LAPPEENRANNAN TEKNILLINEN KORKEAKOULU
LAPPEENRANTA UNIVERSITY OF TECHNOLOGY

TIETEELLISIÄ JULKAISUJA
RESEARCH PAPERS
17

PROCEEDINGS OF THE 4TH FINNISH MECHANICS DAYS

June 5–6, 1991
Lappeenranta, Finland

Edited by Erkki Niemi

LAPPEENRANTA
1991

LAPPEENRANNAN TEKNILLINEN KORKEAKOULU
LAPPEENRANTA UNIVERSITY OF TECHNOLOGY

UDK 621.8
539.2
624

TIETEELLISIÄ JULKAISUJA
RESEARCH PAPERS

17

PROCEEDINGS OF THE 4TH FINNISH MECHANICS DAYS

June 5 - 6, 1991
Lappeenranta, Finland

Edited by Erkki Niemi

Lappeenranta
1991

Scientific Committee

Professor Pekka Neittaanmäki,
University of Jyväskylä

Professor Erkki Niemi (Chairman),
Lappeenranta University of Technology

Senior Assistant Timo Nykänen,
Lappeenranta University of Technology

Professor Matti A. Ranta,
Helsinki University of Technology

Associate Professor Matti Suviolahti,
Lappeenranta University of Technology

Organizing Committee

Associate Professor Heikki Martikka
Professor Erkki Niemi (Chairman)
Senior Assistant Timo Nykänen
Associate Professor Matti Suviolahti
Project Secretary Eija Tauti (Secretary)
Professor Arto Verho

Organizer

Lappeenranta University of Technology
Department of Mechanical Engineering
Centre for Continuing Education

ISBN 951-763-663-6

ISSN 0356-8210

Preface

This volume contains the papers presented at the Fourth Finnish Mechanics Days held in Lappeenranta, Finland, 5 - 6 June 1991. The First Finnish Mechanics Days were held in Oulu in 1982, the Second in Tampere in 1985 and the Third in Otaniemi (Helsinki) in 1988. Although these meetings have traditionally had a national character, five invited quest speakers from Estonia gave the Lappeenranta meeting an international flavour.

The purpose of the Finnish Mechanics Days is to gather researchers and postgraduate students in the field together for stimulating discussions on their research work. The science of mechanics includes a wide range of themes and it is always useful, especially for the younger participants, to gain an understanding of the various problems, and the way common ideas of science can be used to solve them.

The number of papers presented has been steadily growing, which reflects the important role this basic science plays in modern society. The proceedings of the earlier Mechanics Days have been multi-lingual, many papers having been written in Finnish. This time the organisers thought that the use of English throughout the volume would greatly enhance its value as a review of the state-of-the-art of mechanics research in Finland today.

The Organizing Committee wishes to express its sincere gratitude to all authors for their hard and successfull work in preparing contributions.

Erkki Niemi

Contents

Preface

NONLINEAR DEFORMATION WAVES IN SOLIDS WITH APPLICATION IN NONDESTRUCTIVE TESTING 1
Jüri Engelbrecht

ON THE COMPUTER AIDED OPTIMAL STRUCTURAL DESIGN 11
Pekka Neittaanmäki

VIBRATION PROJECT IN HELSINKI UNIVERSITY OF TECHNOLOGY 25
E. Pennala, K. Kantola, E. Porkka, R. Karbasi

Session FINITE ELEMENT METHOD

NUMERICAL HOMOGENIZATION USING THE FINITE ELEMENT METHOD 43
Juha Aliranta, Stig-Göran Sjölind

A FINITE BEAM ELEMENT FOR LAYERED STRUCTURES 49
Matti Leskelä

FINITE ELEMENT DESIGN SENSITIVITY ANALYSIS FOR A CLASS OF NONLINEAR PROBLEMS 55
Raino A. E. Mäkinen

P-ADAPTIVITY APPLIED TO THE SOLUTION OF FIELD AND PLANE STRESS PROBLEMS 63
Seppo Orivuori

A NEW NONCONFORMING FINITE ELEMENT METHOD FOR INCOMPRESSIBLE ELASTICITY 75
Rolf Stenberg, Djebar Baroudi

ON SOME BILINEAR ELEMENTS FOR REISSNER-MINDLIN PLATES 79
Rolf Stenberg, Teemu Vihinen

Session VIBRATIONS

DYNAMICALLY LOADED BEAM ON AN ELASTIC HALF-SPACE 87
Olli Majamäki, Jari Puttonen

RIDE VIBRATIONS OF AN AGRICULTURAL TRACTOR DRIVING ON AN ASPHALT ROAD 95
Mikko Niskanen

EVOLUTION OF NONLINEAR SHEAR WAVES 103
Urmas Valdek

EXPERIMENTAL MODAL ANALYSIS AND COMPARATIVE FEM-ANALYSIS OF A GASTURBINE FOUNDATION PLATE 111
Pentti Varpasuo

CHAOS AND ANOMALOUS CHAOTIC TRANSIENTS OF THE BOUNCING-BALL DYNAMICS 119
Heikki M. Isomäki, Marek Franaszek

Session FLUID FLOW

NON-NEWTONIAN FLUID MODELS IN ELASTOHYDRODYNAMIC LUBRICATION 125
Hannu Iivonen, Bernard J. Hamrock

NUMERICAL CALCULATIONS OF FREE CONVECTION FLOWS IN A TALL VERTICAL CAVITY 133
Tuomas Paloposki, Eero-Matti Salonen

AN APPLICATION OF THE INERTIA FORCE METHOD IN FLUID MECHANICS 143
Eero-Matti Salonen

NUMERICAL SIMULATION OF COMPRESSIBLE FLUID FLOW USING UPWIND METHODS 151
Timo Siikonen

COMPUTER SIMULATION OF INJECTION MOULD FILLING 159
Seppo Syrjälä

Session MARINE TECHNOLOGY

A NONLINEAR ALGORITHM FOR SIMULATING BERTHING OF A SHIP 169
Pekka Hautamäki

INFLUENCE OF DAMPING AND FEEDBACK CONTROL TO DYNAMIC CHARACTERISTICS OF CANTILEVERED PIPES ASPIRATING FLUID 179
Matti Kangaspuoskari, Jari Laukkanen, Antti Pramila

MEASUREMENT AND ANALYSIS OF THERMAL ICE THRUST 187
Mauri Määttänen

Session BUILDING STRUCTURES

AUTOMATIC DESIGN OF STEEL FRAMES IN A CAD-SYSTEM 197
Markku Heinisuo, Arto Möttönen, Tuula Paloniemi, Paavo Nevalainen

STRESSES AND DISPLACEMENTS IN A REINFORCED CONCRETE GROUND SLAB DUE TO THE FRICTION BENEATH THE SLAB 205
Mikko Kilpeläinen

STABILITY OF ARCHED ROOF MADE OF PROFILED STEEL SHEETING 215
Juha Hyvärinen, Pentti Mäkeläinen

Session MATERIAL BEHAVIOUR

INTEGRATED PHOTOELASTICITY OF GLASS 225
H. Aben, S. Idnurm, J. Josepson, K.-J. Kell, A. Puro

DEVELOPMENT OF DEFLECTION AND STRESSES IN WOODEN BEAMS UNDER CYCLIC CHANGES OF SURROUNDING HUMIDITY 233
Antti Hanhijärvi

COMPUTER AIDED MEASUREMENT OF STEEL AND COMPOSITE MACHINE ELEMENTS AND SIMULATION BASED ON MICRO- AND MACROMECHANICS 243
Heikki Martikka, Harri Eskelinen, Raimo Suoranta

THERMOMECHANICAL MODELLING OF WATER SATURATED POROUS MEDIUM 253
Martti Mikkola

DISLOCATION CORE STRUCTURES IN METALS 261
Juhani von Boehm, Risto M. Nieminen

Session BUCKLING

INFLUENCE OF THE FOUNDATION TO THE COMPRESSIVE STRENGTH OF THIN PLATES 267
Paavo Hassinen; TKK

USE OF CURVATURE APPROXIMATION IN AN ANALYSIS OF BEAM AND PLATE BENDING PROBLEMS 277
Reijo Kouhia, Petri Piila

ELASTIC BUCKLING OF THIN-WALLED STRUCTURES USING SPLINE FINITE STRIP METHOD 285
Simo Nikula

SOLUTION OF FLEXURAL-TORSIONAL STABILITY PROBLEM FOR A COLUMN HAVING SINGLY SYMMETRIC OPEN CROSS-SECTION 295
Seppo Salonen, Juha Paavola

Session APPLICATIONS

ON THE OPTIMAL DESIGN OF RIGID-PLASTIC ANNULAR PLATES WITH PIECEWISE CONSTANT THICKNESS 303
Andrus Salupere

OPTIMAL DESIGN OF GEOMETRICALLY NON-LINEAR RIGID-PLASTIC STRUCTURES 311
Jaan Lellep

FLOW CALCULATION IN A PRESSURE-JET HELICOPTER ROTOR BLADE 319
Jukka Mikkonen

AUTOMATED FINITE ELEMENT ANALYSIS OF CRACKED STRUCTURES 327
Timo P. J. Mikkola

FRACTURE ASSESSMENT PROGRAM SYSTEM FOR PRACTICAL ENGINEERING APPLICATIONS 335
Heikki Raiko, Timo P. J. Mikkola

ON FACTORS AFFECTING THE FATIGUE LIFE OF WELDED COMPONENTS USING THE HOT-SPOT APPROACH 343
Teuvo Partanen

ON THE SPRING CONSTANT IN OPEN SECTION JOINTS 351
Timo Björk

Session BASIC PRINCIPLES

A PROGRAM FOR SYSTEMATIC CALCULATION OF DIMENSIONLESS PRODUCTS 361
Jouni Freund, Satu M. Räsänen

USE OF LOCAL RECTANGULAR COORDINATES IN VARIOUS STRUCTURAL ANALYSES 369
Juha Paavola, Eero-Matti Salonen

COMPLEMENTARY WORK, PSEUDOSTRESSENERGY AND STRESSENERGY 377
Pertti Holopainen

NONLINEAR DEFORMATION WAVES IN SOLIDS WITH APPLICATION IN NONDESTRUCTIVE TESTING

JÜRI ENGELBRECHT
Institute of Cybernetics
Estonian Academy of Sciences
Akadeemia tee 21, SU-200108
TALLINN, ESTONIA

ABSTRACT

Nonlinear mathematical models governing the deformation waves in solids are briefly analyzed. The emphasis is put on the evolution equations describing single waves. These equations which are also widely used in other branches of physics give an adequate description of the main physical effects causing the distortion of wave profiles. Such an approach turns out to be useful in nondestructive testing of material properties.

INTRODUCTION

Nonlinearity plays an essential role in most of the physical processes. The widely accepted understanding that linear description is basic and possible nonlinearity leads only to a certain perturbation, has been proved to be erroneous /1/. On the contrary, the world around us is nonlinear and a linear description is just an exception, although it is still widely used for "everyday purpose". Nonlinearity has to be always taken into account in qualitative changes.

In solid mechanics nonlinearity is often related to plasticity and, therefore, the importance of being nonlinear is there perhaps more easily accepted than in other branches of science. Theory of elasticity, however, is mostly used in its linear version based on infinitesimal deformations and the linear Hooke's law. It is interesting to mention that in early days of mechanics many constitutive laws were proposed to connect stress and strain, the Hooke's law being one among others, mostly nonlinear ones. The growing

needs of engineering in the 18th century have picked up the Hooke's law which has led to simple expressions for many practical problems. The fascinating story of this facet of the human thought is given by Bell /2/.

Despite such a traditional "linear thinking", contemporary mechanics of solids accepts nonlinearity as a basic notion /3/. Even more, nonlinear theory of mechanical oscillations has been a cornerstone for contemporary nonlinear dynamics and chaos (see, for example, /4/). The paradigm about the unpredictable behaviour of deterministic, nonlinear dynamical systems has changed our views about the governing laws of Nature. Unpredictability plays an important role not only in physics and related fields, but also in philosophy /1,5/.

This paper covers only one problem in nonlinear solid mechanics, i.e., the propagation of nonlinear deformation waves. The nonlinear theory of elasticity is taken as a basis and the corresponding mathematical models for nonlinear deformation waves are constructed /6/. The physical background is analyzed and the asymptotic evolution equations derived. These equations give a concise but sufficient description of wave processes in solids. Further, the possible application of nonlinear theory in nondestructive testing is briefly described. This description is mostly based on the results obtained in the Institute of Cybernetics, Estonian Academy of Sciences during the last decade.

NONLINEAR MATHEMATICAL MODELS

The conceptual approach in constructing the mathematical models of wave motion is based on the following hierarchical sequence /6/:

- basic principles (initial assumptions and conservation laws);
- constitutive theory (auxiliary postulates which together with conservation laws form a closed system);
- mathematical model (auxiliary assumptions about the character of field variables and approximations of the constitutive equations).

The details of such an approach can also be found in several textbooks /3,7/. Here we shall briefly analyze where and how the nonlinearity comes in.

The first source is of the geometrical character. The strain theory E_{KL} is related to the components of the displacement vector U_K by

$$2E_{KL} = U_{K,L} + U_{L,K} + U_{M,K} \cdot U_{M,L} , \tag{1}$$

where comma denotes the differentation with respect to material coordinates X_L and the summation convention is applied to every repeated index which run over 1,2,3. The nonlinearity in (1) is usually referred to as geometrical nonlinearity. In physical terms it means that the theory of finite deformations is taken into account /3/. Next, the principle of equipresence should be followed which here means that at least all the quadratic terms should be accounted for in other expressions. We see later that there are cases when the accuracy of quadratic terms is not sufficient.

Another important source responsible for nonlinearities is of the physical character and related to the constitutive equation(s). If only the theory of elasticity is taken into account, then we may consider everything to be embedded in the expression of the Helmholtz free energy F

$$\rho_0 F = \frac{1}{2}\lambda I_1^2 + \mu I_2 + \gamma_1 I_1^3 + \gamma_2 I_1 I_2 + \gamma_3 I_3 +$$
$$+ \kappa_1 I_1^4 + \kappa_2 I_1^2 I_2 + \kappa_3 I_1 I_3 + \kappa_4 I_2^2 , \tag{2}$$

where ρ_0 is the initial density; I_1, I_2, I_3 are the algebraic invariants of the deformation tensor (1) and the Greek symbols are used for elastic moduli: λ and μ - the second order or the Lamē moduli, γ_1, γ_2, γ_3 - the third order and κ_1, κ_2, κ_3, κ_4 - the fourth order moduli. For longitudinal waves one should take the third order moduli into account /6,7/, for shear (transverse) waves - both the third and the fourth order moduli /7,8/. In the latter case, the cubic terms appear in governing equations.

In addition to these, some other nonlinearities may arise. For example, the body forces may be of the nonlinear character /9/, the thermal /10/ and viscous /11/ effects may involve new nonlinear terms, etc. The examples of nonlinear mathematical models can be found in several momographs /3,7,12/. As a result, a mathematical model based on the theory of elasticity in the three-dimesnional Cartesian system may be represented as

$$\rho_0 \ddot{U}_N - C_{NKLM} U_{K,LM} = 0 , \tag{3}$$

where $C_{NKLM} = C_{NKLM}(U_{I,J})$ and the dot denotes the differentation with respect to time. The nonlinearities (both geometrical and physical) are put into C_{NKLM}'s. Tn theory of fluids which is usually written in spatial (not material, as (3)) coordinates, additional nonlinearities arise due to con-

vective terms /3/. System (3) must be solved subject to initial and boundary conditions in order to determine the wave field in a solid under inspection.

METHODS OF ANALYSIS

In mathematical terms, system (3) is a quasilinear system of partial differential equations. In many cases, the governing system like (3) may even be more complicated involving more variables (for example, temperature T /10/) and/or integral operators (in the case of relaxing media /11/). The integration of such systems represents a difficult problem of mathematical physics. However, even in the linear case when finite deformations and physical nonlinearities are neglected, the number of exact solutions describing the dependence of the field variables on the initial conditions is rather small. The number of exactly solvable nonlinear problems is certainly much smaller. This is the main reason why approximate methods in wave motion are so intensely developed. Generally speaking, the approximate methods used in the wave propagation theory may be divided into three main groups:

(i) the approximate analysis of the exact solution;
(ii) the perturbative analysis of the solution with small (slow) deviation from a known one;
(iii) the simplification of mathematical models (equations) describing the process.

The description of these methods can be found elsewhere /13/, here we concentrate our attention only on the third group (iii). The methods of this group do not simplify the solutions but rather the equations governing the wave process. The simplifying procedures make use of certain small parameters which may either be present in the initial equations (systems of equations) or result from the process (the solution is close to the stationary one, for example). The best results are achieved when the initial system is simplified into a single equation, first order with respect to time (generally speaking) and of arbitrary order with respect to space coordinates. This equation is called an evolution equation. Physically it means that a wave process is separated into single waves, each of them described by its own equation. The best example of such an evolution equation is the well-

known Korteweg-de Vries equation. Its derivation and history form a brilliant chapter in contemporary mathematical physics /14/. The mathematical details of such simplifying procedures are given, for example, in /13/. It should be noted that the main feature of these procedures is the moving frame in which a certain basic (finite) velocity is taken into account. Here we give some examples of possible nonlinear evolution equations governing nonlinear deformation wave processes in solids.

The dimensionality plays a very important role in deriving and solving the evolution equations. Historically, the one-dimensional (1D) processes were modelled first, involving just one spatial coordinate (say, X_1) of propagation. In some cases (waveguides, spherical or cylindrical processes, etc.) this simplified assumption is quite natural and acceptable without serious doubts, in other cases, however, the assumptions justifying the usage of 1D equations need serious analysis. This way or another, the 1D equations are usually of the following form /6,13,14/:

$$\frac{\partial u}{\partial \tau} \pm u \frac{\partial u}{\partial \xi} + a_0 u + a_1 \frac{\partial u}{\partial \xi} + a_2 \frac{\partial^2 u}{\partial \xi^2} + \ldots = 0 \ , \tag{4}$$

where $\tau = \tau(X_1)$ or $\tau = \tau(t)$ and ξ is the moving frame $\xi = \xi(c_0 t - X_1)$ with $c_0 = \text{const}$. Variable u represents either the deformation gradient or the particle velocity. The nonlinearity is modelled by the second term in (4), the sign of which depends on the signs of higher order moduli. The examples of such equations can be found in /6/.

In two-dimensional (2D) case the situation is more complicated and best results are found for representing equations that model the wave-beams generated by bounded inputs. The 2D evolution equations for longitudinal waves were derived and analyzed in /6,15/ and for shear waves - in /8/. For example, the 2D evolution equation for longitudinal waves is

$$\frac{\partial}{\partial \xi}\left(\frac{\partial u}{\partial \tau} \pm u \frac{\partial u}{\partial \xi} + \ldots\right) = H\left(\frac{\partial^2 u}{\partial \eta^2} + \frac{1}{\eta} \frac{\partial u}{\partial \eta}\right) \tag{5}$$

with $\eta = \eta(X_2)$ and H standing for the so-called diffraction parameter. In physical terms, the r.h.s. of (5) models the slow distortion perpendicular to wave motion in X_1 and in this case the cylindrical symmetry in X_2 is taken into account.

A rather complicated example is given in /16/ for describing the waves in soft tissues, the properties of which can be put somewhere between solids and fluids. The equation is of type (5) involving in the l.h.s. nonlinearity, small-scale inhomogeneity, large-scale inhomogeneity, attenuation in the form of exponential decay and relaxation.

APPLICATIONS

G.Maugin has said /12/: "On certain occasions one wants to benefit from the nonlinearities. On other occasions, one wants to avoid them." What are the main features in wave motion due to nonlinearity? In this paper, attention is paid to basic nonlinearities (geometrical and physical) in the absence of external forces. There is an important point - beside the nonlinearities, other effects of the same order must be taken simultaneously into account and that makes the final mathematical model very complicated. Any combination of viscosity, relaxation, dispersion, temperature, etc. with nonlinearity leads to novel physical conclusions (again in contrast to a linear model of elasticity) /16/.

Generally speaking, the possible features of a nonlinear model in contrast to a linear one are the following:

(i) spectral changes (i.e., changes in wave profiles);
(ii) coupling of waves;
(iii) phase changes;
(iv) interaction with other effects of the same order.

As a consequence, some nice "linear ideas" are lost, including, for example, superposition of solutions and the applicability of integral transform methods.

The spectral changes lead to the generation of higher harmonics and in a certain limit shock waves may be formed causing the stress concentrations. This is an example of a case when nonlinearities should (if possible) be avoided. On the other hand, however, all the changes listed above are informative in a certain sense. If we treat waves as carriers of information as in nondestructive testing (NDT) - then there is a benefit from nonlinearities. Further a brief description of this extremely interesting branch of mechanics is given.

In mathematical terms, the problem of NDT is actually an inverse problem which can be stated as follows: for a given equation (system)

$$L(u) = 0 \tag{6}$$

and for given initial and/or boundary conditions together with a measured variable u at certain τ (or X_1), the unknown coefficients of L(u) must be found. If L(u) is given as system (1), then we come to the inverse problem of the basic system. If L(u) is given as an evolution equation (4) or (5),

then we come to the asymptotic inverse problem /17/.

The asymptotic inverse problem has several advantages compared with the inverse problem of the basic system:

(i) the asymptotic inverse problem is the Cauchy problem being more investigated while the inverse problem of the basic system involves the boundary conditions;

(ii) the solution of an evolution equation corresponds exactly to the experimental technique because as a rule, the receivers (transducers) registrate one certain wave and the space-recording corresponds to the solution of an evolution equation at a certain fixed τ;

(iii) the direct solution of an evolution equation is usually less extensive as compared to the solution of the corresponding basic system.

The accuracy of measurements in the ultrasound region of initial excitations (MHz region) needs digitizing with timelags in the interval of nanoseconds. This is possible using contemporary experimental devices /18/. The information can be extracted from the analysis of a measured pulse that involves:

- changes in spectral amplitudes;
- attenuation due to dissipation;
- decay due to diffraction;
- deformation of the surfaces of equal phase due to dispersion and diffraction, etc.

It is clear that an inverse problem can be ill-posed and the information about the properties of the sample cannot always be uniquely determined. Such an example is the case of a viscoelastic (Voigt model) nonlinear medium. Here we come to the 1D Burgers equation in the dimensionless form /6,7/

$$\frac{\partial u}{\partial \tau} - u \frac{\partial u}{\partial \xi} = \Gamma^{-1} \frac{\partial^2 u}{\partial \xi^2} , \tag{7}$$

where Γ is the acoustic Reynolds number

$$\Gamma = 3|1+m_0| u_0 \tau_c n_0^{-1} . \tag{8}$$

Here m_0 is the dimensionless coefficient of quadratic nonlinearity /6/, u_0 is the maximum amplitude of the initial excitation, τ_c is the wavelength and n_0 is the kinematic viscosity. The structure of Γ shows that in this case the solution of an inverse problem gives a combination of physical parameters and m_0 and n_0 cannot be found separately from one experiment. More-

over, the solution of (8) for large time (distances) shows that the dependence on the initial conditions is lost /19/ while the solution depends only upon the main moment (i.e., energy) of the initial condition. This fact leads to a situation where there is a conditionally well-posed inverse problem only in a certain space of independent coordinates where the dependence on initial conditions still exists.

After showing the difficulties in solving the inverse problems, we still want to stress the importance of such problems in mechanics of solids, in seismology, in biomechanics, etc. The frequency intervals of excitations are different for various problems and various media demanding the different scaling in asymptotic procedures /13/ for deriving the evolution equations. These nonlinear equations form an interesting class of equations which are intensively studied. They give an adequate description of the wave process in a physical sense together with a good correspondence to the experimental techniques. NDT is just one branch of applications where evolution equations enable to enhance the outcome.

ACKNOWLEDGEMENT

The author is grateful to the LOC of the 4th Finnish Symposium on Mechanics for the invitation and travel funds.

REFERENCES

1. West B.J., An Essay on the Importance of Being Nonlinear. Springer, Berlin et al, 1985.

2. Bell J.F., The experimental foundations of solid mechanics. In: Encyclopedia of Physics, vol. VIa/1, ed. by C.Truesdell. Springer, Berlin et al, 1973, 1-778.

3. Eringen A.C., Non-Linear Theory of Continuous Media. McGraw Hill, New York, 1964.

4. Moon F.C., Chaotic Vibrations. Wiley - Interscience, New York et al, 1987.

5. Prigogine I and Stengers I., Order out of Chaos. Heinemann, London, 1984.

6. Engelbrecht J., Nonlinear Wave Processes of Deformation in Solids. Pitman, London, 1983.

7. Bland D.R., Nonlinear Dynamic Elasticity. Blaisdell, Waltham MA, 1969.

8. Valdek U., Evolution of nonlinear plane-polarized transverse waves in a half-space. PhD Thesis, Tallinn Techn. Univ., 1988 (in Russian).

9. Engelbrecht J. and Khamidullin Y., On the possible amplification of nonlinear seismic waves. Phys. Earth Plan. Int., 1988, 50, 39-45.

10. Szekeres A., and Farkas I., Application of the modified law of heat conduction and state equation to dynamical problem of thermoelasticity. Periodica Polytechnica, 1984, 28, 163-170.

11. Ravasoo A., Some remarks on the quasi-linear theory of viscoelasticty. Research Rep. Mech 5/90, Inst. of Cybernetics, 1990 (to appear in Proc. Estonian Acad. Sci., Phys.-Math.).

12. Maugin G.A., Nonlinear Electromechanical Effects and Applications. World Scientific, Singapore, 1985.

13. Engelbrecht J.K., Fridman V.E. and Pelinovski E.N., Nonlinear Evolution Equations. Longman, London, 1988.

14. Miles J.W., The Korteweg-de Vries equation: a historical essay. J. Fluid Mech., 1981, 106, 131-147.

15. Peipman T., Nonlinear wave processes in a medium with dispersion. PhD Thesis, Tallinn Techn. Univ., 1984 (in Russian).

16. Engelbrecht J.K. and Chivers R.C., Evolution equations and ultrasonic wave propagation in biological tissues. Phys.Med.Biol., 1989, 34, 1571-1592.

17. Engelbrecht J., Recent results on nonlinear waves and inverse problems in acoustoelasticity. Atti Accad. Pel. Pericolanti, 1981, 59, 5-23.

18. Bacon D.R., Nonlinear ultrasonic fields: theory and experiment. Proc. Inst. Acoust., 1986, vol. 8, part 2, 39-46.

19. Rudenko O.V. and Soluyan S.I., Theoretical Foundations of Non-Linear Acoustics. Plenum Press, New York, 1977.

ON THE COMPUTER AIDED OPTIMAL STRUCTURAL DESIGN

PEKKA NEITTAANMÄKI

University of Jyväskylä, Department of Mathematics
P.O. Box 35, SF 40351 Jyväskylä, Finland

Abstract. In this paper the problem of optimal structural design is formulated and some practical examples are illustrated. In the second part an overview of the literature of optimal structural design, applications and software is given.

1. INTRODUCTION

The primary problem often facing designers of structural systems is determing the shape of the structure. In spite of graphical work stations and modern software for analyzing the structure, finding the best geometry for the stucture by "trial and error" is still a very tedious and timeconsuming task. The goal in optimal structural design (structural optimization, or redesign) is to computerize the design process and therefore shorten the time it takes to design new products or improve the existing design. Structural optimization is already used in certain applications in the automobile, marine, aerospace industries and in designing truss and shell structures (with minimum weights). In general, however, the structural optimization is just beginning to penetrate the industrial community. The integrated FEM (Finite Element Method) and CAD (Computer Aided Design) technologies within optimization loop will (hopefully quite soon) fully computerize the design loop.

In Fig. 1.1 (a) we see the traditional CAD/FEM–system and in Fig. 1.1 (b) the new generation of CAD/FEM–system.

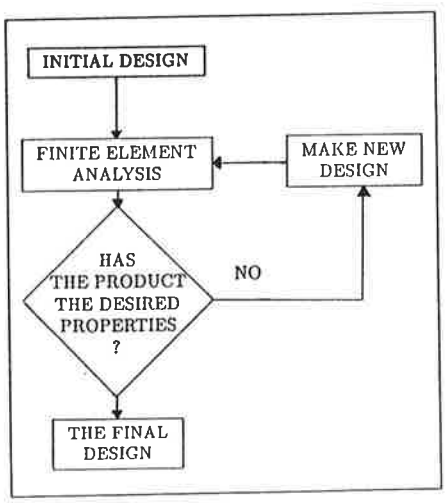

Shape design in traditional CAD system

(a)

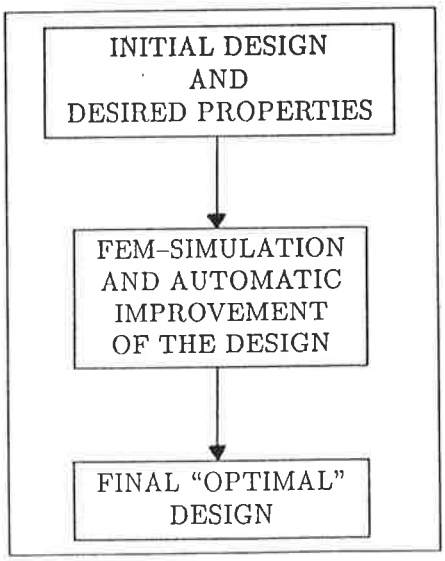

Optimal shape design system

(b)

Figure 1.1.

Parameters chosen to describe the design (geometry) of the system are called design variables. The design parameters can be either finite dimensional (vector) or distributed parameters. Optimal structural design problems can be divided roughly into three classes: domain optimization, optimal sizing and topology optimization.

In domain optimization (or variable boundary optimization) the shape of the domain is sought. Usually the problem is reduced to finding a vector function which defines the unknown boundary. In chapter 2 we shall formulated the domain optimization problem in an abstract setting and give some practical problems which lead to this setting.

In optimal sizing we usually assume that the layout of the structure is given and we try to find optimal sizes of the structural members. The sizes of the members are chosen as the design parameters that can be of a vector or distributed type. Typical examples are optimal sizing of a beam (distributed parameter) or optimal sizing of a frame (vector parameter). The literature of optimal sizing problems is very rich (see **Brandt** (1986), **Gajewski and Zyczkowski** (1987)).

Topology optimization deals with the search of optimal lay-out of the system. For example, design the truss such that the weight of the truss is minimized and the truss can carry a given load without collapsing. On the other hand, in topology optimization, the mechanical body can be considered as a domain in space with a high density of material, that is, the body is described by the global density function that assigns the material to certain areas that are part of the body. Topology optimization problems have an on-off nature and are therefore extremely difficult to solve in the distributed case. For some topology optimization type of problems see **Kohn and Strang** (1986), **Bendsøe and Kichuchi** (1988), **Bendsøe** (1989), **Bendsøe and Rodrigues** (1989).

2. Domain optimization

2.1. Setting of the problem.

Let $\Omega \in \mathcal{O}$ (= set of admissible domains) be a domain for which we want to find an optimal design (an optimal geometrical layout). We suppose that $\mathcal{O}$ is a subset of some larger family $\tilde{\mathcal{O}}$; $\mathcal{O} \subseteq \tilde{\mathcal{O}}$.

With any $\Omega \in \tilde{\mathcal{O}}$ we associate a space $V(\Omega)$ of functions, defined on Ω. In order to handle the situation mathematically, we introduce topologies in $\tilde{\mathcal{O}}$ and in $\{V(\Omega) \mid \Omega \in \tilde{\mathcal{O}}\}$. If Ω_n , $\Omega \in \tilde{\mathcal{O}}$, we have to define what it means that

$$\Omega_n \xrightarrow{\mathcal{O}} \Omega \,. \tag{2.1}$$

Analogously, if $y_n \in V(\Omega_n)$, $y \in V(\Omega)$, Ω_n, $\Omega \in \tilde{\mathcal{O}}$, then we specify the convergence

$$y_n \to y \,. \tag{2.2}$$

Let

$$\Omega \in \mathcal{O} \to y(\Omega) \in V(\Omega) \tag{P}$$

be a mapping which with any domain $\Omega \in \mathcal{O}$ associates the solution of a state problem (given by equations, inequalities etc. in Ω) and let

$$G = \{(\Omega, y(\Omega)) \mid \Omega \in \mathcal{O}\} \tag{2.3}$$

be its graph.

Finally, let $I(\Omega, y)$ with $\Omega \in \mathcal{O}$,and $y \in V(\Omega)$ be a cost function (criterion function), whose restriction on G will be denoted by $J(\Omega)$, i.e.

$$J(\Omega) = I(\Omega, y(\Omega)). \tag{2.4}$$

The *abstract optimal shape design problem* is stated as follows:

$$\textbf{(P)} \qquad \begin{cases} \text{Find } \Omega^* \in \mathcal{O} \text{ such that} \\ J(\Omega^*) \leq J(\Omega) \text{ for all } \Omega \in \mathcal{O}. \end{cases}$$

We will say that $(\Omega^*, y(\Omega^*))$ is an optimal pair for $(\mathbf{P})$.

A large range of important optimal shape design problems which arise in structural mechanics, acoustics, electric fields, fluid flow and other areas of engineering and applied sciences can be formulated. Typically,

$$J(\Omega) = \int_\Omega dx \text{ (minimization of the weight)},$$

$$J(\Omega) = \int_\Omega (y(x))^2\, dx \text{ (minimization of displacements)},$$

$$J(\Omega) = \int_\Omega (\nabla y(x))^2\, dx \text{ (minimization of stresses)},$$

$$J(\Omega) = \int_{\partial\Omega} \frac{\partial}{\partial n} y(x)\, dx \text{ (minimization of contact stresses or boundary flux)}.$$

2.2. Industrial applications.

We shall present a collection of optimal shape design problems which would be interesting as well from an industrial point of view. For the technical background of these problems as well as numerical solution we refer to **Haslinger and Neittaanmäki (1988)**,**Haug and Céa** (1981)and **Pironneau** (1984).

Example 2.1. Maximization of the torsional rigidity of an elastic shaft.

Consider the torsion of the elastic shaft shown in Fig. 2.1.

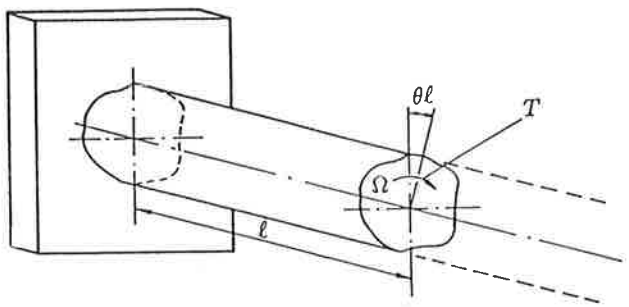

Figure 2.1.

Let Ω denote the cross-section of the shaft. A torque, T, is applied to the shaft at its free end, resulting in a unit angle of twist, θ. From the St Venant theory of torsion, the elastic deformation of the system is governed by the elliptic boundary value problem

$$-\Delta u = 2 \quad \text{in } \Omega \tag{2.5}$$

$$u = 0 \quad \text{on } \partial\Omega \tag{2.6}$$

where u is the Prandtl stress function. The torque–angular deflection relation is given by $T = GR\theta$, where G is the shear modulus of the material of the shaft and R is the torsional rigidity of the shaft given by

$$R(\Omega) = 2\int_{\Omega} u(x)\,dx \ .$$

The problem of optimal shape design of Ω is given by

$$\min_{\Omega\in\mathcal{O}} I(\Omega; u(\Omega)) \ , \tag{2.7}$$

where

$$I(\Omega; u(\Omega)) = -R(\Omega) \ ,$$

$u(\Omega)$ solves (2.5), (2.6) and

$$\mathcal{O} = \{\Omega \subset \mathbf{R}^2 \mid \text{meas}(\Omega) \le A,\ A > 0 \text{ is given and } \Gamma \text{ is Lipschitz}\} \ .$$

Example 2.2. Minimization of the weight of a thermal diffuser.

Consider the problem of finding an optimal shape for a minimum-weight thermal diffuser with *a priori* specifications on the input and output thermal power flux.

We assume that the thermal diffuser has a volume D symmetrical with respect to the z-axis (cf. Fig. 2.2 (a)) whose boundary surface is made up of three regular pieces: the mounting surface Σ_1 (a disc perpendicular to the z-axis with its centre at $(0,0,0)$), the lateral adiabatic surface Σ_2 and the interface Σ_3 between the diffuser and the heatpipe saddle (a disc perpendicular to the z-axis with its centre at $(0,0,L)$).

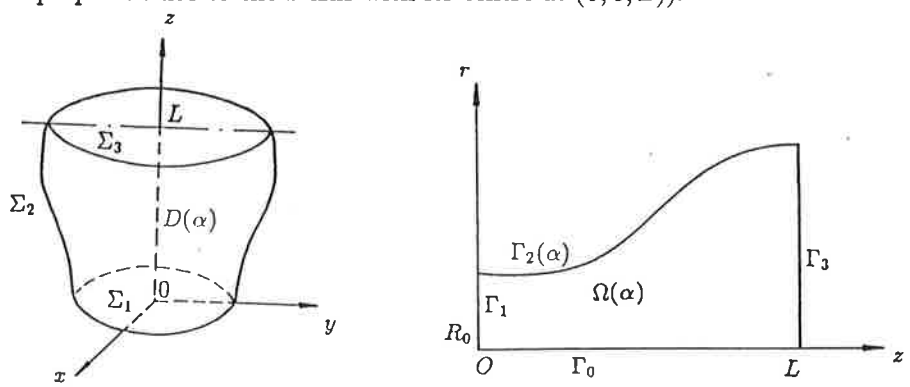

(a) (b)

Figure 2.2.

The temperature distribution over this volume $D(\alpha)$ is the solution of the stationary heat equation

$$\Delta u = 0 \qquad \text{in } D(\alpha) \tag{2.8}$$

with the following boundary conditions on the surface $\Sigma = \Sigma_1 \cup \Sigma_2 \cup \Sigma_3$ (on the boundary of D)

$$\frac{\partial u}{\partial n} = q_{\text{in}} \qquad \text{on } \Sigma_1 \tag{2.9}$$

$$\frac{\partial u}{\partial n} = 0 \qquad \text{on } \Sigma_2 \tag{2.10}$$

$$u = u_3 \qquad \text{on } \Sigma_3,\ u_3 = \text{constant}, \tag{2.11}$$

where $\dfrac{\partial u}{\partial n}$ is the normal derivative on the boundar surface Σ. The parameter q_{in} appearing in (2.9) is the uniform inward thermal power flux at the source (positive constant). The radius R_0 of the mounting surface Σ_1 is fixed so that the boundary surface Σ_1 is fixed in the design problem. Using the axial symmetry of our problem, one can consider the situation in $\mathbf{R}^2$ so that the class of shapes for the diffuser be characterized by a constant $L > 0$ and a positive function $\alpha(z)$, $0 \le z \le L$, with $\alpha(0) = R_0 > 0$. The domain, whose shape we are looking for, is (see Fig. 2.2. (b))

$$\Omega(\alpha) = \{(z,r) \in \mathbf{R}^2 \mid 0 < z < L,\ 0 < r < \alpha(z),\ \alpha \in U_{\text{ad}}\}\ ,$$

where

$$U_{\text{ad}} = \{\alpha \in C^{0,1}([0,L]) \mid \alpha(0) = R_0\}\ .$$

Domain $\Omega(\alpha)$ is bounded by Γ_0, Γ_1, $\Gamma_2(\alpha)$ and Γ_3 (see Fig. 2.2), where

$$\Gamma_2(\alpha) = \{(z,r) \in \mathbf{R}^2 \mid z \in [0,L],\ r = \alpha(z)\}\ .$$

In this case

$$\mathcal{O} = \{\Omega(\alpha) \mid \alpha \in U_{\text{ad}}\}\ .$$

With the assumption that the diffuser is made up of homogeneous material of uniform density (no hollows) the design objective is to minimize the functional of the volume of $\Omega(\alpha)$:

$$J(\alpha) = \pi \int_0^L (\alpha(z))^2\, dz\ ,$$

subject to the constraint on the outward thermal power flux at the interface Γ_3 between the diffuser and the heatpipe saddle:

$$\sup_{(z,r)\in\Gamma_3} -\frac{\partial u}{\partial n}(z,r) \le q_{\text{out}}\ ,$$

where q_{out} is a specified positive constant.

The optimal shape design problem reads

$$(\mathbf{P}) \qquad \begin{cases} \underset{\alpha \in U_{ad}}{\text{Minimize}} \left\{ J(\alpha) = \pi \int_0^L \alpha(z)^2 \, dz \right\} \\ \text{subject to} \quad \sup_{(z,r)\in\Gamma_3} -\dfrac{\partial u(\alpha)(z,r)}{\partial n} \le q_{\text{out}} \ , \end{cases}$$

where $u = u(\alpha)$ is the solution to the state problem

$$\frac{1}{r}\frac{\partial u}{\partial r} + \frac{\partial^2 u}{\partial r^2} + \frac{\partial^2 u}{\partial z^2} = 0 \qquad \text{in } \Omega(\alpha) \tag{2.8'}$$

$$\frac{\partial}{\partial n} u = q_{\text{in}} \qquad \text{on } \Gamma_1 \tag{2.9'}$$

$$\frac{\partial}{\partial n} u = 0 \qquad \text{on } \Gamma_0 \cup \Gamma_2(\alpha) \tag{2.10'}$$

$$u = u_3 \qquad \text{on } \Gamma_3 \ . \tag{2.11'}$$

Example 2.3. Optimization of the shape of the poles of an electromagnet.

This problem is of interest for example in the manufacturing of very large electromagnets and in magnetic tape storage on computers. Fig. 2.3 (a) illustrates the two-dimensional approximation of the physical domain. By symmetry we can restrict the design analysis to one-fourth of the domain only (see Fig. 2.3 (b)). So the domain of interest, Ω, is given by $\Omega =]0, a[\times]0, b[$. It consists of three different subdomains, Ω_F, Ω_C, $\Omega_A = \Omega_{A,i} \cup \Omega_{A,e}$ of *ferric, copper* and *air* materials, respectively. Moreover, we have a subregion $D \subset \Omega_{A,i}$ where constant magnetic field is desired (Fig. 2.3 (a)).

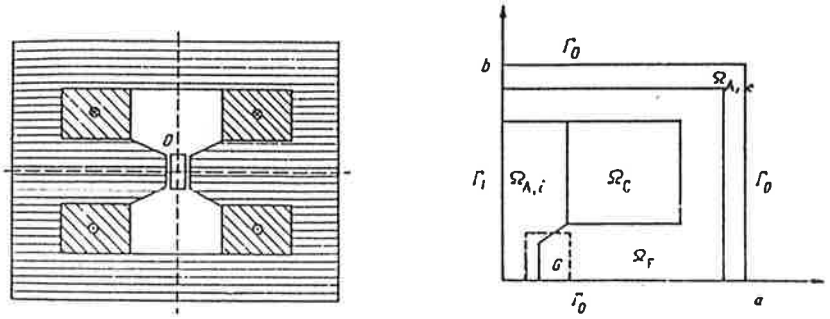

(a) (b)

Figure 2.3.

Our aim is to design a part of the boundary $\partial(\Omega_{A,i} \cap \Omega_F)$ described by a curve γ such that the graph of γ, denoted by $[\gamma]$, lies inside of a given set G (Fig. 2.3 (b)). We can formulate the *shape design problem* as a minimization problem

$$\min_{\Omega_F \in \mathcal{O}} J(\Omega_F) \ , \quad \mathcal{O} = \{\Omega_F \mid [\gamma] \in G\} \ ,$$

where J is the criterion function given by

$$J(\Omega_F) = \int_D |\nabla A - B_d|^2 \, dx \ ,$$

where A is the electromagnetic potential in Ω and B_d is the desire field in the subregion D.

The electromagnetic potential satisfies the non-linear system

$$\nabla \cdot (\nu_r(|\nabla A|^2, x)\nabla A) = \mu_0 j \text{ in } \Omega \ , \quad A = 0 \text{ on } \Gamma_0 \ , \frac{\partial A}{\partial n} = 0 \text{ on } \Gamma_1 \ ,$$

where $\mu_0 = 4\pi \cdot 10^{-7}\text{MKSA}^{-1}$, j is the x_3-component of the current density vector and

$$\nu_r(|\nabla A|^2, x) = \begin{cases} \nu_A = 1 \text{ MKSA for all } x \in \Omega_A \ , \\ \nu_C = 1 \text{ MKSA for all } x \in \Omega_C \ , \\ \nu_F = e + (f - e)\dfrac{|\nabla A|^{2\alpha}}{|\nabla A|^{2\alpha} + g} \text{ MKSA for all } x \in \Omega_F \ . \end{cases}$$

The constants α, e, f and g above can be fixed by experiments. We choose $e = 5 \cdot 10^{-4}$, $f = 0.175775$, $g = 8758.756$ and $\alpha = 5.419241$.

Example 2.4. Optimization of the header in paper machine.

A header is that part of paper machines, which has to deliver flow coming from pump to number of small pipes as uniformly as possible (Figure 2.4.). It has been quite difficult to design the header just trying different kind of geometries and velocities.

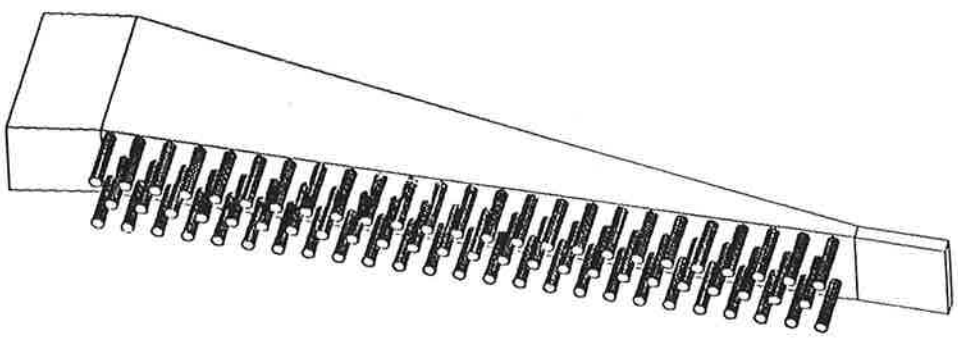

Figure 2.4.

Flowrates in the pipes are effected by controlling recirculation and by changing the shape of the header. To the cost function is chosen the meandistribution of velocities at the end of the pipes. The flow can be modelled by the Navier-Stokes equations.

The design variables are the angle of inflow, the shape of the back wall, the shape of the pipes and recirculation. The shape of the header is assumed to be piecewise linear. When recirculation is changed, we also change velocity of inflow so that the mean value of velocities is constant.

2.3. Remarks on the other applications.

To close this chapter, here we shall mention some more practical applications of optimal shape design. For the marine industry and design of submerged bodies in naval hydrodynamics and related topics see **Bushnell** (1987a, 1987b), **Hughes** (1983, 1986), **Pedersen and Nielsen** (1987), **Angell, Hsiao and Kleinman** (1986) and **Souli** (1988), for antenna structures and flexible structures see **Eschenauer** (1982, 1988), **Bendsøe** (1988) and **Bendsøe, Olhoff and Taylor** (1986); on automobile design see **Bennett and Botkin** (1981); on design problems in the aerospace industry and related topics see **Arumugam and Pironneau** (1988 a,b), **Esping** (1985), **Esping and Holm**, (1988), **Fernandes** (1988), Rosengren (1986), **Wellen and Bartholomew** (1987) and **Wu and Wu** (1987).

For the design of thermal diffusers for communication satellites see **Delfour, Payre and Zolésio** (1986,1987) and of electromagnets see **Pironneau** (1984), **Börner** (1985), **Arumugam, Neittaanmäki and Salmenjoki** (1988).

Optimal shape design in elasticity, plasticity and contact problems have been handled in **Haslinger and Neittaanmäki** (1988). For biomechanical applications see **Hart, Davy and Heiple** (1984) and for interesting examples see articles by **Babuška** (1986), **Stadler** (1988a) and **Velte and Villaggio** (1982).

There is a rapidly increasing research activity on composite materials, for which see **Bushnell** (1987a), **Kohn and Strang** (1986) and **Eschenauer and Fuchs** (1987). This field lies between the interrelation of structural design optimization, the relaxation of variational problems and homogenization.

3. Concluding remarks on the literature on optimal shape design and related topics

3.1. Survey articles, conference proceedings and textbooks.

Problems of optimum structural design have been formulated and solved by numerous authors for several decades. Studies and solutions published up to the early 20th century, now only of historical interest, are not included in our reference list. They are listed in **Brandt** (1986).

In the book edited by **Brandt** (1986) the authors present a fairly complete list of publications (more than 2100 references up to the year 1980) in the field of structural optimization written mainly from the engineering point of view. More precisely, the list was meant to cover all publications dealing with the fundamental problems of optimization and with the optimum design of building and civil engineering structures (optimization of beams, plates, trusses, columns, arches, frames, shells, hanging structures and lattices, etc.). The bibliography contains relatively few references to modern mathematical treatments of the problems in question.

The book by **Gajewski and Zyczkowski** (1987) is devoted to optimal structural design under stability constraints. Particular attention has been paid to the provision

of a comprehensive list of references (including over 2000 entries) with special emphasis on optimal structural design involving stability constraints.

Comprehensive general reviews of the field of optimal structural design have been published by **Niordson and Pedersen** (1973), **Venkayya** (1978), **Haug** (1981), **Schmit** (1981), **Qian** (1982), **Sheu and Prager** (1968) and by **Haftka and Gandhi** (1986). Conference proceedings edited by **Haug and Céa** (1981), **Lev** (1981) and **Atrek, Gallagher, Ragsdell and Zienkiewicz** (1984) include several survey articles. The conference proceedings edited by **Mota Soares** (1987) also includes among others survey articles on optimal shape design, **Taylor** (1987) deals with distributed parameter optimal structural design problems and their basic formulations and applications, **Olhoff** (1987) considers variational methods in structural optimization and **Mota Soares, Leal and Choi** (1987) consider the boundary element method in the optimal design of structural components. The article by **Papalambros** (1987) contains an outline of knowledge-based systems in optimal design. In the article by **Hörnlein** (1987) the features of about 30 internationally-used software systems for structural design are listed.

There are several monographs on optimal shape or optimal structural design. For those written mainly from the engineering point of view see **Arora** (1989), **Banichuk** (1983), **Bremicker** (1989), **Cyras** (1983), **Farkas** (1984), **Gajewski and Zyczkowski** (1987), **Grinev and Filippov** (1979), **Haftka and Kamat** (1985), **Haslinger and Neittaanmäki** (1988) **Hemp** (1973), **Haug and Arora** (1979) **Lawo** (1986), **Lepik** (1982), **Malkov and Ugodchikov** (1981), **Papalambros** (1988), **Prager** (1974), **Rozvany** (1976, 1987), **Save and Prager** (1985), **Troitskij and Petuchov** (1982), **Vanderplaats** (1984), and, more from the mathematical point of view, monographs by **Haug and Arora** (1979), **Haug, Choi and Komkov** (1986), **Komkov** (1988), **Pironneau** (1984) and **Sokolowski and Zolésio** (1991).

3.2. On software for computed aided structural design.

There are several general purpose CAD and FEM software packages which already include initial modules for linking shape optimization to the design procedure as in **Beckers, Braibant and Fleury** (1985). In **Haftka and Kamat** (1985) a brief survey of packages (developed mainly in the 1970s) for structural optimization is given in Chapter 8.6. In **Hörnlein** (1987) the features of about 30 internationally-used program systems for structural optimization are listed.

We shall close this chapter with a short (and inevitably very incomplete) list of software for optimal structural design. These programs have either been developed from the application-oriented point of view (automobile, marine, aircraft, air space industry etc.) or have been supplemented by optimization modules for multipurpose CAD/FEM program packages. For the latter group of software packages, see the optimization modules of ADINA (**Haririan, Cardoso and Arora** (1987)), ANSYS (**Swanson and Marx** (1985)) and NASTRAN. Integrated packages also include STARS (**Bartholomew and Morris** (1984), **Wellen and Bartholomew** (1987)).

For programs developed especially for design optimization we mention only the following products:

AXIOPT (**Trompette and Marcelin** (1987))
DESAP (**Kiusaalas and Reddy** (1977a, 1977b))
LAGRANGE (**Schittkowski** (1985))
MAESTRO (**Hughes** (1986))
OASIS (**Esping** (1985), **Esping and Holm** (1988))

ODYSSEY (**Bennet and Botkin** (1981))
OPTISEN (**Ward, Patel, Wakeling and Weeks** (1987))
OPTSYS (**Bråmå** (1987), **Rosengren** (1986))
PANDA (**Bushnell** (1987a, 1987b))
PROSS (**Sobieszczanski-Sobieski and Bhat** (1981)).

For more details about program pagages for optimal structural design see **Hörnlein** (1987).

References

Angell, T.S., Hsiao, C.G. and Kleinman, R.E. (1986), *An optimal design problem for submerged bodies*, Math. Meth. Appl. Sci. **8**, 50–76.

Arora, J. (1989), "Introduction to Optimum Design," McGraw-Hill, New York.

Arumugam, G., Neittaanmäki, P. and Salmenjoki, K. (1988), *Sensitivity analysis for the design of an electromagnet*, University of Jyväskylä, Preprint 75.

Arumugam, G. and Pironneau, O. (1988a), *Towards a multipurpose optimal shape design computer code*, in **Zolésio** (1988), pp. 1–17.

Arumugam, G. and Pironneau, O. (1988b), *On the feasibility of riblets for airplanes*, in "System Modelling and Information Science," Lecture Notes in Control and Information Sciences, Springer-Verlag, Berlin.

Atrek, E., Gallagher, R.H., Ragsdell, K.M. and Zienkiewicz, O.C. (eds.) (1984), "New Directions in Optimum Structural Design," John Wiley & Sons, Chichester.

Babuška, I. (1986), *Uncertainties in engineering design: Mathematical theory and numerical experiences*, in **Bennett and Botkin** (1986).

Banichuk, N.V. (1983), "Problems and Methods of Optimal Structural Design," Plenum Press, New York.

Bartholomew, P. and Morris, A.J. (1984), *STARS: A Software Package for Structural Optimization*, in **Atrek, Gallager, Ragsdell and Zienkiewicz** (1984), pp. 617–632.

Beckers, P., Braibant, V. and Fleury, C. (1985), *Shape optimal design – an approach matching CAD and optimization consepts*, in "Optimization in Computer-Aided Design," (ed. J.S. Gero), Elsevier Science Publishers (North-Holland), Amsterdam.

Bendsøe, M.P. (1989), *Shape design as a material distribution problem*, Mat. Report, No. 11 (1989), Danmarks Technishe Højskola.

Bendsøe, M.P. and Kichucki, N. (1988), *Generating optimal topologies in structural design using a homogenization method*, Comput. Methods Appl. Mech. Eng. **71**, 197–224.

Bendsøe, M.P., Olhoff, N. and Taylor, J.E. (1986), *On the design of structure and controls for optimal performance of actively controlled flexible structures*, Mat–Report no. 1986-12, Matematisk Institut, Danmarks Tekniske Højskole.

Bendsøe, M.P. and Rodrigues, H.C. (1989), *Integrated topology and boundary shape optimization of 2–D solids*, Mat. Report No 14 (1989), Mat. Inst. Danmarks Teknishe Højskola.

Bennett, J.A. and Botkin, M.E. (1981), *Automated design for automotive structures*, ASME, New York, 81–DET–91.

Bennet, J.A. and Botkin, M.E. (Eds.) (1986), "The Optimum Shape: Automated Structural Design," Plenum Press, New York.

Bermudez, A. (Ed.) (1988), "Optimal Control of Systems Governed by Partial Differential Equations," Proc. of IFIP Workshop on Optimal Control, Lecture Notes in Control and Information Sciences, Springer Verlag, Berlin.

Brandt, A.M. (1986), "Criteria and Methods of Structural Optimization," Martinus Nijhoff Publishers, Dordrecht.

Bremicker, M., "Dekompositionsstrategie in Anwendung auf Probleme der Gestaltsoptimierung," VDI Verlag, 1989.

Bråmå, T. (1987), *Weight optimization of aircraft structures. OPTSYS – a system for structural optimization*, SAAB Aircraft Division Report TKH R-3512, Linköping.

Bushnell, D. (1987a), *PANDA2 – program for minimum weight design of stiffened, composite, locally lucled panels*, Comput. Struct. **25**, 469–605.

Bushnell, D. (1987b), *Theoretical basis of the PANDA computer program for preliminary design of stiffened panels under combined in-plane loads*, Comput. Struct. **27**, 541–563.

Börner, A.D. (1985), "Mathematische Modelle fur Optimum Shape Design Probleme in der Magnetostatik," Dissertation, Universität Hamburg.

Cyras, A.A. (1983), "Mathematical Models for the Analysis and Optimization of Elastoplastic Systems," Ellis Horwood, Chichester.

Daněk, V. and Mäkinen, R. (1990), *Optimal design for transonic flows*, in "**P. Neittaanmäki** (1990,b)."

Delfour, M., Payre, G. and Zolésio, J.P. (1986), *Optimal parametrized design of thermal diffusers for communication satellites*, Optimal Control Appli. Meth. **7**, 163–184.

Delfour, M.C., Payre, G. and Zolésio, J.P. (1987), *Approximation of nonlinear problems associated with radiating bodies in space*, SIAM Numer. Anal. **24**, 1077–1094.

Eschenauer, H. (1982), *Vector optimization in structural design and its application on antenna structures*, in **Eschenauer and Olhoff** (1983), pp. 146–155.

Eschenauer, H. (1988), *Multicriteria optimization techniques for highly accurate focusing systems*, in **Stadler** (1988), pp. 309–354.

Eschenauer, H. and Fuchs, W. (1987), *Modelling, structural analysis, and optimization of composite structures*, Z. Flugwiss. Weltraumforsch. **11**, 201–210.

Eschenauer, H. and Olhoff, N. (Eds.) (1983), "Optimization Methods in Structural Design," Euromech-Colloquium 164, Bibliographisches Institut, Mannheim.

Esping, B. (1985), *The OASIS structural optimization system*, Report 85–3, Dept. of Aeronautical Structures and Materials, The Royal Institute of Technology, Stockholm.

Esping, B. and Holm. D. (1988), *Structural shape optimization using OASIS*, in "IUTAM Symbosium on Structural Optimization," Melbourne, Feb. 88.

Farkas, J. (1984), "Optimum design of metal structures," Ellis Horwood, Chichester.

Fernandes, C.E. (1988), *Optimum design in fluid mechanics: the finite element approach*, in **Bermudez** (1988).

Gajewski, A. and Zyczkowski, M. (1987), "Optimal Structural Design under Stability Constraints," Martinus Nijhoff Publishers, Dordrecht.

Grinev, W.B. and Filippov, A.P. (1979), "Optimization of Beams Governed by Eigenvalue Problems," (in Russian), Naukova Dumka, Kiev.

Haftka, R.T. and Gandhi, R.V. (1986), *Structural shape optimization*, A survey, Comput. Meths. Appl. Mech. Eng. **57**, 91–106.

Haftka, R. and Kamat, M. (1985), "Elements of Structural Optimization," Martinus Nijhoff, Dordrecht, Netherlands.

Haririan, M., Gardoso, J.B. and Arora, J.S. (1987), *Use of ADINA for design optimization of nonlinear structures.*

Hart, R.T., Davy, D.T. and Heiple, K.G. (1984), *A computational method for stress analysis of adaptive elastic materials with a view toward applications in straininducted bone remodeling*, ASME J. Biomechanical Engineering **106**, 342–350.

Haslinger, J. and P. Neittaanmäki (1988), "Finite element approximation of optimal shape design. Theory and applications," J. Wiley & Sons.

Haug, E.J. (1981), *A review of distributed parameter structural optimization literature*, in **Haug and Céa** (1981), Part I, pp. 3–74.

Haug, E.J. and Arora, J.S. (1979), "Applied Optimal Design, Mechanical and Structural Systems," J. Wiley & Sons, New York.

Haug, E.J. and Céa, J. (eds.) (1981), "Optimization of Distributed Parameter Structures," Parts I & II. Nato Advances Study Institute Series, Series E, Sijthoff & Noordhoff, Alphen aan den Rijn.

Haug, E.J., Choi, K.K. and Komkov, V. (1986), "Design Sensitivity Analysis of Structural Systems," Academic Press, Orlando.

Hemp, W.S. (1973), "Optimum Structures," Clarendon, Oxford.

Hughes, O. (1983), "Ship Structural Design," John Wiley Intersciences, New York.

Hughes, O. (1986), *Computer aided optimum structural design of tension leg platfors*, in "Proc. of CADMO 86: Int. Conf. on Computer Aided Design, Manufacture and Operation in the Marine and Offshare Industries," (Washington, 16.–19. Sep. 1986).

Hörnlein, H.R.E.H. (1987), *Take-off in optimal structural design*, in **Mota Soares** (1987), pp. 901–919.

Kiusaalas, J. and Reddy, G.B. (1977a), "DESAP1 - A Structural Design Program with Stress and Displacement Constraints," Vol I: Theoretical and User's Manual. Vol II: Sample Problems. NASA CR-2797, NASA CR-2798.

Kiusaalas, J. and Reddy, G.B. (1977b), "DESAP2 - A Structural Design Program with Stress and Buckling Constraints," Vol I: Theoretical and User's Manual. Vol II: Sample Problems. NASA CR-2794, NASA CR-2795.

Kohn, R.V. and Strang, G. (1986), *Optimal design and relaxation of variational problems*, Comm. Pure and Appl. Math. **XXXIX**, Part I 113–137, Part II 139–182, Part III 353–378.

Komkov, V. (1988), "Variational Principles of Continuum Mechanics with Engineering Applications, Vol 2, Introduction to Optimal Design Theory," D. Reidel Publ. Company, Dordrecht.

Lawo, M. (1986), "Optimum Structural Design," (in German), Vielveg, Braunschweig.

Lepik, U. (1982), "Optimal Design of Inelastic Structurs Under Dynamic Loading," (in Russian; extended summary in English), Walgus, Tallinn.

Lev, O.E. (ed.) (1981), "Structural Optimization, Recent Developments and Applications," American Society of Civil Engineers, New York, USA.

Malkov, V. and Ugodchikov, A.G. (1981), "Optimization of Elastic Systems," Nauka, Moskva.

Mota Soares, C.A. (ed.) (1987), "Computer Aided Optimal Design: Structural and Mechanical Systems," NATO ASI Series F, Vol 27, Springer-Verlag, Berlin.

Mota Soares, C.A., Leal, R.P. and Choi, K.K. (1987), *Boundary elements in shape optimal design of structural components*, in **Mota Soares** (1987), pp. 605–632.

Neittaanmäki, P. (Ed.) (1990), "Numerical Methods for Free Boundary Problems," Proc. of the Conference on Numerical methods for free boundary problems, Jyväskylä, July 23–27, 1990, ISNM, Birkhäuser, Basel.

Niordson, F.I. and Pedersen, P. (1973), *A review of optimal structural eigenvalues*, in "Proc. 13th Int. Cong. Th. Appl. Mech., Moscow 1972," (eds. E. Becker and G.K. Mikhailov), Springer-Verlag, Berlin, pp. 264–278.

Olhoff, N. (1987), *Structural optimization by variational methods*, in **Mota Soares** (1987), pp. 87–164.

Papalambros, P. (1987), *Knowledge based systems in optimal design*, in **Mota Soares** (1987), pp. 759–804.

Papalambros, P. (1988), *Principles of optimal design: modeling and computation*, Cambridge University Press.

Pedersen, P.T. and Nielsen, N.J.R. (1987), *Structural optimization of ship structures*, in **Mota Soares** (1987), pp. 921–941.

Pironneau, O. (1984), "Optimal Shape Design for Elliptic Systems," Springer series in Computational Physics, Springer-Verlag, New York.

Prager, W. (1974), "Introduction to Structural Optimization," Int. Centre for Mech. Udine, No. 212, Springer-Verlag, Vienna.

Qian, L. (1982), *Structural optimization research in China*, in "Proc. Int. Conf. Finite Element Methods, Shanghai, China," pp. 16–24.

Rosengren, R. (1986), *Shape optimization of solid structures in OPTSYS*, SAAB Aircraft Division Report TKH R–3492, Linköping.

Rozvany, I.N. (1976), "Optimal Design of Flexural Systems," Pergamon, Oxford. Russian version: Strojizdat, Moscow (1980).

Rozvany, I.N. (1987), "Structural Design via Optimality Criteria," Martinus Nijhoff Publishers, Dordrecht.

Save, M. and Prager, W. (1985), "Structural Optimization – Vol. 1, Optimality Criteria," Plenum Press, New York-London.

Schittkowski, K. (Ed.) (1985), "Computational Mathematical Programming," NATO ASI Series F, Vol 15, Springer-Verlag, Berlin.

Schmit, L.A. (1981), *Structural synthesis – its genesis and development*, AIAA Journal **19**, 1249–1263.

Sheu, C.Y. and Prager, W. (1968), *Recent developments in optimal structural design*, Appl. Mech. Rev. **21**, 985–992.

Sobieszczanski-Sobieski, J. and Bhat, R.B. (1981), *Adaptable structural synthesis using advanced analysis and optimization coupled by a computer operating system*, J. Aircraft **18**, 142–149.

Sokolowski, J. and Zolésio, J.P. (1991), "Introduction to Shape Optimization, Shape Sensitivity Analysis," Springer Verlag, to appear.

Souli, M. (1988), *Shape Newton method in naval hydrodynamic*, in **Zolésio** (1988), pp. 286–259.

Stadler W. (1988a), *Natural structural shapes (a unified optimal design philopsophy)*, in **Stadler** (1988b), 355–390.

Stadler W. (1988b), "Multicriteria Optimization in Engineering and in the Sciences," Mathematical Concepts and Methods in Sciences and Engineering 37, Plenum Press, New York.

Swanson, J.A. and Marx, F.J. (1985), "Design Optimization Including Solid Modeling Using the Finite Element Program ANSYS," Swanson Analysis Systems, Inc.

Taylor, J.E. (1987), *Distributed parameter optimal structural design: some basic problem formulations and their applications*, in **Mota Soares** (1987), pp. 3–85.

Troitskij, W.A. and Petuchov, L.W. (1982), "Optimal Design of Elastic Bodies," (in Russian), Nauka, Moscow.

Trompette, Ph. and Marcelin, J.L. (1987), *On the choice of objectives in shape optimization*, Eng. Opt. **11**, 89–102.

Vanderplaats, G.N. (1984), "Numerical Optimization Techniques for Engineering Design with Applications," McGraw-Hill Ser. in Engn., McGraw-Hill, New York.

Velte, W. and Villaggio, P. (1982), *Are the optimum problems in structural design well posed?*, Arch. Rat. Mech. Anal. **78**, 199–211.

Venkayya, V.B. (1978), *Structural optimization: a review and some recommendations*, Int. J. Num. Meth. Eng. **13**, 205–228.

Ward, P., Patel, D., Wakeling, A. and Weeks, R. (1987), *Applications of structural optimization using finite elements*, in **Mota Soares** (1987), pp. 1003–1013.

Wellen, J.H. and Bartholomew (1987), *Structural optimization in aircraft construction*, in **Mota Soares** (1987), pp. 955–970.

Wu, J.Z. and Wu J.M. (1987), *A new theoretical basis for optimal aerodynamic design by wind-tunnel-computer integration*, in "Proc. of Second International Conference on Inverse Design Consepts and Optimization in Engineering Sciences," (ed. G.S. Dulikrawich), pp. 167–186.

Zolésio, J.P. (Ed.) (1988), "Boundary Control and Boundary Variations," Lecture Notes in Control and Information Sciences 100, Springer Verlag.

VIBRATION PROJECT IN HELSINKI UNIVERSITY OF TECHNOLOGY

E. PENNALA K. KANTOLA E. PORKKA R. KARBASI
The Laboratory of Strength of Materials
Faculty of Mechanical Engineering
Helsinki University of Technology
Puumiehenkuja 5 A, SF-02150 ESPOO, FINLAND

ABSTRACT

The Laboratory of Strength of Materials started in 1986 a research project concerning experimental vibration analysis and especially modal analysis. Until now, the research has concentrated on getting experience of measuring complicated structures, like aircraft, and developing a computer program appropriate to modal analysis. In the future the main research areas will be in estimation techniques and in linking analytical with experimental modal model. In this paper the research work and program development work done will be described.

In experimental modal analysis the application of multiple excitation force and measuring of multiple response functions became popular during the last decade. The application of multiple input force results in a more uniform excitation energy distribution and hence more accurate and consistent measured data can be obtained. In the 1980's several multiple input modal parameter estimation methods were developed to take advantage of the new excitation method. These parameter estimation methods use frequency response data due to multiple input force simultaneously to estimate global modal parameters. The characteristics, advantages and limitations of time and frequency domain implementations of these methods will be discussed briefly.

Linking the mathematical model with the experimental model has turned out to be necessary in some practical situations, for instance, when measurements can not be done with desired boundary conditions; ground vibration test of an aircraft is an example of that. On the other hand the mathematical model is flexible when predicting the effects of structural modifications. The paper discusses linking in general, its necessity, applications and problems arising from inaccuracies in the experimental and mathematical models. The methods based on manipulation of system matrices seem to be worth future research.

INTRODUCTION

Vibration behavior may be determined mathematically or experimentally. Experimental analysis is required in order to find out actual modal parameters and mode shapes and to update a mathematical model to represent the actual behavior. In cooperation with the Finnish Air Force, The Laboratory of Strength of Materials started in 1986 a research project concerning experimental vibration analysis

and especially modal analysis. The project was established due to Air Force's need to know vibration behavior of aircraft for flutter analysis. This offered a fascinating possibility for Helsinki University of Technology (HUT) to get advanced equipment for research and education. As a whole HUT was an ideal location for the project as the subsequent flutter analysis is also done in another laboratory of HUT. When choosing location for equipment the need to get good contact with students and young researchers and the possibility to perform research for industry was taken into account. The equipment consists of 16-channel Computer-Aided Testing system (GenRad 2515), minicomputer MicroVAX II, three electromagnetic shakers and instrumentation needed for response measurements.

Until now, the research has concentrated on getting experience of measuring complicated structures, like aircraft, and developing a computer program appropriate to modal analysis. During the existence of the project several vibration analyses for aircraft have been done. Also, many different structures and miscellaneous components have been analyzed for industry. The vibration research facility has been exploited in education, two Master's Thesis have been done and one post graduate work is being made.

In the future the main research areas will be in estimation techniques and in linking mathematical with experimental modal model. In this paper the research and program developing work done will be described.

Figure 1 presents the whole analysis process for aircraft. At first the experimental modal model is created by means of modal analysis. The second phase consists of updating Finite Element Model (FEM) through experimental modal model. All subsequent manipulations, like flutter analysis and estimating the effects of structural modifications will be approximated using FE-model.

In experimental modal analysis the application of multiple excitation forces and measuring of

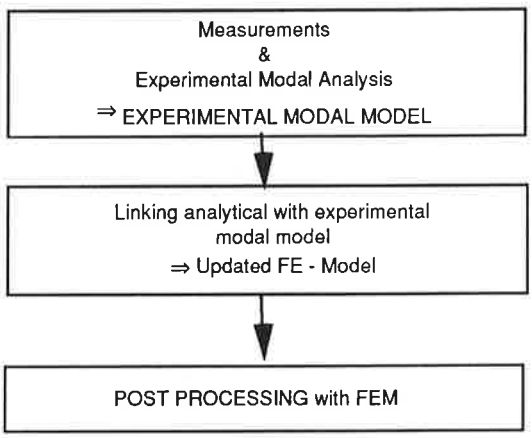

FIGURE 1. A dynamic analysis process for aircraft.

multiple response functions simultaneously became very popular during the last decade. The application of multiple input forces yields more uniform excitation energy distribution to the structure and hence higher quality and more consistent measured data. One extreme advantage of multi-input excitation methods over single input excitation techniques is, that identification of repeated modes is possible. As the modal parameters are global properties of a structure (they do not depend on a measurement location), estimation methods which are able to analyze numerous response functions due to several input forces simultaneously are needed. In the 1980's several such global parameter estimation techniques (eg. time and frequency domain polyreference techniques) have been introduced. The time domain polyreference technique has been our main tool in the estimation of modal parameters. It has also been implemented to self-made computer code, which will be discussed later in this paper.

Updating FE-model through experimental model has turned out to be necessary in many practical situations, for instance, when measurements can not be done with desired boundary conditions; ground vibration test of aircraft is an example of that. On the other hand the mathematical model is very flexible and does not require as much knowledge as using experimental modal model directly when predicting the influence of structural modifications. FE-model is very effective especially when the modifications are relatively small and/or if plenty of different modifications should be investigated. The modification of input file for FE analysis is very simple and the results after modifications will be got fast. In case of large modifications, FEM is not reliable for complicated structures anymore, as there are always inaccuracies present in mathematical models. In such cases the only alternative is to make new measurements and a new experimental model and study if the modifications have yielded desired results.

Trial-and-error method has been the most widely used updating method so far, but nowadays more advanced methods and methods, which require less user interaction have been developed. Linking of models are discussed in greater detail elsewhere in this paper.

Computer programs

There are plenty of commercial computer programs for experimental modal analysis and FE analysis, but only a few codes for linking FE-model with experimental model. Although commercial codes are available, in the Laboratory of Strength of Materials computer programs have been developed for experimental and FE-model creation. This is because commercial programs are generally 'black boxes' which can not be modified or extended by a user. In many cases a client is bound to one software house, because the programs of different software houses do not generally support the same file formats and thus the data transfer between the programs is complicated or impossible. One important aspect was to get more knowledge about the latest methods and deeper insight to the mathematical problems involved in algorithms.

MODALS is an advanced modal analysis software package, which supports most of the features needed in modal analysis and in linking of models, like

- modal parameter estimation,
- modal model validation,
- graphics for function and structural display,
- general function (or block) arithmetics,
- window to other programs,
- tools for combining FE- and modal models,
- programming capability,
- On-Line Help.

MODALS is command language driven and it consists of approximately 100,000 lines of FORTRAN code. MODALS does not support data acquisition, for which a commercial program MODAL-PLUS (by Structural Dynamics Research Corporation, SDRC) is used. The current version of MODALS supports MODAL-PLUS binary file formats and SDRC Universal file formats, but it is easy to add new formats into the code.

In practical analysis the two most important features required of analysis program are, that it is able to handle a large number of modes and wide frequency bandwidth simultaneously. This is because it decreases analysis time notably. MODALS is able to analyze the total analysis band at the same time with maximum of 128 modes. Some theory behind MODALS will be discussed below.

Basic problems present when creating an analysis program may be divided into the following two categories:

1. problems concerning estimation methods and
2. problems how to reduce user interaction.

Problems concerning estimation techniques are on the one hand performance of the method itself, on the other hand mathematical. In most cases a method which is able to analyze the whole frequency band at the same time, without being forced to divide the bandwidth into pieces, is preferable. Frequency domain estimation methods yield typically very ill-conditioned equations, if the frequency range is wide, and thus they are more suitable for narrow bandwidth analysis. Polyreference time domain technique does not have this disadvantage, which is the reason why it has been installed in MODALS. The method should also be able to handle a large number of modes, which also causes numerical difficulties. During the measurement phase, the resolution of the A/D-converter used in data acquisition and selected input range determine the accuracy of measured data. Although the accuracy of measured data is much lower than that used in calculations, the computation accuracy and the algorithms have a remarkable influence on the results. Mathematical problems may be decreased by using stable mathematical routines. In MODALS implementation orthogonal decomposition like QR and Singular Value Decomposition have been used for solving linear equations and eigenvalue problems instead of elementary decomposition (Gaussian elimination). The roots of a

polynomial are solved using companion matrix approach instead of normal polynomial root solvers. Although the residue (mode shape) calculation is mathematically straightforward and stable, it is sometimes difficult to get valid values because of modes present outside the analysis frequency range. It is possible to estimate the effects of out-of-range modes if the residues are calculated in frequency domain, that is not possible in time domain estimation. Thus, in MODALS implementation the residues are calculated in frequency domain.

All estimation techniques which use a wide frequency band generate more roots (natural frequencies and damping values) than are really present in the system. So some of the estimated roots are computational, which should be separated from physical roots. This needs very much interaction between the user and the program and for complicated structures it is normally the most time consuming phase in modal analysis. There is nowadays a couple of methods for detecting computational modes, but none of them is 'fool-proof'. We have investigated this problem quite a lot, but it is still unsolved. In MODALS implementation, a self-developed criterion based on how well the characteristic polynomial is satisfied, is used. This criterion works completely for analytical data (all computational modes will be found), but generally for real data app. only one half of the computational modes is found. This is due to the fact that measurement errors, nonlinearities etc. bluff the algorithm to think that the mode is physical. We are sure that much can be done in this field and thus the developing of a better method is one of the main research areas of the project now.

The FE analysis is performed with Finite Element solver FESAP, which is based on SAP IV [1]. The original code has been modified very widely and plenty of new features have been added to the program. The current version contains app. 21000 lines of FORTRAN code.

FESAP supports many special features useful in the linking process. The natural frequencies and mode shapes are calculated directly without a transformation of the structure stiffness matrix and mass matrix to a reduced form, which yields more accurate results. The ability to solve the eigenvalue problem for a free-free model is very important, for instance, when analyzing aircraft. In many applications the nodal points do not coincide with the measured ones and hence the visual and mathematical comparison of analytical and experimental mode shapes is difficult. This problem can be overcome by displacement extrapolation, which means that the displacements of an arbitrary point in space can be defined using rigid links. Extrapolation is effective, as it does not increase the number of unknowns and the size of system matrices and hence the solution time will not increase.This feature is extremely important for instance in aircraft applications, as they are normally modeled using simple beam elements. Mass output for elements, element groups and for the whole model is important when the mass distribution is under study. The possibility to select the nodal point whose displacements are to be output is also a useful new feature.

Initial stiffness distributions (needed in the updating process) are sometimes determined by static tests. For a visual study and analysis of static test data the computer program REGRESSIO has been developed.REGRESSIO uses a linear regression analysis to fit a straight line to a force-displacement curve. An arbitrary measured data value may be suppressed/unsuppressed interactively. The results,

which are discrete flexibility factors, may then read into MODALS for future manipulation.

The most important aspect of a general purpose computer program is the ease with which it can be modified, extended and updated. This is because new methods are developed and better numerical procedures are available. Every program is designed to be modified and extended easily by the user; additional options and new features may easily be added. The programs are coded using FORTRAN 77 language. The graphics is based on Tektronix graphics.

Program developing will concentrate on MODALS. The need to develop FESAP is small, as according to present knowledge it supports all required features. The main area in developing of MODALS is better estimation techniques, updating methods and methods which reduce user interaction.

Computer codes presented have been used successfully in analysis of aircraft. In Figure 2 the usage of different programs is presented.

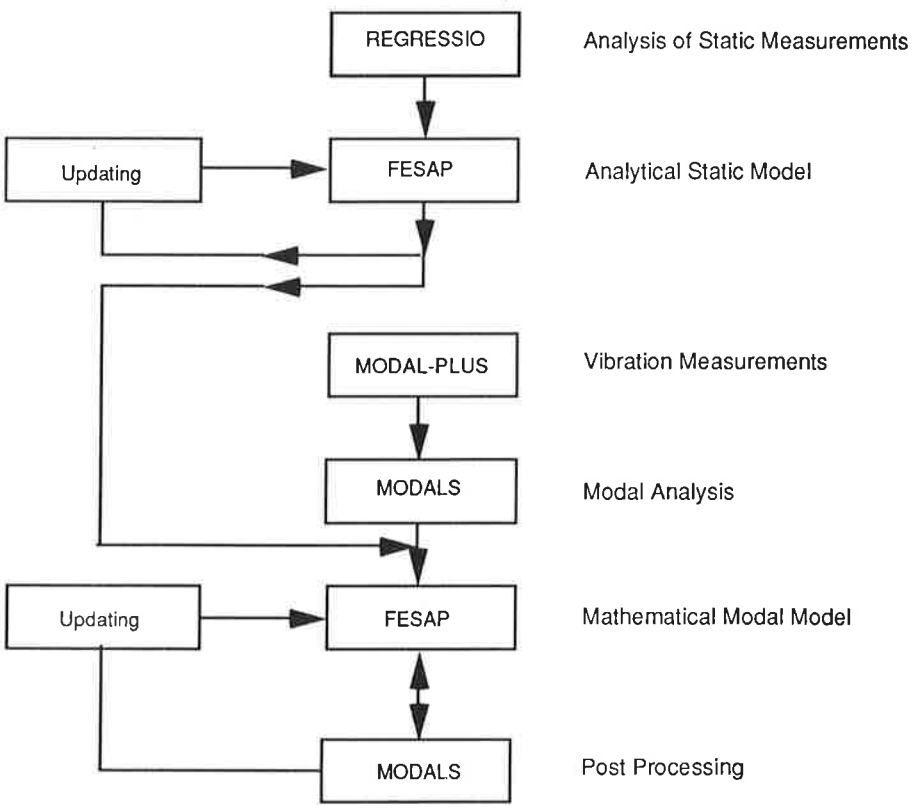

FIGURE 2. Computer programs used in creation of modal models.

POLYREFERENCE COMPLEX EXPONENTIAL TECHNIQUE

One of the most popular multiple input time domain methods namely Polyreference Complex Exponential Technique has been recently installed in modal analysis software package MODALS. The theory background of this method together with one of the frequency domain methods, called Frequency Domain Polyreference Method, will be discussed briefly. Some practical viewpoints concerning the installation of estimation method in MODALS also will be presented. The characteristics, advantages and limitations of methods will be compared to show basic differences between time and frequency domain methods.

Theory

The time domain Polyreference Complex Exponential Technique uses the impulse response function data obtained by inverse Fourier-transform of measured FRF's to extract modal parameters.

The impulse response function between a particular response location and a particular input location of a viscously damped system can be expressed as a linear combination of damped complex exponentials of modes contributing in the frequency range of interest as

$$h_{ij}(t_k) = \sum_{n=1}^{N} \left(A_{ij,n} e^{s_n k\delta T} + A^{*}_{ij,n} e^{s^{*}_n k\delta T} \right) = \sum_{n=1}^{2N} A_{ij,n} U_n^k \,, \qquad (1)$$

where

$s_n = -\zeta_n \omega_n + j\omega_n \sqrt{1-\zeta_n^2}$,

$h_{ij}(t_k)$ = impulse response function between response location i and input location j,

N = number of modes in the frequency range of interest,

n = mode number,

$A_{ij,n}$ = residue for mode n at response location i due to an input at location j,

δT = analysis time increment = $0.5 / (f_{max} - f_{min})$,

ω_n = $2\pi f_n$, where f_n = natural frequency,

ζ_n = relative damping,

* = denotes a complex conjugate.

In a similar fashion an expression for impulse response functions between a particular response location and all input locations can be formulated using matrix notation as

$$\{h_i(t_k)\} = [W][U]^k \{A_i\} \,, \qquad (2)$$

where [W] contains the modal participation factors. The modal participation factors indicate how well a mode is excited from different input locations. Note that only the left hand side of the equation is known and the equation is nonlinear in unknowns. It can be proved that the complex exponentials and the columns of modal participation matrix are the eigenvalues and corresponding eigenvectors of a matrix polynomial of the form

$$[I][W][U]^{p} + [\alpha_1][W][U]^{p-1} + \ldots + [\alpha_p][W][U]^{0} = 0 \ , \tag{3}$$

where $pL \geq 2N$ (L = number of input forces). This matrix polynomial is the characteristic polynomial of the system. The matrix polynomial formulation enables the Polyreference method to find repeated roots of maximum multiplicity of input locations.

Using equations (2) and (3), an autoregressive equation can be derived as

$$\sum_{k=0}^{p-1} [\alpha_{p-k}]\{h_i(t_k)\} = -\{h_i(t_p)\} \ . \tag{4}$$

To determine coefficient matrices of the characteristic polynomial, equation (4) can be used to form a set of linear equations to solve unknown coefficients. Once the coefficient matrices have been solved, the resonance frequencies, damping ratios and modal participation factors of the system can be determined by solving the eigenvalues and eigenvectors of matrix polynomial. Then equation (2) can be used to form a set of linear equations to calculate residues in the time domain. The residues can be calculated also in the frequency domain using an alternative formulation. Hereby, the time domain polyreference parameter estimation is a two stage procedure, first all impulse response functions are used to determine a set of poles and then the residues are calculated for a particular response function. In both stages, a set of linear equations is used to determine unknowns. From the numerical point of view, the autoregressive and matrix polynomial formulation used to solve modal parameters have been found to be stable [2].

In MODALS implementation, a singular value decomposition algorithm is used to solve the unknown coefficient matrices. The companion matrix approach is used to solve the roots of matrix polynomial and the corresponding eigenvectors are calculated directly from equation (3). These algorithms have been found to be able to solve problems involving polynomials of order up to 256 successfully.

Until now, the major difficulty has been with modal participation factors of perfectly repeated roots, which can be considered not to be the case in practice. The algorithm detects repeated roots successfully, but fails to solve the corresponding modal participation factors, which yields incorrect residues (mode shapes). However, if there is a very small difference between roots, the modal participation factors will be estimated correctly.

Frequency Domain Modal Parameter Estimation

The frequency domain modal parameter estimation techniques offer an alternative way to extract modal parameters from FRF's in their natural domain. An expression of FRF of a viscously damped system can be written either in a partial fraction form as

$$H_{ij} = \frac{L_{ij}}{\omega^2} + \sum_{n=1}^{N} \frac{A_{ij,n}}{j\omega - s_n} + \frac{\overset{*}{A}_{ij,n}}{j\omega - \overset{*}{s}_n} + U_{ij} , \tag{5}$$

or in a rational fraction form as

$$H_{ij} = \frac{\sum_{k=0}^{m} a_k (j\omega)^k}{\sum_{k=0}^{n} b_k (j\omega)^k} , \tag{6}$$

where

n	$\geq 2N$
m	$\geq n+2$
H_{ij}	= FRF between response location i and input location j
L	= lower residual term
U	= upper residual term

Let's have a quick overview on the theory of Frequency Domain Polyreference Method. The expression for displacement and velocity FRF's between all response and input locations can be formulated as

$$\begin{aligned} [H] &= [\Phi]\left[j\omega [I] - [s_n] \right]^{-1} [W] \\ [\dot{H}] &= [\Phi][s_n]\left[j\omega [I] - [s_n] \right]^{-1} [W] , \end{aligned} \tag{7}$$

where $[\Phi]$ denotes the mode shape matrix and the residual terms have been neglected for simpilicity. It can be shown that there must exist a matrix A such that

$$[A][\Phi] = [\Phi][s_n] , \tag{8}$$

where the eigenvalues of matrix A are the poles of the system and the corresponding eigenvectors are mode shape vectors. Matrix A can be calculated using the following equation

$$[A][H] = [\dot{H}] \quad . \tag{9}$$

Once the poles and the mode shapes have been calculated the modal participation factors can be determined using equation (7) [3].

Comparison of Methods

The time domain methods use mostly impulse response functions obtained by inverse Fourier transform of measured FRF's, introducing new sources of analysis error like time domain leakage. Another, perhaps more serious, problem using a time domain method is that only the poles within the frequency band of analysis can be detected, since

$$e^{s_n \delta T} = e^{s_n \delta T + j2\pi m} \quad , \qquad \delta T = \frac{1}{2(f_{max} - f_{min})} \quad . \tag{10}$$

As a consequence of this fact it is possible neither to calculate the modes outside the frequency range of analysis nor to take into account residual effects of these modes on the modes located inside the subband of analysis. This fact makes the time domain methods more convenient for analyzing of wide frequency bands. The major advantage of the time domain over frequency domain implementation is the fact that these algorithms have been found to have stable numerical characteristics.

In the frequency domain methods the FRF's are used directly, which makes it possible to analyze also the FRF's with unequal frequency increment. The influence of modes outside the frequency range of analysis can also be taken into account by calculating modes outside the frequency band or by using residual terms. However, most of these methods yield ill-conditioned polynomial formulations, which are found to be numerically unstable, especially when a wide frequency band is analyzed. These facts make the frequency domain methods more convenient for analysis of a narrow frequency band [4].

UPDATING FE-MODEL THROUGH EXPERIMENTAL MODAL MODEL

Effects of the structural modifications on the dynamic behavior can be predicted if the dynamic behavior of the original structure is known. In practice this requires the formation of an experimental modal model. If the individual modificatios are large, it is profitable to repeat measurements, otherwise it is preferred to update FE-model through experimental model. Modifications can be easily modeled by FE-method, which enables fast and accurate solution of the new response.

Applications

Updating of a FE-model creates the basis for reliable prediction of the influences due to the structural and environmental changes. Updated FE-model can be used e.g. in response and flutter analyses and with care in stress analysis.

The aim of the FE-model updating is to improve the operation of a device and the endurance limit against fatigue or to specify acceptable dynamic environment in the transport and mounting. Updated FE-model can be used in the assessment of restraint variations and to determine modes which are not on the measured frequency range. These modes are reliable only if an adequate number of elements and modes have been used in updating.

FE-model updating is mainly applied to vehicles, massive and rotating machines and to very sensitive structures. Some applications are associated with acoustic design and devices, which exploit vibrations. Lack of the appropriate computer programs and their high prices restrict updating in practice.

Requirements of Models and Problems in Modeling

Excitation, measurement and analysis techniques and the analyst's experience have the largest effect on the accuracy of the experimental modal model. Unknown restraints and structural parameters, discrete parameter distributions and joints raise difficulties in FE modeling, too. Nonlinearities and low frequency resolution in measured data may degrade the accuracy. Most structures are partly non-proportionally damped, which causes the measured modes to be complex. In the FE-method, structure is normally assumed to be undamped, which yields real modes i.e. normal modes. Although the damping is ignored, updating can be completed in most cases with success. This requires some more work and more complicated algorithms. Measurements are often contaminated by systematic and non-systematic (noise) errors. Non-systematic errors are normally smoothed away automatically in mathematical routines during modal analysis. In contrast, systematic errors in measured data form a potential error source for updating process. If systematic errors have not been identified during the analysis phase, completely wrong conclusions may be drawn and thus, the basis for the updating process is erroneous. Of course, a FE-model which is updated through an erroneous experimental model is not a reasonable basis for structural modifications.

Existing Methods

Until the 1970's the only updating method was the trial-and-error method, in which the modeler changes FE-model using his own experience and various error descriptions. Since the 1970's there have been successful efforts to develop systematic and automatic methods for the updating process (Fig.3) and hence some of the modern methods manipulate the system matrices directly.

Tools for trial-and-error method: Direct comparison is based on visual investigations and on simple mathematical criteria. On the xy-plane, where abscissa represents measured quantities and ordinate mathematical quantities, equal values form a straight line of slope one. In the case of mode

shapes the slope of the regression line iscalled as 'Modal Scale Factor' (MSF). MSF is calculated between the modes Φ_i and Φ_j according to the following equation

$$MSF = \frac{\{\Phi_i\}^T\{\Phi_j\}}{\{\Phi_j\}^T\{\Phi_j\}} . \tag{11}$$

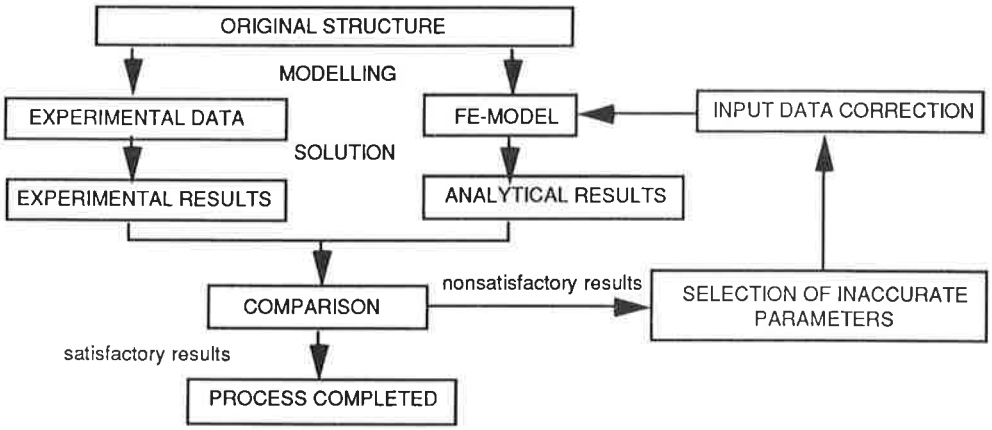

FIGURE 3. Updating FE-model through experimental modal model.

The regression line can be used to determine inaccuracies in the behavior of the FE-model; reasons for bad results are very hard to locate. However, direct comparison is often used in rough updating before a more advanced method will be applied. Direct comparison is analogous with the visual inspection of mode shapes, which is a clear and practical method to locate errors in the response of a FE-model.

The modal assurance criterion (MAC) is a scalar value between zero and one representing the correlation between two mode shapes ($\{\Phi_i\}$ and $\{\Phi_j\}$), and it is defined as [5]

$$MAC = \frac{\left|\{\Phi_i\}^T\{\Phi_j\}\right|^2}{\{\Phi_i\}^T\{\Phi_i\}\{\Phi_j\}^T\{\Phi_j\}} . \tag{12}$$

MAC is usually used as a simplified orthogonality test. In practice the mode shapes are considered the same if MAC-value is greater than 0.9, and entirely different if the MAC-value is smaller than 0.1. Uneven measurement mesh may cause difficulties in interpretation of MAC values.

COMAC is used in calculation of the correlation of magnitudes of the mode shape coefficients (interpretation as above). COMAC for the i:th degree of freedom is calculated using experimental mode shapes (E) and analytical (A) as follows [5]

$$COMAC(i) = \frac{\left\{ \sum_{n=1}^{N} \left| ({}_i\Phi_{A,n})\,({}_i\Phi_{E,n}) \right| \right\}^2}{\sum_{n=1}^{N} ({}_i\Phi_{A,n})^2 \cdot \sum_{n=1}^{N} ({}_i\Phi_{E,n})^2}, \qquad (13)$$

where K is the total number of correlating mode shapes and ${}_i\Phi$ refers to the mode shape coefficient of response location i. The accuracy of COMAC can be improved by setting the mode shapes into the same phase and not taking the absolute value until the end of summation.

COMAC and MAC are used in rough updating especially when there are many degrees of freedom. Pure mode shape comparison does not tell anything about the reasons for erroneous behavior.

Synthesized frequency response functions (FRF) are formed by natural frequencies (f_n), mode shapes (Φ_n), modal masses (m_n) and relative dampings (ζ_n). By comparing these FRFs to the measured ones the accuracy of the element model can be checked. FE eigenanalysis leads normally to real mode shapes, when the synthesized FRF H is formed between point i and j by using N mode shapes as stated in the equation 5.

$$H_{ik} = \sum_{n=1}^{N} \left(\frac{A_{ik,n}}{j\omega + \zeta_n \omega_n - j\omega_n \sqrt{1 - \zeta_n^2}} + \frac{A_{ik,n}^{*}}{j\omega + \zeta_n \omega_n + j\omega_n \sqrt{1 - \zeta_n^2}} \right), \qquad (14)$$

where

$$A_{ik,n} = \frac{{}_i\Phi_n \, {}_j\Phi_n}{m_n} = \text{residue.}$$

Models with few measured points can be easily compared over the whole frequency range. Mode indicator functions, which contain information about multiple FRFs ease the comparison of large models. Comparison of synthesized FRFs aids the advanced methods described below.

Methods based on the classic Berman method: Classic Berman method [6] (Fig. 4) is a noniterative updating process, where no eigenanalysis is needed. Input data of the method consists of experimental mode shapes (Φ), natural frequencies (f) and reduced system mass matrix M and stiffness matrix K. Changes of the system matrices are minimized in the updating process. Iteration

can be used to check the convergence. The theory and associated equations of these methods are presented in reference [6].

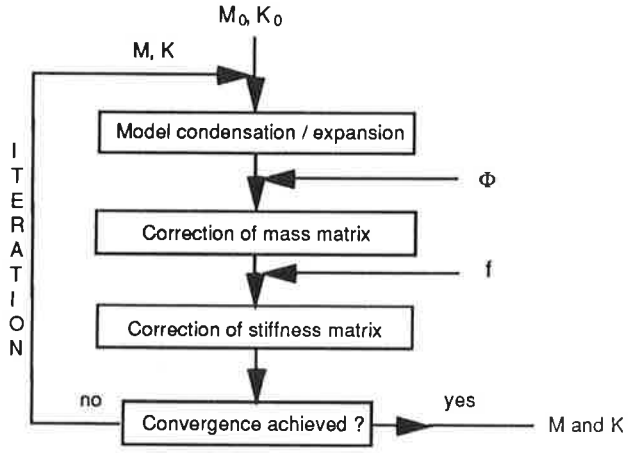

FIGURE 4. Classic Berman method.

Updating methods based on the classic Berman method often yield reduced system matrices, which satisfy experimental results but may present additional modes. Although the updating is very accurate with reduced system matrices, they can not be converted to the changes of the FE-model.

Sensitivity analysis: Iterative sensitivity analysis (Fig.5) presupposes the eigensolution on each cycle. Both global and local parameters are selected as updating objects. Global parameter is e.g. modulus of elasticity, and local parameters could be element parameters, concentrated masses and restraints.

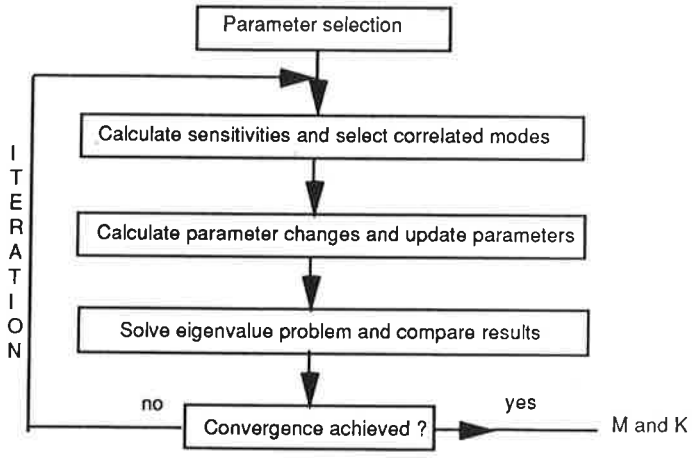

FIGURE 5. Sensitivity analysis of eigenfrequencies.

Let us now concentrate on sensitivity analysis of natural frequencies. Sensitivity of natural frequency f for the parameter P (element of sensitivity matrix S) can be calculated by using finite differences as

$$\frac{\delta f_i}{\delta P_j} \approx \frac{df_i}{dP_j} = \frac{f_i(P) - f(P_j+dP_j)}{dP_j} . \tag{15}$$

Parameter changes can be calculated by Bayesian technique /7/, which allows weighting of experimental and element parameters. For an underdetermined system, the following equation is presented

$$\{dP\} = [C_p][S]^T \left[[C_r] + [S][C_p][S]^T \right]^{-1} \{df\} , \tag{16}$$

where [C] is the weighting matrices. Subscript p refers to parameters and r to responses. Weighting matrices contain proportional reliabilities on their diagonal. Weighting affects the ratio of the accuracies of model parameters and the accuracy of response.

Modes may change places during the updating process and hence they must be ordered after each iteration cycle. Iteration is continued until the predefined convergence criterion is fulfilled.

Changes obtained by sensitivity analysis have clear physical meaning, because it manipulates directly physical parameters of the FE-model. Reduction of the FE-model is unnecessary. The time consuming eigensolution can be considered a disadvantage.

Conclusions

The success of updating FE-model through experimental modal model depends on accuracy of the experimental model and the FE modeller's experience. Inaccuracies in experimental model are due to systematic errors in measured data and unexperience of the analyst. Problems in FE-modeling are concentrated on unknown restraints, joints and unknown structural parameters.

Methods based on the classic Berman method are superior in cases where updated FE-model is used directly without making any changes to the model e.g. in response analysis. That is due to the fact that the physical meaning of the structural parameters has been lost during the updating process. If the changes of the system matrices could be converted to the structural parameters, methods based on the classic Berman method would be practical and accurate updating methods. In the sensitivity analysis the structural parameters are changed directly and thus the physical meaning of the parameters is preserved. Unfortunately, the time consuming iteration process decreases the value of the sensitivity analysis as a practical updating method. The most practical tools for trial-and-error method are MAC, COMAC and visual inspection of mode shapes.

Basic tools for trial-and-error method, as MAC, COMAC and visual comparison of mode shapes

and FRFs are installed into MODALS program. The installation of sensitivity analysis and methods based on the classic Berman method is postponed; the aim will be to combine the advantages of these two methods. Perhaps, the future updating method will construct reduced system matrices by Berman methods and apply sensitivity analysis to the reduced system matrices directly.

The updating methods described in this paper are used successfully in many simple cases. FE-model updating of an aircraft has also been completed using the trial-and-error methods.

SUMMARY

The project has reached a level where it is possible to make experimental modal analysis for complicated structures. Nowadays self-made computer programs are used especially for experimental modal analysis, but for updating FE-models, as well. Experience got from using the programs shows that the programs are appropriate to experimental modal analysis and to the linking of experimental and analytical models. However, it is necessary to continue developing MODALS.

The installation of a sophisticated frequency domain multiple input modal parameter estimation method could enable us to take advantage of both time and frequency domain implementations and thereby more confidence concerning extracted modal parameters could be achieved. The improving methods already installed in MODALS also seems to be potential research area.

Fundamental investigations according to the literature have been done concerning the updating process. This is, however, not enough and research work concerning more sophisticated updating methods should be done. Basic tools for trial-and-error method have been installed into the program MODALS. The installation of more sophisticated methods will be done in the future.

REFERENCES

1. Bathe, K.-J., Wilson, E.L. and.Peterson, F.E., SAP IV, A structural analysis program for static and dynamic response of linear systems, report no. EERC 73-11. University of California, 1974.

2. Deblauwe, F., Brown, D.L. and Allemang, R.J., The polyreference time domain technique. Proceedings of the 5th International Modal Analysis Conference. London, England Apr. 6-9 1987. Union College, Schenectady, New York 1987. Vol.II pp.832-845.

3. Zhang, L., Kanda H. and Lembregts, F., Some applications of frequency domain polyreference modal parameter identification method. Proceedings of the 4th International Modal Analysis Conference. Los Angeles, California, Feb. 3-6, 1986.Union College, Schenectady, New York 1986. Vol.II. pp.1237-1245.

4. Leuridan,J., Lipkens, J., Van der Auweraer, H., and Lembregts, F., Global modal parameter estimation methods: an assessment of time versus frequency domain implementation. Proceedings of the 4th International Modal Analysis Conference. Los Angeles, California, Feb. 3-6, 1986..Union College, Schenectady, New York 1986. Vol.II. pp.1586-1595.

5. Lieven, N.A.J. and Ewins, D.J., Spatial correlation of mode shapes, the coordinate modal assu-

rance criterion (COMAC). Proceedings of the 6th International Modal Analysis Conference. Kissimmee, Florida, Feb. 1-4, 1988..Union.. College, Schenectady, New York 1988. Vol.I. pp.690-695.

6. Caesar, B., Update and identification of dynamic mathematical models. Proceedings of the 4th International Modal Analysis Conference. Los Angeles, California, Feb. 3-6,1986. Union College, Schenectady, New York 1986. Vol.I. pp.394-401.

7. Dascotte, E. and Vanhonacker, P., Development of an automatic mathematical model updating program. Proceedings of the 7th International Modal Analysis Conference. Las Vegas, Nevada, Jan. 30 - Feb.2, 1989. Union College, Schenectady, New York 1989. Vol.I. pp.596-602.

NUMERICAL HOMOGENIZATION USING THE FINITE ELEMENT METHOD

Juha Aliranta and Stig-Göran Sjölind
Engineering Mechanics Laboratory
Department of Mechanical Engineering
University of Oulu
SF-90570 OULU, FINLAND

ABSTRACT

Overall elastic properties of composite materials are frequently calculated using simple averaging methods. In cases where the material has simple symmetry properties, analytical homogenization methods has also been applied, but in more complicated cases numerical methods has to be resorted to.

In this study a numerical homogenization method based on the use of the FEM is presented. A representative volume element (RVE) of the complex composite material was modelled using three dimensional finite elements. Overall stiffness properties were calculated in this way for the RVE. These properties were used in later stages of homogenization or directly in structural finite element calculations.

The presented homogenization method has been applied in several consequtive stages in analysing vibrational behavior of spirally wound paper tubes made of anisotropic materials containing various distributions of voids.

INTRODUCTION

Spirally wound paper tubes are fabricated by immersing paperboard strips in an adhesive bath and then winding the strips around a mandrel in a staggered fashion. Paperboard strips have orthotropic material properties with principal directions of orthotropy coinciding with lenght, width and thickness directions of the strip. After winding the principal directions of the paperboard do not coincide with the geometric axis of the tube and the tube wall will contain various distributions of voids appearing between the individual strips [1].

Spirally wound paper tubes are commonly used in industry as a centre cores for winding paper or film during production operations. The winding is done

under tension, subjecting tubes to external radial pressure. The stress distribution in wound paper is important for developement of sound rolls suitable for shipping. Models to estimate stresses in paper during this winding process have been developed [1, 2]. A closed form elasticity solution is developed to predict stresses and strains in spirally wound paper tubes loaded axisymmetrically [3].

In this study the influence of fabrication operating variables on the stiffness and vibration properties of spiral paper tubes has been studied by using the numerical homogenization method.

METHODS

The homogenization method

When investigating the effective stiffness moduli of composite materials, there are a few possibilities of experimental characterization, but they do not lead to the entire anisotropy elastic matrix. Therefore authors (Willis, Hashin, Halpin,...) have developed several theoretical methods to obtain global or effective constitutive elastic coefficents [4]. One of these methods is the so called homogenization method.

The objective of the homogenization method is to determine average homogenous global constitutive relationships for the composite material from known constitutive properties and distributions of the microscopic constituents. For this purpose a representative volume element (RVE) of the material is analysed. The RVE is a typical small element of the composite material.

Upper and lower limits (in energy manner) for the elastic properties of anisotropic materials can be obtained by Voight´s model and by Reuss´ model, respectively. In the Voight´s model the RVE is assumed to have a uniform strain field $\{\varepsilon^o\}$ and in the Reuss´ model a uniform stress $\{\sigma^o\}$ field [5]. Some authors (Begis [4] and Persson [6]) have used the Voight´s model to predict the effective properties of composite materials. In the Voight´s model equation 1 is used to estimate the effective stiffness properties of anisotropic elastic materials.

$$V\{\varepsilon^o\}^T[E^*]\{\varepsilon^o\} \geq \int_V \{\varepsilon\}^T[E]\{\varepsilon\}dV = \int_s \{F\}^T\{u_o\}ds \qquad (1)$$

where

V is the volume of the RVE
$\{\varepsilon^o\}$ is a uniform strain vector
$[E^*]$ is an average material stiffness matrix
$\{\varepsilon\}$ is the strain vector in the RVE
$\{F\}$ is a force vector
$\{u^o\}$ is a prescribed displacement boundary condition vector
$[E]$ is the material stiffness matrix in the RVE.

The numerical homogenization

In the numerical homogenization we need the theory of the homogenization method, but the effective properties of the anisotropic material has been estimated by using the FEM. In the numerical homogenization we may use equation 1 to calculate the effective properties of the anisotropic material. When we apply prescribed displacement boundary conditions to the RVE, which are the same as in the case of a uniform strain field, the equation 1 can be approximated by

$$\{\varepsilon^o\}^T[E^*]\{\varepsilon^o\} \cong \frac{1}{\bar{V}}\{\varepsilon^o\}^T\int_V [E]\{\varepsilon\}dV \qquad (2)$$

For example if we want to calculate terms of the average material stiffness matrix [E^*], we need to calculate stresses in the RVE. When we substitute $\{\varepsilon^o\}^T = \{1\ 0\ 0\ 0\ 0\ 0\}$, we get the first column $\{E^*_{i1}\}$ of the average material stiffness matrix [E*]. Now we may write equation 2 in the form

$$\{E_{i1}\} \cong \frac{1}{\bar{V}}\int_V [E]\{\varepsilon\}dV = \frac{1}{\bar{V}}\int_V \{\sigma\}dV \qquad (3)$$

It must be noted, that in the equation 2 there are applied prescribed displacement boundary conditions on the RVE, but other points are free.

APPLICATIONS

In this study we have used the numerical homogenization to study operating variables of a spirally wound paper tube. The analysis is based on a representative volume element (RVE), which includes a void and has anisotropic (orthotropic) material properties. The RVE has been analysed by FEM (ABAQUS) using three dimensional finite elements.

Figure 1 a)...d) shows all stages in the analysis of the spiral paper tube. In the first stage, figure 1 a), there has been calculated the average material stiffness matrix of the RVE. Figure 1 a) shows the representative volume element of the tube. In the second stage, figure 1 b), we have used a plane model of the half pitch of the spiral paper tube. By using the plane model the modelling of the half pitch of the tube was easier. Figure 1 b) shows a plane model of the half pitch of the tube. The colored element is the RVE. In the third stage, figure 1 c), there has been made a beam element from the half pitch of the tube by calculating the stiffness matrix of the half pitch of the tube. Figure 1 c) shows a half pitch of the tube, which has been made by transforming the plane model to a cylinder. In the fourth stage, figure 1 d), there has been calculated natural frequencies of the tube by using beam element, which was calculated in the stage 1 c). Figure 1 d) shows the whole structure. The colored part of the tube is a half pitch of the tube.

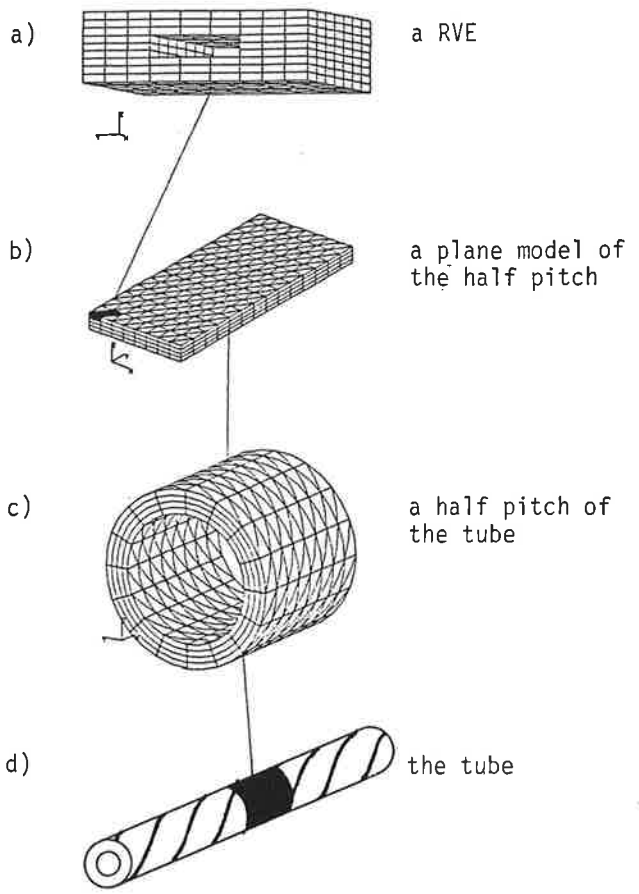

FIGURE 1. All stages in the analysis of the tube.

Figure 2 shows one of the prescribed displacement boundary conditions, which has been used in the numerical homogenization method. From equation 4 we see which kind of load cases we have to use when we are calculating the average material stiffness matrix of the RVE by using the numerical homogenization method in the first stage.

$$\begin{bmatrix}\sigma_{11}\\ \sigma_{22}\\ \sigma_{33}\\ \tau_{23}\\ \tau_{31}\\ \tau_{12}\end{bmatrix} = \begin{bmatrix} E_{1111} & E_{1122} & E_{1133} & E_{1123} & E_{1131} & E_{1112}\\ E_{2211} & E_{2222} & E_{2233} & E_{2223} & E_{2231} & E_{2212}\\ E_{3311} & E_{3322} & E_{3333} & E_{3323} & E_{3331} & E_{3312}\\ E_{2311} & E_{2322} & E_{2333} & E_{2323} & E_{2331} & E_{2312}\\ E_{3111} & E_{3122} & E_{3133} & E_{3123} & E_{3131} & E_{3112}\\ E_{1211} & E_{1222} & E_{1233} & E_{1223} & E_{1231} & E_{1212}\end{bmatrix} \begin{bmatrix}\varepsilon_{11}\\ \varepsilon_{22}\\ \varepsilon_{33}\\ \gamma_{23}\\ \gamma_{31}\\ \gamma_{12}\end{bmatrix} \qquad (4)$$

When we calculate stresses over the volume of the RVE and put $\varepsilon_x = 1$ and other strains are zero ($\{\varepsilon\}^T = \{\ 1\ 0\ 0\ 0\ 0\ 0\ \}$), we get eguation 3.

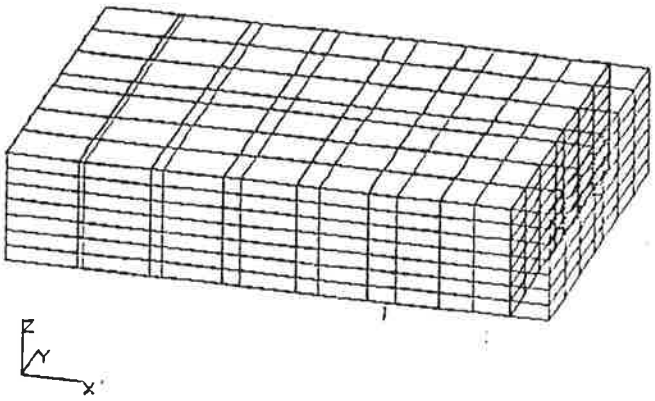

FIGURE 2. Load case $\varepsilon_x = 1$ for the RVE.

Figure 2 shows load case $\varepsilon_x = 1$, where the prescribed displacement boundary conditions are same as in the uniform srain field $\varepsilon_x = 1$, but in this case inner points are free.

In the third stage we have calculated the stiffness matrix of the beam element. Figure 3 shows degrees of freedom of the beam element.

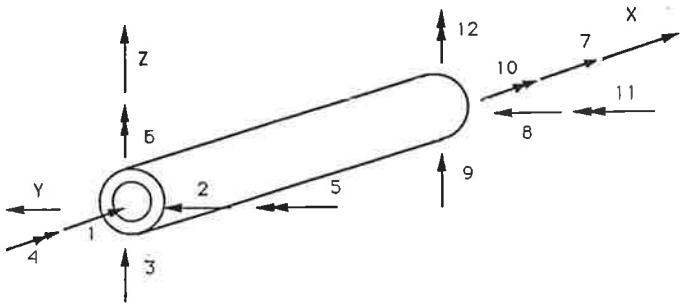

FIGURE 3. The beam element.

CONCLUSION

The tube, which is made of an anisotropic material, has been analysed in several stages. The first stage is to use numerical homogenization method to calculate the overall stiffness properties of the anisotropic material containing various distributions of voids. The second stage is to use the calculated overall moduli of the anisotropic material to calculate the stiffness matrix of a beam element, the lenght of which is a half pitch of the spirally wound tube. The last stage is to use the beam stiffness matrices to analyse vibration properties of the spirally wound tube.

The influence of operating variables on the stiffness has been studied by calculating the first natural frequency of the tube. The first measured natural frequencies are about 41 Hz and the first calculated natural frequencies are about 37 Hz.

The natural frequencies of spirally wound tube obtained by the finite element analysis agree quite well with the measured ones.

REFERENCES

1. Altmann H.C., Formulas for Computing the Stresses in Center-Wound Rolls. Tappi 51 (4), 1968, pages 176 - 179

2. Yagoda H.P., Resolution of a Core problem in Wound Rolls. ASME journal of Applied Mechanics 47, 1980, pages 847 - 854

3. Gerhardt T. D., External pressure loading of spiral paper tubes: theory and experiment. In: Perkins R. W. Mechanics of cellulosic and polymeric materials. ASME, New York, 1989, pages 237 - 245

4. Begis D., Bestagno A., Duvaut G., Hassim A., Nuc M., A new method of computing global elastic moduli for composite material. INRIA Rapport de recherches 195, 1983, pages 1 - 22

5. Whitney J.M., McCullough R.L., Micromechanical materials modeling. Technomic Publishing Company Inc., Lancaster 1990, 231 pages

6. Persson L.E., Person L., Svanstedt N., Wyller J., An intoduction to the homogenization method. Högskolan i Luleå, Luleå 1989, 62 pages

A FINITE BEAM ELEMENT FOR LAYERED STRUCTURES

MATTI LESKELÄ
Research Council for the Technical Sciences,
Academy of Finland
Geologintie 1, SF 90570 OULU, FINLAND

ABSTRACT

The well-known basic plane beam element has two nodes, and its three degrees of freedom on both nodes comprise axial and transverse displacements, together with rotation. Plane elements with in-plane displacements on nodes have been used in beam problems employing inter-connected members e.g. layered beams and composite beams. However, the plane beam elements can also be applied when special type finite elements for layered beams are derived. This paper introduces a transformed beam element which has the same number of degrees of freedom as the basic element. Its stiffness coefficients are easily transformed to meet the requirements of the internal connection structure of the system. The coefficients of the stiffness matrix can be obtained by superimposing displacement states of the basic element in such a way that only one displacement component in the transformed element is non-zero at a time.

INTRODUCTION

Plane beam elements having three degrees of freedom on nodes, ie. rotation and two displacements, can also be employed to solve problems of layered structures when the degrees of freedom are transformed to allow the elements to be interconnected on top of others. This makes them feasible for the manipulation of sandwich structures in which different layers have differing rigidities. The stiffness matrix is formulated by deriving the changes required using the matrix of an ordinary beam element.

The Timoshenko beam element

Timoshenko's beam theory /1,2/ allows for shear deformation when considering the displacement state of the beam, so that the stiffness equation can be written as

$$\begin{pmatrix} N_i \\ V_i \\ M_i \\ N_j \\ V_j \\ M_j \end{pmatrix} = \frac{EI}{(1+\theta)L} \begin{bmatrix} \frac{EA}{EI}(1+\theta) & 0 & 0 & -\frac{EA}{EI}(1+\theta) & 0 & 0 \\ & 12/L^2 & 6/L & 0 & -12/L^2 & 6/L \\ & & (4+\theta) & 0 & -6/L & (2-\theta) \\ & & & \frac{EA}{EI}(1+\theta) & 0 & 0 \\ & SYMM & & & 12/L^2 & -6/L \\ & & & & & (4+\theta) \end{bmatrix} \begin{pmatrix} u_i \\ v_i \\ \varphi_i \\ u_j \\ v_j \\ \varphi_j \end{pmatrix} \quad (1)$$

where abbreviations $\theta = 12EI/GA'L^2$, $A' = A/\alpha$ are used. EI and EA are the flexural and axial stiffnesses respectively, and A is the cross-sectional area.

α is the shear coefficient of the cross-section, used here in order to consider the distribution of the shear stresses on the cross-section. Timoshenko defines it simply as the ratio of the shear stress at the centroid to the average shear stress (the stresses are calculated according to the technical flexural theory).

When the coefficient θ approaches zero, the stiffness coefficients of the technical flexural theory are obtained. The need to consider shear deformations depends on the material properties involved in the problem.

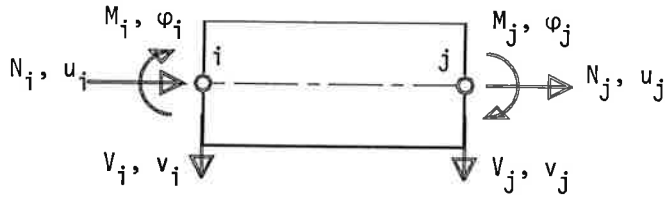

FIGURE 1: Degrees of freedom in two-noded plane beam element

TRANSFORMATION OF THE DEGREES OF FREEDOM

A beam element suitable for layered structures is such that its nodes can be connected flexibly to the nodes of another element by applying spring elements between appropriate nodes. The degrees of freedom on the end nodes of the ordinary element are therefore divided into three nodes, each having now only one degree of freedom, axial or transverse displacement (FIGURE 2.). The top and bottom nodes, *'ti'* and *'bi'* take care of the longitudinal displacements and the middle one, situated on the centroidal axis, moves transversely.

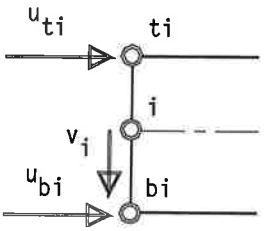

FIGURE 2: Degrees of freedom on the transformed element

DERIVATION OF STIFFNESS COEFFICIENTS

The coefficients of the stiffness matrix for the layered element are now derived by introducing a positive displacement on one node while the others are kept zero and considering the force components of the ordinary element needed to produce this.

The nodal displacement $u_{ti} > 0$ is taken as an example and the forces required to impose the state of Figure 3 are introduced. The displacement state is determined using axial displacement $u_i = \eta_b u_{ti}$ and rotation $\varphi_i = u_{ti}/h$ in the ordinary element. These are produced by the forces

$$N_i = \{EA/L\}u_i = - N_j \qquad (2a)$$

$$V_i = \{6EI/(1+\theta)L2\}_{\varphi_i} \quad (2b)$$

$$M_i = \{(4+\theta)EI/(1+\theta)L\}\varphi_i \quad (2c)$$

$$M_j = \{(2-\theta)EI/(1+\theta)L\}\varphi_i \quad (2d)$$

The axial forces on nodes *ti* and *bi* can be arranged so that these result in a total axial force N_i and a bending moment M_i. To produce N_i, the components N_{tn} and N_{bn} are required and the moment is produced by the force couple $N_{tm} = -N_{bm} = M_i/h$,

$$N_{tn} = \eta_b N_i/(\eta_t + \eta_b) = \eta_t N_i \quad (3a)$$

$$N_{bn} = \eta_t N_i/(\eta_t + \eta_b) = \eta_b N_i \quad (3b)$$

The equations (3) are based on the requirement that N_{tn} and N_{bn} should satisfy the condition of an axial deformation state. The resultant forces on the nodes are then

$$N_{ti} = N_{tn} + N_{tm}$$
$$= \eta_t\eta_b(EA/L)u_{ti} + \{(4+\theta)EI/(1+\theta)Lh^2\}u_{ti} \quad (4a)$$

$$N_{bi} = N_{bn} + N_{bm}$$
$$= \eta_b^2(EA/L)u_{ti} - \{(4+\theta)EI/(1+\theta)Lh^2\}u_{ti} \quad (4b)$$

Accordingly, for the j-end one must write

$$N_{tj} = (-\eta_t\eta_b(EA/L) + \{(2-\theta)EI/(1+\theta)Lh^2\})u_{ti} \quad (4c)$$

$$N_{bj} = -(\eta_b^2(EA/L) + \{(2-\theta)EI/(1+\theta)Lh^2\})u_{ti} \quad (4d)$$

Transverse forces depend only on the rotation, and due to u_{ti} they are written as

$$V_i = -V_j = \{6EI/(1+\theta)L^2h\}u_{ti} \quad (4e)$$

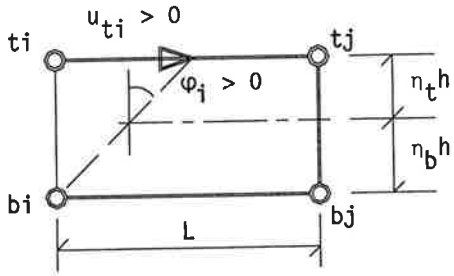

FIGURE 3: Correspondence between a nodal displacement and the rotation of the element end face

Correspondingly, one of the displacements u_{bi}, utj and u_{bj} at a time is set to be non-zero and the force components required are considered. The resulting vector for the nodal forces is

$$\{F_e\} = \{N_{ti}\ N_{bi}\ V_i\ N_{tj}\ N_{bj}\ V_j\}^T \quad (5a)$$

and the vector for the displacements is

$$\{U_e\} = \{u_{ti}\ u_{bi}\ v_i\ u_{tj}\ u_{bj}\ v_j\}^T \tag{5b}$$

The stiffness matrix $[S_e]$ in the equation for an element,

$$\{F_e\} = [S_e]\{U_e\} \tag{6}$$

is

$$[S_e] = \begin{bmatrix} [S_1] & [S_2] \\ [S_2]^T & [S_3] \end{bmatrix}$$

the submatrices of which, $[S_1]$, $[S_2]$ and $[S_3]$, are given in detail in the appendix.

As in all beam elements, the transverse deformations are not considered inside the element. If the system contains substantial compressive layers, they can be allowed for by calibrating the stiffness of the transverse coupling springs so that the flexibility of the layer corresponds to the settlement of the spring.

DISCUSSION

The elements explained above have been found to behave well, due to their similarity in nature to Timoshenko beam elements, which are not sensitive to errors caused by selection of the dimensions, and the overall accuracy of the solution is good provided that the length of the elements is much less than the length of the structure.

The elements have been used for the analysis of composite beams having incomplete interaction, for which purpose the lengths of the elements were chosen directly according to the spacing of the connectors, ie. the lengths were less than the total depth of the cross-section. When the non-linearity of the spring elements was considered, together with the non-elastic material behaviour, the true properties of composite beams could be determined /4/. Figure 4 presents a typical two-layer connected composite element having vertical and horizontal coupling springs. The vertical springs take care of the compression between layers and the horizontal springs allow for the longitudinal shear and slipping at the connection interface.

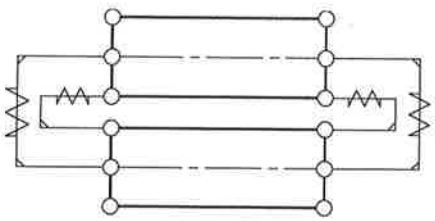

FIGURE 4: A two-layer beam element composed with coupling springs

The nodes capable of longitudinal displacement can be used to couple reinforcing springs (axial elements), which are suitable for the modelling of pre-tensioning effects or reinforcement in concrete structures. Figure 5 shows the principle of connecting a reinforcing axial element to a flexural element.

If no slip is considered, the axial *'a'* is assembled directly to the stiffness matrix of the *'lbe'* element. The slip between the axial and flexural elements could be modelled by using horizontal coupling springs which have the same properties as the load-slip function of the reinforcement.

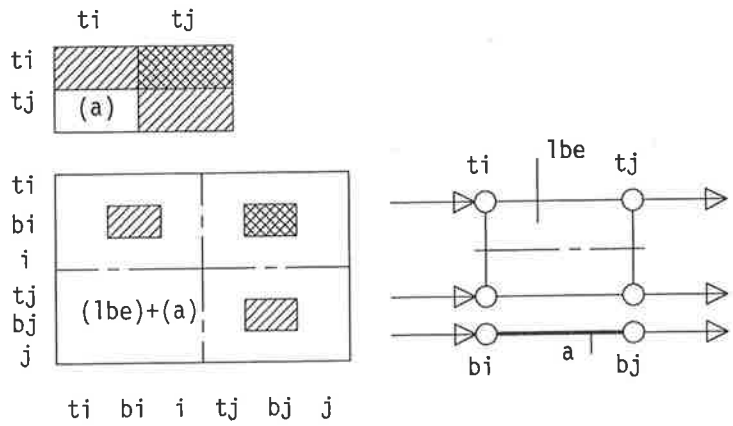

FIGURE 5: Assembly of the stiffness coefficients of an axial element to the stiffness matrix of an layered beam element

REFERENCES

1. Timoshenko, S., Goodier, J.N., Theory of Elasticity. Kongakusha Company Ltd, Tokyo 1968.

2. Owen, D.J.R., Hinton, E., Finite Elements in Plasticity, Theory and Practice, Pineridge Press Limited, Swansea, U.K., 1980.

3. Cowper, G.R., The Shear Coefficient in Timoshenko's Beam Theory. Journal of Applied Mechanics V.33 1966, pages 335 - 340.

4. Leskelä, M., Calculation models for concrete-steel composite beams, considering partial interaction. University of Oulu, Department of Civil Engineering, Oulu 1986. Acta Univ. Oul. C 36.1986. Artes Constr. 8.

APPENDIX

The stiffness matrix of the transformed element is written with the aid of its submatrices as

$$[S_e] = \begin{bmatrix} [S_1] & [S_2] \\ [S_2]^T & [S_3] \end{bmatrix}$$

where the submatrices are written in the most common case

$$[S_1] = \begin{bmatrix} \eta_b^2 SCA+SCF1 & \eta_t\eta_b SCA-SCF1 & SCF3 \\ & \eta_t^2 SCA+SCF1 & -SCF3 \\ SYMM & & SCF4 \end{bmatrix}$$

$$[S_2] = \begin{bmatrix} -\eta_b^2 SCA+SCF2 & -\eta_t\eta_b SCA-SCF2 & -SCF3 \\ -\eta_t\eta_b SCA-SCF2 & -\eta_t^2 SCA+SCF2 & SCF3 \\ SCF3 & -SCF3 & -SCF4 \end{bmatrix}$$

$$[S_3] = \begin{bmatrix} \eta_b^2 SCA+SCF1 & \eta_t\eta_b SCA-SCF1 & -SCF3 \\ & \eta_t^2 SCA+SCF1 & SCF3 \\ SYMM & & SCF4 \end{bmatrix}$$

SCA = EA/L, SCF1 = $(4+\theta)$EI/$(1+\theta)$Lh^2, SCF2 = $(2-\theta)$EI/$(1+\theta)$Lh^2

SCF3 = 6EI/$(1+\theta)$L^{2}h, SCF4 = 12EI/$(1+\theta)$L^3

h = $(\eta_t + \eta_b)$H

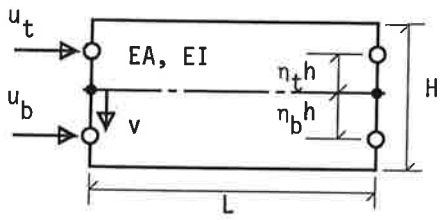

FINITE ELEMENT DESIGN SENSITIVITY ANALYSIS FOR A CLASS OF NONLINEAR PROBLEMS

RAINO A. E. MÄKINEN
Academy of Finland /
Dept. of Mathematics, University of Jyväskylä
P.O. Box 35, SF–40351 JYVÄSKYLÄ, FINLAND

ABSTRACT

Design sensitivity analysis is performed for the finite element system arising from the discretization of nonlinear potential problems using isoparametric Lagrangian elements. The calculated sensitivity formulae are given in a simple matrix form, which makes it easy to include sensitivity calculations into existing finite element codes.

INTRODUCTION

Shape optimization problems are optimal control problems where the control is some geometrical parameter [4], [7]. Traditionally optimal shape design is associated with structural optimization. However, any shape optimization problem which is governed by an elliptic partial differential equation can be solved numerically using the same techniques. In this work we consider the case where the state problem is approximated by the finite element method. Although the continuous setting of the problem may be a distributed control problem, the numerical optimization problem always has a finite number of parameters.

By design sensitivity analysis we mean computing derivatives of the finite element solution with respect to nodal coordinates of the finite element mesh. Although the geometric sensitivity analysis is one of the most crucial steps in numerical shape optimization, it is still considered extremely elaborate and difficult even for linear problems. This is probably due to the bad form in which most of the sensitivity formulae are presented. In these formulae there are usually too much explicit dependence on certain application or element type. This implies unstructured programs which are difficult to debug and maintain.

In what follows we develop the geometric sensitivity analysis in matrix form for a class of nonlinear potential equations. We assume that the continuous problem is discretized using isoparametric Lagrangian elements. A sensitivity analysis of this type for linear elasticity problems has already been done by Brockman [2], [3]. In addition we show how to compute efficiently the sensitivity of a functional depending on the finite element solution. The results can be applied in numerical realization of optimal shape design problems, where the system is governed by these nonlinear problems.

SENSITIVITY OF THE DISCRETE SOLUTION VECTOR OF A NONLINEAR POTENTIAL EQUATION

Consider the nonlinear potential problem with mixed boundary conditions

$$(1)\qquad \begin{cases} -\nabla\cdot\big(\rho(x,|\nabla u|^2)\nabla u\big) = f & \text{in } \Omega\subset \mathbf{R}^n,\ n=2,3 \\ u = 0 & \text{on } \Gamma_1 \\ \rho(x,|\nabla u|^2)\nabla u\cdot n = g & \text{on } \Gamma_2. \end{cases}$$

Here $\partial\Omega = \Gamma_1\cup\Gamma_2$, $f\in L^2(\Omega)$, $g\in L^2(\Gamma_2)$ and $\rho : \mathbf{R}^n\times\mathbf{R}\to\mathbf{R}$ is a given smooth function. We assssume that for given data the problem (1) is an elliptic problem and has an unique (weak) solution.

The range of physical problems falling into this category is large. Moreover, a general nonlinear elasticity problem can be handled analogously. One has to replace the potential u by a displacement field $\vec{u}$, the gradient ∇u by a strain tensor $\varepsilon(\vec{u})$, the source term f by a body force $\vec{f}$, the boundary flux g by a surface traction $\vec{g}$ and $\rho\nabla u$ by a nonlinear stress-strain relation $\sigma(\vec{u}) = \rho(\varepsilon(\vec{u}))\varepsilon(\vec{u})$.

We discretize the problem (1) using Lagrangian finite elements of order k. Then the discrete analoque of problem (1) reads as

$$(2)\qquad \begin{aligned} u_h\in V_h :\quad & \int_{\Omega_h}\rho(x,|\nabla u_h|^2)\nabla u_h\cdot\nabla v_h\,dx \\ & = \int_{\Omega_h} f v_h\,dx + \int_{\Gamma_{2h}} g v_h\,ds \quad \forall v_h\in V_h, \end{aligned}$$

where $V_h = \{\varphi\in C^0(\Omega_h)\mid \varphi|_{T_e}\in P^k(T_e),\ \varphi|_{\Gamma_{1h}} = 0\}$ is the piecewise polynomial finite element space and $\Omega_h = \cup T_e$ is the finite element mesh. The matrix form of problem (2) is the system of nonlinear equations

$$(3)\qquad \mathbf{K}(\mathbf{q})\,\mathbf{q} = \mathbf{f},$$

where $\mathbf{K}(\mathbf{q})$ is the "stiffness" matrix and $\mathbf{f}$ is the "force" vector respectively. The unknown vector $\mathbf{q}$ contains the nodal values of u_h.

Suppose now that the nodes of the finite element mesh depend on a real parameter α. Our aim is to find the sensitivity of the solution vector $\mathbf{q}$ with respect to α, i.e. to find $\partial\mathbf{q}/\partial\alpha$. In what follows we will denote $(\ )' = \partial(\ )/\partial\alpha$.

If the nodes of the finite element mesh depend smoothly on α, we may use the implicit function theorem and differentiate (3) to obtain

$$(4)\qquad [\mathbf{K}(\mathbf{q})]'\,\mathbf{q} + \mathbf{K}(\mathbf{q})\,\mathbf{q}' = \mathbf{f}'.$$

The terms $[\mathbf{K}(\mathbf{q})]'\,\mathbf{q}$ and $\mathbf{f}$ can be computed element by element using the relations

$$(5)\qquad \mathbf{K}(\mathbf{q})\,\mathbf{q} = \sum_e \mathbf{P}^e\mathbf{K}^e(\mathbf{q}^e)\,\mathbf{q}^e \quad \text{and} \quad \mathbf{f} = \sum_e \mathbf{P}^e\mathbf{f}^e.$$

Here $\mathbf{P}^e$ is the "local-to-global" expanding matrix, $\mathbf{P}^{e\mathrm{T}}$ is the "global-to-local" gathering matrix and $\mathbf{q}^e = \mathbf{P}^{e\mathrm{T}}\mathbf{q}$ (vector of nodal values of u_h associated to the e:th element).

In the case of isoparametric elements each element T_e is obtained from the parent element $\hat{T}$ ($[-1,1]^n$, for example) by the mapping $\hat{T} \to T_e : \ \xi \mapsto x(\xi)$. Let

$$\mathbf{N} = \begin{pmatrix} \varphi_1 \\ \vdots \\ \varphi_m \end{pmatrix} \quad \text{and} \quad \mathbf{L} = \begin{pmatrix} \partial\varphi_1/\partial\xi_1 & \dots & \partial\varphi_m/\partial\xi_1 \\ \vdots & \ddots & \vdots \\ \partial\varphi_1/\partial\xi_n & \dots & \partial\varphi_m/\partial\xi_n \end{pmatrix} \tag{6}$$

be the matrices containing the values of the shape functions and their derivatives for the parent element. Denote by $\mathbf{J} = \left[\frac{\partial x_j}{\partial \xi_i}\right]_{i,j=1}^{n}$ the Jacobian of the mapping $\xi \mapsto x(\xi)$. Finally let

$$\mathbf{X}^e = \begin{pmatrix} X_1^1 & \dots & X_n^1 \\ \vdots & \ddots & \vdots \\ X_1^m & \dots & X_n^m \end{pmatrix} \tag{7}$$

be the matrix containing the nodal coordinates of the e:th element. (In what follows, we omit the superscript e as we are now working with the e:th element). At a point $x(\xi)$ the cartesian derivatives of the shape functions are now given by $\mathbf{B} = \mathbf{J}^{-1}\mathbf{L}$ and the Jacobian by $\mathbf{J} = \mathbf{LX}$.

Gaussian quadrature with integration points and weights (ξ^k, W_k), $k = 1, ..., K$ is then used to perform the numerical integration needed for computing the element stiffness matrix, resulting

$$\mathbf{K}^e(\mathbf{q}^e) = \sum_{k=1}^{K} W_k \, \rho(x^k, s_k) \, \mathbf{B}_k^{\mathrm{T}} \mathbf{B}_k |\mathbf{J}_k|, \tag{8}$$

where $s_k = |\nabla u_h(x^k)|^2$, $x^k = x(\xi^k)$, $\mathbf{B}_k = \mathbf{B}(\xi^k)$, $\mathbf{J}_k = \mathbf{J}(\xi^k)$ and $|\mathbf{J}_k| = \det \mathbf{J}_k$.

The following results give the formulae for computing $\mathbf{q}'$. For the proofs, see [2] and [5].

LEMMA 1. *The sensitivity of the "strain-displacement" matrix $\mathbf{B}_k$ is given by*

$$\mathbf{B}_k' = -\mathbf{B}_k \mathbf{X}' \mathbf{B}_k. \tag{9}$$

LEMMA 2. *For the sensitivity of the determinant we have*

$$|\mathbf{J}_k|' = |\mathbf{J}_k| \sum_{j=1}^{m} \nabla\varphi_j(x^k)^{\mathrm{T}} (X^j)'. \tag{10}$$

LEMMA 3. *The sensitivities of s_k and x^k are given by*

$$(x^k)' = (\mathbf{X}')^{\mathrm{T}} \mathbf{N}_k \tag{11}$$

and

$$s_k' = 2(\mathbf{B}_k \mathbf{q}^e)^{\mathrm{T}} \mathbf{B}_k' \mathbf{q}^e + 2(\mathbf{B}_k \mathbf{q}^e)^{\mathrm{T}} \mathbf{B}_k (\mathbf{q}^e)'. \tag{12}$$

LEMMA 4. *The sensitivity of* $\rho(x^k, s_k)$ *is given by*

$$\rho(x^k,s_k)' = 2\,\frac{\partial\rho(x^k,s_k)}{\partial s}(\mathbf{B}_k\mathbf{q}^e)^{\mathrm{T}}\mathbf{B}_k'\mathbf{q}^e + (\nabla_x\rho(x^k,s_k))^{\mathrm{T}}(\mathbf{X}')^{\mathrm{T}}\mathbf{N}_k + 2\,\frac{\partial\rho(x^k,s_k)}{\partial s}(\mathbf{B}_k\mathbf{q}^e)^{\mathrm{T}}\mathbf{B}_k(\mathbf{q}^e)' \tag{13}$$

THEOREM 1. *The term* $[\mathbf{K}^e(\mathbf{q}^e)]'\,\mathbf{q}^e$ *is given by*

$$[\mathbf{K}^e(\mathbf{q}^e)]'\,\mathbf{q}^e = \mathbf{S}^e(\mathbf{q}^e)\,\mathbf{q}^{e\prime} + \mathbf{T}^e(\mathbf{q}^e)\,\mathbf{q}^e, \tag{14}$$

where

$$\mathbf{S}^e(\mathbf{q}^e) = \sum_{k=1}^{K} C_k\,\mathbf{B}_k^{\mathrm{T}}\mathbf{B}_k\mathbf{q}^e\mathbf{q}^{e\mathrm{T}}\mathbf{B}_k^{\mathrm{T}}\mathbf{B}_k \tag{15}$$

$$\mathbf{T}^e(\mathbf{q}^e) = \sum_{k=1}^{K}\Big(C_k\,\mathbf{B}_k^{\mathrm{T}}\mathbf{B}_k\mathbf{q}^e\mathbf{q}^{e\mathrm{T}}\mathbf{B}_k^{\mathrm{T}}\mathbf{B}_k' + D_k\,(\mathbf{B}_k')^{\mathrm{T}}\mathbf{B}_k + D_k\,\mathbf{B}_k^{\mathrm{T}}\mathbf{B}_k' + E_k\,\mathbf{B}_k^{\mathrm{T}}\mathbf{B}_k + F_k\,\mathbf{B}_k^{\mathrm{T}}\mathbf{B}_k\Big) \tag{16}$$

and

$$C_k = 2\,W_k|\mathbf{J}_k|\partial\rho(x^k,s_k)/\partial s, \qquad D_k = W_k|\mathbf{J}_k|\rho(x^k,s_k)$$
$$E_k = W_k|\mathbf{J}_k|(\nabla_x\rho(x^k,s_k))^{\mathrm{T}}(\mathbf{X}')^{\mathrm{T}}\mathbf{N}_k, \qquad F_k = W_k|\mathbf{J}_k|'\rho(x^k,s_k). \tag{17}$$

In the absence of surface terms (i.e. $g \equiv 0$) the element force vector is given by

$$\mathbf{f}^e = \sum_k W_k f(x^k)\mathbf{N}_k|\mathbf{J}_k|. \tag{18}$$

Differentiating (18) we get

THEOREM 2. *The sensitivity of* $\mathbf{f}^e$ *is given by*

$$(\mathbf{f}^e)' = \sum_k W_k\left(\nabla_x f(x^k)^{\mathrm{T}}(x^k)'\mathbf{N}_k|\mathbf{J}_k| + f(x^k)\mathbf{N}_k|\mathbf{J}_k|'\right). \tag{19}$$

Performing the assembly process, we get the following expression for the sensitivity of the solution vector:

THEOREM 3. *The sensitivity of* $\mathbf{q}$ *is given as the solution of the linear system of equations*

$$\Big(\mathbf{K}(\mathbf{q}) + \mathbf{S}(\mathbf{q})\Big)\,\mathbf{q}' = \mathbf{f}' - \mathbf{T}(\mathbf{q})\,\mathbf{q}. \tag{20}$$

REMARK. In the equations (9)–(19) the only matrix depending on a specific application (mesh topology, design parametrization, etc.) is $\mathbf{X}'$. All other matrices are available from the assembly of the system (3). In practise the nonlinear system (3) is solved only approximately. Therefore the equation (20) also holds approximately only. To get accurate numerical values for the sensitivities it is recommended to solve system (3) as accurately as possible. It is beneficial to use Newton-Raphson method in solving equation (3), as after convergence of the Newton-Raphson iteration the coefficient matrix in (20) is (approximately) the one used in the last iteration.

ON THE ADJOINT STATE TECHNIQUE FOR THE SENSITIVITY OF A FUNCTIONAL

Let $\boldsymbol{\alpha} = (\alpha_1, ..., \alpha_M) \in \mathbf{R}^M$ be a parameter vector and let $F : \mathbf{R}^M \times \mathbf{R}^N \to \mathbf{R} : (\boldsymbol{\alpha}, \mathbf{q}) \mapsto F(\boldsymbol{\alpha}, \mathbf{q})$ be a cost or a constraint functional. The sensitivity of F with respect to α_s, $s = 1, ..., M$ is given by

$$\frac{dF}{d\alpha_s} = \frac{\partial F}{\partial \alpha_s} + (\nabla_q F)^{\mathrm{T}} \frac{\partial \mathbf{q}}{\partial \alpha_s}. \tag{21}$$

The form of equation (21) is not suitable when the gradient of F with respect to $\boldsymbol{\alpha}$ is needed as it requires M solutions of the linear system (20). Employing the standard adjoint equation technique of optimal control theory to eliminate $\frac{\partial \mathbf{q}}{\partial \alpha_s}$ we obtain

$$\frac{dF}{d\alpha_s} = \frac{\partial F}{\partial \alpha_s} + \mathbf{p}^{\mathrm{T}} \left(\frac{\partial \mathbf{f}}{\partial \alpha_s} - \mathbf{T}^{(s)}(\mathbf{q})\, \mathbf{q} \right), \tag{22}$$

where $\mathbf{p}$ is the solution of the adjoint equation

$$\Big(\mathbf{K}(\mathbf{q}) + \mathbf{S}(\mathbf{q}) \Big) \mathbf{p} = \nabla_q F. \tag{23}$$

Now the computation of $\nabla_{\boldsymbol{\alpha}} F$ requires only one solution of the linear system (23).

APPLICATIONS

In this section we shortly list some state equations of form (1) which have appeared in optimal design litterature.

Sensitivity analysis for axisymmetric Poisson's equation. An important application is the axisymmetric Poisson's equation

$$-\nabla \cdot \Big(2\pi r \nabla u(r, z) \Big) = 2\pi r\, f(r, z). \tag{24}$$

Equation (24) may descibe a temperature distribution in an axisymmetric structure or an ideal fluid flow in an axisymmetric nozzle, for example. In this case $\rho(x, s) = 2\pi\, x_1$. As the problem is linear the adjoint problem (23) has the same coefficient matrix. When direct methods are used for the solution of (3) one may solve (23) eficiently using the existing factorization of the coefficient matrix.

Sensitivity analysis for magnetic field. Electromagnetic behaviour is governed by the Maxwell's equations for the magnetic field $\vec{H}$ and the magnetic induction $\vec{B}$. Introducing the vector potential $\vec{A}$, $\vec{B} = \nabla \times \vec{A}$ the Maxwell's equations reduce into equation

$$\nabla \times (\rho \nabla \times \vec{A}) = \vec{j}, \tag{25}$$

where $\vec{j}$ is the current density and ρ is the magnetic reluctivity. Let the domain under consideration be given as $\Omega = \Omega_{air} \cup \Omega_{copper} \cup \Omega_{iron}$. In this case the function ρ is of the form

$$\rho(x, |B|^2) = \begin{cases} 1/\mu_0, & x \in \Omega_{air} \cup \Omega_{copper} \\ r(|B|^2), & x \in \Omega_{iron}. \end{cases} \tag{26}$$

Assuming that $\vec{A} = (0,0,u)$ and $\vec{j} = (0,0,j_3)$, the problem then reduces into the nonlinear potential problem

$$-\nabla \cdot (\rho(x, |\nabla u|^2)\nabla u) = j_3. \tag{27}$$

Although the mapping $x \mapsto \rho(x,s)$ is not continuous, no problems arise if the finite element boundaries coincide with the material boundaries. The results of Theorems 1–2 are now directly applicable.

We note that in ref. [6] the sensitivity analysis was performed for this problem in the case of P^1 triangular elements. As in both cases area coordinates were employed the sensitivity formulae presented there cannot be utilized in the case of higher order elements.

Sensitivity analysis for subsonic compressible flow. In two dimensions compressible gas flow is described by the compressible potential equation

$$\nabla \cdot \big(\rho(|\nabla u|^2)\nabla u\big) = 0. \tag{28}$$

The velocity of the flow is given by $\vec{v} = \nabla u$ and the density of the gas by

$$\rho(|\vec{v}|^2) = \rho_0 \left(1 - \frac{\gamma - 1}{\gamma + 1}|\vec{v}|^2\right)^{\frac{1}{\gamma - 1}} \quad (\rho_0 \text{ and } \gamma \text{ positive constants}). \tag{29}$$

When the flow is subsonic then the equation (29) with suitable boundary conditions is an elliptic boundary value problem. In [1] a shape optimization problem for a lifting airfoil was formulated and solved using P^1-elements. Again Theorems 1–2 enable one to use higher order elements too.

CONCLUSIONS

The sensitivity formulae presented in this paper are both simple to program correctly and efficient as basic linear algebra subroutine (BLAS) packages can be utilized. Our approach is general as it applies to all isoparametric Lagrangian finite elements. General purpose programs can be easily developed as the dependence on the specific application can be isolated into separate modules. The same approach can clearly be applied to different state problems (elasticity, Navier-Stokes, etc).

REFERENCES

1. F. Angrand, *Optimum design for potential flows*, Int. j. numer. methods fluids **3** (1983), 265–282.
2. R. A. Brockman, *Geometric sensitivity analysis with isoparametric finite elements*, Commun. appl. numer. methods **3** (1987), 495–499.
3. R. A. Brockman and F. Y. Lung, *Sensitivity analysis with plate and shell finite elements*, Int. j. numer. methods eng. **26** (1988), 1129–1143.
4. J. Haslinger and P. Neittaanmäki, "Finite Element Approximation for Optimal Shape Design," John Wiley & Sons, Chichester, 1988.
5. R. Mäkinen, *Finite-element design sensitivity analysis for non-linear potential problems*, Commun. appl. numer. methods **6** (1990), 343–350.
6. A. Marocco and O. Pironneau, *Optimum design with Lagrangian finite elements: Design of an electromagnet*, Computer Methods in Applied Mechanics and Engineering **15** (1978), 277–308.
7. O. Pironneau, "Optimal Shape Design for Elliptic Systems," Springer-Verlag, 1984.

P-ADAPTIVITY APPLIED TO THE SOLUTION OF FIELD AND PLANE STRESS PROBLEMS

SEPPO ORIVUORI

Imatran Voima Oy, Rakennusosasto
P.O. Box 112, SF-01601 VANTAA, FINLAND

ABSTRACT

This paper describes a method to reveal the errors in the FEM-models. The two error sources: inappropriate jumps in the stress field at interelement boundaries and the lack of satisfaction of governing equations, are transformed into physical quantities with which we can easily measure the errors. In what follows we describe the solution refinement strategy in which the element approximation properties are improved by adding hierarchical edge and bubble modes. This is done only in those parts of the model where error measures exceed the desired accuracy. Examples showing the functionality of the solution refinement method described are also presented. Examples deal with stationary temperature distributions and plane stress problems.

INTRODUCTION

The finite element based programs are becoming more and more user-friendly. They can be used with little knowledge of the solution method. This have caused a growing pressure to estimate the error content of the solution obtained and hopefully even make it better. There are several methods to get some information about the errors in FEM-solution. A priori estimates try to guide meshing so that the largest element size is below a certain limit to guarantee the desired accuracy of the results. Instead of these, a posteriori error analysis methods are used in practical applications. The early literature from the late 1970's /1/ was far too mathematical for civil engineers. Later on this mathematics was translated to a more practical form to be applied in practice. /2/, /3/, /4/ and /5/ are some examples of such papers. Guided by the error estimates the refinement can be carried out using the three different methods: the h-method, the p-method or the hp-method. In the h-method the new nodal point grid is created, in the p-method degrees of polynomials within elements are increased. The error measures used in the papers are often various norms which are difficult to realize by an engineer utilizing FEM-programs. In the present paper the error measures have a clear physical meaning. Two years ago we started to develop ADAFEM-program in Imatran Voima Oy using the p-adaptivity to make it sure that results of the FEM-program are within preassigned error tolerance.

THEORETICAL BACKGROUND

Field problems

Field problems are governed by the flow balance equation

$$\nabla^T \mathbf{q} + Q = 0 \tag{1}$$

where ∇ is the gradient operator, $\mathbf{q}$ is the flux vector and Q is the source term. Components of the flux vector can be related to gradients of a scalar potential by

$$\mathbf{q} = - \mathbf{k}\nabla\phi \tag{2}$$

where $\mathbf{k}$ is a matrix of material properties and ϕ is a potential describing the phenomenon, for example temperature in heat conduction problems.

For orthotropic two-dimensional problems Eq. (1) and (2) can be written as

$$\frac{\partial q_x}{\partial x} + \frac{\partial q_y}{\partial y} + Q = 0 \tag{3}$$

and

$$\begin{aligned} q_x &= - k_x \frac{\partial \phi}{\partial x} \\ q_y &= - k_y \frac{\partial \phi}{\partial y} \end{aligned} \tag{4}$$

where q_x and q_y are the components of the flux vector along global x- and y-axis, respectively; k_x and k_y are the material properties controlling the flow in global x- and y-direction, respectively.

Boundary conditions which are valid on the points of the boundary of the solution domain are

$$q_n = - k_n \frac{\partial \phi}{\partial n} = \bar{q}_n \tag{5a}$$

or

$$q_n = \alpha (\phi - \phi_o) \tag{5b}$$

or

$$\phi = \bar{\phi} \tag{5c}$$

where the subscript n indicates the direction along the normal to the boundary, $\bar{q}_n$ is the prescribed flux, α is the parameter controlling the flow, for example the heat transfer coefficient in heat conduction problems, ϕ_o is a known function and $\bar{\phi}$ is the prescribed boundary value for the unknown potential ϕ.

TWO-DIMENSIONAL ELASTIC STRESS PROBLEMS

The two equilibrium equations for the plane stress problems are

$$\frac{\partial \sigma_x}{\partial x} + \frac{\partial \tau_{xy}}{\partial y} + b_x = 0 \tag{6}$$

$$\frac{\partial \tau_{xy}}{\partial x} + \frac{\partial \sigma_y}{\partial y} + b_y = 0 \tag{7}$$

where σ_x , σ_y and τ_{xy} are the three stress components defining the two-dimensional plane stress problems; b_x and b_y are the components of the body force along x- and y-direction, respectively. Stress-strain relations are

$$\boldsymbol{\sigma} = \mathbf{D}\boldsymbol{\varepsilon} \tag{8}$$

where $\boldsymbol{\sigma} = [\sigma_x \ \sigma_y \ \tau_{xy}]^T$ is the vector of stress components specifying the plane stress state, $\boldsymbol{\varepsilon} = [\varepsilon_x \varepsilon_y \gamma_{xy}]^T$ is the vector of corresponding elastic strain components and $\mathbf{D}$ is the elasticity matrix having the form

$$\mathbf{D} = \frac{E}{1-\upsilon^2} \begin{bmatrix} 1 & \upsilon & 0 \\ \upsilon & 1 & 0 \\ 0 & 0 & (1-\upsilon)/2 \end{bmatrix} \tag{9}$$

in isotropic conditions. E and υ stands for the Young's modulus and the Poisson's ratio of the material, respectively. The strains induced by displacements can be calculated using formulas

$$\varepsilon_x = \frac{\partial u}{\partial x} - \varepsilon_{0,x} \tag{10}$$

$$\varepsilon_y = \frac{\partial v}{\partial y} - \varepsilon_{0,y}$$

$$\gamma_{xy} = \frac{\partial u}{\partial y} + \frac{\partial v}{\partial x}$$

where u and v are the displacement functions along the x- and y-axis, respectively; $\varepsilon_{0,x}$ and $\varepsilon_{0,y}$ are the initial strains in x- and y-direction, respectively.

Boundary conditions which are valid on specific parts of the boundary of the solution domain are

$$\mathbf{u} = \bar{\mathbf{u}} \tag{11a}$$

or

$$\sigma_x \cos(nx) + \tau_{xy} \cos(ny) = \bar{T}_x \tag{11b}$$

$$\tau_{xy} \cos(nx) + \sigma_y \cos(ny) = \bar{T}_y$$

where $\mathbf{u} = [u \ v]^T$ is the vector of unknown displacement functions, the bar above the symbol indicates prescribed value, cos(nx) and cos(ny) are the direction cosines of the normal to the boundary and $\bar{T}_x$ and $\bar{T}_y$ are the traction components.

ERRORS IN THE FEM SOLUTION

The linear equation system whose solution gives the approximate nodal values for the unknown function is often obtained applying the minimum principle of the total potential energy or the Galerkin method in the displacement based finite element methods. These solutions fulfill the displacement continuity conditions to a certain degree between the elements, the over-all equilibrium conditions are satisfied at global and at element levels as well. The pointwise satisfaction of the equilibrium equations (1), (6) and (7) are not generally guaranteed. The normal component of the flux vector by Eq. (5a) and the stress field calculated using Eq. (8) is generally discontinuous across the common element interfaces. Displacement boundary conditions (5c) and (11a) can be assumed to be exactly satisfied.

Errors in field problems

Substituting the approximate solution for the element

$$\phi = \mathbf{N}\mathbf{a}^e \tag{12}$$

where **N** is the row vector of shape functions utilized to describe the behaviour of the unknown function ϕ and $\mathbf{a}^e$ is the column vector of degrees of freedom associated with each shape function, into Eq. (3) and (4), we get

$$-\left(k_x \frac{\partial^2 \mathbf{N}}{\partial x^2} + k_y \frac{\partial^2 \mathbf{N}}{\partial y^2}\right) \mathbf{a}^e + Q = r^e \tag{13}$$

where the material properties were assumed to be constants over the elements. r^e of Eq. (13) describes the pointwise error in the domain of element e. Integrating the absolute value of r^e over the volume V_e of the element e we obtain

$$e^e = \int_{V^e} |r^e| dV \tag{14}$$

which is a measure of the error of FEM solution over the element e.

The jump in the value of normal flux along the interelement boundaries ij between elements e_1 and e_2 can be evaluated using Eq. (5a)

$$j_q^{ij} = - k_{n2} h_2 \frac{\partial \mathbf{N}}{\partial n} \mathbf{a}^{e2} + k_{n1} h_1 \frac{\partial \mathbf{N}}{\partial n} \mathbf{a}^{e1} \tag{15}$$

where h_1, h_2, k_{n1} and k_{n2} are the thicknesses and material properties of the elements e_1 and e_2, respectively. The direction of the normal can be chosen to be outwards with respect to the element e_1. a^{e1} and a^{e2} are the values of the degrees of freedom for element e_1 and e_2, respectively. Integrating the jump over the common interface we obtain

$$e_q^{ij} = \int_{ij} | j_q^{ij} | dS \tag{16}$$

which measures the erroneous discontinuity of the normal flux.

Errors in plane stress problems

Substituting the displacement field obtained for the element e in the Eq. (10), which are further inserted in Eq. (8), we get the stress field in a point under examination

$$\hat{\sigma} = \mathbf{D}\mathbf{B}\mathbf{a}^e - \sigma_o \tag{17}$$

where **B** is the strain-displacement matrix $\varepsilon = \mathbf{B}\mathbf{a}^e - \varepsilon_o$ and σ_o is the initial stress vector. Putting these approximate stresses in the equilibrium equations (6) and (7) we get

$$\frac{\partial \hat{\sigma}_x}{\partial x} + \frac{\partial \hat{\tau}_{xy}}{\partial y} + b_x = r_x^e$$

$$\frac{\partial \hat{\tau}_{xy}}{\partial x} + \frac{\partial \hat{\sigma}_y}{\partial y} + b_y = r_y^e \tag{18}$$

where $r_x{}^e$ and $r_y{}^e$ represent unbalance in x- and y-direction. Integrating the absolute values of these unbalance terms over the volume V_e of the element e we obtain

$$e_x^e = \int_{V^e} |r_x^e| dV$$

$$e_y^e = \int_{V^e} |r_y^e| dV \tag{19}$$

which measure the errors within each element.

Erroneous jumps in stress field across the interelement boundaries ij can be evaluated as follows: calculate the stress components at each point of the boundary ij using Eq. (17) for both elements, then transform these stress components into normal and tangential components, see Fig. (1), and finally integrate the absolute values of the thickness weighted stress differences over the area of the boundary, we get

$$e_\sigma^{ij} = \int_{ij} |\hat{\sigma}_n^{e1} h_1 - \hat{\sigma}_n^{e2} h_2| dS$$
$$e_\tau^{ij} = \int_{ij} |\hat{\tau}_s^{e1} h_1 - \hat{\tau}_s^{e2} h_2| dS \qquad (20)$$

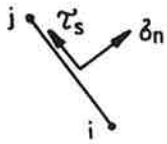

FIGURE 1. Normal and tangential stress component on the boundary ij

ELEMENT SHAPE FUNCTIONS

The unknown function $u(\xi,\eta)$ within each element is approximated using formula

$$u(\xi,\eta) = \sum_{i=1}^{m} N_i(\xi,\eta) a_i + \sum_{i=m+1}^{m+k} N_i a_i + \sum_{i=m+k+1}^{m+k+1} N_i a_i \qquad (21)$$

in which the shape functions N can be grouped in three classes. The first class consists of the shape functions of the basic element, i=1...m, where m=4 or m=8 for the 4- or 8-noded isoparametric element. The second class, i=m+1...m+k, are edge modes defined below. The third class, i=m+k+1...m+k+1, includes bubble modes which are also defined below. In Eq. (21) a_i, i=1...m, are the approximate nodal values of the unknown function, parameters a_i, i=m+1...m+k+1, indicate the participation factor of each hierarchical shape to the solution. One possible choice for the hierarchical edge modes uses functions which are defined as an integral of the Legendre's polynomial

$$P_n(\xi) = \int_{-1}^{\xi} L_{n-1}(x) dx, \qquad (22)$$

where

$$L_n(x) = \frac{1}{2^n n!} \frac{d^n}{dx^n} ((x^2-1)^n) \qquad (23)$$

is the Legendre's polynomial of order n, where $n > 1$ or $n > 2$ for the 4-noded or 8-noded elements, respectively. Edge modes of order n for each of the four edges of the 4- or 8-noded isoparametric element are

$$N_j (\xi,\eta) = P_n(\xi) P_o(\eta) \qquad (24a)$$

$$N_{j+1} (\xi,\eta) = P_1(\xi) P_n(\eta) \qquad (24b)$$

$$N_{j+2} (\xi,\eta) = P_n(\xi) P_1(\eta) \qquad (24c)$$

$$N_{j+3} (\xi,\eta) = P_o(\xi) P_n(\xi) \qquad (24d)$$

where

$$P_o(\xi) = (1-\xi)/2 \quad \text{and} \quad P_1(\xi) = (1+\xi)/2$$

Bubble modes can be defined by

$$N_k(\xi,\eta) = \xi^i \eta^j (1-\xi^2)(1-\eta^2) \tag{25}$$

where i and j are non-negative integers.
Figure 2 depicts the 4th order edge mode

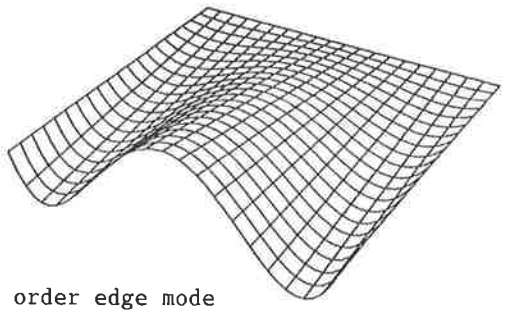

FIGURE 2. 4th order edge mode

ABOUT THE REFINEMENT STRATEGY

The errors are uniformly distributed in the optimal models. So the average errors are computed in field problems using Eq. (14) and (16)

$$E = (\sum_{e=1}^{N} e^e)/N \tag{26a}$$

and

$$J = (\sum_{1}^{M} e_q^{ij})/M \tag{26b}$$

where N is the total number of the elements and M is the number of edges in the model. Similar average errors for plane stress problems are obtained using Eq. (19) and (20)

$$E = \max \left(\frac{1}{N}\sum_{e=1}^{N} e_x^e \;,\; \frac{1}{N}\sum_{e=1}^{N} e_y^e\right) \tag{27a}$$

and

$$J = \max \left(\frac{1}{M}\sum_{1}^{M} e_\sigma^{ij} \;,\; \frac{1}{M}\sum_{1}^{M} e_\tau^{ij}\right) \tag{27b}$$

The dimension of the terms (26a), (26b) and (27a), (27b) is energy/time and force, respectively. This makes it possible to estimate magnitude of these errors comparing them to the energy/time fed into the model in field problems and to the absolute value of the largest reaction force component in stress problems. The new degrees of freedom are added using the following strategy: the average errors (26a) and (26b) or (27a) and (27b) being less than a certain percentage of the above mentioned reference value the solution is assumed to have a desired accuracy. Otherwise the next higher hierarchical edge mode, (24a)...(24d), is added (depending on the edge) to each 'perpendicular' edge to the boundary where errors exceed the preassigned percentage of the reference value. The unbalances in the equilibrium equations (14) or (19) exceeding the same limit cause the bubble modes (25) to be added to the appropriate elements.

EXAMPLES

Example 1

As a first example we consider an one-dimensional heat conduction problem of Fig. 3. Heat is generated with a rate Q=1 W/m³ in elements 7-10 and the temperature = 1 °C is prescribed at x=3. All the other surfaces except x=3 are insulated. The original FEM-solution with 4-noded elements gives piecewise linear solution with exact nodal values (supercon-vergence). Analytic solution is T=2.12 between x=0 and x=1.2, parabolic between x=1.2 and 2.0, linear from value T=1.8 at x=2.0 to value T=1. at x=3, see Fig. 4. According to the Eq. (16) and (14) there is jump error = 0.02 W on boundaries 13-14 and 21-22 and jump error = 0.04 W on boundaries 15-16, 17-18 and 19-20 and unbalance = 0.04 W in elements 7-10, see Fig. 5. Following the refinement strategy presented second order edge modes are added to the edges shown with * in Fig. 6 and bubble mode $(1-\xi^2)(1-\eta^2)$ is also added to the elements 7-10 shown with K1 in Fig. 6. With these refinements the exact analytical solution is obtained.

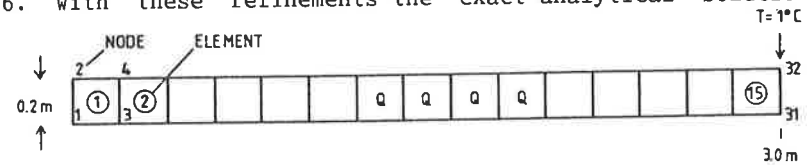

FIGURE 3. Finite element mesh for the original FEM-solution. Thermal conductivities are: $k_x=k_y=1$ W/m/°C

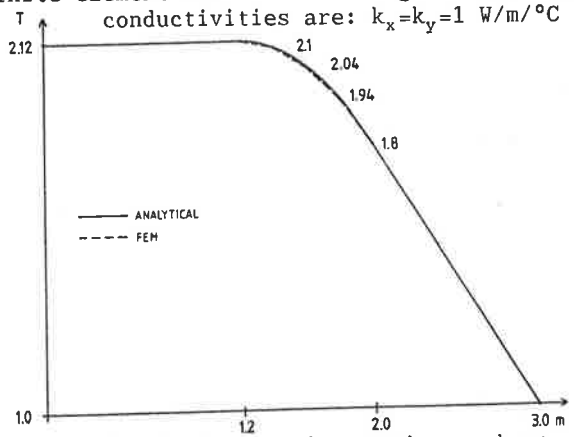

FIGURE 4. Analytical solution to the stationary heat conduction problem = solid line; original FEM-solution = broken line

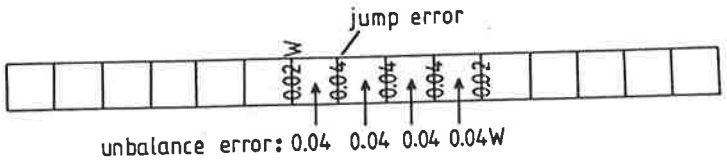

FIGURE 5. Errors in the original FEM-solution. The dimension of the error is W

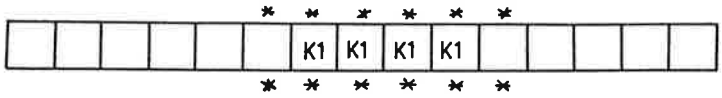

FIGURE 6. Hierarchical modes added to the original FEM-solution. One * means 2nd order edge mode, K1 indicates the bubble mode $(1-\xi^2)(1-\eta^2)$

Example 2
As a second example we consider a cantilever beam shown in Fig 7.

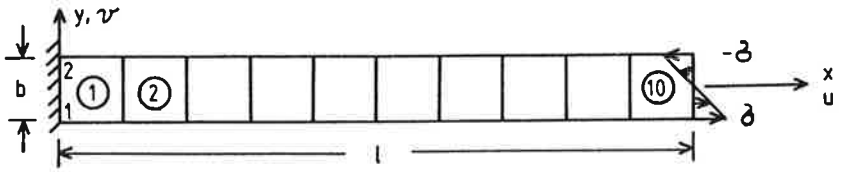

FIGURE 7. Finite element mesh for the cantilever beam subject to bending moment M at the free end. $E=3.0*10^7$ kN/m^2, $\upsilon=0.3$, M=0.15 kNm (σ=3000 kN/m^2), b=0.1 m, l= 1.0 m and thickness of the elements h = 0.03 m.

Analytical solution to the problem is $u(x,y) = -(M/EI)xy$, $v(x,y) = (M/EI)(x^3-\upsilon y^2)/2$, $M(x) = M$ and $Q(x) = 0$, where I is the moment of inertia $= hb^3/12$, M(x) and Q(x) are the bending moment and shear force distributions along the beam. The original FEM-solution using standard isoparametric 4-noded plane stress element is shown in Table 1

TABLE 1 Results of the cantilever beam

	Analytical	Original FEM	With 2nd order edge mode and one bubble	With 6th order edge modes and one bubble
u_{tip}	$1.0000*10^{-4}$	$0.6741*10^{-4}$	$0.9987*10^{-4}$	$0.9992*10^{-4}$
v_{tip}	$0.9993*10^{-3}$	$0.6741*10^{-3}$	$0.9979*10^{-3}$	$0.9990*10^{-3}$
σ_x	3000.	2222.	3000. *)	3000. *)
σ_y	0.	667.	0. *)	0. *)
τ_{xy}	0.	778.	0. *)	0. *)

*) in elements 5-10. Corresponding values for the elements 1-4 differ slightly from these due to the support conditions of the model. u_{tip} is the axial displacement at the free end on its lower surface y=-0.05, σ_x is the axial stress at the same point.

The stress distributions obtained using standard isoparametric 4-noded elements are shown in Fig. 8. The error analysis reveals errors shown in Fig. 9. After adding 2nd order edge modes to the boundaries indicated with at least with one * in Fig. 10. The solution after giving freedom to use edge modes up to 6th order and bubble modes b_0, ξb_0, ηb_0 and $\xi^2 b_0$, where $b_0=(1-\xi^2)*(1-\eta^2)$, uses modes shown in Fig. 10. The need of higher order polynomials in the vicinity of the support is due to the displacement boundary conditions used: u and v fixed, which are different from the analytical solution : u, v and dv/dx zero at (x,y)=(0,0).

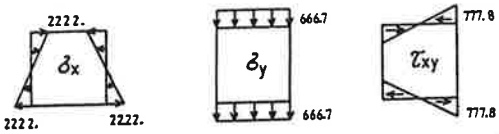

FIGURE 8. Original FEM-solution for stresses in each element

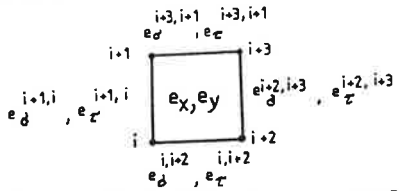

FIGURE 9. Errors in the original FEM-solution evaluated according to the Eq. (20) and (19) are identical for each element. Jump errors are $e_\sigma^{i,i+2}=e_\sigma^{i+3,i+1}=667*0.1*0.03=2.0$ kN, $e_\sigma^{i+2,i+3}=e_\sigma^{i+1,i}=0.$, $e_\tau^{i,i+2}=e_\tau^{i+3,i+1}=2*(0.577*778)*0.1/2*003=1.35$kN (approximate) (1.17=exact), $e_\tau^{i+2,i+3}=e_\tau^{i+1,i}=2*778*0.1*0.03=4.67$ kN and unbalance errors $e_x^{\circ}=0$, $e_y^{\circ}=(2*778/0.1+2*667/0.1)*0.1*0.1*0.03=8.67$ kN

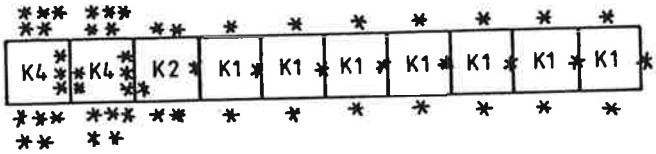

FIGURE 10. Hierarchical modes used in the refined solution, number of stars indicates the order of the edge mode used: one star = 2nd order polynomial, two stars = 3rd order etc.; K1 = one bubble mode, K2 = two bubble modes etc.

Example 3

As a third example we consider a thick pressurized tube. FEM-model of one quadrant of the unit thickness slice of the tube is shown in Fig. 11.

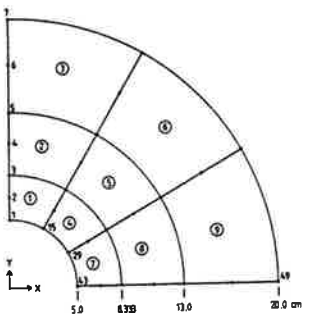

FIGURE 11. Thick tube. Internal pressure p=10 kN/cm^2. Symmetrical boundary conditions on the horizontal and vertical boundaries. E=10000 kN/cm2 and υ=0.3. Because only plane stress elements are available the plane strain can be simulated inputting value $E/(1-\upsilon^2)$ for the Young's modulus and value $\upsilon/(1-\upsilon)$ for the Poisson's ratio.

Original FEM-solution using the 4-noded elements, analytical solution and the two refined solutions are shown in Fig. 12.

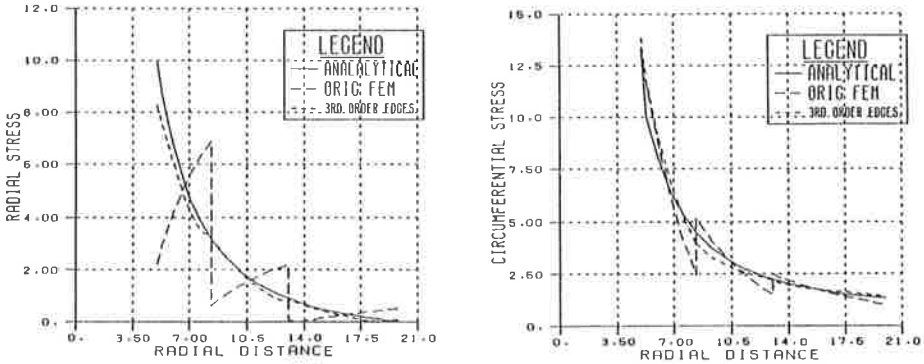

FIGURE 12. Radial and tangential stress distribution for the thick tube subject to internal pressure. Results for the refinement: up to 3rd order edge modes are used and no bubble modes, are also shown

Fig.13 represents the results using 8-noded elements.

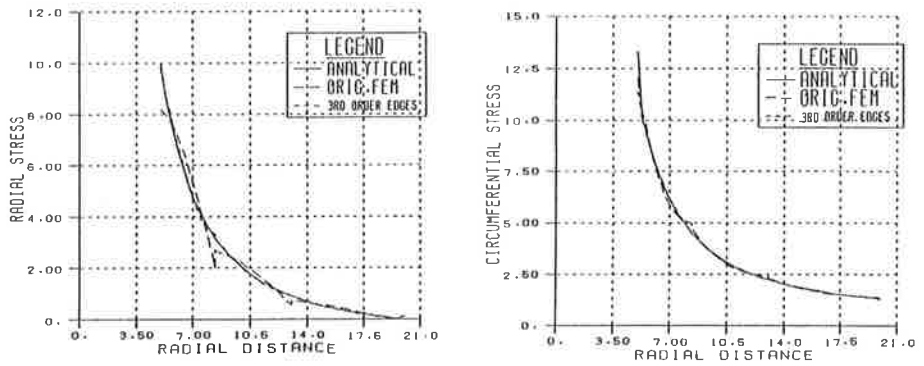

FIGURE 13. As in Figure 12, but 8-noded isoparametric elements are used

CONCLUSIONS

An a posteriori error analysis system have been devised which can adaptively refine the original FEM-solution. At present the linear equation system containing hierarchical degrees of freedom are solved by a direct method, frontal solution technique. To improve the solution efficiency some iteration procedure could be used. The refinement strategy can also be improved by calculating some quantity with which we can decide beforehand which hierarchical modes reduce error most effectively. The ideas presented in the paper can also be extended to the plate in bending problems.

REFERENCES

1. Babuska I. and Rheinboldt W.C, A-Posteriori Error Estimates for the Finite Element Method. Int.J.num.Meth.Engng, Vol 12, 1978, pages 1597-1615

2. Zienkiewicz O.C., J.P de S.R Gago and Kelly D.W, The Hierarchical Concept in Finite Element Analysis. Computers & Structures, Vol 16, 1983, pages 53-65

3. Kelly D.W, J.P de S.R. Gago and Zienkiewicz O.C, A Posteriori Error Analysis and Adaptive Processes in the Finite Element Method: Part I Error Analysis, Part II- Adaptive Mesh Refinement. Int.J.num.Meth. Engng, Vol 19, 1983, pages 1593-1619 and 1621-1656

4. Ainsworth M, Zhu J.Z, Craig A.W and Zienkiewicz O.C, Analysis of the Zienkiewicz-Zhu A-Posteriori Error Estimator in the Finite Element Method. Int.J.num.Meth.Engng, Vol 28, 1989, pages 2161-2174

5. Zienkiewicz O.C, Zhu J.Z and Gong N.G, Effective and Practical h-p-Version Adaptive Analysis Procedures for the Finite Element Method. Int.J.num.Meth.Engng, Vol 28, 1989, pages 879-891

A NEW NONCONFORMING FINITE ELEMENT METHOD FOR INCOMPRESSIBLE ELASTICITY

Rolf Stenberg
Faculty of Mechanical Engineering
Helsinki University of Technology
Djebar Baroudi
Laboratory of Fire Technology
Technical Research Centre of Finland
02150 Espoo, Finland

ABSTRACT

We present a new nonconforming method for the plain strain problem. In the element a continuous piecewise linear approximation is used for one component of the displacement whereas the other components is approximated with piecewise linear functions continuous only at midpoints of element edges. For this method we can show that it does not lock in the incompressible limit.

INTRODUCTION

In the pioneering work by Crouzeix and Raviart [1] it was shown that an optimally convergent method for the Stokes equations is obtained by using a triangular mesh with a piecewise constant approximation for the pressure combined with linear nonconforming approximations for both components of the velocity. This method has however not become very popular, probably due to high number of degrees of freedom.
For conforming methods it easy to see that a stable Stokes element will give an element for the plain strain elasticity problem that will not lock in the incompressible limit; cf. e.g. [2]. In the case of the linear nonconforming element of Crouzeix and Raviart the situation is different. The corresponding plain strain element, with the pressure locally eliminated, would give a displacement method with nonconforming approximations for both component of the displacement. It is easy to see (cf. [2, pp. 250-251]) that in that method spurious mechanisms can occur and hence the method is not of practical use.
Let us also recall that the standard conforming linear element locks in the incompressible limit.
In this paper we present a linear element suffering from neither locking nor mechanisms. The idea is simple: one uses conforming elements for one of the displacement component and conforming for the other.
This element can combined with a piecewise pressure also be used for the Stokes problem and compared with the method of Crouzeix-Raviart it has the advantage that the number of degrees of freedom is considerably reduced.

THE ELEMENT

We consider the plain strain problem: Find the displacement $\mathbf{u} = (u_1, u_2)$ minimizing the energy of the linearly elastic body, i.e.

$$E(\mathbf{u}) = \min_{\mathbf{v} \in \mathbf{V}} E(\mathbf{v})$$

with

$$E(\mathbf{v}) = \int_\Omega \left[\mu\, \varepsilon_{ij}(\mathbf{v})\, \varepsilon_{ij}(\mathbf{v}) + \frac{\lambda}{2} (\varepsilon_{ii}(\mathbf{v}))^2 \right] d\Omega - \int_\Omega f_i\, v_i\, d\Omega - \int_{\Gamma_t} g_i\, v_i\, d\Gamma,$$

where the summation convention is used. $\mathbf{f} = (f_1, f_2)$ is the given body force, $\mathbf{g} = (g_1, g_2)$ the traction acting along the part Γ_t of the boundary of the region Ω originally occupied by the body. μ and λ are the Lamé parameters and $\mathbf{V}$ is the set of kinematically admissible displacements

$$\mathbf{V} = \{\ \mathbf{v} \mid \mathbf{v}_{|\Gamma_d} = (u_{0,1}, u_{0,2}),\ E(\mathbf{v}) < \infty\ \},$$

i.e. the displacement is fixed along the other part Γ_d of the boundary. $\boldsymbol{\varepsilon} = \{\varepsilon_{ij}\}$ is the strain tensor.
Let us now define our method. We introduce a triangulation $\mathcal{T}_h$ of $\bar{\Omega}$ and seek the approximate displacement from $\mathbf{V}_h = \mathrm{V}_{1,h} \times \mathrm{V}_{2,h}$, with

$$\mathrm{V}_{1,h} = \{\ v \mid v \text{ is linear in every triangle of } \mathcal{T}_h, \text{continuous at midpoints of interelement boundaries and equal to } u_{0,1} \text{ at midpoints of element edges lying on } \Gamma_d\ \},$$
$$\mathrm{V}_{2,h} = \{\ v \mid v \text{ is continuous in } \Omega,\ \text{linear in every triangle of } \mathcal{T}_h \text{ and equal to } u_{0,2} \text{ on } \Gamma_d\ \}.$$

The degrees of freedom for this element are the following: The values of the first displacement component at the midpoints of the edges and the values of the second component at the vertices of the triangle. Note that the element stiffness matrix is easily obtained from that of the standard "constant strain triangle" by a simple change of the degrees of freedom.
The approximation is then obtained from the condition

$$E_h(\mathbf{u}_h) = \min_{\mathbf{v} \in \mathbf{V}_h} E_h(\mathbf{v})$$

with

$$E_h(\mathbf{v}) = \sum_{T \in \mathcal{T}_h} \int_T \left[\mu\, \varepsilon_{ij}(\mathbf{v})\, \varepsilon_{ij}(\mathbf{v}) + \frac{\lambda}{2} (\varepsilon_{ii}(\mathbf{v}))^2 \right] d\Omega - \int_\Omega f_i\, v_i\, d\Omega - \int_{\Gamma_t} g_i\, v_i\, d\Gamma\ .$$

Since the basis functions are discontinous the approximate energy above is defined as the sum over each element. The approximations for the strain and stress tensors must also be defined separately on every triangle T in $\mathcal{T}_h$:

$$\boldsymbol{\varepsilon}_{h|T} = \boldsymbol{\varepsilon}(\mathbf{u}_h)_{|T} \quad \text{and} \quad \boldsymbol{\sigma}_{h|T} = \left(2\mu\, \boldsymbol{\varepsilon}(\mathbf{u}_h) + \lambda\, \varepsilon_{ii}(\mathbf{u}_h)\, \mathbf{I}\right)_{|T}\ .$$

These we compare with the exact strain $\boldsymbol{\varepsilon}$ and stress

$$\boldsymbol{\sigma} = 2\mu\, \boldsymbol{\varepsilon}(\mathbf{u}) + \lambda\, \varepsilon_{ii}(\mathbf{u})\, \mathbf{I}$$

and we can prove the following result.

THEOREM. *There is a positive constant C, independent of the Lamé parameter λ, such that*

$$\|\boldsymbol{\varepsilon} - \boldsymbol{\varepsilon}_h\|_0 + \|\boldsymbol{\sigma} - \boldsymbol{\sigma}_h\|_0 \leq Ch(|\mathbf{u}|_2 + |\boldsymbol{\sigma}|_1). \qquad \blacksquare$$

Here h is the mesh parameter, i.e. the maximum diameter of all triangles in $\mathcal{T}_h$, $\|\cdot\|_0$ denotes the L^2-norm and $|\cdot|_i$, $i = 1, 2$, stand for the Sobolev space seminorms; cf. [2, pp. 266-267].

The above estimate is "optimal", i.e. the convergence rate $\mathcal{O}(h)$ is the best one can obtain using piecewise linear basis functions. Furthermore, the positive constant C is independent of the Lamé parameter λ which means that the method will not lock near incompressibility. Let us recall that in a method that locks one can only get an error estimate with a constant that blows up in the incompressible limit when $\lambda \to \infty$ (i.e. when the Poisson ratio $\nu \to 1/2$).

REMARK. If the domain and boundary conditions are such that the regularity estimate

$$\|\mathbf{u}\|_2 + \|\boldsymbol{\sigma}\|_1 \leq C\|\mathbf{f}\|_0,$$

is valid, then we also have the optimal L^2- estimate for the displacement:

$$\|\mathbf{u} - \mathbf{u}_h\|_0 \leq Ch^2(|\mathbf{u}|_2 + |\boldsymbol{\sigma}|_1). \qquad \blacksquare$$

A NUMERICAL EXAMPLE

We will present some preliminary numerical results for (a slight modification of) a standard test problem simulating a cantilever beam subject to a parabolically varying end shear [2, pp. 219-255]. We choose $\Omega = (0, L) \times (-c, c)$ and let the exact solution be

$$u_1(x_1, x_2) = -\frac{P(1-\nu^2)}{4c^3E}\, x_2 \left\{ 3\big(L^2 - (L - x_1)^2\big) + \Big(\frac{2-\nu}{1-\nu}\Big)(x_2^2 - c^2) \right\},$$

$$u_2(x_1, x_2) = \frac{P(1-\nu^2)}{4c^3E} \left\{ (L - x_1)^3 - L^3 + x_1 \Big(\frac{(4+\nu)c^2}{1-\nu} + 3L^2 \Big) + \Big(\frac{3\nu}{1-\nu}\Big)(L - x_1)\, x_2^2 \right\}.$$

This problem is solved by giving the displacement on $\Gamma_d = \{\ (x_1, x_2) \mid x_1 = 0,\ x_2 \in [-c, c]\ \}$ and the traction along the three other sides. By symmetry only half of the domain is computed. The data employed in the calculations are

$$P = -1, \quad L = 16, \quad c = 2, \quad E = 1, \quad \nu = 0.3 \text{ and } 0.499.$$

We perform the calculations for two meshes. The finer mesh of Figure 1 is obtained by first dividing the domain into 4×8 rectangles and then subdividing each rectangle into two triangles. With this mesh the number of degrees of freedom is 153.

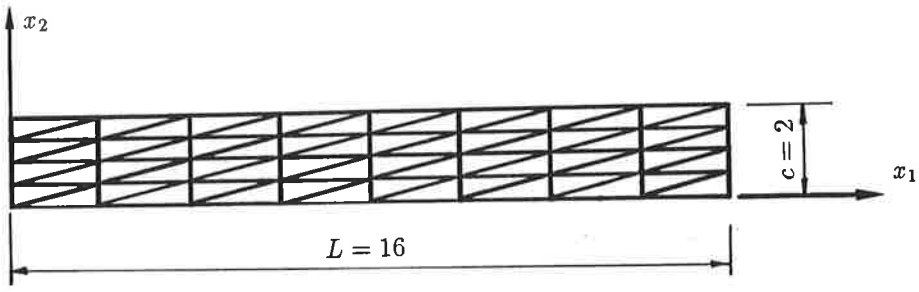

FIGURE 1

The coarser mesh of Figure 2 gives 99 degrees of freedom.

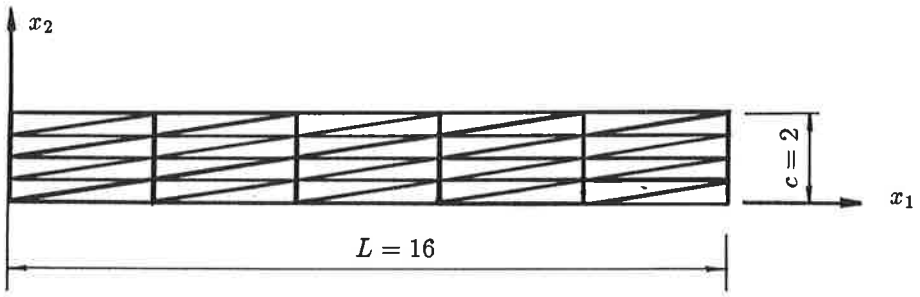

FIGURE 2

In Table 1 we present the normalized vertical tip displacement (i.e. at the point $(L, 0)$) for the two meshes and two values of the Poisson ratio. For comparision we quote the results given in [2, p. 221] obtained for the standard bilinear quadrilateral element with full and selective integration. The mesh for these elements is a 4×8 quadrilateral mesh i.e. the rectangular mesh in Figure 1. The number of degrees of freedom are in this case 90 and should therefore be compared to the results of our method with the mesh of Figure 2.

Method	Degrees of freedom	$\nu = 0.3$	$\nu = 0.499$
Nonconforming, Figure 1	153	1.023	1.021
Nonconforming, Figure 2	99	1.035	1.031
Quadrilateral, full integration [2]	90	0.904	0.334
Quadrilateral, selective integration [2]	90	0.912	0.937

TABLE 1. Normalized tip displacement for plain strain beam

These results show that the present method does not lock and in addition that it is competitive with the selectively integrated quadrilateral element.

REMARK. It is perhaps not entirely correct to compare our results with those given in [2], since there the boundary conditions where given by the symmetry condition, the traction along the rest of the boundary and three displacement components at two corners. With our nonconforming basis functions the corner value of the nonconforming displacement component is not so easily prescribed and hence we have chosen the alternative above. However, the tendency for a method to lock increases when more boundary displacements are fixed. Hence, there is no reason to believe that the results for the quadrilateral methods would be better when the diplacement is assigned on Γ_d. It should also be noted that to prescribe the displacement at a finite number of points is not variationally correct. ■

REFERENCES

1. Crouzeix, M., Raviart, P.A.: Conforming and nonconforming finite element methods for solving the stationary Stokes equations. RAIRO Anal. Numér., R-3 (1973) 33-76
2. Hughes, T.J.R.: The Finite Element Method: Linear Static and Dynamic Analysis. Prentice-Hall 1987

ON SOME BILINEAR ELEMENTS FOR REISSNER-MINDLIN PLATES

Rolf Stenberg and Teemu Vihinen
Faculty of Mechanical Engineering
Helsinki University of Technology
02150 Espoo, Finland

ABSTRACT

We discuss three simple bilinear quadrilateral plate bending elements: the selectively-reduced integrated element, the MITC4 element of Bathe-Dvorkin and a new modification to this. We show by numerical examples that the two first methods suffer from certain deficiences which are removed in our modification of the MITC4 element. The numerical examples confirm the results of the numerical analysis of the methods.

INTRODUCTION

Let us recall the Reissner-Mindlin formulation of the bending of a plate. The basic unknowns are the deflection w and the rotation $\boldsymbol{\beta}$ determined from the condition that they minimize the energy, i.e. $(w, \boldsymbol{\beta})$ satisfy

$$E(w,\boldsymbol{\beta}) = \min_{(v,\boldsymbol{\psi})\in\mathcal{K}_{ad}} E(v,\boldsymbol{\psi}), \tag{1}$$

with the energy defined as

$$\begin{aligned} E(v,\boldsymbol{\psi}) = \frac{t^3}{2}a(\boldsymbol{\psi},\boldsymbol{\psi}) + \frac{G\kappa t}{2}\int_\Omega |\boldsymbol{\psi}-\nabla v|^2\, d\Omega - \int_\Omega g\, v\, d\Omega \\ + \int_{\Gamma_M} \mathbf{M}\cdot\boldsymbol{\psi}\, d\Gamma - \int_{\Gamma_S} Q\, v\, d\Gamma. \end{aligned} \tag{2}$$

Here Ω is the region occupied by the plate, g is the applied load, t is the thickness of the plate, G is the shear modulus and κ is the "shear correction factor". The bending energy is given by the bilinear form

$$a(\boldsymbol{\beta},\boldsymbol{\psi}) = \frac{E}{12(1-\nu^2)}\int_\Omega [(1-\nu)\,\boldsymbol{\varepsilon}(\boldsymbol{\beta}):\boldsymbol{\varepsilon}(\boldsymbol{\psi}) + \nu\ \mathrm{div}\,\boldsymbol{\beta}\ \mathrm{div}\,\boldsymbol{\psi}]\, d\Omega, \tag{3}$$

where E and ν denote the Young modulus and Poisson ratio, respectively. The kinematically admissible deflections and rotations are denoted by $\mathcal{K}_{ad}$. On the boundary parts Γ_M and Γ_S the moment $\mathbf{M}$ and normal shear force Q are prescribed, respectively. We recall that the shear force of the plate is given by

$$\mathbf{Q} = G\kappa t(\boldsymbol{\beta} - \nabla w). \tag{4}$$

The problem in the analysis and design of finite element methods the critical issue is the behaviour of the element for "thin" plates. Hence, one usually studies the problem where the applied load and prescribed boundary moment and normal shear force all are proportional to t^3, i.e.

$$f = t^3 \bar{f}, \qquad \mathbf{M} = t^3 \bar{\mathbf{M}}, \qquad Q = t^3 \bar{Q}, \tag{5}$$

with $\bar{f}$, $\bar{\mathbf{M}}$ and $\bar{Q}$ independent of t. This ensures that the exact problem has a finite limit solution when $t \to 0$, cf. [1]. Below we will also make this assumption. In an analysis it is also useful to introduce the scaled shear force $\mathbf{q} = t^{-3}\mathbf{Q}$ and the following Helmholtz decomposition of it (cf. [4])

$$\mathbf{q} = \nabla r + \mathbf{rot}\, p\ . \tag{6}$$

In the next section we will define the three finite element methods and recall what is known about their performance. The last section is devoted to our numerical examples.

THE FINITE ELEMENT METHODS

In all three methods the standard isoparametric bilinear elements are used for both components of the rotation and the deflection, i.e. we use the space

$$\mathcal{K}_{ad}^h = \{\ (v,\psi) \in \mathcal{K}_{ad} \mid (v,\psi)_{|K} \in [Q_1(K)]^3\ \forall K \in \mathcal{C}_h\ \} \tag{7}$$

where $\mathcal{C}_h$ denotes the partitioning of the domain into quadrilaterals.
In the first method we minimize the following energy expression in $\mathcal{K}_{ad}^h$:

$$\begin{aligned} E_h(v,\psi) = \frac{t^3}{2} a(\psi,\psi) + \frac{G\kappa t}{2} \int_\Omega |\mathbf{R}_h(\psi - \nabla v)|^2\ d\Omega - \int_\Omega g\, v\ d\Omega \\ + \int_{\Gamma_M} \mathbf{M}\cdot\psi\ d\Gamma - \int_{\Gamma_S} Q\, v\ d\Gamma, \end{aligned} \tag{8}$$

with the reduction operator $\mathbf{R}_h$ defined from

$$(\mathbf{R}_h\psi)_{|\text{element}} = \text{ value of } \psi \text{ at the midpoint of the element.} \tag{9}$$

The approximate shear force is calculated from

$$\mathbf{Q}_h = G\kappa t\, \mathbf{R}_h(\boldsymbol{\beta} - \nabla w). \tag{10}$$

This means that an selective reduced integration (SRI) is used; the bending energy is calculated with the 2×2 Gauss rule and the shear term with one point quadrature. We will refer to the element as "SRI".
This element is presented in most recent textbooks on finite elements such as [6,7]. However, the element is usually not recommended without restrictions. It is well known that the approximation obtained for the deflection can be bad, see e.g. the "pergola roof" example (p. 334) and Fig. 5.3.20 of [7]. Another problem with the element is that it can give rise to a highly oscillating (non-physical) shear. This seems to be widely known although not explicitely stated in the literature until quite recently [10].

From a theoretical point of view the problems with this element is not surprising. An analysis shows directly, that in general the method cannot converge optimally. However, if the plate is clamped along the boundary and if rectangular elements are used, then it is possible [9] to derive the following error estimate for the method:

$$\|\nabla w - \nabla w_h\|_0 + \|\nabla \boldsymbol{\beta} - \nabla \boldsymbol{\beta}_h\|_0 \leq Ch(\|w\|_5 + \|\boldsymbol{\beta}\|_4 + \|\mathbf{q}\|_1), \tag{11}$$

Here $(w_h, \boldsymbol{\beta}_h)$ denotes the finite element solution and h denotes the mesh parameter. Above we have used the standard notation for Sobolev space norms (cf. e.g. [5,7]) and in particular $\|\cdot\|_0$ denotes the L^2-norm, i.e.

$$\|\boldsymbol{\psi}\|_0^2 = \int_\Omega |\boldsymbol{\psi}|^2 \, d\Omega. \tag{12}$$

It should be pointed out the positive constants C in the error estimates in this paper are all independent of the thickness t, which shows that the methods do not "lock". It should be remarked that the above estimate is far from optimal since it requires considerable smoothness of the exact solution (compare with the optimal estimate (16) below). Furthermore, the analysis given in [9] shows that the convergence is a consequence of the assumptions of rectangular elements; for general quadrilaterals the method will not converge. This we will below show numerically.

A considerable improvement over the SRI element is the MITC4 element introduced by Bathe and Dvorkin [3]. (This element is very similar to both the T1 element of Hughes and Tezduyar [7] and MacNeals QUAD4 element [11].) The element differs from the SRI in the way the reduction operator is defined. For simplicity we will here only define it in case of rectangular elements and refer to [3] for the general definition using covariant interpolation. For an element $K \in \mathcal{C}_h$ we introduce the space

$$\boldsymbol{\Gamma}_K = \{\ \mathbf{s} = (s_1, s_2) \mid s_1 = a_1 + b_1 y,\ s_2 = a_2 + b_2 x\ \} \tag{13}$$

and define $\mathbf{R}_h \mathbf{s}_{|K} \in \boldsymbol{\Gamma}_K$ through

$$\int_T \left[(\mathbf{R}_h \mathbf{s} - \mathbf{s}) \cdot \boldsymbol{\tau}\right] ds = 0 \quad \text{for every edge } T \text{ of } K. \tag{14}$$

The method is then defined from

$$E_h(w_h, \boldsymbol{\beta}_h) = \min_{(v,\psi) \in \mathcal{K}_{ad}^h} E_h(v, \boldsymbol{\psi}), \tag{15}$$

with E_h as defined in (8) and the above reduction operator. The shear force is then calculated from (10).

The full numerical analysis of this method has not yet been carried out. Only the case of rectangular elements have been considered [1,2]. The analysis of [1,2] show that the method is closely connected to the well known $Q_1 - P_0$ element for the Stokes problem. Hence, anticipating an analysis where the results of [4] and [13] would be combined it seems likely that the case when the mesh $\mathcal{C}_h$ is obtained by uniformly dividing a coarser quadrilateral mesh into 4×4 elements (see [13] for the details) can be handled. This would give the following estimate

$$\|\nabla w - \nabla w_h\|_0 + \|\nabla \boldsymbol{\beta} - \nabla \boldsymbol{\beta}_h\|_0 \leq Ch(|w|_2 + |\boldsymbol{\beta}|_2 + |r|_2 + |p|_1 + t\,|p|_2) \tag{16}$$

However, it is well known that for the Stokes problem the pressure obtained with the $Q_1 - P_0$ method does not converge in general. Hence the analysis of the Stokes problem given in [13] will not give any useful estimate for the shear. For the Stokes problem it is, however, known that a certain filtering (cf. [13]) will produce a convergent pressure, but it is not clear how this filtering should be carried over to a possible filtering of the shear. These theoretical results are in accordance with some recent numerical calculations which show that the MITC4 can give rise to an oscillating shear. In the next section we will give some further numerical evidence on this.
Next, let us turn to our modification of the MITC4 method. We still use the same finite element spaces but we modify the energy expression to be the following

$$E_h(v,\boldsymbol{\psi}) = \frac{t^3}{2}a(\boldsymbol{\psi},\boldsymbol{\psi}) + \frac{G\kappa t^3}{2(t^2+\alpha h^2)}\int_\Omega |\mathbf{R}_h(\boldsymbol{\psi}-\nabla v)|^2\, d\Omega - \int_\Omega g\, v\, d\Omega + \int_{\Gamma_M} \mathbf{M}\cdot\boldsymbol{\psi}\, d\Gamma - \int_{\Gamma_S} Q\, v\, d\Gamma\,, \tag{17}$$

where α is a positive constant. The approximation for the shear force is then obtained from

$$\mathbf{Q}_h = \frac{G\kappa t^3}{(t^2+\alpha h^2)}\,\mathbf{R}_h(\boldsymbol{\beta}-\nabla w). \tag{18}$$

Below this element will be referred to by "STAB". This method is an example of a recent stabilization technique for mixed finite element approximations. In connection with Reissner-Mindlin plates this approach was first proposed in [12] and [8], but in those papers it was required that the approximation for the deflection is one degree higher than the approximation for the rotation. To obtain equal order approximations is more difficult. In [4] we, however, proposed and analyzed a triangular element with linear approximations for both the deflection and the rotation. The above element is the quadrilateral analog to this. Again it seems more than likely that the analysis of [4] can be carried out for this element as well. This would lead to the estimate (16), with the difference that it would now be valid for an arbitrary regular (in the usual sense, cf. [5]) quadrilateral mesh. Another difference to the original MITC4 is that we now also get an estimate for the shear force, cf. [4]:

$$\|\mathbf{Q}-\mathbf{Q}_h\|_0 \le Ct^3(|w|_2 + |\boldsymbol{\beta}|_2 + |r|_2 + |p|_1 + t\,|p|_2). \tag{19}$$

We see that we can only show that the the shear force is bounded in the L^2-norm, and hence it does not necessarily converge. Numerical results also support this; the L^2 convergence rate can wary depending on the smoothness of the solution. However, we should emphasize that for the preceeding two methods, SRI and MITC4, one cannot prove this estimate and hence it is expected that of the three methods the last one will give the best shear. This we will also show by numerical examples.

COMPUTATIONAL EXAMPLES

To show the defiences with the SRI and MITC4 elements it is suffient to consider a very simple test problem: a clamped square Kirchhoff plate (i.e. the limit solution obtained when $t \to 0$) with a uniform load. In the calculations we choose the side length of the plate equal to unity and we use the symmetry and discretize only one square of the

plate. We have chosen $\nu = 0.3$, $t = 0.01$ (since we consider the Kirchhoff solution the thickness used in the calculations act as a penalty parameter) and $\alpha = 0.1$. First we consider a finite element partitioning of $N \times N$ equal squares, see the figure below.

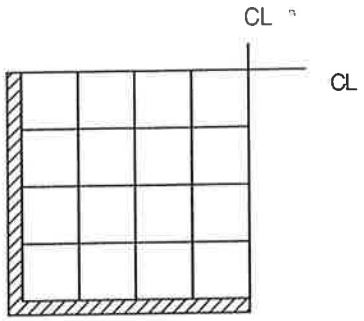

FIGURE 1. Example of a uniform mesh ($N = 4$)

With such a mesh all three methods work well. Next, we consider a distortion of this mesh obtained by moving each interior node at random within a square centered at the node and with sidelength $0.4h$ (h is the sidelength of the original element). In Figure 2 we show the three meshes obtained in this way.

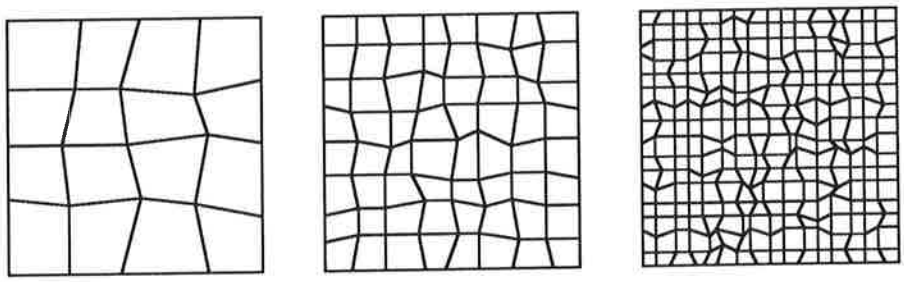

FIGURE 2. The distorted meshes

In Tables 1-6 we list the normalized L^2-errors for the deflection, the normal moment and the normalized shear force, for the uniform and distorted meshes, respectively.

TABLE 1. The error $\|w - w_h\|_0/\|w\|_0$ for the uniform meshes

N	SRI	MITC4	STAB
4	0.0697	0.0699	0.0408
8	0.0161	0.0161	0.0095
16	0.0026	0.0027	0.0025

TABLE 2. The error $\|w - w_h\|_0/\|w\|_0$ for the distorted meshes

N	SRI	MITC4	STAB
4	0.1505	0.0768	0.0408
8	0.0795	0.0187	0.0094
16	0.0328	0.0032	0.0030

TABLE 3. The error $\|M_x - M_x^h\|_0/\|M_x\|_0$ for the uniform meshes

N	SRI	MITC4	STAB
4	0.3292	0.3292	0.3291
8	0.1668	0.1668	0.1668
16	0.0837	0.0837	0.0837

TABLE 4. The error $\|M_x - M_x^h\|_0/\|M_x\|_0$ for the distorted meshes

N	SRI	MITC4	STAB
4	0.3847	0.3434	0.3407
8	0.2165	0.1764	0.1747
16	0.1145	0.0878	0.0873

TABLE 5. The error $\|Q - Q_x^h\|_0/\|Q\|_0$ for the uniform meshes

N	SRI	MITC4	STAB
4	0.2546	0.2772	0.2757
8	0.1328	0.1761	0.1760
16	0.0784	0.1172	0.1174

TABLE 6. The error $\|Q - Q_x^h\|_0/\|Q\|_0$ for the distorted meshes

N	SRI	MITC4	STAB
4	3.0856	0.4701	0.3295
8	3.3147	0.5508	0.2402
16	2.2985	0.2531	0.1784

From the results we directly see that the distortion of the mesh completely distroys the accuracy in the deflection and shear for the SRI method. For the MITC4 the distortion does not affect the accuracy of the moment, but we see that the deflection and shear become worse. We also see that the accuracy of all variables stays the same in our modification of the MITC4.

These results are in complete agreement with theory. As we mentioned, the analysis of the SRI given in [9] use the assumption that the elements are rectangular. For the MITC4 we mentioned that only a partial error analysis can be made whereas our modification of MITC4 is uniformly stable.
One might object that the distorted meshes presented above are somewhat artificial and only constructed in order to catch the SRI and MITC4, and that no mesh generator would produce a mesh like this. However, we would like stress that we chose the square domain only for simplicity (and because the exact solution is available) and that our distorted meshes should be considered as models of coarse meshes for a problem with a complicated geometry.
It should, however, be even more convincing to see that some of the drawbacks with the unstable methods are already seen with meshes which are much less distorted. It seems to have been common kowledge that many methods give bad shears (cf. the introduction to [8]) but to our knowledge this has only recently been explicitely reported in [10]. We will now give some numerical examples similar to those given in [10]. We again start from the uniform finite element partitionings but we now move only one node. The three meshes we obtained are shown below.

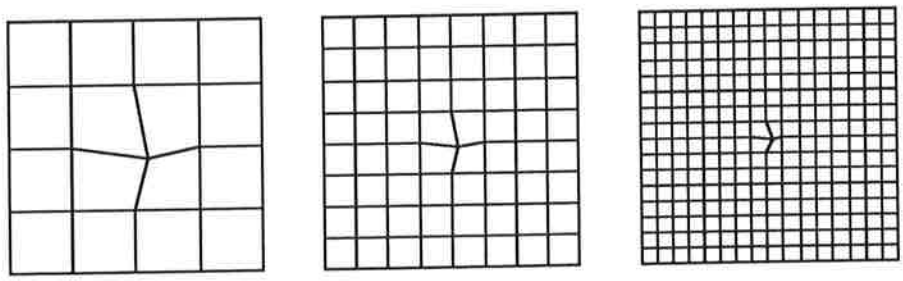

FIGURE 3. The meshes with one node moved

TABLE 7. The error $\|Q - Q_x^h\|_0 / \|Q\|_0$ for the meshes with one node moved ($t = 0.01$)

N	SRI	MITC4	STAB
4	3.9151	0.6448	0.2886
8	1.2244	0.1808	0.1781
16	0.3906	0.1175	0.1177

The errors for the shears are given in Table 7 and when this is compared with Table 5 we see that for the this minor change of the mesh has a disastrous effect on the accuracy for the shear obtained with the SRI. For the MITC4 the shear is very bad for the coarsest mesh but gets better when the mesh is refined. This is due to the stabilizing effect the thickness has when it is of the same order of magnitude as the mesh length. We chose it equal to 0.01, but if we change it to 0.001 this severly affects the accuracy of the shear of the MITC4 as can bee seen from table 8. This is a good indication that the method is not uniformly stable. With our stabilization of the MITC4 the shear is not significantly affected by neither the mesh distortion nor the change of the thickness t.

TABLE 8. The error $\|Q - Q_x^h\|_0/\|Q\|_0$ for the meshes with one node moved and $t = 0.001$

N	SRI	MITC4	STAB
4	29.504	6.4140	0.2893
8	27.260	2.1085	0.1787
16	11.264	0.2150	0.1180

REFERENCES

1. K.J. Bathe and F. Brezzi, On the convergence of a four node plate bending element based on Reissner-Mindlin theory. The Mathematics of Finite Elements and Applications V. MAFELAP 1984. J. R. Whiteman Ed., Academic Press 1985. 491-503
2. K.J. Bathe and F. Brezzi, A simpified analysis of two plate bending elements - The MITC4 and MITC9 elements, In NUMETA 87, Vol. 1, Numerical Techniques for Engineering Analysis and Design, G.N. Pande and J. Middleton, Eds. Martinus Nijhoff Publishers 1987, D46/1
3. K.J. Bathe and E. Dvorkin, A four node plate bending element based on Mindlin-Reissner plate theory and mixed interpolation. Int. J. Num. Meths. Eng. **21** (1985) 367-383
4. F. Brezzi, M. Fortin and R. Stenberg, Error analysis of mixed-interpolated elements for Reissner-Mindlin plates. Mathematical Models and Methods in Applied Sciences **1** (1991). To appear
5. P.G. Ciarlet, The Finite Element Method for Elliptic Problems. North-Holland, Amsterdam 1978
6. R.D. Cook, D.S. Malkus and M.E. Plesha, Concepts and Applications of Finite Element Analysis. Third Edition. John Wiley 1989
7. T.J.R. Hughes, The Finite Element Method. Linear Static and Dynamic Analysis. Prentice-Hall 1987
8. T.J.R. Hughes and L.P. Franca. A mixed finite element formulation for Reissner-Mindlin plate theory: Uniform convergence of all higher-order spaces. Comp. Meths. Appl. Mech. Engrg. **67** (1988) 223-240
9. C. Johnson and J. Pitkäranta, Analysis of some mixed finite element methods related to reduced integration. Math. Comput. **38** (1982) 375-400
10. D. Lasry and T. Belytschko, Transverse shear oscillations in four-node quadrilateral plate elements. Computers and Structures **27** (1987) 393-398
11. R.H. MacNeal, Derivation of element stiffness matrices by assumed strain distribution. Nucl. Engrg. Design **70** (1982) 3-12
12. J. Pitkäranta, Analysis of some low-order finite element schemes for Mindlin-Reissner and Kirchhoff plates. Numer. Math. **53** (1988) 237-254
13. J. Pitkäranta and R. Stenberg, Error bounds for the approximation of Stokes problem with bilinear/constant elements on irregular quadrilateral meshes. The Mathematics of Finite Elements and Applications V. MAFELAP 1984. J. R. Whiteman Ed., Academic Press 1985. 325-334

DYNAMICALLY LOADED BEAM ON AN ELASTIC HALF-SPACE

OLLI MAJAMÄKI, JARI PUTTONEN
Civil Engineering Department
Imatran Voima Oy
P.O. Box 112, SF-01601 Vantaa, Finland

ABSTRACT

In the study, the dynamic interaction between an elastic beam and an elastic half-space is examined. The system is subjected to harmonic external forces. The analysis of the beam-subgrade system is performed applying a global stiffness solution. The beam is discretized by the finite element method. The subgrade impedance matrix is formed by inverting a compliance matrix constructed through the use of the Green's function. The Green's function is determined for a harmonic vertical point load on the surface of the subgrade. On the interaction surface, a complete contact is assumed in the vertical direction and a frictionless boundary condition is applied in the horizontal direction. The practical example presented relates to the behaviour of a gas-turbine foundation. The results pointed out that the flexibility of the foundation give the main contribution to its dynamic behaviour.

INTRODUCTION

Machine Foundation: In the design of the machine foundation a basic goal is to limit vibrations to amplitudes which will allow the satisfactory operation of the machine. Traditionally the machine foundation is a massive and rigid reinforced concrete

structure which acts as a high-tuned system. Nowadays, the frequencies of machines have increased leading to the situation, where structural solutions, which give a low-tuned support for the machine, are prefered. The aim of the study is to develop a method to analyse flexible machine foundations resting on the soil considering the frequency dependency of the dynamic behaviour of the soil medium. A computer program based on the theory presented has been made as a part of the study.

Impedance Functions: In soil dynamics, impedance is defined as a ratio of a the steady-state force to the resulting displacement of a massless foundation on the soil medium. The dynamic force and displacement are generally out of phase. So the displacement can be divided into two parts, one in phase or 180° out of phase and the other 90° out of phase with the exciting force. It is therefore convenient to define impedance as a complex-valued function.

Impedance functions are commonly presented as a function of the dimensionless frequency ratio a_0, defined by

$$a_0 = \frac{\omega B}{c_T}, \tag{1}$$

where ω is the angular frequency of exitation, B a critical foundation dimension like the radius of a circular foundation or one half of the width of a rectangular foundation. c_T is the shear wave velocity of the soil. Impedance funktions K_z are often introduced in the form

$$K_z = K(k + ia_0c), \tag{2}$$

in which K is the static stiffness of the medium, k and c are real dimensionless functions. The real component reflects the stiffness and inertia of the supporting medium. The imaginary component reflects the radiation damping of the medium. The values of impedance functions are calculated separately for each exitation frequency. Impedance functions for rigid body models can be found from References /1/,/2/ and /4/.

Flexible Foundation: If the natural frequencies of the foundation itself are much more higher than the natural frequencies of the modes in which the foundation behaves as a rigid-body, then the foundation can be considered rigid compared to the soil. If the natural frequencies of the foundation are much more higher than the main frequencies of dynamic forces, then the foundation is rigid compared to the loading. In practical situations, it is important to study carefully if a rigid-body model is a realistic one.

GREEN'S FUNCTION

The Green's function is determined for a harmonic point load of unit amplitude. The load with the angular frequency of ω is acting normal to the surface of an elastic half-space. This is also called Lamb's problem /6/. Cylindrical coordinates are used. The load is acting in the origin and in the direction of the axis z. The half-space occupies the region $z \geq 0$.

In a three-dimensional elastic homogenous and isotropic medium, the governing equations of motion with cylindrical symmetry are

$$(\lambda + 2\mu)\frac{\partial}{\partial r}\left(\frac{q}{r} + \frac{\partial q}{\partial r} + \frac{\partial w}{\partial z}\right) + \mu\left(\frac{\partial^2 q}{\partial z^2} - \frac{\partial^2 w}{\partial r \partial z}\right) = \rho\frac{\partial^2 q}{\partial t^2}, \quad (3)$$

$$(\lambda + 2\mu)\frac{\partial}{\partial z}\left(\frac{q}{r} + \frac{\partial q}{\partial r} + \frac{\partial w}{\partial z}\right) - \mu\left[\frac{\partial q}{\partial r \partial z} - \frac{\partial^2 w}{\partial r^2} + \frac{1}{r}\left(\frac{\partial q}{\partial z} - \frac{\partial w}{\partial r}\right)\right] = \rho\frac{\partial^2 w}{\partial t^2}, \quad (4)$$

where λ and μ are the Lamé constants, q is the radial displacement, w the vertical displacemet and ρ is the density of the medium.

Displacements q and w may be introduced through the potential functions ϕ and χ /3/

$$q = \frac{\partial \phi}{\partial r} + \frac{\partial^2 \chi}{\partial r \partial z}, \quad (5)$$

$$w = \frac{\partial \phi}{\partial z} - \frac{1}{r}\frac{\partial \chi}{\partial r} - \frac{\partial^2 \chi}{\partial r^2}. \quad (6)$$

There is a discontinuity in the normal stresses under the point load and $\tau_{rz} = 0$ on the surface. The solution is obtained by using the Hankel transform, and the Green's function for the vertical displacement on the surface of the half-space is /9/

$$w_{z=0} = -\frac{1}{2\pi\mu}\int_0^\infty \frac{\alpha k^2}{(2\zeta^2 - k^2)^2 - 4\alpha\beta\zeta^2} J_0(r\zeta)\zeta d\zeta, \quad (7)$$

where $\alpha^2 = \zeta^2 - \omega^2/c_L^2 = \zeta^2 - h^2$ and $\beta^2 = \zeta^2 - \omega^2/c_T^2 = \zeta^2 - k^2$. c_L is the velocity of the compression wave and c_T is the velocity of the shear wave in the half-space.

The improper integral in Equation (7) cannot easily be evaluated because of the oscillatory nature of the integrand. The denominator $F(\zeta)$ has also a simple pole s, called Rayleigh pole. s is a root of $F(s) = 0$. In the current application, contour integration over the complex plane is used to include the contribution from the Rayleigh pole and the branch cuts associated with the points of $\sqrt{\zeta^2 - h^2}$ and $\sqrt{\zeta^2 - k^2}$. To avoid standing waves, one half of the residue of the Rayleigh pole must be substracted from

it /12/. So it is convenient to introduce the Bessel function J_0 as a combination of two Hankel funktions /11/

$$J_0(r\zeta) = \frac{1}{2}H_0^{(1)}(r\zeta) + \frac{1}{2}H_0^{(2)}(r\zeta). \tag{8}$$

Conture integration is evalued in two parts. The Rayleigh pole is placed below the real axis to point out that waves are propagating away from the point force /5/. Finally the Green's function can be written in the following form

$$w_{z=0} = \frac{1}{2\pi\mu}\left[Res_1 + Int_1 + Int_2 + Int_3 + i\left(Res_2 + Int_4 + Int_5\right)\right], \tag{9}$$

where

$$Res_1 = \frac{\pi\alpha k^2}{16s^2 - 8k^2 - 4\left(\frac{\beta}{\alpha}s^2 + \frac{\alpha}{\beta}s^2 + 2\alpha\beta\right)} Y_0(s), \tag{10}$$

$$Int_1 = \int_0^\infty \frac{2}{\pi} \frac{\sqrt{\zeta^2 + h^2}k^2}{\left(2\zeta^2 + k^2\right)^2 - 4\sqrt{\zeta^2 + h^2}\sqrt{\zeta^2 + k^2}\zeta^2} K_0(r\zeta)\,\zeta d\zeta, \tag{11}$$

$$Int_2 = -\int_0^h \frac{\sqrt{h^2 - \zeta^2}k^2}{\left(2\zeta^2 - k^2\right)^2 + 4\sqrt{h^2 - \zeta^2}\sqrt{k^2 - \zeta^2}\zeta^2} Y_0(r\zeta)\,\zeta d\zeta, \tag{12}$$

$$Int_3 = -\int_h^k \frac{4\sqrt{k^2 - \zeta^2}\left(\zeta^2 - h^2\right)k^2}{\left(2\zeta^2 - k^2\right)^4 + 16\left(\zeta^2 - h^2\right)\left(k^2 - \zeta^2\right)\zeta^4} Y_0(r\zeta)\,\zeta^3 d\zeta, \tag{13}$$

$$Res_2 = \frac{\pi\alpha k^2}{16s^2 - 8k^2 - 4\left(\frac{\beta}{\alpha}s^2 + \frac{\alpha}{\beta}s^2 + 2\alpha\beta\right)} J_0(s), \tag{14}$$

$$Int_4 = -\int_0^h \frac{\sqrt{h^2 - \zeta^2}k^2}{\left(2\zeta^2 - k^2\right)^2 + 4\sqrt{h^2 - \zeta^2}\sqrt{k^2 - \zeta^2}\zeta^2} J_0(r\zeta)\,\zeta d\zeta, \tag{15}$$

$$Int_5 = -\int_h^k \frac{4\sqrt{k^2 - \zeta^2}\left(\zeta^2 - h^2\right)k^2}{\left(2\zeta^2 - k^2\right)^4 + 16\left(\zeta^2 - h^2\right)\left(k^2 - \zeta^2\right)\zeta^4} J_0(r\zeta)\,\zeta^3 d\zeta. \tag{16}$$

In Equations (10)-(13) Y_0 is the Neumann function and K_0 the modified Bessel function of the third kind. The Green's function can easily be evaluated numerically from Equation (9), because the improper integral Int_1 coverges rapidly.

Poisson's ratio ν of the half-space cannot be factored out of the solution. Figure 1 shows the dependence of the Green's function on ν. r describes the distance between the points of exitation and response. The solid line presents the real part of the Green's function and the dashed line presents the imaginary part.

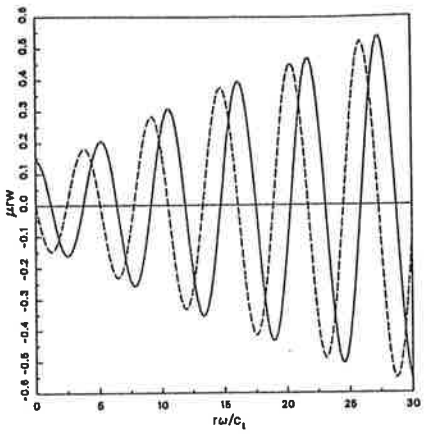

Figure 1. Green's function. Poisson's ratio $\nu = 0.1$.

SOIL STRUCTURE INTERACTION

Subgrade Impedance: The contact area A is divided into regtangular subregions. Figure 2 shows the discretization graphically. It is assumed, that the traction can be considered constant over each subregion. Only the relationship between vertical surface response and vertical surface exitation is taken into account. A single term v_{ij} of the compliance matrix can be determined by integrating over the subregion A_j

$$v_{ij} = \frac{1}{A_j} \int \int_{A_j} w_{z=0}(\omega, r, c_L, c_T) da. \tag{17}$$

The subgrade stiffness matrix $\mathbf{K}_s$ is obtained as an inversion of the compliance matrix.

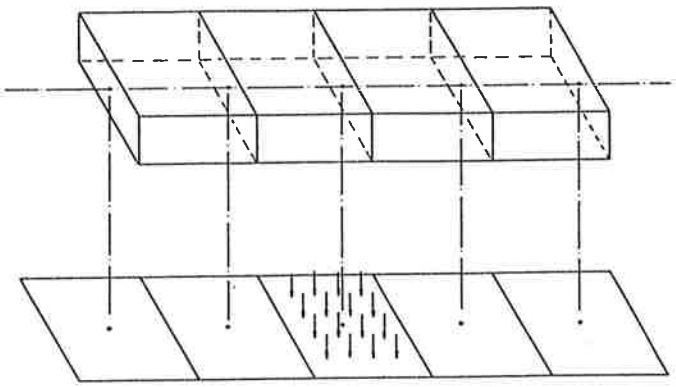

Figure 2. Subgrade discretization.

System Equations: The discretization process involves the definition of nodal points the plane of which coincides with both the surface of the supporting medium and the middle plane of the beam. The reaction force $\mathbf{R}$ between the medium and the

structure is

$$\mathbf{R} = \mathbf{K}_s \mathbf{U}_s, \tag{18}$$

where $\mathbf{U}_s$ is the vertical displacement on the surface of the soil. The dynamic behaviour of the system is described by the equation

$$(\mathbf{K}_{str} - \omega^2 \mathbf{M}_{str})\mathbf{U}_{str} + \mathbf{R} = \mathbf{F}, \tag{19}$$

in which $\mathbf{K}_{str}$ is the stiffness, $\mathbf{M}_{str}$ the mass of the structure and $\mathbf{F}$ is the dynamic force. At nodal points conditions of equilibrium and compatibility are enforced between the surface of medium and the structure. Thus Equation (19) can be written in the form

$$\mathbf{K}_{red}\mathbf{U} + \mathbf{K}_s\mathbf{U} = \mathbf{F}, \tag{20}$$

where $\mathbf{K}_{red}$ include the stiffness and inertial properties of the structure. Finally, a full complex system impedance matrix $\mathbf{K}$ can be obtained by combining $\mathbf{K}_s$ and $\mathbf{K}_{red}$ and, thus

$$\mathbf{K}\mathbf{U} = \mathbf{F}. \tag{21}$$

Rigid Beam Foundation: In order to test the accuracy of the computer program developed, the behaviour of a rigid, massless beam in frictionless contact with the surface of an elastic half-space is studied. The system is excited by a point load. The results pointed out that when aspect ratio is larger than two and dimensionless frequency ratio does not exceed the value $a_0 = 1.5$, the responses computed fall within 10% of the rigid plate values presented in the litterature /8/. Figure 3a shows the effect of L/B for the real part of vertical compliance, when $\nu = 0.25$. Figure 3b shows the corresponding values for the imaginary part of compliance. With the method described, the transverse contact stress is assumed to be uniform. This is the main reason that the beam model cannot describe the behaviour of the plate in high frequencies.

EXAMPLE

A gas-turbine, which has the electric power of 40 MW, is fixed to a concrete block. The length of the footing is 21 m, width 4 m and thichness 1.3 m. The total mass of the foundation is 270000 kg, which is only a little more than the mass of the machine 210000 kg. The operating frequency of the turbine is 85 Hz and the rotating mass 10000 kg. For the generator, corresponding values are 50 Hz and 19000 kg.

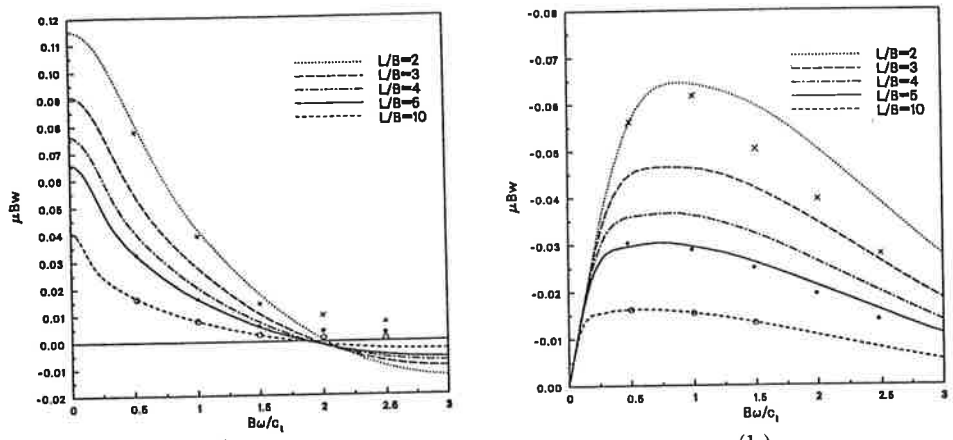

Figure 3. Effect of L/B for compliance function.

The foundation was analysed using the program developed in the study. The footing was modelled by beam elements and it was located on the surface of the half-space. The dimensionless frequency ratio a_0 was 1.5 at the operating frequency of the turbine and 0.88 at the operating frequency of the generator. The amplitudes of exitation under operating conditions were determined according to the VDI 2060 /10/ and the eccentricity used was $e \cdot \omega$=2.5 mm/s. The rotating mass was assumed to be concentrated on the axes. The mass of the machine was described by discrete masses and discrete moments of inertia.

At the operating frequencies the amplitude profile of the gas-turbine foundation is illustrated in Figure 4. The solid line presents the flexible beam model and the dashed line presents the rigid body model.

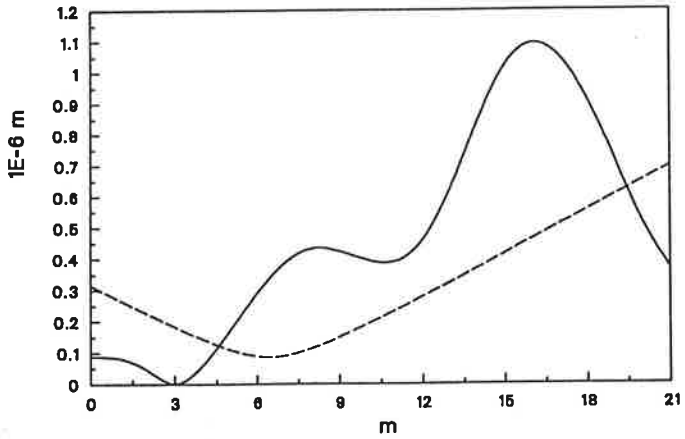

Figure 4. Amplitude profile /7/.

CONCLUSIONS

The dynamic force-displacement relationships for the harmonic vertical motion of the flexible beam resting on an elastic half-space have been obtained. The beam model is useful when aspect ratio is larger than two and dimensionless frequency ratio is less than 1.5. These restrictions can be avoided by using a plate model which is the next step of the study. The example presented pointed out the importance to take into account the flexibility of the foundation.

REFERENCES

1. Banerjee P. K. 1987. Dynamic Behaviour of Foundations and Buried Structures. Belfast. The Universities Press. p.270.
2. Dorby R., Gazetas G. 1986. Dynamic Response of Arbitrarily shaped Foundations. Journal of Geotechnical Engineering, Vol. 112, No. 2. pp. 109-135.
3. Eringen A. C., Suhubi E. S. 1975. Elastodynamics. Volume II. Linear Theory. New York. Academic Press. p. 1003.
4. Gazetas G. 1983. Analysis of machine foundation vibrations: state of the art. Soil Dynamics and Earthquake Engineering, Vol. 2, No. 1. pp. 521-559.
5. Graff K. F. 1975. Wave Motion in Elastic Solids. Oxford. Clarendon Press. p. 649.
6. Lamb H. 1904. On the Propagation of Tremors over the Surface of an Elastic Solid. Philosophical Transaction, Vol. 203, pp. 1-42.
7. Majamäki O. 1990. Dynamically Loaded Structure on the Elastic Half-Space. Thesis of M.Sc. Helsinki University of Technology. pp. 76. (In Finnish).
8. Savidis S., Sarfeld W. 1980. Verfahren und Andvendung der dreidimensionalen dynamischen Wechselwirkung. Vortraege der Baugrundtagung. DGEG, Essen. Selbstverlagt. pp. 47-78.
9. Thiel M. 1982. Soil-Pile Interaction in Horisontal Vibration. Thesis of Ph.D. Lyngby. Tecnical University of Denmark. p. 98.
10. VDI 2060. 1966. Beurteilungsmaßstäbe für den Auswuchtzustand rotierender starrer Körper. p. 8.
11. Whittaker W. L. 1979. Dynamic Analysis of Flexible Plates Bearing on the Elastic Half-Space. Thesis of Ph.D. Pittsburgh. Carnegie-Mellon University. p. 184.
12. Wong H. L. 1975. Dynamic Soil - Structure Interaction. Thesis of Ph.D. Pasadena. California Institute of Technology. p. 240.

RIDE VIBRATIONS OF AN AGRICULTURAL TRACTOR DRIVING ON AN ASPHALT ROAD

MIKKO NISKANEN
Valmet Tractor Works
P.O.Box 557, SF-40101 Jyväskylä
Finland

ABSTRACT

Strong ride vibrations on a smooth road occur when the excitation coming from the wheels is at the same frequency as one of the natural frequencies of the tractor on its tyres. At normal road speeds the eccentricity of the wheels is the main cause of strong ride vibrations.

With the help of a computer model the effects of structural improvements to the tractor's dynamic behaviour have been investigated. By changing the weight distribution, wheelbase and tyre stiffnesses it is not possible to achieve good performance in field conditions and avoid resonance on the road at the same time.

We also tested two different kinds of springs at the rear power lift. Firstly, we used the electronic power lift control as an active spring. Secondly, we installed passive springs to the power lift.

Laboratory measurements and test drives were made on a tractor with front and rear weights. In test drives the rear wheels had eccentricity greater than normal in our tractors. The time limit for maintaining proficiency (ISO 2631) at the resonance speed increased with active springs from 7 minutes to 2 hours and with passive springs to 8 hours. The displacement amplitudes at the driver's seat decreased with active springs by about 75 % and with passive springs by about 90 % when driven at resonance speed.

INTRODUCTION

Strong ride vibrations may occur when an agricultural tractor is driven on a smooth road with heavy load and at a certain speed. The strong vibrations are harmful to the driver, because they reduce the driving comfort and can even be dangerous for the health.

In figure 1 is shown measured displacement at the rear axle of a tractor with heavy rear weight. The displacement is scaled to correspond with 1 mm eccentricity at the rear wheels. The displacement is only slightly greater than eccentricity at the rear wheels when the driving speed is under 25 km/h.

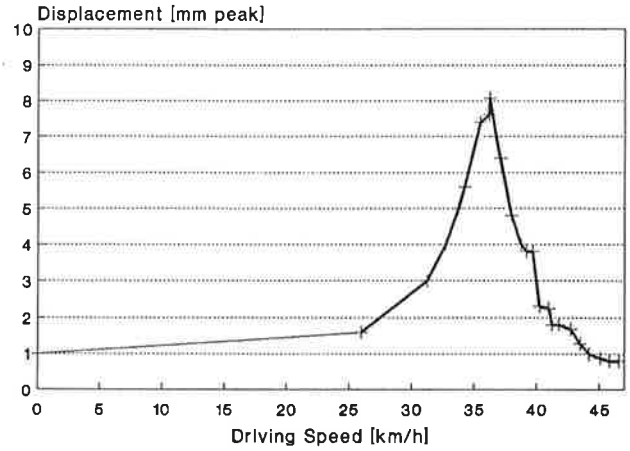

FIGURE 1: Measured displacement at the rear axle of the tractor.Tractor with heavy rear weight driven on a smooth road. Eccentricity at the rear wheels 1 mm.

Displacement reaches a peak at the driving speed of about 35 km/h and then decreases rapidly when the speed is still increased. It is the typical shape of a resonance phenomenom. So we may assume, that strong ride vibrations on a smooth road occur when the exltation coming from the wheels is at the same frequency as one of the natural resonant frequencies of the tractor on its tyres. Pitch and bounce modes of the tractor are the most critical, because they are at frequencies of around 1-3 Hz. The rolling speeds of the wheels are in the same region when the tractor is driven at road speeds. The eccentricity of the wheels is the main cause of strong ride vibrations of an agricultural tractor driven on smooth road.

COMPUTER MODEL CALCULATIONS

Pitch and bounce modes of a tractor with heavy front and rear weights are shown in figure 2. In pitch mode the rotation center is situated between the axles and in bounce mode outside the wheelbase. The mode shapes are calculated with a computer model. The model is made of a tractor weighing 4000 kg and equipped with front weights (450 kg) and a framework with extra weight at the power lift. The mass of the rear weight is 1500 kg, which corresponds to a 4-furrow reversible plough. With the help of this computer model the effects of the structural improvements to the dynamic behaviour of the tractor have been investigated.

The effect on the natural frequency of the pitch mode when the positions of tractor components have been changed one at a time is shown in figure 3. The position of engine, gearbox, PTO-box and cab has very little effect on the natural frequency. The effect of wheelbase is much more significant. In practice the rear wheels can't be moved backwards without lenghtening the hitch links. So, by moving the front axle 800 mm forward the natural frequency of the tractor rises to 1.6 Hz, which means a resonance speed of about 30 km/h if the rear wheels are eccentric.

In figure 4 is shown the effect of tyre stiffnesses on the natural frequency of the tractor body. Increasing the tyre stiffenesses by factor of 2.5 would rise the natural frequency of the pitch mode to the value of 2.1 Hz, which corresponds to a reconance speed of 40 km/h when the rear wheels are eccentric. In practice diagonal tyres would increase the stiffness by about 50 % and dual wheels by about 100 % compared to reference tyres.

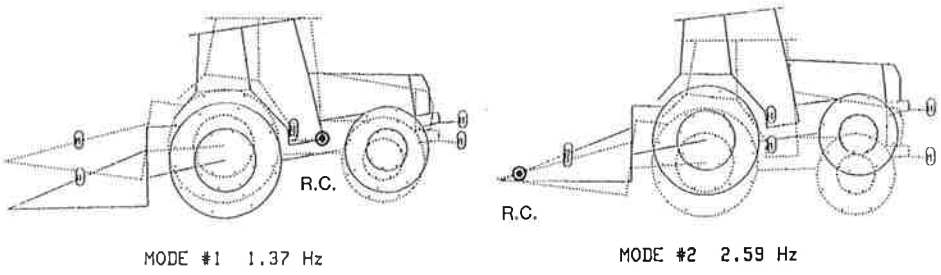

FIGURE 2: Calculated mode shapes of the tractor with front and rear weights. R.C. = rotation center.

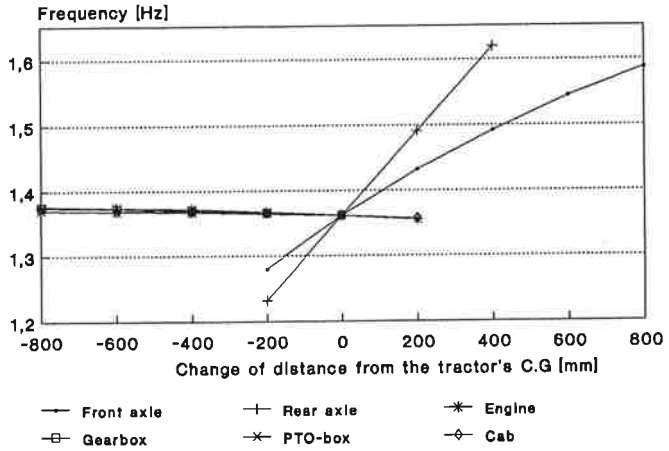

FIGURE 3: Calculated natural frequency (pitch mode) of the tractor body. The effect of change in weight distribution of the tractor with front and rear weights.

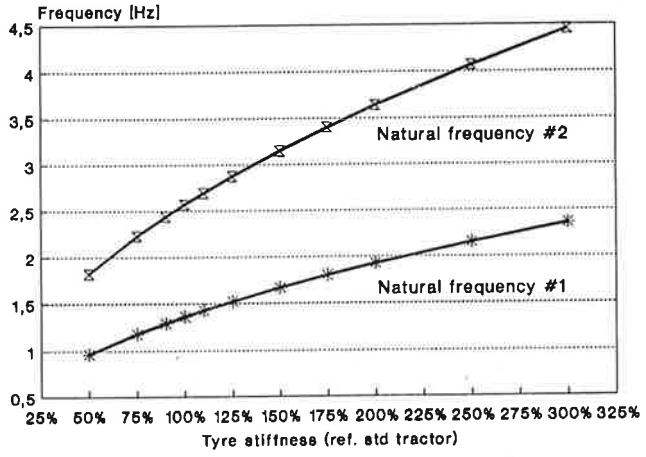

FIGURE 4: Calculated natural frequencies of the tractor body with front and rear weights. The effect of change in tyre stiffnesses.

Calculated displacement under driver's seat when the tractor is driven on smooth road at different speeds is shown in figure 5. The rear wheels have eccentricity of 1 mm. The red curve is the standard tractor, the green curve is the tractor with weight distribution changed to optimum and the blue one is the tractor with optimum weight distribution and diagonal tyres. The weight distribution change and stiffer tyres would increase the resonance speed from 25 km/h to 36 km/h, but the maximum driving speed in Finland is 40 km/h, so it's not enough. So by changing the weight distribution, wheelbase and tyre stiffnesses it is not possible at the same time to achieve both good performance in field conditions and to avoid resonance situation on the road when the tractor is loaded with heavy weights.

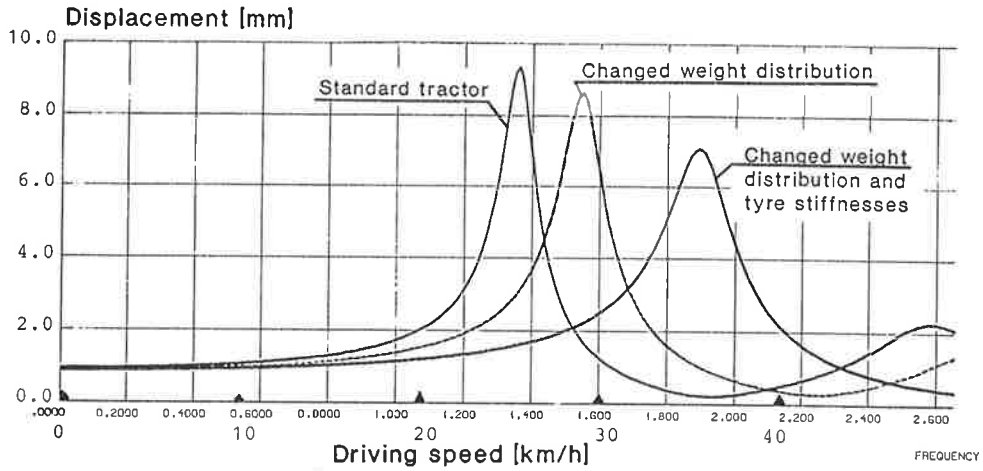

FIGURE 5: Calculated displacement under driver's seat when the tractor with front and rearweights is driven on a smooth road and there is 1 mm eccentricity at the rear wheels. The effect of changes in tractor boby weight distribution and tyre stiffnesses.

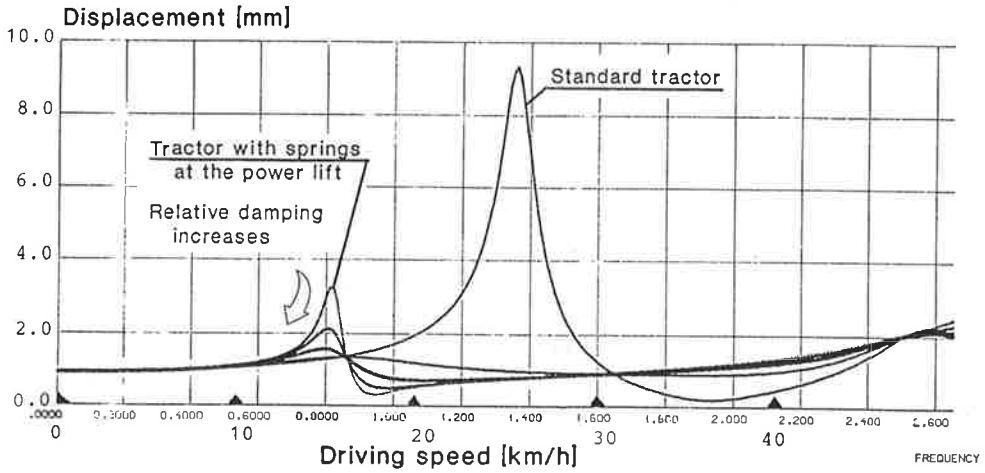

FIGURE 6: Calculated displacement under driver's seat when the tractor with front and rear weights is driven on a smooth road and the rear wheels have 1 mm eccentricity. Tractor with springs at the power lift is compared to standard tractor.

The best way to reduce ride vibrations on a smooth road is to keep the rolling radius variation of the wheels as small as possible. The variation should be under 1 mm, but in practice it is difficult to achieve. Another way to avoid resonances is to attach the implements to the tractor with springs. Figure 6 shows the effect of springs on the displacement under driver's seat. When the power lift is equipped with springs, a new mode shape is born, let's call it 'lift mode'. This is the relative movement between the tractor and the rear weight; and its natural frequency depends heavily on the stiffness of the power lift springs. If this new natural frequency is low enough, the natural frequencies of the tractor body will increase significantly. With light damping at the power lift, the resonance of the lift mode is clearly seen, but the displacement under driver's seat is, however, much smaller than in tractor without springs. When the damping at the power lift is increased, the resonance peak in the displacement curve disappears.

LABORATORY MEASUREMENTS

In a real tractor, we tested two different kinds of springs at the power lift (fig.7). Firstly, we used the electronic power lift control as an active spring. It works only if the implement is attached both with the lower links and the top link and the centre of gravity of the implement is well behind the end of the lower links. Secondly, we installed passive springs with quite heavy damping to the power lift.

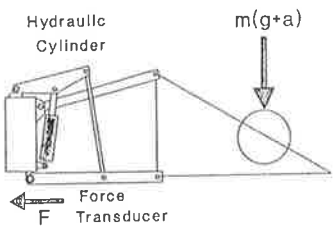

ACTIVE SPRINGS

Force F is kept constant by moving the hydraulic cylinder ⇨ acceleration at the rear weight is kept constant

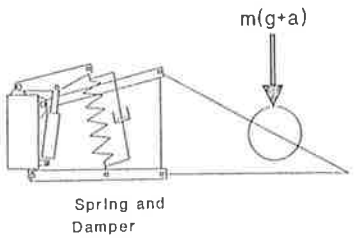

PASSIVE SPRINGS

Spring constant at the C.G of the rear weight: 56 kN/m

Damping constant at the C.G of the rear weight: 3600 Ns/m

FIGURE 7: Principles of springed power lift.

Laboratory measurements and test drives were made on tractor with 450 kg front weight and 1500 kg rear weight. In the laboratory we made a modal analysis for the tractor (fig.8). Measured mode shapes of the tractor without springs (fig.9) are about the same as the calculated ones (fig.2). Natural frequencies are little higher than the calculated ones, because the stiffness of a rolling tyre is lower than the stiffness of a non-rolling tyre, and we used the values of rolling tyres in the computer model. In figure 10, are the synthesized displacement/force- transfer functions at the rear axle of the tractor calculated with the help of the modal model. The resonance of the pitch mode is clearly seen, and the amplitude at the resonance frequency decreases by about 50 % (compared to the tractor without springs) using active springs and by about 75 % using passive springs.

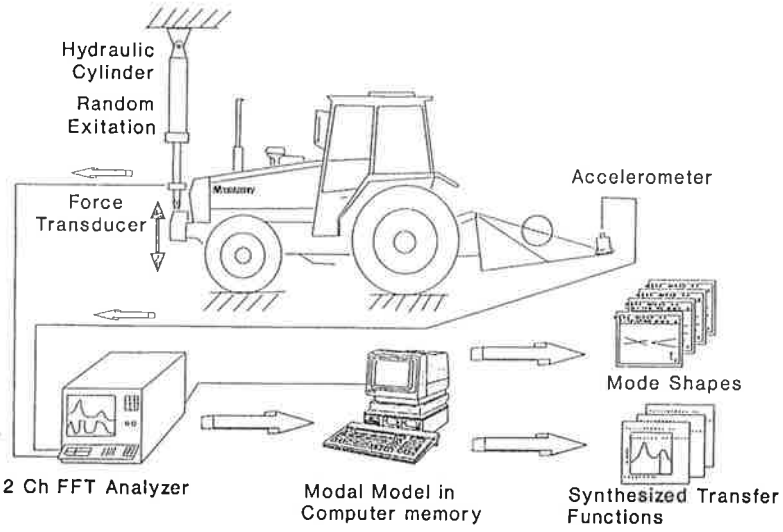

FIGURE 8: Laboratory measurements of the tractor.

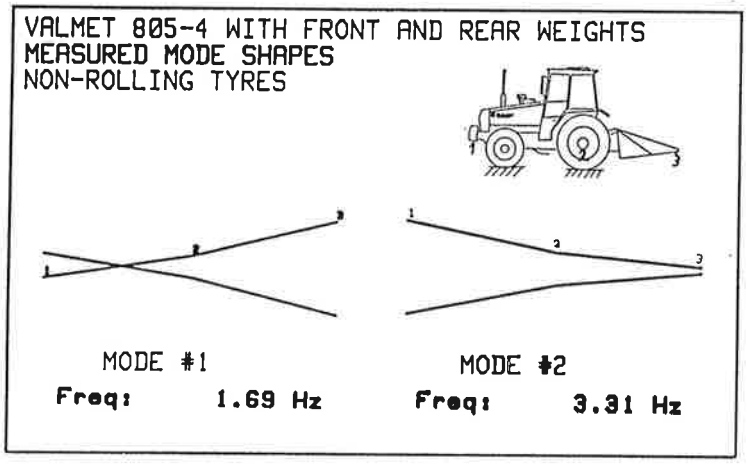

FIGURE 9: Measured mode shapes of the tractor with front and rear weights.

TEST DRIVES ON THE ROAD

In test drives the tractor was driven on a smooth road at the resonance speed of the tractor without springs. Rear wheels had eccentricity greater than normal in our tractors. Fig. 11 shows the horizontal/vertical displacement of the drivers seat. As you can see the tractor without springs has the greatest displacement. With active springs at the power lift the displacements in both directions have decreased by about 75 % and with passive springs by about 90 %.

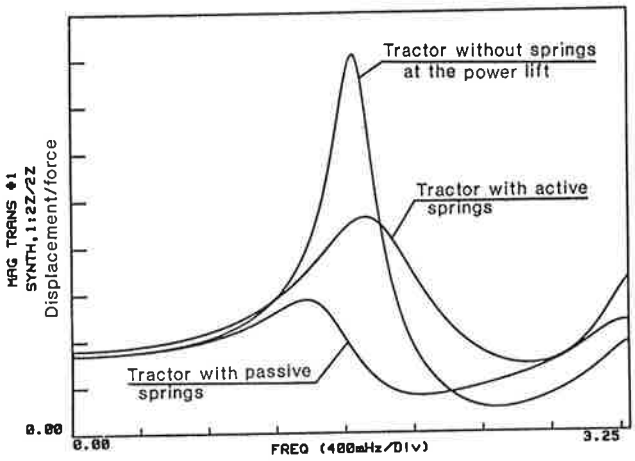

FIGURE **10**: Synthesized displacement/force transfer functions. Displacement and force at the rear axle of the tractor with front and rear weights.

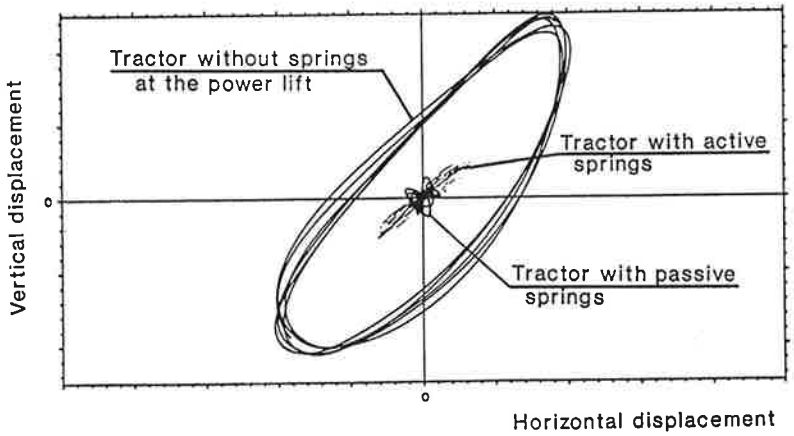

FIGURE **11**: Horizontal and vertical displacement of the driver's seat. The tractor with front and rear weights is driven on a smooth road at the resonance speed.

In figure 12 the vertical acceleration of the driver's seat is compared to ISO 2631 boundaries. Daily exposure time to maintain proficiency when driving the tractor without springs at resonance speed would be about 1 hour. With active springs at the power lift daily exposure time could be about 8 hours and with passive springs about 9 hours.

In figure 13 is the horizontal acceleration of the driver's seat compared to ISO 2631 boundaries. When driving the tractor without springs , daily exposure time to maintain proficiency would be about 7 minutes. With active springs at the power lift daily exposure time could be about 2 hours and with passive springs about 8 hours.

If the vertical and the horizontal accelerations are calculated together, the daily exposure times to maintain proficiency are 7 minutes for the tractor without springs, 2 hours for the tractor with active springs and 8 hours for the tractor with passive springs.

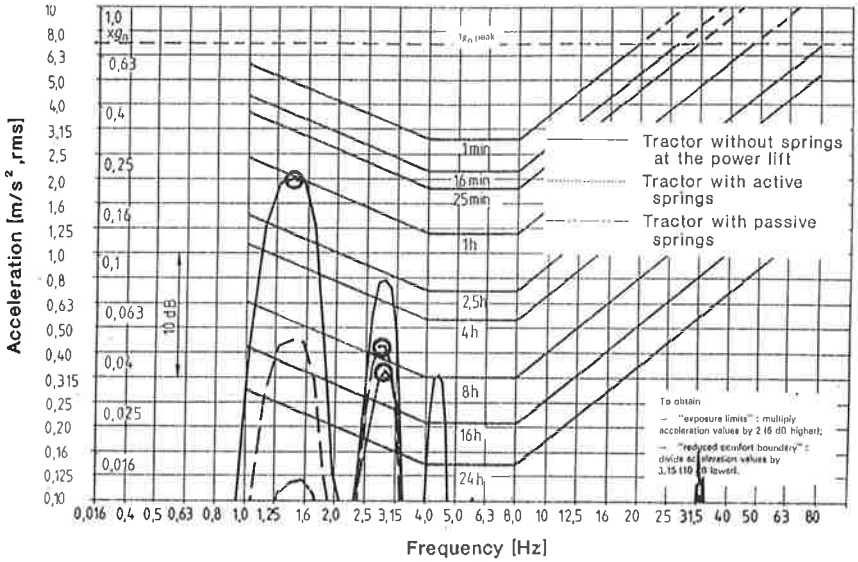

FIGURE **12**: Vertical acceleration of the driver's seat compared to ISO 2631 "fatique-decreased proficiency boundaries". The tractor with front and rear weights is driven on a smooth road at the resonance speed.

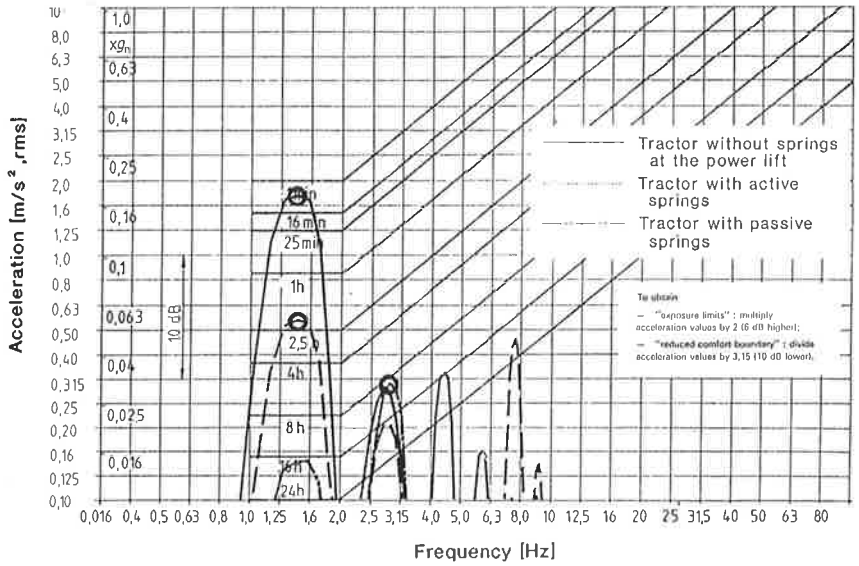

FIGURE **13**: Horizontal acceleration of the driver's seat compared to ISO 2631 "fatique-decreased proficiency boundaries". The tractor with front and rear weights is driven on a smooth road at the resonance speed.

With passive springs at the power lift the driver can't notice the resonance phenomenom between the wheel excitation and the natural frequencies of the tractor at normal road speed. Springs at the power lift are an effective way to reduce ride vibrations when the tractor is driven on a smooth road. They also improve the driveability of the tractor when it is driven over a single bump.

EVOLUTION OF NONLINEAR SHEAR WAVES

URMAS VALDEK
Department of Mechanics, Institute of Cybernetics
Estonian Academy of Sciences
200 108 TALLINN, ESTONIA

ABSTRACT

The two-dimensional problem of propagating nonlinear shear waves in solids by a bounded input is considered. Mathematical model is based on a special modified constitutive equation of the continuous nonlinear viscoelastic medium [1]. Using appropriate scaling of dependent and independent variables, the two-dimensional evolution equation of shear waves is derived. The evolution process of shear waves is analyzed by means of this equation. The effects of geometrical and physical nonlinearities, dissipation and diffraction are taken into account.

INTRODUCTION

The evolution equation approach has been widely used in dynamics of liquids and gases. In dynamics of solids such an asymptotic description is less used, but several problems are rather well analyzed. For example, one-dimensional longitudinal waves in solids have been described by the Burgers equation, which takes into account dissipation according to the Voigt model [2]. In the case of relaxing media, the evolution equation is, generally speaking, of integro-differential type. The two-dimensional evolution equation of longitudinal waves has also been derived and analyzed [3,4]. The corresponding two-dimensional mathematical models of shear waves in solids are much more complicated [5,6]. As to three-dimensional wave

motion then only cases with simplified assumptions are known[7].

In this paper three-dimensional shear waves are investigated on a rather general basis. A special modified constitutive equation of the continuous nonlinear viscoelastic medium is being used [1]. In contrast to the usual models, this constitutive equation permits to explain better the physical meaning of kernel functions, which describe viscous properties of the medium.

MATHEMATICAL MODEL

The Lagrangian strain tensor is taken in its full nonlinear form

$$E_{IJ}(t)= 1/2(U_{I,J}+ U_{J,I} + U_{K,I}U_{K,J}) \qquad (1)$$

where t is time, U_I are the components of displacement vector and a comma denotes the differentiation with respect to Lagrange variables X_I. The indices I,J run over 1,2,3.

It is assumed, that the Kirchoff pseudostress tensor T_{IJ} can be expanded in a Frechet' series in the form [1]

$$\begin{aligned} T_{IJ}(t) = & \int_0^t G^{(1)}_{IJKL}(t,\tau)E_{KL}(\tau)d\tau + \\ & + \int_0^t\int_0^t G^{(2)}_{IJKLMN}(t,\tau,\vartheta)E_{KL}(\tau)E_{MN}(\vartheta)d\tau\, d\vartheta + \\ & + \int_0^t\int_0^t\int_0^t G^{(3)}_{IJKLMNPR}(t,\tau,\vartheta,\nu)E_{kl}(\tau)E_{MN}(\vartheta)E_{PR}(\nu)d\tau\, d\vartheta\, d\nu \end{aligned} \qquad (2)$$

where τ, ϑ, ν are time variables and $G^{(1)}_{IJKL}$, $G^{(2)}_{IJKLMN}$, $G^{(3)}_{IJKLMNPR}$ are relaxation tensors.

Expression (2) is a quasi-linear constitutive equation in case $E_{KL}(t) = 0$ when $t < 0$.

Further, processes in an isotropic medium are considered. In this case relaxation tensors can be expressed by means of scalar relaxation functions and these relaxation functions may be separated into singular and regular parts [8]. Therefore the

constitutive equation can be expressed in the form [1]

$$
\begin{aligned}
T_{IJ}(t) = {} & \lambda(0)\delta_{IJ}E_{KK}(t) + 2\mu(0)E_{IJ}(t) + \\
& + \nu_1(0)\delta_{IJ}E_{KK}(t)E_{LL}(t) + \nu_2(0)\left[E_{IJ}(t)E_{KL}(t)E_{KL}(t) + \right. \\
& \left. + 2E_{kk}(t)E_{IJ}(t)\right] + 2\nu_3(0)E_{IK}(t)E_{KJ}(t) + \\
& + 4\varkappa_1(0)E_{kk}(t)E_{LL}(t)E_{MM}(t)\delta_{IJ} + \\
& + 2\varkappa_2(0)\left[E_{KK}(t)E_{LM}(t)E_{LM}(t)\delta_{IJ} + E_{KK}(t)E_{LL}(t)\right] + \\
& + 3\varkappa_3(0)E_{KK}(t)E_{IL}(t)E_{LJ}(t) + \\
& + 4\varkappa_4(0)E_{KL}(t)E_{KL}(t)E_{IJ}(t) - \\
& - \int_0^t \left[\lambda_1(t-\tau)\delta_{IJ}E_{KK}(\tau) + 2\mu_1(t-\tau)E_{IJ}(\tau)\right]d\tau
\end{aligned}
\tag{3}
$$

where λ, μ are the Lamè constants; ν_1, ν_2, ν_3 are the third-order elastic moduli; $\varkappa_1$, $\varkappa_2$, $\varkappa_3$, $\varkappa_4$ are the fourth-order elastic moduli; $\lambda_1(t)$, $\mu_1(t)$ are the modified relaxation kernel functions, and δ_{IJ} is the Kronecker delta-function.

The instantaneous part of (3) (with time-independent elastic moduli) coincides exactly with the expression of the stress tensor, which has been obtained according to the nine-constant theory of elasticity [6,9]. The similar structure of the linear instantaneous and the regular parts in the expression of stress tensor (3) enables us to interpret the kernel functions $\lambda_1(t)$, $\mu_1(t)$ as the time-dependent Lamè coefficients for the stress-relaxation response to a sudden deformation at time t = 0 [10].

In order to simplify further analysis, vectors $\vec{V}$, $\vec{U}$ and $\vec{U}$ are introduced

$$
\vec{V} = \begin{vmatrix} \dot{U}_1 \\ U_{1,1} \\ U_{1,2} \\ U_{1,3} \end{vmatrix}, \quad \vec{W} = \begin{vmatrix} \dot{U}_2 \\ U_{2,1} \\ U_{2,2} \\ U_{2,3} \end{vmatrix}, \quad \vec{U} = \begin{vmatrix} \dot{U}_3 \\ U_{3,1} \\ U_{3,2} \\ U_{3,3} \end{vmatrix} \tag{4}
$$

Then the equations of motion can be written in the form

$$
\begin{aligned}
& I\frac{\partial \vec{V}}{\partial t} + R^1\frac{\partial \vec{V}}{\partial X_1} + R^2\frac{\partial \vec{V}}{\partial X_2} + R^3\frac{\partial \vec{V}}{\partial X_3} + R^4\frac{\partial \vec{W}}{\partial X_1} + R^5\frac{\partial \vec{W}}{\partial X_2} + R^6\frac{\partial \vec{W}}{\partial X_3} + \\
& \quad + R^7\frac{\partial \vec{U}}{\partial X_1} + R^8\frac{\partial \vec{U}}{\partial X_2} + R^9\frac{\partial \vec{U}}{\partial X_3} +
\end{aligned}
\tag{5}
$$

$$+\int_0^t\Big[L^1(t-\tau)\frac{\partial\vec{V}(\tau)}{\partial X_1}+L^2(t-\tau)\frac{\partial\vec{V}(\tau)}{\partial X_2}+L^3(t-\tau)\frac{\partial\vec{V}(\tau)}{\partial X_3}+$$
$$+L^4(t-\tau)\frac{\partial\vec{W}(\tau)}{\partial X_1}+L^5(t-\tau)\frac{\partial\vec{W}(\tau)}{\partial X_2}+L^6(t-\tau)\frac{\partial\vec{U}(\tau)}{\partial X_1}+$$
$$+L^7(t-\tau)\frac{\partial\vec{U}(\tau)}{\partial X_3}\Big]d\tau=0\quad,$$

$$I\frac{\partial\vec{W}}{\partial t}+S^1\frac{\partial\vec{V}}{\partial X_1}+S^2\frac{\partial\vec{V}}{\partial X_2}+S^3\frac{\partial\vec{V}}{\partial X_3}+S^4\frac{\partial\vec{W}}{\partial X_1}+S^5\frac{\partial\vec{W}}{\partial X_2}+S^6\frac{\partial\vec{W}}{\partial X_3}+$$
$$+S^7\frac{\partial\vec{V}}{\partial X_1}+S^8\frac{\partial\vec{V}}{\partial X_2}+S^9\frac{\partial\vec{V}}{\partial X_3}+ \qquad (6)$$
$$+\int_0^t\Big[M^1(t-\tau)\frac{\partial\vec{V}(\tau)}{\partial X_1}+M^2(t-\tau)\frac{\partial\vec{V}(\tau)}{\partial X_2}+M^3(t-\tau)\frac{\partial\vec{W}(\tau)}{\partial X_1}+$$
$$+M^4(t-\tau)\frac{\partial\vec{W}(\tau)}{\partial X_2}+M^5(t-\tau)\frac{\partial\vec{W}(\tau)}{\partial X_3}+M^6(t-\tau)\frac{\partial\vec{U}(\tau)}{\partial X_2}+$$
$$+M^7(t-\tau)\frac{\partial\vec{U}(\tau)}{\partial X_3}\Big]d\tau=0,$$

$$I\frac{\partial\vec{U}}{\partial t}+T^1\frac{\partial\vec{V}}{\partial X_1}+T^2\frac{\partial\vec{V}}{\partial X_2}+T^3\frac{\partial\vec{V}}{\partial X_3}+T^4\frac{\partial\vec{W}}{\partial X_1}+T^5\frac{\partial\vec{W}}{\partial X_2}+T^6\frac{\partial\vec{W}}{\partial X_3}+$$
$$+T^7\frac{\partial\vec{U}}{\partial X_1}+T^8\frac{\partial\vec{U}}{\partial X_2}+T^9\frac{\partial\vec{U}}{\partial X_3}+ \qquad (7)$$
$$+\int_0^t\Big[N^1(t-\tau)\frac{\partial\vec{V}(\tau)}{\partial X_1}+N^2(t-\tau)\frac{\partial\vec{V}(\tau)}{\partial X_3}+N^3(t-\tau)\frac{\partial\vec{W}(\tau)}{\partial X_2}+$$
$$+N^4(t-\tau)\frac{\partial\vec{W}(\tau)}{\partial X_3}+N^5(t-\tau)\frac{\partial\vec{U}(\tau)}{\partial X_1}+N^6(t-\tau)\frac{\partial\vec{U}(\tau)}{\partial X_2}+$$
$$+N^7(t-\tau)\frac{\partial\vec{U}(\tau)}{\partial X_3}\Big]d\tau=0\quad,$$

where matrices R^m, S^m, T^m, $m = 1,\ldots,9$ consist of physical coefficients and may be functions of $U_{I,J}$. Due to the complicated form of the constitutive equation (3), these matrices are rather complicated. Matrices L^n, M^n, N^n, $n=1,\ldots,7$ consist of relaxation kernel functions. The Eqs.(5),(6),(7) describe the complete wave field in 3D space. The next step is to extract the single waves from system (5),(6),(7) by making use of the asymptotic method [3,11]. The physical description of the problem under consideration is the following. The free surface of the halfspace is subjected to the locally bounded loading, caused either by impact or by an ultrasound transducer. The single wave equations of shear waves are derived using the proper scaling and the proper initial conditions.

EVOLUTION EQUATION

A shear wave is generated by a transverse source on the free surface. Directing the axis X_1 into the halfspace, deformation $U_{2,1}$ is generated at $X_1 = 0$ and is bounded in X_2 and X_3.

The process is described in the reference frame which propagates with the velocity c_1 of a linear shear wave. It is a basic fact for shear waves that the shear component T_{21} of the stress tensor T_{IJ} (3) depends on $U_{2,1}$ and $(U_{2,1})^3$ but does not depend on $(U_{2,1})^2$ [5,9]. Therefore the ray variables for a shear wave in nonlinear theory are established in the following form

$$\xi = c_1 t - X_1 \quad , \qquad (8)$$
$$\tau_1 = \varepsilon^2 X_1 \quad , \quad \tau_2 = \varepsilon X_2 \quad , \quad \tau_3 = \varepsilon X_3$$

Since $U_{2,1}$ is a component of the vector $\vec{W}$, the latter is preferred when $\vec{V}$, $\vec{W}$ and $\vec{U}$ are expanded in series

$$\vec{V} = \varepsilon(\vec{V}_0 + \varepsilon^2 \vec{V}_1 + \ldots) \ ,$$
$$\vec{W} = \vec{W}_0 + \varepsilon^2 \vec{W}_1 + \ldots \ , \qquad (9)$$
$$\vec{U} = \varepsilon(\vec{U}_0 + \varepsilon^2 \vec{U}_1 + \ldots) \ .$$

The following variables are introduced

$$\beta = u u_0^{-1} \quad , \quad u = \dot{U}_2 = - U_{2,1} c_1^{-1} \quad , \quad \sigma = a_1 u_0^2 \tau_c^{-1} \tau_1 \ ,$$
$$\eta = b^{-1} \tau_2 \quad , \quad \gamma = b^{-1} \tau_3 \quad , \quad \zeta = \tau_c^{-1} \xi \ , \qquad (10)$$
$$a_1 = 3/4 |m_1 - m_2| (\varepsilon c_1)^{-2} \quad , \quad c_1 = \mu \rho_0^{-1} \ ,$$

where u_0 is the maximal initial amplitude of the input. In this case the ratios of the elastic constants turn out to obey

$$m_1 = (\lambda + 2\mu + 2\nu_2 + 3\nu_3 + 2\varkappa_4) \ \mu^{-1} \ ,$$
$$m_2 = (\lambda + 2\mu + \nu_2 + 2/3\nu_3)^2 \ [\mu(\lambda + \mu)]^{-1} \ , \qquad (11)$$

and the small parameter for this problem is

$$\varepsilon = 1/2 \ (\ 3|m_1 - m_2|)^{1/2} \ u_0 c_1^{-1} \quad . \qquad (12)$$

Then we obtain a nonlinear equation which describes asymptotically the evolution of a plane-polarized shear wave in three-dimensional space

$$\frac{\partial}{\partial \zeta} \left\{ \frac{\partial \beta}{\partial \sigma} - \left[\ \mathrm{sign}(m_1 - m_2) \beta^2 - \Pi \int_{\zeta} \frac{\partial \beta}{\partial \eta} d\zeta \ \right] \frac{\partial \beta}{\partial \zeta} + \right.$$
$$\left. + \ G \int_0^{\zeta} R\left[(\zeta - \tau)\tau_c / c_1\right] \frac{\partial \beta(\tau, \eta, \sigma)}{\partial \zeta} \, d\tau \right\} = \Delta \frac{\partial^2 \beta}{\partial \eta^2} \qquad (13)$$

Eq.(13) contains two dimensionless parameters which involve dependendence on the ratio τ_c/b

$$\Pi = (\lambda + 2\mu + \nu_2 + 3/2\nu_3)(\lambda + \mu)^{-1}(3|m_1 - m_2|)^{-1/2}\tau_c b^{-1},$$

$$\Delta = - \lambda [2(\lambda + \mu)]^{-1} \tau_c^2 b^{-2} . \qquad (14)$$

Relaxation parameter has the form

$$G = \tau_c c_1^{-1} \varepsilon^{-2} \qquad (15)$$

and we have relaxation kernel function in the form

$$R(\zeta\tau_c/c_1) = \mu_1(\zeta\tau_c/c_1)\ \mu^{-1} . \qquad (16)$$

DISCUSSION

The terms on the right hand side of Eq.(13) describe the effect of diffraction. It can be expected that wave diffraction in solids is influenced by deformation perpendicular to the main displacement vector. Particularly, longitudinal deformations are involved in shear wave diffraction. This becomes obvious if one looks at the system of equations which is available before elimination of $U_{2,1}$ (nonlinear and relaxation terms are omitted here)

$$\begin{cases} \dfrac{\partial U_{1,1}}{\partial \xi} = \varepsilon \dfrac{\mu}{\lambda + \mu} \dfrac{\partial U_{2,1}}{\partial \tau_2} \\ \varepsilon^2 \dfrac{\partial U_{2,1}}{\partial \tau_1} = - \varepsilon \dfrac{\lambda}{2\mu} \dfrac{\partial U_{1,1}}{\partial \tau_2} \end{cases} \qquad (17)$$

On the basis of Eq.(13) and Eqs.(17) it can be expected, that the diffraction of shear waves proceeds mainly in the polarization plane (in the plane τ_1, τ_2), while in the plane τ_1, τ_3 diffraction of the wave beam occurs much more slowly. On that account the shear waves equation remains two-dimensional although the asymptotics is based on the three-dimensional basic equations. This means that in fact the Eq.(13) should describe the three-dimensional evolution process of shear waves in the limits of the applied approximation.

The diffraction parameter Δ for a shear wave is always negative. The sign of the diffraction parameter does not affect the wave amplitude transform but phase shifts, which for

longitudinal waves and shear waves are diametrically opposite.

If deformation $U_{2,1}$ is calculated by means of Eq.(13), then deformation $U_{1,1}$ can be determined in a shear wave-beam

$$U_{1,1} = - \frac{\lambda + 2\mu + \nu_2 + 3/2\nu_3}{2(\lambda + \mu)} U_{2,1}^2 - \\ - \varepsilon \frac{\lambda}{\lambda + \mu} \int_{\xi} \frac{\partial U_{2,1}}{\partial \tau_2} d\xi \quad \sim O(\varepsilon^2) \tag{18}$$

An analogous result for the one-dimensional problem has been obtained by Bland [9]. The effect of finite longitudinal deformation on the shear wave transform causes a complicated nonlinear operator appearing in the Eq.(13). The structure of the integro-differential operator indicates that the process must be asymmetrical in the polarization plane of a beam.

The integro-differential term with the kernel function $R(\zeta)$ in Eq.(13) describes viscous properties of a medium. If the relaxation kernel functions in Eq.(3) have the form

$$\lambda_1(t) = - \Lambda_{,t}(t) \quad , \quad \mu_1(t) = - M_{,t}(t) \quad , \tag{19}$$

then the linear part of the constitutive equation (3) may be divided into a pressure and a deviation part according to the usual linear theory of viscoelasticity [1]. In this case it is possible to obtain the two- or three-dimensional model equations with linear dissipation from Eq.(13). In the one-dimensional approximation this equation is reduced to the modified Burgers equation [12].

REFERENCES

1. Ravasoo A. Some remarks on the quasi-linear theory of viscoelasticity (to appear in Proc.Est.Acad.Sci.).

2. Nariboli G.A, Sedov A. Burgers-Korteweg-de Vries equation for viscoelastic rods and plates. J.Math.Anal.Appl., 32 (1970), № 3, 661.

3. Engelbrecht J.Nonlinear wave processes of deformation in solids. Pitman, London, 1983.

4. Peipman T. On distortion of the two-dimensional deformation waves. Proc. Tartu Univ., 659 (1983), 76-82.

5. Valdek U., Engelbrecht J. An asymptotical description of nonlinear longitudinal and transverse deformation waves in half-space. Izvestiya Acad.Sci.USSR, Mechanics of Solids, N° 4, (1986), 101-105 (in Russian).

6. Peipman T., Valdek U., Engelbrecht J. Nonlinear two-dimensional longitudinal and shear waves in solids (submitted to Acoustica).

7. Zabolotskaya E.A. Sound beams in nonlinear isotropic solids. Sov.Phys.-Acoustics, 32 (1986), 474-479 (in Russian).

8. Ilyushin A.A, Pobedriya B.E. Fundamentals of the mathematical theory of thermo-viscoelasticity. Moscow, Nauka, 1970 (in Russian).

9. Bland D.R. Nonlinear dynamic elasticity. Waltham etc., Blaisdell Publ.Co, 1969.

10. Christensen R.M. Theory of viscoelasticity. New York, Academic Press, 1971.

11. Taniuti T., Nishihara K. Nonlinear waves. Pitman, London, 1983.

12. Nariboli G.A., Lin W.C. Anew type of Burgers equation. Z.angew.Math.Mech., N° 53 (1973), 505-510.

EXPERIMENTAL MODAL ANALYSIS AND COMPARATIVE FEM-ANALYSIS OF A GASTURBINE FOUNDATION PLATE

Pentti Varpasuo
Imatran Voima Oy, Rakennusosasto
P.O. Box 112, SF-01601 VANTAA, FINLAND

ABSTRACT

The modal analysis was carried out for common foundation plate of the turbine and the generator before the installation of machinery. In order to excite the modal shapes of the plate, the plate was shaken by a servohydraulic shaker using mainly broad band, white noise type excitation. The plate was excited in three points. The most important modal shapes detected were the following: (1) The rotation around the longitudinal axis of the foundation with the frequency of 21 Hz and the damping ration of 2.5 %; (2) the first verticl bending mode had the frequency of 32 Hz and the damping ratio of 5 %.

In FEM-analysis, the rotation mode around the longitudinal axis was detected at the frequency of 20.71 Hz. In case of other modeshapes the discrepacies berween the computed and the measured eigen frequencies were considerably larger. One reason to this discrepancy seems to be the fact that the excitation from three points only does not wake up all those mode shapes which were detected using FEM-analysis.

INTRODUCTION

The purpose of the experimental part of the investigation was to determine the most important modal parameters of the typical gasturbine foundation plate. The dimensions of the concrete plate were the following: length 21 m, width 4 m and height 1.3 m. The measurements of the foundation plate were carried out before the installation of the turbine-generator set. In experimental modal analysis the structure is described by the sum of simple oscillators. These oscillators are represented by three modal parameters, namely: the eigenfrequency, the associated mode shape and the damping ratio. The basic task of exprimental modal analysis is the determination of the frequency response function. In order to produce a frequency response function experimentally we need the response of the structure in a given point and also we need to know the force which has excited this response. By fitting a mathematical trial function to this frequency response function within the interesting frequency domain the above modal parameters can be solved. Usually structures have tens of eigenfrequencies within the interesting domain so that the

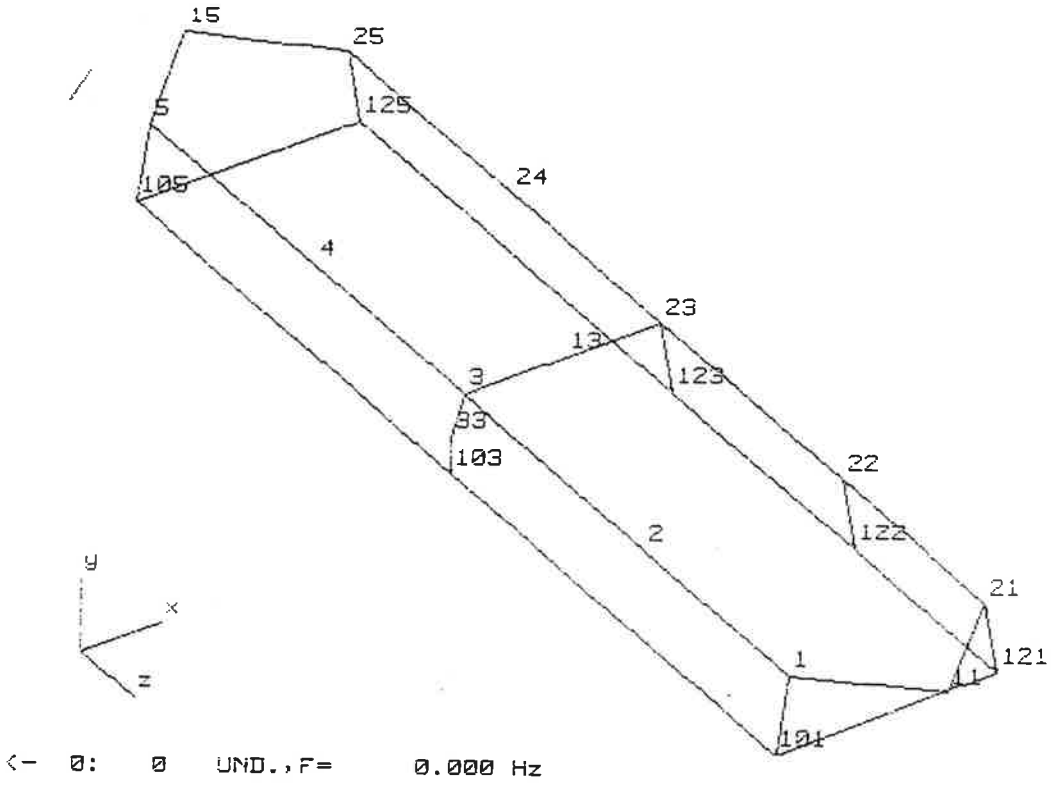

Figure 1. The location of the excitation points and the response points in experimental modal analysis.

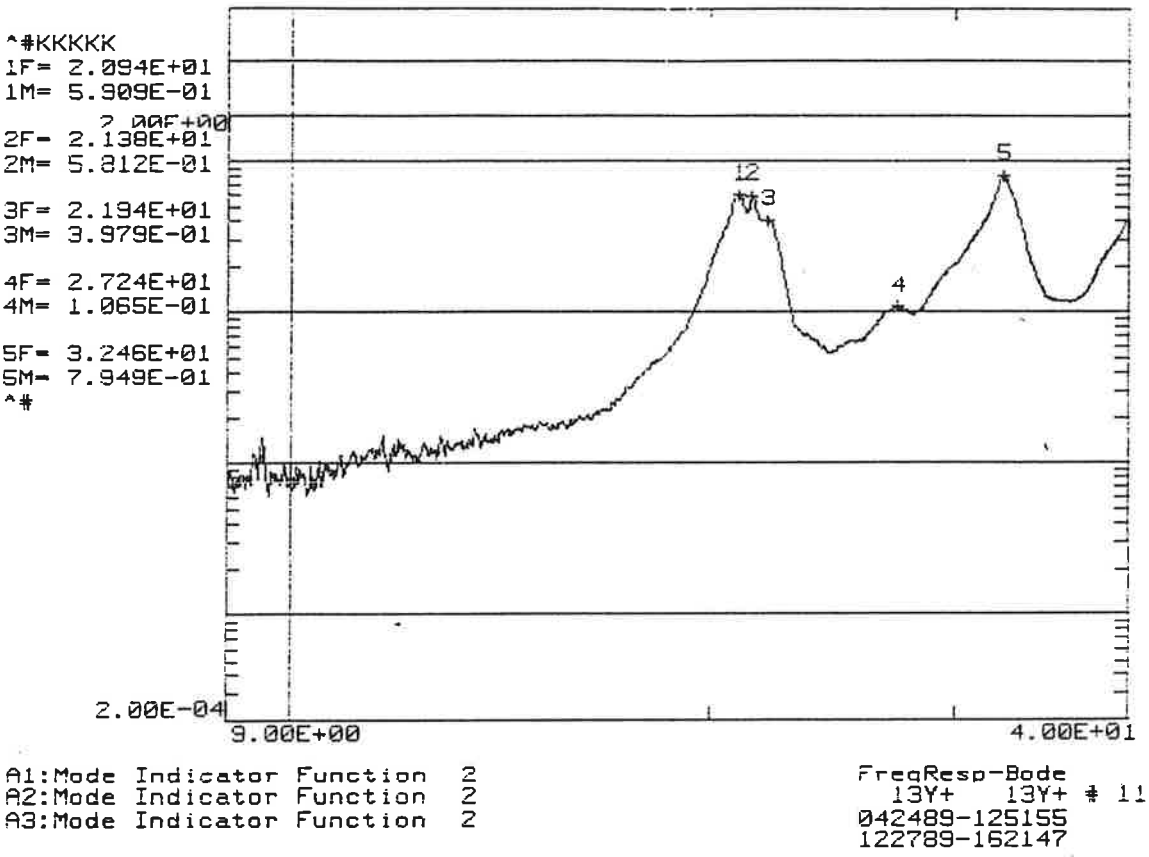

Figure 2. The indicator function when the excitation is applied at point 13Y.

Modal Parameters, PARAM, REF 13Y

Label	Freq	Damping	Amplitude	Phase	Ref	Res	Mode	Flags
1	18.985	0.01194	3.3820E-07	0.422	13Y+	105X-	1	0 0 0 1 1
2	20.040	0.07579	3.5991E-06	2.877	13Y+	15Y+	2	0 0 0 1 1
3	20.893	0.01531	5.4487E-06	1.631	13Y+	105X-	3	0 0 0 1 1
4	21.420	0.01341	4.3647E-06	1.480	13Y+	22Y+	4	0 0 0 1 1
5	22.504	0.01347	1.6047E-06	-1.085	13Y+	105X-	5	0 0 0 1 1
6	23.963	0.01953	2.0849E-06	-2.174	13Y+	105X-	6	0 0 0 1 1
8	26.382	0.01325	3.4676E-07	0.491	13Y+	1Y+	8	0 0 0 1 1
9	27.972	0.02675	3.9012E-06	-2.464	13Y+	1Y+	9	0 0 0 1 1
19	29.716	0.01633	1.6422E-06	1.540	13Y+	1Y+	19	0 0 0 1 1
20	32.011	0.05280	6.6296E-05	-1.425	23Y+	13Y+	20	0 0 0 1 1
21	32.771	0.02835	8.8653E-05	-1.011	23Y+	13Y+	21	0 0 0 1 1

#
#
#
#
#FS
S [cords in use of 30 Available
Rec 2: 20.040 Hz, Z-ROT+Z-TORS
Rec 3: 20.893 Hz, Z-ROT+Z-TORS
Rec 4: 21.420 Hz, Z-TORS+ROT
Rec 5: 22.504 Hz, Z-ROT
Rec 6: 23.963 Hz
Rec 9: 27.972 Hz
Rec 19: 29.716 Hz, 2:ND TORSION
Rec 20: 32.011 Hz, BENDING
Rec 21: 32.771 Hz, BENDING
#

Table 1. The solved eigenfrequencies with corresponding damping ratios for ecitation point 13Y.

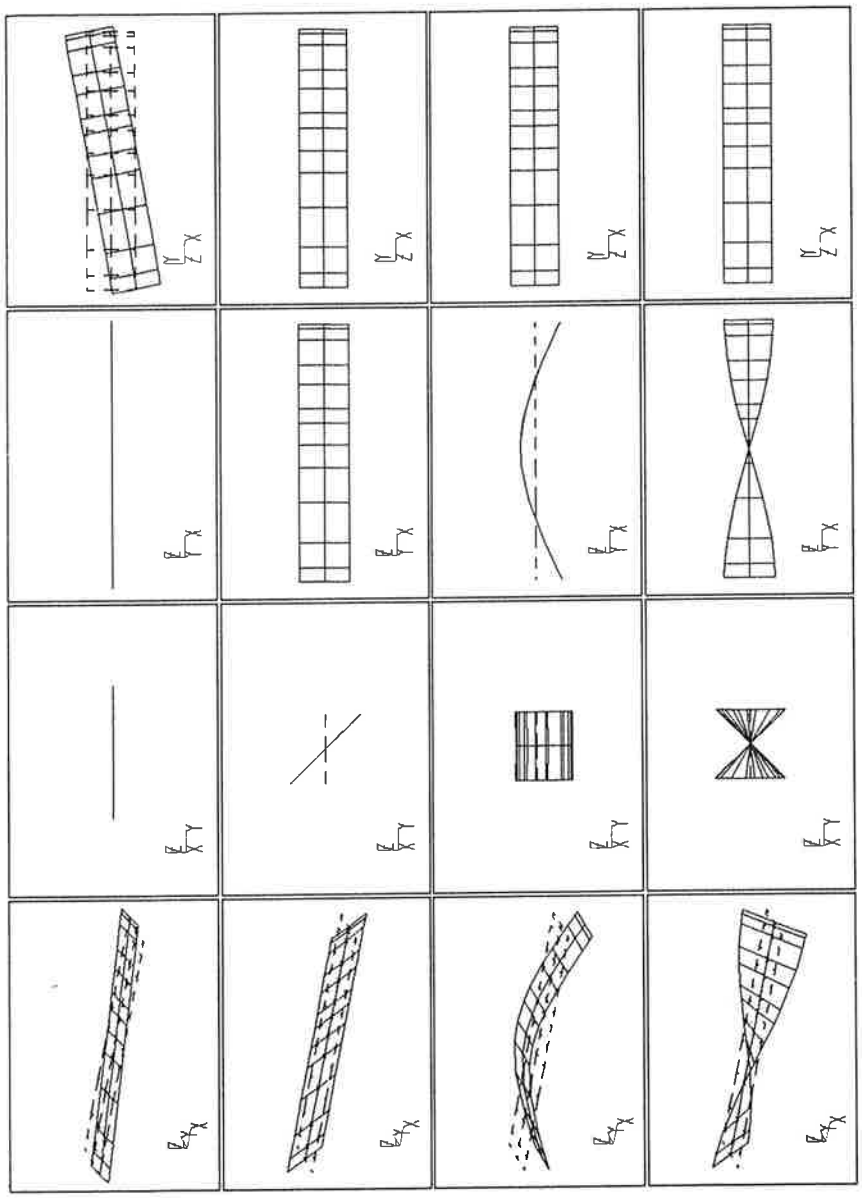

Figure 3. The modal shapes for the eigenfrequencies 20.06, 20.71, 22.21 and 33.13 Hz solved by FEM.

CHAOS AND ANOMALOUS CHAOTIC TRANSIENTS OF THE BOUNCING-BALL DYNAMICS

Heikki M. ISOMÄKI
Faculty of Information Technology
Helsinki University of Technology
SF-02150 Espoo 15, Finland

Marek FRANASZEK
Department of Computer Science
Higher Educational School
PL-30-084 Kraków, Poland

The essence of mechanics is the symmetric structure of the canonical phase space (q,p). This allows us to present the dynamics of an autonomous N degrees-of-freedom system in a 2N-dimensional phase space (or in a 2(N+1)-dimensional one in the nonautonomous case). The history of the motion is then found by solving 2N Hamilton's differential equations of first degree. Due to the special symmetry between q and p the equations can be solved using canonical transformations, which in a completely integrable system produce N (not 2N) independent analytic single-valued first integrals of q and p. These integrals comprise the constants along the calculated trajectory. Hence the trajectory lies on an N-dimensional manifold that in virtue of the Poincaré-Hopf hairy-ball theorem is topologically an N-torus. An N-torus is a naturally periodic object consisting of N independent periodicities. It is fixed by the canonically conjugate action-angle variables. Practically the whole phase space is filled with tori corresponding to different commensurate or incommensurate motions. However, these are not the only essential dynamical objects of the phase space. There are also fixed points, which mostly are elliptic or hyperbolic, and multidimensional separatrices, which connect the hyperbolic points and separate the two kinds of existing tori, the librations and rotations. The interactions and joinings of the separatrices are the key quantities in creating chaotic flows. For integrable systems the generic joining of the separatrix manifolds is smooth and consequently no chaos may exist.

The integrable systems with more than one degree of freedom cannot generally be ergodic on (2N-1)-dimensional energy shell. However, the ergodicity on the lower-dimensional tori is the rule rather than the exception. The simultaneously existing incommensurate trajectories outnumber the commensurate ones on a given energy shell. However, no phase space filling chaos is present. Hence for integrable systems the generic trajectory dimensionality of the dynamics is N. Note the terminology: general equations that can be solved by integrating may still be nonintegrable.

However, even most Hamiltonian systems are nonintegrable. So there remains a question, whether or when the trajectory of the generic dynamics would fill a region in the phase space of dimensionality greater than N. The answer to this question is qualitatively given by the celebrated Kolmogorov-Arnold-Moser (KAM) theorem. It states that in a perturbed near-integrable system most trajectories still lie on tori. However, the surviving tori are mainly incommensurate and there are chaotic trajectories that wander through gaps where commensurate tori have been destroyed. In these gaps bordered by incommensurate KAM surfaces the transversal homoclinic intersections of separatrices

are responsible for hyperbolic chaotic flows. In 2-degrees-of-freedom systems these gaps are disconnected but with more degrees of freedom the gaps form a single connected chaotic region controlled by Arnold's diffusion. Increasing the perturbation this local chaos transforms into global chaos when more and more KAM surfaces start breaking up.

The bouncing-ball dynamics were one of the first mechanisms in which the above KAM analysis has been performed. Several variant configurations have been extensively studied by Fermi, Ulam, Lieberman, Lichtenberg, Cohen, Zaslavsky, Chirikov, Rachko, Brahic, Pustylnikov, Holmes and others. In this paper we study the dissipative variant, which is much less explored.

The engineering systems are usually strongly dissipative. When the dissipation is incorporated in the system the nice theory of mechanics breaks up: the symplectic symmetry and the integrability conditions disappear. The system experiences a structural instability: tori are destroyed and converted into asymptotically stable attractors and the Hamiltonian chaos is removed. However, dissipation does not damp out interesting dynamics. The attractive property related to dissipation splits the chaotic dynamics into two parts: final state chaos and transient state chaos. In these the dynamics may fill exotic and complicated fractal phase-space sets exhibiting noninteger dimensions. These exotic motions can be found together with new commensurate and incommensurate attractors. And in virtue of the recent rapid development of the local and global analysis of nonlinear dynamics it is also evident that many ideas and methods related to the Hamiltonian chaos are carried to the theory of the dissipative chaos.

Why do we bother ourselves about the understanding of irregularity because all problems after all have to be solved numerically? Why don't we just concentrate in developing numerical codes, which we anyway have to resort to? One answer is that the irregularity is closely related to unpredictability. Forecasting and planning are important in the engineering dynamics and hence it is essential to understand how and when deterministic systems produce such irregularities that long-time predictions become impossible. The loss of predictability has such surprising consequences that all feasible numerical codes and computers are exhausted for rather small numbers of time steps in future forecastings. However, even the modest knowledge of the underlying mechanisms creating irregularities may help the engineers to avoid the worst pitfalls.

In many practical applications of the dissipative dynamic systems the transient motions are important. This understandably follows from the fact that in the study of real complex systems it is often impossible to include large number of different interactions in computations and one has to resort to simpler dynamical models in restricted phase spaces. Then the exogenous variables can be thought to play the role of small perturbations or to be added to the system so slowly that the basic deterministic short-time-scale dynamics are essentially valid. Consequently the relevant variables fluctuate in the noisy environment. But with a careful choice of the phase spaces we might expect that much of the fluctuations can be extracted from the underlying endogenous deterministic dynamics if we study the transient motions. Transient motions, on the other hand, can exhibit complexity, which is comparable to chaos but which has time-dependent characteristics. But the lifetimes of transients can be so long that the two dynamics are practically indistinguishable. The repellors form the invariant sets controlling the transients. Repellors are usually found after the boundary crises. A paradigm is the famous one-hump map where by changing the parameter we can find scrambled sets continuously. But if we suppose that those points that convey the motions close to the tangency regions are finally all mapped out then what remains is the non-attracting hyperbolic invariant set, repellor. Moreover, one believes that a chaotic repellor has discontinuities and holes transversal to the unstable direction, i.e., a double-cantor structure. However, in this paper we show how all this need not always be rigorously true and how consequently the transient chaos may be a complex problem of a non-hyperbolic repellor without characteristic holes.

The model studied in this paper is the dissipative bouncing-ball system that is a slightly modified version of the classical Hamiltonian dynamics problem originally raised by Enrico Fermi and Stanisław M. Ulam. In our modified Fermi-Ulam problem

[1,2,3,4,5,6] the ball is made to fly and impact dissipatively on a single sinusoidally vibrating surface under the influence of the gravitational acceleration, which consequently reverses the flight. The complete dimensionless equations of motion comprise a two-dimensional map (t_i, v_i) as follows

$$v_{i+1} = \kappa(2T_i - v_i) + (1+\kappa)\dot{h}_{i+1}, \qquad t_{i+1} = T_i + t_i \tag{1}$$

$$-T_i^2 + v_i T_i + h_i = h_{i+1}, \qquad h_i = H\cos t_i \tag{2}$$

In the above equations of motion t_i is the moment of the i'th surface-ball impact, T_i is the flight time, h is the surface's vertical position, $h_i = h(t_i)$, v_i is the ball's velocity after the i'th impact, H or the reduced number $\lambda = (1+\kappa)H$ denote the amplitude of the surface vibration and κ is the coefficient of restitution. Period-times are given in units 2π below. Our system is dissipative due to the non-elastic impacts with $\kappa = 0.86 < 1$ of the steel-ball experiments [1]. The motions can roughly be divided in simple and complex ones corresponding to $H < 2$ and $H > 2$, respectively [2]. But even the simple motions are very rich and relatively complicated as is depicted, e.g., for $H = 1.8$ with (t,u) basin (Fig. 1), where t=t_i is the moment and u=$v_i - \dot{h}_i$ is the relative velocity for the start of the ball's flight on the surface. In the basin we have five simultaneously stable modes, namely three Zaslavsky-Rachko (ZR) modes, one fixed mute mode and one exotic 3-impact period-3 mode [2,4].

In the following we study the transients of a temporarily-mute mode at $\lambda = 4.95$, which is so called chaotic self-reanimating mode [1,2]. In this mode the ball motion gradually slows down and finally the ball sticks to the surface. This final standstill is the ground state attractor, which follows the bouncing transient. Despite the fact that the motion in the ground state has lost all memory of the previous bouncing transient and is in this sense repeatable, the dynamics need not be really periodic if the transient is chaotic and related to a chaotic repellor. Hence the motions are irregular walks among unstable points because the chaotic bouncing transient always shadows some time the repellor. This is nicely seen in the similarity between a single long transient orbit (Fig. 2a) and the numerically constructed repellor (Fig. 2b) [5].

The repellor in Fig. 2b is constructed by using the Kantz-Grassberger ensemble method [7]. In this repellor we do not find any holes transversal to the unstable direction. In a careful check using two other methods as well, the Nusse-Yorke PIM triple method [8] and the overlapping manifolds method [9], we find the same result. In Figs. 2c and 2d we show how the stable and unstable manifolds touch each other tangentially in vast regions of the phase plane. Moreover, these results are valid for wide ranges of the control parameter H (or λ) [5]. Because basin boundaries embody a chaotic saddle-type repellor a practical consequence is [5] that the stable manifold is very dense with a capacity dimension close to 2 as shown in Fig. 3. The calculated box dimension is ≈ 1.85 by using the uncertainty exponent method of Grebogi, Ott, Yorke and McDonald [10]. Due to this high dimension the computational difficulties increase drastically. For instance, by increasing the initial condition accuracy by huge 6-7 decades in the black region the yield of correct final states increases only by a factor of 10. A detailed discussion about the above and other anomalies of the bouncing-ball problem will be published elsewhere [5,6].

Acknowledgements. We would like to thank Tamás Tél (Eötvös Loránd University), Gert Eilenberger (IFF der KFA Jülich), Michael Thompson (University College London), Francis C. Moon (Cornell University), Olli-Pekka Piirilä (Helsinki University of Technology) and Jukka A. Ketoja (University of Helsinki) for illuminating discussions. We also thank many participants of the workshop Dynamics Days in Düsseldorf in 1990 for beneficial and encouraging comments at our poster [3]. We thank the Finnish State Computing Centre VTKK and Forschungszentrum KFA Jülich for the provision of computational facilities.

References

[1] Z.J.Kowalik, M.Franaszek and P.Pierański, Phys. Rev. **37A**, 4016-4022 (1988).

[2] H.M.Isomäki, Fractal Properties of the Bouncing-Ball Dynamics, in: *Nonlinear Dynamics in Engineering Systems,* edited by W.Schiehlen (Springer, Berlin 1990), p. 125-131.

[3] M.Franaszek and H.M.Isomäki, Atypical Chaotic Transient of the Bouncing-Ball Dynamics, Eleventh Dynamics Days DD11, Düsseldorf, Federal Republic of Germany, 20-23 June 1990, P20.

[4] H.M.Isomäki, Chaos in an Impacting Force Problem, in: *Proc. Second World Congress on Computational Mechanics,* Stuttgart, Federal Republic of Germany, 27-31 August 1990, edited by I. St. Doltsinis, p. 90-93.

[5] M.Franaszek and H.M.Isomäki, Anomalous Chaotic Transients and Repellers of the Bouncing-Ball Dynamics, Phys. Rev. **A**, 6 pages (1991), in press.

[6] H.M.Isomäki and M.Franaszek, in preparation.

[7] H.Kantz and P.Grassberger, Physica **17D**, 75-86 (1985).

[8] H.E.Nusse and J.A.Yorke, Physica **36D**, 137-156 (1989).

[9] T.Tél, Transient Chaos, in: *Directions in Chaos*, vol. **3**, edited by Hao Bai-Lin (World Scientific, Singapore 1990), p. 149-211.

[10] S.W.McDonald, C.Grebogi, E.Ott and J.A.Yorke, Physica **17D**, 125-153 (1985); P.M. Battelino, C. Grebogi, E. Ott, J.A. Yorke and E.D. Yorke, Physica **32D**, 296-305 (1988).

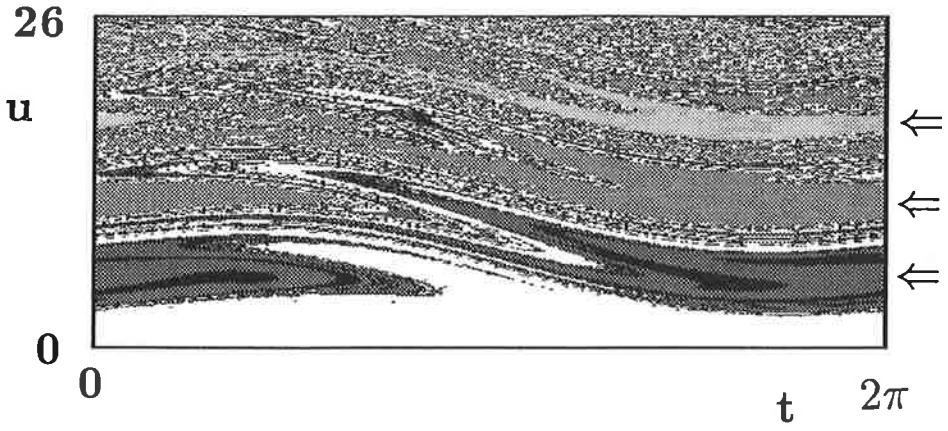

Figure 1. (t,u) basin at $H = 1.8$ with five simultaneous attractors: the white denotes the mute mode basin, the black denotes the exotic 3-impact period-3 mode basin and the grey in three tones denotes the ZR mode 1-impact period-i, i=1,2,3 basins. The main horizontal tongues of the ZR mode basins are marked with arrows.

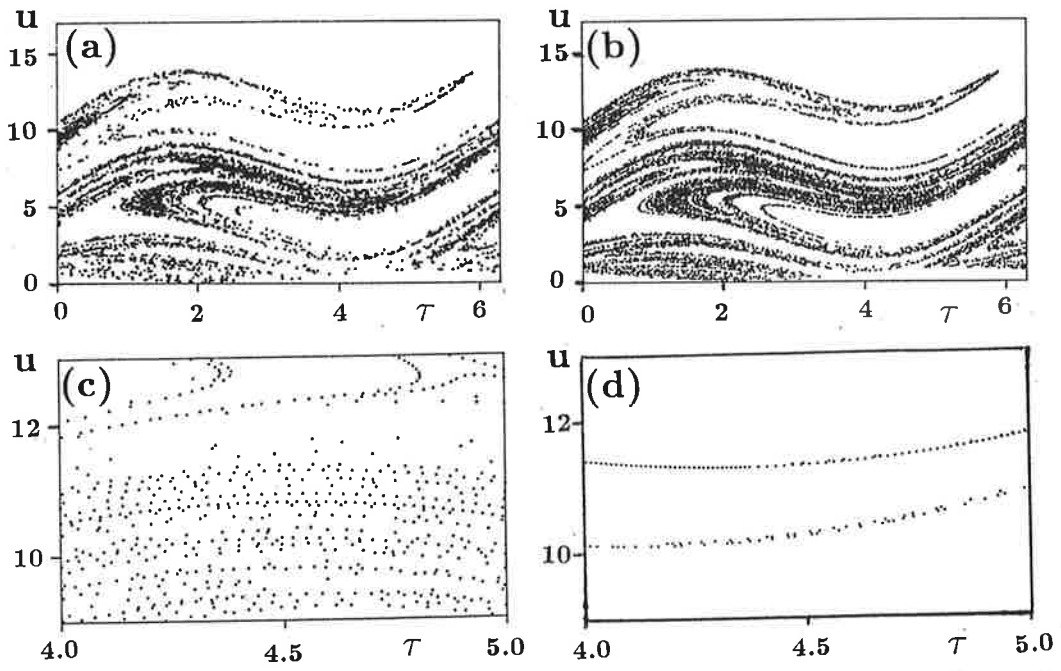

Figure 2. Poincaré sections (τ,u) for $H = 2.661$ ($\lambda = 4.95$), $\tau = t + \pi$. a) single chaotic transient; b) the repellor calculated by the ensemble method. Blow-ups of a region where the stable (c) and unstable (d) manifolds are parallel.

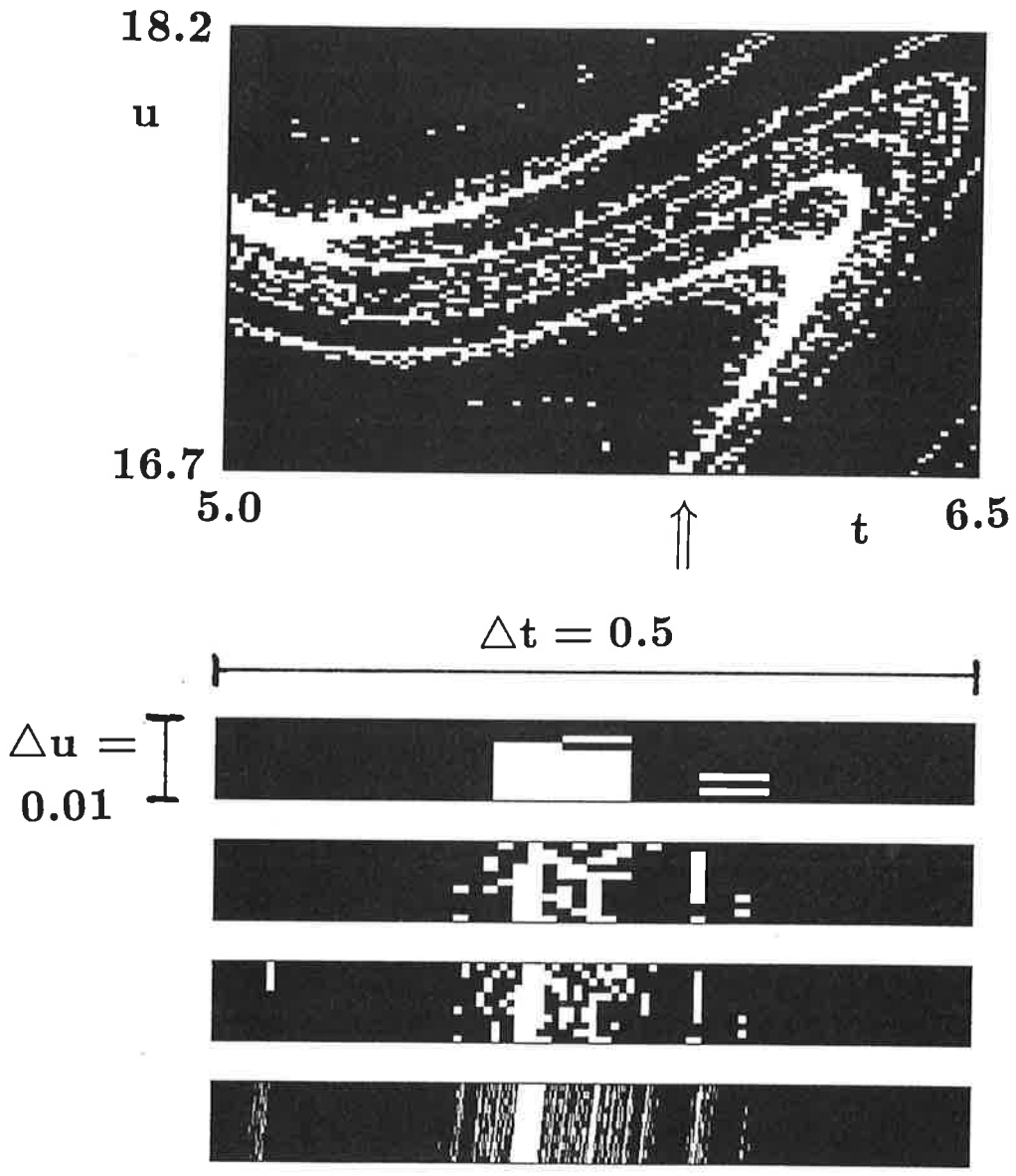

Figure 3. Basin for $H = 2.661$ ($\lambda = 4.95$). The black denotes the chaotic self-reanimating mode basin and the white denotes the ZR 2-impact period-6 basin. The lower part shows the blow-up of a horizontal bar of 0.5 x 0.01 at the white throat of the upper figure marked with an arrow. The refined grids are from the top to the bottom 10, 50,100 and 1000, respectively.

NON-NEWTONIAN FLUID MODELS IN ELASTOHYDRODYNAMIC LUBRICATION

HANNU IIVONEN
Laboratory of Machine Design
Tampere University of Technology
P.O. 527, 33101 Tampere, Finland

BERNARD J. HAMROCK
Department of Mechanical Engineering
The Ohio State University
206 West 18th Avenue, Columbus, Ohio 43210, USA

ABSTRACT

The pressure profiles, the film shapes, and the shear stress distributions for two different non-Newtonian fluid models were compared. The slide-to-roll ratio was varied between 0.0 and 10.0. Results show that the circle model is more severe model than the straight-line model and that the pressure spike vanishes for both models when the slide-to-roll ratio is greater than two. Furthermore, the maximum pressure decreases as the shear stress approaches the limiting shear strength and the non-Newtonian effects become stronger. It was also found that the effects in the film shape and the pressure profile are similar for both models when the shear stress is close to the limiting shear strength. For the straight-line model this requires higher values of the slide-to-roll ratio. The film collapses in the center of the contact when the shear stress is close to the limiting shear strength.

NOMENCLATURE

A	slide-to-roll ratio, $(u_b - u_a) / \bar{u}$
b	semiwidth of Hertzian contact, $R\ (8W/\pi)^{1/2}$
C_S	dimensionless constant, $\pi U/8W$
C_T	dimensionless constant, $2W/\pi$
E	modulus of elasticity, Pa
E'	effective elastic modulus, $2\left[\frac{(1-\upsilon_a^2)}{E_a}+\frac{(1-\upsilon_b^2)}{E_b}\right]^{-1}$, Pa
G	dimensionless materials parameter, $\alpha E'$
H	dimensionless film thickness, hR/b^2
H_{end}	dimensionless film thickness at $X=X_{end}$
h	film thickness, m
h_{end}	film thickness at outlet, m

K	constant, $3\pi^2 U/4W^2$
P	dimensionless pressure, p/p_h
p	pressure, Pa
p_h	maximum Hertzian pressure, $E'b/4R$, Pa
R	equivalent radius, $\left(\frac{1}{r_a}+\frac{1}{r_b}\right)^{-1}$, m
r	radius of curvature, m
S	variable, $\eta\bar{u}/h\,\tau_L = C_S\,(\bar{\eta}/H\,\bar{\tau}_L)$
T	variable, $\left(\frac{h}{\tau_L}\frac{dp}{dx}\right) = C_T\left(\frac{H}{\bar{\tau}_L}\frac{dP}{dX}\right)$
U	dimensionless speed parameter, $\eta_0\bar{u}/E'R$
u	velocity of lubricant in x-direction, m/s
$\bar{u}$	mean velocity, $(u_a + u_b)/2$, m/s
W	dimensionless speed parameter, $w/E'R$
w	applied load per unit length, N/m
X	dimensionless coordinate, x/b
X_{end}	dimensionless outlet meniscus distance
x	coordinate in direction of movement, m
α	pressure viscosity coefficient of fluid, Pa^{-1}
γ	limiting shear strength proportionality constant
$\dot{\gamma}$	shear strain rate, 1/s
η	absolute viscosity of fluid, Pa s
$\bar{\eta}$	dimensionless viscosity, η/η_0
$\bar{\eta}^*$	dimensionless representative viscosity
η_{eff}	effective viscosity, $\tau/\dot{\gamma}$
η_0	viscosity at atmospheric pressure, Pa s
υ	Poisson's ratio
ρ	lubricant density, kg/m^3
$\bar{\rho}$	dimensionless density of lubricant, ρ/ρ_0
ρ_0	density at atmospheric pressure, kg/m^3
τ	shear stress, Pa
τ_0	shear strength at atmospheric pressure, Pa
$\bar{\tau}$	dimensionless shear stress, τ/τ_L
$\bar{\tau}_0$	dimensionless initial shear strength, τ_0/E'
$\bar{\tau}_L$	dimensionless limiting shear strength, τ_L/E'

Subscripts

a	lower surface
b	upper surface
eff	effective

INTRODUCTION

Elastohydrodynamic lubrication is a form of fluid-film lubrication, in which elastic deformation of the contacting surfaces becomes significant. EHL is usually associated with nonconformal contacts, such as rolling-element bearings and gears. In this kind of contact the load has to be carried out by a very small lubrication area. The contact area is usually three orders of magnitude smaller than the contact area in conformal contacts, and for this reason the contact pressure builds up to a very high value (typically 0.7 - 3.0 GPa). This high contact pressure causes significant elastic deformation in the contacting surfaces. Deformations are typically several orders of magnitude greater than the actual minimum film thickness. Furthermore the viscosity of the lubricant can vary by 8 orders of magnitude within the conjunction as a result of the pressure variation. Thus both elastic and pressure-viscosity effects have to be incorporated in the analysis of EHL.

In most EHL analyses the lubricant is assumed to behave in a Newtonian manner. This implies that the shear stress is linearly related to the shear strain rate. This assumption is valid when the sliding speed and the pressure in the conjunction are relatively low. But in nonconformal contacts, where the pressure is high, the lubricant experiences rapid and large pressure variations and, particularly in sliding contacts, high shear rates. The great severity of these conditions has called into question the assumption of Newtonian behavior.

It has been observed by Bair and Winer [1] and Jacobson [2] that at a given pressure and temperature there is a critical shear stress at which the lubricant will shear plastically without any further increase in the shear stress with increasing shear strain rate. This limiting shear strength can be expressed as

$$\tau_L = \tau_0 + \gamma p \,, \tag{1}$$

where τ_L is the limiting shear strength at pressure p, τ_0 is the shear strength at atmospheric pressure, γ is the shear strength proportionality constant, and p is the pressure. A good way to interpret various non-Newtonian models is to use the effective viscosity [3]. It can be defined as

$$\eta_{eff} = \frac{\tau}{\dot{\gamma}} \,, \tag{2}$$

where τ is the shear stress and $\dot{\gamma}$ is the shear strain rate. Using this form, the well-known non-Newtonian models of Bair and Winer [3] can be written as

$$\frac{\eta_{eff}}{\eta} = -\frac{\bar{\tau}}{\ln(1-\bar{\tau})} \tag{3}$$

and

$$\frac{\eta_{eff}}{\eta} = \frac{\bar{\tau}}{\tanh^{-1}\bar{\tau}} \,, \tag{4}$$

where $\bar{\tau} = \tau/\tau_L$.

Houpert and Hamrock [4] used the Eyring model, which can be written as

$$\frac{\eta_{eff}}{\eta} = \frac{(\tau/\tau_E)}{\sinh(\tau/\tau_E)} \,, \tag{5}$$

where τ_E is the shear stress at which the fluid first starts to behave nonlinearly when stress is plotted against shear strain rate.

The behavior of all models presented so far is shown in Fig. 1. It can be seen that in the models of Bair and Winer the effective viscosity approaches zero asymptotically as the shear stress approaches the limiting shear strength, whereas in the Eyring model the effective viscosity decreases slowly and there is no limiting value. In the new model the effective viscosity decreases linearly with increasing shear stress.

New fluid models describing the non-Newtonian behavior of lubricants have been presented lately. One of the most interesting new models is the general model [5], which can written as

$$\frac{\eta_{eff}}{\eta} = \left(1 - \bar{\tau}^n\right)^{\frac{1}{n}}. \tag{6}$$

When n=1 this model becomes the straight-line model

$$\frac{\eta_{eff}}{\eta} = 1 - \bar{\tau}, \tag{7}$$

which was presented by Iivonen and Hamrock [6]. When n=2 it is the circle model

$$\frac{\eta_{eff}}{\eta} = \left(1 - \bar{\tau}^2\right)^{\frac{1}{2}} \tag{8}$$

of Lee and Hamrock [7]. When n is further increased, the general model approaches the viscoplastic fluid behavior shown in Fig. 2. In this paper the film shape, the pressure profile, and the shear stress distribution are compared for n=1 and n=2 (i.e. straight-line and circle models). The method for solving the Reynolds equation is described in [8] in detail and will not be repeated here. Only the relevant equations for both models are presented.

MODIFIED REYNOLDS EQUATIONS

The classical Reynolds equation has been obtained assuming the lubricant behavior to be linear viscous. This equation has to be modified in order to incorporate the new non-Newtonian model into it. In the following analysis the flow is assumed to be steady and isothermal. Furthermore the length of the contact is assumed to be much greater than its width. This allows side leakage to be neglected.

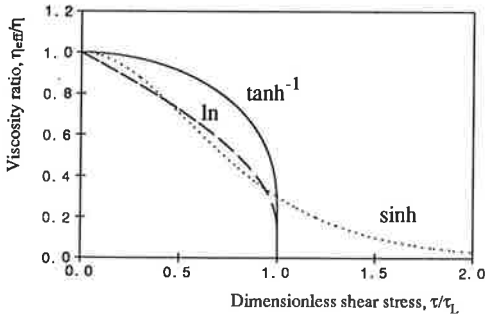

FIGURE 1. Various viscous fluid models.

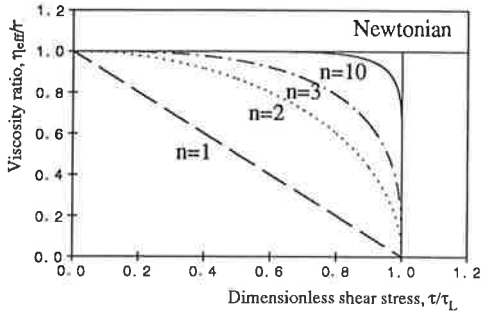

FIGURE 2. General model.

STRAIGHT-LINE MODEL

The modified Reynolds equation for the straight line model can be taken from Iivonen and Hamrock [6]. The straight line model can be rewritten as

$$\dot{\gamma}=\frac{\tau_L}{\eta}\frac{\bar{\tau}}{1-\bar{\tau}}. \tag{9}$$

The shear stress at surface a can be derived as

$$\bar{\tau}_a=1-\frac{e^{AST+T}}{e^{AST+T}-1}T=1-\frac{T}{2}-\frac{T}{2}\coth\left[\frac{(AS+1)T}{2}\right], \tag{10}$$

and at surface b as

$$\bar{\tau}_b=\bar{\tau}_a+T, \tag{11}$$

and the modified Reynolds equation as

$$f=H^3\frac{dP}{dX}+K\bar{\eta}^*\left(\frac{H_{end}}{\bar{\rho}}-H\right)=0, \tag{12}$$

where

$$K=\frac{3\pi^2U}{4W^2} \qquad P=\frac{p}{p_h}$$
$$U=\frac{\eta_0\bar{u}}{E'R} \qquad X=\frac{x}{b} \qquad \bar{\eta}=\frac{\eta}{\eta_0} \tag{13}$$
$$W=\frac{w}{E'R} \qquad H=\frac{hR}{b^2}$$

and

$$\bar{\eta}^*=\frac{T^2/12}{\frac{(AS+1)T}{2}\coth\left[\frac{(AS+1)T}{2}\right]-1}\bar{\eta}. \tag{14}$$

CIRCLE MODEL

The modified Reynolds equation for the circle model can be taken from Lee and Hamrock [7]. The circle model can be written as

$$\dot{\gamma}=\frac{\tau_L}{\eta}\frac{\bar{\tau}}{\left(1-\bar{\tau}^2\right)^{\frac{1}{2}}}. \tag{15}$$

The dimensionless shear stress at surface a can be written as

TABLE 1.
Relevant properties of the oil used.

Viscosity at atmospheric pressure η_0, Pa s	0.01326
Pressure-viscosity coefficient α, Pa^{-1}	1.582×10^{-8}
Limiting shear strength proportionality constant, γ	0.076

$$\bar{\tau}_a = -\frac{T}{2} + AS\left(\frac{1}{A^2S^2} - \frac{T^2}{4}\right)^{1/2}, \tag{16}$$

and the dimensionless shear stress at surface b as

$$\bar{\tau}_b = \bar{\tau}_a + T. \tag{17}$$

Furthermore, the modified Reynolds equation can be written as

$$f = H^3 \frac{dP}{dX} + K\bar{\eta}^*\left(\frac{H_{end}}{\bar{\rho}} - H\right) = 0, \tag{18}$$

where

$$\bar{\eta}^* = \frac{T^3\bar{\eta}/6}{\sin^{-1}e - e}, \tag{19}$$

and

$$e = \bar{\tau}_b\left(1 - \bar{\tau}_a^2\right)^{1/2} - \bar{\tau}_a\left(1 - \bar{\tau}_b^2\right)^{1/2}. \tag{20}$$

RESULTS AND DISCUSSION

One oil, a polyglycol synthetic oil was studied. The properties of that oil are given in Table 1, where the value of γ was taken from [9]. In the analysis the effect of the slide-to-roll ratio A on the film shape, the pressure profile and the shear stress distribution was studied for fixed values of the dimensionless load parameter ($W = 0.6\text{x}10^{-4}$) and the dimensionless speed parameter $U = (1.0\text{x}10^{-11})$. The pressure profiles, the film shapes, and the shear stress distributions at surface a for A=0.0 are shown in Fig. 3. For the operating parameters described above and for low slide-to-roll ratios and low shear stresses, there is no difference between the two models. When the lower body is stationary (A=2.0), the shear stress for the circle model is close to the limiting value, as is shown in Fig. 4. The spike has almost vanished and there is a clear difference in the shear stress between the models. The shear stress is approaching the limiting shear strength faster for the circle model than for the straight-line model. This implies that the circle model is a stronger model to describe the behavior of a non-Newtonian fluid. When A=5.0, the shear stress for the circle model is exteremely close to the limiting shear strength at the central region of the contact, as shown in Fig. 5. This causes changes in the pressure profile and the film shape. The pressure gradient in the inlet region is getting steeper, and an additional nip is forming in the film shape. Results for A=10.0 are shown in Fig. 6. The effects of the non-Newtonian behavior for the circle model are stronger and the maximum pressure is decreasing. The shear

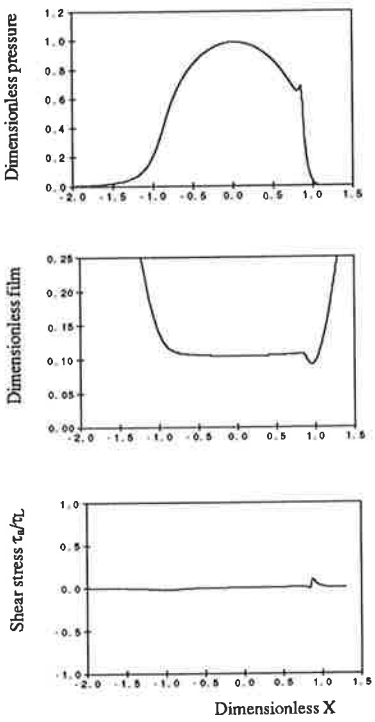

FIGURE 3. Results for A=0.0.

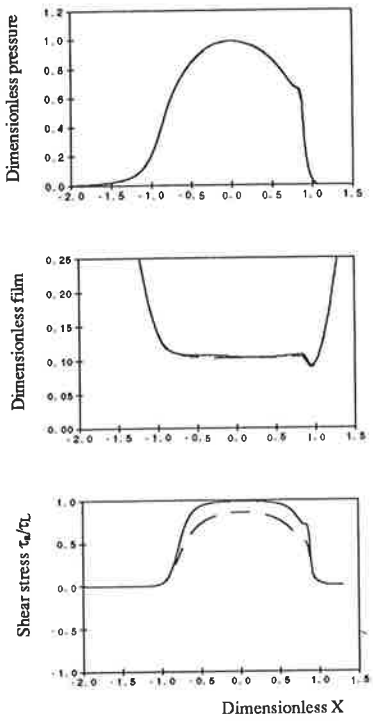

FIGURE 4. Results for A=2.0.

stress for the straight line model has not yet reached the limiting shear strength and thus no distortion can be seen in the pressure profile and the film shape. It can be expected that, as the sliding speed is further increased, similar effects will be seen for the straight-line model as were seen for the circle model. It is also shown in Fig. 6 that the non-Newtonian effects are causing the film collapse in the center of the contact for the circle model.

CONCLUSIONS

The following conclusions were drawn:

1. The circle model is more severe than the straight-line model.
2. For both models the pressure spike vanishes when the slide-to-roll ratio is greater than two.
3. There are no distortions in the pressure profile and the film shape until the shear stress is extremely close to the limiting shear strength.
4. The maximum pressure decreases as the slide-to-roll ratio is increased because the shear stress approaches the limiting shear strength.
5. When the shear stress is close to the limiting shear strength, the results for both models are similar.
6. As the shear stress approaches the limiting shear strength, the film collapses in the center of the contact.

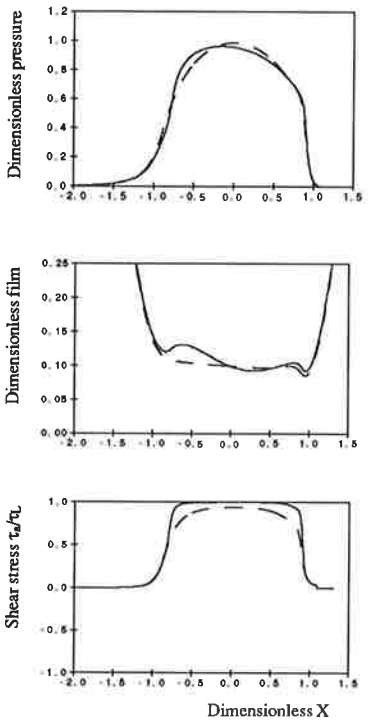

FIGURE 5. Results for A=5.0.

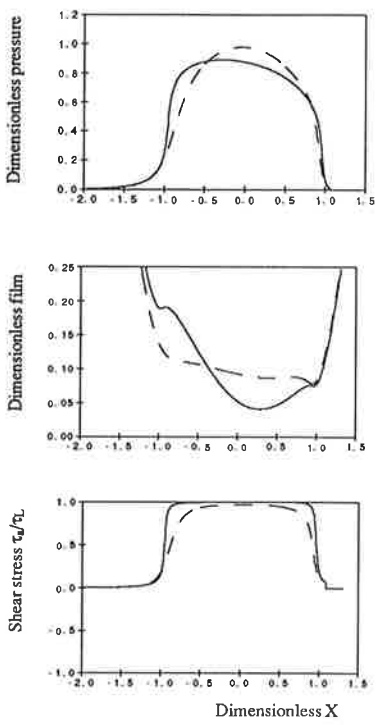

FIGURE 6. Results A=10.0.

REFERENCES

1. Bair, S. and Winer, W.O. (1979) "Shear Strength Measurements of Lubricants at High Pressures", ASME J. Lubr. Technol., vol. 101 (3), pp. 251-257.
2. Jacobson, B.O. (1985) "A High-Pressure-Short-Time Shear Strength Analyzer of Lubricant", ASME J. Trib., vol. 107 (2), pp. 220-223.
3. Bair, S. and Winer, W.O. (1979) "A Rheological Model for Elastohydrodynamic Contacts Based on Primary Laboratory Data", ASME J. Lubr. Technol., vol. (101) (3), pp. 258-265.
4. Houpert, L. and Hamrock, B.J. (1985) "Elastohydrodynamic Lubrication Calculations Used as a Tool to Study Scuffing", Proceedings of the 12th Leeds-Lyon Symposium on Tribology, Mechanical Engineering Publications, Bury St. Edmunds, Suffolk, England.
5. Elsharkawy, A.A and Hamrock, B.J. (1990). "Subsurface Stresses in Micro-EHL Line Contacts". To be published in ASME Journal of Tribology.
6. Iivonen, H. and Hamrock, B.J. (1989). "A New Non-Newtonian Fluid Model for Elastohydrodynamic Lubrication of Rectangular Contacts". In: Proceedings of the 5th International Tribology Conference Eurotrib 89 vol. 2. Edited by Kenneth Holmberg and Ilkka Nieminen. (The Finnish Society for Tribology, Helsinki), 178-183.
7. Lee, R.T. and Hamrock, B.J. (1990). "A Circular Non-Newtonian Fluid Model - Part I - Used in Elastohydrodynamic Lubrication". ASME J. of Trib., vol. 112, pp. 486-496.
8. Iivonen, H. (1990). "Effect of Non-Newtonian Lubricant Behavior on Elastohydrodynamic Lubrication of Rectangular Contacts". Licentiate thesis, Tampere University of Technology, Tampere.
9. Höglund, E. (1984). "Elastohydrodynamic Lubrication - Interferometric Measurements, Lubricant Rheology and Subsurface Stresses", Doctoral Thesis 1984-32D, Luleå University of Technology, Sweden.

NUMERICAL CALCULATIONS OF FREE CONVECTION FLOWS IN A TALL VERTICAL CAVITY

TUOMAS PALOPOSKI & EERO-MATTI SALONEN

Helsinki University of Technology
SF-02150 ESPOO, FINLAND

ABSTRACT

Numerical calculations of the heat transfer by free convection across a tall, vertical cavity filled with air are reported. Two commercial, general-purpose fluid dynamics programs were used in the calculations. The calculated flow fields and temperature fields were in good agreement with theoretical and experimental results found in the literature. The average heat transfer coefficient could be predicted with good accuracy. The onset of the flow instability was also studied, and the multicellular secondary flow was observed.

INTRODUCTION

Rectangular cavities filled with air are commonly used for thermal insulation; they can be found between window glazings, inside walls, and in solar collectors. The heat transfer by free convection across such cavities has been extensively studied both theoretically and experimentally, and the main features of the flow are well understood today. The flow is uniquely determined by the Grashof number Gr, the Prandtl number Pr, and the geometry of the cavity. For practical purposes, it is usually sufficient to determine the average heat transfer coefficient as a function of cavity geometry and wall temperatures. Thus, we are looking for a relationship of the type $\mathrm{Nu} = f(\mathrm{Gr},\mathrm{Pr},\mathrm{geometry})$, where Nu is the Nusselt number.

However, the problem is also of interest to those studying flow instability. As the Grashof number is gradually increased, the flow becomes unstable at $\mathrm{Gr} \approx 10^4$, and a row of steady, two-dimensional convection rolls develops. More complicated, three-dimensional instabilities appear as the Grashof number is further increased, and the flow finally becomes turbulent at around $\mathrm{Gr} \approx 10^9$. The first transition can be studied with rather modest computer resources and therefore provides an excellent benchmark for computational fluid dynamics.

PROBLEM FORMULATION

Consider a rectangular cavity of height H and width L as shown in Fig. 1. The cavity is assumed to be tall (the aspect ratio $\Gamma = H/L \gg 1$) and vertical. In the z-direction, at right angles to the plane of the figure, the cavity is regarded as extending to infinity. Thus, the flow is expected to be two-dimensional.

The left sidewall of the cavity is held at a constant temperature T_1 and the right sidewall at a constant temperature T_2. For the sake of simplicity, let us assume that $T_2 > T_1$. The temperature difference $\Delta T = T_2 - T_1$ is assumed to be small when compared to the average temperature $T_0 = (T_1 + T_2)/2$. The top and the bottom of the cavity are insulated.

The cavity is filled with air at atmospheric pressure p_0. The viscosity η, the thermal conductivity λ, and the specific heat capacity c_p of air are assumed to be constants. The pressure variations are assumed to be small compared with p_0; thus, the density of air can be assumed to be a function of temperature only:

$$\rho = \rho(p_0, T) = \rho_0[1 - \beta_0(T - T_0)] \tag{1}$$

where $\rho_0 = \rho(p_0, T_0)$ and $\beta_0 = \beta(p_0, T_0)$. Here we have introduced the volumetric coefficient of thermal expansion β. Using the ideal gas law, we obtain $\beta_0 = 1/T_0$.

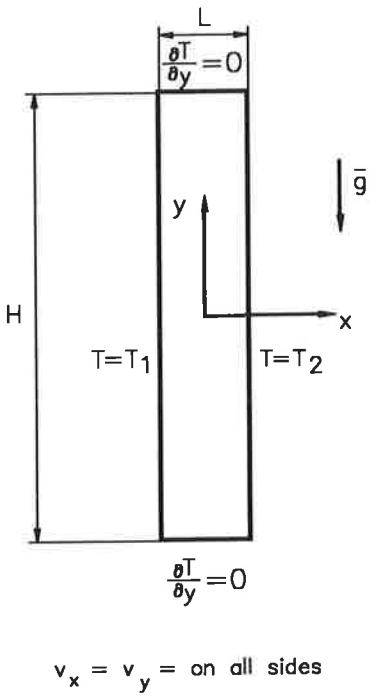

FIGURE 1. A sketch of a tall, vertical cavity.

The conventional Boussinesq equations for steady, two-dimensional flow can now be applied. In dimensionless form they can be written as:

a) *Continuity*

$$\frac{\partial \tilde{v}_x}{\partial \tilde{x}} + \frac{\partial \tilde{v}_y}{\partial \tilde{y}} = 0 \tag{2}$$

b) *Momentum*

$$\tilde{v}_x \frac{\partial \tilde{v}_x}{\partial \tilde{x}} + \tilde{v}_y \frac{\partial \tilde{v}_x}{\partial \tilde{y}} = -\frac{\partial \tilde{P}}{\partial \tilde{x}} + \frac{1}{\mathrm{Gr}}\left(\frac{\partial^2 \tilde{v}_x}{\partial \tilde{x}^2} + \frac{\partial^2 \tilde{v}_x}{\partial \tilde{y}^2}\right) \tag{3}$$

$$\tilde{v}_x \frac{\partial \tilde{v}_y}{\partial \tilde{x}} + \tilde{v}_y \frac{\partial \tilde{v}_y}{\partial \tilde{y}} = -\frac{\partial \tilde{P}}{\partial \tilde{y}} + \frac{1}{\mathrm{Gr}}\left(\frac{\partial^2 \tilde{v}_y}{\partial \tilde{x}^2} + \frac{\partial^2 \tilde{v}_y}{\partial \tilde{y}^2} + \tilde{T}\right) \tag{4}$$

c) *Energy*

$$\tilde{v}_x \frac{\partial \tilde{T}}{\partial \tilde{x}} + \tilde{v}_y \frac{\partial \tilde{T}}{\partial \tilde{y}} = \frac{1}{\mathrm{GrPr}}\left(\frac{\partial^2 \tilde{T}}{\partial \tilde{x}^2} + \frac{\partial^2 \tilde{T}}{\partial \tilde{y}^2}\right) \tag{5}$$

and the boundary conditions are

$$\tilde{x} = -\frac{1}{2}: \quad \tilde{v}_x = \tilde{v}_y = 0, \quad \tilde{T} = -\frac{1}{2} \tag{6}$$

$$\tilde{x} = +\frac{1}{2}: \quad \tilde{v}_x = \tilde{v}_y = 0, \quad \tilde{T} = +\frac{1}{2} \tag{7}$$

$$\tilde{y} = \pm\frac{\Gamma}{2}: \quad \tilde{v}_x = \tilde{v}_y = 0, \quad \frac{\partial \tilde{T}}{\partial \tilde{y}} = 0 \tag{8}$$

These equations have been nondimensionalized by scaling x and y by L, v_x and v_y by U, P by $\rho_0 U^2$, and $T - T_0$ by ΔT. Here $P = p + \rho_0 g y$ is the equivalent pressure and $U = L^2 g \beta_0 \Delta T / \nu$ is the characteristic velocity. The dimensionless parameters in Eqs. (3)–(5) are the Grashof number and the Prandtl number. They are defined as

$$\mathrm{Gr} = \frac{UL}{\nu} = \frac{L^3 g \beta_0 \Delta T}{\nu^2} \tag{9}$$

$$\mathrm{Pr} = \frac{\nu}{a} \tag{10}$$

where $\nu = \eta/\rho_0$ is the kinematic viscosity and $a = \lambda/\rho_0 c_p$ is the thermal diffusivity. The Prandtl number is a function of material properties only; for air at 300 K, $\mathrm{Pr} \approx 0.71$. Equations (2)–(5) and boundary conditions (6)–(8) indicate that the flow inside the cavity is uniquely determined by Gr, Pr, and the aspect ratio Γ.

No analytical solution to the problem described above has been found. However, Batchelor [1] has solved the problem for $\Gamma \to \infty$. The solution is

$$\tilde{P} = \text{constant} \tag{11}$$

$$\tilde{v}_x = 0 \tag{12}$$

$$\tilde{v}_y = -\frac{1}{6}\tilde{x}^3 + \frac{1}{24}\tilde{x} \tag{13}$$

$$\tilde{T} = \tilde{x} \tag{14}$$

Thus, the flow is parallel to the vertical walls: the air rises near the hot wall and sinks near the cold wall. The linear temperature profile indicates that heat is transferred by conduction only (Nu = 1). The Nusselt number is defined as $\mathrm{Nu} = hL/\lambda$, where h is the average heat transfer coefficient.

Experimental observations have shown that in tall cavities, the flow in the center region can be accurately described by Eqs. (11)–(14) (see e.g. [2]). In the top and bottom parts of the cavity, the flow turns around and the flow field is more complicated. As the flow turns around, heat is also convected, and therefore Nu > 1 for cavities with a finite height.

Batchelor also pointed out that laminar flow will only be observed if the Grashof number is sufficiently small. He estimated that the flow will become unstable at Gr > 19000. Later, Vest and Arpaci [3] carried out a more detailed stability analysis. Their theoretical calculations showed that the critical value of the Grashof number is 7900, and that the primary flow instability sets in as a row of steady, two-dimensional vortices. This flow pattern is called multicellular. Vest and Arpaci also verified their theoretical results experimentally using a cavity with $\Gamma = 33$. In the experiments, however, the critical value of the Grashof number was found to be slightly higher ($\mathrm{Gr}_{cr} = 8700$).

At still higher values of the Grashof number, the multicellular flow pattern is disrupted. Three-dimensional and unsteady instabilities appear, and the flow becomes fully turbulent at around $\mathrm{Gr} \approx 10^9$ (see e.g. [2], [4]).

Lee and Korpela [5] presented numerical calculations on two-dimensional unsteady free convection in tall cavities. The calculations were in each case carried out until a steady state was reached. The highest value of the Grashof number in their calculations was 25000. In a cavity with $\Gamma = 20$, the transition to the multicellular flow pattern took place at $10000 < \mathrm{Gr} < 11000$. Lee and Korpela suggested that the higher value of Gr_{cr} compared with the value given of Vest and Arpaci was due to the stabilizing effect of the vertical temperature gradient. For an infinitely tall cavity, $\tilde{T} = \tilde{x}$ and the vertical temperature gradient is zero. For a cavity with a finite aspect ratio, $\tilde{T} = \tilde{T}(\tilde{x}, \tilde{y})$ and the vertical temperature gradient increases as the aspect ratio is decreased. Lee and Korpela also found that the multicellular flow pattern only appeared if the cavity was sufficiently tall; for Gr= 15000, the aspect ratio had to be at least 12.5.

Later, Chait and Korpela [6] analyzed the three-dimensional stability of free convection in tall cavities. They found that the two-dimensional multicellular flow becomes unstable at about Gr= 8600, and concluded that it is not physically meaningful to calculate two-dimensional flow patterns at high values of the Grashof number.

NUMERICAL CALCULATIONS

We studied a cavity of height $H = 0.4$ m and width $L = 0.02$ m; such a high aspect ratio ($\Gamma = H/L = 20$) was chosen to ensure the development of the multicellular flow pattern at high values of the Grashof number. The average temperature T_0 was chosen to be 300 K. Three different values of the Grashof number were used in the calculations: Gr = 8500 ($\Delta T = 8$ K), Gr = 14900 ($\Delta T = 14$ K), and Gr = 21200 ($\Delta T = 20$ K). The lowest value of Gr was chosen to be below the onset of instability, and the two higher values of Gr were chosen to be above the onset of instability.

The calculations were first performed using the FLUENT program, which is based on finite differences and has been developed by Creare Inc. Program version 2.99 was used and the calculations were carried out on a VAX 8350 computer. Four different grids were employed: 9×30, 12×42, 16×58, and 22×82 (horizontal×vertical). All grids were uniform.

All twelve test cases were first calculated using the power-law discretization scheme (the default scheme). The calculated temperature and flow fields were reasonable, and the average heat transfer coefficient could be predicted succesfully. The values of the Nusselt number obtained with Richardson extrapolation are given in Table 1 and compared with calculated and experimental values found in the literature.

TABLE 1

Calculated values of the Nusselt number at different values of the Grashof number and comparison with the numerical results of Lee and Korpela [5] and experimental results of ElSherbiny *et al.* [7]

	Grashof number		
	8500	14900	21200
this study	1.23	1.41	1.56
Lee & Korpela	1.21	1.41	1.55
ElSherbiny *et al.*	1.22	1.42	1.59

However, it has to be noted that ElSherbiny *et al.* applied a different boundary condition for temperature at the top and bottom walls of the cavity. In their apparatus, the top and bottom walls were made of highly conducting material, and a linear temperature profile ($\tilde{T} = \tilde{x}$) was thus established at $y = \pm\Gamma/2$. Since the experimental results are in good agreement with the numerical results, we may assume that for a cavity with $\Gamma = 20$, the thermal boundary conditions at the top and bottom walls are of less importance.

The onset of the flow instability could not be detected using the power-law discretization scheme. The calculations with Gr = 14900 and with Gr = 21200 were therefore repeated using the optional quadratic upwind discretization scheme (called QUICK). Since the QUICK scheme needs more CPU time than the power-law scheme,

the finest grid (22×82) was excluded from the calculations. It was found that when the 16×58 grid was used, two secondary vortices appeared in the cavity. This was observed both at Gr = 14900 and at Gr = 21200. The two other grids (9×30 and 12×42) were too coarse to resolve the flow pattern.

Some calculations were then performed using the FIDAP program, which is based on finite elements and has been developed by Fluid Dynamics International Inc. Program version 4.50 was used and the calculations were carried out on a VAX 8650 computer. The solution strategy for FIDAP calculations was adopted from the Example 7 of the FIDAP manual. This example deals with free convection in a square cavity. Nine-node rectangular elements and two different meshes were employed: 5×20 and 7×28 (horizontal×vertical). Both meshes were uniform. Thus, the degree of accuracy was expected to be similar to that of FLUENT calculations with 12×42 and 16×58 grids, respectively.

The FIDAP calculations with Gr = 8500 were carried out using both meshes. The calculated temperature and flow fields and average heat transfer coefficients were in good agreement with the FLUENT results. The FIDAP calculations with Gr = 14900 and with Gr = 21200 were only carried out using the fine mesh (7×28). At Gr = 14900 the results were in good agreement with the FLUENT results obtained using the QUICK scheme, except that three secondary vortices appeared and that they were stronger. At Gr = 21200 the solution did not converge. The reason for poor convergence is unclear, but we speculate that perhaps FIDAP cannot find a steady, two-dimensional solution at high values of the Grashof number because such flows would also be unstable in real life.

Some results are illustrated in Figs. 2–4. The vertical velocity profiles and the temperature profiles at the midheight of the cavity ($y = 0$) for Gr = 8500 are shown in Fig. 2. The theoretical solutions (Eqs. 13 and 14) and four different numerical solutions are plotted: FLUENT solutions with the 12×42 grid and with the 16×58 grid, and FIDAP solutions with the 5×20 mesh and with the 7×28 mesh. All numerical results are in good agreement with the theoretical profiles. The horizontal velocity profiles along the vertical centerline ($x = 0$) for Gr = 8500 are shown in Fig. 3. In the center region, the horizontal velocities vanish as was predicted by the theoretical solution. Non-zero horizontal velocities can be observed near the top and the bottom of the cavity, in the regions where the flow turns around.

The horizontal velocity profiles along the vertical centerline ($x = 0$) for Gr = 14900 are shown in Fig. 4. Three different numerical solutions are plotted: the FLUENT solution with the power-law scheme and 16×58 grid, the FLUENT solution with the QUICK scheme and 16×58 grid, and the FIDAP solution with the 7×28 mesh. The secondary vortices can be observed in the FLUENT solution with the QUICK scheme and in the FIDAP solution.

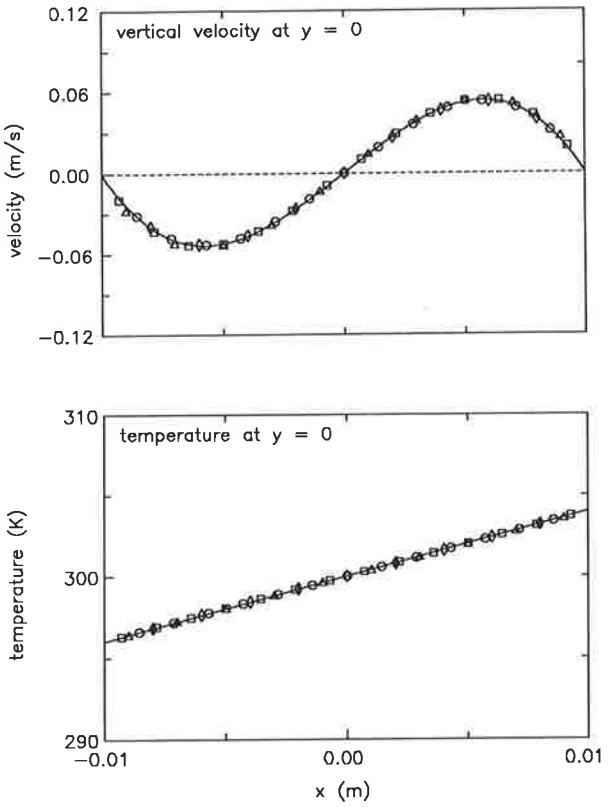

FIGURE 2. Top: the vertical velocity profile at $y = 0$ for Gr = 8500. Bottom: the temperature profile at $y = 0$ for Gr = 8500. The dashed line in the velocity plot corresponds to $v_y = 0$ and is included in the plot for the convenience of the reader. For key see below.

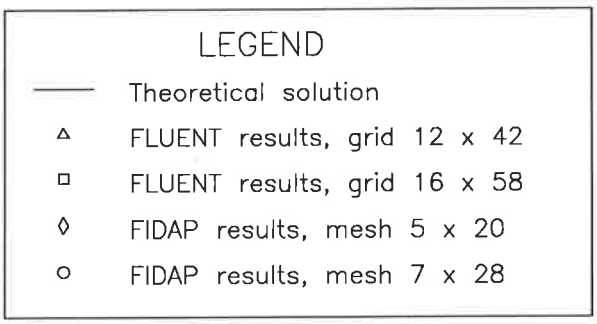

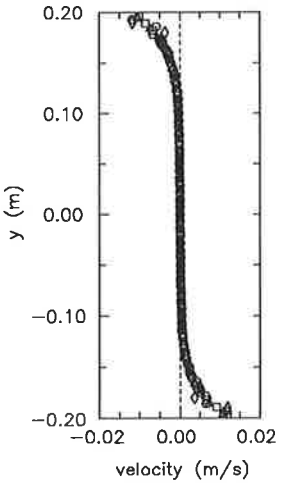

FIGURE 3. The horizontal velocity profile at $x = 0$ for Gr = 8500. The dashed line corresponds to $v_x = 0$ and is included in the plot for the convenience of the reader. For key see previous page.

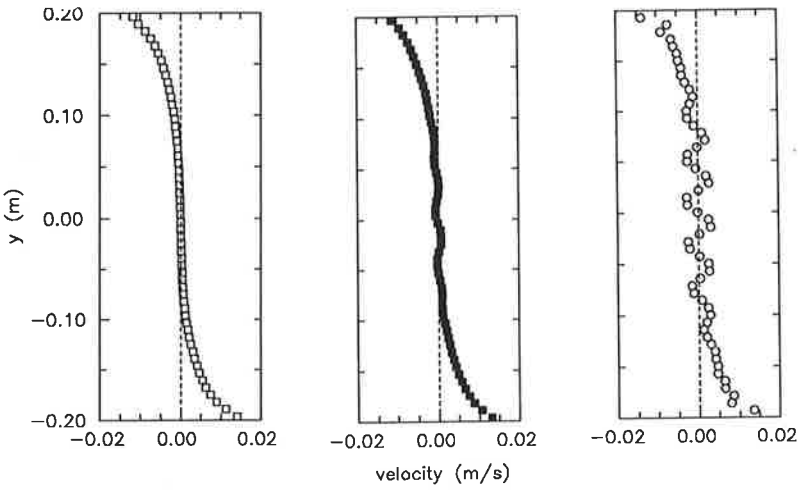

FIGURE 4. The horizontal velocity profile at $x = 0$ for Gr = 14900. Left: FLUENT results with the 16×58 grid and power-law discretization scheme. Middle: FLUENT results with the 16×58 grid and quadratic upstream discretization scheme. Right: FIDAP results with the 7×28 mesh. The dashed lines correspond to $v_x = 0$ and are included in the plots for the convenience of the reader.

CONCLUSIONS

Two commercial, general-purpose fluid dynamics programs were used to calculate the free convection flow of air in a tall, vertical cavity. Both programs gave good results. In fact, the programs could be succesfully used to study flow instability. Further effort is needed, however, to assess their usefulness in more complicated practical problems.

ACKNOWLEDGEMENTS

We wish to thank Professor Helge Andersson for helpful suggestions and Mr. Pertti Kiiski for assistance in drawings.

REFERENCES

1. Batchelor, G. K., Heat transfer by free convection across a closed cavity between vertical boundaries at different temperatures. *Q. Appl. Math.* **12**, 1954, pages 209–233.

2. Eckert, E. R. G. & Drake, R. M. Jr., *Analysis of Heat and Mass Transfer*. McGraw-Hill, New York, 1972.

3. Vest, C. M. & Arpaci, V. S., Stability of natural convection in a vertical slot. *J. Fluid Mech.* **36**, 1969, pages 1–15.

4. Tritton, D. J., *Physical Fluid Dynamics*. Oxford University Press, Oxford, 1988.

5. Lee, Y. & Korpela, S. A., Multicellular natural convection in a vertical slot. *J. Fluid Mech.* **126**, 1983, pages 91–121.

6. Chait, A. & Korpela, S. A., The secondary flow and its stability for natural convection in a tall vertical enclosure. *J. Fluid Mech.* **200**, 1989, pages 189–216.

7. ElSherbiny, S. M., Raithby G. D. & Hollands, K. G. T., Heat transfer by natural convection across vertical and inclined air layers. *Trans. ASME, J. Heat Transfer* **104**, 1982, pages 96–102.

AN APPLICATION OF THE INERTIA FORCE METHOD IN FLUID MECHANICS

EERO-MATTI SALONEN
Institute of Mechanics
Helsinki University of Technology
Otakaari 1, 02150 ESPOO, FINLAND

ABSTRACT

The so called d'Alembert's principle or perhaps more correctly the inertia force method is rarely used in fluid mechanics although one quite often sees applications of the method in particle and solid mechanics. The article first reviews some diverging opinions about the value of the inertia force method in general. Thereafter the method is employed in fluid dynamics making use of certain familiar results from fluid statics. A didactic qualitative derivation of the result, that the pressure decreases in ideal fluid flow at a constriction – which the students find sometimes difficult at first to believe – is finally given.

INTRODUCTION

D'Alembert's principle

In the mechanics literature no generally accepted agreement seems to exist on the actual meaning of the so called d'Alembert's principle. This fact is reflected for instance in the following quotation, Lanczos [1, p. 89]: "It is exactly this apparent triviality which makes d'Alembert's principle such an ingenious invention and at the same time so open to distortion and misunderstanding".

One can divide the interpretations of the principle roughly in two groups which we shall call here the *engineering mechanics interpretation* and the *analytical mechanics interpretation*, respectively.

In the engineering mechanics literature d'Alembert's principle is often said to *reduce dynamics to statics*. As an example let us consider a system consisting of just one particle. Let us write the equation of motion

$$\vec{F} = m\vec{a}\,, \tag{1}$$

where the meaning of the notation is obvious, in the form

$$\vec{F} + \vec{F}^{\mathrm{I}} = \vec{0}\,, \tag{2}$$

where

The pedagogic merit of this procedure is that we can first start the derivations in a simplified situation and finally obtain the general result just by a straightforward modification.

As a second application let us assume that we have solved the equations of motion of a mechanism and as post processing want to determine the bending moment at a certain cross section of a rod at a certain moment of time. Here it is quite convenient to use the inertia force method to convert the problem to a static one as the acceleration is now a given quantity and to employ the familiar routines hopefully obtained during the study of statics.

INERTIA FORCE METHOD AND FLUID MECHANICS

General

If one looks at the index of any particle or solid dynamics book one can nearly always find the term d'Alembert's principle (in the inertia force method meaning used here). In the fluid dynamics literature, however, this is not the case which is a little surprising as the inertia force method can be put to good use in certain situations also there.

Fluid statics

Let us recall the equilibrium equations of fluid statics:

$$-\vec{\nabla}p + \rho\vec{b} = \vec{0} \tag{9}$$

or

$$\vec{\nabla}p = \rho\vec{b}\,, \tag{10}$$

where p is the pressure. The physical meaning of equation (9) or (10) is:

In a fluid statics problem the value of the pressure increases (decreases) in the directions in which the body force has a positive (negative) component and the rate of growth is greatest in the direction of the body force. (11)

The stress tensor can in general be expressed in the form

$$\overleftrightarrow{\sigma} = -p\overleftrightarrow{I} + \overleftrightarrow{\sigma}^{*}, \tag{12}$$

where $\overleftrightarrow{I}$ is the identity tensor and $\overleftrightarrow{\sigma}^{*}$ is the deviatoric stress tensor. For a fluid at rest the deviatoric stress or in this connection the so called viscous stress disappears by definition and we have just

$$\overleftrightarrow{\sigma} = -p\overleftrightarrow{I}\,. \tag{13}$$

This fact makes the stress distribution in a fluid statics problem very simple compared with the solid mechanics one. When the body force field is given, the pressure distribution can be found, at least qualitatively, by just looking at the problem and by making use of statement (11). This is familiar from the hydrostatic pressure distribution due to gravity.

Fluid dynamics

The equations of motion in fluid dynamics are

$$-\vec{\nabla}p + \vec{\nabla}\cdot\overleftrightarrow{\sigma}^{*} + \rho\vec{b} = \rho\vec{a}\,. \tag{14}$$

The apparent difference with respect to the solid mechanics equations (8) is due to the fluid mechanics convention of using the decomposition (12) for the stress. We see that to arrive at the present equation from the fluid statics one (9) we have to make the substitution

$$\rho\vec{b} := \rho\vec{b} - \rho\vec{a} + \vec{\nabla}\cdot\vec{\vec{\sigma}}^{*} \equiv \rho\vec{b}^{e} . \tag{15}$$

The term $\rho\vec{b}^{e}$ introduced could be called the *effective* body force per unit volume. It consists of the real body force ρb, of the inertia body force $-\rho\vec{a}$ and of the viscous body force $\vec{\nabla}\cdot\vec{\vec{\sigma}}^{*}$. Thus on the basis of statement (11) and expression (15):

> *In a fluid dynamics problem the value of the pressure increases (decreases) in the directions in which the effective body force has a positive (negative) component and the rate of growth is greatest in the direction of the effective body force.* (16)

The above result can in some cases be used to obtain a qualitative picture of the pressure distribution. These cases are mainly those where the viscous terms are small because expression $\vec{\nabla}\cdot\vec{\vec{\sigma}}^{*}$ is difficult to estimate. It is also realized that due to the fluid mechanics convention (12), it is perhaps in general not quite correct to call the use of substitution (15) as a pure application of the inertia force method since the effect of viscous stresses must be included, too.

An application

Let us consider the flow of fluid through a constriction (Figure 1(a)). We assume the flow to

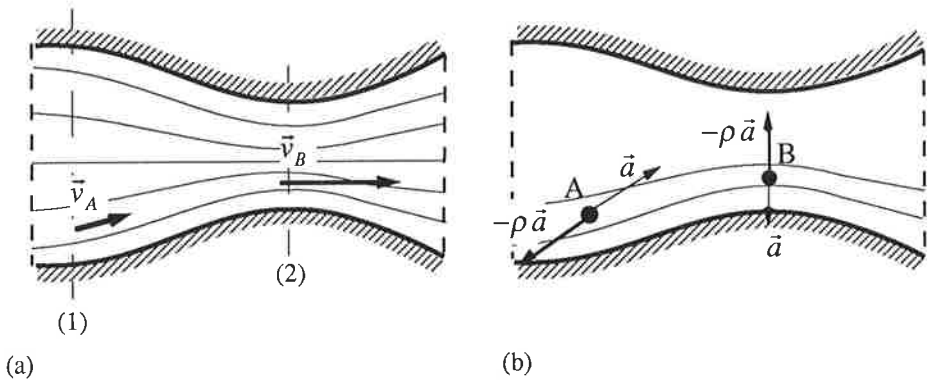

FIGURE 1. (a) Flow through a constriction. (b) Schematic examples of inertia body forces.

be steady, frictionless and incompressible. The well-known Bernoulli equation – obtained through certain mathematical manipulation of the equations of motion – tells among other things that the value of the pressure at section 2 is smaller than at section 1. This result is often found to conflict strongly with the intuitive guess of a layman or even of a fluid mechanics student. The wrong vague argument used goes somewhat along the following lines: Certainly the pressure must increase as the fluid must be forced into a smaller space when advancing towards the constriction.

Let us now explain how the pressure is really changing by employing the inertia force method. The cross sectional areas of the streamtubes must in general clearly decrease

towards the throat. As the fluid is incompressible the velocities must then increase which means that the acceleration component a_t along the streamlines (= streampaths here) must also be directed fowards the throat and, finally, the corresponding inertia force components $-\rho a_t$ must be directed away from the throat. Statement (16) now tells us that when we move along a streamline towards the throat the value of the pressure is really decreasing (we do not consider the possible contributions say due to gravity here).

A fluid particle has also a centripetal component a_n of acceleration directed towards the center of curvature of the streamline. Based on the above observations the qualitative acceleration and corresponding inertia force directions to be to be expected at two typical points A and B are sketched in Figure 1(b). From the latter we see immediately that the pressure is not uniform at the throat but must decrease towards the boundaries.

It should be remarked that if the fluid is compressible we cannot make easy quesses about the velocity distributions of the basis of an assumed streamline distribution because density is no more constant. In such cases the value of the inertia force method is questionable.

CONCLUDING REMARKS

The term d'Alembert's principle carries with it a rather heavy historical burden of different meanings. It is suggested that this term should be avoided in connection with the engineering interpretation discussed above. The term "inertia force principle" or still better the "inertia force method" would seem more appropriate.

The inertia force method can be used to advantage in the teaching of fluid dynamics to give qualitative information about pressure distributions in a very simple and graphic way.

ACKNOWLEDGEMENTS

I wish to thank Mr. T. Paloposki for useful comments on the original manuscript and Mr. R. Huhtanen for processing the figure.

REFERENCES

1. Lanczos C., The Variational Principles of Mechanics. Fourth edition. University of Toronto Press, Toronto, 1974, 418 pages.

2. Rosenberg R.M., Analytical Dynamics of Discrete Systems. Plenum Press, New York, 1977, 424 pages.

3. Rosenberg R.M., d'Alembert and Others on d'Alembert's Principle. Engineering Education, April 1968, pages 959 - 960.

4. Hamel G., Theoretische Mechanik. Springer, Berlin, 1967, 796 pages.

5. Meriam J.L., Dynamics. Second edition. Wiley, New York, 1975, 478 pages.

6. Montgomery D.J., Precedents for use of d'Alembert's Principle. Engineering Education, September 1968, pages 62-63.

7. Osgood W.F., Mechanics. MacMillan, New York, 1948.

8. Panlilio F., Interpreting d'Alembert's Principle. Engineering Education, September 1968, pages 61-62.

NUMERICAL SIMULATION OF COMPRESSIBLE FLUID FLOW USING UPWIND METHODS

Timo Siikonen

Laboratory of Aerodynamics
Helsinki University of Technology
02150 Espoo, Finland

Abstract

The underlying theory of the upwind methods for compressible flow is presented. These methods have been applied in the computer codes developed in the Laboratory of Aerodynamics at the Helsinki University of Technology. Some computational results for an airfoil and a wing are presented. These examples show the relative merits and drawbacks of the upwind differences.

INTRODUCTION

In recent years upwind methods have become popular in the simulation of compressible fluid flow. Upwind methods are intrinsically dissipative and require no additional dissipative terms, which is the case if central differences are applied. Due to the intrinsic dissipation, computational algorithms based on the upwind differences are usually also more robust than the algorithms based on the central differences. The drawback of the upwind methods is the strong numerical dissipation inside shear layers and in the case of low Mach number inviscic flows.

In the case of incompressible flow the upwind concept is applied for the convection terms by employing one-sided difference approximations for derivatives like $\partial u\phi/\partial x$ depending on the sign of the velocity u. The pressure gradient term in the momentum equation can be treated as a source term and it is usually centrally differenced. For a compressible flow the application of the upwind concept is not so straightforward. This is due to the fact that the pressure and the density are strongly coupled, and it is no longer possible to upwind the convection term separately from the pressure gradient.

The use of the upwind methods for compressible flow goes back to Godunov. A description Godunov's method can be found in Ref. [1]. To illustrate the basic idea of upwinding, the one-dimensional equations of gas-dynamics

$$\frac{\partial U}{\partial t} + \frac{\partial F}{\partial x} = 0 \tag{1}$$

are discretisized as

$$U_i^{n+1} = U_i^n - \frac{\Delta t}{\Delta x}[F_{i+\frac{1}{2}} - F_{i-\frac{1}{2}}] \tag{2}$$

Here U is the vector of the dependent variables, $F_{i+\frac{1}{2}}$ is the numerical flux function to be evaluated at the interface between cells i and $i+1$, Δt and Δx are the time-step size and the spatial increment. In order to compute the flux function, Godunov solved the Riemann problem, which is the initial value problem for Eq.(1) with $U(x,0) = U^l$ if $x \leq 0$, or U^r if $x \geq 0$ (see Fig. 1). The solution is self-similar, U is the function of $\xi = x/t$ only. Godunov showed that the numerical flux can be expressed as

$$F = F(U(\xi = 0)) \tag{3}$$

where $U(\xi = 0)$ is the solution of the Riemann problem.

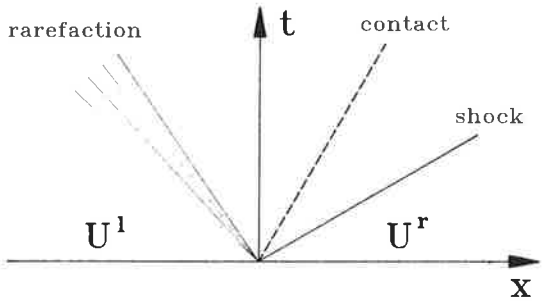

Figure 1 The Riemann problem

The upwind methods presently applied for the simulation of compressible flow are based on the same ideas as Godunov's method. Several so-called approximate Riemann solvers exist. The development of the flow solvers in the Laboratory of Aerodynamics at the Helsinki University of Technology (HUT) is also based on these methods; namely on the approximate Riemann solver of Roe [2] and on the flux-vector splitting method of van Leer [3]. In this paper, the basic principles of these two methods are described. Some computational results from two- and three-dimensional simulations are presented. Both the accuracy and the effect of the numerical dissipation are evaluated.

NUMERICAL METHODS

Governing Equations

Fluid flow is governed by the Navier-Stokes equations. These can be written in a conservative form using Cartesian coordinates as

$$\frac{\partial U}{\partial t} + \frac{\partial F(U)}{\partial x} + \frac{\partial G(U)}{\partial y} + \frac{\partial H(U)}{\partial z} = 0 \tag{4}$$

where $U = (\rho \quad \rho u \quad \rho v \quad \rho w \quad e)^T$ is the vector of conservative variables, ρ the density; the velocity components are u, v and w, and e is the total internal energy. The form of the flux vectors $F(U)$, $G(U)$ and $H(U)$ can be found in any text book of fluid mechanics.

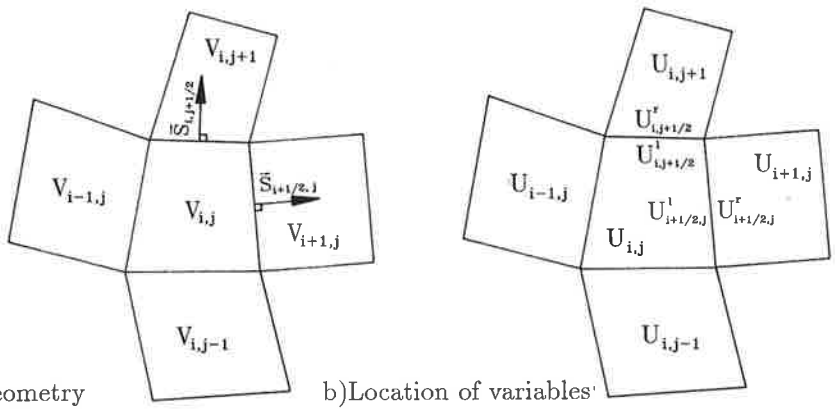

a) Geometry b)Location of variables

Figure 2 Computational grid in a two-dimensional case.

In order to solve Eq.(4) in an arbitrary geometry, a finite-volume technique is applied. The flow equations have an integral form

$$\frac{\partial}{\partial t}\int_V U dV + \int_S \vec{F}(U)\cdot d\vec{S} = 0 \tag{5}$$

for an arbitrary fixed region V with the boundary S. A discrete cell face area can be expressed using the Cartesian base vectors

$$\vec{S} = S_x\vec{i} + S_y\vec{j} + S_z\vec{k} \tag{6}$$

The corresponding unit vector is

$$\vec{n} = n_x\vec{i} + n_y\vec{j} + n_z\vec{k} = \frac{S_x}{S}\vec{i} + \frac{S_y}{S}\vec{j} + \frac{S_z}{S}\vec{k} \tag{7}$$

Performing the integrations of Eq.(5) for a computational cell i shown in Fig. 2a yields

$$V_i\frac{dU_i}{dt} = -\sum_{faces} S\hat{F} \tag{8}$$

where the sum is taken over the faces of the computational cell and

$$\hat{F} = n_xF + n_yG + n_zH \tag{9}$$

Evaluation of the Fluxes

The calculation of the fluxes is performed in two stages. The convective part of the fluxes is evaluated by solving approximately a locally one-dimensional Riemann problem on the cell surfaces. The viscous part is centrally differenced and treated separately from the convective part. In order to compute the derivatives of the viscous terms, the Gauss

theorem is applied for the shifted control volume $V_{i+\frac{1}{2}}$ between the cells i and $i+1$. Details of the discretization of the viscous terms are given in [4].

The calculation of the convective part of the flux is based on the rotational invariance of the flux term, Eq.(9). On a cell surface the convective flux is calculated from

$$\hat{F} = T^{-1}[F(TU)] \tag{10}$$

where T is a rotation matrix. Aftermultiplication by the rotation matrix the fluxes have the same functional form F, as in the case of the Cartesian coordinates. Hence, the flux can be evaluated in the direction normal to the cell surface in a locally one-dimensional fashion.

The solution of the Riemann problem on the cell surface is a time-consuming process. Fortunately, it is possible to solve the problem approximately. There are many ways to do that, see e.g. [5]. In order to calculate the flux, the following definitions are made:

$$\Delta F^+ = F^r - F(U(\xi = 0)), \qquad \Delta F^- = -F^l + F(U(\xi = 0)), \tag{11}$$

Using Eq.(3), the flux function can be written as

$$F = \frac{1}{2}(F^r + F^l) - \frac{1}{2}(\Delta F^+ - \Delta F^-) \tag{12}$$

Eq.(11) also gives $F^r - F^l = \Delta F^+ + \Delta F^- = \Delta F$. The flux differences $\Delta F^{\pm}$ can be considered as parts of ΔF caused by waves travelling to the left and right (see Fig. 1).

Nowadays, the most commonly used approximate Riemann solver is that developed by Roe. In Roe's method the flux difference is replaced by a linearization $\Delta F = A(U^r, U^l)\Delta U$. The form of the Jacobian matrix $A(U^r, U^l)$ is derived in [2]. The flux difference can be rewritten in terms of the right eigenvector $r^{(k)}$ of the Jacobian matrix A, the corresponding eigenvalue $\lambda^{(k)}$, and the inner product $\alpha^{(k)}$ of the left eigenvector with ΔU as

$$\Delta F = \sum_{k=1}^{K} r^{(k)} \lambda^{(k)} \alpha^{(k)} \tag{13}$$

Here, K is the number of equations. In a three-dimensional case $K = 5$. By taking the sign of the eigenvalue into account, the interface flux can be written

$$F = \frac{1}{2}(F(U^r) + F(U^l)) - \frac{1}{2}\sum_{k=1}^{K} r^{(k)} |\lambda^{(k)}| \alpha^{(k)} \tag{14}$$

The flux-vector splitting is an alternative approach. The flux function $F(U)$ is divided into positive and negative parts $F(U)^{\pm}$. The interface flux is then computed from

$$F = F^+(U^l) + F^-(U^r) \tag{15}$$

The flux functions used in Van Leer's method are derived in [3].

The first step in the calculation of fluxes either from Eq.(14) or Eq.(15), is the evaluation of the solution vector on both sides of the cell surface (see Fig. 2b). If U^l and U^r are replaced by the average values of the solution vector within each cell, e.g. by U_i and U_{i+1}, the resulting method is first-order accurate. Second-order accuracy is equivalent to an assumption of linear distribution inside the cell. Using this assumption, the cell interface values can be calculated from

$$U^l_{i+\frac{1}{2}} = U_i + \frac{1}{4}[(1-\kappa)(U_i - U_{i-1}) + (1+\kappa)(U_{i+1} - U_i)] \qquad (16a)$$

$$U^r_{i+\frac{1}{2}} = U_{i+1} - \frac{1}{4}[(1-\kappa)(U_{i+2} - U_{i+1}) + (1+\kappa)(U_{i+1} - U_i)] \qquad (16b)$$

Several difference approximations can be obtained by inserting different values for parameter κ. Fully upwinded second-order discretization is obtained by choosing $\kappa = -1$. The second-order method contains no numerical diffusion. However, the fully upwinded discretization implicitly includes fourth-order dissipation. In the case of a viscous flow this leads to an inaccurate solution inside the shear layers. The remedy is to bias the discretization towards the central difference scheme. A good compromise is often to select $\kappa = 1/3$, which leads to a third-order accurate upwind-biased scheme. A so-called QUICK-scheme is obtained by inserting $\kappa = 0.5$, while $\kappa = 1$ yields the central difference scheme. It should be noted that the central difference scheme does not converge unless artificial dissipation terms are added. The role of the artificial dissipation is similar to the intrinsic dissipation of the upwind-biased methods.

Solution Algorithm

In the case of compressible flow the resulting set of non-linear equations can be solved by marching in time. Since the time-step size is limited with explicit time integration, the computer codes developed at HUT utilize an implicit method. Even the use of an implicit method leads to large computation times when the mesh is refined. Efficiency is improved by applying a multigrid acceleration for the convergence. This has a particularly nice feature that the number of iteration cycles does not depend on the grid size. The computer codes of HUT are mainly run on the Cray X-MP supercomputer. The codes are effectively vectorized, and with a sufficiently large mesh almost a tenfold increase in speed is obtained by vectorization. The solution methods are described in detail in Ref. [4].

RESULTS

The computer codes developed at HUT utilize either Eq.(14) or Eq.(15) for the calculation of fluxes. Currently, two- and three-dimensional as well as axisymmetric versions exist. The turbulence is evaluated from an algebraic model. In the following, a few examples of the performed simulations are given. In the two-dimensional cases the flow is over the NACA 0012 airfoil and the flux is calculated using the method of van Leer. The three-dimensional example has been computed using both methods.

An example of the two-dimensional inviscid calculations is given for a flow over the airfoil at Mach number (Ma) equal to 0.63 and angle of attack (α) equal to 2°. The surface pressure is depicted as a non-dimensional pressure coefficient in Fig. 3. It is seen

that the results obtained by the higher-order methods practically coincide, whereas the result of the first-order method is clearly inaccurate. The case has also been calculated by applying a so-called flux-limiter with the fully-upwinded discretization.

The second simulation is at $Ma = 0.85$ and $\alpha = 1°$. The Mach contours are shown in Fig. 4a. In this flow case there is a strong shock on both surfaces of the airfoil. The shock is tracked very accurately; this is a typical and nice feature of the upwind methods. However, the intrinsic dissipation can produce error, which tends to increase the drag coefficient and decrease the lift coefficient. This depends on the discretization and also on other factors, like the angle of attack. This is shown in Fig. 4b, where the drag coefficient is plotted as a function of the angle of attack. The result is for a laminar flow over the NACA 0012 airfoil at $Ma = 0.85$ and Reynolds number (Re) equal to 2000. It is seen that spurious numerical drag increases as the upwind-biasing is increased.

An example of the application of van Leer's method for turbulent flow is given in Fig. 5a. The case is at $Ma = 0.70$, $\alpha = 1.49°$ and $Re = 9 \cdot 10^6$. If the flow is attached, as in this case, or if the separation region is not too large, a reasonable accuracy can be obtained using an algebraic turbulence model. However, when the angle of attack is increased and the flow is highly separated, the accuracy is not satisfactory. This can be seen from Fig. 5b, which shows the experimental and calculated lift coefficients as a function of the angle of attack. The flow conditions are as in Fig. 5a.

As a three-dimensional example, a flow over the ONERA M6 wing has been simulated. The flow is at $Ma = 0.84$, $\alpha = 3.04°$ and $Re = 11.72 \cdot 10^6$. The upper surface pressure distribution as calculated by Roe's method is shown in Fig. 6a. The friction coefficients obtained by both the methods are plotted in Fig. 6b in a chordwise plane at about midspan. In this case the difference between the predictions is small. Generally, van Leer's method is not as accurate as Roe's method in the simulation of shear layers. Also in this case van Leer's method predicts a somewhat higher drag than Roe's method.

CONCLUSIONS

The basic principles of the upwind discretization methods have been given. Two methods have been applied for the simulation of compressible flow. The results show that especially the shock waves are accurately reproduced with upwind methods. In viscous cases upwind-biased methods should be employed in order to avoid the spurious numerical dissipation inside shear layers.

REFERENCES

1. Richtmyer, R.D., Morton, K.W., Difference Methods for Initial Value Problems, Interscience Publishers, New York, 1967.

2. Roe, P.L., Approximate Riemann Solvers, Parameter Vectors, and Difference Schemes, J. Comput Phys., Vol. 43, pages 357-372, 1981.

3. Van Leer, B., Flux-Vector Splitting for the Euler Equations, Lecture Notes in Physics,

Vol. 170, pages 507-512, 1982.

4. Siikonen, T., Hoffren, J., Laine, S., A Multigrid LU Factorization Scheme for the Thin-Layer Navier-Stokes Equations, 17th ICAS Congress, Stockholm, 1990, pages 2023-2034.

5. Roe, P.L., A Survey of Upwind Differencing Techniques, Lecture Notes in Physics 323, pages 69-78, 1989.

a) b)

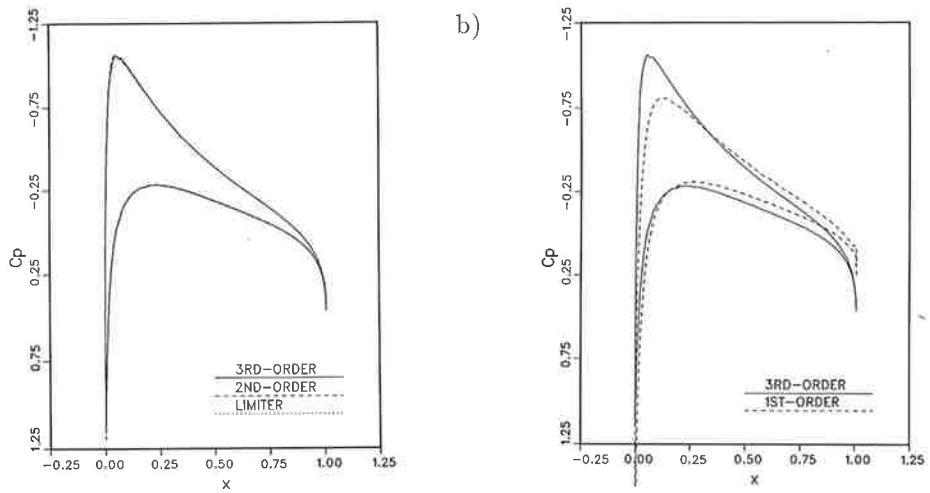

Figure 3 Surface pressure coefficient for the NACA 0012 airfoil at $Ma = 0.63$, $\alpha = 2°$. a) higher-order methods, b) comparison with the first-order method.

a) b)

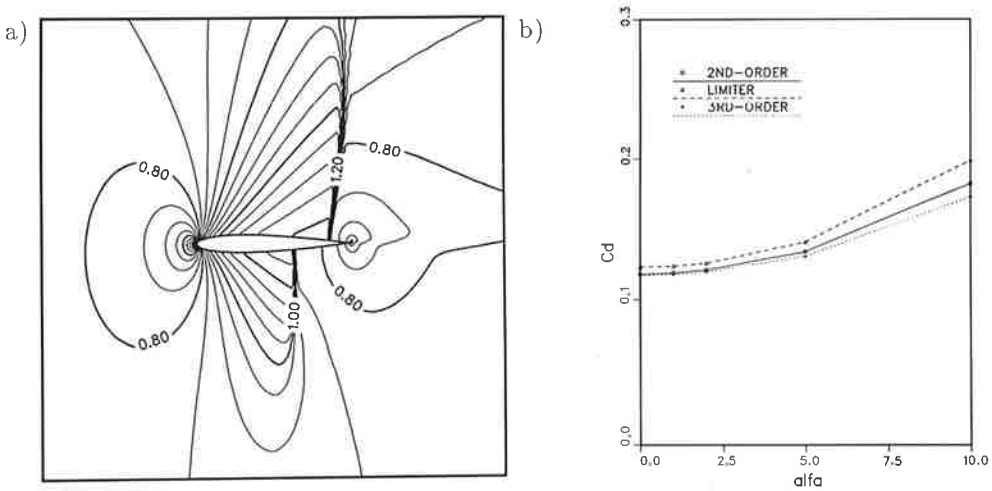

Figure 4 a) Mach contours at $Ma = 0.85$, $\alpha = 1°$, b) drag coefficient as a function of the angle of attack at $Ma = 0.85$, $Re = 2000$.

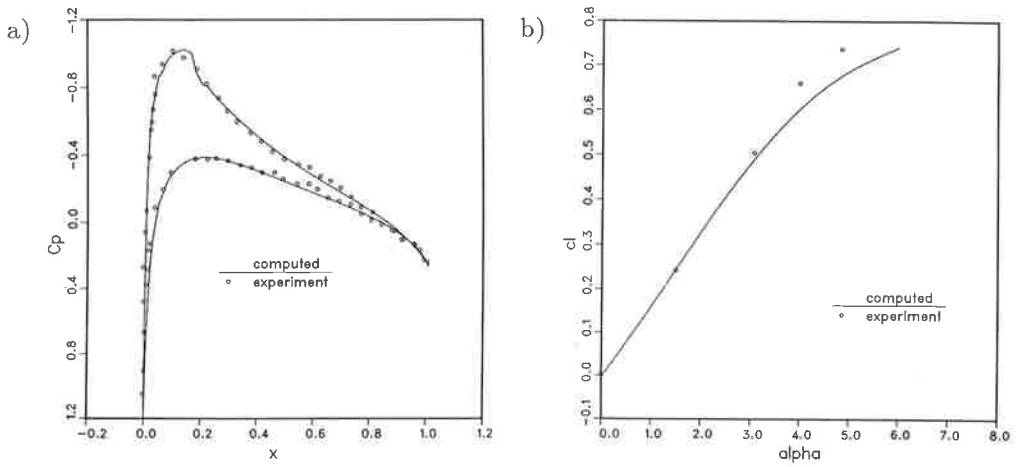

Figure 5 a) Pressure coefficient distribution at $Ma = 0.70$, $\alpha = 1.49°$ and $Re = 9 \cdot 10^6$, b) Lift coefficient versus angle of attack.

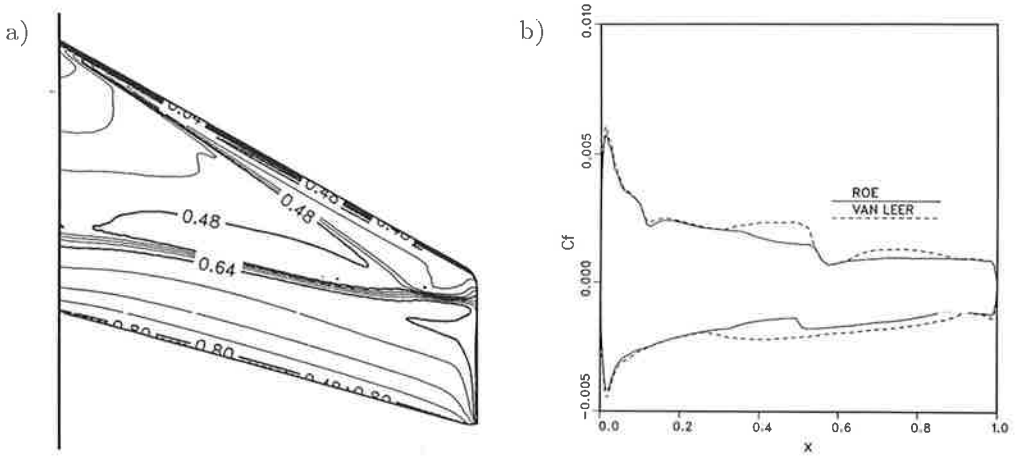

Figure 6 a) Pressure distribution on wing upper surface at $Ma = 0.84$, $\alpha = 3.06°$ and $Re = 11.72 \cdot 10^6$, b) comparison of skin friction coefficients in a chordwise plane at about midspan.

COMPUTER SIMULATION OF INJECTION MOULD FILLING

SEPPO SYRJÄLÄ
Department of Mechanical Engineering
Tampere University of Technology
P.O. Box 527, SF-33101 TAMPERE, FINLAND

ABSTRACT

In this paper a theoretical model is presented for the simulation of injection mould filling. The Hele-Shaw approximation is used to simplify the general flow equations, which are then solved over the flow domain utilizing the analogy between the mould filling and conduction phase change. Numerical computations are performed using a finite-element code ABAQUS. Calculated results in rectangular cavity with varying thickness are provided and good agreement is found between the current predictions and the predictions and experimental results previously presented in the literature.

INTRODUCTION

From a commercial standpoint, the injection moulding is one of the most important polymer processing operations. It is used in a wide spectrum of mass production industries, ranging from toy production to automobile bumper fabrication. The moulding cycle may be conveniently divided into three separe stages, namely, filling, packing and cooling. During filling, polymer melt, produced in an injection moulding machine by the shearing action of a rotating screw combined with external heating, is injected into the mould cavity. Once the mould cavity has been completely filled, additional material is forced into the cavity under high pressure in order to compensate for the subsequent shrinkage due to solidification of the polymer melt. Finally, cooling is continued until sufficient solidification is achieved so that the polymer part may be ejected from the mould without damage. The entire sequence is then repeated in a cyclic manner.

For years, injection moulding knowledge has been based on experience and empiricism and traditionally "trial-and-error" has been one of the key factors in mould design procedure. Considerable time and money is often required to test and, if needed, modify the mould before production may begin. However, the demand for a shorter lead time in product innovation and a higher product quality and the appearance of new materials on the market, for which no experience exists, make the "trial-and-error" approach no longer acceptable. Consequently, increasingly interest has been focused on the computer-aided simulation of injection moulding process. If a computer simulation predicts the process reliably, the design may be checked for possible errors and adapted at an early point in the design process. This would speed up product innovation and reduce costs considerably.

Simulation of injection moulding is mostly concentrated on filling stage, as is the case in this study also. Filling flow simulation may provide significant contributions to the mould design and subsequent process optimization. For example, it becomes possible to observe filling faults such as air entrapments and weld lines and correct these by a change of feed point(s), polymer or process conditions before mould making.

The modelling of mould filling is based on general conservation equations. However, due to the fact that the filling process is very complex, major simplifications are needed. A number of studies have been published, which deal with the simulation of injection mould filling with various simplifications and only few studies are mentioned here. The first attempts were limited to one-dimensional flow in simple geometries, like a rectangular strip with edge gating [1] or a circular disk with center gating [2]. However, in order to be able to model the filling behaviour in more arbitrary mould cavities, one-dimensional treatment is inadequate. Due to the physical nature of the filling process, Richardson [3] suggested that it may be analysed using the Hele-Shaw approximation [4]. This considerably reduces the complexity of the governing equations, as is shown below in this paper, but however describes reasonably the flow behaviour during the filling process. After that, Hele-Shaw formulation has become a standard way to analyse the polymer melt flow into a mould cavity. Various analytical solutions, based upon the Hele-Shaw flow, have been given for simple rectangular cavities [5,6]. Numerical studies have applied finite-difference method [7], finite-element method [8,9] and finite-difference method with body-fitted curvilinear coordinates [10]. From the rheological point of view an inelastic non-Newtonian model for the viscosity is usually found to be adequate in filling flow simulations, although elastic effects may be important in some circumstances. In most of the studies mentioned above a power-law viscosity model is applied.

The major additional complication in the mould filling simulation is the fact, that the position of the advancing melt front is not known a priori, but has to be determined as a part of the solution procedure. In fact, mould filling problem belongs to a more general class of problems, commonly known as moving boundary problems. Considerable information about these kind of problems is available in the literature [11,12]. There are two basic approaches for moving boundary problems in terms of meshing, namely fixed mesh and moving mesh. In mould filling simulations fixed meshes are usually employed. In fixed mesh approach, calculation mesh has been pre-selected to contain the entire mould cavity and the flow front locations are determined at various times during the filling by an interpolation procedure (for more details see for example references [8] and [12]). In moving mesh approach, calculation mesh is generated at each time step to contain only the fluid domain. This kind of approach for the mould filling simulation is presented in reference [10].

THEORETICAL BACKGROUND OF INJECTION MOULD FILLING

In the present study, the modelling of injection mould filling is based on the isothermal flow. The general equations of continuity and momentum [4] are simplified by assuming the fluid, i.e. polymer melt, to be incompressible and by neglecting the elastic and gravitational effects during the filling. Further simplifications are possible, since the Reynolds number, defined with the cavity gapwidth as a characteristic lenght, is typically very small due to the extremely high viscosity of polymer melt, indicating that viscous forces are dominant and inertial forces can be neglected in the momentum equations. In addition, since the gapwidth of the mould cavity is small compared with other dimensions (injection moulded parts are typically thin walled), the velocity and pressure variations in the gapwise direction can be neglected and the shear stresses through the gapwidth can be assumed to be dominant compared

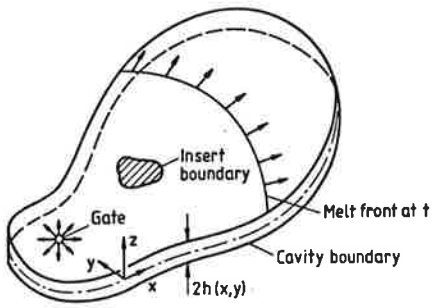

FIGURE 1. Sketch of a thin cavity and the coordinate system.

with in-plane stresses. The assumptions stated above reduce the problem locally to a two-dimensional one and lead to the Hele-Shaw formulation [4].

Adopting the cartesian coordinate system shown in Figure 1, where x- and y-coordinates are in the plane directions and z-coordinate is in the gapwise direction and following the assumptions stated above, the momentum equations reduce to

$$-\frac{\partial p}{\partial x} + \frac{\partial}{\partial z}\left(\eta \frac{\partial u}{\partial z}\right) = 0 \tag{1}$$

$$-\frac{\partial p}{\partial y} + \frac{\partial}{\partial z}\left(\eta \frac{\partial v}{\partial z}\right) = 0 \tag{2}$$

where $p(x,y)$ is the pressure, $u(x,y,z)$ and $v(x,y,z)$ are the velocity components in the x- and y-directions and η is the viscosity. In general case it is dependent on the shear rate, which under the present assumptions is given by

$$\dot{\gamma} = \left[\left(\frac{\partial u}{\partial z}\right)^2 + \left(\frac{\partial v}{\partial z}\right)^2\right]^{1/2} \tag{3}$$

The continuity equation expressed in terms of the gapwise-averaged velocity components is

$$\frac{\partial (h\bar{u})}{\partial x} + \frac{\partial (h\bar{v})}{\partial y} = 0 \tag{4}$$

where h is the half of the gapwidth and gapwise-averaged velocity components $\bar{u}(x,y)$ and $\bar{v}(x,y)$ are defined as

$$\bar{u}(x,y) = \frac{1}{2h}\int_{-h}^{h} u(x,y,z)\, dz \tag{5}$$

$$\bar{v}(x,y) = \frac{1}{2h}\int_{-h}^{h} v(x,y,z)\, dz \tag{6}$$

Appropriate boundary conditions in the z-direction are given by

$$u = v = 0 \qquad \text{at } z = \pm h \tag{7}$$

$$\frac{\partial u}{\partial z} = \frac{\partial v}{\partial z} = 0 \qquad \text{at } z = 0 \tag{8}$$

which describe, that the velocity components are zero at the cavity walls and symmetric velocity profile is assumed in the gapwise direction.

The above equations can be rearranged into a form that is more suitable for the numerical calculations. Since the pressure is independent of z (in present approximation), the integration of momentum equations (1) and (2) with respect to z together with the boundary condition (8) results in

$$\frac{\partial u}{\partial z} = \frac{z}{\eta}\frac{\partial p}{\partial x} \tag{9}$$

$$\frac{\partial v}{\partial z} = \frac{z}{\eta}\frac{\partial p}{\partial y} \tag{10}$$

The second integration together with the boundary condition (7) gives

$$u = -\frac{\partial p}{\partial x}\int_z^h \frac{\hat{z}}{\eta}\, d\hat{z} \tag{11}$$

$$v = -\frac{\partial p}{\partial y}\int_z^h \frac{\hat{z}}{\eta}\, d\hat{z} \tag{12}$$

Performing these integrations, using integration by parts, and making use of expressions (5) and (6), the gapwise-averaged velocities can be written as

$$\bar{u}(x,y) = -\frac{S}{h}\frac{\partial p}{\partial x} \tag{13}$$

$$\bar{v}(x,y) = -\frac{S}{h}\frac{\partial p}{\partial y} \tag{14}$$

where a quantity S(x,y) (a measure of fluidity of the melt) is defined as

$$S = \int_0^h \frac{z^2}{\eta}\, dz \tag{15}$$

Expressions (13) and (14) can be combined with the continuity equation (4) to give the following equation for the pressure field

$$\frac{\partial}{\partial x}\left(S\frac{\partial p}{\partial x}\right) + \frac{\partial}{\partial y}\left(S\frac{\partial p}{\partial y}\right) = 0 \tag{16}$$

The shear rate is also easy to express in terms of pressure gradient by substituting (9) and (10) into (3) with the result

$$\dot{\gamma} = \frac{z}{\eta}\left[\left(\frac{\partial p}{\partial x}\right)^2 + \left(\frac{\partial p}{\partial y}\right)^2\right]^{1/2} \equiv \frac{z}{\eta}|\nabla p| \tag{17}$$

In order to be able to calculate the quantity S, defined by equation (15), the expression for the viscosity is needed. In a simple case with the Newtonian fluid, the expression for S is readily obtained as

$$S = \frac{h^3}{3\mu} \tag{18}$$

where μ is a Newtonian viscosity. In a general case with the non-Newtonian fluid, where the viscosity is dependent on the shear rate, the integration of equation (15) must usually be performed numerically. In particular, for the power-law model the expression for S is obtainable in a closure form. In the case of power-law model the viscosity is written as

$$\eta = m\dot{\gamma}^{n-1} \tag{19}$$

where m and n are constants which depend on the polymeric material used. Combining (19) with (17) the expression for the viscosity becomes as

$$\eta = m\left(\frac{z|\nabla p|}{m}\right)^{(n-1)/n} \tag{20}$$

and further by substituting (20) into the definition (15) and performing the integration, the following expression for S is obtained

$$S = \frac{n}{1+2n}\left(\frac{1}{m}\right)^{1/n} h^{(1+2n)/n} |\nabla p|^{(1-n)/n} \tag{21}$$

The governing equation (16) is of elliptic type and boundary conditions need to be specified along all the boundaries (see Figure 1). The non-penetration condition (i.e the requirement that the normal velocity vanish) along the cavity and insert boundaries results in

$$\frac{\partial p}{\partial n} = 0 \tag{22}$$

At the entrance gate the specified volumetric flow rate is given by

$$2\oint_C \left(-S\frac{\partial p}{\partial n}\right) ds = Q \tag{23}$$

where Q is the flow rate across the entire gap and C denotes any line contour which encloses the gate. Two conditions are needed on the moving boundary, i.e. advancing melt front, one to determine the boundary itself, since the position is not known a priori, and the other to complete the solution of the equation (16). Since the advancing flow front is in a direct contact with vented air, its pressure is atmospheric (assuming the cavity to be properly vented). Taking the atmospheric pressure as a reference value the boundary condition for the moving melt front can be written as

$$p = 0 \tag{24}$$

The requirement of mass balance across the advancing melt front gives the following additional condition

$$-S\frac{\partial p}{\partial n} = h\mathbf{V}\cdot\mathbf{n} \tag{25}$$

where $\mathbf{n}$ is a unit normal vector on the melt front pointing away from the melt domain and $\mathbf{V}$ is a velocity vector at the same point on the front.

It is worth noting, that although the injection mould filling is clearly time-dependent process, the governing equation (16) under present formulation is independent of time. In spite of that, the entire model is time-dependent, since the solution domain i.e. the region filled by melt, which is governed by the boundary condition (25), changes with time. This kind of treatment of the time-dependent phenomena is usually termed as quasi-steady.

SOLUTION PROCEDURE

As briefly discussed above, the mould filling belongs to a general class of problems, usually termed as moving boundary problems. Another typical moving boundary problem is heat conduction with phase change. In fact, as is shown in Appendix, the mould filling and a special case of heat conduction with phase change are analogous problems. Although the symbols in the governing equations

and boundary conditions have different and unrelated physical meaning, they are identical as far as the mathematical solution is concerned. The similarity of governing equations and conditions at the moving boundary are readily seen (see Appendix). As regards the other boundary conditions in the mould filling, the condition (22) for the outer and the insert boundary corresponds physically the situation of an insulated boundary in the heat conduction analysis, whereas the boundary condition (23) at the entrance gate corresponds the constant heat flux boundary condition.

Due to the analogy between mould filling and conduction phase change, the techniques proposed for conduction phase change problems [13] are applicable also for mould filling problems. This fact is utilized in the present study and the commercial finite-element code ABAQUS [14], which is capable to solve conduction problems with change of phase, is used to solve the equations of mould filling.

Although, in principle, the equations and boundary conditions are similar in mould filling and conduction phase change problems, there are some fundamental differences in a physical sense concerning the material properties. In heat conduction analysis the latent heat is usually constant throughout the whole domain, whereas in mould filling analysis the analogical quantity h may change due to the changes of cavity thickness. However, this does not cause any problems in the calculations. In the case of thermal conductivity situation is more involved. It is known that in a general non-linear heat conduction analysis thermal conductivity is dependent on the main variable temperature, whereas in the non-linear mould filling analysis with a non-Newtonian viscosity the analogical quantity S is not dependent on the main variable pressure, but on the pressure gradient (see equation (21)). In order to implement this information into the analysis, some modifications for the algorithm that computes the conductivity are required. In the case of the Newtonian viscosity the value of S may be readily obtained from equation (18) with the result that the governing equation becomes linear.

RESULTS AND DISCUSSION

As an illustration and to check the suitability of the proposed analogy for the mould filling simulations, calculated flow front locations are presented for a rectangular cavity with varying thickness using the Newtonian model. Predicted and measured results presented in the literature are also given.

The cavity and the finite-element mesh used in the calculations are shown in Figure 2, where also cavity dimensions are given. Constant volumetric flow rate at the gate is such that the total filling time is 1 s. Predictions for the melt front positions at various time steps are shown in Figure 3. Calculated and experimental results presented in reference [9] for the same situation are shown in Figure 4. The filling patterns in Figures 3 and 4 are principally similar indicating that the analogy presented in this study can be applied for solving the mould filling problem. The results presented in this paper are limited to the Newtonian case, whereas in practise the viscosity of polymer melts usually depends on the shear rate. As described above the shear rate dependence of the viscosity can be included into the analysis. Some results with the power-law model are presented in reference [15], where also some convergence problems, concerning especially the starting solution, are discussed and the methods to overcome these problems are presented.

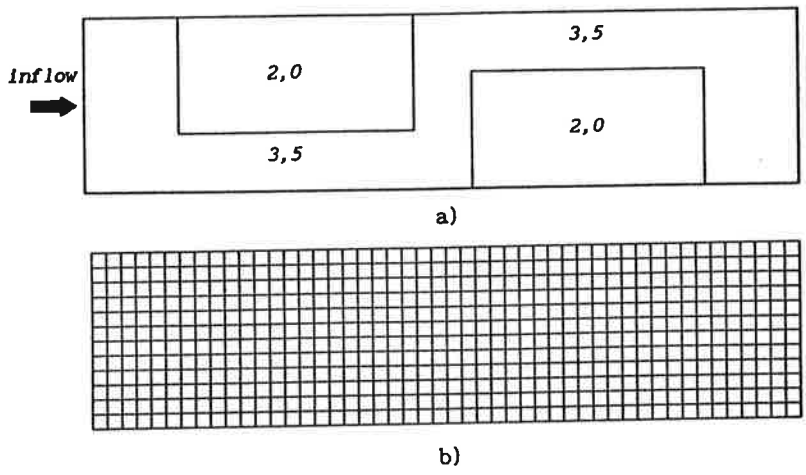

FIGURE 2. a) A rectangular cavity (152 mm × 38 mm) used in the calculations. Numbers indicate cavity thickness in millimeters b) A finite element mesh used in the calculations (48 × 12, linear rectangular elements).

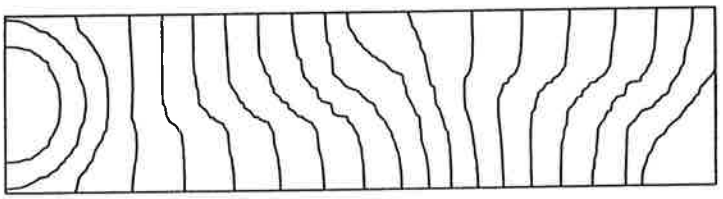

FIGURE 3. Calculated flow fronts at t = 0.05, 0.1, 0.15, 0.2, 0.25, 0.3, 0.35, 0.4, 0.45, 0.5, 0.55, 0.6, 0.65, 0.7, 0.75, 0.8, 0.85, 0.9 and 0.95 s (total filling time 1 s).

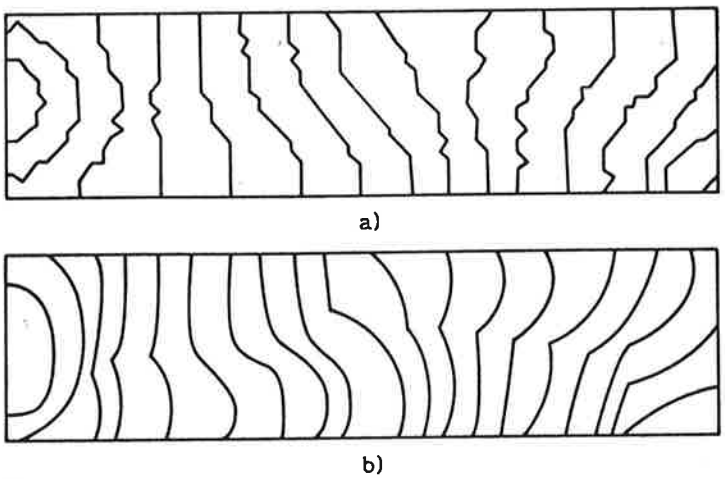

FIGURE 4. a) Calculated and b) experimental flow fronts presented in [9].

The major shortcoming in the present model is the assumption of isothermal flow conditions. To keep the cooling time short enough and thus to allow the mould to be re-used at a sufficiently high rate, the walls of the mould cavity are maintained at a temperature significantly below the solidification temperature of the polymer melt leading to a non-isothermal character of the filling process. This may affect to the filling flow conditions due to the temperature dependence of the viscosity. Another consequence is the formulation of a solid skin layer at the walls of the cavity during the filling. The direct effect of boundary solidification is the constriction of the flow path, which leads to increased pressure drop. However, as was discussed in [9], in many cases reasonably good predictions for the advancing melt front positions are available using isothermal flow assumption, because the time period of filling stage is typically very short and because the thermal conductivity of polymer melts is very low. On the other hand, in the mould cavities which include extremely thin sections, say under 1 mm, temperature changes should be taken into consideration.

As mentioned above, injection mould filling simulations are almost entirely based on purely viscous flow considerations. As known in actual practise the polymer melts exhibit both viscous and elastic effects [16]. However, the simulation of viscoelastic fluid flows is a very difficult task even in simple geometries [17], not to mention the fact that cavity geometries typically used in injection moulding are extremely complex. There are, however, some qualitative information available in the literature, concerning the role of melt elasticity in the mould filling [18]. It may be concluded that in the regions with abrupt or sudden contraction or expansion the elasticity can make considerable contribution to the pressure drop and, that the net effect of elasticity is always to increase the pressure drop above what it would be for an inelastic fluid of the same viscosity.

CONCLUSIONS

Theoretical background of injection mould filling process with appropriate approximations is presented. The solution of mould filling process is based on the analogy between mould filling and conduction phase change and the commercial finite-element code ABAQUS is used for the numerical computations. The capability of the model is demonstrated by analysing the filling of rectangular cavity with varying thickness with the Newtonian fluid. The flow front predictions are in good agreement with the results previously presented in the literature.

REFERENCES

1. Harry, D.H. & Parrott, R.G., Numerical simulation of injection mold filling, *Polym. Eng. Sci.*, **10**, 209-214 (1970).

2. Kamal, R.M. & Kenig, S., The injection molding of thermoplastics, *Polym. Eng. Sci.*, **12**, 294-308 (1972).

3. Richardson, S., Hele-Shaw flows with a free boundary produced by the injection of fluid into a narrow channel, *J. Fluid Mech.*, **56**, 609-618 (1972).

4. Schlichting, H., *Boundary Layer Theory*, McGraw-Hill, 1968.

5. White, J.L., Fluid mechanical analysis of injection mold filling, *Polym. Eng. Sci.*, **15**, 44-50 (1975).

6. Kamal, M.R. & Kuo, Y. & Doan, P.H., The injection moulding behavior of thermoplastics in thin rectangular cavities, *Polym. Eng. Sci.*, **15**, 863-868 (1975).

7. Hieber, C.A. & Shen, S.F., Flow analysis of the non-isothermal two-dimensional filling process in injection moulding, *Israel J. Technology*, **16**, 248-254 (1978).

8. Hieber, C.A. & Shen, S.F., A finite-element/finite-difference simulation of the injection-molding filling process, *J. Non-Newtonian Fluid Mech.*, **7**, 1-32 (1980).

9. Krueger, W.L. & Tadmor, Z., Injection molding into a rectangular cavity with inserts, *Polym. Eng. Sci.*, **20**, 426-431 (1980).

10. Subbiah, S., Traffort, D.L. & Güceri, S.I., Non-isothermal flow of polymers into two-dimensional, thin cavity molds: a numerical grid generation approach, *Int. J. Heat Mass Transfer*, **32**, 415-434 (1989).

11. Crank, J., *Free and Moving Boundary Problems*, Oxford Press, 1984.

12. Wang, H.P. & Lee, H.S., Numerical techniques for free and moving boundary problems, in *Computer Modeling for Polymer Processing* (ed. C.L. Tucker), 369-401, Hanser Publishers, 1989.

13. Fukusako S. & Seki, N., Fundamental aspects of analytical and numerical methods on freezing and melting heat transfer problems, in *Annual Review of Numerical Fluid Mechanics and Heat Transfer* (ed. T.C. Chawla), 351-402, Hemisphere Publishing Corporation, 1987.

14. *ABAQUS User's Manual*, Version 4.8, HKS Inc., 1989.

15. Syrjälä, S., Numerical modelling of injection mould filling and cooling, *Lic. Thesis*, Tampere University of Technology, 1991.

16. Bird, R.B., Armstrong, R.C. & Hassager, O., *Dynamics of Polymeric Liquids*, John Wiley & Sons, 1987.

17. Keunings, R., Simulation of viscoelastic fluid flow, in *Computer Modeling for Polymer Processing* (ed. C.L. Tucker), 403-469, Hanser Publishers, 1989.

18. Isayev, A.I. & Upadhyay, R.K., Flow of polymeric melts in juncture regions of injection moulding, in *Injection and Compression Molding Fundamentals* (ed. A.I. Isayev), 137-225, Marcel Dekker, 1987.

APPENDIX: *Analogy between mould filling and conduction phase change*

Assumptions for the conduction phase change problem:

1. Two-dimensional melting case, where solid region is initially at the melting temperature.
2. Quasi-steady-state situation i.e. the latent heat effect dominates compared with the sensitive heat.

Symbols:

T	temperature	p	pressure
T_m	melting temperature	p_o	atmospheric pressure
k	thermal conductivity	S	measure of fluidity
L	latent heat	h	half of the cavity gapwidth

$\mathbf{n}$ unit normal vector on the moving boundary

$\mathbf{V}$ velocity vector on the moving boundary

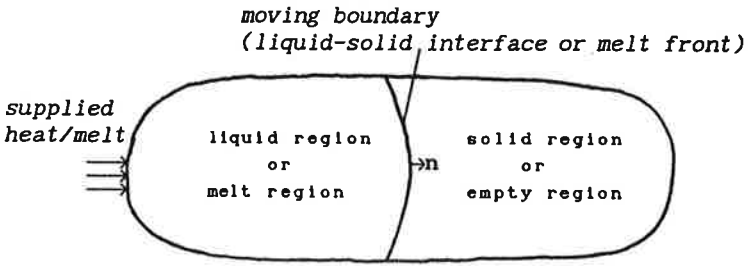

FIGURE. Schematic representation of conduction phase change or mould filling.

	MOULD FILLING	*HEAT CONDUCTION WITH MELTING*
Governing equations:	$\frac{\partial}{\partial x}\left(S\frac{\partial p}{\partial x}\right) + \frac{\partial}{\partial y}\left(S\frac{\partial p}{\partial y}\right) = 0$	$\frac{\partial}{\partial x}\left(k\frac{\partial T}{\partial x}\right) + \frac{\partial}{\partial y}\left(k\frac{\partial T}{\partial y}\right) = 0$
Conditions at moving boundary:	$p = p_o$ $-S\frac{\partial p}{\partial n} = h\mathbf{V}\cdot\mathbf{n}$	$T = T_m$ $-k\frac{\partial T}{\partial n} = \rho L\mathbf{V}\cdot\mathbf{n}$

Analogical quantities: $p \propto T$; $S \propto k$; $h \propto L$; $\rho \equiv 1$

A NONLINEAR ALGORITHM FOR SIMULATING BERTHING OF A SHIP

PEKKA HAUTAMÄKI
Engineering Mechanics Laboratory
Department of Mechanical Engineering
University of Oulu
Linnanmaa SF-90570 OULU, FINLAND

ABSTRACT

A time-step-method based simulation program gives the possibility to take into account most of the factors that have an effect on ship's kinetic energy to find out the loads on fenders and mooring ropes. The simulation is based on the solution of linear second order differential equations for six degrees of freedom where the nonlinearities are taken into account by re-evaluating all changing parameters at every time step. The solution is divided to two parts of which the particular solution is for the first order wave forces and the homogeneous solution for all other external forces. Compared with the test results found in literature the agreement of the results given by the program was often very good but also some variencies could be seen. This was supposed to follow from the fact that all the test arrangements were not known in details, but also, because there still are some effects the adapted theories don't consider.

INTRODUCTION

The traditional equation based on the kinetic energy of the ship fixed with various kind of coefficients doesn't take into account all factors that have an effect on the energy to be absorbed by the fenders. The equations for wind, current and ice loads on ship don't include ship movements or the kinetic energy of an ice float. The wave loads transmitted to fenders are highly dependent on the dynamic properties of a mooring system and they can't be determined by simple equations. Full scale tests are too expensive to make and results of small scale tests don't always convince. One solution to the problems mentioned above is computer simulation.

SIMULATION ALGORITHM

The algorithm is based on a set of linear second order differential equations for six degrees of freedom. The equations are solved in ship coordinate system by a time-stepping procedure with all external and reaction forces evaluated at every time step. During simulation two right-handed Cartesian coordinate systems are used. The ship coordinate system is fixed in ship's body with the origin at the center of gravity and the main coordinate system fixed in space. The solution to one cycle of simulation loop is a combination of homogeneous and particular solutions.

FIGURE 1. The coordinate systems used in the algorithm.

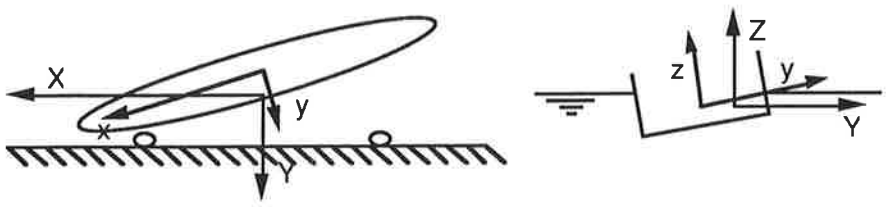

Homogeneous Solution

In solution of the homegenous matrix equation

$$[M_O](q_O'') + [C_O](q_O) + [K_O](q_O) = (0) \qquad (1)$$

where

$[Mo]$	mass matrix for homogenous solution
$[C_O]$	dissipation matrix - " -
$[Ko]$	stiffness matrix - " -
(q_o)	vector of general coordinates

with the well-known solution formulas all constant or slowly varying forces are taken into account by evaluating the instantaneous virtual position of equilibrium as one of the two needed initial conditions for every time step (the other one is the velocity at the end of the previous step)

$$q_{oi}\,(t_n=0) = F_i / k_i \qquad (2)$$

where

i	= 1, 2, ... 6 index of directon
n	n:th time step
i	instantaneous spring constant

$$F = F_A+F_c+F_W{}^{II}+F_l+F_R+F_H+F_T$$

F_A	wind force
F_C	current force
$F_W{}^{II}$	second order wave force (drift force)
F_l	ice force (crushing or drifting)
F_R	reaction forces of mooring system including restoring rorces
F_H	hydrostatic side forces (cushion effects near solid quaywalls)
F_T	special forces like the pushing effect of a tugboat

The new position of the ship in main coordinates is found out when the small deflections arisen during one time step are firstly transformed into the main coordinate system and then added to the previous position coordinate values.

The length of one time step depends on the maximum deflection allowed to arise on fenders and mooring ropes during one step. The greater the nonlinearity of mooring system is the smaller the deflection may be. However, there is a reasonable limit for the shortest time value because of round-off-errors and for the maximum time, because the bigger time value is the less the linearised system corresponds the real system.

Particular solution

In this part of solution the first order wave forces are considered

$$[M_I^I](q_I) + [C_I](q_I') + [K_I](q_I) = (F_W^I) \qquad (3)$$

The time value is equal to the simulated time but also here the matrices and the force vector are evaluated at every time step. Irregular waves are described as a sum of regular wave components and the solution consists of responses for every single wave component solved in the ship coordinate system and the transformed into the main coordinate system.

$$q_{1i}(t) = \sum_{j=1}^{n} Q_{ij} \cos(\omega_j t - \varepsilon_j - \alpha_{ij}) \qquad (4)$$

$$v_{1i}(t) = -\sum_{j=1}^{n} \omega_j Q_{ij} \sin(\omega_j t - \varepsilon_j - \alpha_{ij})$$

where

n	number of wave component
Q	amplitude coefficient
ω	wave frequency
ε	basic phase angle of a wave component
α	phase angle between motion and force

Matrices

The mass matrix is a sum of the ship mass matrix and the added mass matrix. Inertial effects of water caused by ship movements affecting back the ship are taken into account by the added mass matrix.

$$[M] = [M_s] + [A] = \begin{bmatrix} m & & & & & \\ & m & & & & \\ & & m & & & \\ & & & J_1 & & \\ & & & & J_2 & \\ & & & & & J_3 \end{bmatrix} + \begin{bmatrix} a_{11} & & & a_{15} & & \\ & a_{22} & & a_{24} & & \\ & & a_{33} & & & \\ & a_{42} & & a_{44} & & \\ a_{51} & & & & a_{55} & \\ & & & & & a_{66} \end{bmatrix} \qquad (5)$$

where

$[Ms]$	mass matrix of a ship
$[A]$	added mass matrix

Because of the assumed symmetry planes in ship's body the mass matrix is almost diagonal, but the center of gravity of the ship is generally on different level than the center of bouyancy, hence the deviatoric terms $a_{15} = a_{51}$ and $a_{24} = a_{42}$ have to be included. This concerns also the damping matrix C, where the single coefficients are evaluated as a sum of potential and inertial components [2].

$$[C] = \begin{bmatrix} c_{11} & & & & c_{15} & \\ & c_{22} & & c_{24} & & \\ & & c_{33} & & & \\ & c_{42} & & c_{44} & & \\ c_{51} & & & & c_{55} & \\ & & & & & c_{66} \end{bmatrix} \qquad [K] = \begin{bmatrix} k_{11} & & & & k_{15} & k_{16} \\ & k_{22} & & k_{24} & & k_{26} \\ & & k_{33} & k_{34} & k_{35} & \\ & & & k_{44} & k_{45} & k_{46} \\ & symm. & & & k_{55} & k_{56} \\ & & & & & k_{66} \end{bmatrix} \tag{6}$$

The stiffness matrix K is defined by instantaneous spring constants of the tensioned mooring lines and fenders in contact. Also the coefficients of the restoring forces and moments caused by the water have to be included in terms k_{33}, k_{44} and k_{55}.

Forces

The equations for wind and current forces F_A and F_C are based on dynamic pressure, in which shape of structure is taken into account with drag coefficients [3, 4, 5, 6]

$$F_i(\varphi) = 1/2\, \rho c_i(\varphi) v^2 A_i \tag{7}$$

where

i = 1, 2 and 6 for current force
i = 1, 2, 4 and 6 for wind force
p density of air or water
v speed of wind or current
c drag coefficient
φ drift angle
A wind or hull area, including moment arm in directions 4 and 6

The equation for wind and current driving an icefloat has the form [7]

$$F = cqA \tag{8}$$

where

c drag coefficient for ice/wind or ice/water
$q = 1/2\, p\, U^2$ dynamic pressure
U speed of wind at 10 m's altitude or speed of current at -0,5 m's level under ice
A area of an icefloat
p density of air or water

If an icefloat is crushing against ship's hull the force is [8]

$$F = \sigma h b \tag{9}$$

where

σ effective strength of ice
h thickness of ice
$b = b(s)$ the breadth of crushing area is a function of penetrated distance depending on the shape of ship's hull

Simulation of an icefloat's impact on ship's hull is based on the law of energy

conservation which is assumed to have the form [1, 9]

$$W_{I0} - W_{I1} = W_{IC} + W_K + W_P - W_{ID} \tag{10}$$

where

W_{I0} - W_{I1} the kinetic energy of ice at the moments $t = t_o$ and $t = t_1$

W_{IC} the energy needed for crushing

W_K the part of energy transferred to kinetic energy of a ship and w at er

W_P potential energy reserved in mooring ropes and fenders

W_{ID} the increase of kinetic energy of ice during the time $t_1 - t_o$ caused by wind and current

Irregular waves are described as a sum of small regular wave components. The force effects are divided to the first order wave forces depending on single waves and to the second order wave forces, also called the drift forces, depending on wave group properties on a longer time period.

The strip theory is used to get total force on ship, hence the first order wave force in each direction of freedom i is evaluated as a sum of n regular wave force components on N cross-sectional elements

$$F_{Wi}^{I}(t) = \sum_{j}^{n}\sum_{k}^{N}(A_{ijk} \cos \omega_j t + B_{ijk} \sin \omega_j t) \Delta x_k \tag{11}$$

where Δx_k is the length of section element. A and B are elemental force constants consisting of inertial, damping and displacement components [10]. The ISSC-formula [11] is used for describing spectral densities of natural waves and to determine and the parameters of single wave components [12]. In formulating the equation for the second order wave forces the works of Løken, Olsen [13] and Faltinsen [5] (s. [1]) have been used

$$F_{Wi}^{II}(t) = \sum_{j}^{n}\sum_{m}^{n}\sum_{k}^{N}(a_j a_m \cos ((\omega_m - \omega_j)t - (\varepsilon_m - \varepsilon_j)) T_k^i \Delta x_k \tag{12}$$

where

i = 1, 2 and 6 directions of motion

a amplitude

T_k transfer coefficent which depends on the shape of the hull and the drift angle

The water between a berthing ship and a solid quaywall squeezes which introduces a cushion effect that represents an extra force on the ship. Let's assume the ship's hull is long enough, so that the water flow around the ship can be neglected. Based on the Bernoulli equation of pressure there is a balance between the amount of water running down under the ship and the rise of water level. After few manipulations [1] it follows that the lateral force caused by the unbalance between the static pressures on the opposite sides of the hull can be evaluated by the formula

$$F_H = -1/2\, \rho g \sum z_{hk}(z_{hk} + 2D) \Delta x_k \tag{13}$$

where

$z_{hk} = v_k |v_k| D^2 / (2g d_k^2)$ instantaneous hydraulic level

$k = 1, 2, \ldots N$ section elements

D	draft
v	velocity at the point of hull
d	distance between hull and quaywall

FIGURE 2. Comparison between a berthing ship and interconnected vessels.

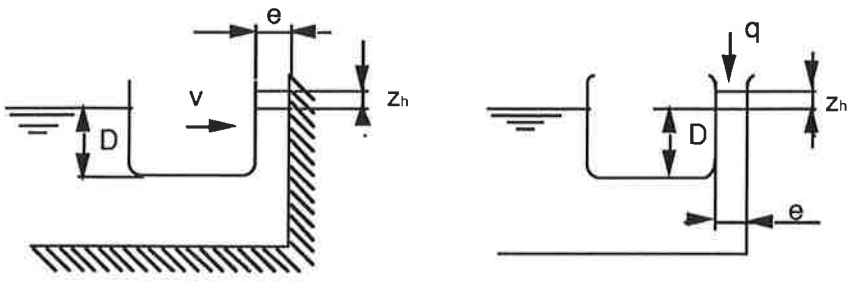

Special features of simulation

The hydrodynamic effects, damping and added masses, are formulated for most directions of motion as functions of circular frequencies which on the other hand are depending on damping and added masses. In homogeneous solution this dependency relation can be solved by giving suitable initial values to the frequencies and during next loops of simulation letting both parameters to find their right values which also are changing all the time because of changing conditions. In particular solution there are n different circular frequencies because of the n regular wave components but the ship is using only one frequency at time in each direction. This frequency is evaluated here as a mean value of the latest halth period of motion of the ship.

Sometimes the matrices are singular or they are too close the singularity. In that situation the algorithm tries to solve smaller and better combinations of degrees of freedom separately and join those solutions together.

Because of the continuous analysing of the situation also things like the friction between ship's hull and fenders, hanging and pre-tensioning the ropes in the way decided previously, hysteretic dissipation in fenders made of viscoelastic materials and the effects caused by flexible structures and pre-tensioned extra fenders behind active ones can be taken into account.

RESULTS

The results given by the simulation program PRESS are compared below to some test results found in the literature. Blokk and Dekker [15, 16] have done tests with a model of 200000 DWT tanker at a scale 1:75 to find out the effects of eccentricity, fender stiffness and initial speed of a ship on fender energy during ship's impact. In figure 3a the strike of fender is shown as a function of initial speed and fender stiffness. The results of centric impact measured by Blokk and Dekker agree very well with the simulated ones. In figure 3b the strike of fender is given as a function of time in centric impact. The measured and simulated curves coinside well on the compressive phase but not on the recoiling phase. After Blokk and Dekker the phases are not symmetrical because during the recoiling phase the ship has to move "upstream". This effect is not taken into account in the simulation algorithm.

The results concerning the effect of eccentricity given by simulation are compared with the results given by Saurin [14] in figure 4. The symbol a means the distance from the point of contact to the center of gravity of the ship. The impact energy W is compared with the energy W_o

FIGURE 3. Stroke of fender as a function of fender stiffness, initial speed of a ship and (b) time.

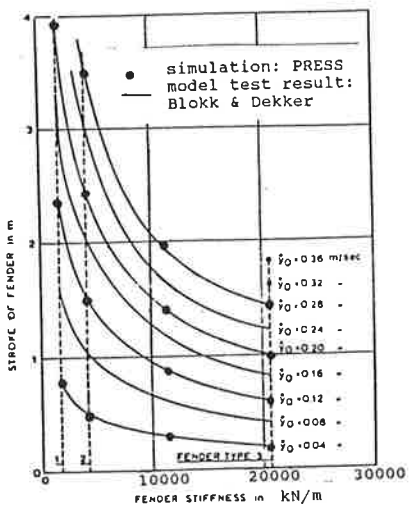

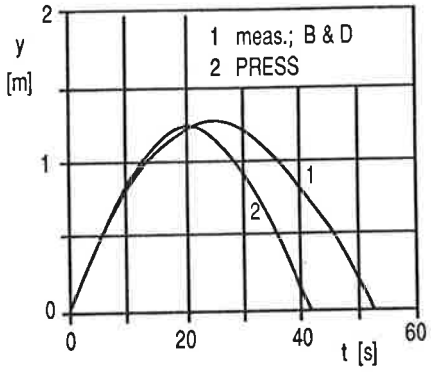

Ship	200000 DWT tanker
condition	fully loaded
scaled	1 : 75

on centric impact. After simulation the sliding of ship's hull along the fender's face has an influence on fender energy. The stiffness coefficient in the direction of the surface of the fender is two times the coefficient in the direction of compression. When the friction coefficient μ is large enough to stop the sliding, the situation corresponds the test conditions and the theory, and the agreement is good. The ship in Saurin's tests was a 32000 DWT tanker scaled 1:60.

FIGURE 4. The influence of eccentricity on fender energy after Saurin [14] and simulation.

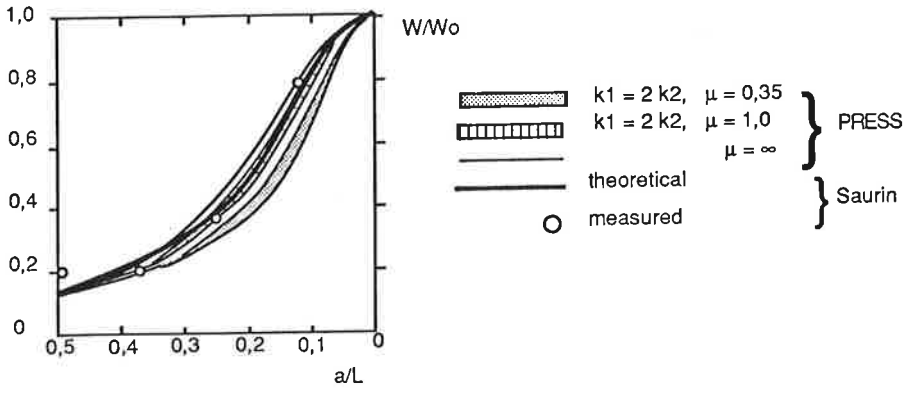

In figure 5 there is an example about the collision of an icefloat with a moored ship where the crushing force, the speed of ice, the responses of the ship and the total reaction force are plotted as a function of time. The ice float is hitting the ship at a straight angle.

INFLUENCE OF DAMPING AND FEEDBACK CONTROL TO DYNAMIC CHARACTERISTICS OF CANTILEVERED PIPES ASPIRATING FLUID.

Matti Kangaspuoskari, Jari Laukkanen, Antti Pramila
Engineering Mechanics Laboratory
Department of Mechanical Engineering
University of Oulu
Linnanmaa SF-90570 OULU,FINLAND

ABSTRACT

The theoretical background of the FEM program system developed by the authors for analysing stability of fluid conveying pipes is presented. Parametric studies concerning the effect of damping and non-Lagrangian coupling by means of feedback control are made.

INTRODUCTION

This paper presents an investigation into the dynamics and stability of a long cantilevered pipe aspirating fluid by FEM. For a long time it has been known that the flow velocity necessary to cause flutter in a cantilevered pipe discharging fluid is so high that it is unlikely to be encountered in practice. However, if long flexible pipe is aspirating fluid from the free end and conveying it to the supported end the pipe is inherently unstable, i.e. the critical velocity is zero [1]. The arrangement represents an idealization of an ocean mining system where pipe is aspirating mixture of water and nodules and conveying them to the ship. The real marine riser system does not lose stability at infinitesimally small flow velocity because of damping caused by friction between the pipe and external fluid.

In marine risers the cross section is varying, there are point masses due to the itermediate pump stations and flexible supports due to mooring equipment, which are difficult to model analytically but are well suited to finite element analysis. Also it is very easy study the effect of a non-Lagrangian coupling to the system when the FEM is used. The non-Lagrangian coupling by means of feedback control may stabilize the system if it is in opposite phase with the unstable eigenmodes. The FEM has been applied to gyroscopic nonconservative problems as early as 1971 [2], but to the knowledge of the authors no commercial FEM-program contains possibilities for analysing dynamics of fluid conveying pipes with all its essential features-gyroscopic and centrifugal terms. The purpose of the present study has been to develop such a FEM-program. Thus far only free vibration have been considered [3],[4].

EXTENDED HAMILTON'S PRINCIPLE AND FEM DISCRETISATION

The system under consideration consists of a pipe of length L with cross-sectional area A, flexural rigidy EI, mass per unit length m_p, axial load P, and conveying fluid, mass per unit length m_f, with a constant axial velocity u. Extended version of Hamilton`s principle [5] taking into account the energies associated with inflow and outflow, is employed in deriving the equations necessary.

It states that

$$\delta \int_{t_1}^{t_2} (T - V)\, dt - \int_{t_1}^{t_2} m_f u (\dot{w} + u w')\, \delta w_{/x=L}\, dt = 0 \qquad (1)$$

where the possible free end is at x=L. T is the kinetic energy of the system and V is the potential energy of the system. A dot indicates differentiation with recpect to time t and a prime indicates differentiation with recpect to the spatial coordinate x. δ is the variation symbol.

The kinetic energy of the pipe and fluid is

$$T = \frac{1}{2} \int_0^L [\, m_p \dot{w}^2 + m_f u^2 + m_f (\dot{w} + uw')^2 \,]\, dx$$

$$+ \frac{1}{2} \sum M_j \dot{w}_j^2 + \frac{1}{2} \sum J_j \dot{w}_j'^2 \qquad (2)$$

where Mj and J_j are the mass and moment of inertia of the possible concentrated masses on the pipe.

The potential energy is

$$V = \frac{1}{2} \int_0^L (EIw''^2 + Pw'^2 - 2qw)\, dx + \frac{1}{2} \sum k_j w_j^2 + \frac{1}{2} \sum k_{v_j} w_j'^2 \qquad (3)$$

where k_j and k_V are the translational and rotational stiffnesses of the possible flexible supports and q is the external transverse loading per unit length.

The fluid is assumed to be incompressible and the potential energy of the fluid is zero.

The equation of motion using expressions (1),(2) and (3) is

$$(m_p + m_f)\, \ddot{w} + 2 m_f u \dot{w}' - (P - m_f u^2)\, w'' + EIw'''' = q \qquad (4)$$

If damping is taken into account the equation of motion must be changed. Internal viscous damping causes an extra term E^*Iw''''. and external viscous damping causes a term cw on the left hand side of equation (4).

By using the typical FEM trial

$$w = [\,N\,]\{\,\bar{a}\,\} \tag{5}$$

where [N] is the shape function matrix and a contains the nodal displacements and slopes, i.e.

$$\{\bar{a}\}^T = [w_1\,,\, w_1'\,,\, w_2\,,\, w_2'\,,\, \ldots\,] \tag{6}$$

we obtain from the first term of Hamilton's principle (1) the discrete equation system

$$[\,M\,]\,\{\ddot{\bar{a}}\} + [\,G\,]\,\{\dot{\bar{a}}\} + [\,K\,]\,\{\bar{a}\} = \{\bar{F}\} \tag{7}$$

where

$$[\,M\,] = \int_0^L (\,m_f + m_p\,)\,[\,N\,]^T\,[\,N\,]\,dx \tag{8}$$

$$[\,G\,] = \int_0^L m_f u\,(\,[\,N\,]^T\,[\,N\,]' - [\,N\,]'^T\,[\,N\,]\,)\,dx \tag{9}$$

$$[\,K_p\,] = \int_0^L E\,I\;[\,N\,]''^T\,[\,N\,]''\;dx \tag{10}$$

$$[\,K_f\,] = \int_0^L (\,P - m_f u^2\,)\,[\,N\,]'^T\,[\,N\,]'\;dx \tag{11}$$

$$\{\bar{F}\} = \int_0^L [\,N\,]^T\,q\;\;dx \tag{12}$$

If the translation of the end of the pipe is possible, the last integral of Hamilton's principle (1) adds

$$\Delta G_{2n-1,2n-1} = m_f u \quad \text{and} \quad \Delta K_{2n-1,2n} = m_f u^2 \tag{13}$$

Thus G matrix is no more skew-symmetric and the stiffness matrix K becomes unsymmetric.

The point masses, flexible supports and dashpots at the nodes cause additions to the corresponding diagonal elements of [M], [K] and [C].

If damping is taken into account, we obtain the equations of motion

$$[\,M\,]\,\{\ddot{\bar{a}}\} + [\,C + G\,]\,\{\dot{\bar{a}}\} + [\,K\,]\,\{\bar{a}\} = \{\bar{F}\} \tag{14}$$

where the total damping matrix C is the sum of the internal damping C_i and external damping C_e.

Damping matrices are

$$[C]_l = \frac{E^*}{E}[K_p] \quad \text{and} \quad [C]_e = \int_0^L c\,[N]^T[N]\,dx \tag{15}$$

The non-Lagrangian coupling by means of feedback control can be taken into account by following expressions

$$[M]\{\ddot{\bar{a}}\} + [G]\{\dot{\bar{a}}\} + [[K] + \alpha[H]]\{\bar{a}\} = \{\bar{0}\} \tag{16}$$

$$[M]\{\ddot{\bar{a}}\} + [[G] + b[H]]\{\dot{\bar{a}}\} + [K]\{\bar{a}\} = \{\bar{0}\} \tag{17}$$

$$[[M] + \kappa[H]]\{\ddot{\bar{a}}\} + [G]\{\dot{\bar{a}}\} + [K]\{\bar{a}\} = \{\bar{0}\} \tag{18}$$

where a,b,k are the feedback gains and H is the feedback matrix. H has zeros everywhere except for a one in row i, column j. In equation (16) we have a displacement sensor, in (17) a velocity sensor and in (18) an acceleration sensor.

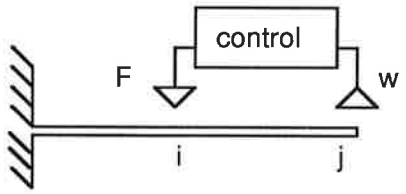

Figure 1. Feedback control.

PARAMETRIC STUDIES

Following nondimensional quantities are used (19)

$$U_{cr} = \left(\frac{m_f}{EI}\right)^{1/2} u_{cr} L \qquad \beta = \frac{m_f}{(m_f + m_p)} \qquad C = \frac{c L^2}{\sqrt{EI(m_p + m_f)}}$$

$$e^* = \frac{E^*}{L^2 E}\left(\frac{EI}{(m_f + m_p)}\right)^{1/2} \qquad D = \frac{d L}{\sqrt{EI(m_p + m_f)}} \qquad A = \frac{\alpha L^3}{EI}$$

$$B = \frac{b L}{\sqrt{EI(m_p + m_f)}} \qquad \Gamma = \frac{\kappa}{m_p} \qquad \gamma = \frac{(m_p + m_f) g L^3}{EI}$$

All the comparisons have been made using 24 elements. The mass ratio b used was equal to 0.5

Figure 2 shows the effect of the external viscous damping C, to the critical velocity of cantilevered pipe aspirating fluid. In figure 3 we have a dashpot, damping coefficient d, at the free end. Critical velocity seems to be linear function of the damping and the bigger is damping the bigger is critical velocity. Both systems loses stability by flutter.

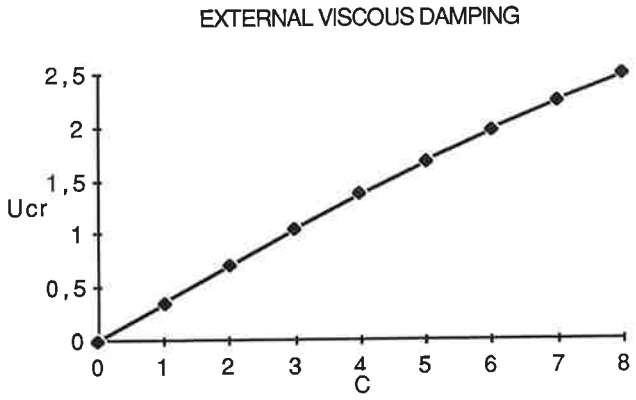

Figure 2 : The effect of the external viscous damping.

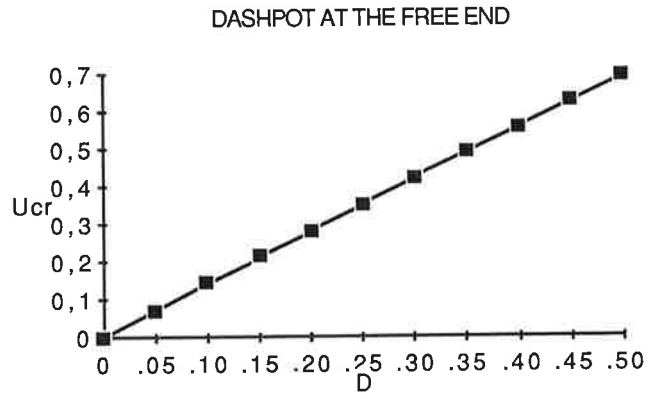

Figure 3 : Dashpot at the free end of the pipe.

Next let us consider figure 4, where we have internal viscous damping e^*.With small values of damping system loses stability by flutter and critical velosity is small. If $e^* > 0.5*10^{-4}$ flutter is ruled out and system loses stability by divergence at first eigenmodes. At the point $e^* = 2.0*10^{-4}$ the first eigenmode regains stability and after that the critical velocity is quite high.

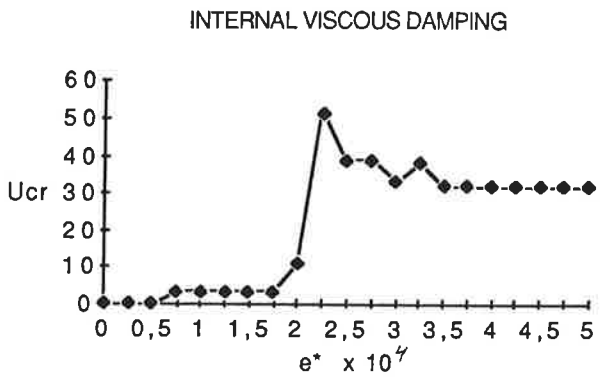

Figure 4 : The effect of internal viscous damping.

Figure 5 shows the effect of the feedback control by a velocity sensor B to the critical velocity of cantilevered pipe aspirating fluid. Nondimensional external damping C was set equal to 1. The sensor j was used was at the free end of the pipe (x=L) and the actuator i was at point (x=L/2).

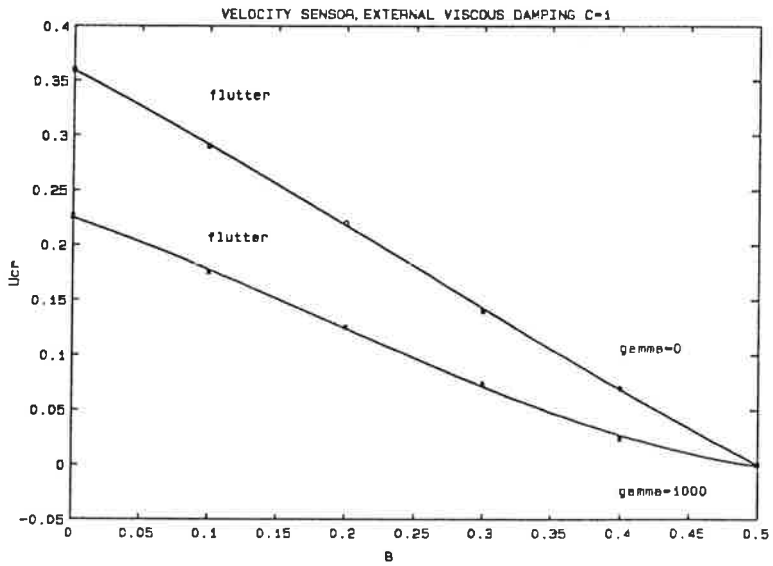

Figure 5 : The effect of feedback control, velocity sensor.

The feedback could be propotional to displacement or acceleration, in the same way. In all these three cases the critical velocity seems to be almost linear function of the feedback gain and the bigger is feedback the lower is critical velocity. At last we can find feedback value when critical velocity is zero, i.e. damped system is unstable at zero velocity. The reason for this effect is that even this kind of single sensor/actuator pair can stabilize only one eigeimode, in continous systems we have alweys higher eigenmodes where feedback force is in phase with response. Structural damping can be written in form

$$\xi_i = \frac{\alpha}{2\omega_i} + \frac{\beta}{2}\omega_i \qquad (20)$$

In the case of a = 0 we have Rayleigh damping propotional to stiffness in form $\xi_i = \eta * \omega_i$. With feedback control we stabilize lower eigenmodes and Rayleigh damping stabilizes those higher modes where feedback force is in phase with response. In figure 6 we have damping $\xi_i = 0.02 * \omega_i$ and acceleration control Γ. In this figure we obtain that critical velocity is growing if feedback gain is increased.

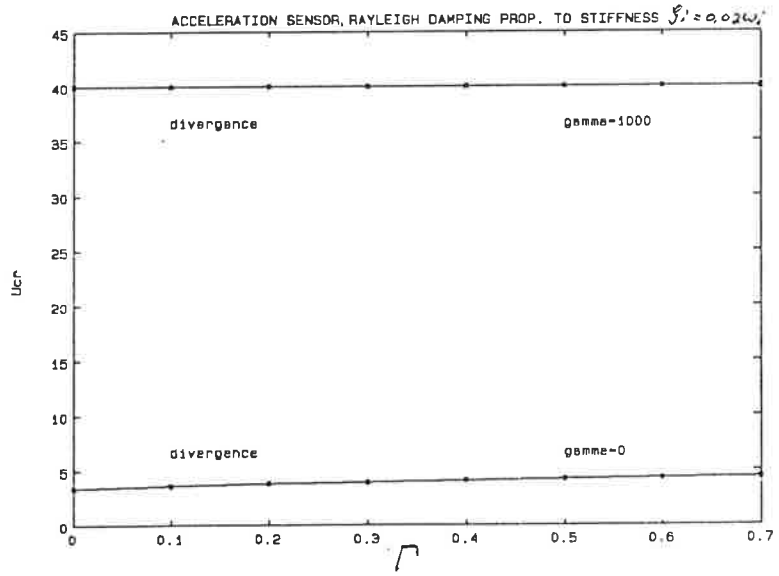

Figure 6 : Acceleration sensor, Raylaight damping propotional to stifness.

CONCLUSIONS

Stability of pipes aspirating fluid has beed studiet using the FEM. The starting point for the discretisation is the extended Hamilton´s principle. The non-Lagrangian coupling by means of feedback control is taken into account.

Some parametric studies for the stability of cantilevered tube with external, internal and pointwisely applied damping are presented. Also the effect of different kind of feedback sensors at the case of external viscous damping and Rayleigh damping propotional to stiffness are presented.

The results obtained that the effect of damping can be either stabilizing or destabilizing depending on the configuration and other parameters involved. (Fig. 2-4).

The critical velocity of a cantilevered tube with external viscous damping and feedback control is decreased if feedback gain is increased (fig. 5). In continous system have allways eigenmodes where feedback force is in phase with response and these modes are unstable.

If system have Rayleigh damping propotional to stiffness by form $\xi_i = \eta * \omega_i$ situation is different. (Fig.6). With feedback control we can stabilize lower eigenmodes and structural damping stabilize higher modes, even those where feedback force is in phase with response. In this aspect the minimization of feedback gain is worthwhile.

REFERENCES

[1] PAIDOUSSIS, M.P., LUU, T.P., Dynamics of a pipe aspirating fluid, such as might be used in ocean mining. ASME Journal of Energy Resources Tecnology, vol. 107, 1985, pp. 250-255.

[2] MOTE, C.D., JR., Nonconservative stability by finite element. Journal of the Engineering Mechanics Division of ASME, vol. 97, 1971, pp. 645-656.

[3] PRAMILA, A., LAUKKANEN, J., LIUKKONEN, S., Dynamics of short and long tubes conveying fluid using FEM, Tampere University of Technology Department of Mechanical Engineering, Applied Mechanics, Report 46, Tampere 1988.

[4] PRAMILA, A., LAUKKANEN, J., LIUKKONEN, S., Dynamics and stability of short fluid conveying pipes using Timoshenko elements. Journal of Sound and Vibration. (in press).

[5] MCIVER, D.B., Hamilton´s prinsiple for systems of changing mass. Journal of Engineering Mathemetics, vol. 7, 1973, pp. 249-261.

MEASUREMENT AND ANALYSIS OF THERMAL ICE THRUST

MAURI MÄÄTTÄNEN
Department of Mechanical Engineering
Helsinki University of Technology
SF-02150 Espoo, Finland

ABSTRACT

Thermal ice expansion can cause significant loads against channel walls. The problem was studied in a Sino-Finnish project to utilize the Yin-Mi canal also during the winter time as an aqueduct for the city of Beijing. In situ thermal ice pressure measurements were conducted by installing pressure sensing plates into the ice. A numerical model is then needed for calculating the corresponding thermal thrust. This is accomplished by observing transient temperature history and nonlinear creep in the ice sheet.

Instrumentation, measurements, theoretical model and analysis methods are described. Results indicate that the effects of air temperature changes in the thermal pressure of ice can be simulated reasonably well. This enables to predict thermal thrust also in more stringent conditions than what were met during the short measurement period. Error sources of the present method are discussed and improvements for the further research proposed.

INTRODUCTION

Thermal ice pressure is a result of ambient air temperature transients. Numerical predictions for ice are however far less reliable than for more common materials in thermal stress analysis in structural mechanics. The reason is in the mechanical properties of ice. Ice is anisotropic material with rheological behaviour. Even though level ice can be modelled as an orthotropic plate for engineering purposes, it still has gas or brine inclusions, cracks, thickness variations, etc., which reduce mechanical properties. There is usually a temperature gradient through the ice thickness, which has a strong effect on elastic modulus and creep rate.

Snow above the ice sheet is an effective insulator, and if snow is drifted, aerial temperature distributions will also occur. In addition turbulent winds are present during air temperature transients. Hence, only at large, statistical average thermal ice pressure can be calculated, locally there will be variations.

The method for calculation of thermal ice pressure starts by solving the heat conduction equation in the ice sheet. From the known temperature histories it is then

possible to solve thermal stresses by observing ice rheological models and boundary conditions. The total thrust can then be integrated through the thickness.

Thermal ice thrust can be measured directly at boundaries or indirectly by gauges embedded in the ice sheet. The former method is preferred, because the result is readily usable in the design of similar structures. If ice pressure is measured a numerical model is needed to translate ice pressure into local ice thrust and further into thrust against boundaries.

Measurements in the field are prone to ambient weather and it is unlikely to hit an optimum combination of snow and ice thickness, and air temperature rates to match maximum design conditions. In laboratory, in the other hand, it is impossible to duplicate conditions in the nature. Hence, to utilize both the in-field data and the numerical model looks the most promising approach. The numerical model can be first calibrated and then applied for the most stringent design conditions.

Thermal ice thrust causes each winter damage to shoreline, channel walls, bridge piers, marinas, etc. This paper is a by-product of winter water flow control project in Yin Mi Canal, North of Beijing, China. Earlier this man made canal was drained for the winter but the increasing demand of water required its winter operation as well. Information was needed to judge whether the original canal wall construction can withstand thermal ice thrust. Thermal ice pressure was measured in the winter 1990 and an analysis procedure was developed to predict total thrust and further to predict maximums.

THERMAL THRUST MEASUREMENT

A direct method to measure thermal ice thrust is to make an instrumented wall panel. Conventional load cells can be used but the difficulty is in waterproofing the load sensing plate, and preventing it from freezing on the foundation. The foundation should be as stiff as the original wall in order not to change ice load paths at or near the instrumented panel. Water level changes are another problem. Due to variations many instrumented panels would be needed for reliable measurements. This approach appeared to be too expensive.

An indirect method is to measure the thrust inside the ice sheet, which has to be balanced by an equal boundary reaction, provided the gauges are sufficiently close to the wall. It is possible to measure ice thermal stresses in different layers through the thickness or to use a gauge that directly integrates the average pressure.

Soil mechanics type of instrumentation has been applied for measuring ice stresses. Flat panels [3,4,7], small stiff cylindrical gauges, vibrating wire pressure sensitive diaphragm, strain gauged cylinder [4], vibrating wire cylinder (also plane state of stress) [2], etc. Thin liquid filled flat panels, based on measuring their internal pressure, are most popular. Their registration ratio is close to 1:1 at wide range of panel to ice stiffness ratios, Eq.1 and Fig. 1.

$$\frac{\sigma}{\sigma_1} = \frac{\frac{E_1}{E} + \frac{H}{2D}}{\left(\frac{E_1}{E}\right)\left(1 + \frac{H}{2D}\right)} \qquad (1)$$

where σ is the true stress and σ_1 the measured pressure, E_1 and E are the gauge and ice modulus of elasticity, H the gauge thickness and D the diameter.

The registration dependence can be calculated by elastic analysis [1], but in practise the situation is more complicated due to ice creeping faster at edges where the panel is most stiff. After a while creep relaxation makes the registration ratio to approach that of an infinitely stiff panel [4].

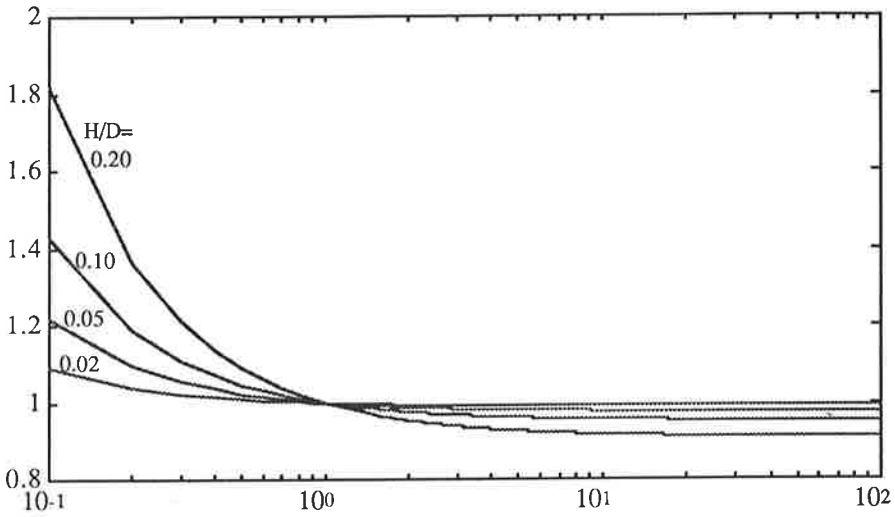

Figure 1. The ratio of true ice pressure to the measured gauge pressure, (registration ratio), versus gauge to ice modulus of elasticity ratio, Eq.1.

If a flat panel panel extents exactly through the ice thickness an average ice pressure, and hence thrust, is directly measured. However, this is not recommended due to easier heat conduction in the gauge which will cause local melting near bottom, and bridging at the top layer of ice. Flat panels are therefore embedded totally inside the ice sheet and will measure only average pressure for a part of ice thickness. Only compressive unidirectional stresses can be measured. With three gauges it is possible to solve the components of the plane state of stress.

For this research a 108 mm diameter, 7 mm thick oil filled flat panel, Fig. 2, was designed, manufactured and calibrated in laboratory, [5]. Commercial pressure transducers were used to measure the internal pressure. With the chosen geometry the measured pressure follows closely the actual ice pressure, as $E_{oil}/E_{ice} > 0.2$ and H/D = 0.065, compare Fig. 1. In the analysis of measurement data the calibration data was was used. It includes the effects of pressure transducer and amplifiers in addition to the gauge mechanical registration ratio.

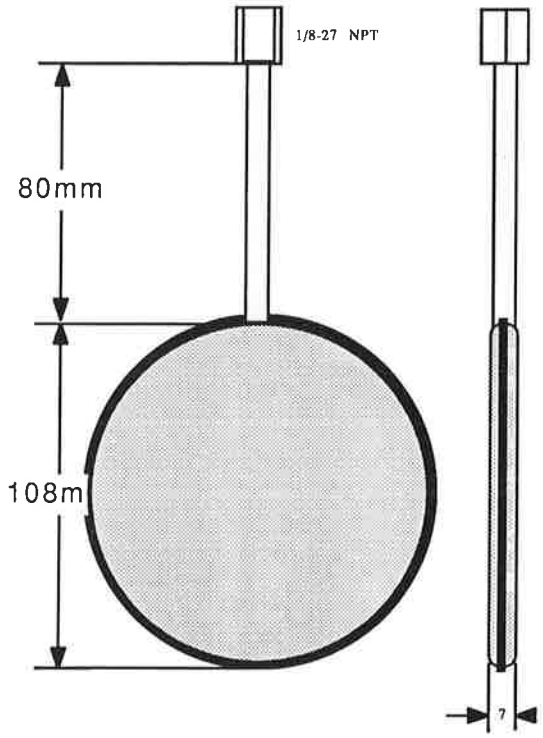

Figure 2. Ice pressure gage.

HEAT CONDUCTION

Average thermal thrust analysis allows ice cover temperature distribution to be modelled in one dimension only. Time dependent temperature distribution T(z,t) through the thickness is covered by the differential equation:

$$\frac{dT}{dt} = a\frac{d^2T}{dz^2} \qquad (2)$$

where a=1.15E-6 m^2/s, is the ice thermal diffusivity. For a more complicated analysis the heat flux due to solar radiation should be added. Also the heat exchange from the air and water to the ice could be observed, which would need the knowledge of heat exchange coefficients, temperatures and velocities both at air and water interfaces. However Eq. 2 can be simply used by assuming a known ice top surface temperature history, which already includes the effects of snow isolation and heat exchange from the air and sun. Temperature at the bottom of ice sheet can be assumed to be 0 °C. The solution for linearly changing surface temperature can be found by using Fourier series:

$$T(z,t) = (1 - \frac{z}{d})(T_o+bt) + \sum_{n=1}^{\infty} \frac{2\,b\,d_n^3}{a\,d}(e^{-at/d_n^2} - 1)\sin\frac{z}{d_n} \qquad (3)$$

where d is ice thickness, b temperature rate, and $d_n = d/n\pi$. The first term in the right hand side does not fulfil the differential equation 1. It can be regarded as a time dependent initial condition upon which the solution of heat conduction is superposed. Another possibility to solve Eq. 2 is a convolution type integral, [6].

$$T(z,t) = \frac{z}{2}(\pi a)^{\frac{-1}{2}} \int_{t_0}^{t} (t - \tau)^{\frac{-3}{2}} T(0,\tau)\, e^{\frac{-z^2}{4a(t-\tau)}}\, d\tau \qquad (4)$$

In practice as the temperature profile is smooth only few terms in the Fourier-series solution, say $n<10$, is needed for accurate enough results. A general temperature history can be superposed by adding different temperature rates b with a time shift corresponding to the change of initiation times. To simulate typical temperature transients a simple model in Fig. 3 can be adopted. The initial temperature T_0 represents ice top surface temperature after a long cold period when ice temperature distribution has established to be linearily varying through the thickness. Then temperature rises to T_1 in t_1 hours, and stays constant until a decrease starts at time t_2, etc. By varying parameters in Fig. 3, different thermal transients can be simulated, e.g daily fluctuations. As the heat diffusion is slow, variations are much smoother soon below the top surface, and hence the "corners" in the simplified top layer temperature history have little effect on overall behaviour in practise.

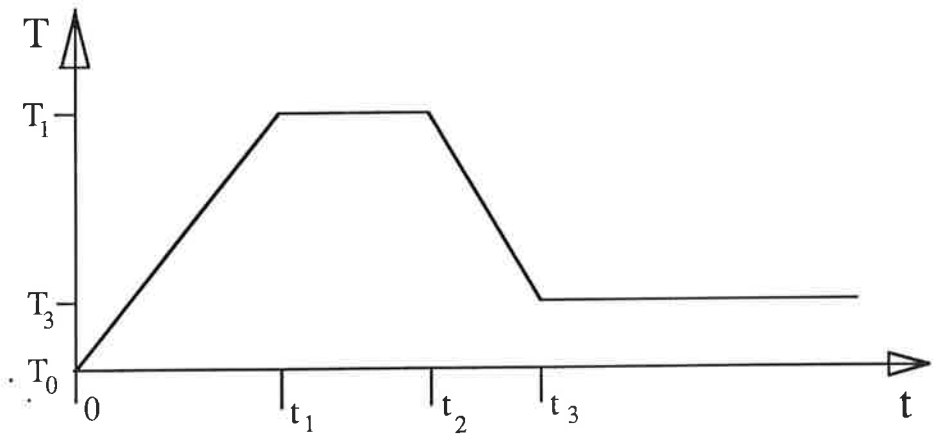

Figure 3. Thermal transient at ice surface.

THERMAL STRESSES AND THRUST

A great many of ice rheological models have been presented. Main features include elastic response, transient creep (delayed elasticity) and nonlinear creep. These models have been established in laboratory conditions for homogeneous ice in uniaxial creep tests. Only limited creep data is available for multiaxial state of stress. In field the situation is more complicated due to inhomogenities in ice. Thermal stress predictions with laboratory rheological models yield to too high stress levels. The reason is partly in size factor, which includes the effects of pore

and brine inclusions, cracks, and eccentric compression, which make the full size ice more compliant. A semi-empirical creep equation for river and lake ice, [3], observes the elastic response and nonlinear creep effects:

$$\frac{d\sigma}{dt} = A\frac{dT}{dt} - B\left(\frac{1}{1-T}\right)^{m}\left(\frac{\sigma}{s}\right)^{n} \qquad (5)$$

where A= 45 kPa/^{o}C, observes the coefficient of thermal expansion and the modulus of elasticity of ice, B=2.2E-13 kPa/s is creep parameter, reference stress s=1 Pa, exponent m=0.2 and n=1.8. It can be seen that there is an effect on creep rate by the temperature T. E.g. in -15 ^{o}C creep rate is only 57 % from that at zero temperature. Creep exponential n=1.8 is smaller than what is the customary 3.0 for the ice. However the value n=1.8 is based on experimental in-field test data with actual river ice, [3], as well as the other parameters in Eq. 5.

The temperature rate can be calculated by derivating Eq. 3 in relation to time:

$$\frac{dT}{dt} = b\left(1-\frac{z}{d}\right) - \sum_{n=1}^{\infty}\frac{2\,b\,d_n}{d}\,e^{-at/d_n^2}\,\sin\frac{z}{d_n} \qquad (6)$$

Again superposition with corresponding time shifts allows to construct arbitrary temperature rate histories, e.g. according to Fig. 3.

At last the total ice thrust P can be calculated by integrating thermal stresses from Eq. 5 through the thickness of ice sheet:

$$P(t) = \int_0^d \sigma(z,t)dz \qquad (7)$$

A Fortran program to observe Eq. 2-7 was written to solve thermal stresses in the ice by finite difference method and the total thrust. For the numerical solution ice thickness is divided into 20 layers. Temperatures, temperature rates and stresses with time at each layer will be calculated and the total ice thrust integrated. Samples of analysis results are presented in Fig. 5 and 6.

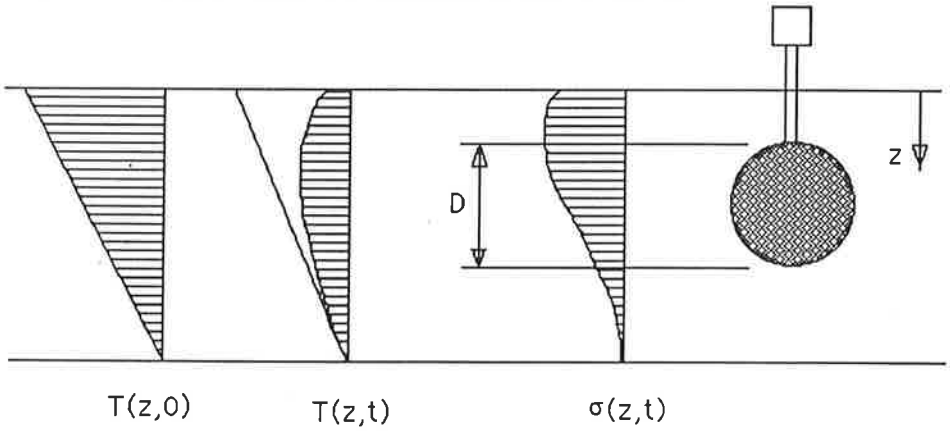

Figure 4. The location of pressure cell in stress field.

To compare pressure cell reading with the analytical model an average of ice pressure at those layers of the ice sheet, that are in contact with the pressure cell, is calculated, Fig. 4. In present tests these layers were between 5 and 15 cm from the top surface of ice. Also the circular shape of the pressure cell disk has to be taken into account. Then this average pressure can be compared to measured pressure and further to the total ice thrust.

APPLICATION EXAMPLE

Measurements were conducted at two locations in the Yin Mi Canal. Ice thickness was less than anticipated and only four transducers could be installed. During the test period temperatures were rising and caused in the second location the center of canal to melt open making thermal ice thrust measurements obsolete. In the first location some good data was gathered at the beginning of test period.

The environmental data on January 25, 1990, was used to test and calibrate the numerical model. Temperature rise time in the air has been about 6 - 8 hours. Due to boundary layer effects the minimum ice top surface temperature has been less than that of air. Hence the data for initial conditions, parameters in Fig. 3, have been chosen to be: t_1=6 hours, t_2=9 hours and t_3=15 hours, and temperatures T_0=-12 °C, T_1=-0 °C and T_3=T_0. The maximum thermal pressure occurs a little after time t_2 and hence the final temperature T_3 has no significant effect.

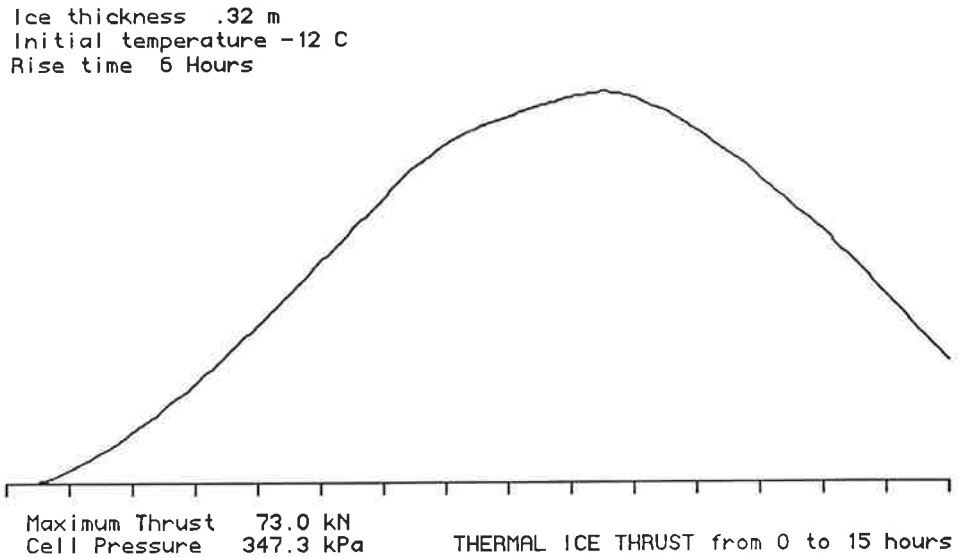

Figure 5. Thermal ice thrust, 0.32 m thick ice.

The results of analysis are plotted in Fig. 5. The calculated maximum thermal thrust is 73 kN/m, and pressure in the measuring cell 347 kPa. The predicted pressure is in good agreement with the measured 380 kPa. If instead of the assumed initial temperature -12 °C, a value of -14 °C is used, the predicted pressure would exceed the measured one by 5 %. The same effect results if only 10 % higher value is chosen for the empirical modulus of elasticity value, (1 GPa instead of 0.9 GPa in coefficient A in Eq. 5).

The effect of warm up time is insignificant, now less than 6 % when the warm up time is varied from 2 to 10 hours. The maximum thrust occurs with 9 hour warm up time. More important is time t_2 when the next cooling phase starts.

DISCUSSION

With the theoretical model it was possible to get a good fit with the measured data. Hence the model can be used to predict thermal ice pressures in other conditions. Highest possible thermal pressures will occur with an optimum warming rate for each ice and snow thickness. The ice also has to be over 24 hours in low temperature before warming up starts.

Ice thermal thrust is almost linearly dependent on the total temperature change. With thin ice the ice thickness has a significant effect, but with over 0.3 m thickness the daily temperature fluctuations are getting too fast to induce highest pressures, Fig. 5. The warm-up time with no snow isolation should be 9 hours already for 0.3 m thick ice. For a 0.5 m ice thickness over 20 hours are needed. As a maximum with 12 °C temperature rise a total thrust of 100 kN/m and a cell pressure of 370 kPa can be expected for a 0.5 m thick ice, Fig.6.

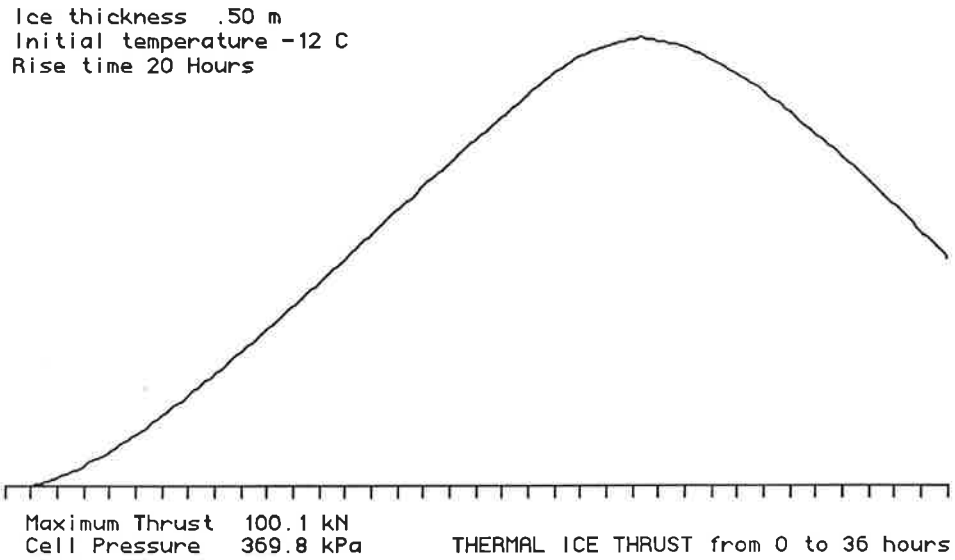

Figure 6. Thermal ice thrust, near optimum rise time.

The numerical model used rigid boundary conditions. The total ice thrust will be significantly reduced if the walls of the canal are resilient. With rigid concrete walls maximum thermal pressure can be expected.

The ice thickness across the canal was not even. At the center ice thickness was about two thirds of that near the walls. Hence the stresses at the center will be 50 % higher and creep relaxation about two times faster. Hence total ice thrust will be smaller in the case of uneven ice thickness profile. As the measured pressure in the cell was higher than the numerically predicted, it suggests, that a higher empirical modulus of elasticity value than 0.9 GPa, in coefficient A in Eq. 5,

should be used. A reliable application of theoretical model needs also to measure the ice thickness profile across the channel.

In the measurement data there was an evident decay of daily thermal pressure peaks. First natural explanation is that at the beginning of measurement period the air temperature change occurred in a much colder temperature, which reduced creep relaxation. Another is that due to daily fluctuations there will be residual stresses, which will counterbalance new thermal stresses. Third explanation is that the average air temperature was rising which made ice softer and stresses smaller. Another chance is that warm water in the canal had an access to pressure cell in the relatively thin ice, hereafter the better heat conduction in the steel may have caused a melt cavity around the pressure cell inducing the decrease of pressure readings.

The indirect thermal thrust measuring allows a simple instrumentation to be used but needs a theoretical model to relate pressure readings to total thrust. For the numerical model calibration, ice top surface temperature history and ice thickness profile across the channel have to be measured. Then it is possible to adjust the site specific parameters in the numerical model to reliably predict thermal ice thrust also in other design conditions that cannot be met during usually short measurement periods.

REFERENCES:

1. Chen A.: Ice pressure censor inclusion factors. Transactions of the ASME 82/Vol. 103, March 1981.

2. Cox G.: A preliminiary investigation on thermal ice pressures. Cold Regions Science and Technology 9 (1984), pp 221-229.

3. Fransson L: Thermal Ice Pressure on Structures in Ice Covered Waters. Doctoral thesis, Luleå University of Technology, 1988:67 D, Sweden.

4. Hamza H. and Blanchet D: A study of the creep effect upon the response of a pressure sensor embedded in an ice sheet. Cold Regions Science and Technology 9 (1984), pp. 97-107.

5. Keinänen H: Jääpainemittausjärjestelmä ja asennus, (Ice pressure measurement arrangements and installation, In Finnish), Report No 2/90, Helsinki University of Technology, Laboratory for Strength of Materials, Espoo, Finland.

6. Langleben M: On the thermal diffusivity of sea ice. Proc. IAHR symposium on Ice 1986, Vol-I, pp 569-578, University of Iowa, Iowa City, USA

7. Templeton J: Measurement of sea ice pressures. Proc. POAC-79, Vol-I, pp. 73-87. The Norwegian Institute of Technology, Trondheim 1979.

AUTOMATIC DESIGN OF STEEL FRAMES IN A CAD-SYSTEM

MARKKU HEINISUO, ARTO MÖTTÖNEN, TUULA PALONIEMI, PAAVO NEVALAINEN
Insinööritoimisto KPM-suunnittelu Oy
Yliopistonkatu 60 C, 33100 TAMPERE, FINLAND

ABSTRACT

The paper deals with one possibility to automatic design procedure for steel frames. The program generates the calculation model from the geometric model and checks the strength of the frame. The special 2.5 dimensional analysis is performed for the profiles of the frame and the plastic theory is used for the design of the joints. The effects of boundary conditions of joints for the final design is studied.

INTRODUCTION

There has been a software development project taking place at KPM-suunnittelu Oy during last two years. The project is financed partly by TEKES. The aim of the project is to develop the CAD-system for the design of steel sructures. This includes both the preparation of the drawings for manufacturers and the calculations concerning the strength of the sructure. The present paper deals with the 2.5-dimensional analyzing method for the steel frames. The CAD-system includes also the design of joints. Paper /1/ gives some general information concerning the CAD-system developed.

CALCULATION MODEL

First, the designer creates the geometry of a structure in the plane. The designer chooses profiles and connections for the initial calculations. The designer can change profiles or connections or some initial data afterwards to obtain better result. The plane geometry is built into the system by using the special recursive algorithm which makes the system very flexible. The same algorithm controls both the geometry of the frame and the geometry of the joints. E.g. cutting lists of the profiles can be plotted from this geometrical model.

The program generates automatically an analysis model for the linear plane frame program from a geometrical model. The program generates four finite elements between structural joints so the error in the linear buckling analysis is small enough for design purposes when considering the column type elements. There are no flexible joints generated automatically in the program to the model, yet. The designer can create flexible joints by introducing small springs to the joints if he thinks it is necessary. The program generates automatically also the calculation models of the joints from the geometrical model. The joints are modelled by

using small eccentricity elements which cause discontinuities to bending moments (Fig. 1). Any systematic procedure to create these small elements could not be found in the literature so these elements for specific joints must be considered case by case.

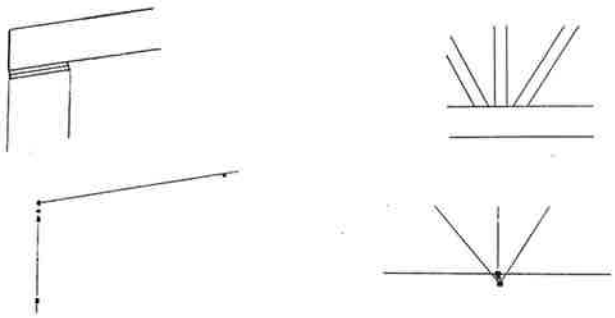

Figure 1. Eccentricity elements of joints

Next the designer gives loadings to the frame. Loads can be either forces or displacements. The continuous loads can be given for groups of elements. After the loads and support conditions are given the program calculates nodal displacements by using the usual beam elements of six degrees of freedoms. Firstly, the linear elastic analysis is done. The KPM-FRAME-program is used for this purpose and the normal output of the frame program is then available. The designer can draw the displaced frame and e.g. shear force diagrams of the frame for the different loading cases. Next step in the program is either to check the strength of the joints or the strength of the profiles chosen by the designer.

DESIGN OF PROFILES

The program checks the strength of profiles in 3-5 points per element. The Finnish code B7 /2/ is used. The design philosophy of that code is near the ideas of the forthcoming EUROCODE. The program checks capacities against the axial forces, shear forces and bending moments and the von Mises strengths of the elements following the rules in the codes. The cross-sectional properties of the profile are calculated according to elastic or plastic theory the latter occurring occassionally when allowed by Finnish codes. Load factors, material strength factors and material strenghts can be given following local codes. The designer gets the information of the used capacities of the profiles in the special report seen in Fig. 2.

Next the stability of the plane frame system is checked by calculating the critical elastic collapse load factor n of the structure. This procedure gives the eigenvalue for the plane frame buckling and this eigenvalue is used for each beam- or column-type elements when designing these elements ie. when checking the state of the stress according to the codes. The critical axial load, the Euler load, is the eigenvalue times the axial load in the most

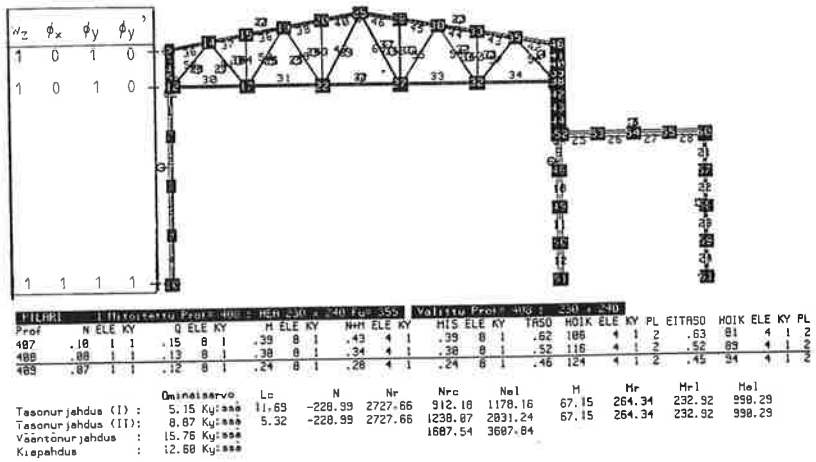

Prof	N	ELE	KY	Q	ELE	KY	M	ELE	KY	NHM	ELE	KY	MIS	ELE	KY	TASO	HOIK	ELE	KY	PL	EITASO	HOIK	ELE	KY	PL
487	.10	1	1	.15	8	1	.39	8	1	.43	4	1	.39	8	1	.62	106	4	1	2	.63	81	4	1	2
488	.08	1	1	.13	8	1	.38	8	1	.34	4	1	.38	8	1	.52	116	4	1	2	.52	89	4	1	2
489	.07	1	1	.12	8	1	.24	8	1	.28	4	1	.24	8	1	.46	124	4	1	2	.45	94	4	1	2

	Ominaisarvo	Lc	N	Nr	Nrc	Nel	M	Mr	Mrl	Mel
Tasonurjahdus (I) :	5.15 Kyllää	11.69	-228.99	2727.66	912.18	1178.16	67.15	264.34	232.92	998.29
Tasonurjahdus (II):	8.87 Kyllää	5.32	-228.99	2727.66	1238.87	2031.24	67.15	264.34	232.92	998.29
Väantonurjahdus :	15.76 Kyllää				1687.54	3687.84				
Kiepahdus :	12.68 Kyllää									

Figure 2. Profile report

critical cross-section of the element. The program creates automatically the stiffness matrix and the geometrical matrix of the elastic plane system for the linear elastic buckling analysis. The designer chooses the designing eigenvalue for the specific element. The system proposed by Yang et al /3/ uses automatically the lowest eigenvalue for the design. It can be seen from Fig. 3 that this is not necessarily the designing eigenvalue e.g. for the columns of the frame. There are also special elements in the frame whose buckling length can be estimated beforehand and these are programmed to the system in order to minimize the calculation time. These are e.g. the bracings of the trusses for which the buckling length = 0.9 times the system length is used.

After that program generates the 3-dimensional calculation model for beam- and column-type elements of the structure. These elements are proposed by the designer. This 3-dimensional analysis is done only for elements with open cross-section. The elements with closed cross-section do not usually need any torsional or lateral buckling analysis. The program uses the beam elements of 14 degrees of freedoms /4/ for this 3-dimensional analysis. The splines for axial and lateral displacements are the normal polynomials and the splines for torsional displacements are the exact solutions of

Vlasov's theory; i.e. hyperbolic functions. In this early stage of the project these 3-dimensional elements are used for the calculation of elastic collapse loads for out of plane buckling, torsional buckling and lateral buckling. After that the strength tests demanded by codes can be done.

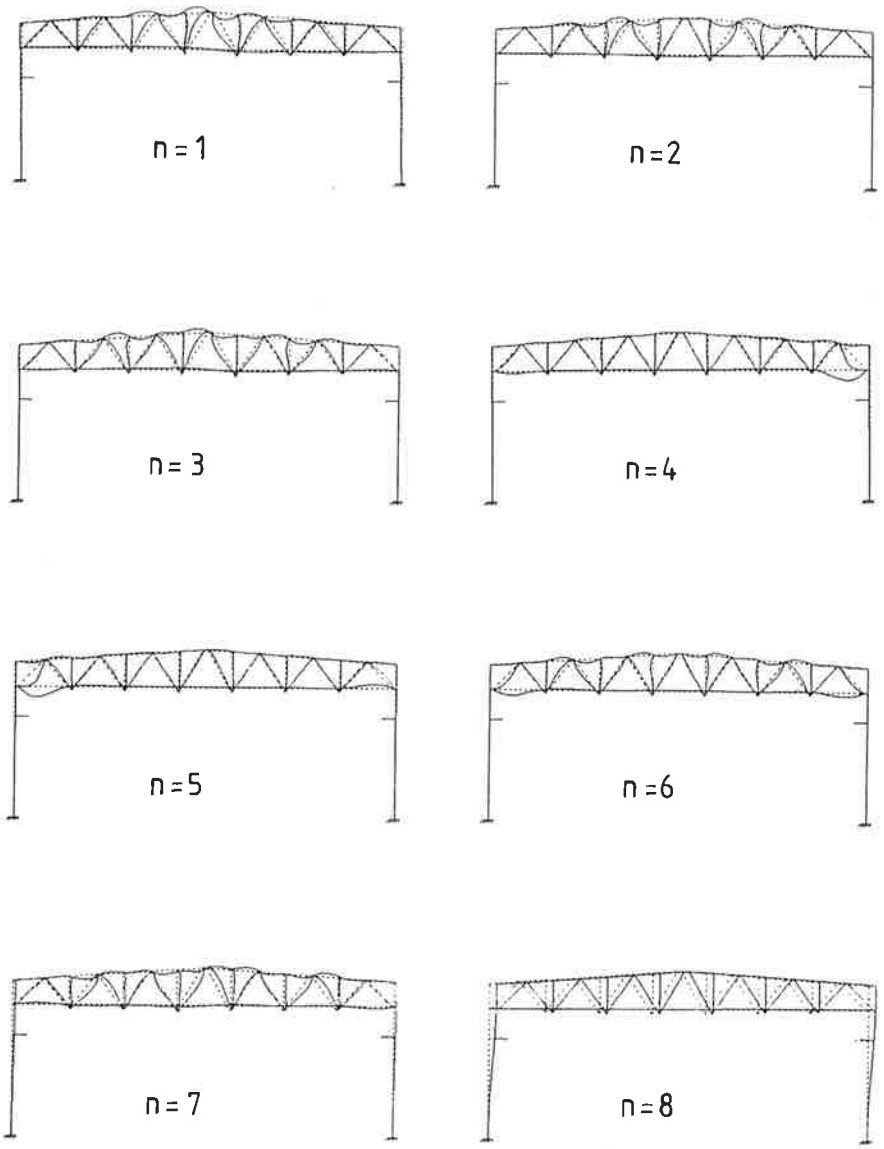

Figure 3. Buckling modes of a frame

It is seen that this 3-dimensional analysis needs four extra degrees of freedoms per node compared to the plane analysis. The three dofs are the same as in the plane analysis and the loading is transferred by the program to these nodes as displacement loads. The two of these extra dofs caused some difficulties in the project because not much information concerning them was found in the literature. These two dofs are the torsional and warping displacements of the cross-section. The information designer needs are the boundary conditions in the joints of steel frames when using this kind of 3-dimensional finite element for design purposes.

The first diploma thesis done within this project dealt with this problem /5/. Some results concerning the effect of torsion and warping in the joints for the critical loads and for the final design values of steel frames were found by doing some parametric studies for the joints which are important in every day design routines. The crane beam or the bracing of the wall (Fig. 4) was modelled by using the rotational spring element and the usual slaving technique for the column.

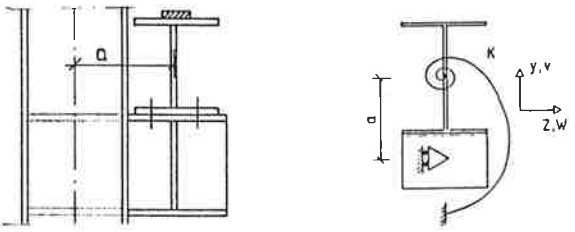

Figure 4. Modelling of a joint

The torsional and lateral buckling loads were calculated by changing the stiffness of the rotational spring and the location of the lateral support. These critical loads were compared to the critical loads of the column supported by the infinitely stiff rotational support at the same place as the rotational spring (Fig. 5). As a conclusion it is said that the crane beam can be considered as the support which can prevent the torsional and lateral displacements if the cross-sectional properties of the crane beam are about the same as those of the column. Moreover, it was found that the warping displacement did not have much effect to the design of the column.

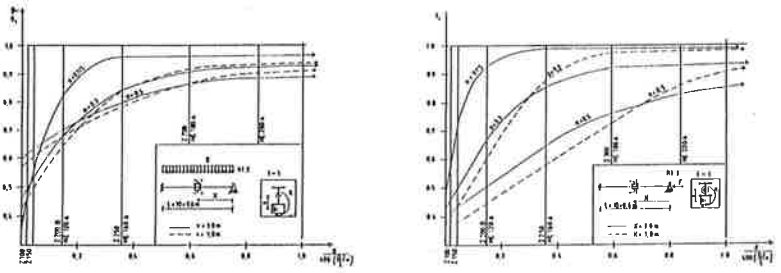

Figure 5. Critical loads of a column

Some calculations were also done concerning the ground conditions under the column. The parametric studies were based on the simple rotational spring model and the ground was modelled by using the deformation model proposed by Cederfelt /6/. It was found that the most of the deformation takes place under the concrete footing, not much deformation takes place in the joint between the concrete footing and the steel column. Moreover it was found that stiffening the ground under the footing must be payed special attention if the joint is modelled as rigid one. There can be found some more information on this subject in Ref. /5/.

DESIGN OF JOINTS

The second diploma thesis of the project deals with the design of joints. The joints are designed following the plasticity theory by using forces calculated by the forementioned linear plane frame program. The design of the joints is almost the same than that proposed by the EUROCODE. That is so because there are more detailed rules given for the design of joints than in the Finnish codes of practise. The program can currently design welded joints between tubular structures, bolted joints between columns and footings and between columns and beams. The extra load factor (n+1)/n is used for the joints which cause second order moments for the frame and if the joints may have some deformation which is not taken into account in calculations.

The joints between tubular structures are designed following the book of Wardenier /7/. The program performs checks of dimensions of the joint and the capacity of the joint. Figure 6 presents the typical report of the joint design of the tubular structure. The program checks the gometrical properties of the joint and the punching shearand the effective width criteria and cord wall buckling and cord face failure by yielding as seen in the figure.

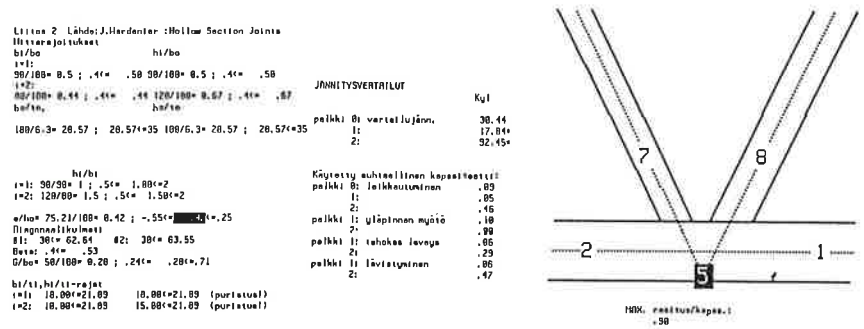

Figure 6. RHS-joint report

When analysing the bolted joints the general plasticity check of the end plate according to Zoetemeijer /8/ is done by the program. Moreover, the program checks if there is enough space between bolts and the profile or the edge of the profile. These parts of the program are made to be very general so they can be used when designing many kinds of joints. The four plastic mechanisms seen in Fig. 7 including the prying effect are always checked for the

bolted joint according to Ref. /8/. These mechanisms can occur in the end plate of the joint or in the flange of the column etc. Figure 8 presents the examples of the cases where these mechanisms are used. The Ref. /9/ is also used for the design of the column footings and the parts of the Ref. /10/ are used for the design of column-beam connections. Figure 9 presents the typical report of the design of the bolted connection.

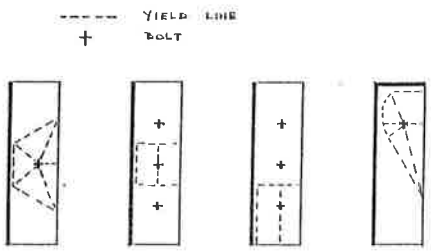

Figure 7. Plastic mechanisms

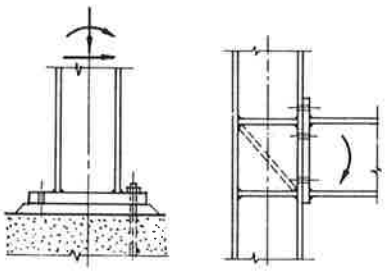

Figure 8. Bolted connections

Liitos 1 Lähde:SBI: Pelarfot,1987

PULTTIMITAT
pulttien minimietäisyys reunasta:
1.5*D=36<= 40.00
pulttien minimietäisyys profiilista:
1.6*(D+8mm)=51.2<= 45.00
pienin reikäväli:
3.0*D=72<=100.00

	Kyl	
kosketusmatka [yp0,yp1]		
yp0=	-97.35	mm
yp1=	-240.00	mm
Kuormitusaaure:		
Puristusvoima:	-15.60	kN
Tukimomentti:	7.00	kNm
Betoni jännitys:	0.68	N/mm^2
Ruuvivoima:		
1	21.67	kN
4	21.67	kN
Ruuvi jännitys:		
1	90.39	N/mm^2
4	90.39	N/mm^2
Ruuvin rajoittava mekanismi:		
1	P+L2	
4	P+L2	
Käytetty suhteellinen kapasiteetti:		
Täytevalun puristus:	.33	(Pelarfot,1987,Stålbyggnadsinstitutet)
Ruuvien voima/vetolujuus:	.27	(RIL 173-1988)
Pohjalevyn plastisuus:	.30	(...balkkolom verbindingen,1983,Zoetemeijer)
Pohjalevyn taivutus:	.00	(Teräsrak.suunnittelu,1989)
Hitsisaumakapasiteetti 2	.43	

Max rasitus/kapasit.
.00<=.83

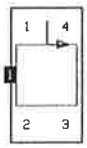

Figure 9. End plate joint report

1. Heinisuo M., Möttönen A., Paloniemi T., Nevalainen P., KPM-TERÄS-CAD tuotekehitysprojekti, Julkaisematon käsikirjoitus

2. Teräsrakenteet. Rajatilamitoitusohjeet 1988: mitoitustaulukot ja käyrästöt, RakMK:n ohjeet B7, RIL, Helsinki 1988

3. Yang Y-B., Kuo C-C., Automatic Design System for Steel Frames, CIVIL-COMP 89, London 1989

4. Annila A., Avoimen ohutseinämäisen sauvan stabiiliuden määrittäminen elementtimenetelmällä, Diplomityö, TTKK, Tampere, 1988

5. Paloniemi T., Teräspilarin liitosten kolmiulotteisen käyttäytymisen vaikutus mitoitukseen, Diplomityö, TTKK, Tampere, 1990

6. Cederfeldt L., Hallbygnader, Publikation 53, Stålbyggnadsinstitutet, Stockholm, 1977

7. Wardenier J. Hollow Section Joints, Delft University Press, 1982

8. Zoetemeijer Ir. P., Samenvatting van het onderzoek op geboute balkkolom verbimdigen, Technische Hogeschool Delft, 1983

9. Pelarfot, Stålbyggnadsintitutet, 1987

10. Rissanen J. Pulttiliitosten lujuusanalyysi sovellettuna CAD-järjestelmään, Diplomityö, TTKK, Tampere, 1986

STRESSES AND DISPLACEMENTS IN A REINFORCED CONCRETE GROUND SLAB DUE TO THE FRICTION BENEATH THE SLAB

MIKKO KILPELÄINEN
Department of Civil Engineering
University of Oulu
P.O. BOX 191, SF-90101 OULU, FINLAND

ABSTRACT

The shrinkage of a reinforced concrete ground slab produces friction between the slab and its subbase. Friction forces act horizontally on the slab.

The article deals with the stresses and the displacements in a slab caused by those forces. The vertical loading of the slab is supposed to be uniformly distributed and therefore the friction forces act rotationsymmetrically.

First the loading and the stresses and the displacements of a circular slab are examined in a polar coordinate system. Then the loading and stresses and displacements of a rectangular slab are examined in a rectangular coordinate system based on different simplifying procedures.

INTRODUCTION

The shrinkage of a reinforced concrete ground slab is directed towards the shrinkage centre of the slab (point 0, Fig. 1a). This movement produces friction forces between the slab and its subbase. Those forces are directed oppositely with the shrinkage movement (Fig. 1b). The forces give rise to tension stresses in the slab, because of which the cracking of the slab may occur.

The magnitude of the friction force H is depending on the horizontal movement of the slab and on the pressure and the friction coefficient between the slab and its subbase.

For the sake of simplicity the friction is mostly supposed to be totally developed, i.e. independent on the magnitude of the movement. If the slab thickness is constant and if the loading is uniformly distributed, the friction force H can be obtained from the equation

$$H=\mu \cdot p=\mu \cdot (\gamma_c \cdot h+q) \ , \qquad (1)$$

where μ is the friction coefficient, p the pressure of the subbase [MN/m^2], γ_c is the volumetric weight of concrete [MN/m^3], h the thickness of the slab [m] and q the uniformly distributed load [MN/m^2].

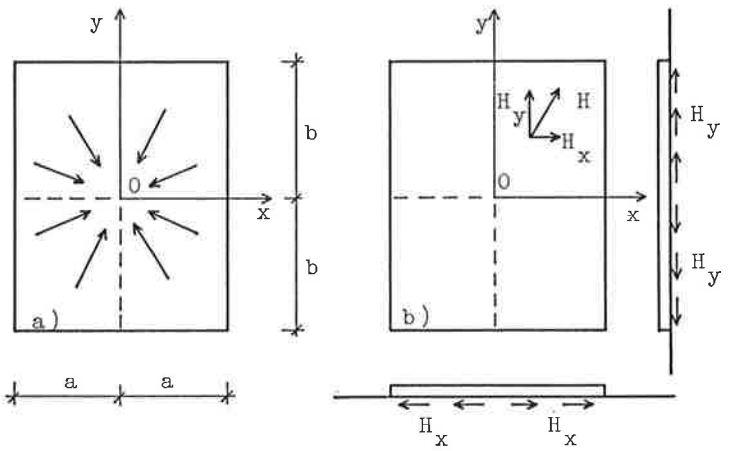

Figure 1. The shrinkage movement a) and the friction forces b) of a concrete ground slab.

This paper deals with circular and rectangular slabs having constant slab thickness. They are supposed to rest on an even subbase and to have constant friction coefficient μ. The loading of the slab is supposed to be uniformly distributed, i.e. q=constant, because of which the friction force H is uniformly distributed as well. In this kind of ideal case, the shrinkage centre is located at the centre of the slab.

CIRCULAR SLAB

Let's examine a circular slab with radius R (Fig. 2a) in a polar coordinate system, the origin of which is located at the centre of the slab. Let's take a differential slab element for the closer examination (Fig. 2b). The stresses acting on the element are shown in Fig. 2b as well.

As a consequence of the equilibrium of the forces acting on the element we obtain (h=constant)

$$\frac{d\sigma_r}{dr}+\frac{\sigma_r-\sigma_\varphi}{r}+\frac{H}{h}=0 \qquad (2)$$

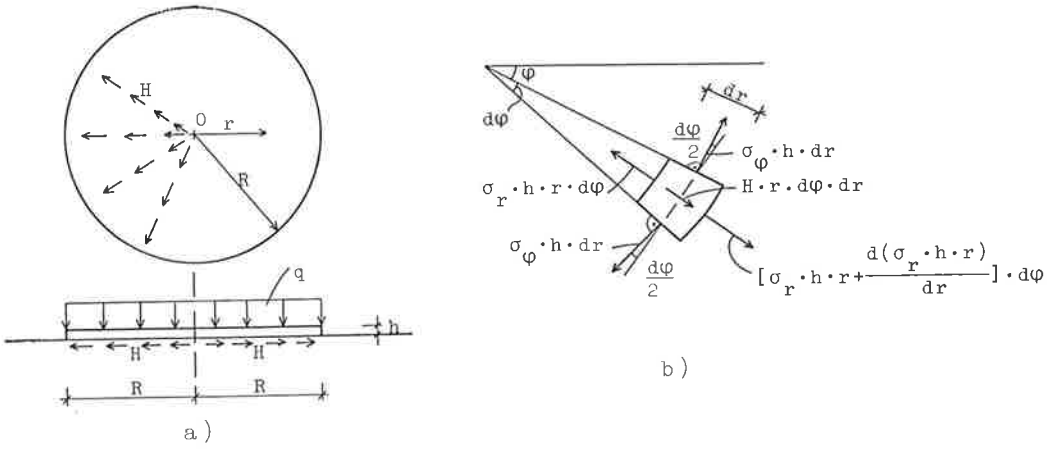

Figure 2. A circular concrete ground slab a) and a slab element b).

According to Hooke's law we obtain

$$\sigma_r = \frac{E}{1-\nu^2} \cdot (\varepsilon_r + \nu \cdot \varepsilon_\varphi) \ , \qquad \sigma_\varphi = \frac{E}{1-\nu^2} \cdot (\varepsilon_\varphi + \nu \cdot \varepsilon_r) \ , \tag{3a,b}$$

where E is the modulus of the elasticity of the slab [MN/m^2], ν the Poisson's ratio and ε_r and ε_φ are the radial and the tangential strain of the slab.

Using the radial displacement u we can write

$$\varepsilon_r = \frac{du}{dr} \ , \qquad \varepsilon_\varphi = \frac{u}{r} \tag{4a,b}$$

Substituting the equations (4) and (3) to the equation (2) we obtain

$$\frac{d}{dr}\left[\frac{1}{r} \cdot \frac{d(r \cdot u)}{dr}\right] + \frac{(1-\nu^2) \cdot H}{E \cdot h} = 0 \tag{5}$$

By integrating the equation (5) twice we obtain

$$u = -\frac{(1-\nu^2) \cdot H}{3 \cdot E \cdot h} \cdot r^2 + \frac{C_1}{2} \cdot r + \frac{C_2}{r} \tag{6}$$

Using the equilibrium of the forces, which act on the slab element, we obtain

$$\frac{d\sigma_x}{dx}+\frac{d\tau_{yx}}{dy}+\frac{H_x}{h}=0\ , \qquad \frac{d\sigma_y}{dy}+\frac{d\tau_{xy}}{dx}+\frac{H_y}{h}=0 \tag{11a,b}$$

If we assume, that $\tau_{xy}=\tau_{yx}$=constant, we obtain σ_x and σ_y from the equations

$$\sigma_x=\frac{H}{h}\cdot\int_x^a\frac{x}{\sqrt{x^2+y^2}}\cdot dx\ , \qquad \sigma_y=\frac{H}{h}\cdot\int_y^b\frac{y}{\sqrt{x^2+y^2}}\cdot dy \tag{12a,b}$$

After integration the equations (12) reduce to

$$\sigma_x=\frac{H}{h}\cdot\left(\sqrt{a^2+y^2}-\sqrt{x^2+y^2}\right)\ , \qquad \sigma_y=\frac{H}{h}\cdot\left(\sqrt{x^2+b^2}-\sqrt{x^2+y^2}\right) \tag{13a,b}$$

Since

$$\frac{du}{dx}=\varepsilon_x=\frac{1}{E}\cdot(\sigma_x-\nu\cdot\sigma_y)\ , \qquad \frac{dv}{dy}=\varepsilon_y=\frac{1}{E}\cdot(\sigma_y-\nu\cdot\sigma_x) \tag{14a,b}$$

we obtain the equations

$$u=\frac{1}{E}\cdot\int_0^x(\sigma_x-\nu\cdot\sigma_y)dx\ , \qquad v=\frac{1}{E}\cdot\int_0^y(\sigma_y-\nu\cdot\sigma_x)dy \tag{15a,b}$$

for the displacements u and v. After integration they can be reduced to the form

$$u=\frac{H}{E\cdot h}\cdot\left[x\cdot\sqrt{a^2+y^2}-(1-\nu)\cdot\left(\frac{x}{2}\cdot\sqrt{x^2+y^2}+\frac{y^2}{2}\cdot\ln\frac{x+\sqrt{x^2+y^2}}{y}\right)\right.$$

$$\left.-\nu\cdot\left(\frac{x}{2}\cdot\sqrt{x^2+b^2}+\frac{b^2}{2}\cdot\ln\frac{x+\sqrt{x^2+b^2}}{b}\right)\right] \tag{16a}$$

$$v=\frac{H}{E\cdot h}\cdot\left[y\cdot\sqrt{b^2+x^2}-(1-\nu)\cdot\left(\frac{y}{2}\cdot\sqrt{x^2+y^2}+\frac{x^2}{2}\cdot\ln\frac{y+\sqrt{x^2+y^2}}{x}\right)\right.$$

$$\left.-\nu\cdot\left(\frac{y}{2}\cdot\sqrt{y^2+a^2}-\frac{a^2}{2}\cdot\ln\frac{y+\sqrt{y^2+a^2}}{a}\right)\right] \tag{16b}$$

The stresses σ_x and σ_y acting at the coordinate axes are presented in Fig. 5. They have been determined from the equations (13). We can recognize, that the stresses have their maximum values in the origin, i.e. at the centre of the slab, where

$$\sigma_{xmax} = \frac{H \cdot a}{h} \quad , \quad \sigma_{ymax} = \frac{H \cdot b}{h} \qquad (17a,b)$$

The corresponding stresses determined by the finite element method using quadratic plane stress elements are shown in Fig. 5 as well. FEMP- program /1/ has been used for computing the diagrams.

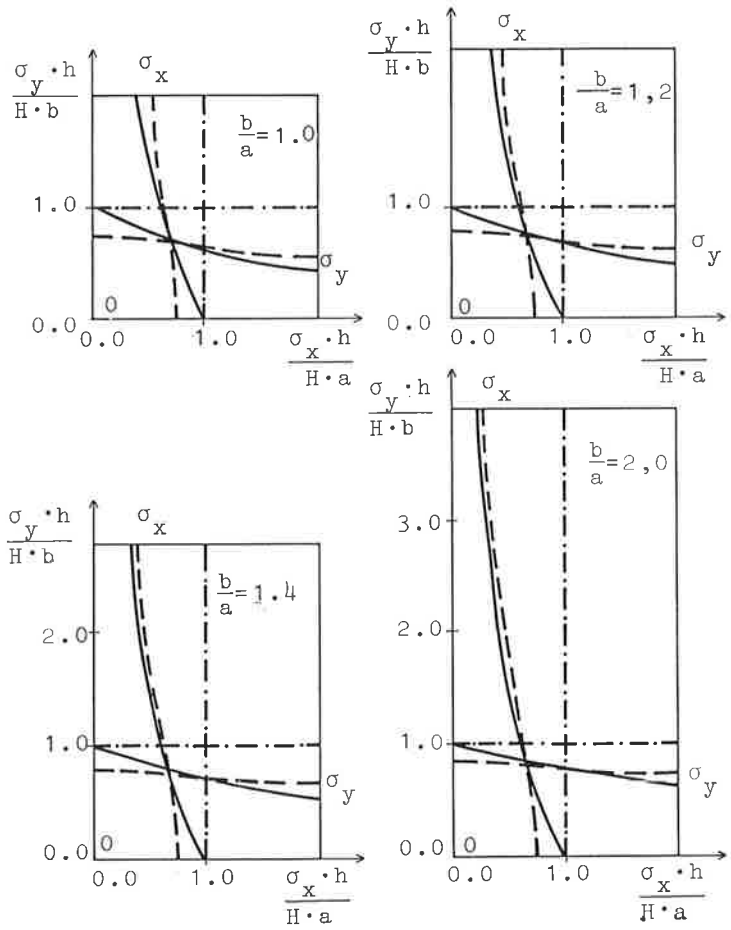

Figure 5. The stresses σ_x and σ_y, which act at the coordinate axes of the slab, according to the equations (13) (——), to the equations (18) (–·–·–) and obtained by the finite element method (- - -). Poisson's ratio ν=0,15.

The tension stresses σ_x and σ_y are often calculated in practice from the equations

$$\sigma_x = \frac{H}{h} \cdot (a-x) \quad , \quad \sigma_y = \frac{H}{h} \cdot (b-y) \tag{18a,b}$$

These stresses have their maximum values at the coordinate axes of the slab, where they can be computed from the equations

$$\sigma_{xmax} = \frac{H \cdot a}{h} \quad , \quad \sigma_{ymax} = \frac{H \cdot b}{h} \tag{19a,b}$$

The equations (19) are identical with the equations (17). The diagrams of the stresses obtained from the equations (18) are presented in Fig. 5. as well.

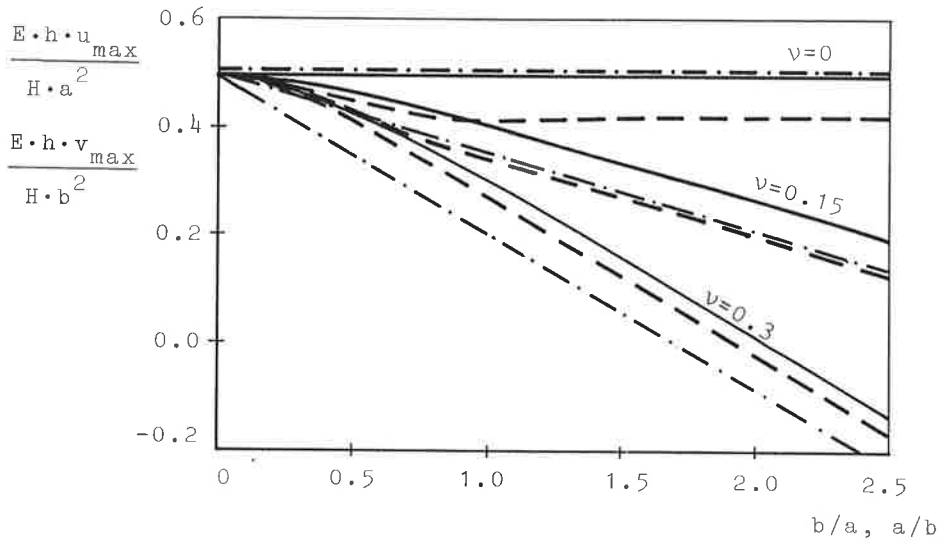

Figure 6. The displacements u_{max} and v_{max} of the midpoints of the edges of a rectangular slab, according to the equations (20) (——), to the equations (21) (–·–·–) and obtained by the finite element method (- - -).

The displacement u has probably its maximum value at the midpoint of the edge of a slab (x=a, y=0) and correspondingly v its maximum value at the midpoint of the other edge (x=0, y=b). Using the equations (16) we can write for the maximum values of those displacements the following dimensionless equations:

$$u_{max} = \frac{H \cdot a^2}{2 \cdot E \cdot h} \cdot \left[1+\nu-\nu \cdot \left(\sqrt{1+\beta^2} + \beta^2 \cdot \ln \frac{1+\sqrt{1+\beta^2}}{\beta} \right) \right] , \tag{20a}$$

$$v_{max} = \frac{H \cdot b^2}{2 \cdot E \cdot h} \cdot \left[1+\nu-\nu \cdot \left(\sqrt{\alpha^2+1} + \alpha^2 \cdot \ln \frac{1+\sqrt{\alpha^2+1}}{\alpha} \right) \right] , \qquad (20b)$$

when α=a/b and β=b/a.

On the other hand, using the equations (18) and (14) we can write for the displacements of the midpoints of the slab edges the following expressions:

$$u_{max} = \int_0^a \varepsilon_x \cdot dx = \frac{H \cdot a^2}{E \cdot h} \cdot \left(\frac{1}{2} - \nu \cdot \frac{b}{a} \right), \qquad (21a)$$

$$v_{max} = \int_0^b \varepsilon_y \cdot dy = \frac{H \cdot b^2}{E \cdot h} \cdot \left(\frac{1}{2} - \nu \cdot \frac{a}{b} \right) \qquad (21b)$$

The diagrams of maximum displacements u_{max} and v_{max} are presented in Fig. 6 as functions of the side ratio and of Poisson's ratio, obtained from the equations (20) and (21). The diagrams, which are computed with the finite element method (FEMP- program) are presented in Fig. 6 correspondingly.

SUMMARY

The equations of the horizontal stresses and displacements acting on a circular slab can be written in an ideal case in a closed form. For the rectangular slabs the stresses and displacements must be calculated with the approximate methods.

From three approximate methods investigated in this study the finite element method gives most accurate and smallest values for the stresses and displacements. On the other hand some generally used formulas for manual calculations give most unaccurate and biggest values for them. When we suppose the shear stress of a slab to be constant the stresses and displacements of a slab can be calculated manually with a reasonable accuracy.

The results of this investigation can be applied to the structural analysis of reinforced concrete ground slabs. The nonlinearity of the σ-ε- curve of the concrete, the creep of the concrete, the cracking of the slab and the uneven distribution of the friction cause inaccuracy to the results. The influence of those factors needs further investigations.

REFERENCES

1. Nilsson L. -Oldenburg M., FEMP. An interactive, graphic finite element program for small and large computer systems. Luleå University, Technical report 1983:07T. Luleå, 1983.

2. Kilpeläinen Mikko, Design and analysis of a reinforced concrete ground slab., University of Oulu, Laboratory of structural engineering, publiation 30. Oulu, 1990, 118 pp. (in Finnish).

STABILITY OF ARCHED ROOF MADE OF PROFILED STEEL SHEETING

JUHA HYVÄRINEN and PENTTI MÄKELÄINEN
Department of Structural Engineering
Helsinki University of Technology
Rakentajanaukio 4, SF-02150 ESPOO, FINLAND

ABSTRACT

An investigation of the structural behaviour and design criteria of an arched roof structural system is described. Double shell arch system constructed by using corrugated steel sheets bent to a form of two-layered curved roof vault is specially investigated by applying specific structural model developed for the system. In this model consisting of a plane bar system, transverse hat profiles connecting two curved shell layers together are stated as radial connection bars and stiffness characteristics for these bars simulating structural behaviour of transverse hat profiles are experimentally determined by shear tests. Analyses and calculations made by applying the double shell arch model are based both on geometrically linear and non-linear behaviour of the arch. Stability of the arched roof is also studied in the analyses by determining critical loads both for global buckling of the roof vault and for local buckling of the curved shell layer between transverse hat profiles.

INTRODUCTION

Free span of a steel roof deck can be considerably extended by using an arched roof instead of flat decking with profiled sheetings. These self-supported arched roof-vaults are made of trapezoidally corrugated steel sheetings bent during cold-forming process in form of an arch,

usually having geometrical proportion of L (span) = R (radius). An arched roof structure is especially effective in form of a double-arch system i.e. a two-layered arch of profiled steel sheetings connected with transverse members e.g. with hat profiles. This new type of arched roof system was first developed and patented some three years ago by Austrian company ZEMAN & Co (GmbH) in Vienna. In applications of this arched roof structure, a steel tie-bar connecting arch-bases in span is usually added to the structural system. In Finland this arched roof system was first adopted and applied by company PAAVO RANNILA Oy.

Structural behaviour of arched roof system described above is studied in this research for finding out and introducing design criteria for arch in respect to design specifications and recommendations. This study is made by using specific structural model for two-layered arch with profiled sheetings connected by transverse hat profiles. For this model consisting of a plane bar system, stiffness characteristics of the bars simulating hat profiles between two arched sheetings are experimentally determined.

STRUCTURAL MODEL

Plane Frame Model of the Arch

In the structural model used for analysis and calculations, the original two-layered arch (Fig. 1a) is replaced by a plane frame as illustrated in Fig. 1b. In this frame, the curved parts of profiled steel sheetings between transverse connecting members i.e. hat profiles (spacing 1.2 - 1.5 m) are replaced by straight beam elements. This means that in dimensioning the arch, the original curvature of the arch between hat profiles is to be taken into account as an eccentricity causing extra bending moment to the beam element.

Hat profiles connecting the two profiled steel sheetings are replaced in the model by short bar elements and these bars are assumed to be clamped to the lower and pinned to the upper profiled steel sheeting. Values of the bending and shear stiffness characteristics for these bar elements are experimentally determined.

The so called system lines of the structural model (Fig. 1c) are thus defined by gravity center axes (G.C.A.) of hat profiles and by neutral axes (N.A.) of profiled steel sheetings determined by applying effective cross-sectional area for the compression side of the profiled cross-section.

FIGURE 1.

Structural model of arch.

a) Two-layered arch with profiled sheetings and transverse hat profiles.

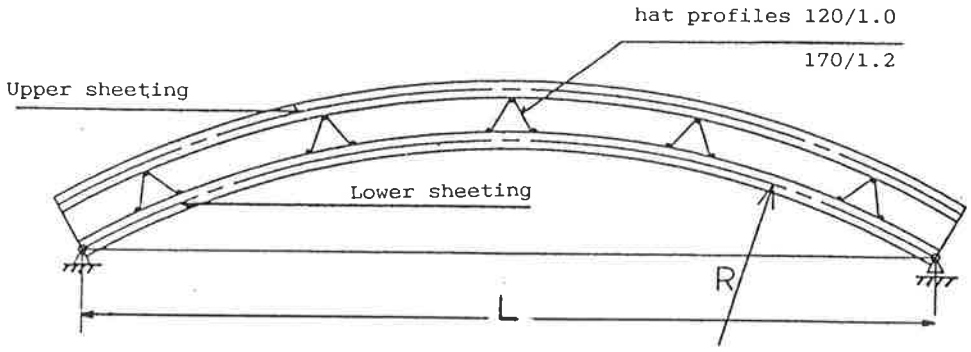

b) Plane frame model of arch.

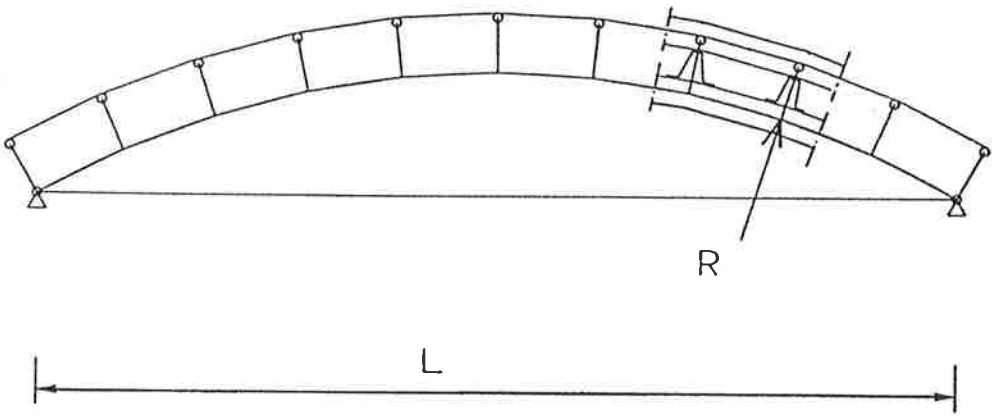

c) System lines of arch model.

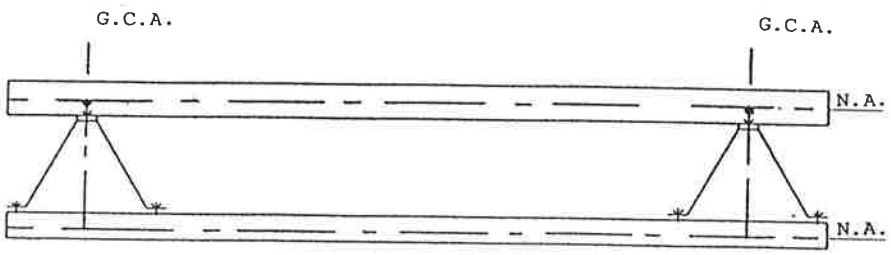

As cross-sectional forces and moments of an arch usually are also dependent upon deflections caused by external loading then for analysing this geometrically non-linear behaviour, calculation methods used are to be based on the second order theory. In this study, both linear and non-linear behaviour of the arch is analysed by using the plane frame model described above.

Cross-sectional and Stiffness Properties for the Model

Longitudinal bars. For calculating bending moment, normal force, and shear force (M,N,V) in an arch cross-section, bending stiffness (EI) and axial stiffness (EA) is to be known in each cross-section of the arch. Because of the local buckling phenomenon on compression side of the cross-section, stiffnesses EI and EA are dependent upon loading state. Thus for determining these stiffnesses, effective cross-sectional areas are to be applied for compressed parts of the profiled sections.

Effective cross-sectional areas can be determined by reducing certain parts (widths) of the profiled section on compression side. Furthermore, in case of edge stiffeners and intermediate flange and web stiffeners reduction for effective area is also to be applied to the sheet thickness (t) on these parts of the compressed cross-section. In this study, effective cross-sectional areas are calculated according to the Finnish code /1/. This corresponds mainly to the Swedish code /2/ and to the German code DIN 18807 /3/.

In case of the two-layered arch made of profiled steel sheetings, for calculating exactly the effective cross-sectional area A_e and the effective moment of inertia I_e of section an iterative procedure is to be applied. In practice, however, values for A_e and I_e can be taken in calculations with an adequate accuracy as minimum values of A and I determined from all possible cases i.e. A_e = minA and I_e = minI. These values are then applied in each cross-section of the arch. Table 1 compares the effective values of A and I as minA and minI with the corresponding gross-values maxA and maxI for profiled sheetings of the arch used in this study.

Transverse bars. Experimental investigation carried out in this study showed that as basic stiffness value EI_0 of hat profile can be taken secant stiffness EI_0-value corresponding load level two third of ultimate load (P_M) i.e. $I_s = I_0$ if $Q \leq 2P_M/3$ (Q = shear force in hat profile). Transverse bending stiffness values EI_0 determined by tests for hat profiles RA-120/1.0 and RA-170/1.2 are listed in Table 2 together with maximum allowable values $Q_{allow.}$ of shear forces caused by nominal loading in validity ranges of I_0-values. For bar elements in

structural model, bending stiffness values EI_H can then be determined with I_0-values by using following formula

$$I_H = (L_H/H)^3 I_0 \qquad (1)$$

where L_H represents theoretical length of bar elements in structural model (distance between neutral axes of sheetings) and H height of hat profiles (120 mm or 170 mm). In cases of variable sheeting thicknesses ($t \neq 0.9$ mm) I_0- and $Q_{allow.}$-values are to be reduced.

TABLE 1.

Minimum effective cross-sectional values A_e and I_e for profiled sheeting sections compared with corresponding gross-sectional values.

Sheeting	t mm	$\frac{I_{min}}{I_{max}}$	$\frac{A_{min}}{A_{max}}$
45/0.7	0.63	0.82	0.82
45/0.9	0.82	0.89	0.88
45/1.1	1.01	0.94	0.92
120/0.8	0.67	0.91	0.75
120/1.0	0.85	0.94	0.82
120/1.2	1.03	0.97	0.88

TABLE 2.

I_0-values for hat profiles 120/1.0 and 170/1.2 with allowable shear force values.

Hat profile	Lower sheet	$I_0 \times 10^{-9}$ m^4/m	$Q_{allow.}$ kN/m
120/1.0	45/0.9	2.73	7
	120/0.9	1.78	7
170/1.2	45/0.9	10.57	12
	120/0.9	8.23	12

STRUCTURAL DESIGN OF ARCH

In basic design of two-layered arch with profiled sheetings connected with hat profiles, combined compression (N) and bending (M) is to be separetaly checked both for upper and lower sheeting section under maximum effect of combined loads. After cross-sectional forces (M,N,V) are determined by usual linear analysis, local and global buckling of arch can be taken into account by following interaction formula

$$(1+0.5\bar{\lambda}_{ki}(1-N_d/N_{Rci}))N_d/N_{Rci} + (1+0.5\bar{\lambda}_{kg}(1-N_d/N_{Rcg}))N_d/N_{Rcg} + (M_d+N_d e/2)/M_R \leq 1 \qquad (2)$$

where N_d = design value of normal force

N_{Rcg} = global buckling force of arch baced on ECCS buckling curve "c"

N_{Rci} = local buckling force of arch-layer between hat profiles based on ECCS buckling curve "c"

M_d = design value of bending moment

$M_R = f_y W_e$ = bending capacity of arch section

e = eccentricity i.e. distance between original curved axis of sheeting and straight axis of sructural model

$\bar{\lambda}_{kg}$ = modified slenderness of arch based on combined cross-section of sheetings

$\bar{\lambda}_{ki}$ = modified slenderness of arch-layer between hat profiles based on sheeting section.

In case when cross-sectional forces (M,N,V) are determined by using non-linear (second-order) theory, formula (2) is reducing to form

$$(1+0.5\bar{\lambda}_{ki}(1-N_d/N_{Rci}))N_d/N_{Rci} + (M_d+N_d e/2)/M_R \leq 1 \qquad (3)$$

In design formulae (2) and (3), for effective cross-sectional area A_e and effective moment of inertia I_e minimum possible values of A and I (minA and minI) are used and also for effective elastic section modulus W_e corresponding minimum value of W in case of pure bending.

In determining values for N_{Rcg} in formula (2) or (3), buckling shape of arch is to be known. In case of a circular arch, critical buckling mode is asymmetric and thus effective buckling length can be determined with multiplying half arch length by a trigonometric factor dependent upon central angle of arch. In case of arch geometry of R = L, this factor is equal to 1.02.

For determining global buckling force N_{Rcg} of two-layered arch, ideal slenderness λ_{id} of double-arch is to be determined for a plane

frame system when interaction between two layers connected by bar elements is to be taken into account. This ideal slenderness can be determined by following formula

$$\lambda_{id} = (\lambda^2 + n\, a\, \lambda_i^2)^{1/2} \qquad (4)$$

where λ = slenderness of arch with fully compact two-layered cross-section

λ_i = slenderness of separate arch sheeting layer between hat profiles having minor section stiffness value

a = constant, $a = 1.3$ for screwed fastenings

n = 2 in case of major axis bending.

Modified slendernesses in design formulae (2) and (3) can be written as follows:

$$\bar{\lambda}_{kg} = \lambda_{id} (f_y/E)^{1/2}/\pi \qquad (5)$$

$$\bar{\lambda}_{ki} = L_i (f_y/E)^{1/2}/\pi i_e \qquad (6)$$

L_i in formula (6) is the length between transverse bar-elements in structural model and i_e is effective radius of gyration of cross-section

$$i_e = (I_e/A_e)^{1/2} \qquad (7)$$

In ECCS buckling curves used for N_{Rci} - and N_{Rcg} -values, choice of type of curve (a,b,c,d) is dependent upon initial imperfections in arch. Usually curve "c" can be used for arch and then maximum initial deflection is assumed as L/400.

In formulae (2) and (3), design bending moment is added by term $N_d e/2$ where distance e is caused by difference between axis of curved sheeting part between hat profiles and corresponding straight line axis in structural model.

DESIGN CALCULATIONS AND COMPARISONS

In design calculation by using a plane bar system as structural model for two-layered arch of profiled steel sheetings connected with transverse hat profiles, validity of the model was tested by comparing results of calculations based on linear (first-order) and non-linear

(second-order) theories. Also influence of horizontal restraint stiffness at base supports on arch behaviour was studied by comparing design calculations in case of horizontally fully restrained support and of tied arch with different axial stiffnesses in the tie between base supports of arch.

Calculations were performed for a fixed arch geometry i.e. L (span) = R (radius) with three L-values of 10, 15 and 22 m. In all cases both linear and non-linear calculation methods were applied. In non-linear case, initial imperfections (max. L/400) according to ECCS buckling curve "c" were assumed in arch geometry as downward initial deflection on half of heavier loading and upward deflection on half of lighter loading. Loading cases were dead load (g = 0.3 - 0.4 kN/m^2) and asymmetric live load (snow) as shown in Fig. 2.

FIGURE 2.

Nominal and design loads for arch R = L = 22 m.

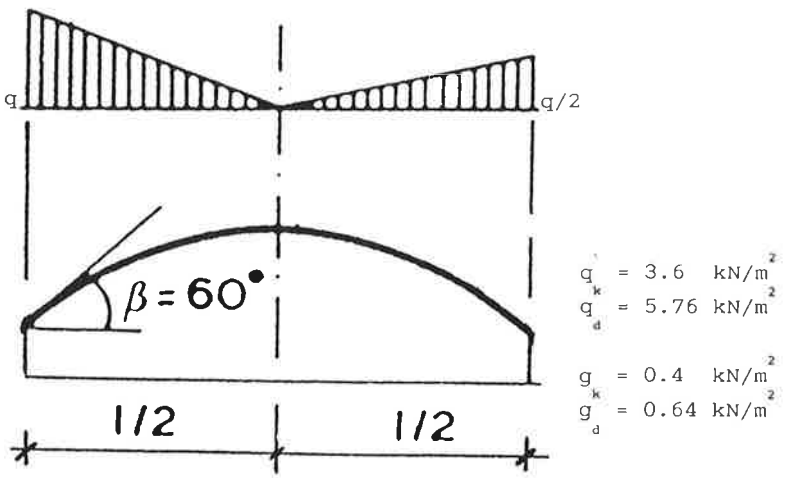

Table 3 shows as an example results of design calculations on arch having span L (=R) = 22 m, both upper and lower sheeting of 120/1.0 (f_y = 320 MPa) and hat profiles of 170/1.2 (f_y = 320 MPa). As can be seen from Table 3, horizontal restraint stiffness at base supports seems to have a minor influence on load-bearing capacity of arch, at the utmost some percents between two extreme restraint stiffness cases of arch supports.

TABLE 3.

Interaction of design stresses (M in kNm and N in kN) for arch R=L =22 m calculated applying formulas (2) and (3).

Case		Lower sheeting		Upper sheeting	
		1. order	2. order	1. order	2. order
	N	40.86	37.20	25.51	36.01
1	M	7.59	10.13	5.97	8.24
	3;4	0.990	0.803	0.707	0.676
	N	40.08	36.64	27.25	37.80
2	M	7.72	10.28	6.06	8.32
	3;4	0.990	0.811	0.733	0.688
	N	39.32	36.08	28.96	39.56
3	M	7.85	10.44	6.15	8.40
	3;4	0.990	0.819	0.759	0.700

Case 1: Horizontally fully restrained base supports
Case 2: Steel tie-bar with cross-sectional area A = 400 mm^2/m
Case 3: Steel tie-bar with cross-sectional area A = 200 mm^2/m

CONCLUSIONS

In analysis made for evaluating structural behaviour and load-bearing capacity of arched roof with profiled sheetings connected with transverse hat profiles, both linear and non-linear calculation methods were applied. It was found out by these calculations that as effective cross-sectional areas and section stiffness values could be chosen minimum values determined on the basis of all possible loading situations of the arch. The effective cross-sectional areas for arched roof sheeting sections can thus be determined correspondingly to values of flat sheeting sections.

Structural model for two-layered arch roof consisting of a plane bar system with double polygonal frame of beam elements connected with transverse bar elements was succesfully used in analyses and design calculations of arch after stiffness values for the bar elements

simulating behaviour of transverse hat profiles between two arched sheetings were experimentally determined in connection of this research project.

Design calculations of the arch were showing that linear calculation methods can be applied with sufficient accuracy within the limits of arch spans (R = 10, 15, 22 m) and geometry (L = R) assumed in this study. It was also observed by analyses and calculations that the influence of horizontal restraint stiffness of arch base supports (i.e. axial stiffness of steel tie-bar between base supports) on stability and load-bearing capacity of arch is relatively small i.e. at maximum in extreme support stiffness cases only some percents on arch capacity values.

ACKNOWLEDGEMENTS

The financial support of company PAAVO RANNILA Oy for this research project is gratefully acknowledged. The authors would also to thank Mr. Martti Koskinen from PAAVO RANNILA Oy for his advices and support throughout the project.

REFERENCES

1. B6, Teräsohutlevyrakenteet. Ohjeet 1989. Ympäristöministeriö. Helsinki. (Finnish Design Code for Cold-Formed Steel Structures).

2. StBK-N5, Tunnplåtsnorm 79. Statens Stålbyggnadskommite 1980. Stockholm. (Swedish Design Code for Cold-Formed Steel Structures).

3. DIN 18807 Stahltrapezprofile im Hochbau. Entwurf 1982. (German Norm for Cold-Formed Steel Structures made of Trapezoidally Profiled Sections).

4. Baehre, R., Untersuchung des Tragfähigkeitsverhaltens von gekrümmten Trapezprofilblechen. (Load-Bearing Capacity of Arched Sheetings with Trapezoidally Profiled Section). Bericht Nr.860618, 1987, TU Karlsruhe. BRD.

5. Hyvärinen, J., Ohutlevyteräksisen kaarikattorakenteen kantavuus ja stabiilius. (Stability and Load-Bearing Capacity of Arched Roof made of Profiled Steel Sheeting). Master's thesis. Helsinki University of Technology. Espoo 1989.

INTEGRATED PHOTOELASTICITY OF GLASS

H. ABEN, S. IDNURM, J. JOSEPSON, K.-J. KELL, A. PURO
Laboratory of photoelasticity
Institute of Cybernetics, Estonian Acad. Sci
21, Akadeemia tee, 200 108 Tallinn, Estonia

ABSTRACT

For analysis of the residual stresses in glass specimen of complicated shape integrated photoelasticity is the most suitable method. However, in the general case theory of the method is very complicated. Theory of integrated photoelasticity is considerably more simple if the birefringence of the specimen is weak or if rotation of the principal axes on the light rays is weak. In case of the glass items one (or both) of these assumptons are often fulfilled.

Theory of integrated photoelasticity in the case of weak birefringence will be briefly considered. Data about stresses in bottles of beer and champagne, and in a fiber preform of nonaxisymmetric form will be presented.

INTRODUCTION

Development of the glass technology (lightweighting of bottles, fabrication of fibers and fiber preforms of complicated cross section, replacement of the annealing technology by the tempering technology etc.) demands more exact knowledge of the residual stresses in glass products. The finite element method can be successfully applied to calculate stresses in glass containers due to external loads [1]. In case of residual stresses the results of calculation are not so reliable since certain hypoteses are to be made concerning

the temperature distribution and change of the material characteristics during different phases of production process. Thus, experimental methods for evaluation of residual stresses are indispensable.

Unfortunately, classical photoelasticity permits only qualitative estimation of residual stresses in glass specimen of complicated shape. However, using integrated photoelasticity [2] several new methods have been developed recently for that purpose.

METHOD

For evaluation of residual stresses the model is put in an immersion bath to avoid refraction of light, and viewed in a polariscope. Dealing with two dimensional objects one can measure the isoclinic parameter and the optical retardation in every point. In the case of three-dimensional stress distribution three types of experimental data can be measured on each ray. Namely, primary and secondary caracteristic directions (α_o and α_*) and characteristic phase retardation γ [2]. In the case of weak birefringence, these are related to components of stress tensor on the ray by simple integral relationships [3]

$$\gamma \cos(\alpha_o+\alpha_*)=C\int_o^{y_*}(\sigma_z-\sigma_x)dy, \tag{1}$$

$$\gamma \sin(\alpha_o+\alpha_*)=C\int_o^{y_*}2\tau_{zx}dy, \tag{2}$$

$$\tan(\alpha_*-\alpha_o)=C^2\left(\int_o^{y_*}(\sigma_z-\sigma_x)\int_o^t 2\tau_{zx}dtdy-\int_o^{y_*}2\tau_{zx}\int_o^t(\sigma_z-\sigma_x)dtdy\right), \tag{3}$$

where C is the photoelastic constant, σ_x, σ_z and τ_{zx} are components of the stress tensor in the plane perpendicular to the light ray, t and y are distances measured along the light ray. It can be shown [3] that these relationships are valid when γ is less than $\pi/2$.

In many cases α_o is equal to α_*. The sum $\alpha_o+\alpha_*$ can be then taken as a double isoclinic parameter 2φ and measurements can be preformed using odinary polariscope. This case has been considered in paper [4]. For example, $\alpha_o=\alpha_*$ if we have an axisymmetric model or when the cilindrical specimen has no gradient along its axis.

Using relationships (1) and (2) and also equations of equilibrium and compability it is possible to determine the axisymmetric stress distribution due to external loads [5].

In the case of axisymmetric stress where axial stress gradient is present we have to preform measurements in two planes separated by a distance Δz. Shear stresses τ'_{zr} and τ''_{zr} in the first and second plane accordingly can be evaluated using equations (2) in these planes. First we have to use simple coordinate transformations and express τ_{zx} through τ_{zr} and after it solve integral equation (2) with respect to τ_{zr} using measured values γ and φ on several rays. Now we can use the equilibrium condition for direction x of a three-dimensional segment cut out from the body (Figure 1).

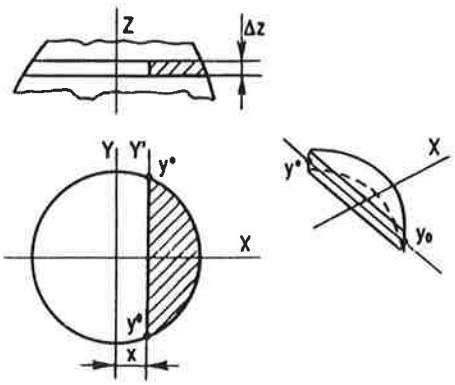

FIGURE 1 Considering the equilibrium condition of a three-dimensional segment.

After some mathematical transformations we get

$$2C\Delta z\int_{y_0}^{y_*}\sigma_x\,dy = \int_x^R \gamma'\sin(2\varphi')\,dx - \int_x^R \gamma''\sin(2\varphi'')\,dx, \qquad (4)$$

where γ', $2\varphi'$ belong to the first- and γ'', $2\varphi''$ to the second plane, R is the radius of the specimen. Equation (4) allows us to elliminate σ_x in equation (1) and it is easy to calculate the distribution of σ_z from there using tomographic methods.

Knowing stresses σ_z and τ_{zr} the meridional stress σ_t on the outer surface of specimen can be determined. In the case of containers the meridional stress on the inner surface can also be evaluated. The meridional stresses play an important role in predicting the reliability of class containers, and therefore their determination is of great importance.

We may study also nonaxisymmetric specimen. In this case the equilibrium condition for x axes allows us to eliminate the stress component σ_x, in eqation (1) and equation (1) can be solved in respect to σ_z using standard tomographic methods. The method of tomography is widely used in medicine for restoring scalar fields [6]. Since we apply the same method for evaluating the stress tensor components, the method is named tensor field tomography [7].

For evaluating the distribution of σ_z we have to preform measurements using many different viewing angles (rotating the specimen round the z axis). Distribution of the axial stress σ_z is determined using Radon inversion.

If the axial stress gradient is not present, we can calculate Airy stress function F. It can be evaluated from the equation

$$\Delta F=\sigma_z-\chi \quad F\big|_R=0, \qquad \partial F/\partial n\big|_R=0, \tag{5}$$

where Δ is Laplace operator χ is a harmonic function, n is the normal to the boundary. If we have found F, other stresses in the plane under investigation can be calculated from the equations

$$\sigma_x = -\partial^2 F/\partial y^2, \qquad (6)$$

$$\sigma_y = -\partial^2 F/\partial x^2, \qquad (7)$$

$$\tau_{xy} = \partial^2 F/\partial x \partial y. \qquad (8)$$

The method for complete determination of stress components described here can be used only in the case of prismatic specimen without axial stress gradient [8].

In the case of specimen of arbitrary shape only distribution of stress component σ_z can be determined (z is the axes around which the specimen is rotated during measurements).

EXPERIMENTAL INVESTIGATIONS

For measurements a polariscope with synchronous rotation of the polarizer and analiser was used. The optical retardation was measured using a compensator. As immersion liquid a mixture of the α-bromnaphtaline and of the sunflower oil was used.

Figure 2 shows the distribution of meridional stresses at the internal and external surfaces of a champagne bottle before and after opening and figure 3 shows the distributions of σ_z in two sections.

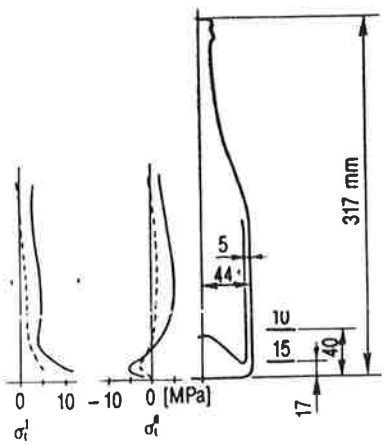

FIGURE 2 Meridional stresses at the internal σ_t^i and external σ_t^e surfaces of a champagne bottle before (-) and after (- - -) opening.

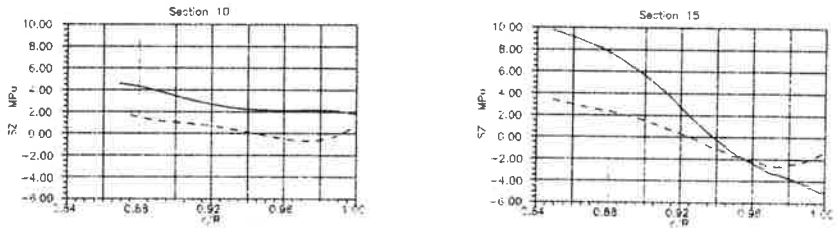

FIGURE 3 Distribution of σ_z in two sections of french champagne bottle before (-) and after (- - -) opening.

Figure 4 shows meridional surface stresses in a beer bottle and Figure 5 the distribution of σ_z through the wall in two sections.

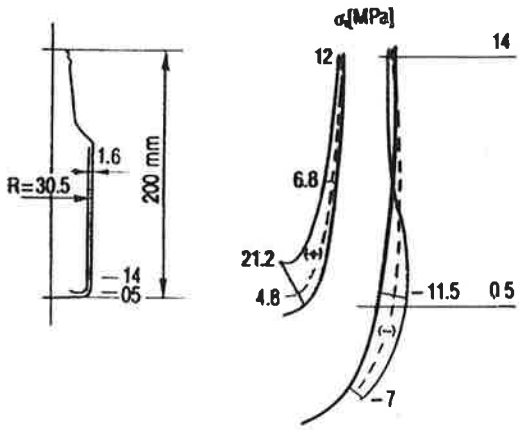

FIGURE 4 Distribution of meridional surface stresses in a beer bottle.

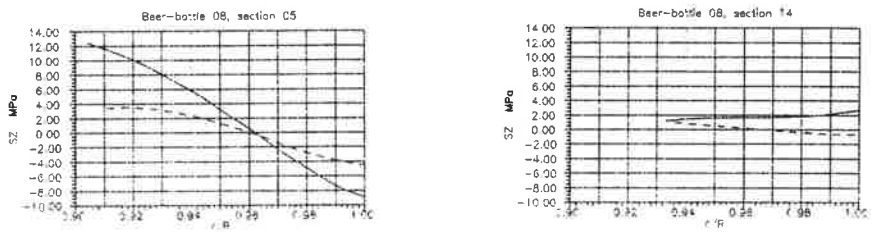

FIGURE 5 Distribution of the longitudinal stress σ_z in a beer bottle.

In figure 6 the axial stress distribution in a fiber preform is shown.

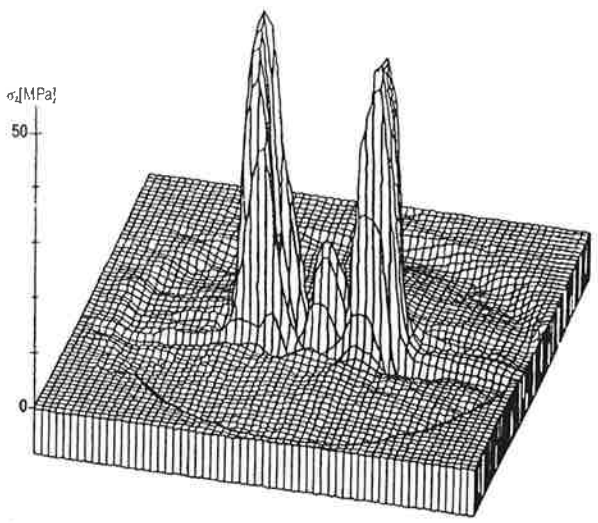

FIGURE 6 A bow tie type fiber preform: distribution of σ_z.

CONCLUSIONS

Using integrated photoelasticity and assuming that birefringence is weak, several methods for the determination of different stress components are developed. Application of the methods is illustrated by examples of experimental investigations.

ACKNOWLEDGEMENT

The autors would like to express their gratitude to Dr V. Matejec from the Institute of Chemistry of Glass and Ceramic materials of the Czeckoslovak Academy of Sciences for furnishing the fiber preform.

REFERENCES

1. Müller-Simon, H., Barklage-Hilgefort H. Strength optimization of glass containers by the finite element method. Glastech. Ber., 1988, 61, N° 12, 348-357.

2. Aben H. Integrated Photoelasticity. McGraw-Hill, New York, 1979.

3. Kell K.-J., Puro A. The case of very weak optical anisotropy in integrated photoelasticity. Optika-Spektrosk. (in Russian, to be published)

4. Aben H., Josepson J., Kell K.-J. The case of weak birefringence in integrated photoelasticity. Optics and Lasers in Engineering, 1989, 11, 145-157.

5. Doyle J. F., Danyluk H. T. Integrated photoelasticity for axisymmetric problems. Exp. Mech., 1978, 18, N° 6, 215-220.

6 Herman GT. Image reconstruction from projections. Acad Press, New York, 1980.

7. Aben H., Kell K.-J. Integrated Photoelasticity as tensor field tomography. ZAMM, 1986, 66, N° 4, T118-T119.

8. Puro A. Determination of residual stresses in long prismatic objects by using integrated photoelasticity. Proc. of Acad. of Sci. USSR. (to be published, in russian)

DEVELOPMENT OF DEFLECTION AND STRESSES IN WOODEN BEAMS UNDER CYCLIC CHANGES OF SURROUNDING HUMIDITY

ANTTI HANHIJÄRVI
Technical Research Centre of Finland (VTT)
Laboratory of Structural Engineering
Kemistintie 3, SF-02150 Espoo, Finland

ABSTRACT

This paper demonstrates the development of stresses and deflection of wooden beams under bending load when the surrounding humidity conditions change in a cyclic manner. A solid wood beam with a small cross-section and a glulam beam with a larger cross-section are considered to study the size effect. The moisture diffusion problem is solved numerically using Fick's second law. The resulting moisture content distributions are used in a structural FE-analysis in which a constitutive equation taking into account the mechano-sorptive creep behavior of wood is adopted. Besides cyclic changes with the moisture content cycles the deflection increases with each cycle. Similarly, the bending stresses show a tendency to change.

INTRODUCTION

The creep of wood is strongly influenced by the changes of its moisture content (ratio of the weigth of contained water to dry weight). These changes arise from the hygroscopic i.e. water absorbing nature of wood and the changes of relative humidity (RH) in the surrounding air. Simultaneous moisture content change and load bring about deformation, which would not be caused by moisture expansion and loading consecutively. This phenomenon is generally called mechano-sorptive creep. An interesting subject that has not yet been thoroughly investigated is what happens to loaded wooden construction members in final use under naturally changing humidity. In the present paper such situations are simulated by analyzing wooden beams under cyclic humidity changes and under constant bending moment using three-dimensional finite element model with mechano-sorptive material properties. Water diffusion characteristics which determine the internal moisture distribution and the constitutive parameters of wood along with the moduli of elasticity are the factors that determine the stress and strain state as a response to a known humidity history and loading.

DIMENSIONS, LOADING AND HUMIDITY CONDITIONS

Two different size beam cross-sections were analysed. The first and smaller one was thought to be cut along the grain so that the pith is located outside the cross-section. The other beam was a glue laminated (glulam) beam with 20 laminae. The dimensions of beams and pith locations for each cut are illustrated in Fig. 1a and b.

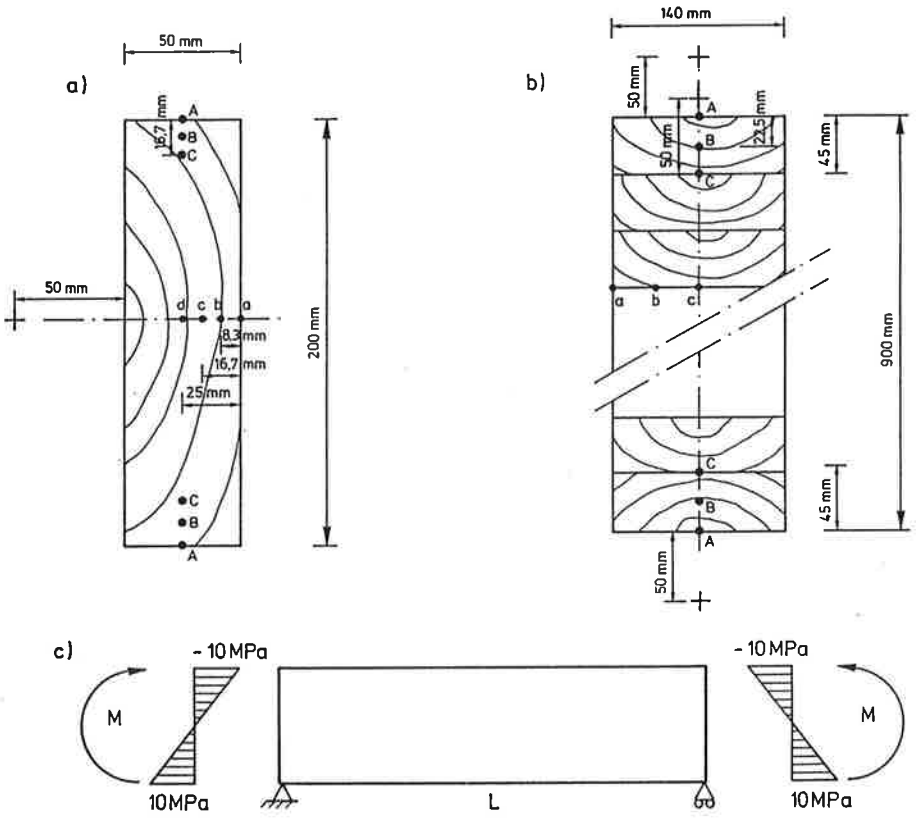

FIGURE 1
a) and b) Cross-sections of analysed beams. c) Loading of beams, L = 1000 mm for the smaller beam and L = 4000 mm for the glulam beam.

The beams were loaded with a constant bending moment with linearly distributed bending stress at the ends. Surface magnitude was 10 MPa compression at the top and tension at the bottom. The loading is illustrated in Fig. 1c.

To simulate the conditions beams undergo in the climatic environment of the Nordic Countries five different humidity histories were used. The annual cycles of humidity in a heated indoors location were modelled with two histories, a moderate one and a severe one:

$$RH = 45\% + 10\% \sin(2\pi t/1yr),\ t = 0 \ldots 2 \text{ yrs}, \quad (1)$$

$$RH = 45\% + 20\% \sin(2\pi t/1yr),\ t = 0 \ldots 2 \text{ yrs}. \quad (2)$$

The annual cycle of humidity in a sheltered non-heated environment was modelled with the following:

$$RH = 75\% + 15\% \sin(2\pi t/1yr),\ t = 0 \ldots 2 \text{ yrs}. \quad (3)$$

Besides annual cycles the humidity fluctuates also in shorter irregular patterns due to the temporary changes in environmental factors. These fluctuations have an irregularly changing amplitude and period. For simplicity they were thought to have a period of about 10 days and an average amplitude of ±10 % RH and were modelled with the following cycle:

$$RH = 45\% + 10\% \sin(2\pi t/10 \text{ days}),\ t = 0 \ldots 20 \text{ days}. \quad (4)$$

The maximum amplitude of these variations was assumed to be ±20% RH and a corresponding cycle is

$$RH = 45\% + 20\% \sin(2\pi t/10 \text{ days}),\ t = 0 \ldots 20 \text{ days}. \quad (5)$$

Besides the cycles described above there are also daily fluctuations in the humidity conditions which have a more regular pattern but because of the relatively slow rate of desorption and adsorption in wood these fluctuations were not considered at all. For all cases the temperature was considered for simplicity as constant at 20°C.

DIFFUSION

The internal moisture distributions in the cross-sections were first calculated by JAM-2 moisture flow program [1] which uses finite difference method to solve Fick's second law of diffusion two-dimensionally:

$$\frac{\partial C}{\partial t} = \frac{\partial}{\partial x}\left(D_x \frac{\partial C}{\partial x} \right) + \frac{\partial}{\partial y}\left(D_y \frac{\partial C}{\partial y} \right), \quad (6)$$

where C denotes water content (kg/m^3) and D_x and D_y are diffusion coefficients.

The moisture distribution was assumed to be constant along the length of the beams. The results of diffusion simulation were converted into input data for the finite element analysis for the calculation of stress state and displacements three-dimensionally.

The values of the diffusion coefficients were assumed to be equal in all directions in the plane perpendicular to grain and their values in different moisture content values were based on litterature [2] and range nearly linearly from $1.0*10^{-10}$ m^2/s at 0.06 moisture content to $2.8*10^{-10}$ m^2/s at 0.20 m.c. The so called sorption curve which gives the

equilibrium moisture content value of wood at any RH value was adopted from Zuritz's numerical curve [5] at 20°C temperature.

STRESS ANALYSIS

The mechanical material behavior of wood was taken into account in the finite element analysis by using the constitutive equation for wood proposed by Ranta-Maunus [3] and its implementation into ABAQUS structural analysis program [4]. The constitutive equation is expressed in one-dimensional form

$$\dot{\epsilon} = \dot{\sigma}/E + (\alpha + m\sigma)\dot{u} \quad , \tag{7a}$$

where ϵ is deformation, σ stress, E modulus of elasticity, u moisture content and α coefficient for moisture expansion. The notation $\dot{}$ stands for the time derivative. The mechano-sorptive parameter m has different values depending on whether wood is drying or wetting:

$$m = \begin{cases} m^-, & \dot{u} < 0, \\ m^+, & \dot{u} > 0, \\ m^{++}, & \text{for first wetting.} \end{cases} \tag{7b}$$

The creep equation (7) does not take into account the "normal" viscoelastic creep so that the only time dependence of the model comes through moisture diffusion.

If relation like (7) is assumed between all components of stress and strain, the constitutive equation can be generalized to a matrix formulation for the purpose of three-dimensional application by the finite element method:

$$\{\dot{\epsilon}\} = [S^e]\{\dot{\sigma}\} + (\{\alpha\} + [S^{ms}]\{\sigma\})\dot{u} \quad , \tag{8a}$$

$$[S^{ms}] = \begin{cases} [S^{ms+}], & \dot{u} > 0 \\ [S^{ms-}], & \dot{u} < 0 \end{cases} \quad , \tag{8b}$$

where $[S^e]$ is the compliance matrix and $[S^{ms}]$ the matrix of the mechano-sorptive coefficients. The effect of the first wetting is neglected and only the long-term effects of mechano-sorptive creep are considered. The numerical values of the matrices are given in Appendix A.

The finite element analysis was performed with ABAQUS structural analysis program using a mesh of three-dimensional 20-node brick elements. The implementation uses Euler forward method for time integration. 48 time increments were used for the annual cycle and 40 increments for the short-term simulations.

RESULTS

The smaller beam was analysed in all humidity conditions described in (1)...(5). The glulam beam was analysed only in the severe annual ones (2) and (3). In all cases the initial moisture distribution was constant throughout the beam. An idea of the variation of the internal moisture content can be obtained through Fig. 2 in which the moisture content resulting from the humidity cycles are shown in some locations of the beams' cross-sections. The moisture content throughout the smaller beam follows well - with only some delay and small damping - the annual changes of the surface moisture content which correspond to the RH value of the surrounding air. But the changes in the innermost parts of the glulam beam have a considerably smaller amplitude and a greater delay. The short-term cycles of surface moisture content seem to be able to penetrate only few mm's from the surface.

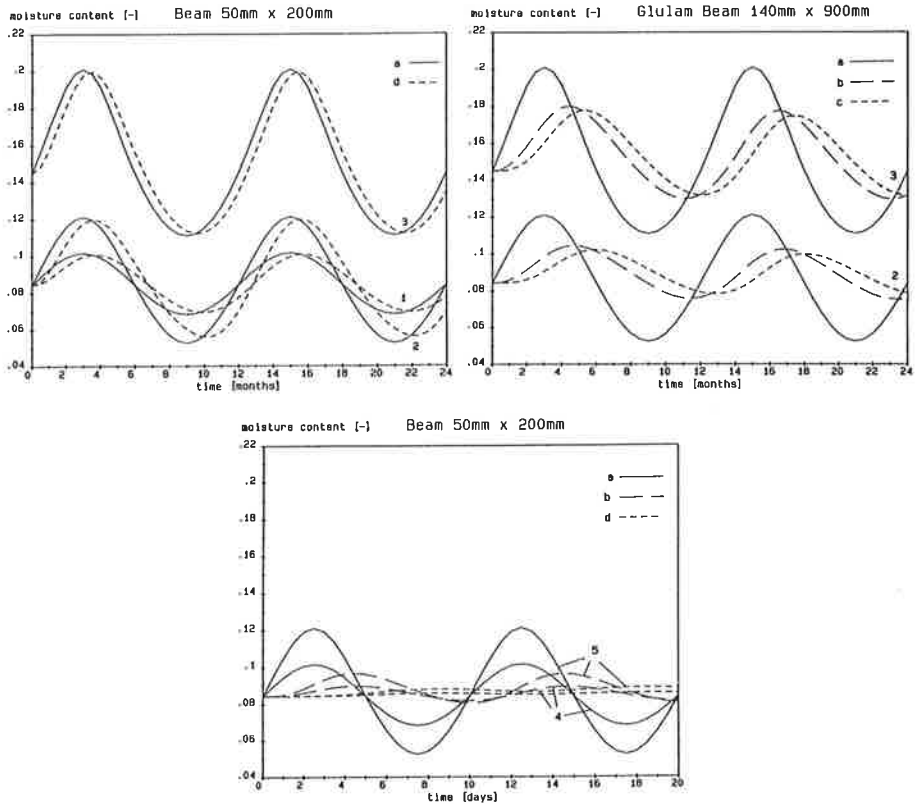

FIGURE 2
Moisture content histories at different locations indicated in Fig. 1. Numbering of the humidity histories:

1) RH = 45%+10%sin(2πt/1yr)
2) RH = 45%+20%sin(2πt/1yr)
3) RH = 75%+15%sin(2πt/1yr)
4) RH = 45%+10%sin(2πt/10 days)
5) RH = 45%+20%sin(2πt/10 days)

The maximum deflection of beams against time is shown in Fig. 3. Besides a periodic change with the cycles of humidity a gradual increase can be seen to take place in all cases. This increase seems to be the greater the severer changes and higher absolute value humidity has.

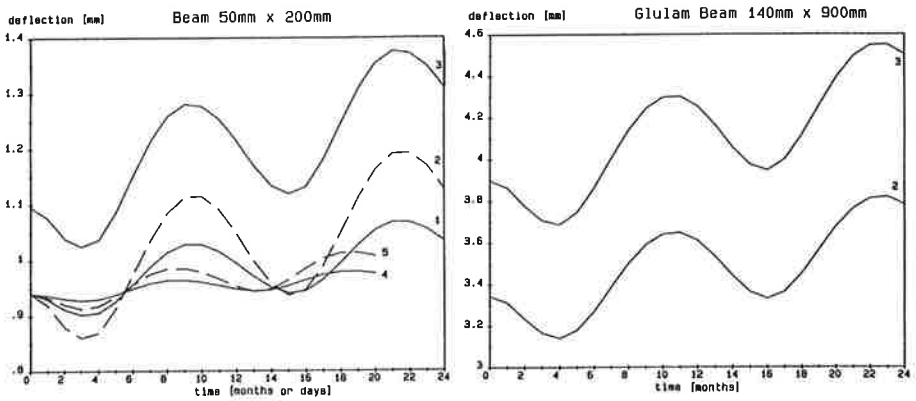

FIGURE 3
Maximum deflection of beams. Numbers refer to humidity histories as in Fig. 2.

The variation of the bending stress with time is illustrated in Fig. 4 at top and bottom surfaces and a small distance underneath the surfaces. The surface stresses vary according to the shrinking and swelling of the surface layer and the layer underneath the surface seems to balance these variations. The reason for the amplitude of these changes in compression to be greater than in tension are the numerical values of the mechano-sorptive parameters that increase the effect of moisture shrinkage and swelling in the case of compression and decrease it in tension. Also a slow tendency of the surface tensile stress to decrease and the compressive stress to increase can be observed.

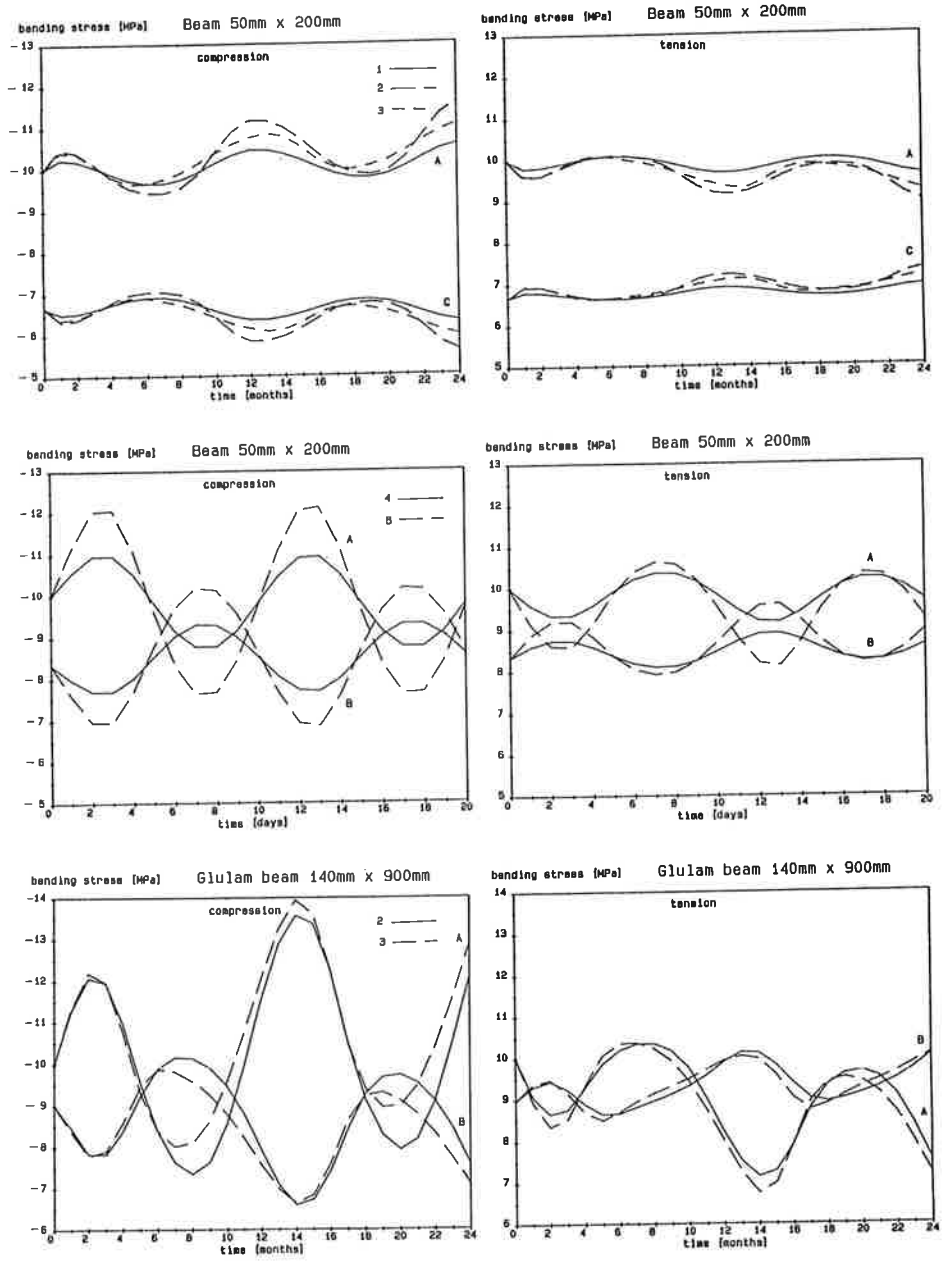

FIGURE 4
Bending stress at surfaces and at some distance underneath them. Letters refer to locations shown in Fig. 1 Numbers refer to humidity histories as in Fig 2.

COMPUTER AIDED MEASUREMENT OF STEEL AND COMPOSITE MACHINE ELEMENTS AND SIMULATION BASED ON MICRO- AND MACROMECHANICS

Heikki Martikka, Harri Eskelinen, Raimo Suoranta
Department of Mechanical Engineering
Lappeenranta University of Technology
P.O.Box 20, SF-53851 LAPPEENRANTA, FINLAND

ABSTRACT

Some tensile and other tests were performed on a low alloy steel with various grain sizes. Experimental results were analyzed using computer programs to obtain true stress- true strain curves. These tests were simulated using dislocation mechanics and dynamics and strain, grain boundary, solution and dispersion hardening theories of multiphase and dispersion alloyed materials. Using these macro- and micromechanical behaviour models the initial discontinuous yielding and the subsequent work hardening was satisfactorily predicted. Temperature and strain rate effects were also considered.

INTRODUCTION

Most nominally homogeneous materials are actually multiphase materials either at macroscopic, microscopic or at both levels. Inclusions and second phase dispersions cause inhomogeneities in the stress and strain fields during deformation. This is due to differences in their elastic, yielding and strain hardening behaviours and morphologies.
The analysis of the plastic deformation and work hardening of multiphase structures is generally done either using micromechanical models or using continuum mechanics. Karlsson and Linden [1] have studied two-phase structures using these methods to calculate plastic deformations of ferrite-pearlite structures having different isotropic yield and work hardening properties. Mechanics of yielding and strengthening are reviewed by Ashby [2] and Martin [3].

This investigation is part of a wider program by which it is aimed to develop and use integratedly micromechanical and macromechanical models for simulating nonlinear material behaviour and test them experimentally.

The objective of the present study was to integrate simple but physically realistic models to simulate observed experimental tensile test results of a low alloy steel.

MATERIALS AND METHODS

The material used in this study was commercial low carbon steel of type Fe 37B SFS 200 with composition (in wt %) 0.13 C, 0.20 Si, 0.51 Mn,

0.017 P, 0.028 S, 0.15 Cr, 0.09 Ni supplied in the form of plates of 3 mm thickness.

Initial state was after hot rolling. Specimens were heat treated to different grain sizes shown in Table 1.

TABLE 1.
Data for specimens

Ser.	Heat	Grain size	HB	ReL	ReH	Rm	Rmt	Rf	Z	Rm/ R8	Rm/ HB
A	initial	.009	139	340	343	447	534	712	.655	3.5	3.2
B	750 C/1h	.012	133	337	338	435	528	801	.675	3.6	3.1
C	900 C/1h	.025	125	322	324	417	500	900	.672	3.5	3.3
D	1050C/1h	.06	100	137	138	227	275	625	.775	3.8	2.3

Legend: ReL = lower yield point, ReH = higher yield point
Rm = nominal UTS, Rmt = true UTS, Rf = true fracture strength after Bridgman correction , Z = reduction in area. Stresses are in (MPa) and grain size D in (mm). HB = Brinell hardness
R8 = nominal yield strength at 8 percent linear strain ≈ DPN ≈ HB hardness

Normal tensile tests and hardness measurements were performed. Microstructure was studied using optical and SEM photography. Typical results are shown in Figure 1.

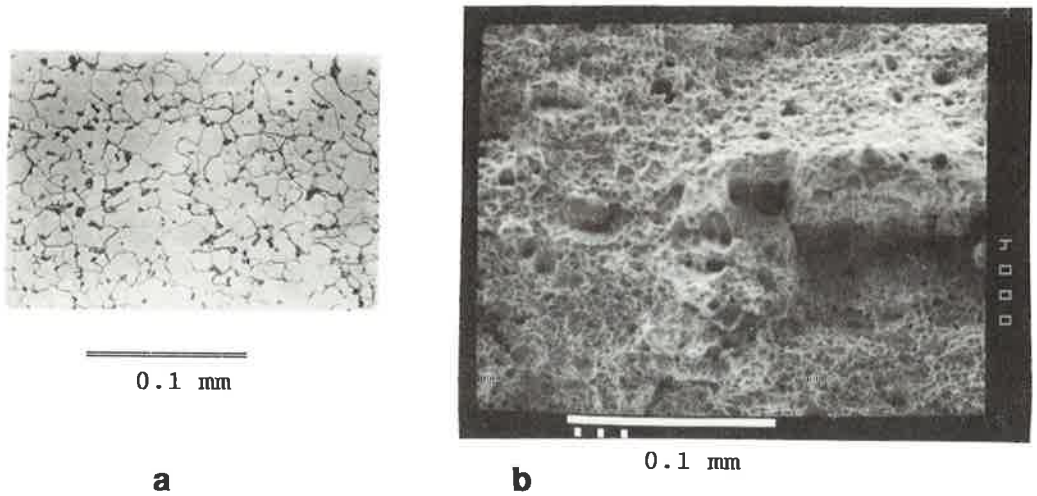

FIGURE 1. Microstructure of a typical steel specimen.
a) Optical photograph showing the typical microstructure of mostly ferrite and low volume fraction of pearlite.(Series B /spec.6). Volume fraction of pearlite is about 0.17.
b) SEM micrograph of series B showing dimple structure typical of ductile fracture (Series B/spec. 4). Dimple size is about 0.01 mm or close to the ferrite grain size.

Tensile test curves were analyzed with a program to obtain fully corrected true stress - true strain curves. A typical tensile test curve is shown in Figure 2 for series B/spec.3. This material has a

microstructure which exhibits a strong discontinuous yield behaviour and strong initial work hardening at the end of the Luders strain.

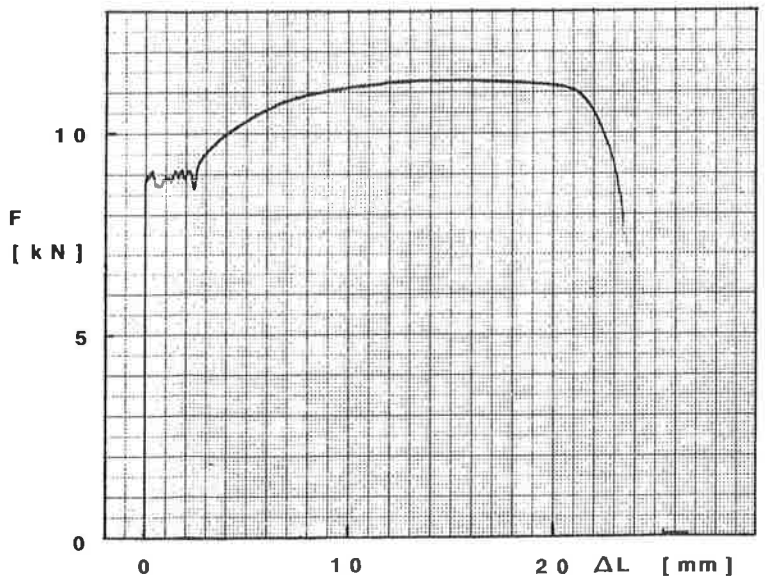

FIGURE 2. Tensile test curve for series B /spec.3. Tensile force is plotted dependent on the elongation of the specimen (initial length 70 mm).

THEORY OF SIMULATIONS

The studied material is composed of aggregates of ferrite and pearlite and a dispersion of inclusions in the ferrite. It is possible to describe the properties of an aggregate in terms of the mechanical behaviour properties of the individual constituents if it is known how strain and stress are distributed between the constituents, and how they interact during deformation.

The macroscopic constituents are individually also microalloyed in their individual microstructures. The ferrite contains in addition of carbon also Si, Mn, Cr and Ni which strengthen the ferrite by solution hardening and by forming inclusions and precipitates.

The yield stress of two ductile phases

If it is assumed that no strain gradients exist at the aggregate level, so that both phases undergo the same strain, then the stresses in each phase are different and the yield stress of the composite will be given by the simple 'law of mixtures':

$$\sigma_y = f\,\sigma_{y1} + (1 - f)\,\sigma_{y2} \qquad (1)$$

where σ_{y1} and σ_{y2} are the yield stresses of the phases in isolation, and f is the volume fraction of phase 1.

The yield stress of a hard phase aggregate in ductile phase

In this situation the hard phase is likely to be undeformed at yield, at which case the yield stress will correspond to that of the matrix.

Thus in pearlite-ferrite structures pearlite is found to have only a small effect on the yield stress. Gladman, Ivor, and Pickering [4] have adopted an equation:

$$\sigma_y = f_1^p \sigma_{y1} + (1 - f_1^p) \sigma_{y2} \quad (2)$$

where σ_{y1} and σ_{y2} are the yield strengths of ferrite and pearlite in isolation, and f_1 is the volume fraction of ferrite, and exponent p was found to have a very low value $p \approx 0.01$, indicating that the yield strength of the aggregate was dependent on the ferrite strength until the structure was almost completely pearlitic.

The yield strength of ferrite

The effect of alloying and polygonal grain size D on the yield strength of ferrite can be described by the Hall-Petch equation:

$$\sigma_y = \sigma_i + k_y D^{-1/2} = \sigma_i + \Delta\sigma_G \quad (3)$$

where σ_i is the friction stress given by ref.[4] as

$$\sigma_i = K + \Delta\sigma_i \quad (4)$$

where

$$\Delta\sigma_i = 37 \text{ (wt\% Mn)} + 83 \text{ (wt\% Si)} + 2918 \text{ (wt\% free N)} \quad (5)$$

and

K = 88 MPa for air cooled material and
K = 62 MPa for furnace cooled material
and k_y = 15.1 (MPa $mm^{1/2}$) when grain size D (mm).

This Hall-Petch formula is typical of a more general formula which takes into account also that yielding may occur continuously or discontinuously and the metal may strain harden by various mechanisms.

$$\sigma_y = \sigma_{Lud} + \Delta\sigma_G + \Delta\sigma_M + \Delta\sigma_T + \Delta\sigma_{KG} \quad (6)$$

Let us consider various terms in eq. (6).

It is now assumed that the intrinsic strength of pure polycrystalline material with some mobile dislocations may be combined to the Luders stress which corresponds to the discontinuous yielding and subsequent continuous yielding.

$$\sigma_{Lud} = K \quad (7)$$

It is also possible to consider them separately as having separate physical origins. Solute hardening is caused when solute atoms pin dislocations and cause a strength increment

$$\Delta\sigma_M = \alpha G c^{1/2} \quad (8)$$

where c is atomic fraction of solute and α is some constant.

Assuming a linearly additive contribution of various sources of strength the solute hardening may be associated to the stress $\Delta\sigma_i$ of eq. (5) proposed in ref.[4]. Thus

$$\Delta\sigma_M = \Delta\sigma_i \quad (9)$$

Increase of dislocation density hinders motion of dislocations and leads to increase of yield strength by an amount:

$$\Delta\sigma_v = \beta\ G\ b\ \rho^{1/2} \qquad (10)$$

where ρ is dislocation density and β is a constant. Dislocations may be classified as geometrically necessary and statistically stored.

In a two-phase alloy deformation gradients cause geometrically necessary dislocations to be stored close to particles. Increment of hardening caused by particles is described by Ashby [2] as

$$\Delta\sigma_T = C_1\ G \left[\frac{b\ f\ \varepsilon_p}{d}\right]^{\frac{1}{2}} \qquad (11)$$

where d is the average particle diameter, ε_p is plastic strain, f is volume fraction of hard equiaxed particles in a ductile matrix with Burgers vector, b, and shear modulus, G. C_1 is a constant [2]:

$C_1 = C_2\ M^{3/2}$,
$C_2 = 0.25$ and
$M = 2$ is orientation factor for bcc crystals.

The factor M is used to transform single crystal shear stress τ vs shear strain g relation $\tau(g)$ into polycrystal $\sigma(\varepsilon)$ relation by $\tau = \sigma / M$, $g = M\ \varepsilon$.

If grain boundaries are regarded as obstacles to slip acting with slip distance equal to grain size D then the increment of yield strength by grain boundaries is described by Ashby [2] as

$$\Delta\sigma_{KG} = C_4\ G \left[\frac{b\ \varepsilon_p}{D}\right]^{\frac{1}{2}} \qquad (12)$$

where

$$C_4 = C_3\ M^{3/2} \quad , \quad C_3 = 0.35 \qquad (13)$$

If the strengthening mechanisms interact strongly like moving dislocations and particles, then the effects of mechanisms must be added nonlinearly as

$$\Delta\sigma = (\Delta\sigma_v^2 + \Delta\sigma_T^2)^{1/2} \qquad (14)$$

Transition from elastic to plastic yielding

The onset of plastic yielding is described by the dynamical theory of discontinuous yielding. This type of yielding is prominent in low alloy carbon steels. Three prerequirements for the occurrence of this type of yielding are proposed:

1. The first requirement is a low initial number of mobile dislocations. In bcc metals the in grown dislocations (10^4 - 10^6 disl/mm^2) are immobilized by interstitial atom locking to give about 1 disl/mm^2 initially. [6]

2. The second requirement is a dislocation velocity v which increases with stress

$$v = \left[\frac{\sigma}{\sigma_o}\right]^n \qquad (15)$$

where σ is the applied stress and σ_o is the stress for unit velocity. It is taken in Ref. [2] as σ_o = 180 MPa for v = 1 mm/s. For iron n = 35 is used according to Wyatt et al. [6].

As the number of dislocations increases a linear work hardening law is assumed [6]:

$$\Delta\sigma = q\,\varepsilon_p \tag{16}$$

Wyatt et al.[6] estimate q = 3000...4000 MPa. In the Luders range the effective hardening rate is smaller. Hence the dislocation velocity is retarded as the back stress $\Delta\sigma$ decreases the effective stress moving the dislocations

$$v = \left[\frac{\sigma - q\,\varepsilon_p}{\sigma_o} \right]^n \tag{17}$$

3. The third requirement is rapid dislocation multiplication, involving double cross slip of screw dislocations and trailing lines of edge dislocation dipoles, which break up into prismatic loops and subsequently generate further dislocations by the Frank-Read type mechanism. The number of active dislocations has been roughly approximated by [6]:

$$\rho = f\,(\,\rho_o + C\,\varepsilon_p{}^a\,) \tag{18}$$

where f is the proportion of dislocations which are mobile (typically 0.1), ε_p is the plastic strain , ρ_o is the initial dislocation density (disl/mm^2). For decarbonized iron $C = 1.6\ 10^7$ and a = 0.8 and for 0.2 per cent iron $C = 4.7\ 10^5$ and a = 1.5 [6]. Now values $C = 1.10^7$ and a = 1 were chosen.

The imposed strain rate $d\varepsilon/dt$ equals the number of mobile dislocations moving with velocity v and contributing strain b

$$\dot{\varepsilon} = 0.5\ b\ \rho\ v \tag{19}$$

where the factor 0.5 averages the various orientations of slip planes.

When equations (17), (18) and (19) are combined then the stress-strain curve at initial discontinuous yielding is obtained as:

$$\sigma = \Delta\sigma + \sigma_{Lud} \tag{20}$$

$$\sigma = q\,\varepsilon_p + \sigma_o \left[\frac{\dot{\varepsilon} * Eraf}{0{,}5\ b\ v_o\ f\ Ranf*Tempf\ (\ \rho_o + C\ \varepsilon_p{}^a\ )} \right]^{1/n} \tag{21}$$

where Eraf is a factor for changing strain rate , Ranf is a random factor for simulating the statistical effect of obstacle distribution on the dislocation velocity and Tempf is a factor used to apply thermal activation.

RESULTS

First the nominal stress-linear strain test curves were converted to true stress - true strain curves. Typical result is shown in Fig. 3 for series B, spec.3.

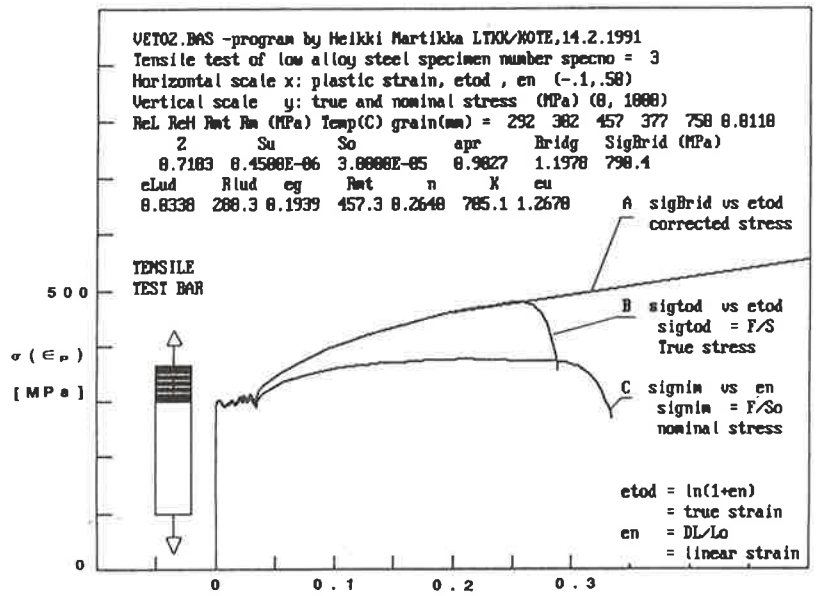

FIGURE 3. Conversion of a test curve to true stress -true strain scale (Series B /spec.3). Curve C shows nominal stress-linear strain, curve B true stress - true strain and curve A shows application of Bridgman correction to curve B.

Results of simulation of the tests are shown in Figures 4 and 5.It may be seen the simulated curves fit reasonably with the experimental curves considering many uncertainties in the theory of the models and their parameters.

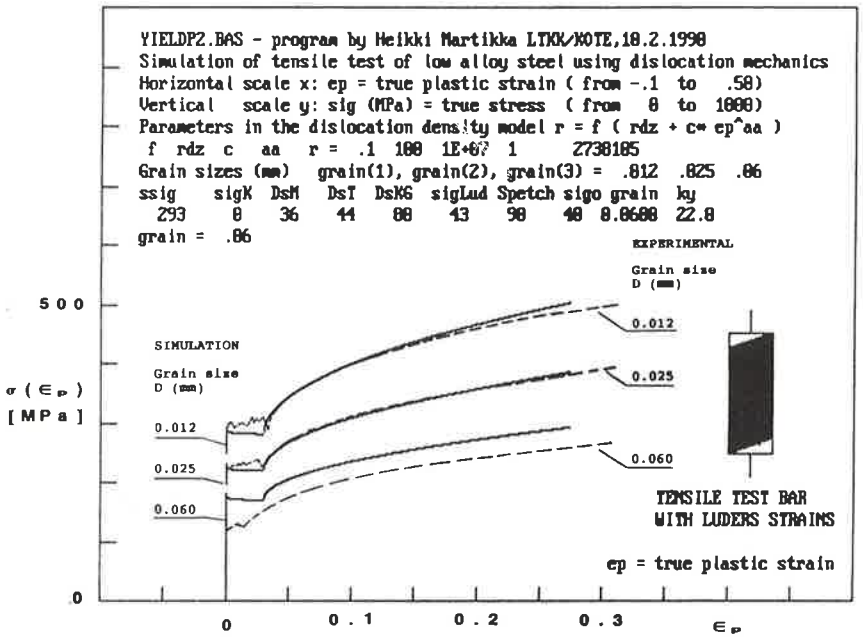

FIGURE 4. Comparison of true stress - true strain curves. Experimental curves and grain sizes D are: B/3 with 0.012 mm, C/11 with .025 and D/16 with 0.06. Simulated curves are plotted with grain sizes D = 0.012, 0.025 and 0.06.

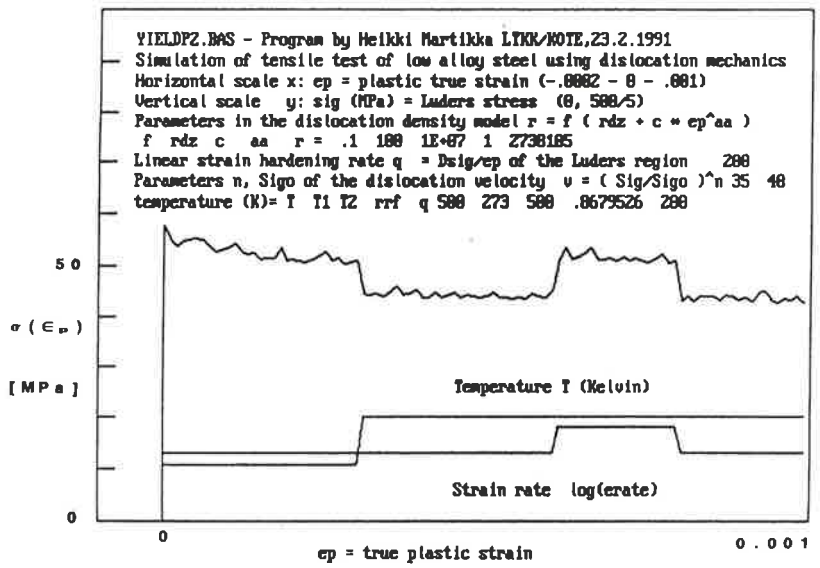

FIGURE 5. Simulation of true Luders stress - true strain tensile test showing initial discontinuous yielding. The curve has been made using a random factor simulating the statistical obstacle distribution effect on the dislocation velocities. The effect of changes of strain rate and temperature are also shown. Effective strain hardening rate is set to q = 200.

DISCUSSION

Tensile tests are commonly used to obtain restricted information about the yielding, work hardening and ductility properties of materials.One goal of this study is to show that much more useful information may be obtained from tensile tests using computer aided analysis and physical models.

It may be seen in Figure 4 that the curves for smaller grain sizes fit quite well with the tests curves but the large grain specimen is softer by 30 MPa than predicted. It may be possible that high temperature annealing has reduced the internal friction stress by this amount. Grain growth and diffusion may have cleaned the ferrite from impurity atoms.This effect is also possible to take into account later. Initial yielding may sensitively depend on actual initial substructure whose model parameters were estimated. The present models were fitted to data using reasonable estimates : ky = 22 ,volume fraction of particles 0.01, diameter 1 μm , initial dislocation density 100 disl/mm^2, a = 1, C = $1 \cdot 10^7$ and σ_o = 40 MPa. It is known [6] that for steels the ratio Rm/DPN is about 3.5. but for series D Rm/HB was only 2.3.

Results of static tests are related to the fatigue strength of steels. For example Grosch [7] gives several empirical models like a typical model by Just

$$\sigma_{bw} = (0.24 + 0.4 \, Z) \, Rm \qquad (22)$$

where σ_{bw} is ideal fatigue strength in rotating bending test. This model agrees with the empirically observed constancy of the ratio σ_{bw}/ Rm = 0.5 for steels with Rm < 1400 MPa only within the range Z ≈ 0.67.. 0.68.

For estimating push-pull fatigue strength amplitude the suggested models are [7]:

$$\sigma_{zdw} = 0.2 \, (Re + Rm) + 57 \quad (MPa) \qquad (23)$$

$\sigma_{zdw} = 0.42\ Rm + 40$

where Re is the yield strength and Rm = UTS tensile strength. Application of these gives the following results:

Small grain series B : $\sigma_{bw} = 224$, $\sigma_{zdw} = 211, 182$
Large grain series D : $\sigma_{bw} = 124$, $\sigma_{zdw} = 130, 135$

This example shows how the usefulness of these microstructure based models may be expanded to predict more accurately some fatigue properties from static test data. It is feasible to incorporate models for estimating thermal activation, strain rate effects, ductile fracture and wear strength.

CONCLUSIONS

1. It may be concluded that the mechanical behaviour of typical steels in tensile tests may be simulated semi-quantitavely using microstructural mechanics of discontinuous yielding and work hardening.
2. One advantage of this method are that detailed physical models are utilized much more effectively when they are unified into a flexible larger model. By comparing these model predictions with analyzed experimental tensile test curves useful insight is obtained for optimizing steel microstructures as an essential part of macroscopic steel structures.
3. Not only static strength but also fatigue properties may be estimated using these models and known empirical models relating static strength and ductility to fatigue strength.
4. Many technical materials exhibit similar behaviour and are amenable to similar analysis. In the next stage of this project relationships between micro- and macrostructural behaviours are studied further with computer aided methods and measurements.

REFERENCES

1. Karlsson B., Linden G., Plastic deformation of ferrite-pearlite structures in steel. Materials Science and Engineering, 17 (1975), p. 209-219

2. Ashby M.F., The deformation of plastically non-homogeneous alloys, in Kelly A., Nicholson R.B. (editors), Strengthening methods in crystals, Applied Science Publishers Ltd, London,

3. Martin J.W., Worked Examples in the Strength of Metals and Alloys, The Inst of Metallurgists, Oxford, 1983,p. 12-56

4. Gladman T., McIvor I.D.,Pickering F.B.,J.I.S.I. 210, 1972, p.916

5. Gladman T., Dulieu D., McIvor I.D., Proc.Conf.'Microalloying '75' , Washington, October 1975, p.32

6. Wyatt H.W., Dew-Hughes D., Metals, Ceramics and Polymers, Cambridge University Press, Cambridge, 1974, p. 417-460

7. Grosch J. (editor), Werkstoffauswahl im Maschinenbau, Expert Verlag, 1988, 263 p.

THERMOMECHANICAL MODELLING OF WATER SATURATED POROUS MEDIUM

MARTTI MIKKOLA
Laboratory of Structural Mechanics
Helsinki University of Technology
Rakentajanaukio 4, 02150 ESPOO

ABSTRACT

The governing equations for the mixture of elastic skeleton and incompressible liquid are derived using the basic principles of continuum mechanics and thermodynamics. The principle of the accompanying local equilibrium state provides the constitutive equations. Darcy's and Fourier's laws follow from the dissipative properties of the mixture. An equation corresponding the classical equation of consolidation by Terzaghi can also be derived.

BASIC CONCEPTS AND NOTATIONS

A completely saturated soil is considered. Soil particles form the skeleton of the porous medium and all the pores are filled with water. The volume fractions of the constituents are β_s (skeleton) and β_w (water).They satify the obvious conditions

$$\beta_s + \beta_w = 1, \beta_s \geq 0, \beta_w \geq 0 \qquad (1)$$

As the soil is saturated, the volume fraction of water equals the porosity of soil $\mathbf{n}$. The true densities of constituents ρ_s and ρ_w are taken as constants. The mass fractions (mass per unit volume of porous medium) are $\rho_s\beta_s$ and $\rho_w\beta_w$. The porous medium is considered as a mixture of constituents, where volume fractions are defined at every point of the continuum.

The velocities of the particles of constituents are denoted by $\vec{\mathbf{U}}_s$ and $\vec{\mathbf{U}}_w$. The relative velocity of water with respect to skeleton is $\vec{\mathbf{U}}_w = \vec{\mathbf{U}}_w - \vec{\mathbf{U}}_s$. The material time derivatives of a quantity $\mathbf{f}$ following constituent k is

$$\frac{d^{(k)}\mathbf{f}}{dt} = \frac{\partial \mathbf{f}}{\partial t} + \mathrm{grad}\mathbf{f}.\vec{\mathbf{U}}_k \qquad (2)$$

The rate of deformation is

$$\mathbf{D}_k = \mathbf{D}\left(\vec{\mathbf{U}}_k\right) = \frac{1}{2}\left\{\mathrm{grad}\mathbf{U}_k + \left(\mathrm{grad}\mathbf{U}_k\right)^T\right\} \tag{3}$$

The displacement vector of skeleton is $\vec{\mathbf{u}}_s$ and the infinitesimal strain tensor is given by the operator $\mathbf{D}$

$$\mathbf{E}_s = \mathbf{D}\left(\vec{\mathbf{u}}_s\right) = \frac{1}{2}\left\{\mathrm{grad}\vec{\mathbf{u}}_s + \left(\mathrm{grad}\vec{\mathbf{u}}_s\right)^T\right\} \tag{4}$$

The general conservation law of continuum mechanics /2/

$$\frac{d}{dt}\int_\Omega A\,d\Omega = -\int_{\partial\Omega} \vec{\mathbf{a}}.\vec{\mathbf{n}}\,d\Gamma + \int_\Omega \mathbf{A}_d\,d\Omega + \int_\Omega \mathbf{A}_p\,d\Omega \tag{5}$$

is frequently used in this paper. In eq.(5), A denotes the quantity studied, $\vec{\mathbf{a}}$ is the flux lost through the surface of the volume considered, $\mathbf{A}_d$ the given rate of production of the quantity and $\mathbf{A}_p$ the unknown rate of production of the quantity. $\vec{\mathbf{n}}$ is the outward unit normal of surface $\partial\Omega$. The local form of the conservation law (5) is

$$\frac{\partial A}{\partial t} + \mathrm{div}\left(A\vec{\mathbf{U}} + \vec{\mathbf{a}}\right) - \mathbf{A}_d = \mathbf{A}_p \quad \text{in } \Omega \tag{6}$$

where $\vec{\mathbf{U}}$ is the velocity of the material.

BALANCE LAWS OF MIXTURE

The balance laws of mass, momentum and energy for the mixture of skeleton and water are derived by use of the general conservation law (6) (see /2/).

The rate of production of mass of constituent k is

$$\theta_k = \frac{\partial}{\partial t}\left(\rho_k \beta_k\right) + \mathrm{div}\left(\rho_k \beta_k \vec{\mathbf{U}}_k\right),\ k \in \{s, w\} \tag{7}$$

The conservation law holds for each constituent

$$\theta_s = 0, \theta_w = 0 \tag{8}$$

The rate of production of linear momentum is

$$\vec{\mathbf{m}}_k = -\mathrm{div}\sigma_k - \vec{\mathbf{f}}_k + \rho_k \beta_k \frac{d^{(k)}\vec{\mathbf{U}}_k}{dt} + \theta_k \vec{\mathbf{U}}_k,\ k \in \{s, w\} \tag{9}$$

The balance of linear momentum is

$$\vec{\mathbf{m}}_s + \vec{\mathbf{m}}_w = \vec{0} \tag{10}$$

σ_k is the stress tensor of constituent k and $\mathbf{f}_k$ the body force per unit volume. The total stress acting on a surface element is $\left(\sigma_s + \sigma_w\right).\vec{\mathbf{n}}$. In the application to the soil problem, the inertia

terms in eq.(9) will be neglected.

The rate of production of energy obtains the form

$$\mathbf{I}_k = \frac{\partial}{\partial \mathbf{t}}\left(\mathbf{e}_k + \frac{1}{2}\rho_k\beta_k\vec{\mathbf{U}}_k.\vec{\mathbf{U}}_k\right) + \mathrm{div}\left\{\left(\mathbf{e}_k + \frac{1}{2}\rho_k\beta_k\vec{\mathbf{U}}_k.\vec{\mathbf{U}}_k\right)\vec{\mathbf{U}}_k + \vec{\mathbf{q}}_k - \vec{\mathbf{U}}_k.\sigma_k\right\} - \mathbf{r}_k - \\ -\vec{\mathbf{f}}_k.\vec{\mathbf{U}}_k,\ \ k\in\{s,w\} \qquad (11)$$

The balance law of energy is

$$\mathbf{I}_s + \mathbf{I}_w = 0 \qquad (12)$$

In eq.(11), $\mathbf{e}_k$ is the internal energy of constituent k per unit volume, $\vec{\mathbf{q}}_k$ the heat flux from the volume to the exterior, $\mathbf{r}_k$ the given rate of production of heat inside the body. Again, the kinetic energy in eq.(11) will be neglected in the application to the soil problem.

ENTROPY INEQUALITY

Next, the second principle of thermodynamics is evoked. The rate of production of entropy per unit volume is

$$\gamma_k = \frac{\partial \mathbf{s}_k}{\partial \mathbf{t}} + \mathrm{div}\left(\mathbf{s}_k\vec{\mathbf{U}}_k\right) + \mathrm{div}\left(\frac{\vec{\mathbf{q}}_k}{\mathbf{T}}\right) - \frac{\mathbf{r}_k}{\mathbf{T}},\ \ k\in\{s,w\} \qquad (13)$$

where $\mathbf{s}_k$ is the entropy of constituent k per unit volume and $\mathbf{T}$ the absolute temperature, which is assumed to be the same for both constituents. Introducing the free energy $\Psi_k=\mathbf{e}_k-\mathbf{T}\mathbf{s}_k$ (per unit volume) and employing the expression (11), eq.(13) can be brought into the form

$$\mathbf{T}\gamma_k = \sigma_k:\mathbf{D}\left(\vec{\mathbf{U}}_k\right) - \left[\frac{\mathrm{d}^{(k)}\Psi_k}{\mathrm{dt}} + \mathbf{s}_k\frac{\mathrm{d}^{(k)}\mathbf{T}}{\mathrm{dt}}\right] - \Psi_k\mathrm{div}\vec{\mathbf{U}}_k - \vec{\mathbf{m}}_k.\vec{\mathbf{U}}_k - \frac{\vec{\mathbf{q}}_k.\mathrm{grad}\mathbf{T}}{\mathbf{T}} + \mathbf{I}_k \qquad (14)$$

According to the second principle, the rate of entropy production is non-negative

$$\mathbf{T}(\gamma_s + \gamma_w) \geq 0 \qquad (15)$$

This is the Clausius-Duhem inequality, which has to be satisfied for all actual evolutions of the mixture. The expression of dissipation in eq.(15) is divided, as usual, into the intrinsic or mechanical dissipation

$$\mathbf{d}_1 = \sum_k\left\{\sigma_k:\mathbf{D}\left(\vec{\mathbf{U}}_k\right) - \frac{\mathrm{d}^{(k)}\Psi_k}{\mathrm{dt}} - \mathbf{s}_k\frac{\mathrm{d}^{(k)}\mathbf{T}}{\mathrm{dt}} - \Psi_k\mathrm{div}\vec{\mathbf{U}}_k - \vec{\mathbf{m}}_k.\vec{\mathbf{U}}_k\right\} \qquad (16)$$

and the thermal dissipation

$$\mathbf{d}_2 = -\sum_k\frac{\vec{\mathbf{q}}_k.\mathrm{grad}\mathbf{T}}{\mathbf{T}} = -\frac{\vec{\mathbf{q}}.\mathrm{grad}\mathbf{T}}{\mathbf{T}} \qquad (17)$$

It is required that both the intrinsic and the thermal dissipation are separately non-negative for any real evolution of the state of the mixture.

CONSTITUTIVE EQUATIONS

The entropy inequality does not directly give any constitutive laws but rather gives a certain condition to be satisfied in admissible evolutions of the phenomenon. As a matter of fact, the constitutive behaviour is determined by the choice of the variables describing the state and the dissipative properties of the material and by the choice of the expressions of the free energy and of the pseudo-potential of the constituents. Here, the set of variables defining the the state of porous medium is chosen

$$\left\{\mathbf{T},\beta_s,\beta_w,\mathbf{D}(\vec{\mathbf{u}}_s)\right\} \tag{18}$$

The volume fractions, however, are not independent but constrained by conditions (1). To begin with, smooth convex functions of volumetric free energies are assumed

$$\Psi_w = \Psi_w(\mathbf{T},\beta_s,\beta_w)$$
$$\Psi_s = \Psi_s\left(\mathbf{T},\beta_s,\beta_w,\mathbf{D}(\vec{\mathbf{u}}_s)\right) \tag{19}$$

The internal constraints (1) imposed on volume fractions are taken into account by adding the indicator function $\mathbf{I}(\beta_s,\beta_w)$ (see /1/) to the sum of free energies of constituents. Hence, the free energy of the mixture takes on the form

$$\Psi = \Psi_s + \Psi_w + \mathbf{T}\mathbf{I}(\beta_s,\beta_w) \tag{20}$$

The indicator function is multiplied by the temperature in order to have the internal energy which does not contain $\mathbf{I}$. The indicator function is a function from $\mathbf{R}^2$ to $\overline{\mathbf{R}} = \mathbf{R}\cup\{+\infty\}$

$$\mathbf{I}(\beta_s,\beta_w) = 0, \text{ if } (\beta_s,\beta_w)\in\mathbf{C}, \ +\infty \text{ otherwise} \tag{21}$$

The set $\mathbf{C}\subset\mathbf{R}^2$ is the convex set defined by the constraints (1) (see FIGURE 1)

$$\mathbf{C} = \left\{(\beta_s,\beta_w)\in\mathbf{R}^2 \,|\, \beta_s+\beta_w = 1, \beta_s\geq 0, \beta_w\geq 0\right\} \tag{22}$$

Thus, the constraints are considered as material properties. By means of the indicator function the free energy is forced to take only the values which comply with the constraints.

Next, the expression of dissipation (16) will be formed.

For water, the smooth expression of free energy $(19)_2$ is used, but the indicator function is added to the free energy of skeleton. To shorten the writing, the notation

$$\mathbf{B}_{kj} = \frac{\partial \Psi_k}{\partial \beta_j} \tag{23}$$

is introduced. For the non-smooth indicator function, the concept of subdifferential is used (see /1/)

$$\left(\hat{\mathbf{B}}_s, \hat{\mathbf{B}}_w\right) \in \partial \mathbf{I}(\beta_s, \beta_w) \tag{24}$$

i.e. the subgradient defined by the set $(\hat{\mathbf{B}}_s, \hat{\mathbf{B}}_w)$ belongs to the subdifferential $\partial \mathbf{I}$ of function $\mathbf{I}$. From FIGURE 1 it can be seen that $\hat{\mathbf{B}}_s = \hat{\mathbf{B}}_w$ in case $\beta_S>0$, $\beta_W>0$ while $\hat{\mathbf{B}}_s \geq \hat{\mathbf{B}}_w$ in case $\beta_S=1$, $\beta_W=0$. Further, it is taken into account that the derivatives $d^{(w)}\beta_j/dt$ and $d^{(s)}\beta_j/dt$ are not independent but according to formula (2) related by

$$\frac{d^{(w)}\beta_j}{dt} = \frac{d^{(s)}\beta_j}{dt} + \vec{\mathbf{U}}_w . \operatorname{grad}\beta_j \tag{25}$$

The expression of dissipation (16) can now be written in the form

$$\begin{aligned} \mathbf{d}_1 = {} & \sigma_s : \mathbf{D}\left(\vec{\mathbf{U}}_s\right) - \frac{\partial \Psi_s}{\partial \mathbf{E}_s} : \mathbf{D}\left(\vec{\mathbf{U}}_s\right) - \Psi_s \operatorname{div}\vec{\mathbf{U}}_s - \left(\mathbf{B}_{ss} + \hat{\mathbf{B}}_s + \mathbf{B}_{ws}\right)\frac{d^{(s)}\beta_s}{dt} + \\ & + \sigma_w : \mathbf{D}\left(\vec{\mathbf{U}}_w\right) - \Psi_w \operatorname{div}\vec{\mathbf{U}}_w - \left(\mathbf{B}_{sw} + \hat{\mathbf{B}}_w + \mathbf{B}_{ww}\right)\frac{d^{(w)}\beta_w}{dt} - \\ & - \left\{\vec{\mathbf{m}}_w - \left(\mathbf{B}_{sw} + \hat{\mathbf{B}}_w\right)\operatorname{grad}\beta_w + \mathbf{B}_{ws}\operatorname{grad}\beta_s\right\} . \vec{\mathbf{U}}_w \end{aligned} \tag{26}$$

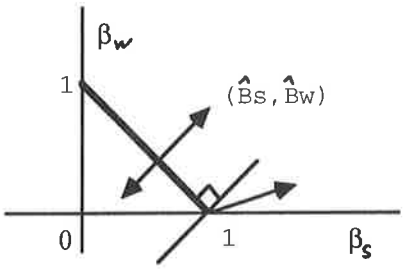

FIGURE 1. Subgradients of the indicator function of convex set $\mathbf{C}$.

The dissipative behaviour of the mixture is assumed to depend on the mass flow of water $\rho_w \beta_w \vec{\mathbf{U}}_w$ (with respect to the skeleton) and on the heat flow

$$\Phi_1 = \Phi_1\left(\rho_w \beta_w \vec{\mathbf{U}}_w\right), \quad \Phi_2 = \Phi_2\left(\vec{\mathbf{q}}\right) \tag{27}$$

The functions of pseudo-potential Φ are required to be convex,

non-negative and zero at the origin.

According to the principle of the accompanying local equilibrium state /3/, the intrinsic dissipation is

$$\mathbf{d}_1 = \frac{\partial \Phi_1}{\partial \rho_w \beta_w \vec{\mathbf{U}}_w} \cdot \rho_w \beta_w \vec{\mathbf{U}}_w \tag{28}$$

which is always non-negative because of the properties of Φ_1. It is required that the intrinsic dissipation (26) equals the expression (28) for any real evolution, i.e. an evolution satisfying the mass balance conditions (8). Thus, the Clausius-Duhem inequality will be satisfied, if the dissipation (26) augmented by mass balance conditions by means of Lagrange multipliers η_s and η_w

$$\mathbf{d}_1 + \eta_s \theta_s + \eta_w \theta_w \tag{29}$$

equals the dissipation (28) for any evolution. This yields the relationships

$$\sigma_s^D = \left(\frac{\partial \Psi_s}{\partial \mathbf{E}_s} \right)^D$$

$$\sigma_w^D = 0$$

$$\mathbf{p}_s = -\frac{1}{3} \mathrm{tr} \frac{\partial \Psi_s}{\partial \mathbf{E}_s} - \Psi_s + \beta_s \left(\mathbf{B}_{ss} + \mathbf{B}_{ws} + \hat{\mathbf{B}}_s \right)$$

$$\mathbf{p}_w = -\Psi_w + \beta_w \left(\mathbf{B}_{sw} + \mathbf{B}_{ww} + \hat{\mathbf{B}}_w \right)$$

$$\frac{\partial \Phi_1}{\partial \rho_w \beta_w \vec{\mathbf{U}}_w} = -\frac{1}{\rho_w \beta_w} \left\{ \vec{\mathbf{m}}_w - \left(\mathbf{B}_{sw} + \hat{\mathbf{B}}_w \right) \mathrm{grad} \beta_w + \mathbf{B}_{ws} \mathrm{grad} \beta_s \right\} \tag{30}$$

Above, the division of second order tensors into deviatoric and spherical parts has been employed, e.g. $\sigma = \sigma^D - \mathbf{p}\mathbf{1}$, $\mathbf{p} = -(\mathrm{tr}\sigma)/3$. The four first equations (30) are the equations of state while the last one is a complementary constitutive equation. The thermal dissipation (17) and the dissipation potential Φ_2 lead to the generalized Fourier law of heat conduction

$$\frac{\partial \Phi_2}{\partial \vec{\mathbf{q}}} = -\frac{1}{\mathbf{T}} \mathrm{grad} \mathbf{T} \tag{31}$$

The complete system of equations is constituted by mass balance equations (8), momentum balance (10), energy balance (12), constitutive equations (30) and (31) and the condition (1), altogether 25 equations. The unknowns are $\mathbf{T}, \beta_s, \beta_w, \vec{\mathbf{U}}_s, \vec{\mathbf{U}}_w, \sigma_s, \sigma_w$, $\vec{\mathbf{q}}$, and $\hat{\mathbf{B}}_s = \hat{\mathbf{B}}_w$, also 25 in number.

APPLICATION

The expressions of free energy (19) and of dissipation potential (27) are still in a rather general form, limited only by the choice of variables, and, consequently, so are also the constitutive equations (30) and (31). Here, a specific choice of free energies is made

$$\Psi_s = \beta_s\left\{-\rho_s C_s T\ln\left(\frac{T}{T_0}\right)+\frac{1}{2}K_s(\mathrm{tr}E_s)^2+\mu_s E_s^D:E_s^D-3\alpha_s K_s(\mathrm{tr}E_s)(T-T_0)\right\}$$

$$\Psi_w = \rho_w\beta_w\left\{-C_w T\ln\left(\frac{T}{T_0}\right)-L\frac{T-T_0}{T_0}\right\} \qquad (32)$$

The coefficients C_s and C_w are the specific heat capacities. The constant L is related to the latent heat of fusion of water ℓ: defining the latent heat as discontinuity of specific internal energy $\ell=\hat{e}^+-\hat{e}^-$, the relationship $\ell=(C_w^+-C_w^-)T_0+L$ follows. T_0 is the temperature of fusion, 0°C in normal conditions. K_s, μ_s and α_s are the bulk modulus, the shear modulus and the coefficient of thermal expansion of skeleton, respectively. Expression $(32)_2$ means that water is considered incompressible. The dissipation potentials are chosen as quadratic functions with constant coefficients k_d and k_T

$$\Phi_1=\frac{1}{2k_d}\left(\rho_w\beta_w\vec{U}_w\right)^2,\Phi_2=\frac{1}{2k_T}(\vec{q})^2 \qquad (33)$$

Use of expressions (32) and (33) in eqs.(30) and (31) results in constitutive equations

$$\sigma_s=\beta_s\left\{2\mu_s E_s^D+K_s\left[\mathrm{tr}E_s-3\alpha_s(T-T_0)\right]-\hat{B}_s\right\}$$

$$p_w=\beta_w\hat{B}_w$$

$$\beta_w\vec{U}_w=-\frac{k_d}{\rho_w}\left\{\mathrm{grad}\left(\frac{p_w}{\rho_w\beta_w}\right)-\frac{\vec{f}_w}{\rho_w\beta_w}\right\}$$

$$\vec{q}=-\frac{k_T}{T}\mathrm{grad}T=-\lambda\mathrm{grad}T \qquad (34)$$

Eq.$(34)_2$ means that the interstitial pressure of water $p_w/\beta_w=\hat{B}_w$ is indeterminate. Eq.$(34)_3$ can be recognized as Darcy's law of water flow in porous medium, and eq.$(34)_4$ is the classical Fourier's law of heat conduction. The coefficient of hydraulic conductivity is $k=k_d g/\rho_w$. g is the acceleration of gravity.

The equations of the problem permit to derive the well-known equation of consolidation of saturated soil by Terzaghi /4/. In fact, denoting the porosity of soil by $n = \beta_w$, and assuming the stress of skeleton also to be spherical, $\sigma_s = -p_s 1$, and the temperature field uniform, the system of equations can be written in the form

$$-\frac{\partial n}{dt} + \mathrm{div}\left[(1-n)\vec{U}_s\right] = 0$$

$$\frac{\partial n}{dt} + \mathrm{div}\left(n\vec{U}_s\right) + \mathrm{div}\left(n\vec{U}_w\right) = 0$$

$$-\mathrm{grad}\left(p_s + p_w\right) + \vec{f}_s + \vec{f}_w = 0$$

$$p_s = -(1-n)K_s \mathrm{div}\,\vec{u}_s + (1-n)u$$

$$p_w = nu$$

$$n\vec{U}_w = -k\left\{\mathrm{grad}\left(\frac{p_w}{\rho_w n g}\right) - \frac{\vec{f}_w}{\rho_w n g}\right\} \qquad (35)$$

u is the true interstitial pressure of water. Further, assuming the total pressure $p = p_s + p_w$ to be independent of time and neglecting the spatial variation of porosity, the equation of consolidation can be derived

$$\frac{\partial u}{\partial t} = k\left[(1-n)K_s + p - u\right]\mathrm{div}\,\mathrm{grad}\left(\frac{u}{\rho_w g}\right) \qquad (36)$$

Eq.(36) is comparable to the equation of Terzaghi, if the modulus of compressibility is taken as

$$M_s = (1-n)K_s + p - u \qquad (37)$$

REFERENCES

1. Frémond M., Mixtures and phase changes in solid mechanics. Proc. of the 3rd Finnish Mechanics Days. Helsinki Univ. of Technology, Inst. of Mech., Otaniemi 1988/26, pages 1-33.

2. Germain P., Mécanique, Tome II. Ellipses, Paris, 1986.

3. Germain P., Nguyen Q.S., Suquet P., Continuum thermodynamics. J.Appl.Mech.ASME, Vol.50,Dec. 1983,pages 1010-1020.

4. Terzaghi K., Erdbaumechanik auf bodenphysikalischer Grundlage. Leipzig-Wien, Franz Deuticke, 1925. 399 pp.

DISLOCATION CORE STRUCTURES IN METALS

JUHANI VON BOEHM and RISTO M. NIEMINEN
Helsinki University of Technology
Otakaari 1, 02150 ESPOO, FINLAND

ABSTRACT

The atomic core structure of the imperfect [112] edge dislocation in gold is studied as a generic example of dislocation core structures in fcc metals. Molecular dynamics simulation is used. The interatomic interactions are modelled by the many-body ATVF and glue models. Newton's equations of motion are solved with the velocity-Verlet algorithm. The computations are carried out using a rectangular geometry with periodic boundaries along the [112]-direction and fixed boundaries determined by the linear elasticity theory in the perpendicular directions. The imperfect [112] edge dislocation appears as two partial [112] dislocations with a stacking fault ribbon in between. The range of the transition from the fcc stacking into the hcp stacking fault is about 20 Å. Most pronounced changes occur near the edge. Detailed atomic core structures are reported.

INTRODUCTION

The (isotropic) elasticity theory gives for the total energy stored per unit length of a straight dislocation the following expression:

$$w_t = \frac{Kb^2}{4\pi}\ln\left(\frac{R}{r_0}\right) + w_0 \qquad (1)$$

where the first term on the right-hand side is the strain energy of the linear elastic field per unit length, K is a constant (energy factor), b is the magnitude of the Burgers vector, R is the outer radius of a circular cylinder within which the energy is evaluated (the dislocation line being the axis of that cylinder), r_0 is the core radius, and w_0 is the core energy per unit dislocation length [1]. When r_0 approaches zero the first term on the right-hand side diverges. This artifact is due to the neglect of the discrete atomic structure.

The purpose of the present study is to obtain realistic atomic core structures in the neighbourhood of a straight edge dislocation. Although we study the special case of the imperfect [112] edge dislocation in gold we believe that our results are generic for face centered cubic (fcc) metals.

The fcc crystal structure of gold is shown in Fig. 1. The [112] edge dislocation (z-axis)

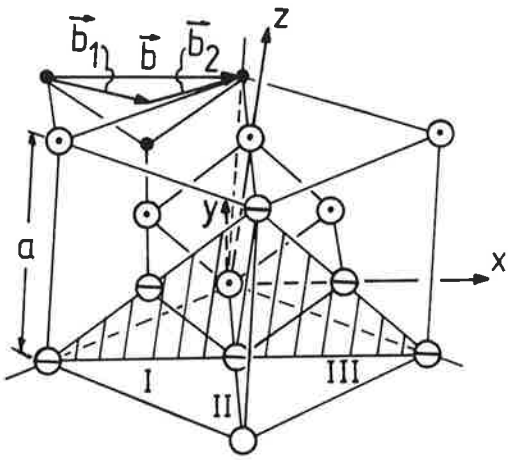

FIGURE 1. Face-centered cubic crystal structure of gold. a denotes the lattice constant and $\boldsymbol{b}$ the Burgers-vector of the perfect [112] edge dislocation. $\boldsymbol{b}_1$ and $\boldsymbol{b}_2$ denote the partial Burgers-vectors. The circles with a bar represent atoms in the $(11\bar{1})$ glide-plane (shaded). The circles with a dot represent atoms in the $(11\bar{1})$-plane which contains the edges of the partial dislocations. The small filled circles represent atoms behind this plane. The open circle represents an atom in the $(11\bar{1})$-plane in front of the glide plane.

can be formed energetically most easily because the corresponding Burgers vector $\boldsymbol{b} = a\boldsymbol{u}_x / \sqrt{2}$ has the smallest possible length and thus minimizes the stored energy proportional to b^2 (Eq. (1)). The $(11\bar{1})$ plane is most densely packed and acts as the glide-plane. However, since $\boldsymbol{b}$ contains two atomic planes, it can be further divided into two partial Burgers vectors $\boldsymbol{b}_1$ and $\boldsymbol{b}_2$:

$$\boldsymbol{b} = \boldsymbol{b}_1 + \boldsymbol{b}_2 = \left(a\boldsymbol{u}_x / \sqrt{2} - a\boldsymbol{u}_y / \sqrt{6}\right)/2 + \left(a\boldsymbol{u}_x / \sqrt{2} + a\boldsymbol{u}_y / \sqrt{6}\right)/2 \ . \tag{2}$$

Since

$$b^2 > b_1^2 + b_2^2 \tag{3}$$

the edge dislocation containing two half-planes has a tendency to separate into two partial dislocations containing one half-plane each.

The starting geometry was prepared as follows [2]. The half-planes I and II were removed (see Fig. 1) and the half-plane III was moved by $-\boldsymbol{b}/2$. Then the atoms for $x > 0$ were displaced using the isotropic elasticity theory [1] by

$$u_x = \frac{b}{2\pi}\left[\arctan\left(\frac{y}{x}\right) + \frac{1}{2(1-\nu)}\,\frac{xy}{x^2+y^2}\right]$$

$$u_y = \frac{b}{4\pi(1-\nu)}\left[(1-2\nu)\ln\left(\sqrt{x^2+y^2}\right) + \frac{x^2}{x^2+y^2}\right] \tag{4}$$

$$u_z = 0$$

and the atoms for $x < 0$ symmetrically with respect to the $x = 0$ plane (ν is the Poisson ratio).

In all cases we used a rectangular geometry with periodic boundaries with the period of $\sqrt{6}a$ or $1.5 \cdot \sqrt{6}a$ containing 12 or 18 atom planes, respectively, in the [112]-direction (z-axis in Fig. 1). The $(1\bar{1}0)$ surfaces were fixed and the $(11\bar{1})$ surfaces were either free or fixed (thickness of the fixed layer 8-10 Å).

METHODS

The traditional pair-potential approximation (PPA) has following deficiences. The Cauchy ratio C_{12}/C_{44} in PPA equals 1 whereas in reality it equals 1.5...3.7 for fcc metals. The energy ratio e_v/e_c (e_v is the vacancy formation energy, e_c is the cohesion energy/atom) in short-ranged PPA equals about 1 whereas in reality it equals 0.25...0.36 for fcc metals. To describe these and also some other properties correctly one must go beyond PPA. One practical way of doing this is to use the recently derived semiempirical many-body approximations where the total energy is written in the following generic form [3-9]

$$V = \frac{1}{2}\sum_{i,j=1}^{N}{}' \Phi\left(\left|\boldsymbol{r}_i - \boldsymbol{r}_j\right|\right) + \sum_{i=1}^{N} U(n_i) \tag{5}$$

where

$$n_i = \sum_{j=1}^{N}{}' \rho\left(\left|\boldsymbol{r}_i - \boldsymbol{r}_j\right|\right). \tag{6}$$

In Eqs. (5) and (6) Φ is the mainly repulsive pair-potential, $\boldsymbol{r}_i$ is the position vector of nucleus i, U is the mainly attractive many-body potential, $'$ indicates that $i = j$ term should be omitted in the summation, n_i is the background density at nucleus i determined by the density functions ρ of the surrounding atoms. By taking the proper derivatives of Eqs. (5) and (6) we get for the force acting on nucleus i the following expression:

$$\boldsymbol{F}_i = -\nabla_i V =$$

$$= -\sum_{j}{}' \left\{\Phi'\left(\left|\boldsymbol{r}_i - \boldsymbol{r}_j\right|\right) + \left[U'(n_i) + U'(n_j)\right]\rho'\left(\left|\boldsymbol{r}_i - \boldsymbol{r}_j\right|\right)\right\} \frac{\boldsymbol{r}_i - \boldsymbol{r}_j}{\left|\boldsymbol{r}_i - \boldsymbol{r}_j\right|} \tag{7}$$

where $'$ in Φ, U and ρ denotes a derivative with respect to the argument.

Newton's equations of motion

$$m\,\ddot{\boldsymbol{r}}_i = \boldsymbol{F}_i \qquad i = 1,2,\cdots,N \tag{8}$$

(m is the mass of the atoms) were solved using the velocity-Verlet algorithm [10]:

$$
\begin{aligned}
&a)\quad \boldsymbol{r}_i(t+\delta t) = \boldsymbol{r}_i(t) + \delta t \boldsymbol{v}_i(t) + \frac{1}{2}\delta t^2 \boldsymbol{a}_i(t) \\
&b)\quad \boldsymbol{v}_i\left(t+\frac{1}{2}\delta t\right) = \boldsymbol{v}_i(t) + \frac{1}{2}\delta t \boldsymbol{a}_i(t) \\
&c)\quad \boldsymbol{a}_i(t+\delta t) = \boldsymbol{F}_i(t+\delta t)/m \quad (\textit{from Eq. (7)}) \\
&d)\quad \boldsymbol{v}_i(t+\delta t) = \boldsymbol{v}_i\left(t+\frac{1}{2}\delta t\right) + \frac{1}{2}\delta t \boldsymbol{a}_i(t+\delta t)
\end{aligned}
\tag{9}
$$

where the time step δt used was 5 fs, $\boldsymbol{v}_i \equiv \dot{\boldsymbol{r}}_i$ and $\boldsymbol{a}_i \equiv \ddot{\boldsymbol{r}}_i$.

The solution of Eqs. (8) corresponds to the normal molecular dynamics (MD) where the number of atoms N, the volume of the system V and the total energy E are constant. We also used modified equations of motion [11,12]

$$
\begin{aligned}
&\ddot{\boldsymbol{r}}_i = \frac{1}{m}\boldsymbol{F}_i - \xi\,\dot{\boldsymbol{r}}_i \\
&\dot{\xi} = \frac{1}{Q}\left(\sum_{i=1}^{N} m\dot{\boldsymbol{r}}_i^2 - n_f k_B T\right)
\end{aligned}
\tag{10}
$$

where ξ is the friction coefficient controlling absolute temperature T, Q is the thermal inertia parameter, n_f is the degrees of freedom (= 3N) and k_B is Boltzmann's constant. The solution of Equations (10) corresponds to the constant - NVT MD. Equations (10) were solved using our modified velocity-Verlet algorithm [13].

RESULTS AND DISCUSSION

All the simulations either with the ATVF [8] or glue model [5,6] and either with free or fixed $(11\bar{1})$ surfaces resulted in a quite similar structures. Figures 2 and 3 show as a typical

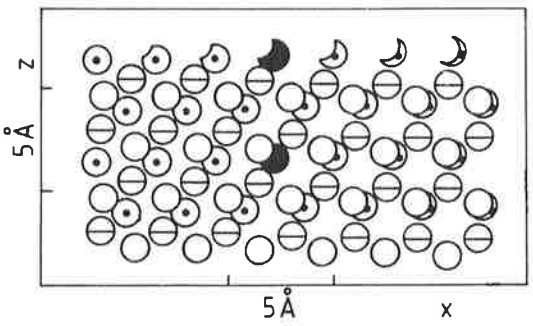

FIGURE 2. The structure of the left partial dislocation. The atoms of the glide plane (circles with a bar) and the two neighbour planes are shown. The filled circles represent the atoms of the edge of the partial dislocation. For further information see Fig. 1 and the text.

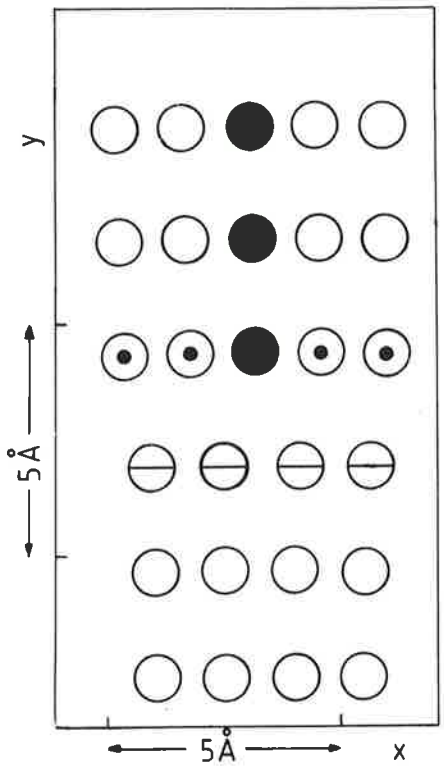

FIGURE 3. The structure near the edge of the left partial dislocation. The filled circles represent the atoms of the extra plane. The circles with a bar belong to the glide plane. For further information see Fig. 1 and the text.

example the structure of the left partial dislocation core obtained from an ATVF constant-NVE MD simulation (Eq. (8), 4694 atoms out of which 408 fixed on the $(1\bar{1}0)$ surfaces, 17880 time steps, free $(11\bar{1})$ surfaces, period $\sqrt{6}a$ with 12 atom planes, x- and y-dimensions of the movable region 180 and 40 Å, respectively). The distance between the left and right partial dislocations is 33 Å that should be compared with the estimated value of 40 Å. It is immediately obvious that the crystal near the edge of the partial dislocation is by no means "bad". The change from the fcc stacking on the left hand side in Fig. 2 to the hcp stacking fault ribbon on the right hand side takes continuously place in the region of about 20 Å. The effect of the extra half plane (black circles in Figs 2 and 3) is to distort the surroundings quite regularly. As can be expected the most pronounced changes occur near the edge.

CONCLUSIONS

This study shows that the molecular dynamics simulation is a powerful method in obtaining microscopic information about extended defects in crystals. This paper presents the detailed atomic structure of the [112] imperfect edge dislocation in the fcc metal gold. The atomic arrangement around the partial dislocation is seen to be quite regular.

ACKNOWLEDGEMENT

The authors would like to thank Mrs. T. Aalto for expert typing of the manuscript.

REFERENCES

1. C. Teodosiu, Elastic Models of Crystal Defects, Springer-Verlag 1982.

2. R.M.J. Cotterill and M. Doyama, Phys. Rev. **145**, 465 (1966).

3. M.S. Daw and M.I. Baskes, Phys. Rev. Lett. **50**, 1285 (1983).

4. M.S. Daw and M.I. Baskes, Phys. Rev. **B29**, 6443 (1984).

5. F. Ercolessi, E. Tosatti and M. Parrinello, Phys. Rev. Lett. **57**, 719 (1986).

6. F. Ercolessi, M. Parrinello and E. Tosatti, Phil. Mag. **A58**, 213 (1988).

7. M.W. Finnis and J.E. Sinclair, Phil. Mag. **A50**, 45 (1984).

8. G.J. Ackland, G. Tichy, V. Vitek and M.W. Finnis, Phil. Mag. **A56**, 735 (1987).

9. M.S. Daw, Phys. Rev. **B39**, 7441 (1989).

10. W.C. Swope, H.C. Andersen, P.H. Berens and K.R. Wilson, J. Chem. Phys. **76**, 637 (1982).

11. W.G. Hoover, Phys. Rev. **A31**, 1695 (1985).

12. D.J. Evans and B.L. Holian, J. Chem. Phys. **83**, 4069 (1985).

13. J. von Boehm and R.M. Nieminen, to appear in the Proceedings of the Europhysics Conference on Computational Physics (CP90) Amsterdam 1990, ed. A.G. Tenner.

INFLUENCE OF THE FOUNDATION ON THE COMPRESSIVE STRENGTH OF THIN PLATES

PAAVO HASSINEN
Department of Structural Engineering
Helsinki University of Technology
Rakentajanaukio 4, SF-02150 ESPOO, FINLAND

ABSTRACT

Buckling strength values of plates supported by an elastic foundation are needed in the design of some civil engineering applications. In the literature several foundation models have been presented beginning from the simple Winkler's foundation model to elastic half space models inclusive nonlinear and tensionless foundations. The paper studies the buckling behaviour of long simply supported plates on elastic foundations. The linear buckling stresses of these plates can in many loading cases be solved analytically and some expressions are given in the paper. The evaluation of the ultimate compressive strength is a more complicated problem. In the paper some numerical results are given and discussed.

INTRODUCTION

The analysis of beams and plates on elastic foundations is a very common problem in the civil engineering practice. The usual question is the influence of the foundation on bending moments, shear forces and deflections of a beam or a plate. The most often used elastic foundation models are the Winkler's foundation, two-parameter foundation models and the elastic half space. Beside the elastic foundation also nonlinear elastic and viscoelastic foundation models are developed especially for the use in geotechnics. The methods of the analysis of beams and plates supported by a foundation depend very much on the chosen foundation model. If the horizontal displacements are neglected, as it is done in most one- and two-parameter models, the solution can be found by solving the governing differential equation for a plate (1), in which the additional parameter is the foundation coefficient C. In a general case a coupled problem of the foundation and the structure has to be solved. To study the behaviour of beams and plates on viscoelastic or nonlinear elastic foundations efficient iterative procedures have been developed. The choice between the foundation models depends usually on the possibilities to define the foundation parameters experimentally.

$$D\nabla^4 w + Cw = q + N_x^o \frac{\partial^2 w}{\partial x^2} + 2N_{xy}^o \frac{\partial^2 w}{\partial x \partial y} + N_y^o \frac{\partial^2 w}{\partial y^2} \qquad (1)$$

In some civil engineering applications beams and plates on an elastic foundation are loaded by compressive forces in their plane and therefore, the buckling strength value of them is needed. Among these e.g. piles and sheetings in the ground and face plates of sandwich panels can be mentioned. The utilization of the stiffness and the strength properties of this lateral support is beside the theoretical interest a thing of the utmost consequence also in the practical design work. This paper discusses the influence of the linear elastic foundation to the behaviour of uniaxially compressed long simply supported plates. The significance of the slenderness of the plate and the stiffness of the foundation are studied and analytical and numerical examples as well as some practical calculation models are given. The paper is limited to local buckling problems. The global buckling phenomena and the interaction between the local and global failure modes in plated structures are not studied.

POTENTIAL ENERGY EXPRESSIONS

The total potential energy of an uniaxially compressed plate with straight boundaries and supported by an elastic foundation can be given to a half buckling wave length by

$$U = U_B + U_S + U_C - V \tag{2}$$

where the strain energy of the bending of the plate

$$U_B = \frac{D}{2}\int_0^a\int_0^b (\Delta w)^2 \, dxdy \tag{3}$$

the strain energy due to the stretching of the middle surface

$$U_S = \frac{t}{2E}\int_0^a\int_0^b (\Delta F)^2 \, dxdy \tag{4}$$

the strain energy of the foundation consisting of an elastic half space

$$U_C = \frac{1}{2}\int_0^a\int_0^b\int_0^\infty (\sigma_x \varepsilon_x + \sigma_y \varepsilon_y + \sigma_z \varepsilon_z + \tau_{xy} \gamma_{xy} + \tau_{yz} \gamma_{yz} + \tau_{zx} \gamma_{zx}) \, dxdydz \tag{5a}$$

or of the foundation with negligible horizontal displacements and stresses

$$U_C = \frac{1}{2}\int_0^a\int_0^b\int_0^\infty (\sigma_z \varepsilon_z + \tau_{yz} \gamma_{yz} + \tau_{zx} \gamma_{zx}) \, dxdydz \tag{5b}$$

or

$$U_C = \frac{1}{2}\int_0^a\int_0^b C\, w^2 \, dxdy \tag{5c}$$

and the work done by the axial force $N_x(y)$

$$V = t\int_0^b N_x(y)\, u(x = a, y)\, dy = \frac{t}{2}\int_0^a\int_0^b N_x(y) \left(\frac{\partial w}{\partial x}\right)^2 dxdy \tag{6}$$

The stresses and displacements are assumed to vanish in a linear way or exponentially over the height of the foundation.

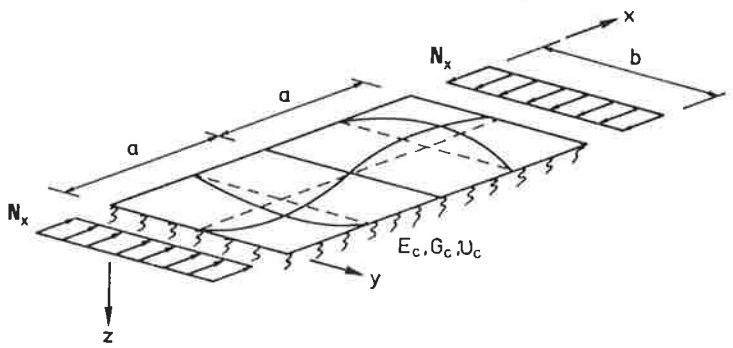

FIGURE 1. Notations used to an uniaxially loaded plate on an elastic foundation.

COMPARISON BETWEEN THE LINEAR BUCKLING STRESSES

When evaluating linear buckling stresses of a long plate strip, simply supported on its longitudinal boundaries (x, y = 0, a) the following sinusoidal expression can be assumed to the deflection w(x,y,z)

$$w(x,y,z) = \Sigma\, h_1(z)\, w_n \sin(\pi x/a) \sin(n\,\pi y/b) \tag{7}$$

where a is an still unknown buckling half wave length. The deflection w and the horizontal displacements u and v in an elastic half space are solved using the Navier's equations for homogeneous isotropic bodies. Complicated mathematical calculations produce the following foundation coefficient to a thick foundation layer with vanishing displacements at the bottom of the foundation and vanishing horizontal displacements on the top of the foundation

$$C_1 = \frac{2\,(1 - \nu_c)\,E_C}{(1 + \nu_c)(3 - 4\nu_c)}\,\pi\,\sqrt{\frac{1}{a^2} + \frac{n^2}{b^2}} \tag{8}$$

which is dependent on the wave length of the buckled plate.

The function $h_1(z)$ to the foundation model with neglected horizontal displacements over the whole depth of the foundation (eqs. 5b, c) is usually written by a simple expression

$$h_1(z) = e^{-kz} \tag{9}$$

k is a decay factor which is solved from the condition $\partial U_C/\partial k = 0$. Assuming $G_{yz} = G_{zx} = G_c$, the method results a foundation coefficient

$$C_2 = \pi\,\sqrt{E_C G_C}\,\sqrt{\frac{1}{a^2} + \frac{n^2}{b^2}} \tag{10}$$

Using the equations (7) with $h_1(z = 0) = 1$ and (5c) and minimizing the total potential energy expression (2) with respect to w_n gives the following equation to the buckling stress

$$\sigma_{cr\,1,2} = K_{1,2}\,\frac{\pi^2 E}{12\,(1 - \nu^2)}\,\left(\frac{t}{b}\right)^2 \tag{11}$$

$$\text{where } K_{1,2} = \left(\frac{1}{\phi} + n^2\phi\right)^2 + R_{1,2}\,\phi^2\,\left(\frac{1}{\phi^2} + n^2\right)^{1/2} \tag{12}$$

$$\phi = a/b \tag{13}$$

$$R_1 = \frac{E_C}{E}\,\frac{12\,(1 - \nu^2)}{\pi^3}\,\frac{2\,(1 - \nu_c)}{(1 + \nu_c)(3 - 4\nu_c)}\,\left(\frac{b}{t}\right)^3 \tag{14}$$

$$R_2 = \frac{\sqrt{E_C G_C}}{E}\,\frac{12\,(1 - \nu^2)}{\pi^3}\,\left(\frac{b}{t}\right)^3 \tag{15}$$

The critical buckling stress is finally found by minimizing the coefficient K with respect to ϕ. The first eigenvalue (n = 1) is shown to be critical in the cases $0 < R_2 < 200$ (Fig. 2).

Several approximate formulae have been given to the critical buckling coefficient K. Using the least squares method the author has defined to the elastic half space foundation model the second and third expressions in table 1. These expressions are exactly valid to steel

plates ($\nu = 0.3$) and to foundations with a Poisson's ratio $\nu_c = 0.25$. The fourth expression in table 1 is found by Davies and Hakmi. It is based on experimental results of polyurethane foamed sandwich panels and is therefore suitable to the practical design work of these panels.

TABLE 1. Approximate buckling coefficients for uniaxially compressed long plates simply supported on their longitudinal edges.

Foundation	Buckling coefficient	Parameter
Winkler's foundation	$K = 2[(R + 1)^{1/2} + 1]$	$R = 0.112 \frac{Cb}{E} \left(\frac{b}{t}\right)^3$
elastic half space E_C, ν_C	$K = 0.703\ R^2 - 0.415\ R + 4.00$	$R = \frac{b}{t}\left(\frac{E_C}{E}\right)^{1/3}$
elastic half space E_C, G_C	$K = 0.985\ R^2 - 0.474\ R + 4.00$	$R = \frac{b}{t}\left(\frac{E_C G_C}{E^2}\right)^{1/6}$
design, el. half space E_C, G_C /2/	$K = [16 + 7\ R + 0.002\ R^2]^{1/2}$	$R = 0.35 \left(\frac{b}{t}\right)^3 \frac{(E_C G_C)^{1/2}}{E}$

An important special case can be found by giving to the equations (11) and (12) $b \to \infty$. Minimizing the buckling stress with respect to the wave length a, the following expressions to the critical wave length and to the stress of this column-type plate strip can be found. The approximate expressions above are based on the Poisson's ratios $\nu = 0.3$ and $\nu_c = 0.25$.

$$a_1 = \pi t \left(\frac{(1 + \nu_c)(3 - 4\nu_c)}{12\,(1 - \nu^2)(1 - \nu_c)}\right)^{1/3} \left(\frac{E}{E_C}\right)^{1/3} \approx 1.816\ t \left(\frac{E^2}{E_C G_C}\right)^{1/6} \tag{16}$$

$$a_2 = \pi t \left(\frac{1}{6\,(1 - \nu^2)}\right)^{1/3} \left(\frac{E^2}{E_C G_C}\right)^{1/6} \approx 1.784\ t \left(\frac{E^2}{E_C G_C}\right)^{1/6} \tag{17}$$

$$\sigma_{cr,1} = 1.8899 \left(\frac{(1 - \nu_c)^2}{3\,(1 + \nu_c)^2 (3 - 4\nu_c)^2 (1 - \nu^2)}\right)^{1/3} (E_C^2 E)^{1/3}$$

$$\approx 0.823\ (E_C G_C E)^{1/3} \tag{18}$$

$$\sigma_{cr,2} = 1.8899 \left(\frac{E_C G_C E}{12\,(1 - \nu^2)}\right)^{1/3} \approx 0.852\ (E_C G_C E)^{1/3} \tag{19}$$

The influence of the foundation stiffness to linear buckling stresses and to the buckling wave lengths in comparison with the pure steel plate ($K = 4.0$, $\phi = a/b = 1.00$) can clearly be seen in the fig. 2.

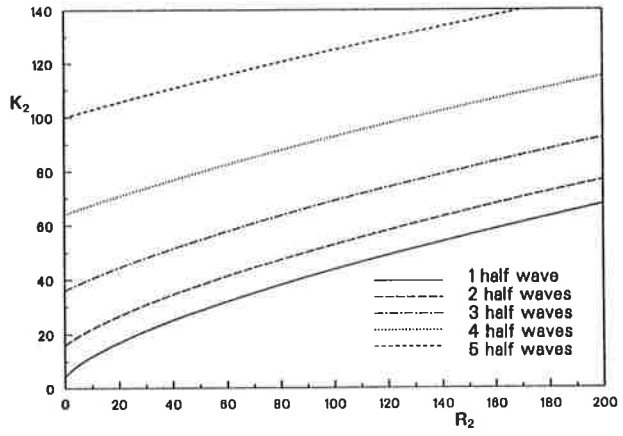

a)

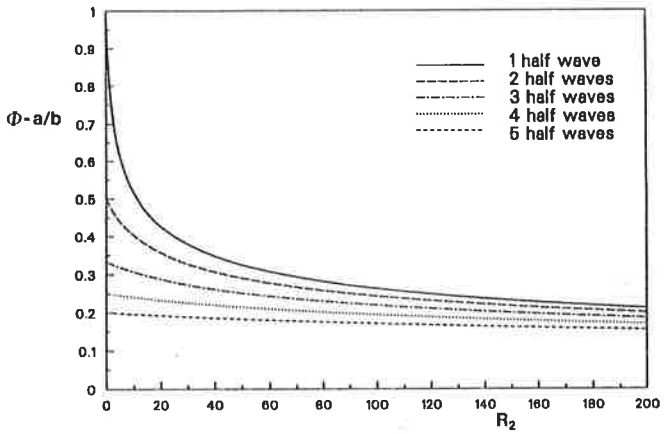

b)

FIGURE 2. a) Buckling coefficients K_2 and b) relative half buckling wave lengths a/b depending on the parameter R_2 and the number of buckling half waves in y-direction.

COMPARISON BETWEEN THE COMPRESSIVE STRENGTHS

In evaluation the compressive strength of plates on elastic foundations the b/t-ratio, the boundary conditions and the yield strength of the plate as well as the stiffness of the foundation are important parameters. One of them can be dominant so, that the plate behaves like a plate without any lateral support, e.g. low b/t-ratios, or like a beam-column in an infinite elastic medium, e.g. very stiff foundation. No analytical models are available to evaluate the ultimate compressive strength of these plates.

For comparison numerical analyses were performed using the ABAQUS finite element code. In the analysis four thin plates were modelled, two of them with and two without a foundation. The plates are simply supported on their longitudinal edges (x, y = a, b) and their b/t-ratios are 100 or 500. The foundation model in the analyses corresponds the elastic half space in which the horizontal displacements are taken into consideration (Fig. 3). The lengths a in the models were defined using the analytical calculation methods and they correspond the first critical wave length.

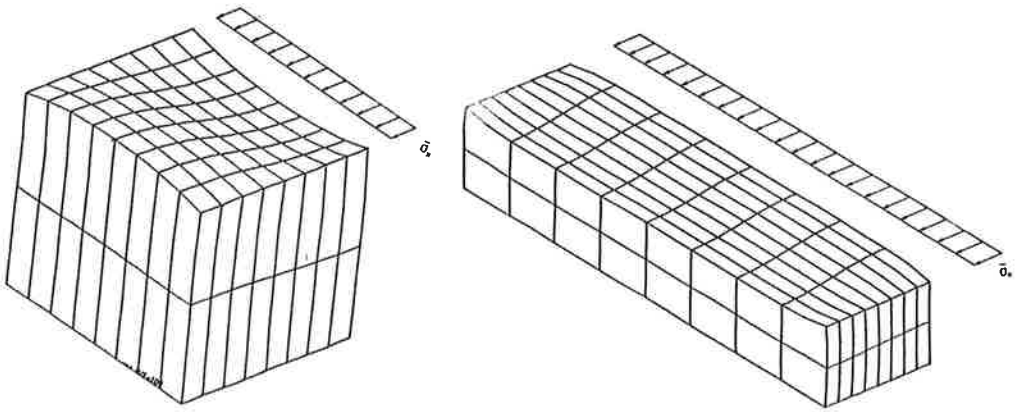

FIGURE 3. Deformed FEM models of thin steel plates on an elastic half space. One half wave length and the full width of the plate is modelled. The faces consist of 8 x 8 8-node shell elements and the foundation of 8 x 8 x 2 20-node solid elements. a) b/t = 100 and b) b/t = 500.

The results of the numerical analysis show the both linear buckling stress and the ultimate compressive strength to increase due to the foundation (fig. 4 and table 2). The increase is more significant to the more slender plate (b/t = 500), to which the foundation is a more dominant stiffening medium compared with the effect of the longitudinal edges. The foundation increases also the post-buckling axial stiffness ($E = d\sigma/d\varepsilon$), the more the more slender the plate is. In the post-ultimate limit state the rigid plates (b/t = 100) show a fast decreasing load bearing capacity while the more slender plates keep the load level high, but are involved in large deformations and deflections.

The buckling wave length decrease with the increase of the stiffness of the foundation. This yields high bending moments and bending stresses in the post-buckling area to plates on an relatively stiff foundation. So the strains caused by axial stresses and bending together exceed the yield strain faster in the plates supported by a foundation than in the plates without lateral continuous support. Large strains are not concentrated to the axial load bearing longitudinal edges, but occur also in the middle surface of the plate, where the high bending stresses are. The plastic strain field in the top and bottom faces of the plates on an foundation is more smooth and wide compared with the plates without foundation, in which the plate is yielding more locally near the longitudinal edges at the ultimate limit state.

a)

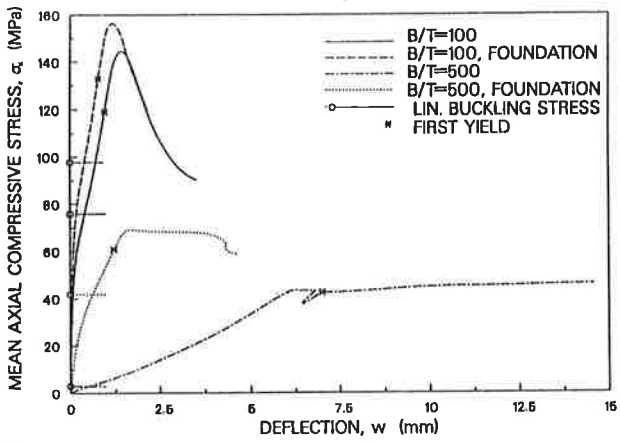

b)

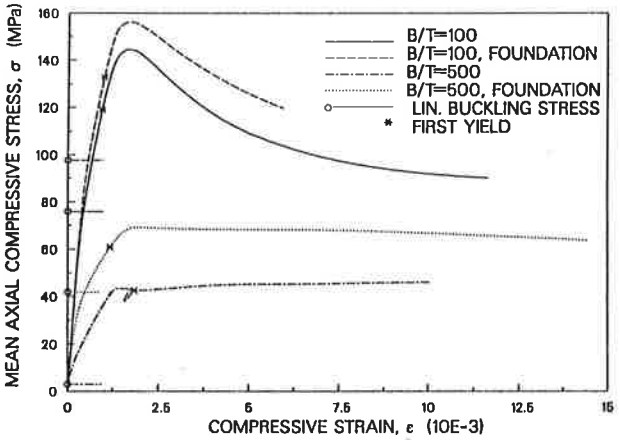

FIGURE 4. a) Out of plate deflection and b) mean axial compressive strain of two steel plates with and without a foundation. $E = 210000$ N/mm^2, $E_C = 1$ N/mm^2, $\nu = 0.3$, $\nu_C = 0.25$ and $f_y = 320$ N/mm^2.

The difference in the strain fields between the plates with and without a lateral foundation and further between the "rigid" (b/t = 100) and "slender" (b/t = 500) plates can be seen in figs. 6 and 7. The relative difference between the ultimate compressive stress and the stress corresponding the first yielding is smaller in the plates supported by a foundation. This is because of the high and wide bending strain fields and reduced bending stiffnesses in a wide area in the plate after the first yield loading level.

For the engineering design work some simplified approximate formulae have been developed to evaluate the compressive strength of an axially loaded long plate supported by a foundation. The fourth expression to the buckling coefficient K in the table 1 /2/ is based on the foundation model no. 2 in the previous chapter (eqs. 5b, 10 and 15). This expression together with the well known Winter's formula (20) is developed and used in the design of face plates for foam core sandwich panels. The formula (20) is found to be valid in the area $0 < R_2 < 200$.

$$\sigma_u = f_y (1 - 0.22/\lambda)/\lambda \leq f_y \qquad (20)$$

where

$$\lambda = \left(\frac{f_y}{\sigma_{cr}}\right)^{1/2} = \frac{\sqrt{12\,(1-\nu^2)}}{\pi}\,\frac{b}{t}\,\sqrt{\frac{f_y}{KE}} \qquad (21)$$

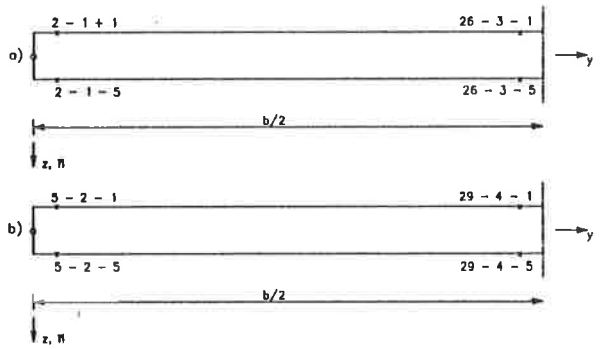

FIGURE 5. Locations of some integration points in the shell elements in the points a) x = a/2 and b) x = a.

a)

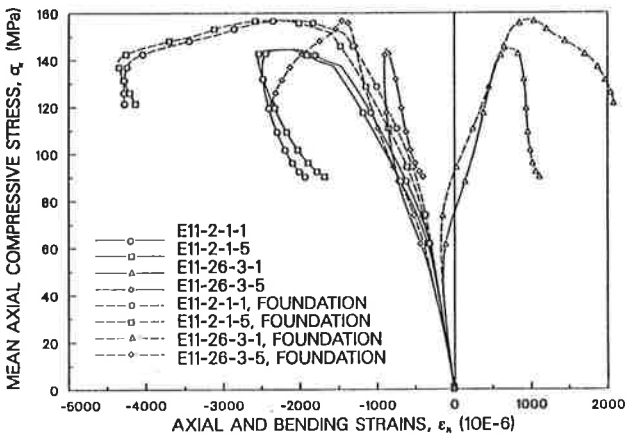

b)

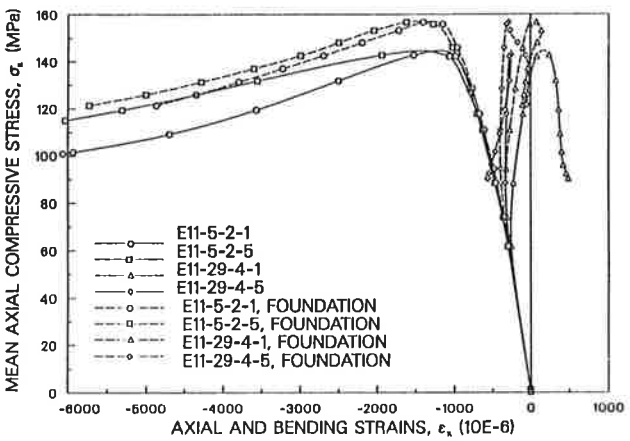

FIGURE 6. Axial strains in the steel plate a) in the place of the maximum out of plate deflection (point x = a/2 in the fig. 1.) and b) in the place of the vanishing out of plate deflection (point x = a in the fig. 1.). b/t = 100. The numbers refer to the locations of integration points in the shell elements in the fig 5.

TABLE 2. Characteristic strength values ($\bar{\sigma}_x$) to the plates used in the comparison. The values on the last line are calculated using the expression (20).

b/t foundation a/b	100 no 1.00	100 yes 0.83	500 no 1.00	500 yes 0.244
linear buckling stress, MPa	75.9	97.7	3.03	41.8
stress corresponding first yielding, MPa	119.0	132.7	42.5	60.8
ultimate strength, MPa	144.5	156.3	43.5	69.1
ECCS-model (20), MPa	139.2	153.9	-	-

a)

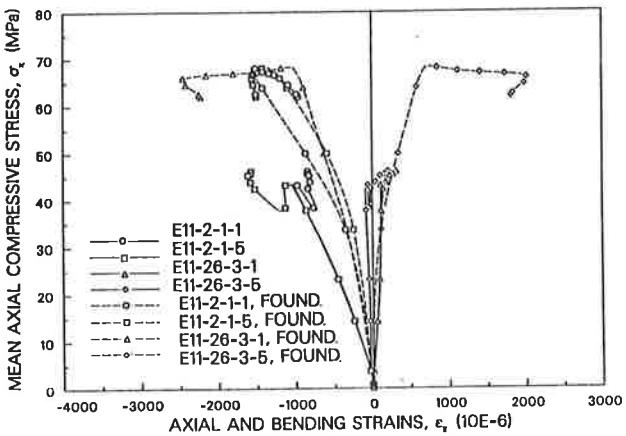

b)

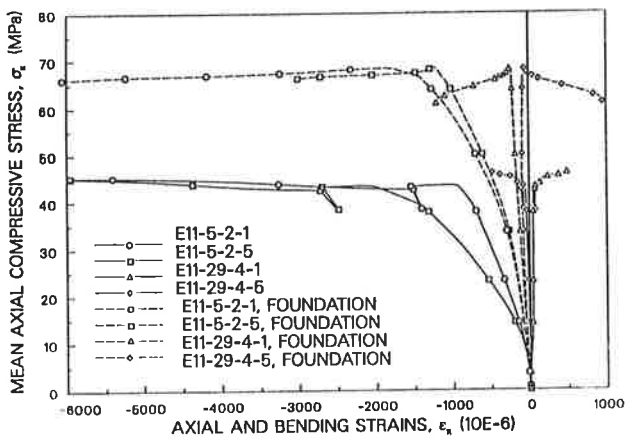

FIGURE 7. Axial strains in the steel plate a) in the place of the maximum out of plate deflection (point x = a/2 in the fig. 1.) and b) in the place of the vanishing out of plate deflection (point x = a in the fig 1.). b/t = 500. The numbers refer to the integration points in the shell elements in the fig 5.

CONCLUSIONS

The foundation under an axially loaded slender plate increases the buckling stress and the compressive strength of the plate. The extent of the increase depends on the b/t- and σ_{cr}/f_y-ratios and on the stiffness of the foundation, so that it is higher to slender plates on a relatively rigid foundation. The foundation changes the shapes of the eigenmodes. The mode with one buckling half wave in the transverse direction is not necessarily the lowest eigenmode to a long simply supported plate. Further, there possibly exist several eigenvalues very near each other, which makes the numerical analyses strongly sensitive to the intitial mode and to the solution strategy.

NOTATIONS

a	half buckling wave length in x-direction
b, b_e	width and effective width of the plate
f_y	yield strength of the plate
n	number of buckling half wave lengths in y-direction
t	thickness of a plate
w w_n	deflection and deflection coefficients of the plate
C, C_1, C_2	foundation coefficients
E	Young's modulus for the plate
E_C, G_C	Young's modulus and shear modulus of the foundation
K, K_1, K_2	buckling coefficients
$N_x(y)$	axial load
R, R_1, R_2,	parameters
ν, ν_C	Poisson's ratio of the plate and of the foundation
λ,	relative slenderness of the plate
ϕ	= a/b
σ_{cr}, σ_u	critical axial stress and compressive strength of the plate

REFERENCES

1. Vlasov V.Z. & Leont'ev U.N., Beams, plates and shells on elastic foundations. Israel Program for Scientific Translations Ltd., Jerusalem 1966.

2. Davies J.M. & Hakmi M.R., Local buckling of sandwich plates. IABSE Report, Vol. 60, p. 533 - 538.

3. Stamm K. & Witte H., Sandwichkonstruktionen. Springer Verlag, Wien. 1974.

4. ABAQUS, User's Manual, Version 4.8. Hibbitt, Karlsson & Sorensen, Inc. 1989.

USE OF CURVATURE APPROXIMATION IN AN ANALYSIS OF BEAM AND PLATE BENDING PROBLEMS

Reijo KOUHIA*
Faculty of Mechanical Engineering
Eindhoven University of Technology
P.O. Box 513, NL-5600 MB EINDHOVEN, THE NETHERLANDS

Petri PIILA
Department of Structural Engineering
Helsinki University of Technology
Rakentajanaukio 4A, SF-02150 ESPOO, FINLAND

ABSTRACT

As an introductory example an approximate calculation of the post-buckling behaviour of the elastica is presented. Using a simple interpolation for curvature, and integrating the displacements from this approximation, yield fairly good results in the whole post-buckling regime with relative ease.

The paper also discusses the generalization of this procedure, which can be utilized in the finite element method. The construction of element equilibrium equations are briefly described.

BACKGROUND

Ideas to this study emanated during the course of structural stability held in the Helsinki University of Technology during the autumn period 1989. Basic aim was to demonstrate the post-buckling behaviour of continuous elastic systems, such like beams, plates and cylindrical shells. For example, evaluation of the post-critical equilibrium path of an inextensional Euler elastica requires lengthly, but however, quite straightforward calculations [2]. Even the approximate procedures result in lengthly manipulations, when the standard potential energy formulation[1] in connection with the perturbation approach is used. Also the validity of results are quite limited.

A simple remedy is to approximate the strain quantities (i.e. curvatures in beam and plate structures) and integrate the displacements, which are only needeed in the expression of the potential of external loads.[2]

*permanent address: Department of Structural Engineering, Helsinki University of Technology

[1] Standard potential energy formulation = strains are derived from assumed displacement field.

[2] And of course to fulfill the boundary conditions.

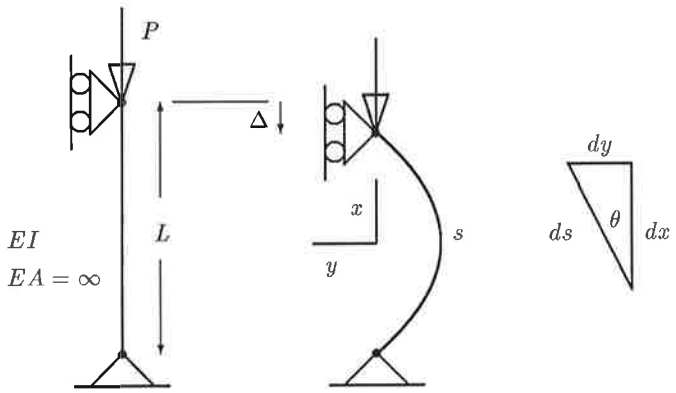

Figure 1: Inextensional simply supported beam.

AN EXAMPLE

As a simple example a uniform inextensional simply supported compressed beam is considered, see Fig. 1. Expression of the total potential energy has the form

$$\Pi_P = \tfrac{1}{2} \int_0^L EI\kappa^2 ds - P\Delta(\kappa), \tag{1}$$

where EI is the bending stiffness, L the length and κ the curvature of the beam. The external compressive force is denoted by P and Δ is the end shortening.

The most simple approximation to the curvature κ is naturally a constant. After a few lines of simple manipulations the potential energy is rewritten as

$$\Pi_P = \tfrac{1}{2} EI\kappa^2 L - PL(1 - \frac{2}{\kappa L} \sin \frac{\kappa L}{2}).$$

From the stationary condition, the following relationship between load and curvature is obtained

$$\frac{PL^2}{EI} = \frac{k^2}{\frac{\sin(k/2)}{k/2} - \cos(k/2)}, \qquad k = \kappa L. \tag{2}$$

Usually the load-displacement curve is of interest. So, to accomplish the analysis the midpoint deflection is expressed as a function of curvature

$$\frac{v}{L} = \frac{1}{k}[1 - \cos(k/2)], \tag{3}$$

and the resulting path is shown in Fig. 2

Much better accuracy is achieved when a trigonometric approximation

$$\kappa(s) = \kappa_0 \cos \frac{\pi s}{L}$$

is used.[3] Integrating the slope angle from the fundamental equation:

$$\frac{d\theta}{ds} = -\kappa, \tag{4}$$

the expression

$$\int_0^{(L-\Delta)/2} dx = \int_0^{L/2} \cos\theta ds = \int_0^{L/2} \cos(\kappa_0 \frac{L}{\pi} \sin\frac{\pi s}{L}) ds$$

$$\Rightarrow \qquad \Delta(\kappa_0) = L[1 - \frac{2}{\pi} \int_0^{\pi/2} \cos(\alpha \sin z) dz],$$

to the end shortening is obtained ($\alpha = \kappa_0 L/\pi, z = \pi s/L$). Expanding the integrand into a Taylor series, integrating and inserting it into the potential (1), the following relation can be obtained from the stationary condition

$$\frac{PL^2}{EI} = \frac{k}{2\sum_{n=1}^{\infty} \frac{k^{2n-1}(-1)^{n+1}}{(2n-1)!\,\pi^{2n}} \left[\prod_{\ell=0}^{n-1} \frac{2n-(2\ell+1)}{2n-2\ell}\right]}, \tag{5}$$

where $k = \kappa_0 L$. The midpoint deflection v is integrated from the expression

$$\int_0^v dy = \int_0^{L/2} \sin\theta ds = -\int_0^{L/2} \sin(\kappa_0 \frac{L}{\pi} \sin\frac{\pi s}{L}) ds,$$

which gives

$$\frac{v}{L} = \frac{1}{\pi} \sum_{n=0}^{\infty} \frac{k^{2n+1}(-1)^n}{(2n+1)!\,\pi^{2n+1}} \left[\prod_{\ell=0}^{n-1} \frac{2n-2\ell}{2n-(2\ell-1)}\right]. \tag{6}$$

Results of Equations (5) and (6) are shown in Fig. 2.

AN ASSUMED CURVATURE BEAM ELEMENT

In this section a simple non-linear beam element is derived from an assumed curvature distribution. As a model problem, a cantilever beam is considered.

Legendre polynomials

$$P_p(\xi) = \frac{c}{(p-1)!} \frac{1}{2^{p-1}} \frac{d^p}{d\xi^p} \left[(\xi^2-1)^p\right] \tag{7}$$

are chosen for the curvature interpolation. The constant c is obtained from the normalization requirement[4]

$$\int_{-1}^{1} P_p^2(\xi) d\xi = 2.$$

[3] Note: s is measured along the beam's axis.

[4] When integrated over the length of an element: $\frac{1}{2} h^{(e)} \int_{-1}^{1} P_p^2(\xi) d\xi = h^{(e)}$.

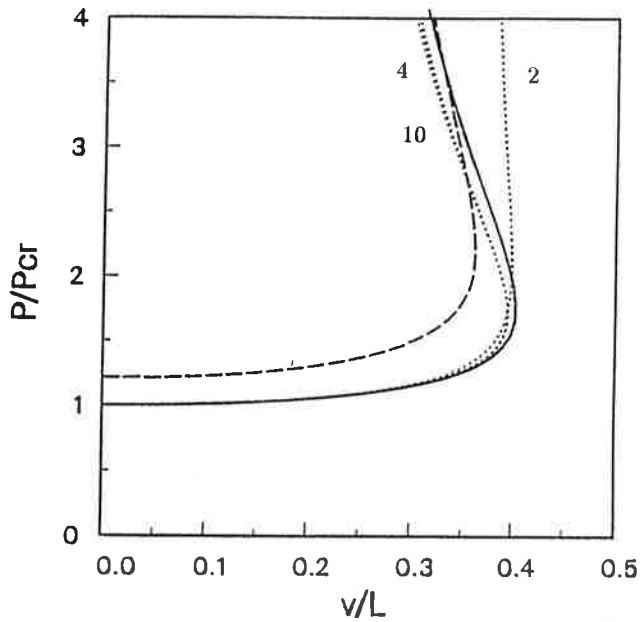

Figure 2: Horizontal deflection at the beam's midpoint. Solid curve is the analytical solution. Dashed line corresponds to Equations (2) and (3). Dotted lines are the results of using Equations (5) and (6), when the sum is taken with two, four or ten terms.

Polynomials up to order three are

$$P_0(\xi) = 1, \quad P_1(\xi) = \sqrt{3}\xi, \quad P_2(\xi) = \tfrac{\sqrt{6}}{2}(3\xi^2 - 1) \text{ and } P_3(\xi) = \tfrac{\sqrt{7}}{6}\xi(15\xi^2 - 9).$$

Thus, the interpolation for the curvature can be expressed as

$$\kappa(\xi) = \sum_{i=0}^{n} P_i(\xi)\kappa_i, \tag{8}$$

where the curvature parameters are denoted by κ_i.

Derivation of the equilibrium equations for an arbitrary element (e) can be started from the basic relationship (4), equations

$$\frac{dx}{ds} = \cos\theta, \qquad \frac{dy}{ds} = \sin\theta, \tag{9}$$

and the potential of an element e

$$\Pi_P^{(e)} = \tfrac{1}{2}\int_0^{h^{(e)}} EI\kappa^2 ds - \int_0^{h^{(e)}} \bar{f}v ds - \int_0^{h^{(e)}} \bar{g}u ds, \tag{10}$$

where $\bar{f}$ and $\bar{g}$ are the distributed vertical and axial loads, respectively. From the fundamental equations (4) and (9), expressions for the axial displacement u and the vertical deflection v can be obtained

$$u^{(e)}(s) = u_1^{(e)} + \Delta u^{(e)}(s) \doteq u_1^{(e)} + h^{(e)} - \int_0^{h^{(e)}-\Delta u^{(e)}} dx = u_1^{(e)} + h^{(e)} - \int_0^{s} \cos\theta ds, \tag{11a}$$

$$v^{(e)}(s) = v_1^{(e)} + \Delta v^{(e)}(s) = v_1^{(e)} + \int_0^s \sin\theta ds, \tag{11b}$$

where $u_1^{(e)}$ and $v_1^{(e)}$ are the displacements at the left end of an element e. Performing transformation to a dimensionless coordinate system $\xi \in [-1, 1]$ and integrating the rotation θ from the equation (4) yields[5]

$$\theta(\xi;\kappa_i) = \theta_1 - \Delta\theta(\xi;\kappa_i),$$

where

$$\Delta\theta(\xi;\kappa_i) = \tfrac{1}{2} h \sum_{i=0}^{n} P_i^1(\xi)\kappa_i$$

and the notation P_i^1 means polynomials which have been integrated from the Legendre polynomials (7) of order i, i.e.

$$P_i^1(\xi) = \int_{-1}^{\xi} P_i(\zeta)d\zeta.$$

Translational displacements (11) can be expressed in the form

$$u(\xi) = u_1 + h[1 - \tfrac{1}{2}\int_{-1}^{\xi} \cos\theta(\zeta;\kappa_i)d\zeta] \quad \text{and} \quad v(\xi) = v_1 + \tfrac{1}{2} h \int_{-1}^{\xi} \sin\theta(\zeta;\kappa_i)d\zeta,$$

which after simple manipulations can be written as

$$u(\xi) = u_1 + h\left\{1 - \tfrac{1}{2}\left[I_c(\xi;\kappa_i)\cos\theta_1 + I_s(\xi;\kappa_i)\sin\theta_1\right]\right\}, \tag{12a}$$

$$v(\xi) = v_1 + \tfrac{h}{2}\left[I_c(\xi;\kappa_i)\sin\theta_1 - I_s(\xi;\kappa_i)\cos\theta_1\right], \tag{12b}$$

where

$$I_c(\xi;\kappa_i) = \int_{-1}^{\xi} \cos\Delta\theta(\zeta;\kappa_i)d\zeta \quad \text{and} \quad I_s(\xi;\kappa_i) = \int_{-1}^{\xi} \sin\Delta\theta(\zeta;\kappa_i)d\zeta.$$

For construction of a practically useful element a nodal degrees of freedom should consist of translational displacements and rotations, i.e. $(u_1, v_1, \theta_1, u_2, v_2, \theta_2)$. However, in the model problem considered, the discretized equilibrium equations can be formulated elegantly by using only rotational degrees of freedom and assuming constant curvature. The curvature parameter κ_0 is expressed in terms of rotations

$$\theta_2 = \theta(1;\kappa_0) = \theta_1 - \Delta\theta(1;\kappa_0) \quad \Rightarrow \quad \kappa_0 = -\frac{\theta_2 - \theta_1}{h}. \tag{13}$$

Carrying out the manipulations on the translational displacements Δu and Δv, give

$$\Delta u = h\left(1 - \frac{2}{\theta_2 - \theta_1}\sin\frac{\theta_2 - \theta_1}{2}\cos\frac{\theta_2 + \theta_1}{2}\right), \tag{14a}$$

$$\Delta v = \frac{2h}{\theta_2 - \theta_1}\sin\frac{\theta_2 + \theta_1}{2}\cos\frac{\theta_2 - \theta_1}{2}. \tag{14b}$$

[5]The element label (e) has been dropped out for convenience.

number of elements	computed critical load P/P_E $P_E = \frac{1}{4}\pi^2 EI/L^2$
1	1.2159
2	1.0525
4	1.0128
8	1.0031
30	1.0002

Table 1: Critical loads of the model problem.

Parameters u_1 and v_1 of an element e are calculated from

$$u_1^{(e)} = \sum_{i=1}^{e-1} \Delta u^{(i)} \quad \text{and} \quad v_1^{(e)} = \sum_{i=1}^{e-1} \Delta v^{(i)}. \tag{15}$$

Inserting now Equations (12),(13),(14), and (15) into the potential (10), the non-linear equilibrium equations expressed in terms of rotations can be obtained from the stationary condition. These parametrized equations can be solved by using a continuation algorithm.

The model problem is solved under a single concentrated compressive load. Obtained critical loads are shown in Table 1. Uniform element meshes are used. Convergence seems to be quadratic as it would be expected.

The above described procedure seems to be difficult to generalize for two-dimensional problems, such like plates and shells. Hence, a more conventional approach to formulate the assumed strain elements is described in the next section. It might also give some insight to the shear locking phenomena.

MORE ON ASSUMED STRAIN ELEMENTS

Formulation of an assumed strain element is started from the generalized variational principle, also called the Hu-Washizu principle, see Ref. [3] p. 434,

$$\Pi_G = \int_V \{a(\varepsilon_{ij}) + \Phi(u_i) - \sigma_{ij}\left[\varepsilon_{ij} - \tfrac{1}{2}\left(u_{i,j} + u_{j,i} + u_{k,i}u_{k,j}\right)\right]\} dV + \int_{S_\sigma} \Psi(u_i) dS, \tag{16}$$

where it is assumed that the displacement field u_i satisfies the kinematical boundary conditions and Φ, Ψ are the body force and surface traction potentials. Straightforward use of the Hu-Washizu principle results in a system where all of the three independent fields: displacements u_i, strains ε_{ij} and stresses σ_{ij} are separately approximated. Practically it is not reasonable to have independent approximations to both strains and stresses. Thereby, stresses are expressed as functions of strains by using the constitutive law $\sigma_{ij} = C_{ijkl}\varepsilon_{kl}$.

Limiting the present discussion only to geometrically and materially linear case, the Hu-Washizu functional for a Timoshenko beam takes the form

$$\Pi_G^* = \tfrac{1}{2}\int_I (EI\kappa^2 + GA\gamma^2) dx - \int_I \bar{f} v dx - \int_I \left[EI\kappa(\kappa + \theta_{,x}) + GA\gamma(\gamma - v_{,x} + \theta)\right] dx,$$

which can be arranged to the form

$$\Pi_G^* = -\tfrac{1}{2}\int_I (EI\kappa^2 + GA\gamma^2)dx - \int_I \bar{f}dx - \int_I EI\kappa\theta_{,x}dx - \int_I GA\gamma(v_{,x} - \theta)dx. \qquad (17)$$

It is well known, that standard approaches to construct a Timoshenko beam element where equal order interpolation for deflection and rotation are used, will lock in a limiting case when the thickness t of a beam tends to zero. This is due to the shear energy term $a_s = \frac{1}{2}\int_I GA(v_{,x} - \theta)^2 dx$ which does not have the possibility to vanish when a beam is subjected to a constant bending moment, because the shear strain will vanish only if $v_{,x} \to \theta$, which is possible only if $v \to 0$ and $\theta \to 0$. A natural way to circumvent this problem is to interpolate deflection by using an interpolation polynomial whose degree is one order higher than the one used for the rotation. So, the approximate displacement field has the possibility to satisfy the vanishing shear strain condition. Fortunately, exactly the same element equilibrium equations are obtained, when a reduced numerical integration is used,[6] which also results in a much more economical computation, especially in materially non-linear cases.

Substituting the interpolations

$$\kappa = \mathbf{N}_\kappa \mathbf{q}_\kappa, \quad \gamma = \mathbf{N}_\gamma \mathbf{q}_\gamma, \quad v = \mathbf{N}_v \mathbf{q}_v \quad \text{and} \quad \theta = \mathbf{N}_\theta \mathbf{q}_\theta$$

into the functional (17), the discrete compatibility and equilibrium equations

$$\begin{bmatrix} \mathbf{A}_{\kappa\kappa} & \mathbf{0} & \mathbf{0} & \mathbf{B}_{\kappa\theta} \\ \mathbf{0} & \mathbf{A}_{\gamma\gamma} & \mathbf{B}_{\gamma v} & \mathbf{B}_{\gamma\theta} \\ \mathbf{0} & \mathbf{B}_{v\gamma} & \mathbf{0} & \mathbf{0} \\ \mathbf{B}_{\theta\kappa} & \mathbf{B}_{\theta\gamma} & \mathbf{0} & \mathbf{0} \end{bmatrix} \begin{Bmatrix} \mathbf{q}_\kappa \\ \mathbf{q}_\gamma \\ \mathbf{q}_v \\ \mathbf{q}_\theta \end{Bmatrix} = \begin{Bmatrix} \mathbf{0} \\ \mathbf{0} \\ \bar{\mathbf{f}} \\ \mathbf{0} \end{Bmatrix} \qquad (18)$$

are obtained from the stationary condition.

If the Legendre polynomials (7) are used in interpolation of strains, i.e κ and γ, the matrices $\mathbf{A}_{\kappa\kappa}$ and $\mathbf{A}_{\gamma\gamma}$ are diagonal

$$\mathbf{A}_{\kappa\kappa} = -EIh\mathbf{I}, \qquad \mathbf{A}_{\gamma\gamma} = -GAh\mathbf{I},$$

where $\mathbf{I}$ is a unit matrix. Thus, the inversion of these matrices, needed in the static condensation process, is an easy task. The other matrices in Equation (18) are

$$\mathbf{B}_{\kappa\theta} = -\int EI\mathbf{N}_\kappa^T \mathbf{N}_{\theta,x} dx, \quad \mathbf{B}_{\gamma v} = -\int GA\mathbf{N}_\gamma^T \mathbf{N}_{v,x} dx, \quad \mathbf{B}_{\gamma\theta} = \int GA\mathbf{N}_\gamma^T \mathbf{N}_\theta dx.$$

In the functional (17) the problems might arise from the last term. However, if a constant approximation for the shear strain and linear interpolation of deflection and rotation are used, it is immediately clear that the contribution from this term will vanish in the limiting case of vanishing shear strain. Hence, exactly the same stiffness matrix than in the reduced integrated standard Timoshenko beam element is obtained.[7]

[6] At least in cases of linear and parabolic interpolation for v and θ.

[7] In this case there is no difference if either constant or constant + linear interpolation is used for the curvature.

In the Reissner-Mindlin plate theory the Hu-Washizu functional has the form, [3] p. 498,

$$\Pi_G = \int_A [a(\mathbf{\Gamma}) - \bar{f}w - M_x(\Gamma_x - \psi_{,x}) - M_y(\Gamma_y - \phi_{,y}) - M_{xy}(\Gamma_{xy} - \psi_{,y} - \phi_{,x}) \\ -Q_y(\Gamma_{xz} - w_{,x} - \psi) - Q_y(\Gamma_{yz} - w_{,y} - \phi)]\, dA - \int_{C_\sigma} (\bar{M}_{xn}\psi + \bar{M}_{yn}\phi + \bar{V}_z w) ds,$$

where the strain energy $a(\mathbf{\Gamma})$ can be divided into bending- and shear energies[8]

$$a(\mathbf{\Gamma}) = a_b(\Gamma_x, \Gamma_y, \Gamma_{xy}) + a_s(\Gamma_{xz}, \Gamma_{yz}) \\ = \tfrac{1}{2} D \left[(\Gamma_x + \Gamma_y)^2 + \tfrac{1}{2}(1-\nu)(\Gamma_{xy}^2 - 4\Gamma_x\Gamma_y)\right] + \tfrac{1}{2} Gt(\Gamma_{xz}^2 + \Gamma_{yz}^2).$$

Rotations ϕ and ψ are related to the right-hand-rule rotations ϕ_x, ϕ_y about x- and y-axes by definitions: $\phi = -\phi_x, \psi = \phi_y$. Using the expressions

$$\begin{aligned} M_x &= D(\Gamma_x + \nu\Gamma_y), & Q_x &= Gt\Gamma_{xz}, \\ M_y &= D(\Gamma_y + \nu\Gamma_x), & Q_y &= Gt\Gamma_{yz}, \\ M_{xy} &= \tfrac{1}{2}(1-\nu)D\Gamma_{xy}, \end{aligned}$$

for the stress resultants, the modified functional

$$\Pi_G^* = -\int_A \{a(\mathbf{\Gamma}) + \bar{f}w\}\, dA \\ + \int_A \{D[(\Gamma_x + \nu\Gamma_y)\psi_{,x} + (\Gamma_y + \nu\Gamma_x)\phi_{,y} + \tfrac{1}{2}(1-\nu)\Gamma_{xy}(\psi_{,y} + \phi_{,x})] \\ + Gt[\Gamma_{xz}(w_{,x} + \psi) + \Gamma_{yz}(w_{,y} + \phi)]\}\, dA + \int_{C_\sigma} \Psi(w, \phi, \psi) ds \qquad (21)$$

is obtained.

Special care to the selection of appropriate interpolation functions of shear strains Γ_{xz} and Γ_{yz} should be paid. Obviously constant values of Γ_{xz}, Γ_{yz} are good choises. However, in a formulation of a well behaving four-node plate element in Ref. [1], a slightly improved selection has been made. Making use of the modified Hu-Washizu functional (21), it is now tried to explain: 'why this particular element behaves well?'

A square plate element subjected to a pure bending ($M_x = M, M_y = M_{xy} = 0$) is considered. The shear strain γ_{xz} obtained from the interpolation of w and ψ contains now terms $(1, x, y, xy)$. If the interpolation of the independent shear variable Γ_{xz} is linear in y-direction and constant in the x-direction, as it is done in Ref. [1], it will be harmless, resulting to zero contribution of the term $\int_A Gt\Gamma_{xz}(w_{,x} - \psi)dA$. Similar reasoning can be done when the plate is bent in the other direction.[9]

References

[1] K.J. Bathe and E.N. Dvorkin. A four-node plate bending element based on Mindlin-Reissner plate theory and a mixed interpolation. *IJNME*, 21:367–383, 1985.

[2] S.P. Timoshenko and J.M. Gere. *Theory of Elastic Stability.* McGraw-Hill, 1961.

[3] K. Washizu. *Variational Methods in Elasticity & Plasticity.* Pergamon Press, 1982.

[8] The bending rigidity of the plate is $D = Et^3/[12(1-\nu^2)]$.

[9] The shear strain Γ_{yz} is interpolated by a linear expression in x-direction and it is constant in y-direction.

ELASTIC BUCKLING OF THIN-WALLED STRUCTURES USING SPLINE FINITE STRIP METHOD

SIMO NIKULA
Department of Mechanical Engineering
Lappeenranta University of Technology
P.O. Box 20, SF-53851 LAPPEENRANTA, FINLAND

ABSTRACT

Spline Finite Strip Method (SFSM) tries to combine well known Finite Element Method (FEM) and less known semi-analytic Finite Strip Method (FSM). In this paper mainly linear elastic buckling of prismatic beam structures is studied.

Spline Finite Strip Method allows use of other boundary conditions than simply supported ends. Loading may consist of longitudinal and transverse normal stresses and of shear stress. These are main differences between FSM and SFSM. Main differences between SFSM and FEM are discussed and demonstrated with a simple example.

Method is compared with semi-analytic Finite Strip and commercial Finite Element packages as ABAQUS and MSC/NASTRAN. SFSM results are taken from references. Special problems with eigenvalue buckling prediction are discussed. Mathematical methods for eigenvalue prediction are discussed briefly.

SFSM seems to be an alternative method for FEM. It requires almost as much numerical processing as FEM. FSM seems to most practical method that can take distortion effects of beam into account. Because of its limitations FSM suits best to comparing alternatives.

INTRODUCTION

Increasing use of thin-walled structures arose the problem of non-classical buckling modes over a decade ago. If for example a high strength column is well designed, it will not

usually buckle in flexural mode. Because of the need to analyze local and distortional modes many researchers worked in the late 70's with Finite Strip Method. FSM was originally developed by Cheung [1] mainly for static analysis of bridges.

In FSM prismatic structure is divided into strips, which are joined at longitudinal nodal lines. In longitudinal direction trigonometric functions are used as shape functions. This shape function is ideal for many cases, because analytical solutions for e.g. local buckling, column flexural buckling and beam lateral buckling under constant moment are trigonometric series too. In transverse direction relatively simple polynomials are used as shape functions. Most popular are linear shape functions for membrane displacements and third order hermit polynomials (beam shape functions) for transverse displacements.

FSM has not been commercially very popular despite of its good qualities. The only applications so far have been made in universities and have been more or less for academic use. Best part of FSM is that it doesn't require much storage in computer and most cases can be solved in a few minutes although every possible buckling length must be solved separately.

There are a few restrictions with FSM. Firstly it is possible to use only simple supports at ends. If one chooses shape functions that would simulate other end conditions, all modes would couple and create enormous bandwidth. In some cases using a few modes may be a good idea, for example Fischer [2] used a few modes simultaneously to handle longitudinal gradient of moment. For many cases it is necessary to take into account interactions at different lengths. Because of orthogonal shape functions FSM can't do that. Interactions at selected length are anyhow taken into account.

SFSM was developed to solve these problems. Carl de Boor [3] made mathematical basis for beta-splines available in the late 70's and in early in the 80's Cheung and Fan [4] devised SFSM for structural analysis. A few years ago Hancock and Lau [5] used SFSM to analyze buckling of flat plates. Most recent developments are handling arbitrary cross-section geometrically nonlinearly [6],[7] and eigenvalue buckling of arbitrary shaped plates using subparametric mapping [8].

SFSM is numerically much heavier than FSM because trigonometric shape functions in longitudinal direction are replaced by series of third order beta-splines. Compared to shell-FEM it has less degrees of freedom due to fact that there are only four dofs per node and quite good longitudinal shape functions. Bandwidth tends to be high in SFSM because each shape function is nonzero over four sections.

ENGINEERING INTRODUCTION TO SPLINE FINITE STRIP

Spline Function

Main difficulty in understanding SFSM is the use of spline function. Engineers who are familiar with displacement based FEM find it rather difficult to cope with function multipliers instead of nodal displacements and rotations. In usual FEM engineer sets nodal

displacement boundary conditions, applies nodal forces and gets nodal displacements as a result from analysis. When spline functions are used this cannot be done directly. Applying end boundary conditions is done by modifying shape functions, nodal forces are divided to four adjacent splines and even displacement results have to be calculated after the analysis. In fact one must know shape functions and boundary conditions to be able to calculate displacement results. These things can be hidden from the user but they may cause some headache to programmers.

Mathematical definition for third order beta-spline can be found in many textbooks. Main point is that it is piecewise defined continuous third order polynomial that has continuous first and second derivates. Its usefulness is based on that it is nonzero only in four intervals. Many authors give definition only for equal spaced B_3-spline [6], but more general approach can also be used [9]. Piecewise definition for B_3-spline is shown in Table 1.

TABLE 1
Definition for B_3-spline.

$\eta \in [\ ]$	$\phi_i(\eta)$
η_{i-2}, η_{i-1}	$A_i(\eta-\eta_{i-2})^3$
η_{i-1}, η_i	$A_i(\eta-\eta_{i-2})^3+C_i(\eta-\eta_{i-1})^3$
η_i, η_{i+1}	$B_i(\eta_{i+2}-\eta)^3+D_i(\eta_{i+1}-\eta)^3$
η_{i+1}, η_{i+2}	$B_i(\eta_{i+2}-\eta)^3$

Where multipliers are:

$$A_i=\frac{1}{h_{i-1}(h_{i-1}+h_i)(h_{i+1}+h_i+h_{i+1})}$$

$$B_i=\frac{1}{h_{i+1}(h_{i+2}+h_{i+1})(h_{i+2}+h_{i+1}+h_i)}$$

$$C_i=\frac{-(h_{i-1}+h_i+h_{i+1}+h_{i+2})}{h_{i-1}h_i(h_{i+1}+h_i)(h_{i+2}+h_{i+1}+h_i)}$$

$$D_i=\frac{-(h_{i-1}+h_i+h_{i+1}+h_{i+2})}{h_{i+2}h_{i+1}(h_{i+1}+h_i)(h_{i+1}+h_i+h_{i-1})}$$

and $h_K=\eta_K-\eta_{K-1}$

Examples of equal spaced and nonequal spaced splines are shown in Fig. 1. Equal spaced is defined by points at -2, -1, 0, 1 and 2. Definition points for nonequal spaced spline are -2, 0, 1, 1.5 and 2.

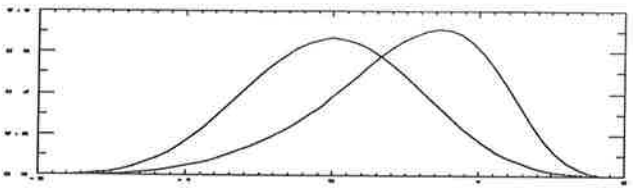

FIGURE 1. Examples of B_3-splines

To satisfy the support conditions at the two ends of the strip, the local splines at and immediately adjacent to the end-point have to be modified in accordance to Table 2, in which the restrictive condition $l_1 = l_2$ has been adopted.

TABLE 2
Modified Local Spline for End Support

Boundary condition	Modified local spline		
	ϕ_{-1}	ϕ_0	ϕ_1
Free	ϕ_{-1}	ϕ_0	ϕ_1
Simple-supported	Eliminated	$\phi_0-4\phi_{-1}$	$\phi_1-\phi_{-1}$
Clamped	Eliminated	Eliminated	$\phi_1-0.5\phi_0+\phi_{-1}$

Tip Loaded Cantilever Beam by Spline Finite Strip

To describe the use of SFSM a step by step solution for tip loaded cantilever beam is given below. Description for studied case is given in Fig. 2. Basic knowledge of elements based on assumed displacement is expected, see e.g. [10] pp. 82.

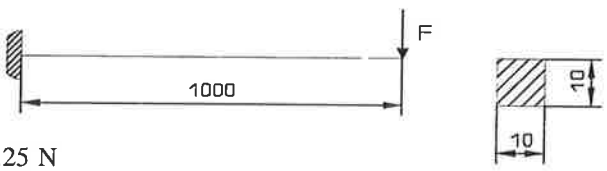

F=5.25 N
E=210 GPa
I=8.33E-10 m^4
Dimensions are given here in mm

FIGURE 2 Description for studied cantilever beam

Because we have only one section and it is of unit length, all the multipliers A_i and B_i are $\frac{1}{3}$ and C_i and D_i are $-\frac{2}{3}$. Shape functions for splines 1 and 2 are given in eq (1).

Shape function for spline 1 is modified and splines -1 and 0 are deleted as described in Table 2.

$$\begin{aligned}\Phi_1(\eta) = & \frac{1}{6}(\eta+1)^3 - \frac{2}{3}(\eta-0)^3 \\ & -0.5\left(\frac{1}{6}(2-\eta)^3 - \frac{2}{3}(1-\eta)^3\right) \\ & + \frac{1}{6}(1-\eta)^3 \\ = & \frac{18\eta^2 - 11\eta^3}{12} \\ \Phi_2(\eta) = & \frac{1}{6}(\eta-0)^3\end{aligned} \tag{1}$$

Strain-displacement matrix is then given by eq (2) and stiffness matrix by eq (3).

$$[B] = \frac{d^2}{d\eta}[N] = [3-\frac{11}{2}\eta,\eta] \tag{2}$$

$$[k] = EI\int_0^1 [B]^T[B]d\eta \approx \begin{matrix} 452.08 & -58.33 \\ sym & 58.33 \end{matrix} \tag{3}$$

Load vector is defined by eq (4). Terms in load vector are obtained by multiplying force and value of shape function at loading point.

$$\{f\} = F\{\phi_1(1),\phi_2(1)\} \approx \{3.0625, 0.875\} \tag{4}$$

Solving these linear equations gives the spline multipliers. These multipliers are in this case 0.01 and 0.025. Displacements at specified places are obtained by calculating dot product of multipliers and shape functions values at those points. E.g. at tip, displacement is given by eq (5), which is same as by beam theory when transverse shear displacement is ignored (Euler-Bernoulli).

$$\delta_{tip} = (\phi_1(1),\phi_2(1))\cdot(0.01, 0.025) = 0.01 \tag{5}$$

COMPARISON BETWEEN DIFFERENT METHODS

Studied case

Only one example is discussed here. Because there was no SFSM program available, case had to be from [6] or from [7]. A plate girder in uniform bending from [7] was selected because interaction between lateral and distortional buckling had been failure mode at short lengths. Girder was simple supported at ends and loaded with uniform bending. Measures are shown in Fig 3.

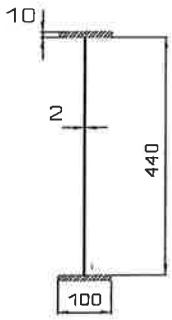

E=210 GPa
Poissons ratio = 0.3

FIGURE 3. Geometry of the plate girder.

Methods used

SFSM results are taken from [7] pp 2.22 - 2.23. FSM calculations are made by own analysis program, which is based on [11]. This program will be available for public use later in this year. FEM calculations are made by ABAQUS [12] and MSC/NASTRAN [13]. With ABAQUS both eigenvalue buckling analysis and nonlinear analysis were carried out. With NASTRAN only eigenvalue analysis was made. In NASTRAN user can select the method used to solve eigenvalue problem. Both Lanczos and enhanced inverse power method (SINV) were used.

Element models

Erp used four to ten sections in longitudinal direction, strips in flanges and eight strips in web. He tested girders of 3, 5, 10 and 20 m. Results were compared with lateral buckling load obtained by beam theory and with approximate analytical method of Hancock.

FSM model used had the same strip configuration as SFSM model. FSM calculations were made at same lengths and moreover at a few lengths varying from 0.2 m to 0.3 m to get hold of local buckling of the web.

FEM calculation were made only for 3 m girder. FEM models were made and postprocessed mainly by Ideas Supertab [14]. Two different meshes were used. First mesh had same division of parabolic shell elements as Erp had in his SFSM model. In ABAQUS element type was S8R5 and in NASTRAN QUAD8. Only symmetric half of length was modelled. Results obtained from this mesh were quite confusing. To get more sight another mesh with only two elements at flanges and six in web but fifteen elements in halflength was made. Meshes are shown at the results section. FEM models were loaded by line loads applied at flanges. These loads were applied by using very thin (0.5 mm) beams.

Models which were solved nonlinearly were perturbed by moving one web node 0.5 mm out of plane at the symmetry plane. In second model material was assumed to be elastic-plastic as follows: first yield 235 MPa and maximum stress of 250 MPa at 5 % plastic strain. Because yielding material was used, all the nodes in loaded end web between flanges were constrained to remain at straight line. Force tolerance (PTOL) was set

to 1 N and moment tolerance (MTOL) to 0.1 Nm. Tolerances were set so tight because of very slender web. In web seven integration points through thickness were used and in flanges only three.

Results

Results for different lengths using analytical solutions, SFSM and FSM are in Table 3.

TABLE 3
Buckling Moments in kNm for a plate girder in uniform bending.

girder length	FSM	SFSM	Hancock	Beam theory
3	89.7	88.7	76.4	97.8
5	38.0	37.8	37.4	41.5
10	15.0	15.0	15.0	15.8
20	7.0	7.0	7.0	7.0

It should however be noticed at local buckling gives slightly lower values than lateral-distortional buckling at 3 m length. Minimum is according to FSM about 76.7 kNm at halfwavelenght of 225 mm. Analytical solution for clamped edges would give 77 kNm (buckling factor K is 39.6 [15] p. 373).

Buckling analysis using FEM gives usually quite nice pictures as can be seen in following figures. In Fig. 4 are FEM models which had only five elements in longitudinal direction. Buckling moment was 54.5 kNm according to ABAQUS (left) and 15.2 kNm (!) according to NASTRAN (right). In Fig. 5 are buckling modes from the second model which had fifteen elements in longitudinal direction. In this model buckling moments were 77.2 kNm (ABAQUS, left) and 65.5 kNm (NASTRAN, right). There was no difference between result obtained by Lanczos method and SINV. Difference between results from ABAQUS and NASTRAN are due to differences in element formulation and not due to solution method.

In Fig. 6 are failure modes obtained from nonlinear ABAQUS solutions. Left model was solved elastically up to 100 kNm and right model up to limit load which was 117 kNm. In both case ABAQUS solver reported negative eigenvalues when solution reached about 80 kNm.

Solution times

FSM model was solved using IBM PS/2 Model 70 microcomputer with 80387 arithmetic coprocessor (Matlab floptest gives 200 kFlops). Total solution time for ten lengths and two eigenvalues for each length was 73 s.

FEM model were solved using VAX 8550 minicomputer (Matlab floptest gives 900 - 1000 kFlops). Solution times are for second model and five eigenvalues. Using ABAQUS only four lowest eigenvalues had converged after 20 iterations (20 iteration vectors) and total CPU time for solution was 1800 s. NASTRAN found five lowest eigenvalues using Lanczos method in 940 s. Using enhanced inverse power method (SINV), solution time was 1100 s. NASTRAN logs I/O time too and it was for Lanczo 2200 s and for SINV 4300 s. CPU time for nonlinear ABAQUS analysis of second model was 7900 s.

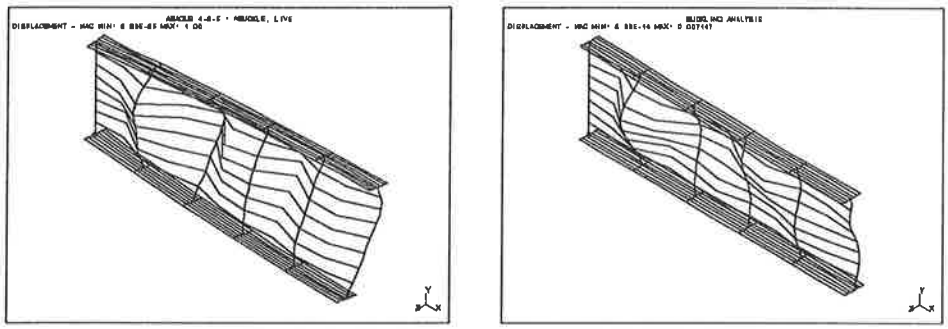

FIGURE 4. Buckling modes of first FEM model

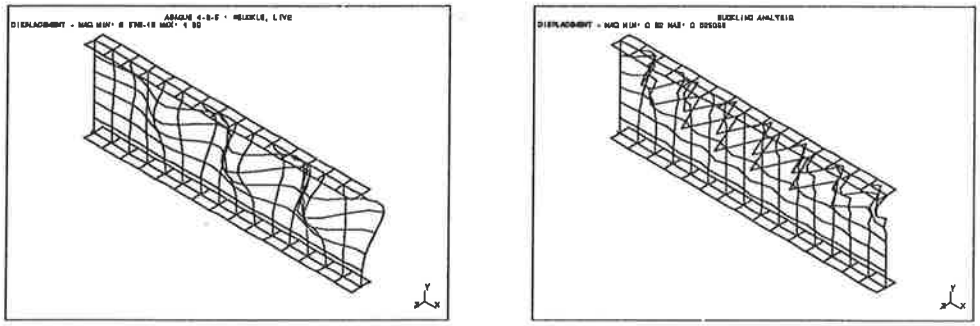

FIGURE 5. Buckling modes of second FEM model

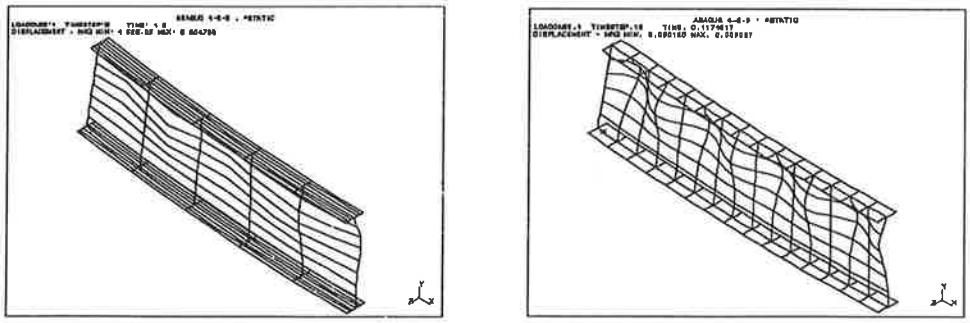

FIGURE 6. Failure modes from nonlinear analysis

DISCUSSION

Although SFSM has many good qualities it does not give solution to main problem. There is no easy way to handle interactions between different modes having different wavelengths. As with FEM quite a lot of elements (sections) must be used to be able to take these interactions into account. When using FEM there are also many difficulties.

Local buckling is quite difficult to handle with eigenvalue methods, because there will be quite a many almost equal sized eigenvalues. Subspace iteration [16], which is used in ABAQUS to solve eigenvalue problem, is not very well suited for problems of this kind. Convergence speed is proportional to ratio of eigenvalues corresponding to last and first iteration vector. On the contrary subspace method seems to work well in FSM, because all the lengths are studied separately. Lanczos method which is available in NASTRAN seems to work better for multiple eigenvalues.

Problems with first FEM-model point out clearly that although quite large aspect ratios can be used in static analysis, this can't be done when buckling is to be solved. Nonlinear analysis using dense mesh can always be used to solve these problems, but it requires too much resources to be useful when comparing different possibilities in engineering work.

SUMMARY AND CONCLUSIONS

Use of thinwalled structures has brought up need to analyze prismatic beam structures so that local behaviour can be taken into account. Anylyzing distortional and nontrivial local buckling cases has brought up new methods like FSM and SFSM.

In FSM trigonometric shape functions make it possible to analyze three dimensional structures as a series of two dimensional mathematical models. Main advantages in using FSM are ease of use and modest hardware requirements.

SFSM replaces trigonometric functions with a series of B_3-splines. This makes it possible to analyze non-simple supported structures. Complicated stress distributions can also be taken into account. In principle interactions between global and local modes can be taken into account, but it requires quite dense mesh.

SFSM may become an alternative method for FEM in future. If analysis programs will be available and they are done with efficient algorithms which take advantage of special forms of matrixes, it may become superior to shell-based FEM. At present FSM seems to suit better for everyday use and for comparing different alternatives. If interactions between local and global modes must be analyzed, nonlinear FEM seems to be the only, although expensive solution.

REFERENCES

1. Cheung, Y.K., Finite Strip Method in Structural Analysis. Pergamon Press, New York, 1976. ISBN 0-08-018308-5.

2. Fischer, M. and Jianzhong, Z., Verzweigungslasten von Beul- und Gesamtstabilitätsproblemen nach der Finite-Streifen-Methode. In: Stahlbau 12/1987.

3. De Boor, C., A Practical guide to Splines. Applied Mathematics Sciences 27. Springer-Verlag, 1978. ISBN 0-387-90356-9.

4. Cheung, Y.K., Fan, S.C. and Wu, C.Q., Spline Finite Strip in Structural Analysis. In Proceedings of the International Conference on Finite Element Methods, Shanghai, pp. 704-709. Science Press, Beijing/Gordon & Breach, New York 1982. (Ref from [8])

5. Lau, S.C.W. and Hancock, G.J., Buckling of Thin Flat-Walled Structures by a Spline Finite Strip Method. In Thin-Walled Structures Vol 4 (1986) pp. 269-294.

6. Kwon, Y.B. and Hancock, G.J., A Nonlinear Elastic Spline Finite Strip Analysis for Thin-Walled Sections. Research Report No. R607, University of Sydney Australia, 1989.

7. van Erp, G.M., Advanced Buckling Analyses of Beams with Arbitrary Cross Sections. PhD Theses. Eindhoven 1989. ISBN 90-9002808-0.

8. Tham, L.G. and Szeto, H.Y., Buckling Analysis of Arbitrarily Shaped Plates by Spline Finite Strip Method. In Computers & Structures Vol. 36. No. 4, pp 729-735, 1990.

9. Tham, L.G., Application of Spline Finite Strip Method in the Analysis of Space Structures. In Thin-Walled Structures 10(1990) pp. 235-246.

10. Cook, R.D., Concepts and Applications of Finite Element Analysis, Second Edition. John Wiley & Sons, 1981. ISBN 0-471-03050-3.

11. Hancock, G.J., Local, Distortional and Lateral Buckling of I-Beams. Research report No B 312, University of Sidney, 1977.

12. ABAQUS User's Manual, Version 4.8. Hibbit, Karlsson & Sörensen Inc, 1989.

13. MSC/NASTRAN User's Manual, Version 66A. The MacNeal-Schwendler Corporation, 1989.

14. SDRC I-DEAS, Level V. Finite Element Modeling, User's Guide. Structural Dynamics Research Corporation, 1990.

15. Allen, H.G. and Bulson, P.S., Background to Buckling. McGraw-Hill Book Company, 1980. ISBN 0-07-084100-4.

16. Bathe, K.J., Finite Element Procedures in Engineering Analysis. Prentice-Hall Inc., 1982. ISBN 0-13-317305-4.

SOLUTION OF FLEXURAL-TORSIONAL STABILITY PROBLEM FOR A COLUMN WITH SINGLY SYMMETRIC OPEN CROSS-SECTION

Seppo Salonen and Juha Paavola
Helsinki University of Technology
Department of Structural Mechanics
Rakentajanaukio 4A, SF-02150 ESPOO, FINLAND

ABSTRACT

The present paper discusses a solution technique applicable to the differential equation system due to the problem of flexural-torsional instability of columns with open cross-sections. The system considered consists of three separate differential equations which are coupled in the general case. Various symmetries of the cross-section release the couplings between these equations. This presentation is limited, for simplicity, to columns with singly symmetric cross-sections in which there are couplings only between two of the governing equations. The applications analysed consist of problems in which the effect of elastic supports on the solution is studied.

INTRODUCTION

A slender column with an open thin-walled cross-section having thus a relatively small torsional rigidity can lose its stability under axial compressive load through a buckling failure caused by bending, torsion or a combination of both these factors. In the case of pure torsional buckling the axis of rotation of the column connecting the shear centres of each cross-section remains straight and each cross-section plane rotates about this axis. In the flexural-torsional stability model the effect of torsion is combined with the conventional Eulerian buckling theories supplying the problem with a new aspect which proves to play an important role in the stability analysis. Analytical procedures predicting the critical behaviour of this kind of columns taking into account also the torsional effects are based on the assumption that the shape of the cross-sections remains unchanged during deformation.

The solution technique conventionally applied in the literature to the problem of flexural-torsional instability is in some extent incomplete. The solution is searched for by assuming certain deflectional and rotational modes of the column which satisfy both the differential equations and the boundary conditions. However, this procedure is

applicable only in those simple cases in which the functions fulfilling the requirements due to boundary conditions can easily be constructed. The aim of this study is to introduce a procedure which could be used to find with ease the complete solution for the problem considered and would be applicable also under various boundary conditions.

FUNDAMENTAL FORMULATION OF THE PROBLEM

The column considered is assumed to be straight having a thin-walled open cross-section. The axial coordinate x coincides with the column axis through the centre of each cross-section. The coordinate axes y, z are the principal axes of the cross-section and the coordinate system used is right-handed. Displacement components of the shear centre in the directions of y and z axes are denoted by v and w, respectively, and the angle of rotation about the column axis correspondingly by φ. The column is loaded at the ends by concentrated compressive loads P the eccentricities of which are e_y and e_z in the directions of the principal axes.

The mathematical formulation of the problem due to flexural-torsional instability, presented in the fundamental textbook [1], is presented by a system of three ordinary differential equations which are coupled if the shear centre and the centre of the cross-section do not coincide with each other or the axial compressive load applied at the ends of the column is eccentric. The problem is formulated by equations

$$\begin{aligned} &EI_y w'''' + Pw'' - P(y_v - e_y)\varphi'' = 0, \\ &EI_z v'''' + Pv'' + P(z_v - e_z)\varphi'' = 0, \\ &EI_\omega \varphi'''' - GI_t\varphi'' + P(r^2 + \beta_y e_y + \beta_z e_z)\varphi'' + P(z_v - e_z)v'' - P(y_v - e_y)w'' = 0, \end{aligned} \tag{1}$$

in which the quantities EI_y, EI_z, EI_ω and GI_t are the both bending, warping and torsional rigidities, respectively, A is the cross-sectional area and coordinates y_v, z_v define the position of the shear center in principal coordinates. The superscript 'prime' means differentiation with respect to the axial coordinate x. In addition, the notations

$$r^2 = \frac{I_z + I_y}{A} + y_v^2 + z_v^2, \quad \beta_z = \frac{1}{I_y}\int_A z(z^2+y^2)dA - 2z_v, \quad \beta_y = \frac{1}{I_z}\int_A y(z^2+y^2)dA - 2y_v$$

are used of which the quantities β_z and β_y are also called WAGNER's coefficients.

Limiting the consideration to columns with singly symmetric cross-sections in which, for example, the z-coordinate line coincides with the axis of symmetry, yields in equations $y_v = 0$ and $\beta_y = 0$. When the loading is assumed, in addition, to be symmetric with respect to the axis of symmetry, i.e. $e_y = 0$, the first one of equations (1) will be separated from the two remaining ones. Thus the problem formulation is

$$\begin{aligned} &EI_y w'''' + Pw'' = 0, \\ &EI_z v'''' + Pv'' + P(z_v - e_z)\varphi'' = 0, \\ &EI_\omega \varphi'''' - GI_t\varphi'' + P(r^2 + \beta_z e_z)\varphi'' + P(z_v - e_z)v'' = 0. \end{aligned} \tag{2}$$

In the continuation, the first one of equations (2) will be left out of consideration. Following the procedure introduced by SIMITSES [2] the two last ones combining the transverse flexural and torsional behaviours can be presented in the form

$$L_1 v + L_2 \varphi = 0, \qquad L_3 v + L_4 \varphi = 0, \tag{3}$$

in which the differential operators are

$$\begin{aligned} L_1 &= EI_z \frac{d^4}{dx^4} + P\frac{d^2}{dx^2}, \qquad L_2 = L_3 = P(z_v - e_z)\frac{d^2}{dx^2}, \\ L_4 &= EI_\omega \frac{d^4}{dx^4} - \Big(GI_t - P(r^2 + \beta_z e_z)\Big)\frac{d^2}{dx^2}. \end{aligned} \tag{4}$$

Since the operators are linear and thus commutative the first one of equations (3) can be operated with L_4 and the second one with L_2 and subtracted from each other. Consequently, a separate function for displacement v is obtained. Operating the first one of equations with L_3 and the second one with L_1 and subtracting yields correspondingly in an identical equation for the angle of rotation φ. These equations

$$(L_1 L_4 - L_2 L_3)v = 0, \qquad (L_1 L_4 - L_2 L_3)\varphi = 0. \tag{5}$$

are ordinary differential equations with constant coefficients and of eighth order. Solutions for them are of the form $v = \exp(\gamma x)$ and $\varphi = \exp(\gamma x)$. Substituting the trial functions into the system (5) results in a corresponding characteristic polynomial of eighth order

$$\gamma^4\{EI_\omega EI_z\gamma^4 + [PEI_\omega - EI_z(GI_t - P\bar{r}^2)]\gamma^2 - P[GI_t - P(\bar{r}^2 - \bar{z}_v^2)]\} = 0, \tag{6}$$

in which the notations $\bar{r}^2 = r^2 + \beta_z e_z$ and $\bar{z}_v = z_v - e_z$ are introduced. Equation (6) has a fourfold root $\gamma = 0$ and the roots

$$\gamma^2 = -b \pm \sqrt{\alpha^2 + \beta^2} = -b \pm \sqrt{b^2 + c}, \tag{7}$$

in which the notations

$$\begin{aligned} b &= P[\bar{r}^2/(2EI_\omega) + 1/(2EI_z)] - GI_t/(2EI_\omega), \\ \alpha &= P[\bar{r}^2/(2EI_\omega) - 1/(2EI_z)] - GI_t/(2EI_\omega), \\ \beta &= P\bar{z}_v/(E\sqrt{I_z I_\omega}), \\ c &= P[GI_t - P(\bar{r}^2 - \bar{z}_v^2)]/(EI_\omega EI_z) \end{aligned} \tag{8}$$

are used. Expression (7) is written in two separate forms of which the first one shows that the term under the square root is always positive. From the second one it can be observed that whether the coefficient c is positive or negative, the characteristic polynomial (6) has two real and two imaginary roots or, alternatively, four pure imaginary roots. The limit $c = 0$ corresponds to the fixed value of the compressive load $P = GI_t/(\bar{r}^2 - \bar{z}_v^2)$. Consequently, the complete solutions for the differential equation system (5) in the region $P < GI_t/(\bar{r}^2 - \bar{z}_v^2)$ are

$$v = A_1 \sinh d_1 x + A_2 \cosh d_1 x + A_3 \sin d_2 x + A_4 \cos d_2 x + A_5 x^3 + A_6 x^2 + A_7 x + A_8, \tag{9a}$$

$$\varphi = B_1 \sinh d_1 x + B_2 \cosh d_1 x + B_3 \sin d_2 x + B_4 \cos d_2 x + B_5 x^3 + B_6 x^2 + B_7 x + B_8, \tag{9b}$$

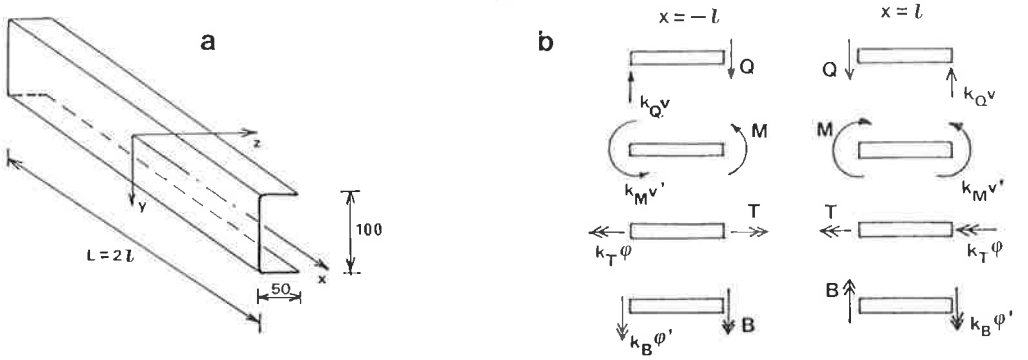

FIGURE 1. (a) Thin-walled column, coordinate system and (b) boundary conditions.

in which the coefficients $d_1^2 = \text{abs}(\sqrt{\text{b}^2 + \text{c}} - \text{b})$ and $d_2^2 = \sqrt{b^2 + c} + b$. Correspondingly, in the region $P > GI_t/(\bar{r}^2 - \bar{z}_v^2)$ the solutions are of the form

$$v = A_1 \sin d_1 x + A_2 \cos d_1 x + A_3 \sin d_2 x + A_4 \cos d_2 x + A_5 x^3 + A_6 x^2 + A_7 x + A_8, \quad (10a)$$

$$\varphi = B_1 \sin d_1 x + B_2 \cos d_1 x + B_3 \sin d_2 x + B_4 \cos d_2 x + B_5 x^3 + B_6 x^2 + B_7 x + B_8. \quad (10b)$$

Inserting the solutions in the original system of equations (3) yields the couplings $B_1 = \lambda_1 A_1$, $B_2 = \lambda_1 A_2$, $B_3 = \lambda_2 A_3$, $B_4 = \lambda_2 A_4$ and $B_5 = A_5 = B_6 = A_6 \equiv 0$ between various constants in which

$$\begin{aligned} \lambda_1 &= (\mp EI_z d_1^2 - P)/(P\bar{z}_v) = P\bar{z}_v/(\mp EI_\omega d_1^2 + GI_t - P\bar{r}^2), \\ \lambda_2 &= (EI_z d_2^2 - P)/(P\bar{z}_v) = P\bar{z}_v/(EI_\omega d_2^2 + GI_t - P\bar{r}^2), \end{aligned} \quad (11)$$

so that only eight independent constants remain. The signs higher up are valid when $P < GI_t/(\bar{r}^2 - \bar{z}_v^2)$ and lower down, correspondingly, when $P > GI_t/(\bar{r}^2 - \bar{z}_v^2)$.

BOUNDARY CONDITIONS

A thin-walled column with length of $L = 2\ell$ is examined. The origin of the coordinate system in which the column is considered is located at the midspan symmetrically with respect to the axial coordinate shown in Figure 1a. The general linearly elastic boundary conditions are assumed in which linear springs resist deflection, rotation, twisting and warping at the ends of the column. The spring constants are denoted with the subscripts referring to the corresponding force quantities. The boundary conditions at the ends of the column, i.e. at $x = \pm\ell$ which are depicted graphically in Figure 1b are [3]

$$\begin{aligned} Q_y(\pm\ell) &= -EI_z v'''(\pm\ell) - Pv'(\pm\ell) - P\bar{z}_v\varphi'(\pm\ell) = \mp k_Q v(\pm\ell), \\ M_z(\pm\ell) &= -EI_z v''(\pm\ell) = \pm k_M v'(\pm\ell), \\ T(\pm\ell) &= -EI_\omega \varphi'''(\pm\ell) + (GI_t - P\bar{r}^2)\varphi'(\pm\ell) - P\bar{z}_v v'(\pm\ell) = \mp k_T \varphi(\pm\ell), \\ B(\pm\ell) &= -EI_\omega \varphi''(\pm\ell) = \pm k_B \varphi'(\pm\ell). \end{aligned} \quad (12)$$

Here the notations Q_y, M_z, T and B for the stress resultants of shear force, bending, twisting and warping moments, respectively, and for corresponding spring stiffnesses

are used. Further, the signs higher up and lower down correspond in each condition to each other. Substituting the solutions for the transverse deflection and torsional angle into the boundary conditions, summing and subtracting mutually the corresponding conditions at each end of the column separates the solution into symmetric and antimetric buckling modes. Thus the coefficient matrix 8×8 of the homogeneous system of equations for constants A_i and B_i will be reduced diagonally to two 4×4 matrices of which the one corresponding to the symmetric solution functions defines the critical load due to symmetric buckling and the other, similarly, the critical load due to antimetric buckling. Transcendental equations yielding in critical load values are obtained by requiring the determinant of each submatrix, separately, to vanish. It is of interest to note that the composition of the determinant, for example in the symmetric case, excludes certain symmetric failure modes due to the rigid body motion which do not represent critical behaviour. Instead, the rigid body motion due to antimetric instability providing the solution with corresponding antimetric failure modes is included in the relevant determinant equation.

It is still worth taking notice of a curious behaviour of the transcendental function which is built up piecewise using two separate solutions (9) and (10). On the limit point, between the two regions defined from the roots of the characteristic polynomial (6) where $P = GI_t/(\bar{r}^2 - \bar{z}_v^2)$, the determinant tends to zero when approached from any region. However, on the limit point the coefficient d_1 utilized in the solutions vanish. At this point the corresponding part of the solution functions have to be replaced by polynomial terms yielding finally in nonzero terms of third and second degree. This new solution will vanish only at a certain fixed value of the length of column producing in the general case a discontinuity of the trancendental function. So, this limit value of the axial load does not represent critical behaviour at the point in question.

NUMERICAL EXAMPLES

Aa an example a column with a thin-walled cold-formed ⊔-cross-section $100 \times 50 \times 4$, shown in Figure 1a, is studied. The geometric properties $A = 737$ mm^2, $I_y = 0.1816$ 10^6 mm^4, $I_z = 1.132$ 10^6 mm^4, $I_t = 4{,}096$ mm^4, $I_\omega = 297.3$ 10^6 mm^6, $z_v = -31.26$ mm, $r^2 = 2{,}759$ mm^2, $e_z = 0$ and the material parameters $E = 2.1$ 10^5 N/mm^2 and $\nu = 0.3$. The length of the column varies from 1 m to 10 m. The yield stress $f_y = 690$ N/mm^2 is selected for practical reasons to cut out too high values of the compressive load. The value of the compressive load which separates the solution to two regions is thus $P = 185.6$ kN. It corresponds to the value of 0.03463 of the scaled non-dimensional variable applied later on the vertical axis of the figures depicting the results obtained.

The aim is to study the effect of various elastic supports on the critical behaviour due to torsional-flexural instability. Among the boundary conditions (12) the cases in which the springs resist arising rotational and torsional angles are selected to be dealt with, whereas the remaining spring constants $k_Q = k_B \equiv 0$. Each constant k_M and k_T, separately, is varied to cover the range from zero to infinity, excluding the zero values which yield in unequilibrated systems. The other boundary conditions stay unchanged.

The computational results, the critical load versus the length of column are shown in Figures 2 and 3. Both of the quantities applied on the coordinate axes are non-dimensional. Similarly, the spring constants are scaled so that rotational springs studied in Figure 2 are varied using the dimensionless factor $k = k_M L/(EI_z)$ and torsional ones,

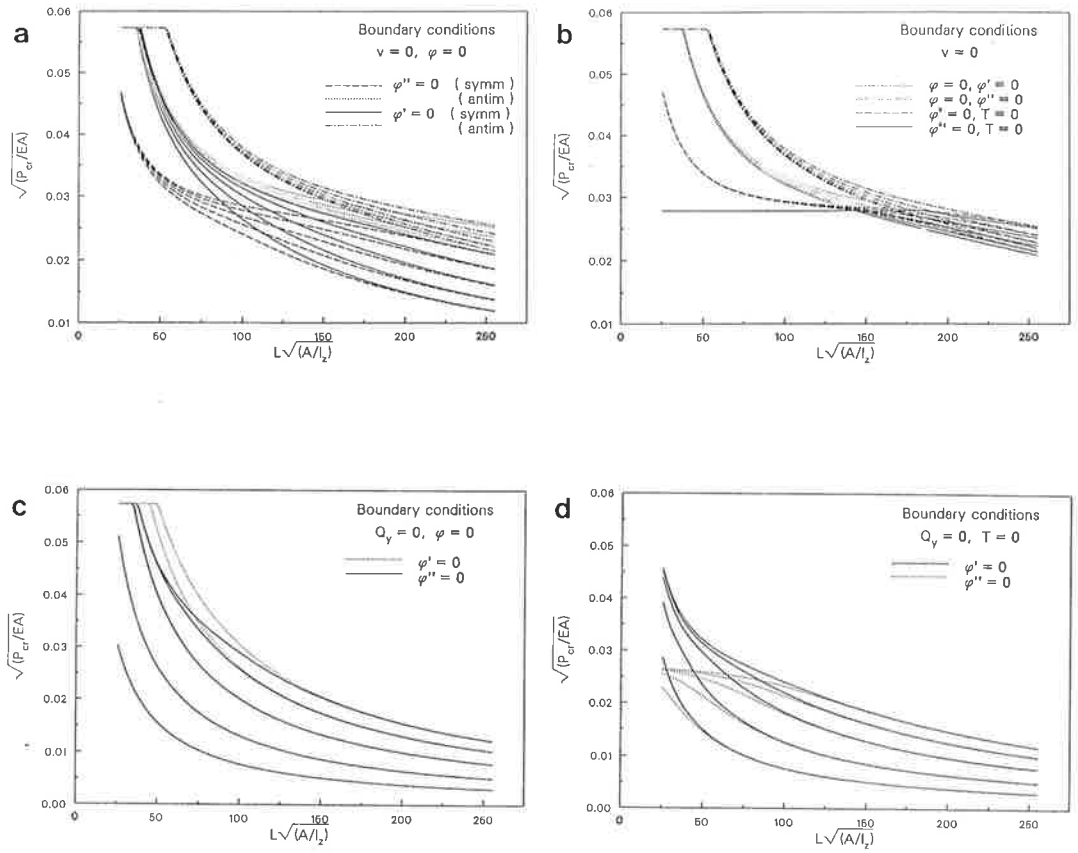

FIGURE 2. Critical load vs. length of a column having rotational springs with stiffnesses $k = 0, 1, \sqrt{10}, 10, \infty$ at each end. In figures (c) and (d) the smallest value of the spring stiffness applied is $1/\sqrt{10}$.

correspondingly, in Figure 3 using $k = k_T L/(GI_t)$.

Figure 2a depicts the case in which the ends of the column are provided with rotational springs while the transverse deflection and twisting are prevented. In addition, various conditions for the derivatives of the angle of twist are considered corresponding to simply supported and clamped ends of the column with respect to torsion. Symmetric failure proves to be most critical for each value of the column length in spite of varying spring stiffnesses which can be seen by comparing the corresponding symmetric and antimetric curves in the figure. It is also to be noticed that for short columns when the torsional behaviour of the column dominates, the influence of the spring stiffness on the value of the critical load is insignificant while the effect of varying boundary conditions with respect to the twisting angle for both the symmetric and antimetric buckling modes is notable. On the other hand, for long columns when the bending is predominant the influence of the spring stiffness is emphasized and the one of boundary conditions decreases. Also, the fact that critical loads due to antimetric buckling for a simply supported column and, correspondingly, due to symmetric buckling for a clamped column coincide, can be verified.

Figure 2b shows the critical load vs. column length due to antimetric failure under

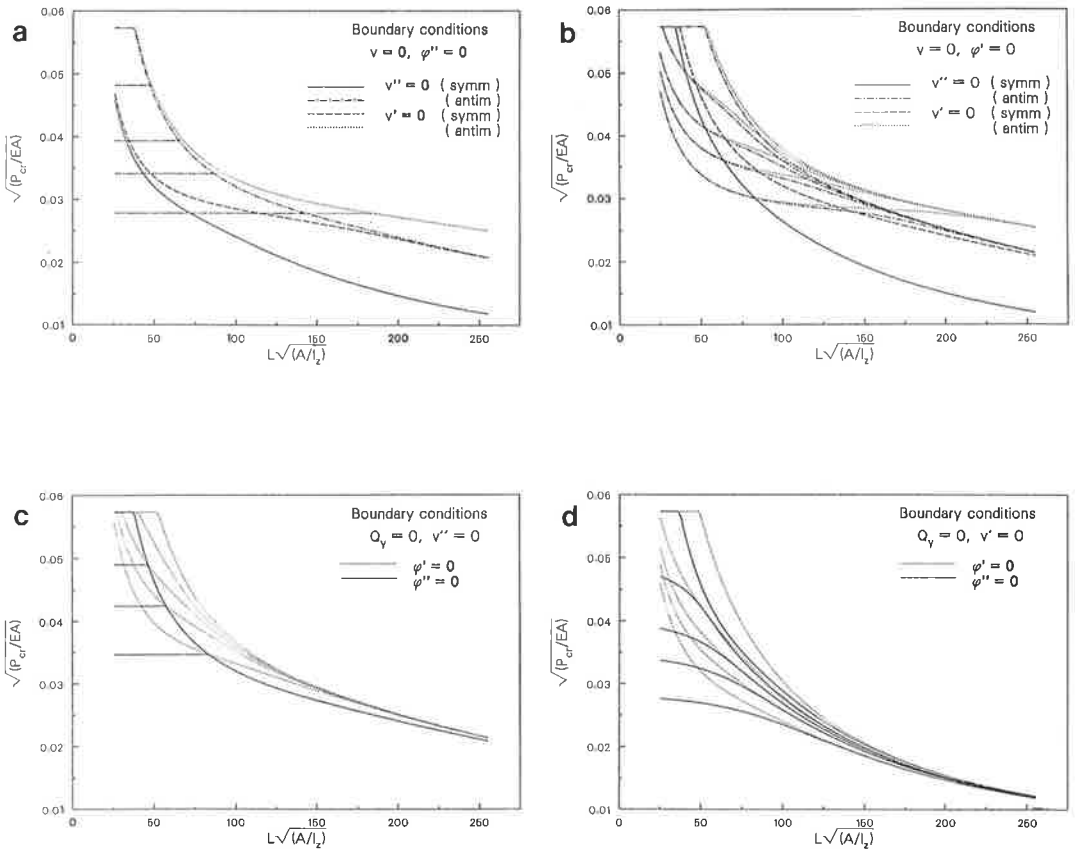

FIGURE 3. Critical load vs. length of a column having torsional springs with stiffnesses $k = 0, 1, 2, 4, \infty$ at each end.

various boundary conditions for the torsional angle. Consideration covers the range from fixed to simply supported columns with respect to the transverse deflection. Attention can be paid for a column having totally free ends with respect to torsion which yields in the critical load value $P = GI_t/\bar{r}^2 = 119.9$ kN (0.02783), independent of the column length. This value corresponds to constant rate of the angle of twist.

Critical loads corresponding to the antimetric failure mode for a column supported with rotational springs and having vanishing shear force at each end are presented in Figures 2c and 2d. Figure 2c shows the results for a stiffer column in which the angle of rotation is not permitted to take place whereas Figure 2d for a more slender one with free rotation at the ends of the column. The rigid body motions due to translation and twisting exclude in these cases the critical symmetric behaviour. Varying boundary conditions for the torsional angle have only a minor effect on the critical load arising only for shorter columns where the torsional behaviour is dominant. When the spring stiffness tends to zero the antimetric rigid body motion will take place yielding in vanishing critical load according to $P = 2kEI_z/L^2$.

Figures 3 depict results corresponding to the critical load value for a column provided with a torsional spring at each end. Critical symmetric behaviour occurs only when the transverse deflection at the ends is prevented, in addition, yielding thus also

in the load value independent of the spring stiffness. Figure 3a shows the distribution of the critical load vs. the length of the column both due to symmetric and antimetric buckling. Here, the transverse deflection is prevented and warping takes place freely at the ends whereas in Figure 3b warping is assumed to be prevented. It can be observed that for long columns the symmetric failure due to bending fixes the critical load and for short ones the antimetric buckling combined with the torsional behaviour is more critical. The antimetric behaviour in Figure 3a is independent of the length according to the expression $P = GI_t(1+k/2)/\bar{r}^2$. It is now obvious that the influence of the boundary conditions concerning the angle of twist disappear when the column length increases and, on the contrary, for short columns the boundary conditions due to deflection has only of a minor significance. The equivalent behaviour between the antimetric simply supported and symmetric clamped columns can again be realized.

Figures 3c and 3d focuse the critical antimetric behaviour of the column in which the boundary condition due to vanishing transverse deflection is replaced by the condition of vanishing shear force. The parallel figures show now the results for a column with whether simply supported or clamped ends with respect to torsion. It is to be noticed that the condition due to vanishing shear force $Q_y = 0$ yields in the equation $v+\bar{z}_v\varphi = 0$ meaning that the displacement of the centre of the cross section is prevented. This boundary condition diverges from that one requiring the displacement of the shear center to vanish applied usually and is stronger yielding in a higher value for critical load. At the same time it presumes twisting to occur about the centre of the cross-section.

The examples considered cover the cases in which both ends of the column are provided with physically equivalent springs. The results presented can, however, be exploited in all common cases encountered in the practice in which a column is provided with a rotational or torsional spring at one end, only. Figures 2 and 3 include thus results for each column having one or two fixed, simply supported or free end. Columns with springs resisting translation or warping at each end can be dealt with, analogously.

CONCLUSIONS

A refined solution procedure for a flexural-torsional problem of an elastic thin-walled column is presented. Especially, the effect of various elastic restraints is studied in the case of a column with a singly symmetric cross-section. The size of the determinant determining the critical load is reduced by treating a structure provided with physically equivalent springs at both ends. This procedure separates the symmetric and antimetric deformation modes. Varying the stiffness of elastic restraints covers the simple basic boundary conditions applied usually. Problems worked on include all possible homogeneous boundary conditions due to restricted rotation and torsion. Solutions calculated are in harmony with the well-known analytical results.

REFERENCES

1. Timoshenko S.P., Gere J.M., Theory of Elastic Stability. 2nd ed., McGraw-Hill 1961.
2. Simitses G.J., An Introduction to Elastic Stability of Structures. Prentice Hall 1976.
3. Mikkola M., Structural Stability. Steel structures RIL 113 Chapters 3 and 4, Helsinki 1975 (in Finnish).

ON THE OPTIMAL DESIGN OF RIGID-PLASTIC ANNULAR PLATES WITH PIECEWISE CONSTANT THICKNESS

ANDRUS SALUPERE
Department of Structural Mechanics
Tallinn Technical University
Ehitajate tee 5, 200108 TALLINN, ESTONIA

ABSTRACT

Rigid-plastic stepped annular plates under uniform pressure load for four types of boundary conditions are considered. Such plate dimensions are sought for which the plate of constant volume has the maximal load carrying capacity.

INTRODUCTION

The problem of the load carrying capacity of two stepped circular plates was solved by Lepik [1] and by König and Rychlevski [2]. Vallner [4,5] examined the load carrying capacity of homogeneous annular plates for different boundary conditions. Lamblin, Guerlement and Save [3] presented optimal parameters for axisymmetrically loaded circular and annular plates with jump nonhomogeneity. They considered simply supported circular plates, annular plates with simply supported outer edge and free inner edge, and annular plates with clamped outer edge and free inner edge.

The aim of this paper is to solve the optimization problem for two-stepped annular plates for four types of boundary conditions (Fig.1), by calculating load carrying capacity. Assuming the plate has a constant volume , optimal parameters for which the load carrying capacity has the maximum value, are to be found.

moments M_1 and M_2 in every s_i and we obtain from (5)-(9) a nonlinear system of equations for p_o, s_i $(i = 2...n-1)$, M_k and $Q(\vartheta)$. From these equations one can calculate quantities p_o, $Q(\vartheta)$ and M_k. Finally, we have a nonlinear system of equations for s_i $(i = 2...n-1)$. This system is solved by the Newton iterative method. For this problem only the solution $\vartheta < s_2 < \ldots < s_{n-1} < 1$ is suitable. Below different cases of boundary conditions are considered.

Case i: The inner edge and the outer edge are clamped (Fig.1i). Seven possible regimes are observed (Fig.3). Additional conditions are

$$0 < M_1(\alpha) < \gamma^2, \tag{12}$$

for regime 2 ;

$$M_k < 1, \tag{13}$$

for regime 3 ;

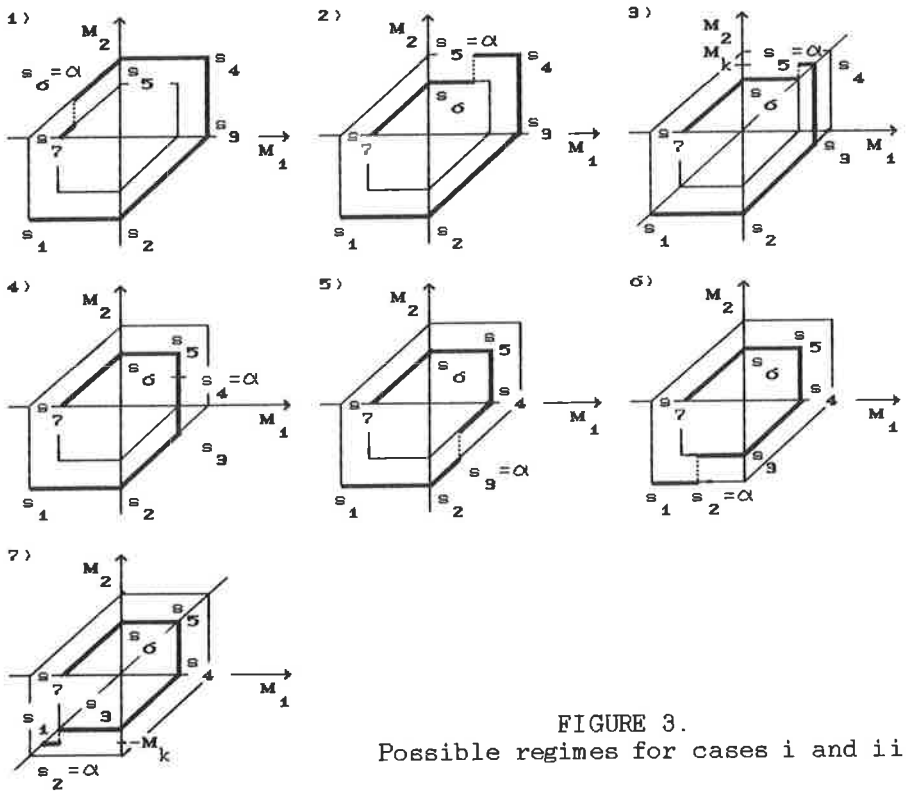

FIGURE 3.
Possible regimes for cases i and ii

$$-\gamma^2 < M_1(\alpha) < 0 \qquad (14)$$

for regime 6 ;

$$M_k > -1, \qquad (15)$$

for regime 7 .

Case ii: The inner edge is clamped and the outer edge is simply supported (Fig.1ii). Six possible regimes are observed. They are analogous with regimes for case i. In the present case regime 1 corresponds to Fig.3-2, regime 2 to Fig.3-3, etc., and regime 6 to Fig.3-7. Now we do not accept intervals $[s_6,s_7]$, because we have the boundary condition $M_1(1) = 0$. Additional conditions are: (12) for regime 1, (13) for regime 2, (14) for regime 5 and (15) for regime 6.

Case iii: The inner edge is simply supported and the outer edge is clamped (Fig.1iii). Six possible regimes are observed (Fig.4). Additional conditions are: (12) for regime 2, (13) for regime 3, and (15) for regime 6 .

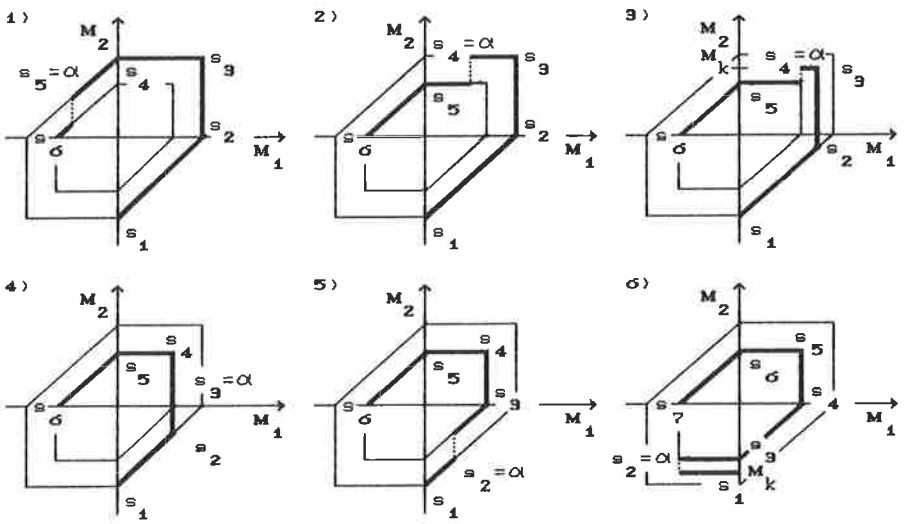

FIGURE 4.
Possible regimes for cases iii and iv

Case iv: The inner edge and the outer edge are simply

supported (Fig.1iv). Five possible regimes are observed (Fig.4). Regime 1 corresponds to Fig.4-2, regime 2 to Fig.4-3 ... and regime 5 to Fig.4-6. We do not accept intervals which correspond to side BC on the Tresca hexagon. Additional conditions are: (12) for regime 1, (13) for regime 2 and (15) for regime 5 .

RESULTS

The problem of the load carrying capacity is solved for four cases and for the following values of parameters α, γ and ϑ : $0.1 \leq \vartheta \leq 0.8$, $\vartheta < \alpha \leq 1$, $0.03 \leq \gamma \leq 1$.

TABLE 1. The load carrying capacity for stepped plates p_o^m which corresponds to the optimal parameters α^m and γ^m, the load carrying capacity for uniform plates p_o^u and the ratio p_o^m/p_o^u.

ϑ	case i			case ii		
	p_o^m	p_o^u	p_o^m/p_o^u	p_o^m	p_o^u	p_o^m/p_o^u
0.1	5.194	3.950	1.315	3.801	2.698	1.409
0.2	6.543	5.273	1.241	4.798	3.662	1.310
0.3	9.078	7.531	1.205	6.655	5.291	1.258
0.4	13.96	11.79	1.184	10.26	8.357	1.228
0.5	24.45	20.87	1.172	17.96	14.89	1.204
0.6	51.08	43.87	1.164	37.30	31.49	1.185
0.7	140.0	120.4	1.163	103.7	86.83	1.194
0.8	623.9	534.2	1.167	458.3	386.2	1.187

ϑ	case iii			case iv		
	p_o^m	p_o^u	p_o^m/p_o^u	p_o^m	p_o^u	p_o^m/p_o^u
0.1	6.863	3.557	1.929	5.154	2.381	2.165
0.2	7.341	4.556	1.611	5.488	3.082	1.781
0.3	9.424	6.302	1.495	6.985	4.292	1.627
0.4	12.92	9.605	1.345	9.748	6.570	1.484
0.5	22.04	16.60	1.328	16.23	11.39	1.425
0.6	41.09	34.19	1.202	30.46	23.49	1.297
0.7	107.5	92.07	1.168	79.48	63.30	1.256
0.8	414.5	400.9	1.034	299.8	275.6	1.088

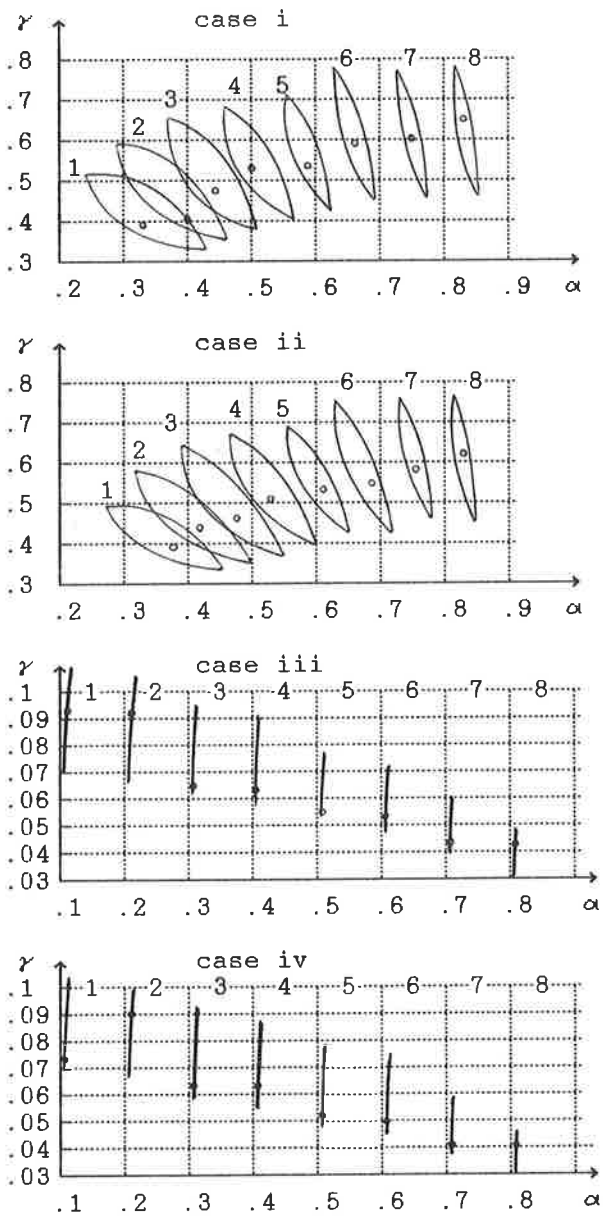

FIGURE 5. Regions which correspond to the condition (17)

We denote the load carrying capacity by p_o and

$$p_o^m = \max_{\alpha,\gamma}(p_o(\alpha,\gamma)). \quad (16)$$

In Fig.5 regions where

$$p_o^m - 0.05p_o^m \le p_o \le p_o^m \quad (17)$$

are presented. Symbols "∘" in Fig.5 mean the optimal parameters α^m and γ^m and they correspond to the maximum values of the load carrying capacity p_o^m. Curve numbers 1-8 correspond to $\vartheta = 0.1 \ldots \vartheta = 0.8$ respectively. It follows from Fig.5 that in the cases iii and iv the extremum point is located close to the inner edge, i.e. we have to put a narrow ring of stiffness near this edge. In Table 1 the load carrying capacity for stepped plates p_o^m which corresponds to the optimal parameters α^m and γ^m, the load carrying capacity for uniform plates p_o^u and the ratio p_o/p_o are given.

CONCLUSIONS

A method for calculating the load carrying capacity for two-stepped rigid- plastic annular plates has been worked out. Numerical data for optimal parameters are given. It follows from these data that the values of the load carrying capacity for two- stepped annular plates can be increased up to 32 per cent for case i, up to 41 per cent for case ii, up to 93 per cent for case iii, up to 117 per cent for case iv, compared with the corresponding plates of uniform thickness. If the parameter ϑ increases, the percentage of economy decreases.

REFERENCES

1. Lepik, Ü., Load carrying capacity of nonhomogeneous plates and shells (in Russian). Izv. Akad. Nauk SSSR, OTN, Mekhanika i Mashinostrojenie. **4**, 1963 pages 167-171
2. König J. A., Rychlevski J., Limit analysis of circular plates with jump homogeneity. Int. J. Solids Structures. **2**, 1966 ,pages 493-513
3. Lamblin D. O., Guerlement G., Save M. A., Solution de dimensionnement plastique de volume minimal de plaques circulaires pleines et sandwiches en présence de contraintes technologiques. Journal de Méchanique théorique et appliquée. **4**, 1985, pages 433-461.
4. Vallner H., On the load carrying capacity of annular plates (in Estonian). Proc. Estonian Agricultural Academy. **17**, 1960, pages 162-175
5. Vallner H., Calculation of the load carrying capacity of rigid-plastic annular plates (in Russian). Inform. Bulletin. VINITI Akad. Nauk SSSR. **2**, 1961, pages 89-98

OPTIMAL DESIGN OF GEOMETRICALLY NON-LINEAR RIGID-PLASTIC STRUCTURES

JAAN LELLEP
Department of theoretical mechanics
Tartu University, 46 Vanemuise, 202400 Tartu, Estonia

ABSTRACT

Problems of optimal design of plastic thin-walled structures are considered taking the post-yield behaviour into account. Material of the structures is assumed to be rigid-plastic obeying Tresca or Mises yield condition. Necessary optimality conditions are established with the aid of the variational methods of the optimal control theory. The minimum weight designs are obtained for cylindrical shells and annular plates.

1. INTRODUCTION

Over past few decades, many authors have developed theoretical and numerical methods for optimal design of elastic and non-elastic members of structures. Clearly, the practical problems in this area are complex. The most of the investigations devoted to the optimization of plastic thin-walled structures have been stated as minimum weight problems for a given collapse load and neglect thus the configuration changes of structures, as shown in the review paper [1] .

A parametrical optimization technique is developed for rigid-plastic cylindrical shells in [2,3] taking the post-yield point behaviour into account. Material of the shells is assumed to obey a piece-wise linear or smooth yield condition. Numerical methods have been used in the case of geometrically non-linear plastic cylindrical shells and annular plates of Von Mises material in [4] . In the present study an attempt is made to establish a general approach to the optimization of geometrically non-linear axisymmetric structures.

2. OPTIMALITY CRITERION AND CONSTRAINTS

Let us consider an axisymmetric plate or shell which operates in the range of plastic deformations. We assume that the deformations are small, but the displacements attain the order of the shell wall thickness. In the case of axisymmetric structures which are subjected to the axisymmetric loads the stress-strain state is also axisymmetric.

Let us assume that the internal loading distribution is given in the form $P=P(x,p_1,\ldots,p_l)$, where the function P is a given function. It is differentiable with respect to $p_1,\ldots,p_l$ and piece-wise continuous with respect to the coordinate x. The parameters $p_1,\ldots,p_l$ are specified or unspecified constants. These assumptions are satisfied, for instance, by the normal pressure of uniform intensity and by the loading of piece-wise constant intensity.

Let $x\in[0,L]$. In order to get sufficient generality of the statement of the problem the interval $(0,L)$ is assumed to be divided into $m+1$ zones, the nodes being at $x=a_j$ $(j=0,\ldots,m+1)$, where $a_0=0$ and $a_{m+1}=L$. In each interval $D_j=(a_j,a_{j+1})$ (here $j=0,\ldots,m$) all cross-sections of the structure are of the same configuration and the dimensions are constants or continuously variable quantities.

The area of the cross-section of the structure may be presented as $S=S_j(x,H,h_1,\ldots,h_m)$ for $x\in D_j$. Here S_j stands for a given differentiable function whereas H is an unknown func-

tion. The constant parameters $h_1,\ldots,h_m$ may be interpreted as the different thicknesses of layers in the case of a non-homogeneous layered structure.

Let us assume that certain restrictions are imposed on the stress-strain state of the structure at the points $x=x_j$ $(j=1,\ldots,k)$ and $x=s_i$ $(i=1,\ldots,n)$, where $x_j \in D_j$. The points of the optimal trajectory $x=s_i$ are associated with the location of absolutely rigid ribs (additional supports). At these points the shear force and the slope of the deflection may have finite discontinuities. At the points x_j and elsewhere these variables are continuous.

The optimization criterion is presented in the form of a Bolza functional

$$J = \sum_{j=0}^{k} \left\{ G_j\left(p_1,\ldots,p_l,h_1,\ldots,h_m,s_1,\ldots,s_n,a_j,a_{j+1},\right.\right.$$
$$\left.\left. W(x_j),\frac{dW(x_j)}{dx},U(x_j)\right) + \int_{D_j} F_j\left(p,s_j,W,\frac{dW}{dx},U\right)dx \right\} \qquad (1)$$

where the functions G_j and F_j are given differentiable functions, whereas W and U stand for the displacements in two directions.

The cost criterion (1) comprises a number of cost functionals associated with particular cases. For instance, the particular case of (1) when $G_0=W(L/2)$, $F_j=0$ corresponds to the minimization of the maximal deflection of a cylindrical shell provided both ends of the shell are fixed on the same manner. In another case when $G_j=h_j(a_{j+1}-a_j)$, $F_j=0$ $(j=0,\ldots,m)$ one has the minimum weight problem of a cylindrical shell of piece-wise constant thickness.

Minimum of the cost criterion is sought for under the condition that the optimal solution satisfies the basic equations of the geometrically non-linear theory of plastic shells as well as the additional constraints. The additional constraints are divided into the groups of global and local constraints. The global constraints are presented as inequalities

$$R_i\left(P,S,W,\frac{dW}{dx},U\right) \le 0; \qquad i = 1,\dots,r \tag{2}$$

and equalities

$$\sum_{j=0}^{k} \int_{D_j} S_{io}\left(P,S_j,W,\frac{dW}{dx},U\right)dx = A_i; \qquad i = 1,\dots,s; \tag{3}$$

where R_i (i=1,...,r) are assumed to be given differentiable functions but S_{io} (i=1,...,s) are piece-wise differentiable. The quantities A_i are given constants. As particular cases of (2) may serve the restrictions which impose upper bounds on the thickness or deflection of the shell.

The local constraints may be expressed in the form of inequalities

$$f_{ij}\left(p_1,\dots,p_l,h_o,\dots,h_m,M_1(x_j),\frac{dM_1(x_j)}{dx},W(x_j),\frac{dW(x_j)}{dx},U(x_j)\right)\le 0, \tag{4}$$

$$i = 1,\dots,p_j; \qquad j \in K$$

and equalities

$$g_{ij}\left(p_1,\dots,p_l,h_1,\dots,h_m,s_1,\dots,s_n,M_1(s_j),\frac{dM_1(s_j\pm)}{dx},\right.$$

$$\left.\frac{dW(s_j\pm)}{dx},U(s_j\pm)\right) = 0; \quad i = 1,\dots,q_j; \; j = 1,\dots,n. \tag{5}$$

where M_1 is the bending moment and f_{ij}, g_{ij} are given functions. The set K is a subset of integers 0,...,k. It may be an empty set, also.

Constraints (4) and (5) express intermediate conditions. If, for instance, at $x=s_j$ the additional rigid ribs are located, one has $W(s_j)=0$; $M_1(s_j)=M_*$. These conditions may be considered as particular cases of (5).

3. BASIC EQUATIONS AND METHODS OF SOLUTION

Material of the shell is rigid-plastic one. The yield surface in the space of moments $M_{1,2}$ and membrane forces $N_{1,2}$ is specified with the aid of the set of inequalities

$$\Phi_{ij}(M_1, M_2, N_1, N_2, H, h_1, \ldots, h_m) \leq 0, \qquad i \in I \tag{6}$$

for each region D_j ($j=0,\ldots,k$). Here Φ_{ij} stand for given functions and I is a fixed set of integers.

A deformation-type theory of plasticity is employed and the deformations components and equilibrium equations are chosen in consistance with the Von Karman non-linear shell theory. Following state variables are introduced

$$y_1=M_1, \quad y_2=\frac{dM_1}{dx}, \quad y_3=W, \quad y_4=\frac{dW}{dx}, \quad y_5=U, \quad y_6=N_1 . \tag{7}$$

The gradientality rule and equilibrium equations may be transformed into a set of the first order equations with respect to the state variables (7). For instance, in the case of a cylindrical shell the set of basic equations has the form

$$\begin{aligned} &y_1' = y_2; \qquad y_2' = N_1\Phi^{1j} - \frac{N_2}{A} + P; \\ &y_3' = y_4; \qquad y_4' = \Phi^{1j}; \qquad y_5' = -\frac{1}{2}y_4^2 + \Phi^{2j} \end{aligned} \tag{8}$$

for each $x \in D_j$, provided the symmetry conditions are met. The primes denote differentiation with respect to x.

In (8) following notation is used:

$$\Phi^{1,2j} = \sum_{i \in I} \nu_i^2 \frac{\partial \Phi_{ij}}{\partial M_1, N_1} . \tag{9}$$

Here ν_i stands for an unknown scalar multiplier whereas Φ_{ij} denote the left-hand sides of equations of the yield surface (6).

Similar equations may be obtained for the case of annular plates. Thus it is reasonable to assume that the state variables satisfy the differential equations

$$y_i' = Y_i(y_1,\dots,y_6,h_1,\dots,h_m,M_2,N_2,H); \qquad i = 1,\dots,6 \qquad (10)$$

and certain algebraic requirements

$$Z_j(y_1,\dots,y_6,h_1,\dots,h_m,M_2,N_2,H,\nu_i) = 0; \qquad j \in Z\,. \qquad (11)$$

Some of the relations of type (11) have to be used for elimination of ν_i from equations (10).

The posed problem consists in the minimization of the functional (1) taking into account the constraints (10) and (11) as well as the plasticity conditions (6) and additional requirements (2) - (5). The problem is considered as a control problem. Necessary optimality conditions are obtained with the aid of the variational methods of the optimal control theory. This yields a set of non-linear differential and algebraic equations which is solved in particular cases of circular cylindrical shells and annular plates.

4. NUMERICAL RESULTS

Let us study the weight minimization of a sandwich cylindrical shell under the condition that the deflections of the design of variable thickness do not exceed the deflections of the associated shell of constant thickness. The shell is hinged at both ends and is subjected to the internal pressure of intensity $P=pN_o/A$ and to the axial force $N_1=n_1N_o$.

In the case of a material which obeys Tresca yield condition the problem may be solved analytically. The non-dimensional face-sheet thickness v may be presented as

$$v = \begin{cases} 1 + \left\{n_1 - p + (p-1)\operatorname{ch}\beta(1-\xi_1)\right\}\dfrac{\operatorname{ch}\beta\xi}{\operatorname{ch}\beta}; & \xi\in(0,\xi_1), \\ p + \dfrac{1}{\operatorname{ch}\beta}\left\{(n_1-p)\operatorname{ch}\beta\xi + (1-p)\operatorname{sh}\beta\xi_1\operatorname{sh}\beta(1-\xi)\right\}; & \xi\in(\xi_1,1), \end{cases} \qquad (12)$$

where $\beta = l\sqrt{N_o/AM_o}$, $\xi = x/l$ and

$$\xi_1 = 1 - \frac{1}{\beta}\sqrt{\frac{2\Phi_m}{p-1}} .$$

Here M_o and N_o stand for the yield moment and yield force, respectively. It is assumed that the stress state of the shell corresponds to the flat $N_2=N_o$ and the stress profile is bounded by the restriction $\Phi(m_1, n_1, n_2, v) \leq 0$. The solution of the equation $\Phi = 0$ with respect to m_1 is denoted by Φ_m.

Economy of the design with the thickness (12) depends on the load parameters and geometry parameter of the shell.For instance, in the case of $\beta=16$; $n_1= 0,2$; $p = 1,4$ one can save 18% of material using the design of variable thickness. For $n_1= 0,4$; $p=1,3$ the maximal saving equals 13%.

In the case of Von Mises material the sets (10), (11) must be integrated numerically.For solving the boundary value problems a modification of the method of adjoint operators was employed.

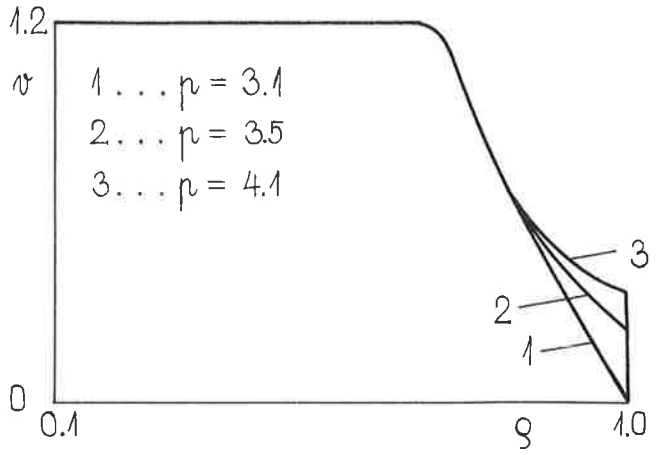

Fig.1. Optimal design of an annular plate.

The optimal material distribution for an annular plate is presented in Fig. 1. The plate is hinged at the outer edge and free at the inner edge. It is subjected to the action of the uniformly distributed transverse pressure. The minimum weight design is established under the condition that the maximum deflections of the plates of variable and constant thicknesses,

respectively, coincide.Curve 1 in Fig.1 corresponds to the limit state. Now the thickness at the outer edge vanishes. When the load increases the thickness at r/R = 1 obtains finite values.Corresponding to these designs savings are equal 14%, 12% and 10%, respectively.

REFERENCES

1. Lellep J., Lepik Ü., Analytical methods in plastic structural design. Eng. Optimiz., 1984, 7, № 3, p. 209-239.
2. Lellep J., Parametrical optimization of plastic cylindrical shells in the post-yield range. Int. J. Eng. Sci., 1985, 23, № 12, p. 1289-1303
3. Lellep J., Optimal design of plastic reinforced cylindrical shells. Control Theory and Adv. Technol.,1989, 5, № 2, p. 119-135.

4M Леллеп Я., Маяк Ю., Оптимальное проектирование жесткопластических кольцевых пластин при условии пластичности Мизеса. Уч. зап. Тартуского ун-та, 1989, 853, с. 38-48.

FLOW CALCULATION IN A PRESSURE-JET HELICOPTER ROTOR BLADE

JUKKA MIKKONEN
Finnish Air Force Depot
P.O. Box 210, SF-33101 TAMPERE, FINLAND

ABSTRACT

The principle of flow calculation in the blade of a pressure-jet helicopter (hollow rotor blades, nozzles at blade tips) is presented. In this calculation method a minimum amount of simplifying assumptions is taken. The blade is divided into elements and practically an exact solution is made for each element. The solution is based on continuity, energy and momentum equations and gas equation of state. Friction, mass forces and heat transfer are taken into account.

The same calculation method is useful when calculating a wind power plant (that produces low pressure rotating a turbine).

SYMBOLS

A	flow area
a_c	Coriolis-acceleration
C	circumference of flow area
c_f	friction factor
c_p	specific heat capacity at constant pressure
e	specific internal energy
F	function, force
F_c	Coriolis-force
$F_{viscous}$	friction force
f	mass force
g	acceleration of gravity (=9.80665 m/s^2)
h	specific enthalpy
M_c	Coriolis-moment
m	mass
$\dot{m}$	mass flow
P_{COMP}	isentropic compressor power

The Coriolis-acceleration of air flowing inside the blade [1, p. 173]:

(1) $a_c = 2\Omega u$

The Coriolis-moment preventing rotation, taking (1) into account:

$$M_C = \int_0^R r dF_C = \int_0^R r dm \cdot a_C = \int_0^R r \rho A dr \cdot 2\Omega u = \int_0^R r m \cdot 2\Omega dr.$$ And

(2) $M_c = m\Omega R^2$

The useful mechanical power, net power P_{NET}, is calculated by subtracting Coriolis-power $M_c\Omega$ from jet power $mu_N V_t$:

(3) $P_{NET} = m(u_N V_t - V_t^2)$

The isentropic compressor power P_{COMP} (using stagnation temperature after compressor T_{COMP}):

(4) $P_{COMP} = mc_p(T_{COMP} - T_a)$

Also (energy balance):

(5) $P_{COMP} = P_{NET} + \frac{1}{2}m(u_N - V_t)^2 + mc_p(T_N - T_a) - mq$

The heat transfer term q represents heating or cooling.

The Flow in the straight part of the blade

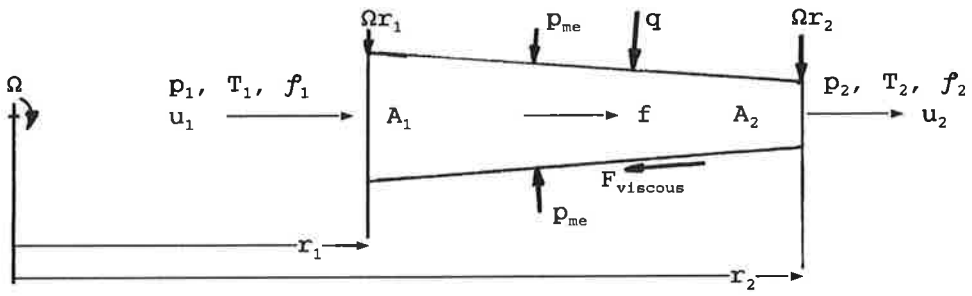

FIG. 2. The flow in a blade element.

Figure 2 represents a blade element. The flow cross-sectional area A in the blade may vary with radius r. The gas (air) flowing in the blade is affected by mass force f (centrifugal force) and friction force $F_{viscous}$. Term q takes heat transfer (air cooling) into account. The following equations [2] are needeed.

Continuity equation:

$$(6) \qquad -\iint_S \rho\bar{V}\cdot d\bar{S} = \frac{\partial}{\partial t}\iiint_V \rho dV$$

Momentum equation:

$$(7) \qquad \iint_S (\rho\bar{V}\cdot d\bar{S})\bar{V} + \iiint_V \frac{\partial(\rho\bar{V})}{\partial t} dV = \iiint_V \rho\bar{f} dV - \iint_S p d\bar{S} + \bar{F}_{viscous}$$

Energy equation:

$$(8) \qquad Q + P_{shaft} + P_{viscous} - \iint_S p\bar{V}\cdot d\bar{S} + \iiint_V \rho(\bar{f}\cdot\bar{V})dV = \iiint_V \frac{\partial}{\partial t}[\rho(e+V^2/2+gz)]dV + \iint_S \rho(e+V^2/2+gz)\bar{V}\cdot d\bar{S}$$

The flow is assumed stationary and 1-dimensional. The height term gz and also P_{shaft} and $P_{viscous}$ are neglected (no mechanical energy transfer). We get:

(9) $$\rho_2 u_2 A_2 = \rho_1 u_1 A_1$$

(10) $$\rho_2 u_2^2 A_2 - \rho_1 u_1^2 A_1 + p_2 A_2 - p_1 A_1 + (A_1 - A_2) p_{me}$$
$$= \rho_{me} A_{me} \cdot \int_{r_1}^{r_2} f dr - \tau_{me} C_{me} (r_2 - r_1)$$

(11) $$h_2 + u_2^2/2 = h_1 + u_1^2/2 + q + \int_{r_1}^{r_2} f dr$$

or (for a calorical perfect gas)

$$c_p T_2 = c_p T_1 + q + \int_{r_1}^{r_2} f dr$$

Now we take a numerical method when solving these equations and use the element mean values p_{me}, ρ_{me}, A_{me}, τ_{me} (shear stress) and C_{me} (circumference of the cross-section) for the element in figure 2.

The centrifugal force term:

(12) $$f = \Omega^2 r$$

The shear stress (c_f =friction coefficient) [4]:

(13) $$\tau = \tfrac{1}{2} \rho u^2 c_f$$

Also the equation of state for a perfect gas (it holds well for air)

(14) $$p = \rho R T$$

is needeed. We assume that the quantities p_1, ρ_1, T_1 and u_1 (fig. 2) must be calculated when other quantities are known (mean values p_{me}, ρ_{me}, etc. are not known). As well p_2, ρ_2, T_2 and u_2 may be unknown quantities. When using equations (9)...(14) a system of nonlinear equations (4 unknown quantities) is obtained. It may be solved by solving the equation

$$(15) \qquad F = u_2 - u_1 + 1/\mathbf{m}\cdot[p_2A_2 - p_1A_1 + (A_1 - A_2)p_{me} - \tfrac{1}{2}\rho_{me}A_{me}\Omega^2(r_2^2 - r_1^2) + \tau_{me}C_{me}(r_2 - r_1)] = 0 ,$$

where

$p_1 = \rho_1 R T_1$

$\rho_1 = \mathbf{m}/u_1 A_1$

$T_1 = T_2 + [u_2^2 - u_1^2 - 2q - \Omega^2(r_2^2 - r_1^2)]/2c_p$

$\tau_{me} = \tfrac{1}{2}\rho_{me} u_{me}^2 C_{fme}$

p_{me}, ρ_{me}, A_{me}, τ_{me} ja C_{me} (circumference) are mean values in the element. First, give some value to u_1 ($u_1 = u_2$). The new value of u_1 is $(u_1)_n$ and it is calculated iteratively (Newton`s method):

$$(16) \qquad (u_1)_n = -F(u_1)/F'(u_1) + u_1 ,$$

where

$$F'(u_1) = -1 - A_1/\mathbf{m}\cdot p_1'(u_1) - A_{me}\Omega^2/2\mathbf{m}\cdot(r_2^2 - r_1^2)\cdot\rho_{me}'(u_1) + C_{me}(r_2 - r_1)/\mathbf{m}\cdot\tau_{me}'(u_1)$$

$$p_1'(u_1) = -\mathbf{m}R/A_1\cdot\left\{[2c_pT_2 + u_2^2 - 2q - \Omega^2(r_2^2 - r_1^2)]/u_1^2 + 1\right\}/2c_p$$

$$\rho_{me}'(u_1) = -\tfrac{1}{2}\mathbf{m}/A_1u_1^2$$

$$\tau_{me}'(u_1) = c_{fme}[-\tfrac{1}{2}\mathbf{m}u_{me}/A_1u_1^2 + \rho_{me}]u_{me}/2$$

During the solving prosess the values of friction coefficient c_{fme} and heat transfer term q are calculated, using suitable correlations. There is no room for these calculations (and for many other rotor calculations) in this paper.

DISCUSSION

Only the main principle of rotor calculation was presented. The considerations of nozzle, rotor net power and so on was not presented here. For this reason no results from these considerations is shown. However, complete helicopter power demand calculations have shown the total power transmission efficiency to be (assuming isentropic compressor) 0.5...0.6.

REFERENCES

[1] Gessow A. and Myers G. C., Aerodynamics of the Helicop ter. 7. edition, 1983. Frederick Ungar Publishing Co., New York.

[2] John D. Anderson, Jr., Modern Compressible Flow with His torical Perspective. Copyright 1982 by McGraw-Hill, Inc.

AUTOMATED FINITE ELEMENT ANALYSIS OF CRACKED STRUCTURES

Timo P.J. Mikkola
Technical Research Centre of Finland (VTT)
Nuclear Engineering Laboratory
Vuorimiehentie 5, SF-02150 ESPOO, FINLAND

ABSTRACT

An automated system has been developed for the analysis of structures containing surface cracks using three dimensional (3D) Finite Element (FE) models. The system has been developed for safety studies of nuclear power plant components where high reliability and accuracy is required. Typical analyzed structures are thick walled nuclear power plant components under pressure and thermal transient loadings. In the validation of the automated analysis capability results from several nearly full-scale tests have been used as well as other published results. The developed system is capable to produce results with high accuracy.

INTRODUCTION

Safety and integrity of nuclear power plant components must be guaranteed in all postulated loading conditions for the plant lifetime. In safety studies flawed structures are often analyzed under severe loading conditions with extremely pessimistic assumptions of e.g. loads, material parameters and crack sizes. The conservatisms are justified due to the fatal consequences of failures, but this may yield overly pessimistic results. In order to reduce the conservatism, large effort is being paid on refining the analysis methods as well as on improving material characterization and on accurate analysis of the real loading conditions.

The accuracy of fracture and fatigue analyses can be improved by using three dimensional (3D) finite element (FE) models for the fracture parameter calculation. The present state-of-the-art in numerical and experimental fracture mechanics and the availability of supercomputers have significantly improved the possibilities to perform such analyses. However, difficulties arise from the large effort needed in preparing 3D FE-models of flawed structures. Also, the accuracy level of the analysis results is often unknown. The analysis models are complicated and the amount of results is large, which makes the accuracy assessment difficult.

At the Technical Research Centre of Finland (VTT) a three year research project has been initiated in 1989 for improving the capability of analyzing flawed structures with fracture mechanics. The project focuses on automating the use of 3D FE-models and on developing methods for accuracy assessment and for directing model refinement, see [4, 5].

The automated system can be used for developing a database solution of the structure for an engineering fracture assessment program VTTSIF [10]. Subsequent analyses with this program can be performed very easily and costly 3D FE-analyses can be avoided. On the other hand, the automated system is at the same time available for a more accurate analysis.

AUTOMATED FE-MODEL GENERATION

The FE-model is created with the ACR-program [3] in two phases. First a surface crack in a plate is modeled and in the second phase this plate model is transformed into the final geometry. For pipes, elbows and pressure vessels the geometry transformation is a simple analytical function. For more complicated structures a very general transformation scheme is being developed using parametric representation of the geometry. With the ACR-program, surface cracks in almost any geometry can be modeled.

The initial plate FE-model is made by using the ACRGEN-program module for writeing a session file for the PATRAN-program [9], which is then used for generating FE-model for the plate. The ACR-program uses mainly basic features of the PATRAN-program and special features are avoided. The ACR-program could be used together with other advanced FE-modeler programs as well. After the plate model is generated, the ACRMOD-program module is used for transforming the geometry, modifying the mesh and adding loads and boundary conditions. Several other modifications are also performed specially for the FE-mesh near the crack tip area. An FE-model for an elbow with a long axial surface crack generated using the ACR-program is shown in Fig. 1.

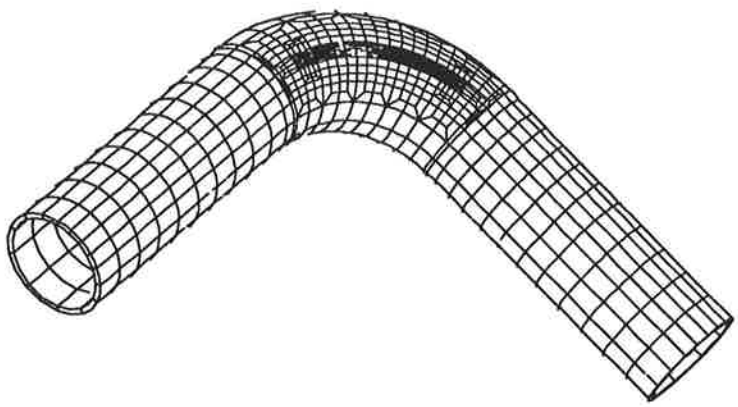

FIGURE 1. An FE-model of an elbow with long axial crack [by Keijo Koski, VTT].

The ACR-program is not intended for replacing an FE-modeler program. The PATRAN-program can be used for generating FE-model for other parts of the structure, adding

loads and boundary conditions and eg. for mirroring the FE-model of the crack area to produce a more complete model of the crack.

Modelling of the Crack Area

The FE-mesh near the crack location developed by the ACR-program is well suited for the use of the virtual crack extension- (VCE) method in J-integral calculation, see Fig. 2. The elements form circular layers around the crack front, which are natural paths for J-integral evaluation. The nodes on the end-planes of these element layers are repositioned on planes perpendicular to the crack front. The nodal points of the innermost element layer can be modified for producing 1/r- or $1/\sqrt{r}$-singularity at the crack tip using the standard techniques for the isoparametric continuum elements [2]. Also other modifications are performed.

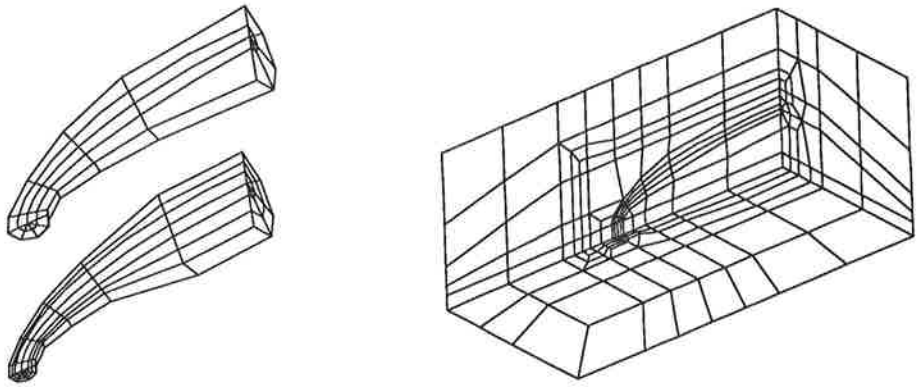

FIGURE 2. Detail of the FE-mesh near the crack with the basic mesh density and a finer mesh density; an FE-model of a shallow crack with several element layers over thickness and separate element layer for cladding material.

The basic FE-mesh at the crack area was initially designed to contain as few elements as possible. The number of element layers around the crack front is two for the basic mesh density and more element layers can be generated, see Fig. 2. Also the number of elements in the crack front direction can be increased as well as the number of elements over ligament. Two standard crack forms are available, namely a semi-elliptical surface crack and a constant depth crack with circular arc at the end. Further, it is possible to define the crack front location directly using cubic spline functions.

Currently the FE-mesh is being developed specially for shallow cracks penetrating an interface between two materials in an inclined angle. This is the case for a shallow crack in the inner surface of a reactor pressure vessel having a cladding layer. Also a special FE-mesh is being developed to be used for the analysis of crack growth by tearing.

Geometry Transformations

The geometry transformations are used for mapping the initial plate to the final geometry of the structure. Transformations have been developed for cylindrical, toroidal and spherical geometries, see Fig. 3. These correspond to the geometries of several typical nuclear power plant components e.g. pipes, elbows and pressure vessels. The transformations do not use any information of the crack itself and thus they can be used for developing circumferential or

axial part through cracks as well as inclined cracks or there may be several cracks in the model. The crack can also be transformed to the inner or outer surface of the final geometry.

The system is being extended to cracks in the nozzle area of a pressure vessel, see Fig. 3. This transformation is based on parametric description of the two surfaces of the structure. With this transformation, practically all thick walled geometries containing a surface crack can be modeled with the ACR-program. Typical applications are modelling of cracks in a pressure vessel nozzle area.

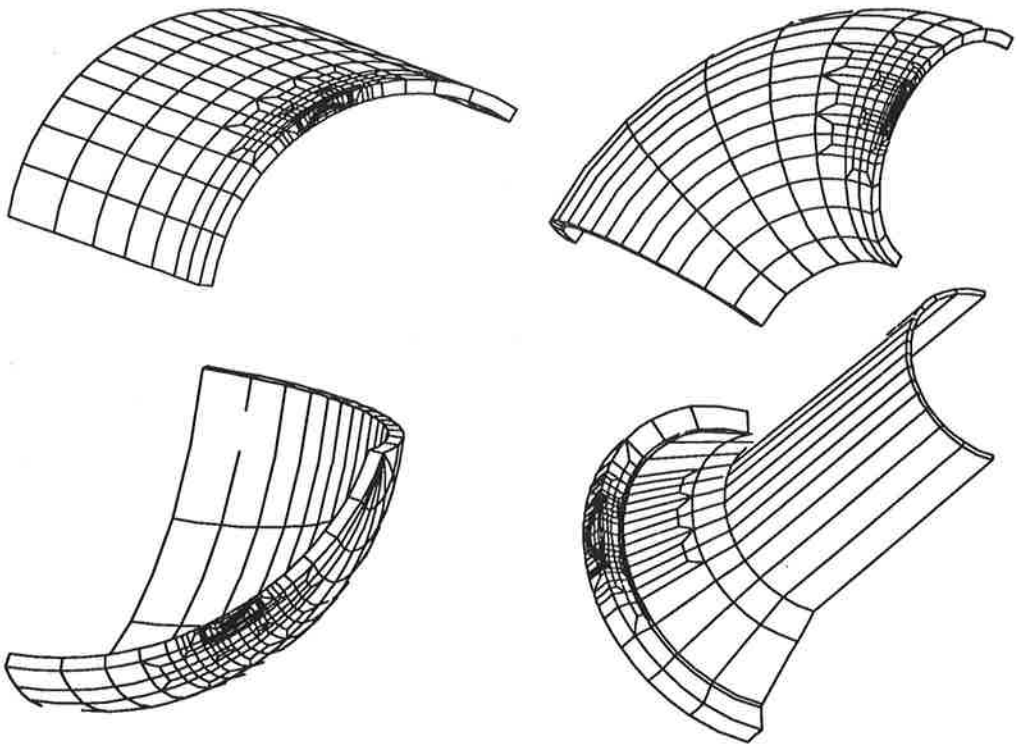

FIGURE 3. Available transformations in the ACR-program.

Generation of Loads and Boundary Conditions

The ACR-program can generate loads and boundary conditions only for the model part formed of the initial plate geometry. The PATRAN-program can always be used for generating loads and boundary conditions for all parts of the FE-model including also the model near the crack.

Pressure and thermal shock load conditions can be generated separately for the six surfaces of the initial 'plate'-model and also on the crack flank surfaces. Several interfaces for user supplied subroutines are available in the ACR-program for specifying the load conditions. This capability has been used eg. for generating transient temperatures for the inner surface of a pressure vessel with a local cooling strip.

The boundary conditions can be generated separately to the same surfaces as the loads. In addition, separate boundary conditions for the corner nodes can be given. The boundary

conditions for each degree-of-freedom (dof) concidered are: fixed, constant for the plane and rotation of the plane over a coordinate axis. The last condition will be generalised to constraining the nodes in a plane to displace as a plane. Special user suplied interface subroutines for the boundary conditions can be used similarly as for the loads for describing special conditions. This capability has been used eg. for a 3D-model to generate boundary conditions calculated with an uncracked axisymmetric model.

ACCURACY CONTROL OF THE RESULTS

The modelling of the tip crack area has been developed to give accurate results for a broad range of crack depths and lengths. The results for a plate with surface crack under tension from [6] have been used as a basic test case when developing the FE-model. The present quality of the generated mesh is clearly satisfactory for most applications.

The developed automated model generating capability cannot guarantee the same accuracy for all possible crack sizes, structure geometries and loading conditions. The transformations may produce bad shaped elements or the user may wish to perform an exceptionally accurate analysis. For these cases, it should be possible to use the ACR-program for generating an initial mesh and then to perform local mesh refinement for improving the accuracy of the results.

The present commercially available FE-programs offer only limited means for local mesh refinement once the mesh is generated. Three practical choices to improve the accuracy are mesh re-design, use of higher order elements (p-version refinement) and element sub-division (h-version refinement). The first one is used in the development of the system but it is not very useful in practical applications. The second method can be used only with a special analysis program unlike the third method, which is applicable with almost all analysis programs. With the third method the only requirement for the analysis program is that it accepts constraint equations.

Results for Surface Crack in a Plate Under Tension

A large matrix of surface crack sizes in a plate under tension load has been analyzed [5] and the results are compared with the results of Newman and Raju [6]. The analyses were made with the 20-noded isoparametric solid element of the ADINA-program [1] and the VTTVIRT-program [12] is used for J-integral evaluation from the ADINA-results.

The FE-models were automatically created using the ACR-program and the basic FE-mesh density with only two element layers around the crack front. For shallow cracks with crack depth of a/t = 0.2 one extra element layer over the ligament was used. Typical results for the scaled stress intensity factor along crack front are shown in Fig. 4 for the crack length a/c = 0.2 for two crack depths. The stress intensity factor is scaled as

$$K = F \sigma_0 \sqrt{\frac{\pi a}{Q}} \qquad (1)$$

where F is the shape factor, σ_0 is the nominal stress and Q is elliptical integral of the first kind. Also the FE-results and results of an analytical formula given in [6] are shown. The results are typical in that all three solutions are inside a narrow band.

The accuracy of the FE-results of Newman and Raju is not known. The analytical formula is result of curve fitting to the FE-results with maximum difference of less than 5 % when compared to the maximum FE-result for corresponding crack size [6]. The present results are in ± 5 % difference band everywhere along crack front for most of the crack sizes and within ± 8 % for all results when referred to the FE-results of [6]. A more complete discussion of the present results is given in [5].

The test matrix was analyzed using full (3*3*3) and reduced (2*2*2) integration and both 1/r- and 1/√r-singularity. Only insignificant changes were found in the results. The VCE-method as implemented in the VTTVIRT-program [12] has proven to be very insensitive of the integration path. The numerical path dependence of J-integral was less than 1 % for all the results, when compared to the mean of all paths. The path dependence measures obviously mesh quality within the integration path. The stress-strain field is dominated by the crack tip singularity and is modeled here using singular elements. It seems reasonable that it is insensitive to the errors in other parts of the mesh.

The modelling of the crack tip singularity is sufficiently accurate. The main source of error for the present models is in the elements connecting the crack tip elements with the regular elements far from the crack. The accuracy of the present results is acceptable in general. In further improvement of the mesh, methods for local refinement should be used.

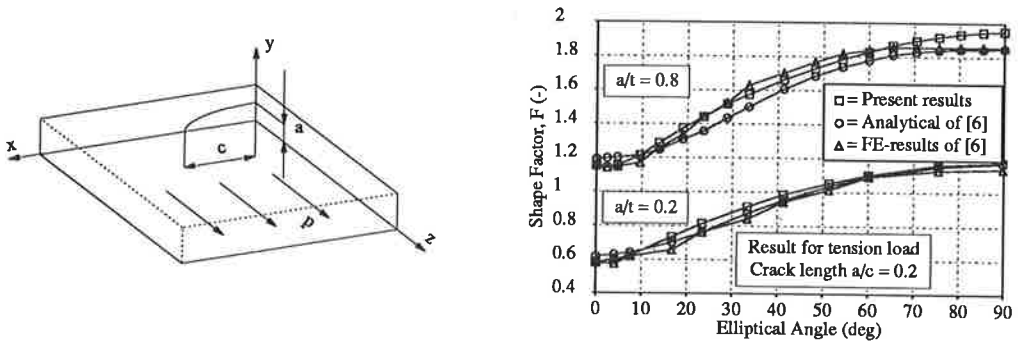

FIGURE 4. Results for a plate with a surface crack under remote tension.

Local Model Refinement Procedure

The h-version model refinement has been used for 2D-models together with an error measure to improve result accuracy [5]. The error measure was based on estimating the error in equilibrium equations for the FE-solution [7, 8] with equation

$$F_i^e = \int_{A_e} \left(\sigma_{ij}^{FE} n_j - t_i \right) dA \qquad (2)$$

where t_i is true (unknown) traction force on element surface A_e, σ_{ij}^{FE} finite-element approximation for the stresses and n_j the surface normal. This is equivalent to integrating the residual error in equilibrium equation over the element volume. The true traction is unknown, but the integral of it over the element surface is zero, while the structure has to be in balance. The unbalanced force was calculated using (2) separately for each element.

The single edge cracked strip under tension was used as the test case. The crack depths a/t = 0.1, 0.2, 0.3, 0.5 and 0.8 were analyzed. The unbalanced force was calculated for each element and minimized by mesh refinement. The 2D-analyses were made with the 8-noded isoparametric plane element of the ADINA-program [1] and J-integrals were calculated with the VTTVIRT-program [12]. The unbalanced force and the mesh refinements were made with the Post3D-program [8].

The mesh refinement was made by sub-dividing the elements with largest unbalanced force. The results for the initial mesh and the mesh after refinement are shown in Fig. 5. The refined meshes are also shown for the three shallow crack models. The stress intensity factor is scaled with formula

$$K = H \sigma_0 \sqrt{\pi a} \, (1 - a/t)^{-1.5} \qquad (3)$$

where σ_0 is nominal stress, a crack depth, t wall thickness and H the shape factor. The solution of [11] is used for comparison and it is drawn with the given accuracy limits ± 0.5 %.

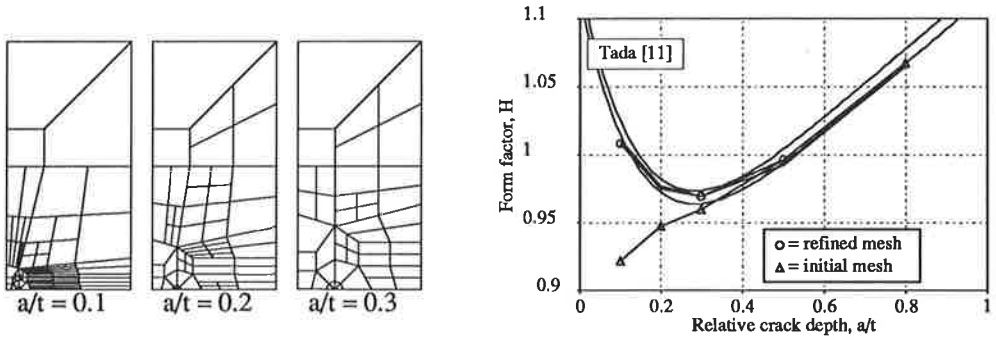

FIGURE 5. Stress intensity factor results for a cracked strip with h-version mesh refinement.

The results for the two deep crack models, a/t = 0.5 and 0.8 were accurate already for the initial mesh and the error was large only for the shallow crack case with a/t = 0.1. For the three shallow cracks a/t = 0.1, 0.2 and 0.3, the mesh was refined until the maximum unbalanced force occurred in the second circular layer of elements at the crack area. The elements in these two layers were not sub-divided.

At first, the unbalanced force weighted with the element strain energy was used to direct the refinement. Only three and two refinements were required for the a/t = 0.2 and 0.3 cases respectively and the resulting meshes are shown in Fig. 5. For the shallow crack model with a/t = 0.1, mesh refinement was made also with unweighted unbalanced force. The final result was found with fewer steps without weighting. The resulting mesh refinement concentrated better to the stress concentration area as can be seen in Fig. 5. At first the stress intensity factor converged rapidly and then the rate of convergence slowed down. This indicated, that the mesh should also be refined at the crack tip area as was suggested also by the unbalanced force.

Preliminary results have shown that the behaviour of the unbalanced force for the 3D-models is similar to that of the plane models [5]. More tests are required to confirm this result and also to find a useful way to compare the unbalanced forces of different models.

CONCLUSIONS

The developed ACR-program significantly reduces the time and costs of performing a full 3D FE-analysis of flawed structures. At the same time the accuracy of the results has been increased. The system can easily be modified for new types of structures. An accuracy assessment procedure is being developed and preliminary results are promising. The error parameter was capable to direct the mesh refinement and yielded accurate results. Further development is required before the error parameter can be used in accuracy assessment for other loading cases and geometries. Also the element sub-division procedure should be extended to 3D-models.

Acknowledgements - This work is a part of the Advanced Structural Analysis System Research Programme (Ra) of Technical Research Centre of Finland (VTT). The financial support of Teollisuuden Voima Oy (TVO) and Imatran Voima Oy (IVO) are gratefully acknowledged.

REFERENCES

[1] ADINA - A Finite Element Program for Automatic Dynamic Incremental Analysis. Report ARD 87-1, ADINA R&D, Inc. 1987.

[2] Koers, R.W.J., Use of Modified Standard 20-node Isoparametric Brick Elements for Representing Stress/Strain Fields at a Crack Tip for Elastic and Perfectly Plastic Material. Int. J. of Fracture 40, pp. 79-110, 1989.

[3] Leinonen, M., Mikkola, T.P.J.: The ACR-program for Automatic Finite Element Model Generation for Part Through Cracks. Technical Research Centre of Finland (VTT), Nuclear Engineering Laboratory, Research Reports 658, 80 p., 1989.

[4] Mikkola, T.P.J., Leinonen, M., Niemi, H., Talja, H.: Automated Fracture Analysis with Three-Dimensional Finite Element Models. Proc. of the 5th International Conference on Numerical Methods in Fracture Mechanics, ed. Luxmoore and Owen. Pineridge Press, Swansea 1990, pp. 545-556.

[5] Mikkola, T.P.J., Niemi, H., Quality Assurance for Fracture Mechanical Finite-Element Analyses. Paper to be presented in the 8th ADINA Conference on July 17.-19., 1991.

[6] Newman, J.C., Raju, I.S.: Analysis of Surface Cracks in Finite Plates Under Tension or Bending Loads. NASA-TP-1578, 1979.

[7] Niemi, H., Criteria for Finite Element Solution Accuracy Assessment. Helsinki University of Technology, Diploma Thesis, 1989, 103 p (in finnish).

[8] Niemi, H., Automatic Refinement of Finite Element Solution . Rakenteiden Mekaniikka, 23(1990)1, ss. 3-22 (in finnish).

[9] PATRAN PLUS User manual, Release 2.4. PDA Engineering, Publication number 2191023, 1989.

[10] Raiko, H., Mikkola, T. P. J., Fracture Assessment Program System for Practical Engineering Applications. IV Suomen Mekaniikkapäivät, 5.-6.6.1991, Lappeenranta, 8 p.

[11] Tada, H., Paris, P., Irwin, G., The Stress Analysis of Cracks Handbook, 2nd ed. Paris Productions Inc., St. Louis, Missouri, 1985.

[12] Talja, H., Elastic-Plastic Fracture Parameters and Their Calculation by Finite Element Method, Helsinki University of Technology, Licentiate's Thesis, 113 p., 1989 (in finnish).

FRACTURE ASSESSMENT PROGRAM SYSTEM FOR PRACTICAL ENGINEERING APPLICATIONS

HEIKKI RAIKO & TIMO P.J. MIKKOLA
Technical Research Centre of Finland (VTT)
Nuclear Engineering Laboratory
Vuorimiehentie 5, SF-02150 ESPOO, FINLAND

ABSTRACT

An efficient program VTTSIF has been developed for engineering fracture and fatigue assessment of flawed structures. The program applies weight function method in stress intensity factor (K_I) evaluation and Paris law for fatigue crack growth calculation. Thermal transient temperatures and stresses can be calculated with a separate program module TEMPS. The VTTSIF-program includes a structural geometry case database which comprises of several basic 2D and 3D solutions. New solutions can be added in the database eg. from literature or developed with the finite element (FE) -method.

INTRODUCTION

In the fracture and fatigue analysis of structures the exact location, shape and size of the crack is often not exactly known. Thus it is very important to be able to perform large matrix of analyses varying the assumptions conserning the crack. Here rapid and easy application is important and thus the use of FE-method alone is hardly practical. The use of fracture mechanical handbooks is always possible. The difficulty is that the number of solutions is limited and for each structure, solutions for several load cases are required. The weight function method [2, 13, 14] allows the fracture parameter estimation under arbitrary loading when only one 'reference' solution is known. The requirements for the 'reference' solution are that the fracture parameter and crack face displacements are known.

The difficulties in applying the weight function method in practise are similar to those of all analytical or semi-analytical methods. The number of known closed form weight function solutions is limited. General procedures for determining weight functions for surface flaws in arbitrary structures do not exist although some attempts in this direction have been presented, see eg. [3, 15]. In application, one is bound to use approximations.

In the VTTSIF-program [5, 6] the weight function method is implemented with the

The parameters K_β can be solved if equation (5) is written for n or more linearly independent (a_α , f_α)-pairs. The accuracy of (5) depends on the number of shape functions.

Crack Face Displacement Field Approximation

In [12] a general method has been given for the displacement field approximation for 2D-cases and this has been further developed eg. in [17]. The crack face displacement field is approximated with

$$u^{(1)}(\xi, a) = \sqrt{8}\,\sigma_0 \frac{(1-\nu^2)}{E}\, a\, \xi^{1/2} \left(F + \sum_{i=1}^{n} G_i\, \xi^i \right) \qquad (6)$$

where ξ = 1 - x/t, x is coordinate from surface, t is the wall thickness, G_i:s are the free parameters, σ_0 scaling stress and F the shape factor of the $K_I^{(1)}$. The first term in (6) gives the required asymptotic behaviour for the displacement at the crack tip. The term G_1 is determined using energy conciderations by applying the weight function equation (1) for the reference load case. Thus for the determination of G_1, only the stress intensity factor solution is required. Two more parameters can be determined using zero displacement curvature and known COD condition at crack mouth [17].

Displacement field approximation has been generalised for 3D-cases in [5] by defining equivalent 2D-crack along the 3D-crack front and in a more general form in [4, 11]. The correct asymptotic near field behaviour at the crack tip is fulfilled with the two latter methods. The difference between the two methods is in the coordinate system used.

Weight Function Method in the VTTSIF-program

The displacement approximation method of [17] has been implemented in the new version of the VTTSIF-program [11]. The old version of the VTTSIF-program [5] used displacement solution with n = 1. The accuracy of the solution is improved especially for deep cracks.

The 3D-solution in the VTTSIF-program is being completely redefined [11]. The solution for the semi-elliptical surface crack is given in a completely new form. With the new method for 3D-surface cracks local stress intensity factors are calculated using equation (5). In addition the weighted average values can be calculated directly from (3) or by using (2) and the solution of (5).

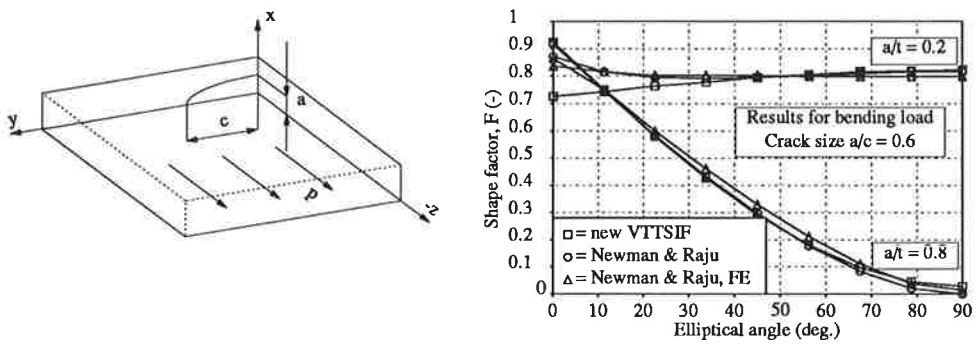

FIGURE 2. Stress intensity factor for a surface crack in a plate under remote bending.

In Figure 2 the solution for a surface crack in a plate under remote bending is given for two crack depths. The analytical solution of [9] for remote tension is used as 'reference' load case. Comparison with the FE- and analytical solutions of [9] for remote bending load shows that the new method is very accurate. Preliminary results show that the accuracy is similar for all crack sizes when a > c for bending type load [11].

Crack Growth Analysis

The crack growth analysis capabilities in the VTTSIF-program [6] are based on application of the Paris' law. This means that the crack growth increment Δa is assumed to be proportional to the cyclic variation of the stress intensity factor ΔK_I according to formula:

$$\frac{da}{dN} = C(\Delta K_{eff})^n \qquad (7)$$

where da/dN is the crack growth per load cycle, C and n are material parameters and $\Delta K_{eff} = K_{Imax} - K_{Imin}$ with possible plasticity correction. The effect of possible plastic phenomenon is taken into account according to the method given in [16].

Three different options are available in the VTTSIF-program for integrating equation (7). In the first method straightforward cycle-by-cycle counting of Δa- and Δc-increments is used. For large number of load cycles this may be unpractical. In the second method the integration is performed with Simpson's formula. For periodical loadings the integration can be performed also in loading blocks. The last method is useful eg. for nuclear power plant components for which several different type loading sets are defined for the period between start-up and shut-down of the plant. The crack growth parameters C and n given in ASME XI for ferritic steel in air or reactor water condition are readily available in the program.

Thermal Transient Stress Analysis

Thermal transient stress analyses can easily be made by a separate infinite series based program module. The program is aimed at simplifying the solution of transient temperature distribution in a flat slab that is insulated on one surface and convectively exposed to a fluid on the other surface. Two basic transient types are considered: 1) the fluid suddenly changes temperature to a new value that is maintained thereafter; and 2) the fluid changes temperature linearly with time. We shall first present analytic formulas for the temperature in the metal as a function of time and position in the wall:

Case 1 - Step change in fluid temperature:

$$T(x,t) = T_0 + (T_f - T_0)\left[1 - \sum_{n=1}^{\infty} c_n \cos(m_n x/a)\, e^{(-m_n^2\theta)}\right] \qquad (8)$$

and Case 2 - Linear change in fluid temperature:

$$T(x,t) = T_0 + (T_f - T_0)\left\{1 - \sum_{n=1}^{\infty} c_n \cos(m_n x/a)\left[1 - e^{(-m_n^2\theta)}\right]/m_n^2\theta\right\} \qquad (9)$$

where

c_n = $(4 \sin m_n) / (2 m_n + \sin 2m_n)$
m_n = n^{th} root of the equation $m \tan m = N_B$
N_B = Biot number = h a/k
h = surface heat transfer coefficient
a = slab thickness
k = thermal conductivity of slab material
θ = Fourier number = α t/a^2
α = thermal diffusivity of slab material
t = time from start of transient
T_0 = initial uniform temperature
T_f = temperature of fluid at time t
x = distance measured from insulated face

The actual temperature transient may be thought of as the superposition of several basic transient types which can be shifted in starting time. This 2D assumption can be used with reasonable accuracy for many practical purposes, for excample pipes and vessels having steam or fluid media inside and thermal insulation outside. The theory of this program module is given in [8].

The local thermal stresses are calculated from temperature distributions by formulas for nonsupported cylindrical shell as follows:

$$\sigma_z = \frac{\alpha E}{1-\nu}\left[\frac{2}{r_o^2 - r_i^2}\int_{r_i}^{r_o} Trdr - T\right] \qquad (10)$$

and

$$\sigma_t = \frac{\alpha E}{1-\nu}\left[\frac{r^2 + r_i^2}{(r_o^2 - r_i^2)\, r^2}\int_{r_i}^{r_o} Trdr + \frac{1}{r^2}\int_{r_i}^{r} Trdr - T\right] \qquad (11)$$

where

σ_z = axial stress component
σ_t = circumferential stress component
ν = Poisson's ratio
E = modulus of elasticity
α = linear coefficient of thermal expansion
r_i = inside radius of the cylinder
r_o = outside radius of the cylinder
T = temperature at radius r
r = radial coordinate

VTTSIF-PROGRAM

The VTTSIF-program is programmed in FORTRAN-77 language in three separate modules. The total amount of code is app. 10 000 card images. The weight function method for stress intensity factor calculation and the crack growth analysis is made in one module, the thermal transients and thermal stresses in an other module called TEMPS and the creation and edition of the input data module is done by a third program module BASE. The program system is installed in large variety of computer platforms; mainframes, engineering workstations and PCs. The requirements for computer hardware is very low and the time required for typical analyses is negligible in most installations. The analysis module gives a ready formatted report page output from all cases analyzed and, furhermore, gives the numerical results in a neutral formattted file, which then can easily be used for graphical post-processing facilities.

The solution types available in the VTTSIF-program are programmed in the form of a structural geometry case database which currently includes:

- single or double edge cracked plate,
- thick cylinder with internal or external, circumferential or longitudinal crack,

- radial edge crack in a disk,
- circumferential crack in a cylindrical bar,
- semielliptic surface crack in a plate,
- semielliptic internal or external longitudinal crack in a cylinder and
- semielliptic internal circumferential crack in a cylinder.

New solutions can easily be added to the database. For a new case only the stress intensity factor solution and corresponding reference stress field are required. The solution for shape factor F must be given as a function of crack size and it must be applicable down to zero crack size. The reference stress field is the stress field caused by the reference load case in the crack plane for an uncracked structure. The COD-solution can also be included in the database, if available.

The new VTTSIF-program can use the database solutions also for direct superposition in calculating the stress intensity factor. This feature is practical especially for 3D-cases, where it is often not possible to produce reference solution for the whole range of crack sizes.

EXAMPLE ANALYSIS

An axisymmetric crack in a pressure vessel wall has been analysed with the VTTSIF-program. The pressure vessel (D_i=4000 mm, t=150 mm) is under constant internal pressure (10 MPa) and the fluid temperature is suddenly changed from +300 °C to a lower value of +100 °C. The thermal transient temperatures and stresses have been analysed with the TEMPS-program, see Fig 3. The stress intensity factors at time t=10, 60 and 600 sec for crack depths from 5 to 130 mm have been analysed with the VTTSIF-program.

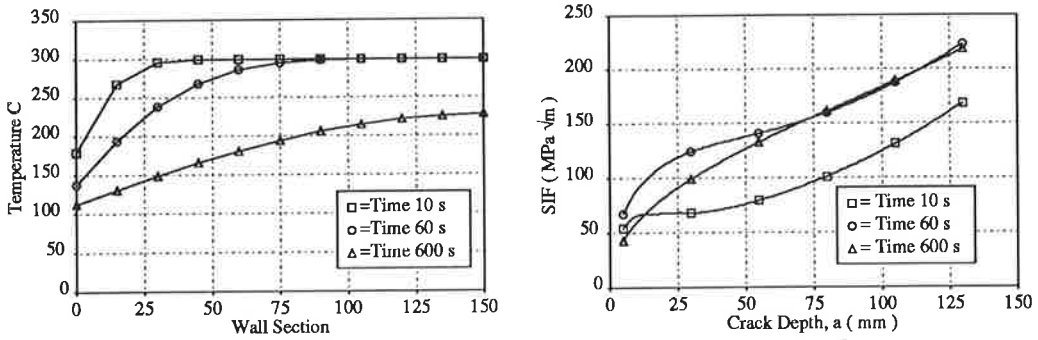

FIGURE 3. Transient temperatures in the wall and the stress intensity factors, respectively.

CONCLUSIONS

An efficient and practical engineering tool for fracture mechanics calculations and crack growth analysis has been presented. The weight function method used to calculate fracture parameters makes the code very effective, so that usual PCs give the computer capasity needed. This kind of an engineering tool makes the fracture analyses so easy and cheap to do that it can be taken into use in everyday planing and design.

REFERENCES

[1] Besuner, P. M., The Influence Function Method for Fracture Mechanics and Residual Fatigue Life Analysis of Cracked Components under Complex Stress Fields, Nuclear Engineering and Design 43(1977), pp. 115-154, North-Holland Publishing Company.

[2] Bueckner, H.F., A Novel Principle for the Computation of Stress Intensity Factors. ZAMM 50,9 (1970), pp. 529-546.

[3] Chen, K.L., Atluri, S.N., Comparison of Different Methods of Evaluation of Weight Functions for 2-D Mixed-mode Fracture Analyses. Engineering Fracture Mechanics, 34(1989)4, pp. 935-956.

[4] Fett, T., The Crack Opening Displacement Field of Semi-elliptical Surface Cracks in Tension for Weight Functions Applications, International Journal of Fracture 36(1988), pp. 55-69, Martinus Nijhoff Publishers.

[5] Kantola, K., Jännitysintensiteettikertoimen Laskeminen Painofunktiomenetelmällä. Technical Research Centre of Finland, Nuclear Engineering Laboratory, technical report YRT-3/86, 1986, 40 pages, (In finnish).

[6] Leinonen, M., VTTSIF-ohjelman Väsymisanalyysivalmiuden Kehittäminen ja Ohjelmakäsikirja. Technical Research Centre of Finland, Nuclear Engineering Laboratory, technical report PAKO-2/89, 1989, 16 pages + 16 app., (In finnish).

[7] Leinonen, M.S., Mikkola, T.P.J., The ACR-program for Automatic Finite Element Model Generation for Part Through Cracks. Espoo 1989, Technical Research Centre of Finland, Research Report 658, 80 pages.

[8] McNeill, D. R., Brock, J. E., Engineering Data File, Charts for Transient Temperatures in Pipes, Heating/Piping/Air Conditioning, November 1971, Reinhold Publishing Corporation, pp. 107 - 119.

[9] Newman, J. C., Raju, I. S., Analyses of Surface Cracks in Finite Plates under Tension or Bending Loads, NASA Technical Paper 1578, Dec 1979.

[10] Nishioka, T., Atluri, S., N., The First Order Variation of the Displacement Field due to Geometrical Changes in an Elliptical Crack, pp. 1-20.

[11] Mikkola, T.P.J., Development of Weight Functions for Surface Cracks. Espoo 1991, Technical Research Centre of Finland, Research Reports (to be published).

[12] Petroski, H.J., Achenbach, J.D., Computation of the Weight Function from a Stress Intensity Factor. Engineering Fracture Mechanics, 10(1978), pp. 257-266.

[13] Rice, J.R., Weight Function Theory for Three-dimensional Elastic Crack Analysis. Fracture Mechanics: Perspectives and Directions (Twentieth Symposium), ASTM STP 1020, R. P. Wei and R. P. Gangloff, Eds., American Society for Testing and Materials, Philadelphia, 1989, pp. 29-57.

[14] Rice, J.R., Some Remarks on Elastic Crack-tip Stress Fields. Int. J. Solids Structures, 8(1972), pp. 751-758.

[15] Sham, T.-L., A Unified Finite Element Method for Determining Weight Functions in Two and Three Dimensions. Int. J.Solids Structures, 23(1987)10, pp. 1357-1372.

[16] Turner, C. E., Methods for Post-Yield Fracture Safety Assessment. Post-Yield Fracture Mechanics, 2nd ed., England, Elsevier Applied Science Publishers Ltd, 1984, pp. 25 - 221. ISBN 0-85334-276-8.

[17] Wu, X., R., Carlsson, J., Wide-range Weight Function for Single Edge Crack in a Finite Width Sheet. Proceedings of the 5th International Conference on Numerical Methods in Fracture Mechanics, Freiburg 1990, pp. 17-28.

ON FACTORS AFFECTING THE FATIGUE LIFE OF WELDED COMPONENTS USING THE HOT-SPOT APPROACH

Teuvo Partanen
Department of Mechanical Engineering
Lappeenranta University of Technology
P.O Box 20, SF-53851 LAPPEENRANTA, FINLAND

ABSTRACT

The effect of hot-spot stress distribution in the direction of fatigue crack growth has been calculated using a fracture mechanics weight function method. The stress distributions calculated were; tension and bending in various combinations; nonlinear stress gradients; stresses of cracks growing from holes. The results indicate that for a constant fatigue life, the hot-spot stress of various stress distribution types which best correlates the life is the stress at a depth of 1 to 2 mm below the surface, and not the stress at the surface. Thus FEM-models must be made accurate enough to define the stress state at this depth. The higher stress gradient at the surface affects the life less than the stress distribution deeper in the crack growth direction. According to the results the hot-spot stress can be defined as the stress at a depth of 1mm under the surface.

INTRODUCTION

The hot-spot approach has been regularly used as a means to predict fatigue life of offshore welded structures, where the nominal stress approach cannot be used due to interaction of the structure and the stress state. Nowadays the hot-spot approach has been adopted to ordinary engineering structures also. The hot-spot approach is based on the surface stress extrapolated to the weld root from measured strains at some distance from the weld root. The surface strain range of the structure and the stress range of laboratory test specimens measured similarly are assumed to be equally damaging in the method. Thus only one Wöhler curve is required in order to predict fatigue life of all structures welded by similar methods. Instead of measuring the strains, finite element calculations are used as a means to determine the hot-spot stress. Fatigue cracks are initiated at defects at the base of notches such as weld toes, where the local peak stress increases very rapidly. In the hot-spot method the peak stress nonlinearity, if discovered by the calculation method, is intended to be excluded by stress extrapolation outside the peak region. Sometimes it is easy, sometimes difficult, to determine the exact hot spot stress by extrapolation, due to stress nonlinearity. In this paper results of a numerical study are presented to show that a more representative and more constant stress under the surface can be used as the hot-spot stress for fatigue life determination.

THEORY

The fatigue life of welded structures is considered to consist of fatigue crack propagation, the initiation period being much less important than in machined components. Fracture mechanics is a valuable tool in determining fatigue crack growth life. Using the superposition principle to determine the stress intensity factor (SIF), only the stress distribution of an uncracked structure in the plane of the growing crack is needed to calculate the stress intensity factor of a crack of arbitrary size and shape, using the weight function method.

By using fracture mechanics it can be shown that the majority of fatigue crack growth life is consumed growing a crack from the initial crack size of a weld defect to a final size of about 10mm, irrespective of the structure size and plate thickness. The fatigue damage process is very fast at the end of the life and only marginal effects on total life can be achieved by considering longer crack lengths than 10mm as failure criteria. Thus it is essential to determine the stress distribution of an uncracked structure in the range of 0 to 10 mm in the crack growth direction. In determining the SIF of varying stress distributions the two important parameters are the total force opening the crack faces and the weighted effect of stress location with respect to the crack tip. Crack growth rate can be determined as a function of the crack length, and the life spent can be integrated consecutively. Various stress distributions giving equal fatigue life can be calculated and plotted for comparison.

Weight function method

By determining stress intensity factors, stresses distributed along crack faces produce different effects depending on the location of the stress considered. In the case of uniformly loaded basic cracks, the stress on the crack mouth is weighted by $2/\pi$ whereas the stress at the crack tip is weighted by infinity, giving an averaged weight of one for the whole crack. The SIF of a crack subjected to an arbitrary stress distribution can be integrated over the crack length using the predetermined stress distribution and an appropriate weight function. Weight functions for various crack types have been developed differing only slightly from one to another. The best known of the weight functions is the Green's function [2] developed for the basic crack, central through thickness crack in an infinite plate.

The stress intensity factor (SIF) can be calculated as

$$K = Y \cdot K_o \tag{1}$$

where

$$K_o = \sigma_o \cdot \sqrt{(\pi \cdot a)} \tag{2}$$

$$Y = \frac{2}{\pi} \cdot \frac{1}{a \cdot \sigma_o} \cdot \int_0^a \frac{\sigma(x)}{\sqrt{[1-(x/a)^2]}}\, dx \tag{3}$$

Weight functions of power law stress distributions

For a power law stress distribution

$$\sigma(x/a) = \sigma_o \cdot \alpha_n \cdot x^n \qquad n = 0,1,2,3 \qquad (4)$$

weight functions Y can be integrated in closed form

$$Y = 1 + \alpha_1 \cdot a \cdot 2/\pi + \alpha_2 \cdot a^2 \cdot 1/2 + \alpha_3 \cdot a^3 \cdot 4/(3 \cdot \pi) \qquad (5)$$

For a power root law stress distribution

$$\sigma(x/a) = \sigma_o \cdot \beta_m \cdot x^m \qquad m = 1/2,\ 1/3,\ 1/4,\ 1/5 \qquad (6)$$

weight functions Y can be integrated numerically

$$Y(m) = y_m \cdot a^m \cdot \beta_m \qquad m = 1/2,\ 1/3,\ 1/4,\ 1/5 \qquad (7)$$

The weight factors y_m of eq. 7. are shown in Table 1.

TABLE 1.
Weight factors y_m of power root stress functions

m	y_m
(1	$2/\pi$)
1/2	0.763
1/3	0.823
1/4	0.859
1/5	0.883

Within 1% accuracy Y(m) can be written as

$$Y(m) = [1 - (1-2/\pi) \cdot m^{(2/\pi)}] \cdot a^m \cdot \beta_m \qquad m = 1,\ 1/2,\ 1/3,\ 1/4,\ 1/5 \qquad (8)$$

Crack Growth Life

The crack growth life predicted using the Paris law

$$da/dN = C \cdot \Delta K^3 \qquad (9)$$

can be numerically integrated for various stress gradients using appropriate weight functions.

Fatigue crack growth life N can be written as

$$N = \frac{1}{C \cdot \Delta\sigma_p^3 \cdot \pi^{3/2}} \int_{a_f}^{a_o} \frac{1}{[Y(m,a) \cdot \sqrt{a}]^3}\, da \qquad (10)$$

Lives for different stress distributions can then be set equal. The calculated maximum stress $\Delta\sigma_p$ of the stress distribution range

considered which gives a life N can be increased or decreased by the reference stress range $\Delta\sigma_o$ and life N_o to give an equal fatigue life N_o

$$\Delta\sigma_p^3 \quad N_o = \Delta\sigma_o^3 \cdot N \qquad \text{or} \qquad \Delta\sigma_p = \Delta\sigma_o \cdot (N/N_o)^{1/3} \tag{11}$$

RESULTS

Fatigue crack growth lives from an initial crack of 0.2mm to a final crack of 10mm have been calculated by numerical integration, taking into account the stress distribution opening the crack faces. The lives have been made dimensionaless by the crack growth life of the basic crack - the crack in an infinite plate subjected to far field tension. In Figures 1a,1b,1c equivalent life stress distributions are shown for various bending - tension stress ratios of linear, square root and cube root stress distributions. The reference tension stress has been defined as the stress at a depth of 10mm.

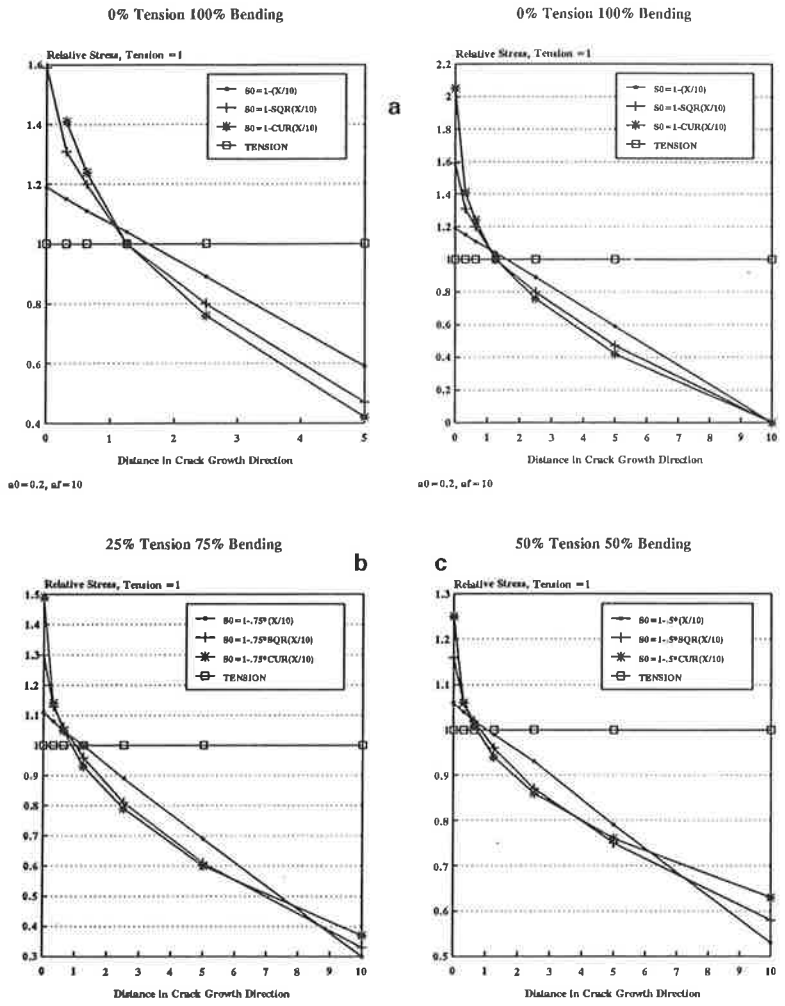

FIGURE 1. Equivalent life bending stress distributions

The calculation approach presented can be applied to various other stress distributions as well. In Figures 2a and 2b equivalent life stress distributions of cracks growing in the stress concentration field of a hole in a wide plate have been presented for various hole radii, large holes and small holes.

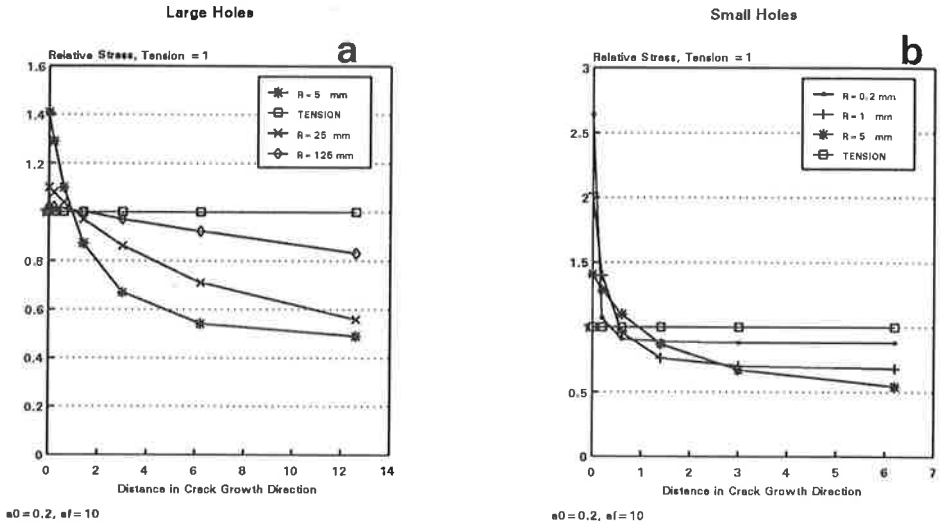

FIGURE 2. Equivalent life hole stress distributions

The effect of the peak stress concentration due to weld reinforcement, known as the Mk-factor and the crack ellipticity have been considered for linear tension to bending stress ratios 0,0.33,0.67 and 1. The results are shown in Figure 3.

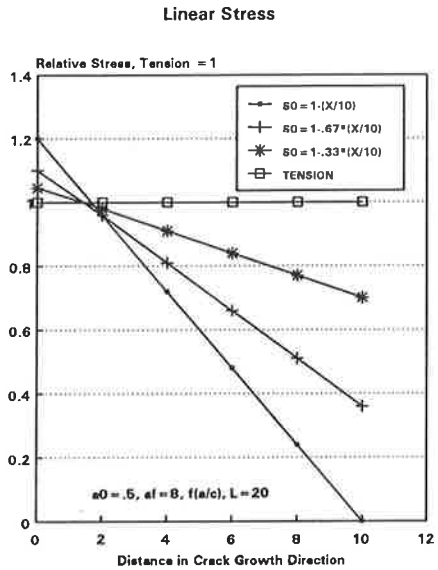

FIGURE 3. Equivalent life bending stress distributions in welds

DISCUSSION

Pure bending as defined by the stresses at the surface and at a depth of 10mm is slightly less damaging than pure tension, 20% less in the stress range. Similar results have been obtained for edge cracks in welds [3]. A representative effective stress can be determined by weighting linearly the nonlinear stress distribution. All the stress distributions intersect the pure tension stress at a crack depth of 1 to 1.5mm.

From the stress distribution of equivalent life hole cracks, it can be seen that the life of cracks initiating from small holes depends on the nominal tension stress range, whereas the life of large hole cracks is strongly dependent on the stress concentration K_t=3 of the hole. In all cases considered the stress at a depth of 1mm describes best the life to be expected, much better than the life scatter 27, as defined merely by the stress concentration factor K_t=3.

Weld crack dimensions were chosen to give, by tension loading, an equivalent life to that of basic crack tension loading. Similar quantitative correlation of bending - tension effective stress as for plane surface cracks was observed.

When calculating the real life of weld toe cracks of thinner plates the real effects of thickness, width and loading must be taken into account. In the case of thin specimens the cracks grow through the plate and also in the width direction. In the present study the effect of stress gradient of thicker plates was studied separately and relatively.

When measuring the strains at the surface of a real structure the strain gauges should be located at distances giving similar through thickness linear distribution and effective extrapolated stress, as defined by the equivalent life method.

CONCLUSIONS

1. Fatigue crack propagation life is dependent not only on the hot-spot stress at the surface of the structure, but also on the stress gradient in the crack growth direction.

2. Fatigue crack growth life in thick plates is a function of the real stress distribution at depths up to about 10mm and is not a function of any dimensionless depth ratio stress.

3. Stress calculated at a depth of 1 mm below the surface correlates well with the fatigue crack growth lives of various calculated stress distributions.

REFERENCES

1. Hobbacher A., Recommendations for assesment of weld imperfections in respect to fatigue. IIW-Doc. XIII-1266-88/XV -659-88 International Institute of Welding, 1988, 30 p.

2. Tada H., Paris P., Irwin G., The Stress Analysis of Cracks Handbook. Del Research Corporation, 226 Woodbourne, St. Louis, Missouri, 63105 (1973)

3. Ferreira Martins J.A and Branco C.A. Moura, Influence of the radius of curvature at the weld toe in the fatigue strength of fillet welded joints. International Journal of Fatigue, N:o 1 January 1989 pp 29-36, 1989 Butterworth & Co (Publishers) Ltd

ON THE SPRING CONSTANT IN OPEN SECTION JOINTS

TIMO BJÖRK
Department of Mechanical Engineering
Lappeenranta University of Technology
P.O. Box 20, SF-53851 LAPPEENRANTA, FINLAND

ABSTRACT

It is well known that semi-rigid joints affect the bending moment distribution in plane frames. This paper presents a method of analysis for a structure with partial restraint joints.

Warping stiffness of a joint is usually considered as a single spring constant. However, in order to obtain the correct overall force distribution in a complete structure, it is important to realise that warping stiffness consists of two components: a carry-over spring constant and a grounding spring constant.

A theory of analysis for the warping spring constants is presented, as well as the principle of determining numerical values for practical joints.

INTRODUCTION

Several papers have been published concerning semi-rigid connections in plane frames loaded by bending moments, (e. g. [1]). However, in space frames or grid structures which are subjected to a torsional moment, warping stiffness of joints is an even more important factor in order to obtain the correct overall nominal stress distribution in a structure. A lattice frame joint in a vehicle frame is a typical example of a structure in which warping stiffness should not be ignored. Another important case for considering the warping stiffness is (flexural-) torsional buckling. The theoretical buckling value may increase fourfold when boundary conditions are changed from free to warp to completely rigid.

Warping stiffness of vehicle structures has been analysed by Beermann and Oehlschlaeger [2],[3]. They analysed the structure using the force matrix approach instead of the displacement method. Therefore they determined the flexibility coefficient based on warping in adjacent members of the joint. This flexibility coefficient of the joint is not actually an inverse value of the stiffness constant.

Mecson and Alade studied the same kind of structure using the relative stiffness approach, where relative stiffness in a completely rigid joint is one, and is zero in a joint free to warp [4]. This method is not very practical when finite beam element analysis is used. Numerical values for warping stiffnesses of the joints studied were based on thin shell element analysis, in the same manner as Beermann and Oehlschlaeger.

Yang developed a beam element method for space frame structures taking into account the warping stiffness of the joints [5]. However, no method for calculation of the stiffness constant for a warping spring was presented.

Ilvonen et al. presented a semi-analytical method for the calculation of a warping spring stiffness constant of an open section joint based on stresses and displacements in the junction line of a branch member section [6]. This method gives relevant information for fatigue design from the stress distribution in a joint. However this analysis requires a very fine element mesh and may give rise to numerical difficulties in some cases.

Even though many of papers have been published dealing with joints with partial restraint warping, the dualistic nature of a warping spring is not considered. In principle every warping spring consists of two components: a **carry over-** and a **grounding spring** constant. This separation is very important in order to obtain correct global bimoment and Saint Venant's torsional moment distributions in the structure.

A finite element method called AGIFAP has been developed in the Laboratory of steel structures at Lappeenranta University of Technology [7]. The program uses 14 d.o.f beam elements and also takes into account warping stiffness of the joint as stiffnesses associated with other degrees of freedom. Main principles of determining the warping constant for an arbitrary open cross section joint, and how it is utilized in the finite element method are presented in this paper.

BIMOMENT TRANSMISSION IN JOINTS

A joint consisting of two I-beam sections with unequal heights is presented in Fig. 1. The profile section may be arbitrary, but the I-beam is the most distinct for demonstrating this phenomenon. The bimoment is marked here by a couple of moment vectors or by triple vector, even if the bimoment is actually rather a scalar rather than a vector. If the branch member is loaded by a bimoment $B_{\omega o}$, only some part of the bimoment (denoted $B_{\omega c}$) is transmitted to the main member and the remaining part $B_{\omega g}$ is grounded in the joint itself. It appears that the grounded part of the bimoment disappears when the flow of the bimoment is traced over the joint.

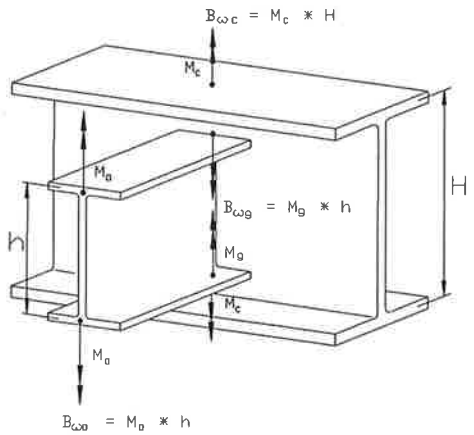

FIGURE 1. A joint loaded by a bimoment

This appears more clearly if we examine the situation shown in Fig. 2. In this case the flanges of the I-beam are grounded with a closed section stub. In relation to grounding of the bimoment the details shown in Figs. 2a and 2b are equal, assuming that the web thickness of the beam is negligibly small. The grounding spring behaves as if there were an external spring support. However, the grounding spring is in practice an internal spring support, in the same way that the bimoment is an internal force, and does not therefore need any external support in order to be in equilibrium.

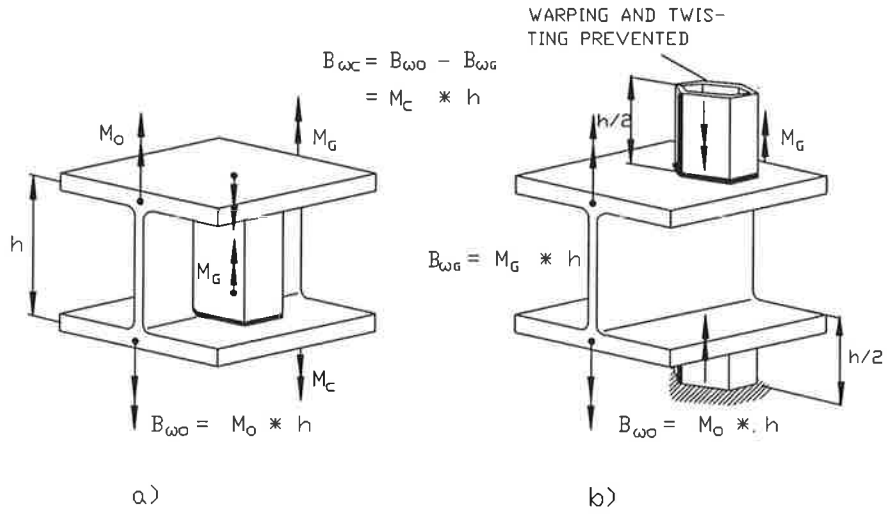

FIGURE 2. Internal and external grounding springs

Analogies between warping grounding and the following phenomena are illustrated in Fig. 3: shear force on an external support (Fig. 3b), leaking pipe juntion analysed by E. Niemi (Fig. 3c) and a short circuit in electrotechnics (Fig. 3d).

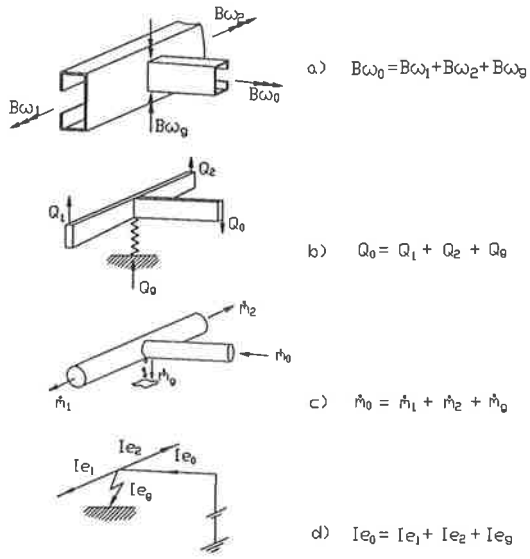

FIGURE 3. Analogies of warping grounding

Fig. 4 shows some joint details, where the dualistic behaviour of a warping spring is obvious. In these cases the total warping spring constant S_ω does not describe very well the flow of the bimoment through the joint.

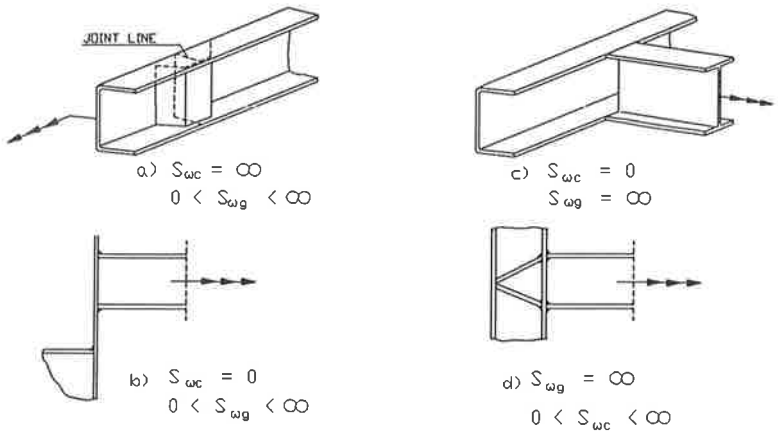

FIGURE 4. Dualistic behaviour of warping grounding

DETERMINATION OF SPRING CONSTANT

In some cases the numerical value of the grounding warping spring is easy to determine using a simple analytical approach (Fig. 5).

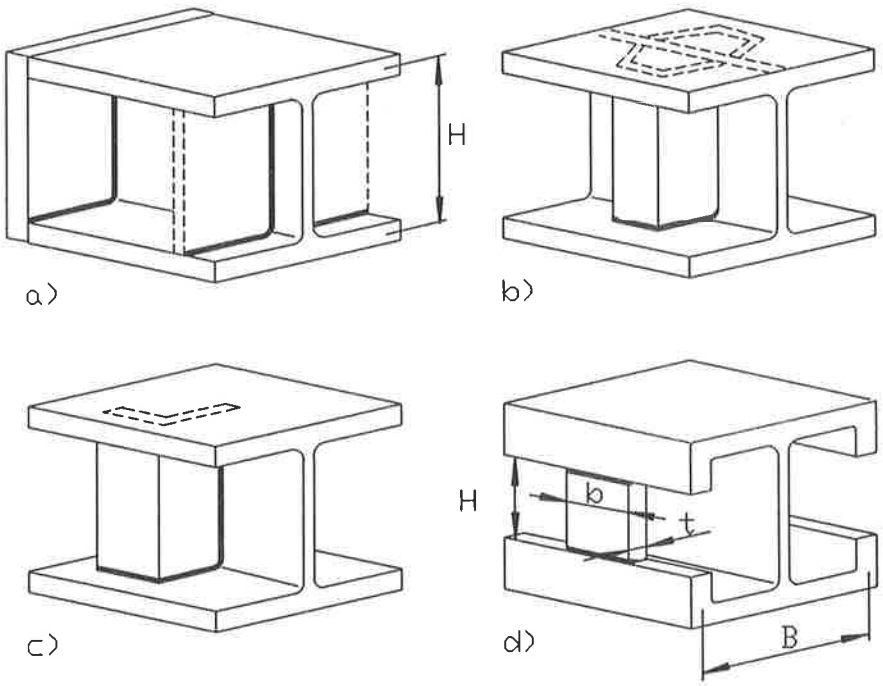

FIGURE 5. Analytical approach for warping grounding springs

If we consider the vertical stiffener(s) as a beam system loaded by torsional moments at each end, we have a simple analytical model for solving the grounded spring constant.

$$S_{\omega g}=G\cdot I_t\cdot H \qquad (1)$$

In equation (1) $G\cdot I_t$ is the torsional stiffness of the stiffeners. The stiffener is in effect a beam loaded by torsional moment and supported elastically at each end, because the flange of the I-beam may prevent free warping at the ends of the stiffener. In the case of end plate or transverse plate stiffeners, the spring constants of supports are zero, and in closed configuration vertical stiffeners they are usually negligibly small. The detail presented in Fig. 5c should be analysed using FEM in order to obtain the correct boundary conditions for the stiffener.

If a stiffener is subjected to a bending load in excess of the torsional load (Fig 5d), the grounding spring constant can be calculated from the following formula

$$S_{\omega g}=\frac{E\cdot B^2\cdot b^3\cdot t}{2\cdot H} \qquad (2)$$

It is impossible to evaluate analytically the warping spring constant of more complicated joints. In particular the determination of a carry over spring constant requires the use of thin shell finite element analysis. By assuming the joint type presented in Fig. 1, it is easy to draw up an analytical model for the joint behaviour shown in Fig. 6.

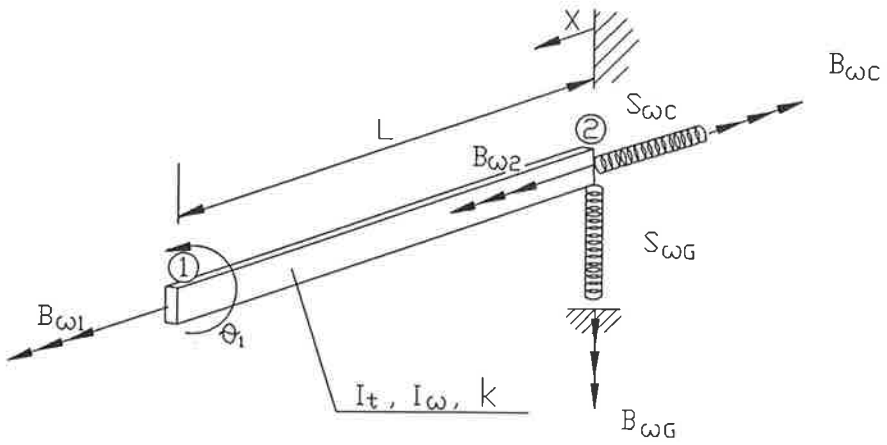

FIGURE 6. Analytical model for determination of warping spring

The loading bimoment and the warping stiffness of the branch member are input values. From the finite element method we obtain the supporting forces and the angle of rotation θ_1 at the end of the branch member. The angle of rotation for a bimoment loaded beam is

$$\theta=C_1\cdot\sinh kx+C_2\cdot\cosh kx+C_3\cdot x+C_4 \qquad (3)$$

where the torsional constant

$$k=\sqrt{\frac{G\cdot I_t}{E\cdot I_\omega}} \qquad (4)$$

Taking into account the boundary conditions we obtain the following equations

when x = 0: $\theta = 0$
$\theta' = B_{\omega 2}/S_\omega$
$\theta'' = B_{\omega 2}/(E \cdot I_\omega)$
$\theta''' = k^2 \cdot \theta'$

x = L: $\theta = \theta_1$
$\theta'' = B_{\omega 1}/(E \cdot I_\omega)$

The spring constant of the joint is

$$S_\omega = \frac{(B_{\omega 1} - E \cdot I_\omega \cdot k^2 \cdot \theta_1) \cdot E \cdot I_\omega \cdot k \cdot \sinh kL}{B_{\omega 1} \cdot (1 - \cosh kL) + k^2 \cdot E \cdot I_\omega \cdot \theta_1 \cdot \cosh kL} \qquad (5)$$

The transmitted bimoment through the joint is calculated from FEM-analysis

$$B_{\omega c} = \sum_i (F_i \cdot y_i \cdot z_i) \qquad (6)$$

where F_i are reaction forces due to the boundary conditions and y_i, z_i are distances from the shear centre of the beam. If the main member is significantly long in the FEM-model, the grounding effects due to Saint Venant's torsional rigidity should not be ignored. The spring constants for carry over and grounded spring can now be determined

$$S_{\omega c} = \frac{B_{\omega c} \cdot S_\omega}{B_{\omega 2}} \qquad (7)$$

$$S_{\omega g} = S_\omega \cdot \left(1 - \frac{B_{\omega c}}{B_{\omega 2}}\right) \qquad (8)$$

where

$$B_{\omega 2} = \frac{S_\omega \cdot k^2 \cdot E \cdot I_\omega \cdot \theta_1}{k \cdot E \cdot I_\omega \cdot \sinh kL - S_\omega \cdot (1 - \cosh kL)} \qquad (9)$$

APPLICATION IN BEAM ELEMENT METHOD

In applications of the beam element method, the carry over spring constant $S_{\omega c}$ will be treated as a normal spring constant between (two) adjacent elements. The grounding spring constant $S_{\omega g}$ is considered as another external supporting spring of the structure. It should be noted that grounding spring is fixed at the end of the element and therefore it is significant which node is grounded in FEM-analysis, as illustrated in Fig. 7a. Fig. 7b shows a joint, in which a gusset plate causes a grounded bimoment for the branch member by a shell stiffness effect as well as for the main member through a plate stiffness effect.

In order to obtain a more correct stress distribution in the main member, the effects of joint eccentricity should be taken into account [8]. If the length of the gusset plate l_p is significant, this part of the main member should be considered as a box beam.

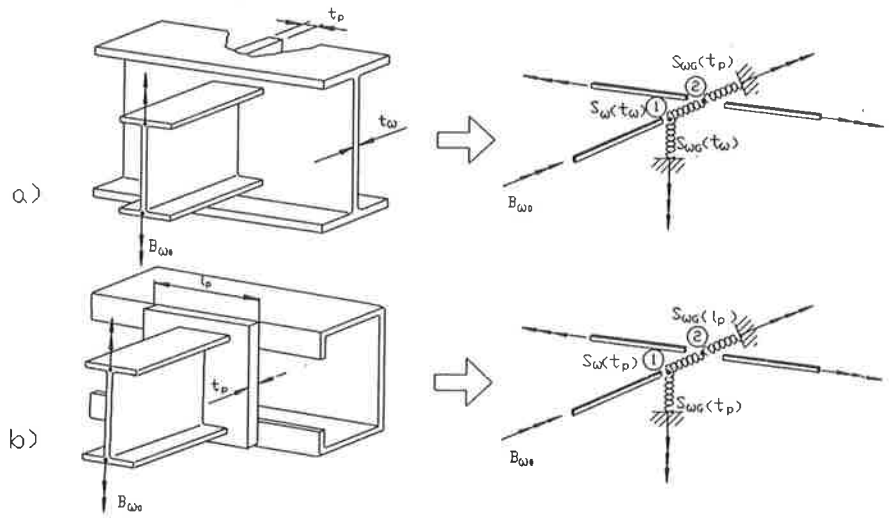

FIGURE 7. Warping springs in beam element model

EXAMPLE

Fig. 8 presents an FEM model with dimensions from the joint type shown in Fig. 7b.

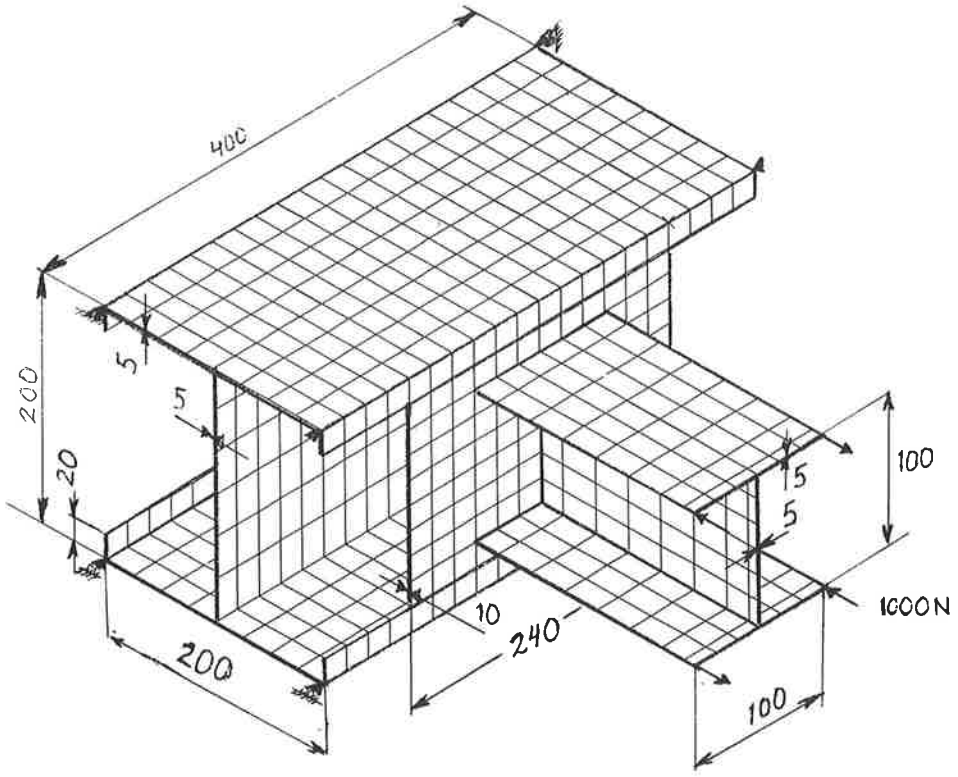

FIGURE 8. FEM-model of analysed joint

Using the principles and equations from the previous chapters the following numerical values can be found for spring constants

$S_{\omega c}$ = 90 MNmm^3/rad
$S_{\omega g}$ = 917 GNmm^3/rad

In order to obtain more sophisticated conclusions about the plate and shell effects on grounding spring constant would require more analyses with different loading and boundary conditions. More numerical examples of typical open section joints are presented by Halme [9].

DISCUSSION

Using the system presented in this paper for the analysis of a warping spring, it is easy to determine the spring contants with respect to bending rotation, axial deflection, shear deflection etc. This method is applied normal as well as eccentric joints. The mesh of the FEM model in this approach does not need to be very fine, because calculations are based on deformation, not on stresses. The branch length may be arbitrary, because it is taken into account in analytical calculations. However, shear deformations due to warping rigidity are not included in the analytical model although they are considered in FEM. This error is quite small considering that the accuracy of the analysis can be increased considerably taking the joint flexibility into account.

REFERENCES

1. Chen W., Joint flexibility in steel frames. Elsevier Applied Science. London 1987

2. Beermann H., Rechnerische Analyse von Nutzfahrzeugetragwerken. Verlag TÜV Rheinland. Köln 1986

3. Oelschlaeger H., Nachgiebige Knoten bei der Torsionberechnung von Nutzfahrzeugerahmen aus offenen Profilen. Automobiltechnische Zeitschrift 86, 3/1984

4. Mecson T., Alade G., Structural analysis of latted frames under torsion. Proceedings, The Institution of Mechanical Engineerings, Vol 190, 38/76

5. Yang Y-B., Linear and nonlinear analysis of space frames with nonuniform torsion using iterative computer graphics. Thesis of Cornell University, 1984

6. Ilvonen R, Vaittiniemi K., Niemi E., Arinarakenteen estetty vääntö liitosten joustavuus huomioonottaen. II Suomen Mekaniikkapäivien esitelmät, TTKK 1985

7. AGIFAP ver. 3.0, User manual. Lappeenranta University of Technology, Laboratory of steel structures. 1991

8. Björk T., Joustavat ja epäkeskiset liitokset palkkielementtimenetelmässä. Tutkimusraportti 1. LTKK, Konetekniikan osasto, 1990

9. Halme T., Kevytprofiililiitosten joustavuuden määritys. Diplomityö, Konetekniikan osasto, LTKK 1988

A PROGRAM FOR SYSTEMATIC CALCULATION OF DIMENSIONLESS PRODUCTS

JOUNI FREUND* and SATU M. RÄSÄNEN**
*Helsinki University of Technology, Otakaari 1, SF-02150 ESPOO, FINLAND
**Turku Inst. of Tech., Sepänkatu 1, SF-20700 TURKU, FINLAND

ABSTRACT

The use of dimensional analysis is quite easy when a relatively small number of quantities is involved in the phenomenon under consideration. The so called dimensionless products can be formed by inspection or just by sensible guessing, though some experience is needed to guide the guesswork. The situation is different if the the number of quantities is large.

The program presented in this article makes the use of Langhaar's method for calculating dimensionless products a systematic exercise. It is believed that for instance persons responsible for teaching dimensional analysis may find the program useful. With this aid the emphasis can be shifted more on the important physical side of the problem.

INTRODUCTION

Dimensional analysis can be used to find a relationship of general type between the quantities in a given physical setting. The outcome of dimensional analysis is that it's not the quantities themselves that matter but rather certain combinations of them. The number of these so called dimensionless groups is smaller than the number of original variables. Consequently the amount of work can be reduced substantially if the relationship among the variables has to be found experimentally. To be concise: The method provides some information about what to plot against what and what not to.

Different ways of calculating the dimensionless products have been presented in the literature. Most of them are based on the Buckingham Pi-theorem, the rest use Rayleigh's method. Different variations of Buckingham's method have been created in order to decrease the calculation work needed or to make dimensional analysis easier for the student, see for instance

[1] and [2]. However, as mentioned in reference [3], the subject can easily obtain the reputation of being 'black art'. This feeling may be shared by the students if rather exotic prescriptions for determination of dimensionless products are given.

Langhaar has described in his book [4] a systematic and straightforward method based on Buckingham's theorem of which the other methods are variations, as noted in reference [5]. Langhaar's method is applicable to all problems of dimensional analysis. Furthermore when applying Langhaar's method one can (and should too) divide the original problem into two simpler subproblems in a natural way. The first subproblem is concerned with the identification of the decisive variables and to transforming the problem of finding the dimensional groups into a linear algebraic one. The second subproblem of solving the system can easily be handled by a student with a moderate experience in linear algebra.

In this paper the authors describe a rather simple program for doing this sometimes tedious linear algebra part. The core of the program is a solver for linear systems of the type $A_{(n,m)}X_{(m)} + B_{(n)} = 0_{(n)}$ with non-matching number of equations n and variables m. The program may have some interest of its own as the calculations are performed by using rational numbers.

REVIEW OF THE METHOD

Let us consider a physical setting with quantities y_i, $i = 1,\ldots,m$. Each of the quantities is thought to consist of a numerical value and dimension having to do with the way to measure the quantity. The quantity itself is sort of invariant, but the numerical value obviously depends on the selected unit of measurement or 'reference stick' or dimension. The dimensions of the basic undefined quantities selected are the basic dimensions. The derived dimensions follow from definitions or from physical laws. Here we do not specify in detail 'the stick of measure', but denote the basic dimensions by a capital antique letter (say L for length).

Buckingham's theorem states that the relationship between the quantities (if it exists) can be expressed in a form including only dimensionless groups. The theorem is based on the fact, that the correctly written underlying equations are dimensionally homogeneous. So any correctly derived equation (say the solution of the equation system) will also be dimensionally homogeneous.

The question is: Given a complete set of quantities describing a physical setting in some system of measurement (say M, L, T), what is the number of the independent dimensionless so called Pi-groups of the form

$$\Pi = y_1^{k1} y_2^{k2} \ldots y_m^{km}, \tag{1}$$

and what are the values of the corresponding rational number valued exponents k_j, $j = 1,\ldots,m$? The independency means here that none of the dimensionless groups can be formed as a

combination of the others. Clearly the exponents in (1) must be chosen to satisfy the dimensional homogeneity condition. So by using the 'take dimension' operator [ ] one gets

$$[1]=[y_1]^{k_1}[y_2]^{k_2}\ldots[y_m]^{k_m}. \tag{2}$$

If the exponents of the dimensions of each variable are arranged as columns to form a matrix, the requirement can be written in the form

$$\begin{bmatrix} a_{11} & a_{12} & \cdots & a_{1m} \\ a_{21} & a_{22} & \cdots & a_{2m} \\ \vdots & \vdots & \ddots & \vdots \\ a_{n1} & a_{n2} & \cdots & a_{nm} \end{bmatrix} \begin{Bmatrix} k_1 \\ k_2 \\ \vdots \\ k_m \end{Bmatrix} = \begin{Bmatrix} 0 \\ 0 \\ \vdots \\ 0 \end{Bmatrix}, \tag{3}$$

where n is the number of basic quantities (often in mechanics $n=3$). Thus the problem of finding the complete set of dimensionless products is transformed into a more familiar one of solving a linear equation system.

SOLUTION METHOD

Some computer methods for solving the linear system have been introduced (see for example [6]). However, there seems to be room for improvements. As the exponents in (2) or equivalently the solutions of (3) are known to be rational number valued, it seems to be natural to work with rational numbers from the beginning. The solution should also be obtained in a form, where the common divisors in the nominator and denominator of each rational number are cancelled out. Furthermore, there should not be any restrictions concerning the coefficient matrix.

In fact it is quite easy to generate a simple and foolproof method, which gives the solution (if it exists) of any linear equation system whatsoever, without any rearrangements concerning the equations and variables [7]. Instead of concentrating on the homogeneous problem (3), we will consider a more general problem

$$A_{(n,m)}X_{(m)}+B_{(n)}=0_{(n)}. \tag{4}$$

where $A_{(n,m)}$ is the coefficient matrix, $X_{(m)}$ is the vector of unknowns and $B_{(n)}$ is the known vector. The subscripts in parenthesis refer to the size of the corresponding matrix or vector.

The problem can be solved by using a straightforward elimination method for systems with non-matching number of equations and unknowns. The equation system is first cast into the equivalent form

$$\begin{bmatrix} I_{(r,r)} & \overline{A}_{(r,m-r)} \\ 0_{(n-r,r)} & 0_{(n-r,m-r)} \end{bmatrix} \begin{Bmatrix} X_{(r)} \\ Y_{(m-r)} \end{Bmatrix} + \begin{Bmatrix} \overline{B}_{(r)} \\ R_{(n-r)} \end{Bmatrix} = \begin{Bmatrix} 0_{(n)} \end{Bmatrix} \tag{5}$$

by means of the Gaussian method with the pivoting scheme: Whenever a zero diagonal element, say a_{ii} , prevents the elimination process, a nonzero entry is searched from the i:th column to the right and from the i:th row downwards. If none is found, the system is already in the wanted form, otherwise after the change of equations i and j and the place of variables i and k the elimination can continue (the nonzero entry is thought to be a_{jk} with $j,k \geq i$). In actual practice no swapping of equations or variables is performed but the needed information is kept in equation usage table $E_{(n)}$. Finally the coefficient matrix will be partitioned into four matrices: An identity matrix, two zero matrices and a matrix depending on the original matrix. Correspondingly the vectors will be partitioned into two vectors. The size of the identity matrix is the rank of the system. The overbars in (5) are used to indicate the dependence of $\overline{A}$ and $\overline{B}$ on A and B, respectively.

Depending on the sizes of the submatrices thus obtained one can make several conclusions about the solution set. (I) Obviously the solution set is empty provided $R_{(n-r)} \neq 0_{(n-r)}$. In this case the equation set contains at least two contradictory equations. (II) The solution set consists of exactly one unique vector provided $R_{(n-r)} = 0_{(n-r)}$ and $r = m$. The situation is the most often encountered because when writing the system one tries to make sure that the number of independent equations are equal to the number of unknowns for obvious reasons. However, the situation does not exclude multiples of some equation. (III) Finally the solution set consists of infinitely many vectors provided $R_{(n-r)} = 0_{(n-r)}$ and $r < m$. The situation results whenever the number of independent equations is smaller than the number of unknowns. The cases (I) and (II) are excluded in dimensional analysis applications, if the problem is posed properly.

In any case the general solution of the equation system (when it exists) can be written in the form

$$\begin{Bmatrix} X_{(r)} \\ Y_{(m-r)} \end{Bmatrix} = -\begin{Bmatrix} \overline{B}_{(r)} \\ 0_{(m-r)} \end{Bmatrix} + \begin{Bmatrix} -\overline{A}_{(r,m-r)} \\ I_{(m-r,m-r)} \end{Bmatrix} \{C_{(m-r)}\} \tag{6}$$

where vector $C_{(m-r)}$ is arbitrary. In order to get the m-r linearly independent solutions forming a complete set, one can choose consecutively one element of $C_{(m-r)}$ as nonzero. One should note that each matrix with nonpositive values for indices should be rejected in (6). For instance, if the original coefficient matrix is a square one and the rank is equal to the number of unknowns, the last term on the right hand side will vanish as well as the lower parts of the vectors.

PROGRAM

The FORTRAN-language program developed and based on the theory described above consists of a simple main program, of a solver and of several small subroutines to handle the rational number arithmetics and input and output operations.

For simplicity each rational number is taken as an integer valued table of two entries. The first entry is the numerator and the second one is the denominator. Thus the arithmetics operates on a quite small subset of rational numbers ranging from 1/M to M, where M is the maximum integer number available. Although the Euclidean algorithm [8] is used to cancel the greatest common divisor out of the numerator and the denominator whenever needed, the solution may fail due to integer overflow. Some other presentation for the rational numbers (say a string of characters) is needed if the program is used in solving problems with a large number of equations or with rational numbers consisting of large prime numbers.

The listing of the program consisting of about 200 lines is obtainable from the authors on request.

EXAMPLE 1

As an example let us consider a simple impact problem, where an elastic ball strikes a rigid stationary plane perpendicularly. The aim is to find a formula, which can be used in predicting the velocity after the impact. As quite complicated if treated otherwise, the problem is well suited for some kind of semi-empirical treatment.

The decisive variables in M, L,T- system are taken to be

Velocity before impact	u_1	LT^{-1},
Radius of the sphere	R	L,
Density of the sphere	ρ	ML^{-3},
Poisson's ratio	ν	1
Young's modulus	E	$ML^{-1}T^{-2}$,
Velocity after impact	u_2	LT^{-1},

The list is by no means exhaustive, but should be taken more as a compromise between accuracy and the experimental work to be performed. It is clear that any real material is dissipative, but the mechanism of making the velocity smaller after each impact has obviously more to do with elastic vibrations, so this effect is neglected. One should note that the strain-stress relationship is not completely described by E alone, if the material (for example rubber) is nonlinear.

The search for dimensionless products of the form (1) results into a linear equation sys-

tem (4) with

$$A_{(3,6)} = \begin{bmatrix} 0 & 0 & 1 & 0 & 1 & 0 \\ 1 & 1 & -3 & 0 & -1 & 1 \\ -1 & 0 & 0 & 0 & -2 & -1 \end{bmatrix}, \quad B_{(3)} = \begin{Bmatrix} 0 \\ 0 \\ 0 \end{Bmatrix}, \tag{7}$$

where the columns of the matrix consists of the exponents of M, L and T for each variable. The program gives three independent Pi–groups: $\Pi_1 = \nu$, $\Pi_2 = E / u_1^2 \rho$ and $\Pi_3 = u_2 / u_1$. So by using Buckingham's theorem, we know that there exists a relationship

$$\Pi_3 = f(\Pi_1, \Pi_2), \tag{8}$$

where the actual form is now intended to be found experimentally for example by taking Π_1 as a curve parameter and plotting Π_3 against Π_2. For small velocities the experiment can be performed for instance by dropping a ball with known material properties on (say) a concrete floor. The relationships $u_1 = \sqrt{2gh_1}$ and $u_2 = \sqrt{2gh_2}$, where h_1 and h_2 are the dropping height and the height the ball will rise after the impact respectively, give the needed ingredient for the experiment.

EXAMPLE 2

The second example is taken from [4] and deals with natural convection in a horizontal pipe concentric with a larger pipe. The space between the pipes is filled with liquid. As the temperature of the pipes is different, steady convection currents are generated by the thermal expansion of the fluid and some heat transportation will occur. The purpose is to find the general form of a formula describing the heat transfer between the pipes. The decisive variables in M,L,T,Θ-system are taken to be (see [4 p.126] for details)

Diameter of the smaller tube	d_1	L,
Diameter of the larger tube	d_2	L,
Acceleration due to gravity	g	LT^{-2},
Temperature difference	$\Delta\theta$	Θ,
Specific heat capacity per unit volume	$c\rho$	$ML^{-1}T^{-2}\Theta^{-1}$,
Thermal conductivity	k	$MLT^{-3}\Theta^{-1}$,
Coefficient of thermal expansion	β	Θ^{-1},
Kinematic viscosity	ν	L^2T^{-1},
Coefficient of heat transfer	h	$MT^{-3}\Theta^{-1}$.

So the problem is to find all the independent solutions of a linear equation system with

$$A_{(4,9)} = \begin{bmatrix} 0 & 0 & 0 & 0 & 1 & 1 & 0 & 0 & 1 \\ 1 & 1 & 1 & 0 & -1 & 1 & 0 & 2 & 0 \\ 0 & 0 & -2 & 0 & -2 & -3 & 0 & -1 & -3 \\ 0 & 0 & 0 & 1 & -1 & -1 & -1 & 0 & -1 \end{bmatrix}, \quad B_{(4)} = \begin{Bmatrix} 0 \\ 0 \\ 0 \\ 0 \end{Bmatrix}. \tag{9}$$

The program gives the set

$$\Pi_1 = \frac{d_2}{d_1}, \quad \Pi_2 = \frac{gk}{c\rho d_1^{3/2}}, \quad \Pi_3 = \beta\Delta\theta, \quad \Pi_4 = \frac{g\nu}{d_1^{3/2}}, \quad \Pi_5 = \frac{gh}{c\rho d_1^{1/2}}, \tag{10}$$

which is not exactly the set given in the reference, but is complete anyway.

ACKNOWLEDGEMENT

We are grateful to Mr. Djebar Baroudi for bringing to our attention the Euclidean algorithm.

REFERENCES

1. Barr, D.I.H., Echelon matrices in dimensional analysis, IJMEE 7, 1979, pages 85-89.

2. Webb, A.I.C., Fryer, J.D., The formation of dimensionless groups, IJMEE 9, 1981, pages 77-82.

3. Taylor, E.S., Dimensional analysis for engineers, Clarendon Press, Oxford, 1974.

4. Langhaar, H.L., Dimensional analysis and theory of models, Wiley, New York, 1951 and Robert E. Krieger Pub. Co., New York, 1980.

5. Barr, D.I.H., Consolidation of the Webb and Fryer procedure for dimensional analysis, IJMEE 10, 1982, pages 279-284.

6. Matthews, F.W, Morfett, J.C., A method of dimensional analysis for computer application, IJMEE 14, 1986, pages 65-73.

7. Kivelä, S.K., Matriisilasku ja lineaarialgebra, Otakustantamo 466, 1980.

8. Agnew, J., Explorations in number theory, Brooks/Cole Publishing Company, 1972.

USE OF LOCAL RECTANGULAR COORDINATES IN VARIOUS STRUCTURAL ANALYSES

Juha Paavola and Eero-Matti Salonen
Helsinki University of Technology
Department of Structural Mechanics and Institute of Mechanics
SF-02150 ESPOO, FINLAND

ABSTRACT

The present paper is concerned with some aspects of teaching structural mechanics. First, the importance of the principle of virtual work as a common basis for both numerical and analytical methods is emphasized. The aim is to introduce a method in which local rectangular Cartesian coordinates are used in a simple and graphic way to derive analytical expressions for strains in any orthogonal curvilinear coordinate system. In numerical work the same method can be utilized allowing the use of well-known expressions for strains in rectangular orthogonal coordinates. As applications of the theory polar coordinates and bending and stretching of a plane beam are considered.

INTRODUCTION

The position of numerical methods - and particularly that of the finite element method - has become more and more important in solving problems of structural mechanics. This fact must be taken seriously into account in the education of the subject to obtain a correct balance between analytical and numerical methods. It is equally clear that the amount of time allotted to be used at the universities for teaching the subject is not probably going to increase at the present time.

It seems that under these circumstances the principle of virtual work should obtain an extremely important role in economizing the teaching by acting as a common basis for both the numerical and analytical methods. The principle is a direct starting point for deriving the governing finite element equations but it can equally well be used for obtaining the corresponding analytical equilibrium equations. The principle describes any structural problem - be it as complicated as anyone wants - as a scalar equation, in which scalar quantities - intensities of internal and external virtual work - are integrated over the volume and surface of the structure. In the evaluation of these invariant scalars one can make use of any coordinate system which does not necessarily need to

be conformable with the geometry of the structure. This flexibility can be made use of in the numerical treatment in the simplest possible way: Only familiar rectangular Cartesian coordinates are employed for expressing strains and stresses at the integration points. The directions of the coordinate axes can further be selected to vary from point to point for instance to take in a simple way into account say an assumption of zero value for a certain stress component.

The finite element method has thus diminished the need to treat problems of mechanics in general curvilinear coordinates. In purely analytical methods with curved structures the use of curvilinear coordinates is naturally still necessary. It is, however, then often enough to work with orthogonal coordinates - if an analytical solution is to be expected to be found. Even in this case the derivation of the expressions needed can be a rather challenging and time consuming task.

The two traditional approaches to do this can be called the differential geometry method and the tensor formalism method. The former is employed mainly in introductory engineering texts and is based on figures of suitable small elements and their free body diagrams to find the strain expressions and equilibrium equations. This approach may in some cases be illustrative but it also easily leaves the student a little unsure of the exactness of the final results. Much depends on the quality of the figures used. The tensor formalism, on the other hand, gives results in no doubt of correctness but this way demands quite a lot of previous knowledge from the student if to be achieved in a reasonable time. In this paper an alternative procedure to the ones described above is presented to derive the governing strain expressions in connection with orthogonal curvilinear coordinates which is believed to be of some didactic value.

To shorten the presentation the relevant formulae for small strains will be given here in two dimensions only as the extensions to three dimensions are quite obvious. As applications of the theory the equations in polar coordinates are considered as well as the bending and stretching problem of a curved plane beam. Only the derivation of strain expressions are considered and the use of the virtual work principle to obtain the equilibrium equations are left untouched in this context.

SOME MATHEMATICAL PREPARATIONS

Three coordinate systems, rectangular Cartesian x, y with unit base vectors $\vec{i}, \vec{j}$, rectangular Cartesian X, Y with unit base vectors $\vec{e}_X, \vec{e}_Y$ and orthogonal curvilinear α, β with unit base vectors $\vec{e}_\alpha, \vec{e}_\beta$ are used. Coordinates x, y and α, β are defined for the whole structure and are employed in the traditional way. The X, Y-system is, however, used as an auxiliary tool in a way to be explained presently.

The partial derivatives $\partial\vec{r}/\partial\alpha$ and $\partial\vec{r}/\partial\beta$ of the position vector $\vec{r}$ with respect to the curvilinear coordinates are tangent vectors to the corresponding coordinate lines and one can thus write

$$\frac{\partial\vec{r}}{\partial\alpha} = H_\alpha \vec{e}_\alpha, \qquad \frac{\partial\vec{r}}{\partial\beta} = H_\beta \vec{e}_\beta, \tag{1}$$

where $H_\alpha = |\partial\vec{r}/\partial\alpha|$ and $H_\beta = |\partial\vec{r}/\partial\beta|$ are the so called LAMÉ coefficients or scale factors, VÄISÄLÄ [1], NOVOZHILOV [2] They can be evaluated from the equations

$$H_\alpha = \left(\frac{\partial\vec{r}}{\partial\alpha}\cdot\frac{\partial\vec{r}}{\partial\alpha}\right)^{1/2}, \qquad H_\beta = \left(\frac{\partial\vec{r}}{\partial\beta}\cdot\frac{\partial\vec{r}}{\partial\beta}\right)^{1/2}. \tag{2}$$

The connection between derivatives evaluated with respect to the X, Y and α, β coordinates will be needed. It is convenient to start from the relationship

$$\begin{aligned} \frac{\partial}{\partial \alpha} &= \frac{\partial X}{\partial \alpha}\,\frac{\partial}{\partial X} + \frac{\partial Y}{\partial \alpha}\,\frac{\partial}{\partial Y}, \\ \frac{\partial}{\partial \beta} &= \frac{\partial X}{\partial \beta}\,\frac{\partial}{\partial X} + \frac{\partial Y}{\partial \beta}\,\frac{\partial}{\partial Y} \end{aligned} \tag{3}$$

obtainable simply by the chain rule. The multipliers $\partial X/\partial \alpha$, $\partial Y/\partial \alpha$, ... can be expressed as follows

$$\begin{aligned} \frac{\partial X}{\partial \alpha} &= \frac{\partial \vec{r}}{\partial \alpha} \cdot \vec{e}_X, \qquad \frac{\partial Y}{\partial \alpha} = \frac{\partial \vec{r}}{\partial \alpha} \cdot \vec{e}_Y, \\ \frac{\partial X}{\partial \beta} &= \frac{\partial \vec{r}}{\partial \beta} \cdot \vec{e}_X, \qquad \frac{\partial Y}{\partial \beta} = \frac{\partial \vec{r}}{\partial \beta} \cdot \vec{e}_Y. \end{aligned} \tag{4}$$

This can be seen by considering the position vector expressed in the form

$$\vec{r} = \vec{r}_O + X\vec{e}_X + Y\vec{e}_Y, \tag{5}$$

where $\vec{r}_O$ is the position vector of the origin of the X, Y-system, by taking into account that $\vec{r}_O$ and the unit vectors $\vec{e}_X$ and $\vec{e}_Y$ are constants and by remembering the meaning of the dot product. Using matrix notations the connection is

$$\begin{Bmatrix} \dfrac{\partial}{\partial \alpha} \\ \dfrac{\partial}{\partial \beta} \end{Bmatrix} = \begin{bmatrix} \dfrac{\partial \vec{r}}{\partial \alpha} \cdot \vec{e}_X & \dfrac{\partial \vec{r}}{\partial \alpha} \cdot \vec{e}_Y \\ \dfrac{\partial \vec{r}}{\partial \beta} \cdot \vec{e}_X & \dfrac{\partial \vec{r}}{\partial \beta} \cdot \vec{e}_Y \end{bmatrix} \begin{Bmatrix} \dfrac{\partial}{\partial X} \\ \dfrac{\partial}{\partial Y} \end{Bmatrix}. \tag{6}$$

Actually, the inverse relationship

$$\begin{Bmatrix} \dfrac{\partial}{\partial X} \\ \dfrac{\partial}{\partial Y} \end{Bmatrix} = \begin{bmatrix} \dfrac{\partial \vec{r}}{\partial \alpha} \cdot \vec{e}_X & \dfrac{\partial \vec{r}}{\partial \alpha} \cdot \vec{e}_Y \\ \dfrac{\partial \vec{r}}{\partial \beta} \cdot \vec{e}_X & \dfrac{\partial \vec{r}}{\partial \beta} \cdot \vec{e}_Y \end{bmatrix}^{-1} \begin{Bmatrix} \dfrac{\partial}{\partial \alpha} \\ \dfrac{\partial}{\partial \beta} \end{Bmatrix} \tag{7}$$

will be needed. This way of representing the connection between the derivatives is very convenient also in numerical calculations from the programming point of view and was probably introduced originally by IRONS and AHMAD [3].

The unit vectors $\vec{e}_\alpha$ and $\vec{e}_\beta$ depend on position and their derivatives with respect to the curvilinear coordinates are required. General expressions for these vectors can be derived, e.g. MALVERN [4]. In this presentation the derivatives will be given in some specific cases and the reader is assumed to be familiar with them. It may be remarked that the use of connections like (3) are essential also in the theory of parametric finite elements so that again numerical and analytical methods can find common features.

DISPLACEMENTS AND STRAINS

With the three coordinate systems there are accordingly three ways to represent the displacement vector:

$$\vec{u} = u_x\vec{i} + u_y\vec{j}, \tag{8a}$$

$$\vec{u} = u_X\vec{e}_X + u_Y\vec{e}_Y, \tag{8b}$$

$$\vec{u} = u_\alpha\vec{e}_\alpha + u_\beta\vec{e}_\beta. \tag{8c}$$

The last one is employed in analytical calculations in 'curved' structures. The expressions for the rectangular small strain components are in the X,Y-system

$$\begin{aligned}\epsilon_X &= \frac{\partial u_X}{\partial X} = \frac{\partial \vec{u}}{\partial X}\cdot\vec{e}_X,\\ \epsilon_Y &= \frac{\partial u_Y}{\partial Y} = \frac{\partial \vec{u}}{\partial Y}\cdot\vec{e}_Y,\\ \gamma_{XY} &= \frac{\partial u_X}{\partial Y}+\frac{\partial u_Y}{\partial X} = \frac{\partial \vec{u}}{\partial Y}\cdot\vec{e}_X+\frac{\partial \vec{u}}{\partial X}\cdot\vec{e}_Y.\end{aligned} \tag{9}$$

The dot product expressions following the familiar forms can be verified directly by differentiating the definition (8b) with respect to the local coordinates having the fixed unit base vectors constant. These expressions are convenient, particularly in numerical algorithms, and they were probably also introduced by IRONS and AHMAD [3].

The strategy to obtain the expressions for the strain components ϵ_α, ϵ_β and $\gamma_{\alpha\beta}$ is based here simply on fixing the origin O of the auxiliary coordinate system X,Y momentarily to an arbitrary point P of the domain and on letting the X- and Y-axes coincide with the tangents to the α- and β-coordinate lines at the origin. Then clearly at the origin $\epsilon_\alpha = \epsilon_X$, $\epsilon_\beta = \epsilon_Y$ and $\gamma_{\alpha\beta} = \gamma_{XY}$.

According to expressions (9) the derivatives of the displacement vector with respect to the local coordinates are required. The so called Jacobian matrix, i.e., the coefficient matrix in equation (6) becomes diagonal at the local origin, so that

$$\begin{bmatrix} \dfrac{\partial \vec{r}}{\partial \alpha}\cdot\vec{e}_X & \dfrac{\partial \vec{r}}{\partial \alpha}\cdot\vec{e}_Y \\ \dfrac{\partial \vec{r}}{\partial \beta}\cdot\vec{e}_X & \dfrac{\partial \vec{r}}{\partial \beta}\cdot\vec{e}_Y \end{bmatrix} = \begin{bmatrix} H_\alpha & 0 \\ 0 & H_\beta \end{bmatrix}, \tag{10}$$

because $\vec{e}_\alpha = \vec{e}_X$, $\vec{e}_\beta = \vec{e}_Y$ and because of expressions (1) the dot products $\partial\vec{r}/\partial\alpha\cdot\vec{e}_Y$ and $\partial\vec{r}/\partial\beta\cdot\vec{e}_X$ disappear. Furthermore the terms $\partial\vec{r}/\partial\alpha\cdot\vec{e}_X$ and $\partial\vec{r}/\partial\beta\cdot\vec{e}_Y$ give the magnitudes of the vectors $\partial\vec{r}/\partial\alpha$ and $\partial\vec{r}/\partial\beta$ which are given by the scale factors. Thus

$$\begin{bmatrix} H_\alpha & 0 \\ 0 & H_\beta \end{bmatrix}^{-1} = \begin{bmatrix} H_\alpha^{-1} & 0 \\ 0 & H_\beta^{-1} \end{bmatrix} \tag{11}$$

and formulae (7) give simply

$$\frac{\partial}{\partial X} = H_\alpha^{-1}\frac{\partial}{\partial \alpha}, \qquad \frac{\partial}{\partial Y} = H_\beta^{-1}\frac{\partial}{\partial \beta} \tag{12}$$

at the local origin. Now

$$\begin{aligned}\frac{\partial \vec{u}}{\partial X} &= H_\alpha^{-1}\Big(\frac{\partial u_\alpha}{\partial \alpha}\vec{e}_\alpha + u_\alpha\frac{\partial \vec{e}_\alpha}{\partial \alpha}+\frac{\partial u_\beta}{\partial \alpha}\vec{e}_\beta+u_\beta\frac{\partial \vec{e}_\beta}{\partial \alpha}\Big),\\ \frac{\partial \vec{u}}{\partial Y} &= H_\beta^{-1}\Big(\frac{\partial u_\alpha}{\partial \beta}\vec{e}_\alpha + u_\alpha\frac{\partial \vec{e}_\alpha}{\partial \beta}+\frac{\partial u_\beta}{\partial \beta}\vec{e}_\beta+u_\beta\frac{\partial \vec{e}_\beta}{\partial \beta}\Big).\end{aligned} \tag{13}$$

Here after evaluating the governing derivatives of unit vectors the expressions are substituted into the strain component formulae (9). It should still be remarked that equations (13) are valid exactly only at the origin of the auxiliary coordinate system.

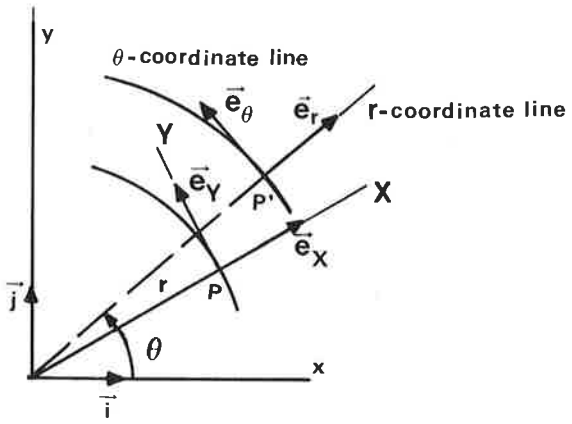

FIGURE 1. Polar coordinate system.

POLAR COORDINATES

As a very simple illustrative application of the preceding theory the case of polar coordinates shown in Figure 1 is considered. Here the roles of α and β are the radius r and the angle θ. The position vector for a point P' is

$$\vec{r} = r\vec{e}_r \tag{14}$$

and the displacement (8c)

$$\vec{u} = u_r\vec{e}_r + u_\theta\vec{e}_\theta. \tag{15}$$

The derivatives of the unit base vectors are found to be simply

$$\frac{\partial\vec{e}_r}{\partial r} = 0, \qquad \frac{\partial\vec{e}_\theta}{\partial r} = 0, \qquad \frac{\partial\vec{e}_r}{\partial\theta} = \vec{e}_\theta, \qquad \frac{\partial\vec{e}_\theta}{\partial\theta} = -\vec{e}_r. \tag{16}$$

Thus

$$\begin{aligned} \frac{\partial\vec{r}}{\partial r} &= \frac{\partial r}{\partial r}\vec{e}_r + r\frac{\partial\vec{e}_r}{\partial r} = \vec{e}_r, \\ \frac{\partial\vec{r}}{\partial\theta} &= \frac{\partial r}{\partial\theta}\vec{e}_r + r\frac{\partial\vec{e}_r}{\partial\theta} = r\vec{e}_\theta \end{aligned} \tag{17}$$

and employing formulae (2)

$$H_r = (\vec{e}_r \cdot \vec{e}_r)^{1/2} = 1, \qquad H_\theta = (r\vec{e}_\theta \cdot r\vec{e}_\theta)^{1/2} = r. \tag{18}$$

The counterparts of equations (13) are here

$$\begin{aligned} \frac{\partial\vec{u}}{\partial X} &= \left(\frac{\partial u_r}{\partial r}\vec{e}_r + \frac{\partial u_\theta}{\partial r}\vec{e}_\theta\right), \\ \frac{\partial\vec{u}}{\partial Y} &= \frac{1}{r}\left(\frac{\partial u_r}{\partial\theta}\vec{e}_r + u_r\vec{e}_\theta + \frac{\partial u_\theta}{\partial\theta}\vec{e}_\theta - u_\theta\vec{e}_r\right). \end{aligned} \tag{19}$$

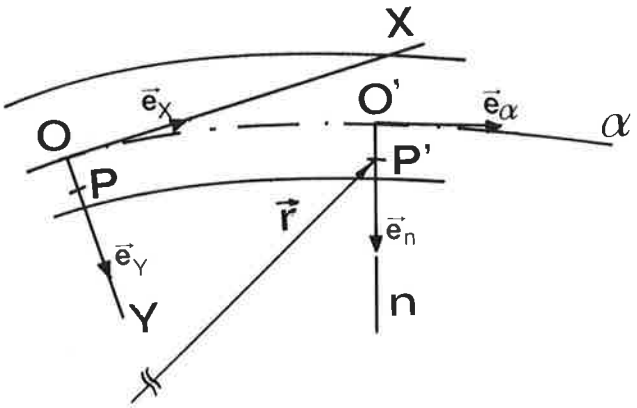

FIGURE 2. Curved beam.

The strain components according to equations (9) at the origin P are finally

$$\begin{aligned} \epsilon_r &= \epsilon_X = \frac{\partial u_r}{\partial r}, \\ \epsilon_\theta &= \epsilon_Y = \frac{u_r}{r} + \frac{1}{r}\frac{\partial u_\theta}{\partial \theta}, \\ \gamma_{r\theta} &= \gamma_{XY} = \frac{1}{r}\frac{\partial u_r}{\partial \theta} - \frac{u_\theta}{r} + \frac{\partial u_\theta}{\partial r}. \end{aligned} \tag{20}$$

These results are in accordance with the ones given in literature. It may still be remarked that the derivation is based on a simple logic which can be applied without alterations to any orthogonal curvilinear coordinate system.

CURVED BEAM

Geometry

A curved plane beam is considered using the notation shown in Figure 2. The notations are altered here from those used in the preceding text to better conform for a possible extension to shells, which is, however, not discussed here, see [5]. The curvilinear coordinate α coincides with the beam axis. Instead of the coordinate symbol β the symbol n is used for the normal measuring the distance from the beam axis. The purpose is to determine the expressions for the strain components $\epsilon_\alpha = \epsilon_X$ and $\gamma_{\alpha n} = \gamma_{XY}$ at a general point P shown in Figure 2. Here it is appropriate, since the normal coordinate is rectilinear, to fix the origin of the auxiliary coordinate system at the point O on the beam axis, as shown in the figure. Another possibility is to define the origin at any point outside the beam axis. This means that the scale factors can no more be spanned on the quantities defined on the axis but have to be determined at each point, separately. In this presentation the former procedure is adopted. The derivation is started with an arbitrary point P' which will finally be let to move to P. The position vector of a point P' can be combined of two parts as follows

$$\vec{r}(\alpha, n) = \vec{r}_{O'}(\alpha) + n\vec{e}_n(\alpha), \tag{21}$$

where $\vec{r}_{O'}$ is the position vector of point O' on the axis. The derivatives of the unit base vectors are

$$\frac{\partial \vec{e}_\alpha}{\partial \alpha} = -\frac{H}{R}\vec{e}_n, \qquad \frac{\partial \vec{e}_n}{\partial \alpha} = \frac{H}{R}\vec{e}_\alpha, \tag{22}$$

whereas the corresponding derivatives with respect to n vanish. The reference to coordinate α is dropped out in the scale factor H and the radius of curvature R, for brevity. Expressions (22) are obtained from the well known FRENET formulae, e.g. VÄISÄLÄ [1]. Here the radius of curvature of the beam axis is considered positive when the center of curvature is on the negative side of the n-axis. The scale factor is defined through the equation

$$\frac{\partial \vec{r}_{O'}}{\partial \alpha} = H\vec{e}_\alpha. \tag{23}$$

If coordinate α is selected to be the arclength s - as is usual - the scale factor is a unit, i.e., $H = 1$. Differentiation of expression (21) gives

$$\begin{aligned} \frac{\partial \vec{r}}{\partial \alpha} &= \frac{\partial \vec{r}_{O'}}{\partial \alpha} + n\frac{\partial \vec{e}_n}{\partial \alpha} = H\vec{e}_\alpha + n\frac{H}{R}\vec{e}_\alpha = H\Big(1+\frac{n}{R}\Big)\vec{e}_\alpha, \\ \frac{\partial \vec{r}}{\partial n} &= \vec{e}_n. \end{aligned} \tag{24}$$

It can be seen that the scale factors corresponding to coordinates α and n at a general point are $H(1+n/R)$ and 1. Here and in the following - in a slight deviation from the treatment for example in the case of polar coordinates - the scale factor H and the radius of curvature R refer to the quantities on the axis only. Equations (12) obtain thus the forms

$$\frac{\partial}{\partial X} = H^{-1}(1+\frac{n}{R})^{-1}\frac{\partial}{\partial \alpha}, \qquad \frac{\partial}{\partial Y} = \frac{\partial}{\partial n}. \tag{25}$$

Displacements and strains

To achieve a one-dimensional conventional theory the displacement assumption of TIMOSHENKO's beam theory is adopted according to which the displacement vector is

$$\vec{u}(\alpha, n) = [u_\alpha(\alpha) - n\theta(\alpha)]\,\vec{e}_\alpha(\alpha) + u_n(\alpha)\vec{e}_n(\alpha). \tag{26}$$

The unknowns are the functions $u_\alpha(\alpha)$, $u_n(\alpha)$ and $\theta(\alpha)$ representing the displacement components of point O' on the beam axis and the rotation of a material fiber originally perpendicular to the axis as positive in the clockwise direction. The only nonzero strain components in expressions (9) are ϵ_X and γ_{XY}. The derivatives of the displacement vector at point P needed can be calculated directly using expressions (25) and (26) yielding

$$\begin{aligned} \frac{\partial \vec{u}}{\partial X} &= H^{-1}\left(1+\frac{n}{R}\right)^{-1}\left[\Big(\frac{\partial u_\alpha}{\partial \alpha} - n\frac{\partial \theta}{\partial \alpha}\Big)\vec{e}_\alpha + (u_\alpha - n\theta)\frac{\partial \vec{e}_\alpha}{\partial \alpha} + \frac{\partial u_n}{\partial \alpha}\vec{e}_n + u_n\frac{\partial \vec{e}_n}{\partial \alpha}\right] \\ &= \left(1+\frac{n}{R}\right)^{-1}\left[\Big(\frac{\partial u_\alpha}{H\partial \alpha} - n\frac{\partial \theta}{H\partial \alpha} + \frac{u_n}{R}\Big)\vec{e}_\alpha + \Big(-\frac{u_\alpha - n\theta}{R} + \frac{\partial u_n}{H\partial \alpha}\Big)\vec{e}_n\right], \\ \frac{\partial \vec{u}}{\partial Y} &= \frac{\partial}{\partial n}\Big[(u_\alpha - n\theta)\vec{e}_\alpha + u_n\vec{e}_n\Big] = -\theta\vec{e}_\alpha \end{aligned} \tag{27}$$

and the strain components, correspondingly ($\vec{e}_\alpha = \vec{e}_X$, $\vec{e}_n = \vec{e}_Y$)

$$\begin{aligned}\epsilon_\alpha = \epsilon_X &= \left(1+\frac{n}{R}\right)^{-1}\left(\frac{\partial u_\alpha}{H\partial\alpha} - n\frac{\partial\theta}{H\partial\alpha} + \frac{u_n}{R}\right),\\ \gamma_{\alpha n} = \gamma_{XY} &= \left(1+\frac{n}{R}\right)^{-1}\left(-\frac{u_\alpha - n\theta}{R} + \frac{\partial u_n}{H\partial\alpha}\right) - \theta.\end{aligned} \tag{28}$$

It is often of interest to find out the parts of incresing power of the normal coordinate n, particularly concerning the coefficients of constant and linear terms. Thus these expressions can be reformulated as

$$\begin{aligned}\epsilon_\alpha &= \frac{\partial u_\alpha}{H\partial\alpha} + \frac{u_n}{R} - \frac{n}{R}\left(\frac{\partial u_\alpha}{H\partial\alpha} + \frac{u_n}{R} + \frac{R\partial\theta}{H\partial\alpha}\right) + O(n^2),\\ \gamma_{\alpha n} &= \left(1 - \frac{n}{R} + O(n^2)\right)\left(\frac{\partial u_n}{H\partial\alpha} - \frac{u_\alpha}{R} - \theta\right).\end{aligned} \tag{29}$$

If the BERNOULLI assumption or the beam theory with vanishing shear deformations is adopted the rotation function can be solved from the latter one of equations (28) or (29) by setting the condition $\gamma_{\alpha n} \equiv 0$. Thus the expression

$$\theta = \frac{\partial u_n}{H\partial\alpha} - \frac{u_\alpha}{R} \tag{30}$$

is obtained. Substituting this into the expression for the axial strain, the former one in equations (28), yields in the form

$$\begin{aligned}\epsilon_\alpha &= \frac{\partial u_\alpha}{H\partial\alpha} + \left(1+\frac{n}{R}\right)^{-1}\left[\frac{u_n}{R} - n\left(\frac{u_\alpha}{R^2}\frac{\partial R}{H\partial\alpha} - \frac{\partial}{H\partial\alpha}\left(\frac{\partial u_n}{H\partial\alpha}\right)\right)\right]\\ &= \frac{\partial u_\alpha}{H\partial\alpha} + \frac{u_n}{R} - n\left[\frac{u_n}{R^2} + \frac{u_\alpha}{R^2}\frac{\partial R}{H\partial\alpha} - \frac{\partial}{H\partial\alpha}\left(\frac{\partial u_n}{H\partial\alpha}\right)\right] + O(n^2).\end{aligned} \tag{31}$$

CONCLUSIONS

A tuitional introduction to the use of fixed rectangular Cartesian coordinates is presented. The procedure illustrated is capable to serve both analytical and numerical purposes. It is also a tool which could be made use of in educational aims to facilitate and lower that threshold interpreted as repulsive towards mechanical problems of structures.

REFERENCES

1. Väisälä K., Vektorianalyysi. 6th ed. WSOY, Helsinki, 1975 (in Finnish).
2. Novozhilov V.V., Thin shell theory. P. Noordhoff Ltd. Translation, London, 1964.
3. Irons B.M. and Ahmad S., Techniques of finite elements. Ellis Horwood, Chichester, 1980.
4. Malvern L.E., Introduction to the mechanics of continuous medium. Prentice-Hall, New York, 1969.
5. Paavola J. and Salonen E.-M., Muodonmuutokset ja kiinteät paikalliset karteesiset koordinaatit (in Finnish, in preparation).

COMPLEMENTARY WORK, PSEUDO STRESS ENERGY AND STRESS ENERGY

PERTTI HOLOPAINEN
Department of Mechanical Engineering
Tampere University of Technology
P.O. Box 527, SF-33101 TAMPERE, FINLAND

ABSTRACT

It has been examined with examples the connection between external complementary work, stress energy and pseudo stress energy and when it is equal to zero. Further, the principle of virtual forces has been presented.

INTRODUCTION

The principle of stationary complementary work for geometrically nonlinear structures has been presented by Oran 1967 /1/. An other formulation has been presented by the author 1974 /2/, /3/. An essential problem in the force method the rotation of rigid body as a function of forces has been examined by the author /3/, /4/.

COMPLEMENTARY WORK FOR GEOMETRICALLY NONLINEAR STRUCTURES

It has been derived by the author in 1974 /2/ the complementary work

$$W_c = \Sigma H_{ij} \overline{\Delta h}_{ij} + U_c \qquad (1)$$

for the finite element method (force method) of elastic structures. In (1)

W_c	external complementary work
U_c	stress energy
H_{ij}	node force of element at the node i and in the direction j = 1, 2, 3 or x, y, z.
$\overline{\Delta h}_{ij}$	relative node displacement caused only by the rigid body rotation of element
$\Sigma H_{ij} \overline{\Delta h}_{ij}$	the pseudo stress energy ΔW_c .

If the rigid body rotations of all elements are infinite as it can be assumed in geometrically nonlinear structures, the pseudo stress energy is equal to zero and it can be set

$$W_c = U_c \qquad (2)$$

where W_c is the same as the Engessers work /5/.

When the structure is rigid body mechanism with one or more degree of freedom, the stress energy is equal to zero, and

$$W_c = \Sigma H^e_{ij} \overline{\Delta h}^e_{ij} \; . \qquad (3)$$

APPLICATIONS

Bar element. Consider a bar element as shown in Fig. 1.

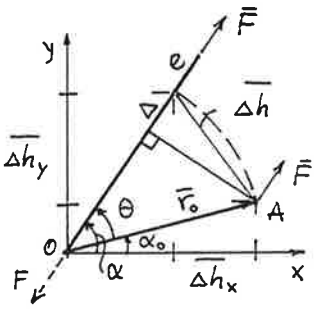

FIGURE 1

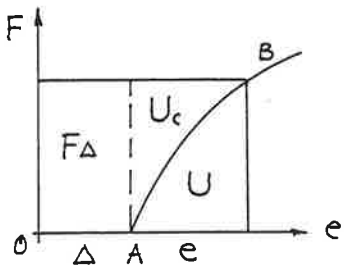

FIGURE 2

The force F turns the bar OA from an initial position α_0 to the moment equilibrium position α so as rigid body and stretch amount e. The external complementary work (see Figs. 1 and 2)

$$W_c = F\Delta + \int_0^F e(F)\,dF$$

$$= \bar{F} \cdot \bar{\Delta h} + U_c \tag{4}$$

$$= H_x \overline{\Delta h}_x + H_y \overline{\Delta h}_y + U_c$$

where the components of $\bar{F}$ have been denoted H_x and H_y and

$$\left.\begin{aligned} F &= \pm\sqrt{H_x^2+H_y^2} \\ \overline{\Delta h}_x &= r_0 \cos\alpha - r_0 \cos\alpha_0 \\ \overline{\Delta h}_y &= r_0 \sin\alpha - r_0 \sin\alpha_0 \end{aligned}\right\} \tag{5}$$

The derivative

$$\frac{\partial W_c}{\partial F} = \Delta + e(F) \tag{6}$$

is the displacement of node A in the direction of F. The derivative

$$\frac{\partial W_c}{\partial H_x} = \overline{\Delta h}_x + e(F)\frac{\partial F}{\partial H_x} = \overline{\Delta h}_x + e_x \tag{7}$$

is the displacement of node A in the direction of H_x.

When the rigid body rotation of the elements are not infinite, the external complementary work W (Eg. 1) is not a complement of the strain energy U as the Engessers work (Ergänzungsarbeit in the German).

The graph of function F in Fig. 2 is the line OAB. When F is equal to zero, the pseudo stress energy $F\Delta \neq 0$ has been produced! But if we note that the complementary work is work of displacements so as the work of forces, we can understand the pseudo stress energy without difficulty.

Beam element. Consider a beam element as shown in Fig. 3.

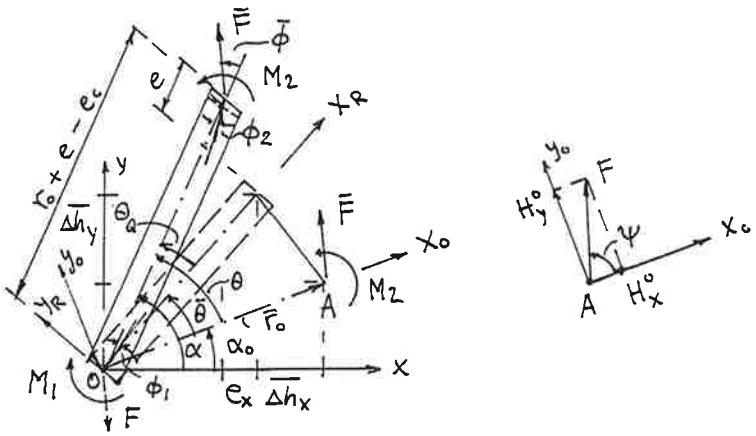

FIGURE 3

Forces F, M_1, M_2 turns the beam OA from an initial position α_0 to the deformed equilibrium position α. The position $\alpha_0 + \bar{\theta}$ is the rigid body orientation from which the moment equilibrium position has been reached. If the deformations e, θ_Q, ϕ_1, ϕ_2, e_c are infinite, the rigid body position is the moment equilibrium position, too.

The external complementary work

$$W_c = \bar{F} \cdot \overline{\Delta h} + (\bar{M}_2 - \bar{M}_1)\bar{\theta} + U_c$$

$$= H_x \overline{\Delta h}_x + H_y \overline{\Delta h}_y + (M_2 - M_1)\bar{\theta} + U_c \qquad (8)$$

where $\bar{F}$ is given in (5), and

$$\overline{\Delta h}_x = r_0(\cos(\alpha_0+\bar{\theta}) - \cos\alpha_0)$$

$$\overline{\Delta h}_y = r_0(\sin(\alpha_0+\bar{\theta}) - \sin\alpha_0)$$

and $\bar{\theta}$ can be calculated as a function of forces.

It can be obtained /6/ for one beam element (Fig. 3)

$$\frac{\partial W_c}{\partial H_x} = \overline{\Delta h}_x + \frac{\partial U_c}{\partial H_x} = \overline{\Delta h}_x + e_x \qquad (9)$$

...

$$\frac{\partial W_c}{\partial M_1} = -\bar{\theta} + \frac{\partial U_c}{\partial M_1} = -\bar{\theta} + \phi_1 \qquad (10)$$

...

Rectangular plate element in plane forces. Consider an element shown in Fig. 4.

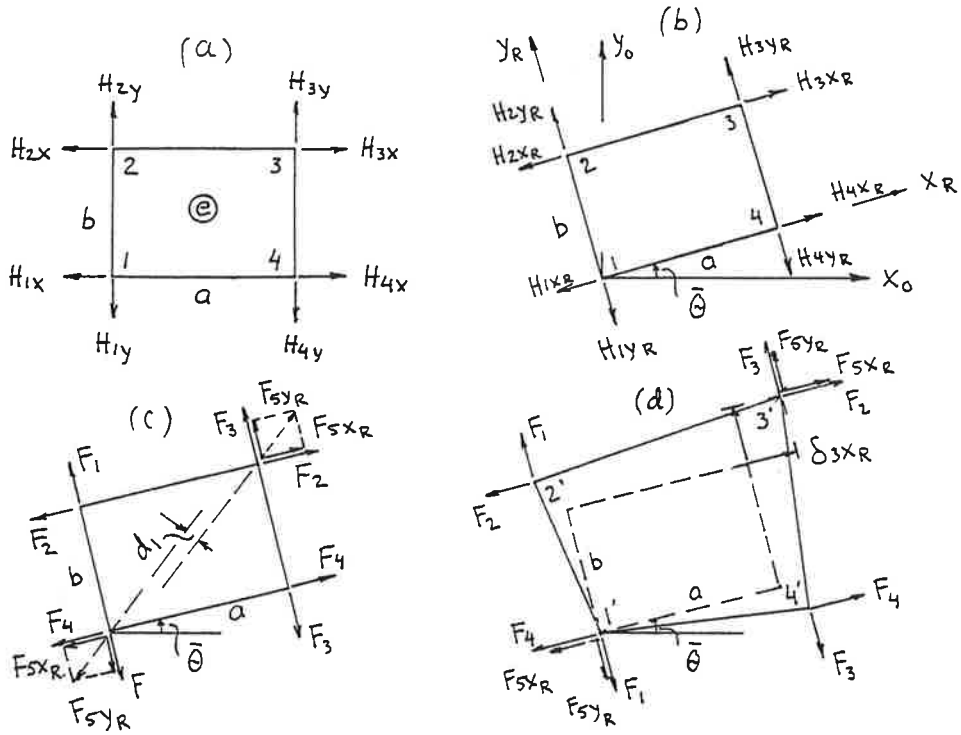

FIGURE 4

In fixed directions the nodeforces have been denoted H^e_{ij} (i = 1...4, j = x, y). Because of the force equilibrium two nodeforces say H_{1x} and H_{1y} can be eliminated. So

$$\left.\begin{aligned} H_{1x} &= H_{3x} + H_{4x} - H_{2x} \\ H_{1y} &= H_{2y} + H_{3y} - H_{4y} \end{aligned}\right\} \qquad (11)$$

The nodeforces H^e_{ij} turn the rectangle 1 2 3 4 from the initial position $\alpha^0(=0)$ (Fig. 4a) to the deformed equilibrium position 1'2'3'4' (Fig. 4d). The position θ(Fig. 4c) is the rigid body orientation (position) from which the moment equilibrium position 1'2'3'4' has been reached by the deformations only. If the element deformations δ_{ij} (i = 2,3,4, j = x_R,y_R) are infinite, the rigid body position is the moment equilibrium position, too, and $d_1 = 0$ in Fig. 4c.

The nodeforces H_{ij} (i = 1...4, j = x,y e has been dropped) can be transformed to rotated direction (Fig. 4b) and for calculation the element deformation δ_{ij} the nodeforces shall be denoted as shown in Fig. 4c where

$$\begin{aligned} F_1 &= H_{2y} & F_{5x} &= H_{3x} - H_{2x} \\ F_2 &= H_{2x} & F_{5y} &= H_{3y} - H_{4y} \\ F_3 &= H_{4y} \\ F_4 &= H_{4x} \end{aligned} \tag{12}$$

The external complementary work

$$W_c = \sum_{i,j} H_{ij}\,\overline{\Delta h}_{ij} + U_c(F_1 \ldots F_4,\ F_{5x},\ F_{5y}) \tag{13}$$

and it can be obtained

$$\frac{\partial W_c}{\partial H_{ij}} = \overline{\Delta h}_{ij} + \sum_k \frac{\partial U_c}{\partial F_k}\,\frac{\partial F_k}{\partial H_{ij}} = \overline{\Delta h}_{ij} + e_{ij}\ , \qquad (i = 2 \ldots 4,\ j = x,y) \tag{14}$$

where

$$\left.\begin{aligned} \overline{\Delta h}_{2x} &= -b \sin \bar{\theta} \\ \overline{\Delta h}_{2y} &= b \cos \bar{\theta} - b \\ &\ldots \end{aligned}\right\} \tag{15}$$

and $\bar{\theta}$ can be calculated as a function of forces.

<u>The rotation of a beam element as a function of forces</u>

The rotation /7/

$$\theta = \begin{cases} \Psi - \bar{\phi}, & \text{when beam is tensioned} \\ \Psi + \bar{\phi} - \pi, & \text{when beam is compressed} \end{cases} \tag{16}$$

In (16)

$$\left.\begin{aligned} \Psi &= \arctan\left(\frac{H^0_y}{H^0_x}\right) \\ \bar{\phi} &= \overline{\arcsin\left(\frac{-\Delta M}{rF}\right)} \end{aligned}\right\} \tag{17}$$

$$\Delta M = M_2 - M_1$$

and H^0_x, H^0_y are the components of F referred to the fixed local coordinate frame Ox_0y_0. The axis Ox_0 joints to the beam axis in the initial state. Under these circumstances the formulas (16, 17) are valid for $\theta \in \left(-\frac{\pi}{2}, \frac{\pi}{2}\right)$. It must be noted the requirement $|\Delta M| \leq r\,F$ in $(17)_2$.

ROTATION OF RIGID BODY AS A FUNCTION OF FORCES

Plate element in plane forces (Fig. 5).

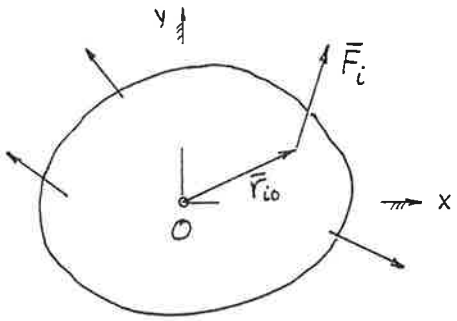

FIGURE 5. Rigid plate in plane forces hinged at 0. In the initial position.

From the moment equilibrium conditions it can be obtained /4/

$$\bar{k} \tan\theta = \frac{\bar{M}_O^0}{N_O^0} \tag{18}$$

where

$$\bar{M}_O^0 = \Sigma\, \bar{r}_{io} \times \bar{F}_i, \quad N_O^0 = \Sigma \bar{r}_{io} \cdot \bar{F}_i \tag{19}$$

$\bar{k}$ is unit vector perpendicular to the plate.

The rotation $\underline{\theta}$ calculated from Eq. (16, 17) or (18, 19) is not the rigid body rotation θ of the deformable body, except, when the element deformation are infinite.

Rigid body in space forces. (Fig. 6)

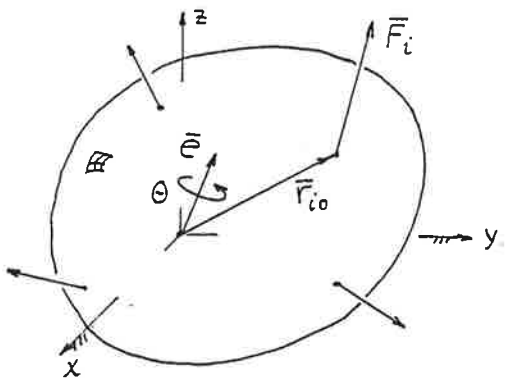

FIGURE 6. Rigid body in space forces hinged at fixed 0 in the initial position.

Because of moment equilibrium conditions

$$\sum_{i=1}^{n} \bar{r}_i \times \bar{F}_i = \bar{0} \tag{20}$$

From the Rodrigues formula (1840)

$$\bar{r}_2 - \bar{r}_1 = \tan\frac{\theta}{2}\,\bar{e} \times (\bar{r}_2 + \bar{r}_1) \tag{21}$$

can be solved ($\bar{r}_2 \triangleq \bar{r}_i$, $\bar{r}_1 \triangleq \bar{r}_{io}$)

$$\bar{r}_i = (1-\cos\theta)(\bar{e} \cdot \bar{r}_{io})\bar{e} + \cos\theta\ \bar{r}_{io} + \sin\theta\ \bar{e} \times \bar{r}_{io} \tag{22}$$

or

$$\bar{r}_i = \underline{A}\ \bar{r}_{io} = (\underline{I}-\underline{B})^{-1}(\underline{I}+\underline{B})\bar{r}_{io}\ , \tag{23}$$

where denoting $\bar{b} = \tan\frac{\theta}{2}\,\bar{e}$ instead of $\bar{b} \times \bar{r}$ the $\underline{B}\bar{r}$ has been written. $\underline{B}$ is a skev-symmetric matrix. The formula $\underline{A} = (\underline{I}-\underline{B})^{-1}(\underline{I}+\underline{B})$ is valid for any ortogonal matrix $\underline{A}$ and is known as Cayley's formula /8/.

Here the stationary principle of potential energy V_0 with subsidiary condition has been applied. For the rigid body shown in Fig. 6

$$\begin{aligned} V_0 &= \Sigma\, \bar{r}_i \cdot \bar{F}_i \\ &= (1-\cos\theta)\bar{e}^{T}\underline{T}\bar{e} + \cos\theta K + \sin\theta\bar{e} \cdot \bar{M}_0^0 \end{aligned} \tag{24}$$

where

$$\begin{aligned} &\underline{T} = \text{matrix of tensor } \Sigma\, \bar{r}_{io}\bar{F}_i \text{ (tensor product)} \\ &K = \Sigma\, \bar{r}_{io} \cdot \bar{F}_i \\ &\bar{M}_0^0 = \Sigma\, \bar{r}_{io} \times \bar{F}_i \end{aligned} \tag{25}$$

and $\bar{r}_i$ has been taken from the equation (22). A new function

$$\mathcal{F} = V_0(\theta,\bar{e}) + \lambda(e^2-1) \tag{26}$$

has been introduced. As a results of unconstrained extremum problem the equations

$$\frac{\partial \mathcal{F}}{\partial \theta} = \sin\theta\ \bar{e}^{T}\underline{T}\bar{e} - \sin\theta\ K + \cos\theta\ \bar{e} \cdot \bar{M}_0^0 = 0 \tag{27}$$

$$\begin{aligned} \frac{\partial \mathcal{F}}{\partial e_x} &= (1-\cos\theta)[2T_{11}e_x + (T_{12}+T_{21})e_y + (T_{13}+T_{31})e_z] + \sin\theta\ M_{0x}^0 \\ &\quad + 2\lambda e_x = 0 \\ \frac{\partial \mathcal{F}}{\partial e_y} &= (1-\cos\theta)[(T_{12}+T_{21})e_x + 2T_{22}e_y + (T_{23}+T_{32})e_z] + \sin\theta\ M_{0y}^0 \\ &\quad + 2\lambda e_y = 0 \\ \frac{\partial \mathcal{F}}{\partial e_z} &= (1-\cos\theta)[(T_{13}+T_{31})e_x + (T_{23}+T_{32})e_y + 2T_{33}e_z] + \sin\theta\ M_{0z}^0 \\ &\quad + 2\lambda e_z = 0 \end{aligned} \tag{28}$$

$$\frac{\partial \mathcal{F}}{\partial \lambda} = e_x^2 + e_y^2 + e_z^2 - 1 = 0 \tag{29}$$

have been obtained. The equations (28) can be written

$$[(1-\cos\theta)\underline{B} + 2\underline{\lambda}]\bar{e} + \sin\theta\ M_0^0 = \bar{0}\ , \tag{30}$$

where $\underline{B} = \underline{T} + \underline{T}'$ is symmetric. $\underline{T}$ is not symmetric except in the moment equilibrium state.

The equation (27) is the same as in /4, p. 115/ derived by the author directly from the moment equilibrium condition.

What is the rigid body orientation of structural element? Definition: The rigid body orientation of element is such one from which the final state can be obtained by the pure deformations.

Consider the plate element in plane forces (Figs. 4). The rigid body rotation θ can be calculated by using the following algorithm.

Alg.

1° Calculate the rotation θ_0 (Fig. 4b)
2° Transform the force H_{ij} to the rotated coordinate frame (Fig. 4b)
3° Calculate the element forces F_i (Fig. 4c)
4° Calculate the element deformations (Fig. 4d)
5° Calculate $\Delta\theta$, of the deformed element
6° If $\Delta\theta < \delta$, go to end, else go to 3°.

$$\bar{\theta} = \theta_0 + \Delta\theta_1 + \ldots \tag{31}$$

THE PRINCIPLE OF STATIONARY COMPLEMENTARY WORK

It can be written

$$\delta W_c = 0 \quad \& \quad \text{equilibrium} \Rightarrow \text{compatibility}$$

The internal forces of structures can be defined from the equilibrium conditions

$$\Sigma\bar{P}_i = \bar{0} \tag{32}$$

$$\Sigma\bar{r}_i \times \bar{P}_i = \bar{0} \tag{33}$$

Because of apply the equations (32, 33) reduntant forces shall be selected. When the structure is geometrically linear, both of the equations (32, 33) are usable and the statistically determinate base system and reduntants for one loop /9/ can be chosen as shown in Fig. 7. When the structure is geometrically nonlinear in equation (33) r_i:s are unknown, too, and the equation (33) is not usable to determine the internal forces as a function of given and reduntant forces. The base system and reduntants shall be chosen as shown in Fig. 8.

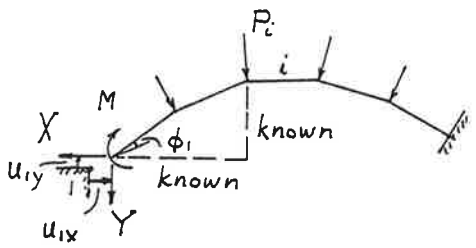

FIGURE 7

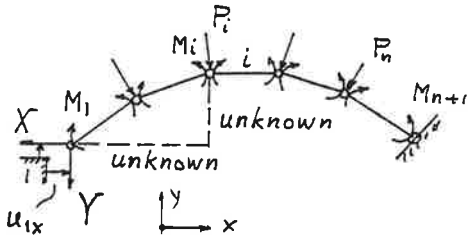

FIGURE 8

It is assumed that the hinges are so dense (Fig. 8) that the elements can be considered geometrically linear or slightly geometrically nonlinear in the final state coordinate frame. The moment equilibrium condition (33) is now used to define the orientation of elements. For example, in the loop shown in Fig. 8 the element forces are

$$H_{ix} = X - \sum_{\nu=1}^{i} P_{\nu x}$$

$$H_{iy} = Y - \sum_{\nu=1}^{i} P_{\nu y} \qquad (i = 1 \ldots n) \tag{34}$$

$$M_1 \ldots M_{n+1}$$

If n bar element has been taken, the two different structures can be assembled. The displacement method is more suitable when analysing the structure shown in fig. 9 (two unknown displacements) and the force method when analysing the structure shown in Fig. 10 (two unknown forces).

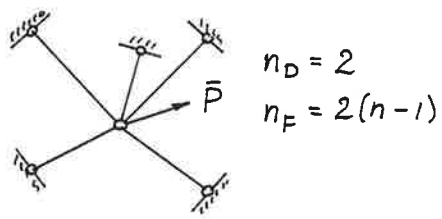

FIGURE 9

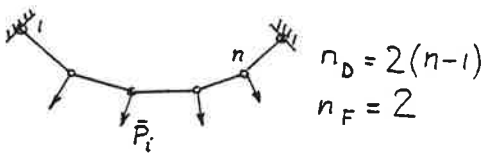

FIGURE 10

THE PRINCIPLE OF VIRTUAL FORCES

From the principle of stationary complementary work can be obtained /6/ (by keeping displacements constant)

$$\frac{\partial W_c}{\partial X_{kj}} = \Sigma \frac{\partial H_{ij}}{\partial X_{kj}} \overline{\Delta h}_{ij} + \frac{\partial U_c}{\partial X_{kj}} = 0 \qquad (k = 1...1,\ j = 1,2,3) \tag{35}$$

$$\frac{\partial W_c}{\partial F_{ij}} = \Sigma \frac{\partial H_{ij}}{\partial F_{ij}} \overline{\Delta h}_{ij} + \frac{\partial U_c}{\partial F_{ij}} = u_{ij} \tag{36}$$

When the equation (35) has been multiplied by the virtual forces δX_i and noted $\frac{\partial H_{ij}}{\partial X_{kj}} = 1$ (the "kinematic" in force space) it can be obtained

$$\delta W_c = \Sigma 1 \cdot \overline{\Delta h}_{ij} \delta X_j + \Sigma e_{ij} \delta X_j = 0 \qquad (i = 1,...) \tag{37}$$

When δX_j:s are free it follows from (37)

$$\overline{\Delta h}_{ij} + e_{ij} = 0 \qquad (i = 1...n,\ j = 1,2,3) \tag{38}$$

The equation (37) has been illustrated in Fig. 11.

It can be seen, that the variation δW_c of external complementary work is not equal to the variation δU_c of internal stress energy except, when rigid body rotations are infinite.

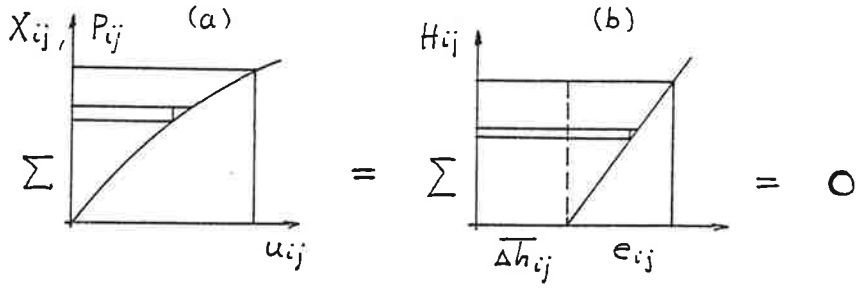

FIGURE 11

EXAMPLE. Consider a loop shown in Fig. 8. For the discontinuous assembly of elements keeping displacements $\bar{u}$, $\overline{\Delta h}_i$, α_i constants

$$\begin{aligned} &-u_{1x}\,\delta X - u_{1y}\,\delta Y - \Sigma\beta_i\,\delta M_i + \Sigma(u_{ix}\,\delta P_{ix} + u_{iy}\,\delta P_{iy}) \\ &= \Sigma[(\overline{\Delta h}_{ix} + e_{ix})\delta H_{ix} + (\overline{\Delta h}_{iy} + e_{iy})\delta H_{iy}] \\ &+ \Sigma(\overline{\Delta\theta}_i - \varphi_i)\delta M_i = 0 \end{aligned} \tag{39}$$

But for equilibrium (34)

$$\begin{aligned} \delta H_{ix} &= \delta X \\ \delta H_{iy} &= \delta Y \end{aligned} \tag{40}$$

δM_i:s are free.

Substituting from (40) in (39) on the right side

$$\begin{aligned} \delta W_c = {} & \Sigma(\overline{\Delta h}_{ix} + e_{ix})\delta X + \Sigma(\overline{\Delta h}_{iy} + e_{iy})\delta Y \\ & - \Sigma(\overline{\Delta\theta}_i - \varphi_i)\delta M_i = 0 \end{aligned} \tag{41}$$

When δX, δY, δM_i $(i = 1...n+1)$ are free

$$\begin{aligned} \overline{\Delta h}_{ix} + e_{ix} &= 0 \\ \overline{\Delta h}_{iy} + e_{iy} &= 0 \\ \overline{\Delta\theta}_i - \varphi_i &= 0 \quad . \end{aligned} \tag{42}$$

In $(42)_3$

$$\overline{\Delta\theta}_i = \bar{\theta}_i - \bar{\theta}_{i-1}, \qquad \varphi_i = \phi_{i,i+1} + \phi_{i,i-1} \tag{43}$$

When the complementary virtual work is equal to zero with equilibrium force system, the structure is in compatible state.

SUMMARY

The complementary work of structures has been considered as a work of displacements. They can be divided into two parts: displacements of rigid body and displacements caused by pure deformations. Correspondingly, the complementary work has been divided into the pseudo stress energy and stress energy. The force equilibrium equations only are usable to determine the internal forces and stresses as a function of given loads and redundants. The stress energy has been written originally in the rigid body coordinate frame and the pseudo stress energy in the global coordinate frame. The connection between rigid body coordinates and global coordinate determined from the moment equilibrium conditions of elements as a function of forces.

REFERENCES

1. Oran C., Complementary energy consept for large deformations. JSD Vol. 93, No. ST1, Feb. 1967.

2. Holopainen P., Application of the principle of stationary complementary work to the analysis of suspension roofs. Int. conf. on tension roof structures, The Polytechnic of Central London, 1974.

3. Holopainen P., The general theory of a suspension cable, 1975 (Dissertation), Helsinki University of Technology.

4. Holopainen P., Statiikka, 1980, 2. ed. 1984. (Handout in the course of statics of rigid bodies), Tampere University of Technology.

5. Engesser F., Ueber statisch unbestimmte Träger bei beliebigen Formänderungs-Gesetze und über den Satz von den kleinsten Ergänzungsarbeit, Zeitschr. d. Architecten u. Ing.-Vereins zu Hannover, Vol. 35, Heft 8, 1889, Spalten 734-744.

6. Holopainen P., Komplementaarisen työn stationaarisen arvon periaatteen soveltaminen tasokehiin, 1983. (Application of the principle of stationary complementary work to the analysis of plane frames, Tampere University of Technology, Applied mechanics, Report 18).

7. Holopainen P., Epälineaarinen mekaniikka, 1984. (Handout in the course of nonlinear structural mechanics, Tampere University of Technology).

8. Bottema O., Roth B., Theoretical kinematics, 1979, North Holland Publishing Company.

9. Morice P.B., Linear structural analysis, Thames and Hudson, London, 1959.

EENRANNAN TEKNILLINEN KORKEAKOULU

TEELLISIÄ JULKAISUJA

. OLKKONEN,TAUNO. Tuotteen tuotantoteknisen suunnittelun ohjaaminen. 1973. 148 s. Väitösk.

. SUVIOLAHTI, MATTI. Yksinkertaisesti tuetun ympyrälieriökuorikaton Hooken kimmolakiin perustuva lujuusopillinen ratkaisu käyttämällä Fourierin sarjakehitelmiä. 1975. 67 s.

3. SUVIOLAHTI, MATTI. Jatkuvan ympyrälieriökuorikaton Hooken kimmolakiin perustuva ja reunaehdot tarkasti toteuttava lujuusopillinen matemaattinen ratkaisu käyttämällä Fourier'n sarjakehitelmiä. 1975. 187 s. Väitösk.

4. SÄÄKSJÄRVI, MARKKU. Eräs puunhankinnan yhteistyömalli: hyödyn jakaminen peliteoreettisena ongelmana. 1976. 115 s. Väitösk.

5. RUOTTU, SEPPO. Aineen, impulssin ja energian siirtyminen turbulen tissa hiukkas-kaasu-suspensiossa. 1976. 46 s. Väitösk.

6. KOSKELAINEN, LASSE. Analysis of pipe networks using linear theories. 1977. 36 s.

7. PENTTINEN, SEPPO. Experimental studies of electromagnetic transitions in the selfconjugated ^{30}P, ^{32}S and ^{34}Cl nuclei through the (p,γ) reaction. 1977. U.s. Diss.

8. KOSKELAINEN, LASSE. A model for optimal design of district heating networks. 1978. 88 s. Diss.

9. LAITINEN, HEIKKI. Determining risk potential through accidents and near-accidents: an empirical study in a steel factory. 1984. 125 s. Diss.

10. LAINE, JOUKO. Calculation of process response with matrices. 1985. 75 s.

11. LUKKA, ANITA. On method and system design for a problem in vehicle routing and scheduling. 1987. 169 s. Diss.

12. HOLSTIUS, KARIN. Project business as a strategic choice: a theoretical and empirical study of project marketing. 1989. 105 s.

13. YLI-HARJA, OLLI. Median filters: extensions, analysis and design. 1989. 173 s. Diss.

14. ZAMANKHAN, PIROOZ. The temperature distribution of viscous fluid flowing in constricted or widened tubes far downstream from the beginning of the heated-section. 1989. 37 s. Diss.

15. HYPPÄNEN, TIMO. An experimental and theoretical study of multiphase flow in a circulating fluidized bed. 1989. 207 s. Diss.

16. MARTIKAINEN, JUKKA. On the effects of welding parameters on weld quality of plasma arc keyhole welding of structural steels. 1989. 132 s. Diss.

ISBN 951-763-663-6
ISSN 0356-8210